AD-A186 440 A DETAILED NUMERICAL GRAPHICAL AND EXPERIMENTAL STUDY 1/5
OF OBLIQUE SHOCK WA (U) TORONTO UNIV DOWNSVIEW
(ONTRRIO) INST FOR AEROSPACE STUDIES. H M GLAZ ET AL
UNCLASSIFIED 01 AUG 86 UTIAS-285 DNA-TR-86-365 F/G 20/4 NL

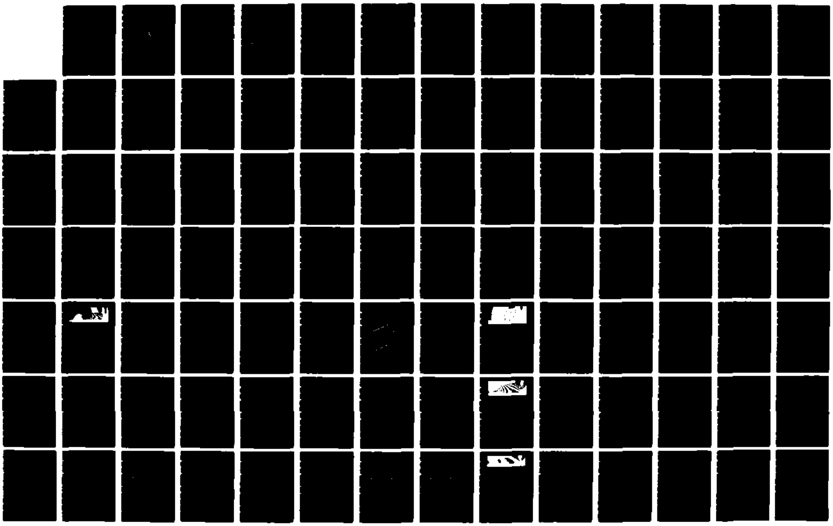

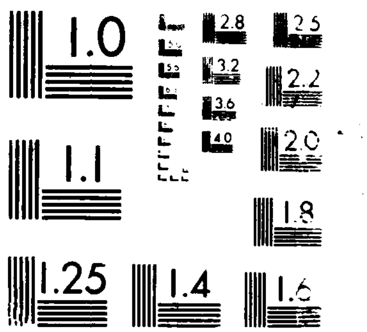

MICROCOPY RESOLUTION TEST CHART
NATIONAL BUREAU OF STANDARDS 1963-A

(12)

AD-A186 440

DNA-TR-86-365

A DETAILED NUMERICAL, GRAPHICAL, AND EXPERIMENTAL STUDY OF OBLIQUE SHOCK WAVE REFLECTIONS

H. M. Glaz, et al.
University of Toronto, Institute for Aerospace Studies
4925 Dufferin Street
Downsview, Ontario, Canada
M3H 5T6

1 August 1986

Technical Report

CONTRACT No. DNA 001-83-C-0266

Approved for public release;
distribution is unlimited.

THIS WORK WAS SPONSORED BY THE DEFENSE NUCLEAR AGENCY
UNDER RDT&E RMSS CODE B344084466 Y99QMXSG00008 H2590D.

Prepared for
Director
DEFENSE NUCLEAR AGENCY
Washington, DC 20305-1000

87 10 2 148

CUT HERE AND RETURN

DISTRIBUTION LIST UPDATE

This mailer is provided to enable DNA to maintain current distribution lists for reports. We would appreciate your providing the requested information.

- ☐ Add the individual listed to your distribution list.
- ☐ Delete the cited organization/individual.
- ☐ Change of address.

NAME: ______________________________

ORGANIZATION: ______________________________

OLD ADDRESS	CURRENT ADDRESS
______________	______________
______________	______________
______________	______________

TELEPHONE NUMBER: (   ) ______________________________

SUBJECT AREA(s) OF INTEREST:

______________	______________
______________	______________
______________	______________

DNA OR OTHER GOVERNMENT CONTRACT NUMBER: ______________________________

CERTIFICATION OF NEED-TO-KNOW BY GOVERNMENT SPONSOR (if other than DNA):

SPONSORING ORGANIZATION: ______________________________

CONTRACTING OFFICER OR REPRESENTATIVE: ______________________________

SIGNATURE: ______________________________

Director
Defense Nuclear Agency
ATTN: [redacted] TITL
Washington, DC 20305-1000

Director
Defense Nuclear Agency
ATTN: [redacted] TITL
Washington, DC 20305-1000

UNCLASSIFIED

SECURITY CLASSIFICATION OF THIS PAGE

REPORT DOCUMENTATION PAGE

Form Approved
OMB No. 0704-0188
Exp. Date: Jun 30, 1986

1a REPORT SECURITY CLASSIFICATION UNCLASSIFIED	1b RESTRICTIVE MARKINGS
2a SECURITY CLASSIFICATION AUTHORITY N/A since Unclassified	3 DISTRIBUTION / AVAILABILITY OF REPORT Approved for public release; distribution is unlimited.
2b DECLASSIFICATION / DOWNGRADING SCHEDULE N/A since Unclassified	
4 PERFORMING ORGANIZATION REPORT NUMBER(S) UTIAS Report No. 285	5. MONITORING ORGANIZATION REPORT NUMBER(S) DNA-TR-86-365
6a NAME OF PERFORMING ORGANIZATION University of Toronto Institute for Aerospace 6b OFFICE SYMBOL (If applicable)	7a NAME OF MONITORING ORGANIZATION Director Defense Nuclear Agency
6c ADDRESS (City, State, and ZIP Code) 4925 Dufferin Street Downsview, Ontario, Canada M3H 5T6	7b ADDRESS (City, State, and ZIP Code) Washington, DC 20305-1000
8a NAME OF FUNDING / SPONSORING ORGANIZATION 8b OFFICE SYMBOL (If applicable) SPAS/Ullrich	9 PROCUREMENT INSTRUMENT IDENTIFICATION NUMBER DNA 001-83-C-0266
8c ADDRESS (City, State, and ZIP Code)	10 SOURCE OF FUNDING NUMBERS PROGRAM ELEMENT NO: 62715H PROJECT NO: Y99QMXS TASK NO: G WORK UNIT ACCESSION NO: DH008038

11 TITLE (Include Security Classification)

A DETAILED NUMERICAL, GRAPHICAL, AND EXPERIMENTAL STUDY OF OBLIQUE SHOCK WAVE REFLECTIONS

12 PERSONAL AUTHOR(S)

Glaz, H. M.; Colella, P.; Glass, I. I.; and Deschambault, R. L.

13a TYPE OF REPORT	13b TIME COVERED	14 DATE OF REPORT (Year, Month, Day)	15 PAGE COUNT
Technical	FROM 850930 TO 860801	860801	388

16 SUPPLEMENTARY NOTATION

This work was sponsored by the Defense Nuclear Agency under RDT&E RMSS Code B344084466 Y99QMXSG00008 H2590D.

17 COSATI CODES		
FIELD	GROUP	SUB-GROUP
20	11	
20	6	

18 SUBJECT TERMS (Continue on reverse if necessary and identify by block number)

Oblique Shock-Wave Reflections; Numerical Simulations; Interferometry - Isopycnics; Shock-Tube Flows

19 ABSTRACT (Continue on reverse if necessary and identify by block number)

An extensive series of numerical calculations of oblique-shock-wave reflections in air and argon have been performed using a version of the second-order Eulerian Godunov scheme for inviscid compressible flow. This scheme is among the best of the upwind schemes developed in recent years.

The results have been compared with the best available interferometric data from the UTIAS 10 cm x 18 cm shock tube, for fifteen different cases. The objective of this portion of the study was to assess the accuracy of the computer code in computing two-dimensional shocked flow of an inviscid perfect gas. A significant portion of our analysis is devoted to the question of the extent of influence of viscous and vibrational nonequilibrium effects on the experimental flow fields.

20 DISTRIBUTION / AVAILABILITY OF ABSTRACT ☐ UNCLASSIFIED/UNLIMITED ☒ SAME AS RPT ☐ DTIC USERS	21 ABSTRACT SECURITY CLASSIFICATION UNCLASSIFIED
22a NAME OF RESPONSIBLE INDIVIDUAL Sandra E. Young	22b TELEPHONE (Include Area Code) (202)325-7042 22c OFFICE SYMBOL DNA/CSTI

DD FORM 1473, 84 MAR — 83 APR edition may be used until exhausted. All other editions are obsolete.

SECURITY CLASSIFICATION OF THIS PAGE

6a. NAME OF PERFORMING ORGANIZATION (Continued)

Studies

19. ABSTRACT (Continued)

Further parametrized series of calculations were performed in an effort to study the feasibility of numerically constructing inviscid transition lines in the (M_s, θ_w)-plane. Good agreement with analytic predictions was found for low values of M_s and, as might be expected, there are substantial discrepancies for $M_s = 8.75$. The possibility of using such numerical results in the formulation of accurate transition criteria is discussed.

Overall, the computer code has been found to represent a significant predictive capability. The future extension of the code to permit the detailed modelling of nonequilibrium and viscous effects is, however, an important objective.

SUMMARY

An extensive series of numerical calculations of oblique-shock-wave reflections in air and argon have been performed using a version of the second-order Eulerian Godunov scheme for inviscid compressible flow. This scheme is among the best of the upwind schemes developed in recent years.

The results have been compared with the best available interferometric data from the UTIAS 10 cm x 18 cm shock tube, for fifteen different cases. The objective of this portion of the study was to assess the accuracy of the computer code in computing two-dimensional shocked flow of an inviscid perfect gas. A significant portion of our analysis is devoted to the question of the extent of influence of viscous and vibrational nonequilibrium effects on the experimental flow fields.

Further parametrized series of calculations were performed in an effort to study the feasibility of numerically constructing inviscid transition lines in the (M_s, θ_w)-plane. Good agreement with analytic predictions was found for low values of M_s and, as might be expected, there are substantial discrepancies for $M_s = 8.75$. The possibility of using such numerical results in the formulation of accurate transition criteria is discussed.

Overall, the computer code has been found to represent a significant predictive capability. The future extension of the code to permit the detailed modelling of nonequilibrium and viscous effects is, however, an important objective.

PREFACE

We are grateful to Mr. Ralph Ferguson for his extensive programming work for these calculations as well as his tireless help in preparing the figures. We thank also Ms. Karen Hibbert for her help in the latter task. Discussions with Dr. George Ullrich and Dr. Allen Kuhl are very much appreciated. The efforts of Ms. Mary Stroik on the many versions of the manuscript for this report are acknowledged with thanks.

The financial assistance received from the U.S. Department of Energy at the Lawrence Berkeley Laboratory under Contract DE-AC03-78SF00098; from the U.S.Defense Nuclear Agency under DNA Task Code Y99QAXSG and DNA Contract 001 83-C-0266; from the Naval Surface Weapons Center Independent Research Fund; from the U.S. Air Force Office of Scientific Research under Grant 82-0096; and from the Natural Science and Engineering Research Council of Canada is acknowledged with thanks.

TABLE OF CONTENTS

LIST OF ILLUSTRATIONS

LIST OF ILLUSTRATIONS (Continued)

LIST OF ILLUSTRATIONS (Continued)

LIST OF ILLUSTRATIONS (Continued)

LIST OF ILLUSTRATIONS (Continued)

LIST OF ILLUSTRATIONS (Continued)

Figure | Page

LIST OF ILLUSTRATIONS (Continued)

Figure Page

SECTION 1

INTRODUCTION

A direct comparison is made for fifteen basic cases of oblique shock-wave reflections between interferometric results obtained at the University of Toronto Institute for Aerospace Studies (UTIAS) 10 cm x 18 cm Hypervelocity Shock Tube and numerical results obtained by using a current computational method for solving the Euler equations of compressible flow. Additional parametrized sequences of calculations are presented to assess the utility of the present numerical method in constructing the various reflection-transition lines (RR - SMR, SMR - CMR, CMR - DMR; see Figs. 1 & 2) for inviscid flows in the shock-wave Mach-number, wedge-angle(M_s, θ_w) -plane. An additional parametrized sequence has been calculated in order to study the validity of the boundary-layer displacement theory to account for the "von Neumann paradox."

Over the past five years, extensive experimental and analytical data were obtained for these problems (Ben-Dor & Glass 1978, 1979, 1980; Ando & Glass 1981; Lee & Glass 1982; Shirouzu & Glass 1982; Deschambault & Glass 1983; Deschambault 1984; Hu 1984; Hu & Glass 1985; Hu & Shirouzu 1985; Wheeler and Glass 1985; Wheeler 1985). We refer the reader to these references for an extensive discussion of the theory of oblique shock-wave reflections, an introduction to the history of the field, and further references.

With the advent of modern computers, it has become possible to attempt the computation of such problems using finite difference schemes. The state-of-the-art in this area was surveyed in Ben-Dor & Glass 1978 and Deschambault & Glass 1983; these authors concluded that advances in numerical technique would be required before numerical results could be viewed with the same confidence as experimental data. The main object of this report is to demonstrate that the numerical method used herein is sufficiently accurate to be placed on a nearly equal footing with experimental methods in the analysis of perfect, inviscid, compressible flows. However, further development work is needed in the numerical modelling of nonequilibrium, viscous flow fields.

This study deals exclusively with results for air and argon; the experimental data for these results may be found in Deschambault 1984 where they are discussed in detail. Many other related calculations have been performed with our computer code, and we briefly describe them here. Recent experimental data for SF_6 has also been obtained and is reported in Hu 1985

and Hu & Glass 1985. An analogous numerical-experimental study to the present report for SF_6 may be found in Glaz et al 1985. An interesting problem is posed by assuming a polytropic gas, fixing M_s and θ_w, and allowing γ = ratio of specific heats to be a varying parameter. This problem is well-suited to a numerical study and the results using our numerical method are presented in Colella & Glaz 1984 and Berger et al 1985. Finally, a computer code has been developed for the problem of a spherical explosion reflecting off an ideal surface; the numerical method is virtually identical to that used in obtaining the results for this report. Calculations using this code are presented in Colella & Glaz 1984 and Colella et al 1985. The results of these calculations show that the high M_s, DMR flow fields of planar oblique shock wave reflection have a lot in common with the Mach stem region flow fields of the spherical explosion problem just after the RR-DMR transition, although there are significant structural differences downstream of the triple point, presumably due either to unsteadiness or the different boundary conditions.

A portion of the calculations which are studied in this report have appeared in Colella & Glaz 1982, 1984 and Glaz et al 1985. The latter paper includes an expanded discussion of some of the overall issues involved in comparing experimental results to approximate solutions of a perfect inviscid flow. In this report, we concentrate on presenting the complete set of calculations including a discussion of each comparison or parametric series. The plan of the report is as follows. In Section 2, the terminology of oblique shock-wave reflections is reviewed and some notation is defined. Sections 3 and 4 are devoted to experimental techniques and the numerical method, respectively. In Section 5, the results are presented and Section 6 is an extended summary.

SECTION 2

OBLIQUE SHOCK-WAVE REFLECTIONS

The four types of pseudo-stationary oblique shock-wave-reflection patterns are shown in Figure 1 and consist of (a) regular reflection (RR), (b) single Mach reflection (SMR), (c) complex Mach reflection (CMR) and (d) double Mach reflection (DMR). Figure 1 illustrates the definitions of wedge angle θ_w, triple-point trajectory angles, χ, χ', various shock waves I, R, R', M, M', slip surfaces S,S' and the flow regions 1-5 produced by the foregoing reflections, the angle δ between the incident I and reflected R shock waves is also shown as well as the angle ω' between R and the wall or R and the triple-point-trajectory angle χ. The bow shock stand-off distances s and the length L, between the wedge corner and the reflection point or Mach stem are also indicated. Such qua ities can be measured experimentally or predicted numerically and provide important information on the state of the gas whether frozen, non-equilibrium or equilibrium (Shirouzu & Glass 1982; Hu 1985; Hu & Glass 1985).

The equations of gas dynamics are, in Cartesian coordinates,

$$
\begin{aligned}
\rho_t + (\rho u)_x + (\rho v)_y &= 0 \\
(\rho u)_t + (\rho u^2+p)_x + (\rho uv)_y &= 0 \\
(\rho v)_t + (\rho uv)_x + (\rho v^2+p)_y &= 0 \\
(\rho E)_t + (\rho uE+up)_x + (\rho vE+vp)_y &= 0
\end{aligned}
\tag{1}
$$

where ρ is the density, $\underline{u} = (u,v)$ is the velocity field, $E = \frac{1}{2}(u^2+v^2) + e$ is the total specific energy, e is the specific internal energy, and p is the pressure. The system is closed by specifying an equation-of-state (EOS),

$$p = p(\rho, e). \tag{2}$$

We shall often use the polytropic EOS,

$$p = (\gamma-1)\rho e, \tag{3}$$

where $\gamma > 1$ is the ratio of specific heats.

If real gas and viscous effects can be ignored [i.e., equations (1), (2) hold], the problem has no intrinsic length-scale, suggesting the use of the self-similar or pseudo-stationary coordinate system $(\xi,\eta) = [(x-x_0)/(t-t_0), (y-y_0)/(t-t_0)]$ where (x_0,y_0) are the coordinates of the wedge corner and t_0 is the time at which the incident shock wave reaches the corner. Following Jones et al 1951, the system (1) may be transformed to pseudo-stationary coordinates and becomes, in conservation form,

$$\begin{aligned}
(\rho\tilde{u})_\xi + (\rho\tilde{v})_\eta &= -2\rho \\
(\rho\tilde{u}^2+p)_\xi + (\rho\tilde{u}\tilde{v})_\eta &= -3\rho\tilde{u} \\
(\rho\tilde{u}\tilde{v})_\xi + (\rho\tilde{v}^2+p)_\eta &= -3\rho\tilde{v} \\
(\rho\tilde{u}\tilde{H})_\xi + (\rho\tilde{v}\tilde{H})_\eta &= -\rho(\tilde{u}^2+\tilde{v}^2) - 2\rho\tilde{H}
\end{aligned} \tag{4}$$

where

$$\begin{aligned}
\tilde{u} = u - \xi,\ \tilde{v} &= v - \eta, \\
\tilde{H} &= \tfrac{1}{2}(\tilde{u}^2+\tilde{v}^2) + h
\end{aligned} \tag{5}$$

and $h = e + p/\rho$ is the specific enthalpy. We refer to $(\tilde{u},\tilde{v})$, $\tilde{H}$ as the self-similar velocity field and self-similar total enthalpy, respectively. In addition we define

$$\tilde{M}^2 = (\tilde{u}^2 + \tilde{v}^2)/c^2 \tag{6}$$

where c = sound speed and we refer to $\tilde{M}$ as the self-similar Mach number. The system (4) is, evidently, the steady Euler equations with the addition of source terms. We note that the ratio s/L is constant, for given initial conditions, for self-similar solutions of the non-stationary equations, just

as s is constant for steady supersonic flow. In this and other ways a change to pseudo-stationary coordinates is very useful in the analysis of these flow fields and will be used in this study.

In particular, the type of reflection pattern is a function of the incident shock-wave Mach-number M_s, the wedge angle θ_w, and the gas equation of state. The transition boundaries in the (M_s,θ_w)-plane for oblique shock-wave reflection are reproduced from Lee and Glass (1982) in Figure 2 for real air and a polytropic equation of state with $\gamma = 1.40$. The analogous figure for argon ($\gamma = 5/3$) may be found in this reference. The construction of the transition lines is based on various (heuristic) transition criteria and the numerical calculation of the jump conditions at reflection and triple points. These criteria, which have been the subject of extensive investigation in the literature, are summarized in Lee and Glass (1984) and Shirouzu and Glass (1983). In Sec. 5, the numerical results will be used to partly assess the validity of some of these criteria as well as the overall accuracy of the transition diagram, Figure 2.

The fourfold partition of the (M_s,θ_w) plane illustrated in Figure 2 is quite coarse relative to the rich phenomenology present in these flow fields. Some other features that may be similarly partitioned (see Ben-Dor and Glass 1979) are (a) whether or not the reflected shock is detached or attached to the wedge corner; (b) in the attached case, whether the flow at the corner is subsonic or supersonic; (c) for RR whether the flow is subsonic or supersonic (in pseudo-stationary coordinates) at the reflection point and (d) for SMR, CMR and DMR whether or not M "toes-out" or "toes-in".

A comprehensive study of these issues is beyond the scope of this report, but they will be discussed as appropriate in the comparison of experimental and numerical results in Sec. 5.

SECTION 3

EXPERIMENTAL TECHNIQUES

The experiments for the present study were performed in the UTIAS 10 cm x 18 cm Hypervelocity Shock Tube. A design, performance and calibration study of the original facility can be found in Boyer 1964. More recent and detailed descriptions of the shock tube appear in Bristow 1971 and Ben-Dor and Whitten 1979. Further details of the experiments associated with the present work can be found in Deschambault 1984.

3.1 EXPERIMENTAL FACILITY.

The basic shock tube facility consists of a 1.4m long driver and a 12.2m channel. The initial pressure in the channel can be easily varied from near vacuum to atmospheric conditions. At the end of the channel is a test section containing high-quality interferometric windows through which the shock tube flows may be observed. A 23-cm diameter field-of-view Mach-Zehnder interferometer (Hall 1954) in conjunction with a giant-pulse ruby-laser is used to record simultaneous dual-wavelength (λ=694.3nm and 347.2nm) infinite-fringe interferograms of the two-dimensional flow-fields. This allows the direct observation of the flow-field isopycnics (lines of constant density). The 15ns pulse generated by the ruby laser effectively freezes all motion, thereby producing sharp, clear images.

Two methods were used to produce the incident shock-wave Mach-numbers for the present study. For shock-wave Mach-numbers less than 6 a cold-gas driver was employed. The diaphragm consisted of several layers of mylar-polyester films. With the proper choice of driver gas, CO_2 or He, and diaphragm thickness, the desired shock-wave Mach-number could be obtained in the test gas upon rupture.

For shock-wave Mach-numbers greater than 6 combustion-driver techniques were used. Specially scribed stainless steel diaphragms were burst by the constant-volume combustion of a stoichiometric mixture of O_2 and H_2 diluted with 70% He. Combustion was initiated by the impulsive heating of a 0.38-mm diameter tungsten wire through the discharge of a 45μF 13kV capacitor.

The reflection patterns were generated by the impingement of normal shock

waves with steel wedges. The wedges were bolted firmly to the bottom wall of the facility to ensure rigidity. The sides of the wedges were flush with the inside walls and interferometric windows of the shock-tube test-section

3.2 DATA REDUCTION TECHNIQUES.

The infinite-fringe interferograms enabled the recording of small relative density changes of the various shock tube flows. The density difference $\Delta\rho$ between the two adjacent fringes of the same color is related to the wavelength λ of the light source (694.3nm and/or 347.2nm) and the Gladstone-Dale constant K ($2.274 \times 10^{-4} m^3/kg$ for air, λ = 589.6nm and $1.574 \times 10^{-4} m^3/kg$ for Ar, λ = 694.3nm) and is expressed by the relation $\Delta\rho = \lambda/KL$, where L is the depth of the test section (10.16cm).

To obtain quantitative values for the isopycnics the following method was employed. From the initial conditions of the experiment, i.e., shock-wave Mach-number, wedge angle, initial pressure and temperature, the thermodynamic states around the reflection point for RR and the triple point for MR were calculated using two- and three-shock theory (Ando 1981). These were used as reference states from which all other density values could be obtained using the above relation.

The wall-density distribution plots were obtained directly from the interferograms. The origin was defined to be the reflection point of a RR or the foot of the Mach stem of a MR. The corner of the wedge was defined to be a distance L from the origin. All absolute distances were then scaled by L giving a value of 1 to the distance from the origin to the wedge corner. Where possible the center of the isopycnic intersecting the wedge surface was used to locate the value of the density at that point.

For some of the experimental results presented here, it was necessary to use test gases with very low initial densities and pressures relative to atmospheric conditions. As a result, several interferograms show the effects of vibrational nonequilibrium which must be taken into account when analysing the corresponding interferograms. The relaxation zones are clearly visible and appear as additional fringe shifts in the post-shock flow-field parallel to the frozen incident shock front. Behind the reflected shock wave, the characteristic signature of a relaxing gas is the nearly tangential incidence of the isopycnics and the reflected shock wave.

SECTION 4

NUMERICAL METHOD

The numerical results presented in this paper have been calculated with a version of the Eulerian second-order Godunov scheme for nonstationary gas dynamics of a type considered by Colella and Woodward 1984. The version of the scheme used here is presented in Colella and Glaz 1982,1983, including the modifications required for non-polytropic gases.

The method is a finite-difference scheme for systems of hyperbolic conservation laws in one space-like dimension: for multidimensional applications such as the shock-on-wedge problem, we employ operator splitting. Differencing is in conservation form and the numerical fluxes are computed by solving zone interface Riemann problems whose time-centred left and right states are computed from the characteristic form of the equations. This technique leads to second-order accuracy in smooth flow and ensures that the method is centred upstream. In practice, the method is very stable and robust. In the immediate vicinity of a strong shock, some dissipation is required; this has been accomplished by smoothly degrading the scheme to the first-order Godunov scheme in such regions. The degree of degradation is a function of the shock thickness and strength.

For argon, we have used a perfect (frozen) gas equation of state with $\gamma = 5/3$. If the shock tube test gas was air, the equation of state was chosen to be either a perfect (frozen) gas with $\gamma = 7/5$ or the Hansen 1959 real air equation of state as modified by Deschambault 1984 for the present application. The efficient solution of the Riemann problem in the context of our second-order Godunov method for an arbitrary equation of state is treated in Colella and Glaz 1982,1983. Also, these papers demonstrate that the choice of equation of state has a substantial influence on the quantitative numerical results, as might be expected.

As noted in the preceding section, vibrational non-equilibrium, which is only temperature dependent, can be significant for moderate to high Mach numbers when the test gas is air (at high Mach numbers dissociation effects are also density dependent): for the argon cases considered here we expect the gas to remain frozen. The choice of an appropriate equation of state for the air calculations depends mainly on the vibrational relaxation length l_v, behind the shock waves I, R, M of Figure 1. If $l_v \gg l$ (where l is a characteristic flow length arising in the problem; for the present

experiments, $l \sim 0.1mm$), then the gas is frozen and the perfect gas equation of state is correct. If $l \gg l_v$, then the gas is in equilibrium and the Hansen equation of state for real air is used. Finally, if $l_v \sim l$, then neither the frozen nor the equilibrium hypothesis is appropriate, and the flow is said to be in non-equilibrium. We have numerically treated such cases as equilibrium flow fields by using the Hansen equation of state, although the only correct procedure would be to solve an extra partial differential equation representing a rate equation for vibrational relaxation (and for dissociation at high Mach numbers). This decision will be an important issue in our discussion of these cases in Sec. 5.

The computational mesh and our problem initialization procedure is illustrated in Figure 3. Note that these figures are drawn from right to left to conform with the experimental interferograms. We have used a square (i.e., $\Delta x = \Delta y$ = constant) mesh for all of the computations in Sec. 5. Because the flow is pseudo-stationary, the choice of Δx is immaterial.

The initial data are taken as U_0, M_s where $U = (\rho, p, u, v,)^T$ is the state vector and M_s is the initial shock-wave Mach-number. From these data and the given equation of state, the post-shock state U_1 may be calculated. To initialize the two-dimensional calculation, these data are placed on the grid far upstream (ca. 60-75 zones) of the corner, as illustrated in Figure 3a; interpolation of conserved quantities [i.e. $U^C = (\rho, \rho u, \rho v, \rho E)^T$] is used for zones that straddle the incident shock. However, this is a very poor representation of the numerical shock because any shock-capturing scheme will diffuse a shock wave over two or more zones in the computational mesh. The resulting structure is referred to as a discrete travelling wave (i.e., a mesh function that depends only on x - Vt, where V is the vector velocity of the wave and equals the shock speed in magnitude for a discrete shock wave). Starting with any initial data (e.g., the one zone U_0 - U_1 jump described above) satisfying the Rankine-Hugoniot conditions, the solution will tend as the number of time-steps becomes large towards the appropriate discrete travelling wave, plus other low-amplitude waves that we refer to as "starting error", with the starting error separating from the travelling wave. For the present application, it is very important to ensure that the starting error is eliminated before the shock wave is allowed to reflect, and we proceed as follows. First, the computer code is allowed to run until the shock wave

reaches the corner, and the situation in Figure 3b is reached. In this figure, the region immediately behind the shock and about 2-3 zones thick is the discrete travelling wave and the small (less than 5%) relative amplitude disturbances further downstream is the one-time starting error. The computer code then arbitrarily changes the flow field to that illustrated in Figure 3c, i.e., the discrete travelling wave (arbitrarily set to exactly 4 zones in the computer code) is retained but the starting error is replaced by the post-shock state U_1.

At this point, the flow field becomes truly two-dimensional and the computer code is now run without further interruption until the end of the calculation is reached.

The boundary conditions for this problem, which are standard, are discussed in detail in Colella and Glaz 1983. We remark here that our treatment of the intersection of the incident shock with the upper or left-hand boundary or both is not entirely consistent with the discrete travelling wave and leads to the introduction of a low relative amplitude (ca. 1%) wave behind the incident shock at its intersection with the boundary. This wave, which we call a boundary error, may lead to a rather unaesthetic structure in the contour plots and it can impinge on the disturbed flow field behind the reflected shock. Examples will be noted in Sec. 5.

All calculations were performed on a CRAY I at Los Alamos National Laboratory, Los Alamos, New Mexico. The computer code was designed to take significant advantage of the machine's vector architecture. Each calculation in Sec. 5 required 15-40 min. c.p. time with most in the range of 20-30 min. Much of this time is wasted on the extra grid points introduced to eliminate the starting error as well as grid points outside the reflected shock. Also a fine mesh is only really needed in the Mach-stem region. Thus, an intelligent adaptive mesh structure could reduce these times substantially.

SECTION 5

COMPUTATIONAL RESULTS

A direct comparison of experimental results and numerical calculations is presented in Sec. 5.1 for fifteen cases of oblique shock-wave reflections. For eight of the cases in air, the computation has been performed twice, once with a perfect gas EOS with $\gamma = 1.4$ and once with the Hansen EOS. Thus, twenty-three computations are reported on in this part. In Sec. 5.2, the results of several parametrized sequences of calculations are presented to demonstrate the capability of our numerical method to compute the correct transition in the (M_s,θ_w) -plane. An additional sequence is presented in this part to demonstrate (upon comparison with experimental data) the effect of boundary-layer displacement on the RR-DMR transition.

5.1 COMPARISON OF EXPERIMENT WITH CALCULATION.

The initial conditions for the fifteen cases are listed in Table I along with the computational mesh (NX,NY) and the equation of state selected for each case (and it is noted where two choices of EOS were made for a case). All four wave configurations are represented in the range of (M_s,θ_w) considered. The following data are presented for each case: experimental isopycnics; computed isopycnics using the same density levels as were obtained in the experiment; wall distribution plots, q vs x/L, with $q = p/p_0$, ρ/ρ_0, e, $\tilde{u}$ and with the ρ/ρ_0 plot including a comparison with experiment; whole flow field contour plots, using thirty equally spaced contours, of the quantities $\rho,e,p,\tilde{M},u,v,\tilde{u},\tilde{v},\tilde{H}$; in a "blowup" frame in the vicinity of the Mach stem or reflection point, contour plots, using thirty equally spaced contours of $\rho,e,p,\tilde{M},\tilde{H}$ are shown along with the experimental isopycnics, self-similar streamlines, and a self-similar velocity vector field plot. For those cases involving a comparison of two calculations with differing EOS, the contour plots of actual isopycnics are shown together with the interferogram, and an additional wall distribution plot is added comparing ρ/ρ_0 vs. x/L for the two calculations and the experiment on the same graph.

In order to assist the reader in interpreting the graphical output, we make several general comments here, which are not repeated below for each case. It is regretted that many interesting phenomena are not commented on in the text, but we felt it useful to present the entire set of figures. First, for those cases involving two calculations, the subscript "P" refers to the

perfect gas calculation and the subscript "H" refers to the Hansen calculation; in the event that such a figure is referenced in the text without a subscript, the context determines which (or both) figures are being discussed. Concerning the contour plots, the coordinate system is oriented with the origin at the corner point, the x or ξ direction along the wedge surface after reflection, the y or η direction perpendicular to the wedge and facing upwards in the figure; however, we have reversed orientation for the wall plots and have set $x/L = 1.0$ at the corner and $x/L = 0.0$ at the reflection point or the intersection of the Mach stem with the wedge surface. We regret that we have not matched the length L in the plots of the calculations with the corresponding interferograms. The contour plots of those quantities which may take on positive or negative values use solid (dashed) lines to represent positive (negative) contour levels. The zero level is always the last solid contour. In particular, the sonic line in the $\bar{M}$ plots can always be easily found. The most important feature of an equally spaced contour plot for compressible flow is that discontinuities are clearly visible because several contour levels overwrite each other on the plot, at the location of the discontinuity. When plotting density contours using the levels prescribed by the available experimental fringes, this effect is still present but degraded to varying degrees for the different cases. In particular, density levels between ρ_1 and ρ_2, etc. may not be present at all, although in many cases we arbitrarily inserted extra contours for aesthetic reasons.

Referring to Figure 7 (i.e., Case 4), the generic features of the various plots are discussed (the notation "Figure N" is used when it would not be useful to consider Figure 7 as an example). First, most pages have a heading with certain information: "MS", "ALP" are M_s, θ_w in the notation of the text; NR and NZ are the number of mesh points in the calculation and correspond to Table I; "P_0" is p_0, the initial shock-tube pressure; KBEG is the first point (viewing from right to left) in the x-direction after the reflection point; and the word "PERFECT" or "HANSEN" appears to denote the EOS. Notice that (NR-KBEG) by NZ is the appropriate aspect ratio, rather than NR by NZ. Figures 7a and b are presented on the same page and all plots are uniformly labelled according to the table appearing along with these figures. When comparing an interferogram (Figure 7a in this example) with the associated calculated isopycnics (Figure 7b here), the effect of an EOS mismatch in the

calculation of ρ_2/ρ_0 and ρ_3/ρ_0 can be striking and misleading. Recall, see Section 3, that these density values are calculated for the interferogram using a specific choice of equilibrium EOS. A numerical computation using a different choice of EOS will automatically get different values and shift all of the contours away from their correct locations. An excellent example of this effect is Figure 12b4 where most of the isopycnics have been shifted into the numerical shock layers associated with the reflected shock and the second Mach stem. Concerning Figures 7d and e, we note the following: (1) the $\bar{M}$ plots in both figures show that the disturbed flow is subsonic everywhere except in Region 2 where the flow is entirely supersonic, (2) contact or slip surfaces tend to show more clearly in the plots of e and $\bar{H}$ than in ρ and this is especially true of the boundary of the vortex rollup as may be noted by comparing these three plots in Figure 7e; of course, this effect is caused by the different effects the Rankine-Hugoniot jump conditions have on the number of contours appearing in the shock layers for the different quantities and, it should also be noted, the EOS or the value of γ in the case of the polytropic EOS has a large effect, (3) shock waves can be distinguished from slip surfaces by comparing the pressure plots with plots of ρ, e, $\bar{M}$, etc., (4) distinguishing compressions from rarefactions can usually be done with the pressure contours alone (e.g., if a compression steepens to form a shock) or in conjunction with the wall pressure plot, Figure 7c; determining the direction in which a wave faces is often of interest and is not usually obvious although sometimes the $\bar{u}$ plot in Figure Nc can be used for waves normal to the wall, (5) the $\bar{H}$ plots are not constant states because of the source terms in eqn. 4; it follows from the Rankine-Hugoniot conditions that $\bar{H}$ does not change across a shock wave and this can be seen clearly in Figures 7d and e for the second Mach stem and the reflected shock wave, although there is some slight nonmonotone variation inside the numerical shock layer. It is also true that $\bar{H}$ does not jump across the incident shock wave and the first Mach stem despite appearances to the contrary in Figures 7d and e. Close inspection (not obvious to the reader in most instances in Figures Nd and e) reveals that $\bar{H}$ is the same in each of Regions 0-3 at the first triple point and the variation of $\bar{H}$ in the numerical shock layers is enough to cause this layer to be filled in with several additional contour levels, (6) the visual appearance in Figure 7c of streamlines ending in the interior of the calculation is, of course, just a plotter error (the density of

streamlines is fixed for reasons of efficiency), 7) the velocity vector plot, Figure 7e shows how this vector jumps across shock waves and aligns itself with slip surfaces and the wall boundary conditions.

The discussion of many of the cases refers to hand measurements of ξ and ξ'. The accuracy of these measurements is not usually very good: however, differences between measurements (e.g., regarding the two calculations of the same case using different choices of EOS) is much more reliable.

<u>Case 1</u>: $M_s = 2.05$, $\theta_w = 60^0$, RR, Argon. Comparison of the experimental and numerical isopycnics (Figures 4a, b) show them to be in good agreement with an error of about one fringe at the start of the subsonic region. The wall density distribution (Figure 4c) disagrees by about the same amount. It may be observed that the density contour levels curve sharply towards the reflection point just above the wedge surface, an effect that is not present in the experimental results. The blowup plots of $\tilde{M}$, $\tilde{H}$ exhibit this effect as well, even in the supersonic region. This numerical error is referred to as "wall heating" and is commonly observed in shock capturing calculations as shown, for example, in Noh 1976. Wall heating affects only the density, temperature, etc., and not the pressure (Figure 4d). It may be seen to account for part of the observed error in this case, including the slight error in the value of the reflected shock wave density ρ_2 on the wall. In addition, the error in the stand-off distance of the bow shock s, relative to the experimental distance from the reflection point P to the corner L is about 6.2%.

<u>Case 2</u>: $M_s = 1.26$, $\theta_w = 45^0$, RR, Air. Figures 5b and c show that the quantitative agreement between experiment and calculation is very poor for this case, and the results are largely independent of the choice of EOS. Furthermore, the angle between the wedge and the reflected shock as well as other gross flow field quantities are in substantial error, even though the isopycnic patterns are in excellent qualitative agreement. A possible explanation for this severe error may be found by considering the ratio ρ_2/ρ_0 as a function of M_s, fixing $\theta_w = 45^0$. It turns out that $\rho_2(M_s{=}1.26) = 2.49\rho_0$ and $\rho_2(M_s{=}1.24) = 2.09\rho_0$, whereas the calculation has $\rho_2/\rho_0 = 2.2$. In other words, the slope $d(\rho_2/\rho_0)/dM_s$ is so steep in the

region of interest that small errors in either the numerical method or experimental measurement can lead to large errors in ρ_2. For further discussion of this type of consideration, see Hu and Shirouzu 1985. Noting that the disturbed flow field is wholly subsonic, Figure 5a, and that this case is close to the RR-SMR transition boundary, it is also possible to speculate that the experiment is actually an SMR despite this not being visible on the interferogram or in the calculations. The full resolution of this disagreement should be possible with the adaptive mesh version of our code, see Berger et al 1985, used in a region of parameter space around $(M_s, \theta_w) = (1.26, 45^0)$. A posteriori, it is seen that studying the results for both choices of EOS was not useful.

<u>Case 3</u>: $M_s = 1.50$, $\theta_w = 45^0$, SMR, Air. Comparison of the interferogram and the calculated isopycnics, Figures 6a and b, shows excellent qualitative agreement and approximately a one fringe error quantitatively. This agreement continues for $x/L \sim 1.0$ since the experimental corner flow field is inviscid. We measure $\chi = 1.0^0$ and 0.5^0 for the calculation and experiment, respectively. Since the Mach stem is only 3-4 computational zones high, possible explanations for this disagreement include numerical error due to lack of resolution and the existence of viscous boundary-layer effects in the experiment. The disagreement in the wall density profiles, Figure 6c, for $x/L < 0.5$ may be due to several causes: the possibility of viscous effects along the wedge, the possibility of the numerical wall-heating error interacting with the slip surface, and the difficulty in precisely locating the intersection of a fringe with the wedge in the interferogram. Some of the contour plots in the blowup frame, Figure 5e, illustrate the difficulties. The different choices of EOS proved not to be important for this case.

<u>Case 4</u>: $M_s = 3.03$, $\theta_w = 47^0$, DMR, Air. The calculated and experimental wave patterns, Figures 7a and b, are in excellent qualitative agreement, including a relatively sharp slip surface emanating from the second triple point. The interferogram shows a different orientation for fringe c and an extra fringe d under the reflected shock between the two triple points, which may be an indication that the gas is relaxing in this region. The differences due to the choice of EOS are small, but noticeable. In particular, the values of χ and χ' are close to the experimental result for

the Hansen EOS but are too large by about 1° for the γ = 1.4 results. It should be noted, however, that $\theta_w = 47^0$ is very close to the RR-DMR transition line and the boundary layer defect may have had some effect on χ, χ' in the experiment. Also, the vortex rollup is closer to the leading Mach stem for the Hansen calculation than for the perfect gas calculation, Figure 7e; the interferogram does not show the rollup moving ahead at all, presumably due to viscous effects. As is typical for DMR results, the flow field is of mixed type with region 2 being supersonic and the remainder being subsonic, Figure 7d. Also typical is the relative strength of the contact surface and vortex rollup in the $\bar{H}$ plots, Figure 7e; the waviness of this surface in the numerical results is a hint of the physical Kelvin-Helmholtz instability apparent in the interferogram. Concerning the wall density plots, Figure 7e, the Hansen EOS calculation is a few percent high on the peak value even after correcting the discrepancy in ρ_3/ρ_0. The interferogram, of course, cannot exhibit the sharp inviscid peak and valley in the rollup region of the calculation. The relative displacement of these structures between the two calculations follows directly from the differences in the calculated values of χ'. The viscous corner region, as expected, is not reproduced well in the calculations.

<u>Case 5</u>: M_s = 2.65, $\theta_w = 30^0$, CMR, Air. Comparing the interferogram with the density contours in Figures 8a and d, it may be seen that excellent overall agreement was obtained for the wave system except in the corner region. The comparisons using the experimental isopycnics, Figures 8a and b, differ by a larger degree. The differences in the vortex rollup pattern are clearly the result of experimental viscous effects. Figures 8d and e show a small supersonic region at the triple point, which is typical of CMR results.Another interesting feature of this flow field is the presence of three points along the wedge surface where $\bar{u}$ = 0 (see the $\bar{u}$ contour plot, Figure 8d, and the $\bar{u}$ wall plot, Figure 8c); the first two occur at the leading and trailing edges of the vortex rollup pattern and the third appears much further downstream. This pattern is pervasive (except, see Case 7) for those Mach reflections with a vortex rollup. We measure $\chi = 8.6^0$ for the perfect gas calculation and $\chi = 8.3^0$ for the Hansen EOS calculation and the experiment. The calculated values of ρ/ρ_0 in the region $0.0 \leq x/L \leq 0.2$ are in good agreement with the interferogram, Figures 8a and c, once the

calculation of ρ_3/ρ_0 is corrected for χ and the choice of EOS, and the different rollup patterns are taken into account. The larger disagreements in comparing the experimental isopycnics, Figure 8a, and the wall density distributions, Figure 8c, downstream of the vortex might be explained by the viscous effects providing different boundary conditions for the subsonic inviscid flow field between the rollup and the corner region (where these effects are substantial).

<u>Case 6</u>: $M_s = 5.07$, $\theta_w = 30^0$, CMR, Argon. The isopycnic patterns are in excellent agreement, despite the availability of relatively few fringes, Figures 9a and d, except for the corner region and the details of the vortex rollup pattern. The quantitative agreement, Figures 9a, b and c and measurements of χ, are also very good except in the corner.

<u>Case 7</u>: $M_s = 10.37$, $\theta_w = 10^0$, CMR, Air. The experimental results, Figure 10a, show strong relaxation effects in the disturbed flow field behind the reflected shock (this is indicated by the near tangential incidence of the fringes to the shock), and the incident shock jump appears almost in equilibrium. Also, the wedge surface does not appear to be perfectly straight in the photograph, which indicates that the sidewall boundary-layer-diffraction effects may be significant. There is reasonably good qualitative agreement (disregarding the real-gas effects) in the isopycnic patterns, Figure 10d, although the kink is more pronounced in the experiment than in the calculation. In evaluating the wall density plots, Figure 10c, it should be noted that the data points were evaluated assuming frozen-triple-point conditions while the calculation implicitly used the equilibrium Hansen EOS for the same task. Also, we estimate $\chi \simeq 13.0^0$ for the experiment and measure $\chi = 15.0^0$ for the calculation; the corner attachment angle is 20.5° for the experiment and 25.5° for the calculation. The latter difference is very large and is clearly the result of the difference between an equilibrium shock jump and a strongly relaxing shock jump at the corner. The former difference is probably also a real gas effect, and would have a strong influence on the kink structure. The vortex rollup patterns are in remarkably close qualitative agreement, although we note the rollup is closer to the leading Mach stem, which has a somewhat greater toe-out, in the experiment than in the calculation. An unusual feature of this flow field is that $\tilde{u}$ has

just one zero on the wedge surface, located at the leading edge of vortex rollup. Comparing with the discussion in Case 5, this suggests that as the (M_s, θ_w) - plane is traversed from the low M_s, high θ_w region to the high M_s, low θ_w region and restricting to cases for which a vortex rollup pattern is present, the number of zero crossings of $\bar{u}$ along the wedge surface smoothly bifurcates between one and three. The results for Cases 14 and 15 substantiate this conjecture; the former lies near the transition point and has three zero crossings while the latter lies just beyond the transition (and the lone zero crossing ahead of the vortex rollup is pushed foward into the shock layer). Also, the contact surface is more unstable in the calculation than in the experiment. These two effects are opposite to those usually holding in our results. Thus, it seems that quite good quantitative agreement could be obtained for x/L small in the wall density plots if the rollup patterns could be spatially lined up, the Hansen EOS used in evaluating the data, and the corner jump conditions changed to provide the correct downstream boundary condition for the subsonic portion of the flow field, Figure 10d. The dip in Figure 10c at $x/L \sim 0.25$ is due to the boundary error.

<u>Case 8</u>: $M_s = 1.66$, $\theta_w = 40^0$, SMR, Air. The isopycnic patterns, Figures 11a, b and d, as well as the wall density plots, Figure 11c, are in excellent qualitative and quantitative agreement. The only noticeable difference between the two calculations is that the value of ρ_3/ρ_0 is in better agreement when using the Hansen EOS and this aligns the overall wall density plots closer to the experiment. There is a larger error for x/L large which is probably explained by viscous effects in the corner region for the experiment. The EOS effect on the values of ρ_3/ρ_0 is worth commenting on in detail, since the small value of M_s precludes significant real-gas effects. Assuming a perfect gas and a Mach stem normal to the wedge surface at the triple point, one may compute $\rho_3/\rho_0 = [(\gamma+1)M_0^2]/[(\gamma-1)M_0^2 + 2]$ where $M_0 = M_s \csc \psi_0$ and $\psi_0 = \pi/2 - (\theta_w + \chi)$ which implies that ρ_3/ρ_0 is sensitive to the value of χ at low shock-wave Mach numbers and/or high values of $(\theta_w + \chi)$ and that $d(\rho_3/\rho_0)/d\chi < 0$. For this case, $\chi \sim 3.5^0$ in both calculations but is slightly less in the Hansen calculation which is enough to account for the wall density results presented in Figure 11c. Noting that the calculations compute ρ_3/ρ_0 and account for the EOS, χ, and any deviation from normality of the Mach stem automatically, while the experimenter must make the assumptions

above and measure χ by hand, one sees that the differences in the various results are outweighed by the agreements. Also, boundary layer-displacement may be a factor because of the relatively low value of χ.

<u>Case 9</u>: $M_s = 2.87$, $\theta_w = 40^0$, DMR, Air. Comparing the density contour plots, Figure 12d, with the interferogram, we see that there is excellent overall qualitative agreement for both calculations. This agreement is maintained only for the perfect gas calculation when comparing the experimental isopycnics, Figure 12b; of course, the experimental data reduction used a frozen triple point analysis. The vortex rollup pattern, the corner flow field, and the second triple point flow field differ considerably, however. Taking up the latter point first, we note that this case is near the CMR-DMR transition boundary, irrespective of the choice of EOS. Also, we measure $\chi = 5.3^0$ for the perfect gas calculation, $\chi = 5.0^0$ for the Hansen EOS calculation and $\chi = 4.5^0$ for the experiment. Thus, it is not unreasonable for the calculations to contain a much stronger second Mach stem and sharper second triple point than the experiment, which is close to CMR. The effects of boundary-layer displacement might also play a role. The experimental contact surface is very diffusive and this effect may prevent the vortex from moving forward towards the Mach stem, in conjunction with the presumed boundary-layer effects. The peak stagnation density (see the $\bar{u}$ vs. x/L plots in Figure 12c) behind the vortex is substantially higher in the calculations; we can conjecture that this is due to the sharper DMR structure and the nondiffusive contact surface of the calculation. In view of these effects and the differing boundary conditions at the upstream stagnation point and the corner, the wall density results, Figure 12c, are actually in good agreement. The Hansen EOS results must be corrected for the data reduction technique and there is otherwise little difference in the two calculations. In particular, the bunching of the fringes, in Figure $12b_H$, at the second Mach stem is due to the mismatch in Regions 2 and 3 between the experiment and the Hansen calculations.

<u>Case 10</u>: $M_s = 3.72$, $\theta_w = 40^0$, DMR, Air. The analysis for this case follows closely that for Case 9, although the interferogram, Figure 13a, is clearly DMR as are the calculations. It is likely that there is a relaxation fringe underneath the reflected shock between the two triple points. We

measure $\chi = 5.5^0$ for the perfect gas calculation, $\chi = 5.2^0$ for the Hansen EOS calculation, and $\chi = 5.0^0$ for the experiment; the differences in the measurements of χ' are similar. Referring to the $\tilde{M}$ contour plots, Figures 13d and e, one sees that the sonic line is coincident with the second Mach stem; this always occurs in our clear DMR results and it is a useful criterion in distinguishing the CMR-DMR transition. Other typical flow field features are (1) the transition of the second Mach stem to a continuous compression near its intersection with the main contact surface, Figures 13d and e, and (2) the existence of two stagnation points O_1 and O_2, one behind the vortex and the other just below the S-M' intersection and above the wedge, see the $(\tilde{u},\tilde{v})$ vector field plots, Figure 13e; note that the self-similar streamlines are singular at these two points. Also, the pressure attains local maxima at these two points, Figure 13e, and the $\tilde{u}$ contour plots, Figure 13d, show $\tilde{u} = 0$ at O_1 and O_2. Concerning the wall density plots, Figure 13c, the agreement is closer than it appears because the data points in the range $0.18 < x/L < 0.425$ need to be shifted to the right to account for the different relative locations of the second triple point; such a shift lines up the plots but the peaks are still off as in Case 9.

Case 11: $M_s = 4.62$, $\theta_w = 40^0$, DMR, Air. The analysis is similar to Cases 9-10. There is probably a relaxation fringe underneath the reflected shock which is stronger in the interferogram, Figure 14a, then for some of the other cases. We measure $\chi = 6.0^0$ for the perfect gas calculation and $\chi = 5.0^0$ for the Hansen EOS calculation and the experiment; there are similar differences for χ'. The quantitative agreement between the experiment and the perfect gas calculation is very good away from the corner in both the isopycnic plot, Figure $14b_p$, and the wall density plot, Figures 14c and c_p. A shift of data points as in Case 10 leads to nearly exact agreement for $0.16 < x/L < 0.35$ and the peak density error at the stagnation point is very small, relative to Cases 9-10. This is perhaps due to a reduced relative influence of viscous effects in the region, although the interferogram shows significant instabilities in the contact surface and a vortex rollup pattern similar to these two cases. It is interesting to note that in Cases 9-11 the Hansen EOS provides better agreement with the experiment in terms of gross flow field features (e.g., χ, χ') but worse agreement on quantitative details such as wall density curves (we are discussing the situation, of course, after

the data have been corrected for the choice of EOS). The present case exemplifies this fact in that the Hansen EOS calculation shows exact agreement on χ but is badly off on peak density along the wall.

<u>Case 12</u>: M_s = 2.03, θ_w = 27^0, SMR, Air. The agreement between calculation and experiment is extremely strong in all respects, Figures 15a, b and c, and is the best of all the fifteen cases. Quantitatively, the isopycnics are off by about one fringe and the wall density plot shows similar agreement except in a small region near the corner. The contact surface spreads out in the experiment and does not rollup as much as in the calculation.

<u>Case 13</u>: M_s = 8.70, θ_w = 27^0, DMR, Air. The interferogram, Figure 16a, exhibits substantial real gas effects and even the Hansen EOS does not model the isopycnic shapes and locations very well. The relaxation length, ℓ_v, is about 0.1 x L for the incident shock and the fringes are at nearly tangential incidence to the reflected shock. Also, the relaxing gases in the Mach stem region have obscured the contact surface and part of the roll-up pattern. The density contour plot, Figure 16d, and the interferogram show very good agreement. The rollup patterns substantially agree, although the contact surface normal to the wall S_n at x/L ~ 0.02 and the backwards facing shock wave W_b normal to the wall at x/L ~ 0.065 in the calculation, Figure 16e, are either not resolved or are lost due to viscous effects in the interferogram. Both calculation and experiment exhibit a strong toe-out of the first Mach stem; the kink on this shock surface may be near transition to a new triple point in view of the possible existence of an extra slip surface S_e emanating from this point, see the u contour plot, Figure 16d, and the $\tilde{M}$ plots, Figures 16d and e. The vector field plot, Figure 16e, shows the existence of a pseudo-stationary stagnation point O_2 near the intersection of the two slipstreams, in addition to the one at the center of the vortex O_1; indeed, there is a two-dimensional region around O_2 where the flow appears to be stagnated. Our measurements show that χ = 9.6^0 and χ' = 9.0^0 for the calculation, and that χ = 7.5^0 and χ' = 7.8^0 for the experiment. The measured corner attachment angles are 33.5° and 23.0° for the calculation and experiment, respectively. This nonequilibrium effect (which apparently is poorly modelled with the equilibrium Hansen EOS) explains the large

disagreement near $x/L = 1.0$ in the wall density plots, Figure 16c. After correcting the data for the Hansen EOS, there are large errors in the wall density plot in the range $x/L < 0.5$. Possible explanations include the large error in downstream boundary condition at $x/L = 1.0$, the large difference in χ and χ', viscous effects and differences in rollup pattern, and general relaxation effects, of course, the nonequilibrium flow field likely contributes to the other three effects. Overall, real-gas effects have an extensive impact on the flow field dynamics for this case and the equilibrium calculation was unable to reproduce many of the details.

<u>Case 14</u>: $M_s = 7.19$, $\theta_w = 20^0$, C/DMR, Air. The interferogram, Figure 17a, shows clearly that the experimental flow field is neither frozen nor in equilibrium, including the disturbed flow beneath the reflected shock. A more detailed discussion of equation of state and nonequilibrium effects in the numerical analysis of this case is available in Colella and Glaz 1985. The triple point angle χ is nearly in exact agreement, and the rollup patterns and Mach stem toe-out agree qualitatively, Figure 17d. The attached shock wave at the corner is bifurcated in the interferogram and supersonic in the calculation, a possible relaxation effect, although viscous effects may be important too. The experiment and calculation both show this case lying near the CMR-DMR transition boundary. Lee and Glass 1982 conjecture that this transition occurs when the sonic line just reaches the kink; the $\tilde{M}$ contours, Figures 17d and e, bear this out quite well. After allowing for the EOS correction of the wall data, a possible small shift for the vortex location, and the different corner structures, the wall density plots show surprisingly strong agreement; the dip at $x/L \sim 0.35$ is an excellent example of the computational boundary error.

<u>Case 15</u>: $M_s = 8.86$, $\theta_w = 20^0$, DMR, Air. The calculated density contours, Figure 18d, and the interferogram, Figure 18a, show good overall agreement, including many flow field details. The vortex rollup patterns are very close, although viscous effects in the experiment preclude detailed agreement. The vortex is pushed foward very close to the Mach stem in both calculation and experiment; the calculation shows a wave interaction W in this region which does not appear in any of the other cases. This is seen most clearly in the blowup plots, Figure 18e. The details of this portion of the

flow field are lost in the interferogram and are underresolved in the calculation. However, this flow field pattern is reproduced in the interferogram of Experiment 974 from Deschambault 1984 for which M_S = 10.18, θ_w = 20^0 and is in air. This interferogram is reproduced here in Figure 18f. Vibrational relaxation effects are pervasive in the experiment, Figure 18a, including the Mach stem region. The failure of the fringes to merge into the second Mach stem as the contours do in the calculation, Figure 18d, is probably a real-gas effect. The corner attachment angle is 27° for the calculation and about 21° - 23° for the experiment. The calculation has a supersonic corner and relaxation effects dominate the experimental results in the corner region. We measure χ = 12.2^0 for the calculation and χ = 10^0 for the experiment, and χ' = 12.5^0 for the calculation and 11.2° for the experiment. Overall, nonequilibrium effects preclude a realistic quantitative comparison for this case.

5.2 TRANSITION SEQUENCES.

Four sets of parametrized sequences of calculations are presented in this section. The purpose of the first three sets of calculations is to assess the potential of detailed computational results in constructing oblique shock-wave-transition boundaries (see Figure 2) and in validating theories explaining these transitions. Each set contains two sequences of calculations, one for a perfect gas with γ = 1.4 and one using the Hansen EOS. The following data is presented for each case: whole flow field contour plots, using thirty equally spaced contours, of the quantities ρ, $\tilde{M}$; in an appropriate "blowup" frame in the vicinity of the triple point or reflection point, contour plots, using thirty equally spaced contours, of the quantities $\rho, e, p, \tilde{M}, \tilde{H}, \tilde{u}$, along with the streamlines and vector field associated with the pseudo-stationary velocity $(\tilde{u}, \tilde{v})$. The purpose of the fourth set is to demonstrate the boundary-layer defect theory by presenting a parametrized sequence of inviscid calculations for argon (treated as a perfect gas with γ = 5/3) near the RR-DMR transition boundary and comparing with an experimental result. For this set, only whole flow field density contours are presented.

<u>Set 1</u>: Here, an attempt is made to locate the SMR-CMR and CMR-DMR boundaries for θ_w = 45^0, Air; 1.30 < M_S < 2.60, perfect gas with γ = 1.40;

$1.50 < M_s < 2.30$, Hansen EOS; in increments of $\Delta M_s = 0.1$. The results are presented in Figures 19 and 20. Considering the $\tilde{M}$ plots in the vicinity of $M_s = 1.70$, we see that the sonic line has moved into region 2 for the cases with $M_s > 1.70$ and that the extent of the supersonic region increases with increasing shock-wave Mach number. Assuming that the SMR-CMR transition occurs when region 2 becomes supersonic at the triple point (see Lee and Glass 1982), it follows that the $M_s = 1.70$ case is a CMR and the cases where $1.30 < M_s < 1.70$ are SMR's because region 2 is entirely subsonic for these cases. It may be noted that for $M_s = 1.30$, the Mach stem M and the slipstream S are only barely visible and the case appears like an RR. The differences due to EOS effect are not marked at these M_s values, but the Hansen $M_s = 1.60$ results provide a slightly earlier CMR than the perfect gas calculation. The results agree reasonably well with the analytic transition diagram, Figure 2. Also, it would not be unreasonable for the reader to view Figures 19 and 20 and take these transitions at slightly higher M_s values, which would have the effect of making the comparison with Figure 2 somewhat less close.

In view of the small values of χ in this region, it would be useful to restudy these cases with a refined mesh in the triple-point region (using an adaptive mesh algorithm, Berger et al 1985), thereby substantially eliminating the effects of numerical error near the wall boundary and allowing sufficient resolution to separate the results for the two choices of EOS. Also, the severe slope $d\theta_w/dM_s$ of the transition curves at $M_s \simeq 1.70$ argues for increased resolution.

We now consider the $\rho, \tilde{M}$ plots in the range $2.20 < M_s < 2.40$. One theory for the CMR-DMR transition (see Lee and Glass 1982) is that the flow at the first triple point should be supersonic with respect to the motion of the kink. Because the flow immediately beneath the reflected shock and between the two triple points is constant, this criterion is equivalent to requiring that the sonic line (in pseudo-stationary coordinates) intersect the kink. Also, the sonic line should have the same tangent at the kink as the second Mach stem, because the flow is supersonic ahead and subsonic behind this discontinuity. Finally, the density contours may be expected to begin coalescing as the shock wave is about to form. Using these criteria, the calculations show that the $M_s = 2.30$, perfect gas case is a weak DMR and that

the M_S = 2.40, perfect gas case is a clear-cut DMR; for the Hansen calculations, the M_S = 2.20 can be considered a DMR and the M_S = 2.10 case is a CMR. These results are also in reasonable agreement with the analytic results for the perfect-gas transition at $\theta_w = 45^0$, see Figure 2. Note that Figure 2 indicates that no DMR can exist in this range of M_S for $\theta_w = 45^0$. However, it has been found experimentally that the CMR-DMR transition line meets the SMR-CMR transition line where it joins the RR-MR line. The exact shape of this curve is not known, although it would be expected to lie much closer to the present numerical values. Insofar as this observation is due to inviscid, equilibrium effects, the numerical results are further corroborated. It would be of great interest to pursue the numerical studies in the neighborhood of the coincidence of the SMR-CMR and CMR-DMR lines.

It is also worth noting that in this set, the isopycnic shapes and distributions resemble those for RR until $M_S \simeq 1.60$, where a loop exists at the wedge corner and the next fringe away from this loop is bowed towards it. This effect becomes increasingly prominent as M_S increases through the CMR range, loops begin to form near the slipstream as DMR approaches, and prominently so as M_S increases through the DMR range. For smaller values of θ_w, such isopycnic distributions can occur for smaller values of M_S (see Figure 15, M_S = 2.03, $\theta_w = 27^0$). The foregoing gives some insight into the changing overall wave patterns as the (M_s,θ_w) - plane is traversed.

<u>Set 2</u>: The CMR-DMR transition is studied for M_S = 4.0, Air; $29^0 < \theta_w < 34^0$ perfect gas with $\gamma = 1.40$; $25^0 < \theta_w < 30^0$, Hansen EOS; in increments of $\Delta\theta_w = 1^0$. The results are presented in Figures 21 and 22. The analytic CMR-DMR transition, Figure 2, for M_S = 4.0 takes place at $\theta_w \simeq 32^0$ for a perfect gas and $\theta_w \simeq 26^0$ for the Hansen EOS. The EOS effect is predicted correctly, that is, $\theta_w \simeq 32^0$ for a perfect gas and 20° for the Hansen EOS so that this transition line is shifted up by about 3°. It is worth noting that the calculated Mach stems are not perpendicular to the wedge at the triple point; this is an assumption in the analytic calculations leading to Figure 2 (see Lee and Glass 1984). Also, it would not be unreasonable to require the calculated kinks to clearly sharpen up to a new triple point before assuming a DMR transition.

Set 3: The SMR-CMR and CMR-DMR transitions are studied for M_s = 8.75, Air: $6^0 \leq \theta_w \leq 10^0$ and $22^0 \leq \theta_w \leq 26^0$, perfect gas with $\gamma = 1.40$; $5^0 \leq \theta_w \leq 9^0$ and $15^0 \leq \theta_w \leq 19^0$, Hansen EOS; in increments of $\Delta\theta_w = 1^0$. The results are presented in Figures 23 and 24. The analytic SMR-CMR transition (Figure 2) for M_s = 8.75 takes place at $\theta_w \sim 3^0$ for a perfect gas and at $\theta_w \sim 6^0$ for the Hansen EOS. According to our criteria involving the M sonic line, none of the reported calculations with $\theta_w \leq 10^0$ are CMR with the possible exception of the $\theta_w = 9^0$ Hansen EOS result. Thus, the calculated transitions differ from the analytic results by at least 3°. Once again, none of the calculated Mach stems are perpendicular to the wedge at the triple point. The analytic CMR-DMR transition, Figure 2, for M_s = 8.75 takes place at $\theta_w \sim 23^0$ for a pefect gas and at $\theta_w \sim 16^0$ for the Hansen EOS. The calculations show transition at θ_w no greater than 22° for a perfect gas and at $\theta_w \sim 15\text{-}16^0$ for the Hansen EOS. This represents close agreement. Here as well, the Mach stems are not perpendicular to the wedge at the triple point. It should be noted that the experimental results are not in close agreement with either of the two transition lines (see Figure 2) at such high values of M_s. Consequently, new criteria may have to be found so that better agreement can be obtained for the SMR-CMR-DMR transition lines (see Deschambault and Glass 1983, and Hu and Glass 1985).

Set 4: M_s = 7.10, Argon (perfect gas with $\gamma = 5/3$); $49^0 \leq \theta_w \leq 55^0$, in increments of $\Delta\theta_w = 1^0$; $\theta_w = 52.75^0, 53.75^0$; $53.1^0 \leq \theta_w \leq 53.5^0$ in increments of $\Delta\theta_w = 0.1^0$. The purpose of this set of calculations is to estimate the inviscid RR-DMR transition boundary and, by comparison with experimental results, to demonstrate and quantify the well-known disagreement between theory and experiment for this issue (see, for example, Shirouzu and Glass 1982). An experimental interferogram for $\theta_w = 49^0$ and all of the computational results are presented in Figure 25. Noting the results in the range $53.0^0 \leq \theta_w \leq 53.5^0$ and comparing with the experiment, a value of $\Delta\theta_w \sim 4.0 - 4.5^0$ may be inferred as the "boundary-layer defect" (see Hornung and Taylor 1982; Shirouzu and Glass 1982; Wheeler and Glass 1985) for the M_s = 7.10 RR-DMR transition. We are referring, in particular, to the substantial disagreement concerning the extent of the Mach stem region relative to the entire flow field. We have attempted to calculate the precise RR-DMR transition point by plotting the height of the Mach stem relative to L

against θ_w for the computations and extrapolating the curve to zero height, Figure 26. The result is θ_w = 53.35° which disagrees moderately with the theoretical results of θ_w = 54.4° in Lee and Glass, 1982. We remark that this error may be caused by an unnoticed bias in our measuring technique (done by simply using a ruler on the computer-generated contour plots of the blow-up Mach stem region (not shown)), lack of numerical resolution when the Mach stem is only 1-2 zones high, or a numerical error in the post-shock flow field at the wall. In any case, the error is small relative to the viscous-inviscid difference and it is also possible that the theoretical inviscid prediction of θ_w = 54.4° does not apply when the entire disturbed flow field is taken into account. Higher resolution calculations using an adaptive mesh scheme, Berger et al 1985, will be carried out in an effort to settle this issue. This set of calculations also illustrates the dramatic collapse of the complex DMR-pattern into the simple RR-pattern as θ_w changes by a fraction of a degree (see Figures 25l and m).

SECTION 6

CONCLUSIONS

A computer code has been developed for the inviscid, perfect gas shock-on-wedge problem and the results have been compared with the best available experimental data. The code is based on contemporary methodology in the numerical analysis of hyperbolic conservation laws, and has only recently been available.

Good to excellent qualitative agreement has been obtained in all cases of direct comparison, and this applies to structures beneath the reflected shock such as the vortex roll-up as well as coarser criteria such as the reflection pattern. Quantitatively, the results are very good for flow fields without observable nonequilibrium or viscous effects, except for Case 2. The error in this case is probably a result of the relatively large variation of the solution with respect to small increments in the problem parameters in the vicinity of the parameter values defining this case. When nonequilibrium or viscous effects are present, the quantitative error can be 10-15% and we may recall Case 11 which has a much larger, and unexplained error.

Although not entirely proven, it appears that the computer code represents a substantial predictive capability for the shock-on-wedge problem restricted to inviscid, perfect gases. Even for viscous, real gas flow fields, the computational results provide a significant amount of information, including highly resolved flow-field structures.

Significant non-equilibrium and viscous effects have been demonstrated in the shock wave diffraction experiments. Much of this could be inferred without the numerical study, but the latter can provide a quantitative estimate of the various effects. In particular, vibrational relaxation is observed in the high shock wave Mach number cases, and this can have large-scale effects on criteria such as the corner attachment angle and type (subsonic or supersonic) and viscous effects are important in determining the vortex roll-up pattern and the wedge corner flow field. Although these effects occur in thin layers or small regions, they may have an effect on the quantitative results in the inviscid portion of the flow field.

The capability of the computer code to discriminate between very small increments in problem parameters (M_s, θ_w, and the equation of state, although the latter has not been treated here) has been demonstrated.

By using parametrized sequences of calculations, it would be possible to construct transition boundaries in the (M_s, θ_w)-plane. Of course, the transitions obtained would be dependent on the transition criteria used in their construction; our use of the sonic criterion in self-similar coordinates shows how the infinite amount of data potentially available from a calculation can be invaluable in evaluating one of the proposed criteria.

The discussion of transition set 1 in Section 5 illustrates how parametrized numerical calculations can be used to elucidate details of the flow field transition not otherwise available. It is quite possible that such results will prove useful in the discovery of more precise analytic transition criteria, in the future. For the high M_s transitions, the inviscid numerical results provide a guide for the analysis of inviscid transition criteria in a parameter regime where analytic-experimental agreement has been relatively poor and where nonequilibrium phenomena are hard to avoid in the experiments. Of course, the formulation of transition criteria for viscous, nonequilibrium flow fields is not assisted by the present computer code.

Also we have been able to validate the conjecture that the RR-DMR. transition is offset in experiments by a boundary-layer defect.

In Section 5, several calculations were noted where our analysis could be greatly improved with a more efficient adaptive mesh in the vicinity of the Mach stem. Obtaining the necessary resolution with the present computer code would be overly expensive if carried out on a production basis for a large number of calculations. Using the methods of Berger and Colella 1985, Berger et al 1985, we expect to overcome this problem and revisit some of the cases discussed in this report. Additionally, we are working on techniques to reduce further or eliminate the starting error and boundary error from our results.

In future work, we intend to modify our computer code and include an approximation for vibrational relaxation. We expect that this work will settle some of the questions raised in this paper. The results presented here demonstrate, however, that a valid approximate solution method for the Navier-Stokes equations will be required if complete agreement between experiment and calculation is demanded. Despite these shortcomings, the comparison of the present numerical simulations with interferometric data from RR, SMR, CMR and DMR experiments are probably the best available to date.

1. Ando, S., "Pseudo-Stationary [illegible] Reflections in Carbon Dioxide - Domains and Boundaries," [illegible], UTIAS Tech. No. [illegible] (1981).

2. Ando, S. and Glass, I. I., "Domains and Boundaries of Pseudo-Stationary Oblique-Shock-Wave Reflections [illegible]," Proc. [illegible] Int'l. Symp. on the Military Applications of [illegible], Defence Res. Est. Suffield, Ralston, Alberta, Canada, [illegible] (1981).

3. Ben-Dor, G. and Glass, I. I., "Nonstationary Oblique-Shock-Wave Reflections: Actual Isopycnics and Numerical Experiments," AIAA J. 16 (1978), pp. 1146-1153.

4. Ben-Dor, G. and Glass, I. I., "Domains and Boundaries of Non-Stationary Oblique-Shock-Wave Reflexions. 1. Diatomic Gas," J. Fluid Mech. 92 (1979), pp. 459-496.

5. Ben-Dor, G. and Glass, I. I., "Domains and Boundaries of Non-Stationary Oblique-Shock-Wave Reflexions. 2. Monatomic Gas," J. Fluid Mech. 96 (1980), pp. 735-756.

6. Ben-Dor, G. and Whitten, B. T., "Interferometric Techniques and Data Evaluation Methods for the UTIAS 10 cm x 18 cm Hypervelocity Shock Tube," Univ. of Toronto, UTIAS Tech. No. 208 (1979).

7. Berger, M. and Colella P., "Local Adaptive Mesh Refinement for Shock Hydrodynamics," (forthcoming, 1985).

8. Berger, M., Colella, P. and Glaz, H. M. "Wave Bifurcations for Self-Similar Two-Dimensional Shocked Flows," (forthcoming, 1985).

9. Boyer, A. G., "Design, Instrumentation and Performance of the UTIAS 4 in x 7in Hypersonic Shock Tube," Univ. of Toronto, UTIAS Report No. 99 (1964).

10. Bristow, M. P. F., "An Experimental Determination of the Polarizability for Singly Ionized Argon," Univ. of Toronto, UTIAS Report No. 158 (1971).

11. Colella, P. and Glaz, H. M., "Numerical Modelling of Inviscid Shocked Flows of Real Gases," Proc. 8th Intl. Conf. on Numerical Methods in Fluid Dynamics, Aachen, 1982, ed. E. Krause, Springer-Verlag, Berlin.

12. Colella, P. and Glaz, H. M., "Numerical Computation of Complex Shock Reflections in Gases," Proc. 9th Intl. Conf. on Numerical Methods in Fluid Dynamics, Saclay, 1984, ed. Soubbaramayer and J. P. Boujot, Springer-Verlag, Berlin.

13. Colella, P. and Glaz, H. M., "Efficient Solution Algorithms for the Riemann Problem for Real Gases," to appear J. Comp. Phys. (1985).

14. Colella, P., Ferguson, R., Glaz, H. M., and Kuhl, A., " Mach Reflection from an HE Explosion," (forthcoming, 1985).

15. Colella, P. and Woodward, P. R., "The Piecewise-Parabolic Method (PPM) for Gas-Dynamical Simulations," J. Comp. Phys. 54, (1984), pp. 174-201.

16. Deschambault, R. L. and Glass, I. I., "An Update on Nonstationary Oblique-Shock-Wave Reflections: Actual Isopycnics and Numerical Experiments," J. Fluid Mech. 131 (1983), pp. 27-57.

17. Deschambault, R. L., "Nonstationary Oblique-Shock-Wave Reflections in Air," Univ. of Toronto, UTIAS Report No. 270 (1984).

18. Glaz, H. M., Colella, P., Glass, I. I., and Deschambault, R. L., "A Numerical Study of Oblique Shock-Wave Reflections with Experimental Comparisons," to appear Proc. R. Soc. Lond. 13 (1985).

19. Glaz, H. M., Glass, I. I., Hu, J. C. J., Walter, P., "Oblique Shock Wave Reflections in SF_6: A Comparison of Calculation and Experiment," (forthcoming, 1985).

20. Hall, J. G., "The Design and Performance of a 9 Inch Plate Mach-Zehnder Interferometer," Univ. of Toronto, UTIAS Report No. 27 (1954).

21. Hansen, C. F., "Approximations for the Thermodynamic and Transport Properties of High-Temperature Air," NASA TR R-50 (1959).

22. Hornung, H. G. and Taylor, J. R., "Transition from Regular to Mach Reflection of Shock Waves Part 1. The Effect of Viscosity in the the Pseudosteady Case," J. Fluid Mech. 123 (1982), pp. 143-153.

23. Hu, J. T. C., "Pseudo-Stationary Oblique-Shock-Wave Reflections in a Polyatomic Gas - Sulfur Hexafluorid," Univ. of Toronto, UTIAS Technical Note No. 253 (1985).

24. Hu, J. T. C. and Glass, I. I., "An Interferometric and Numerical Study of Pseudostationary Oblique-Shock-Wave Reflections in Sulfur Hexafluoride (SF_6)," submitted to the Proceedings of the Royal Society of London (1985).

25. Hu, J. T. C. and Shirouzu, M., "Tabular and Graphical Solutions of Regular and Mach Reflections in Pseudo-Stationary Frozen and Vibrational-Equilibrium Flows," Univ. of Toronto, UTIAS Report No. 283 (forthcoming, 1985).

26. Jones, D. M., Martin, P. M. E., and Thornhill, C. K., "A Note on the Pseudo-Stationary Flow Behind a Strong Shock Diffracted or Reflected at a Corner," Proc. Roy. Soc. A 209 (1951), pp. 238-247.

27. Lee, J.-H. and Glass, I. I., "Domain and Boundaries of Pseudo-Stationary Oblique Shock-Wave Reflections in Air," Univ. of Toronto, UTIAS Report No. 262 (1982). See also Prog. Aero.Sci. 21 (1984), pp. 53-80.

28. Noh, W. F., "Numerical Methods in Hydrodynamic Calculations," Lawrence Livermore National Laboratory, Report No. UCRL-52112 (1976)

29. Shirouzu, M. and Glass, I. I., "An Assessment of Recent Results on Pseudo-Stationary Oblique-Shock-Wave Reflections," Univ. of Toronto, UTIAS Report No. 264 (1982).

30. Wheeler, J., "A Resolution of the von Neumann Paradox," Univ. of Toronto, UTIAS Tech. Note No. 256 (1985).

31. Wheeler, J. and Glass, I. I., "A Reconsideration of the von Neumann Paradox," (forthcoming, 1985).

32. Woodward, P. R., and Colella, P., "Numerical Simulation of Two-Dimensional Fluid Flow with Strong Shocks," J. Comp. Phys. 54 (1984), pp. 115-173.

Table 1. Initial conditions, equation of state, and computational mesh for each experimental case.

CASE	FIGURE	GAS	TYPE	Θw	Ms	Po (k Pa)	ρo (gm/cc)	EOS	NX	NY
1	4	Argon	RR	60^{o}	2.05	20.00	3.23×10^{-4}	$\gamma = 5/3$	355	90
2	5	Air	RR	45^{o}	1.26	101.12	1.146×10^{-3}	$\gamma = 1.4$ Hansen	350	160
3	6	Air	SMR	45^{o}	1.50	50.66	5.73×10^{-4}	$\gamma = 1.4$ Hansen	375	160
4	7	Air	DMR	47^{o}	3.03	3.33	3.77×10^{-5}	$\gamma = 1.4$ Hansen	500	120
5	8	Air	CMR	30^{o}	2.65	13.33	1.52×10^{-4}	$\gamma = 1.4$ Hansen	390	125
6	9	Argon	CMR	30^{o}	5.07	4.00	6.45×10^{-5}	$\gamma = 5/3$	420	140
7	10	Air	CMR	10^{o}	10.37	6.67	7.53×10^{-5}	Hansen	400	140
8	11	Air	SMR	40^{o}	1.66	33.33	3.8×10^{-4}	$\gamma = 1.4$ Hansen	375	135
9	12	Air	DMR	40^{o}	2.87	16.67	1.9×10^{-4}	$\gamma = 1.4$ Hansen	420	110
10	13	Air	DMR	40^{o}	3.72	6.00	6.87×10^{-5}	$\gamma = 1.4$ Hansen	420	100
11	14	Air	DMR	40^{o}	4.62	2.80	3.19×10^{-5}	$\gamma = 1.4$ Hansen	420	90
12	15	Air	SMR	27^{o}	2.03	33.33	3.87×10^{-4}	$\gamma = 1.4$	350	130
13	16	Air	DMR	27^{o}	8.70	4.10	4.76×10^{-5}	Hansen	440	85
14	17	Air	C/DMR	20^{o}	7.19	8.00	9.29×10^{-5}	Hansen	420	120
15	18	Air	DMR	20^{o}	8.86	4.10	4.65×10^{4}	Hansen	500	110

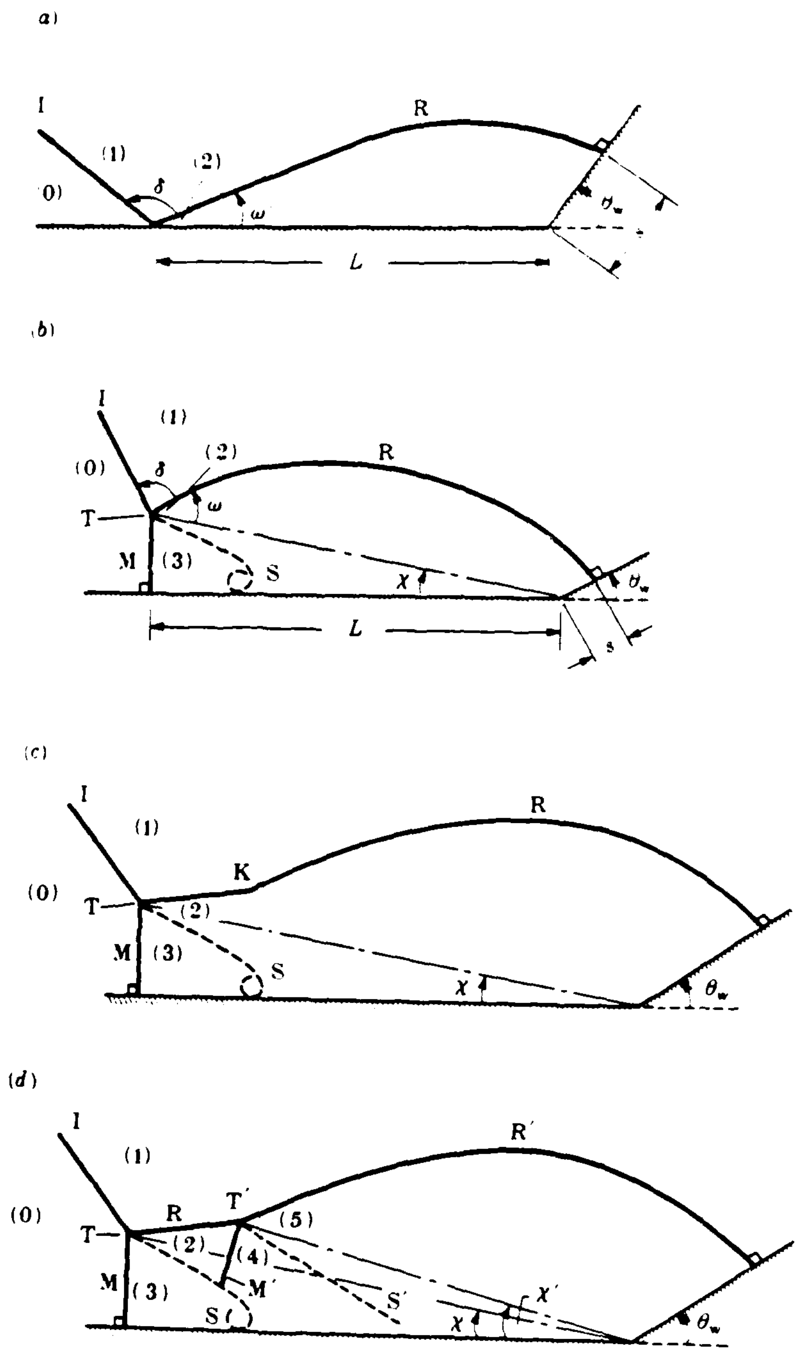

Figure 1. Schematic diagrams of types of oblique shock-wave reflections: (a) RR; (b) SMR; (c) CMR; (d) DMR; also definitions of L and s.

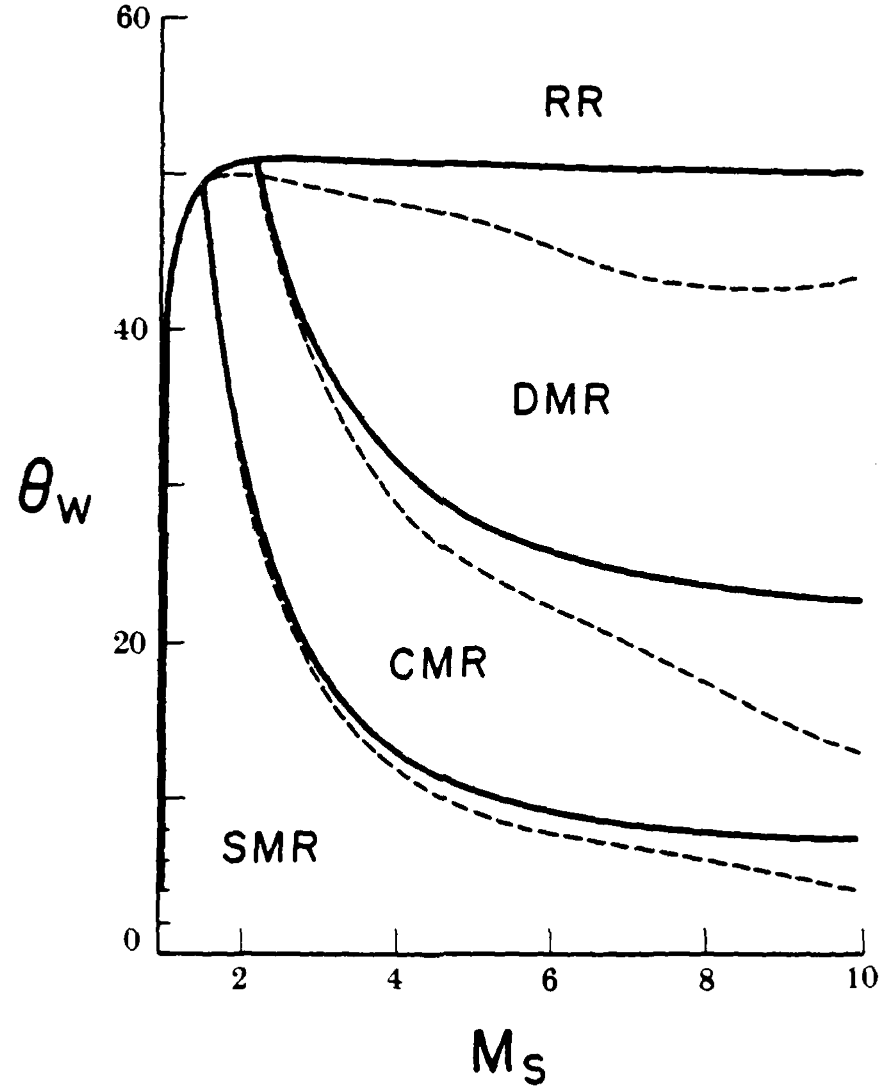

Figure 2. Regions of RR, SMR, CMR, and DMR and their transition boundaries in the (M_s, θ_w)-plane for perfect (frozen) air solid lines and imperfect (equilibrium) air broken lines, p_0 = 2.00 kPa, T_0 = 300 K, γ = 1.40.

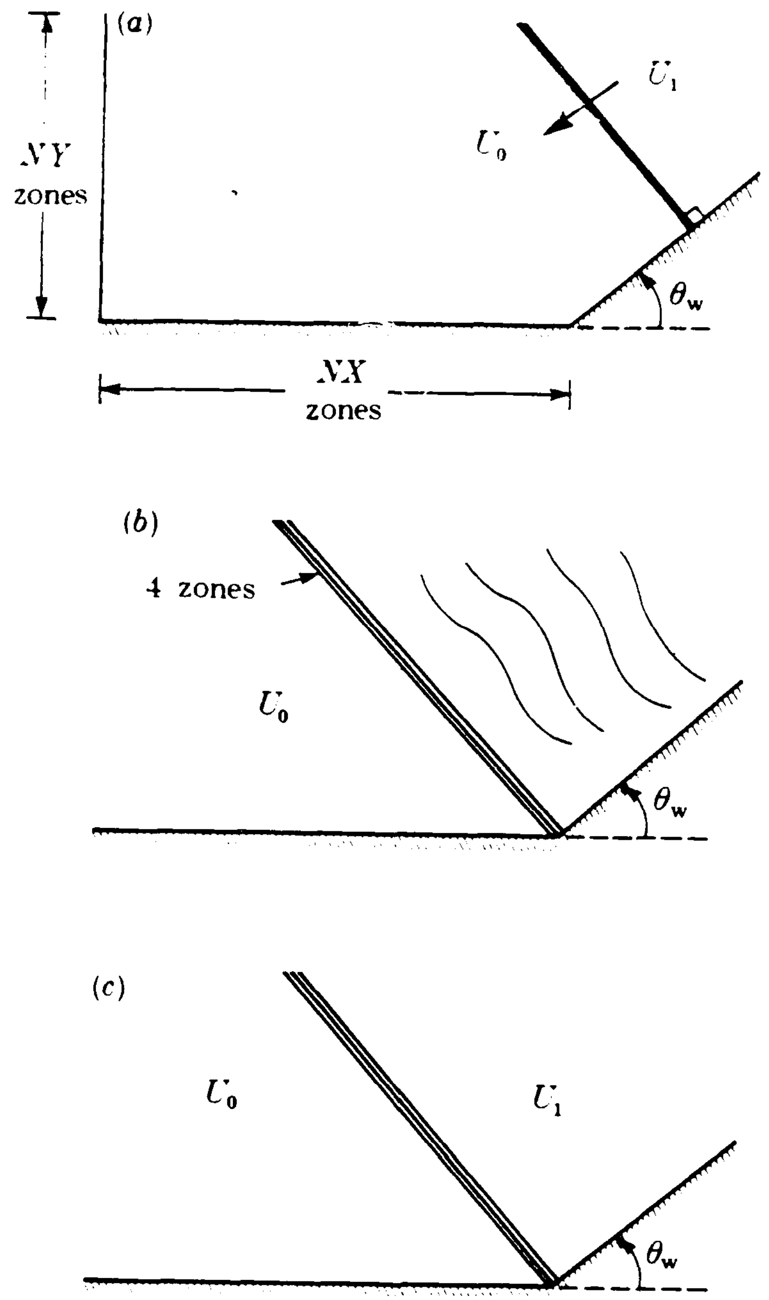

Figure 3. Numerical scheme for flow initialization; (a) starting procedure; (b) shock reaching corner; (c) elimination of small disturbances.

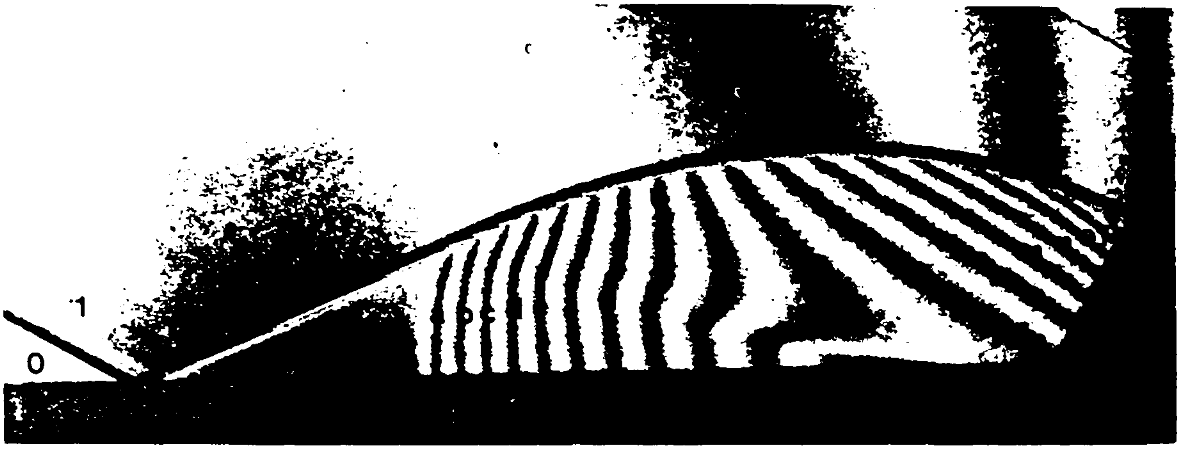

Region	ρ/ρ_0	Region	ρ/ρ_0
0	1.00	h	3.86
1	2.33	i	3.80
2	4.38	j	3.73
a	4.32	k	3.67
b	4.25	l	3.60
c	4.19	m	3.54
d	4.12	n	3.47
e	4.06	o	3.41
f	3.99	p	3.34
g	3.93	q	3.28

Figure 4a. Interferogram

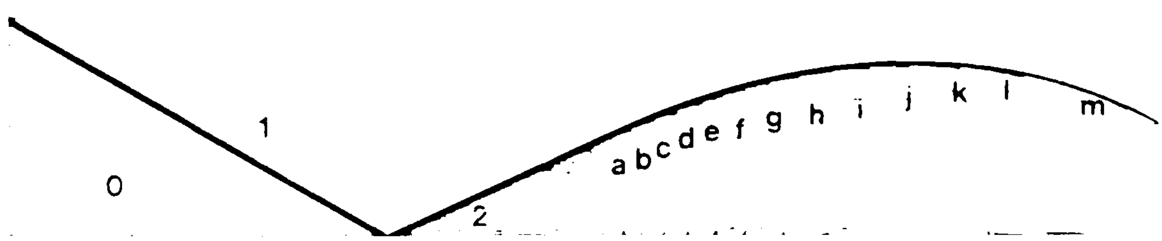

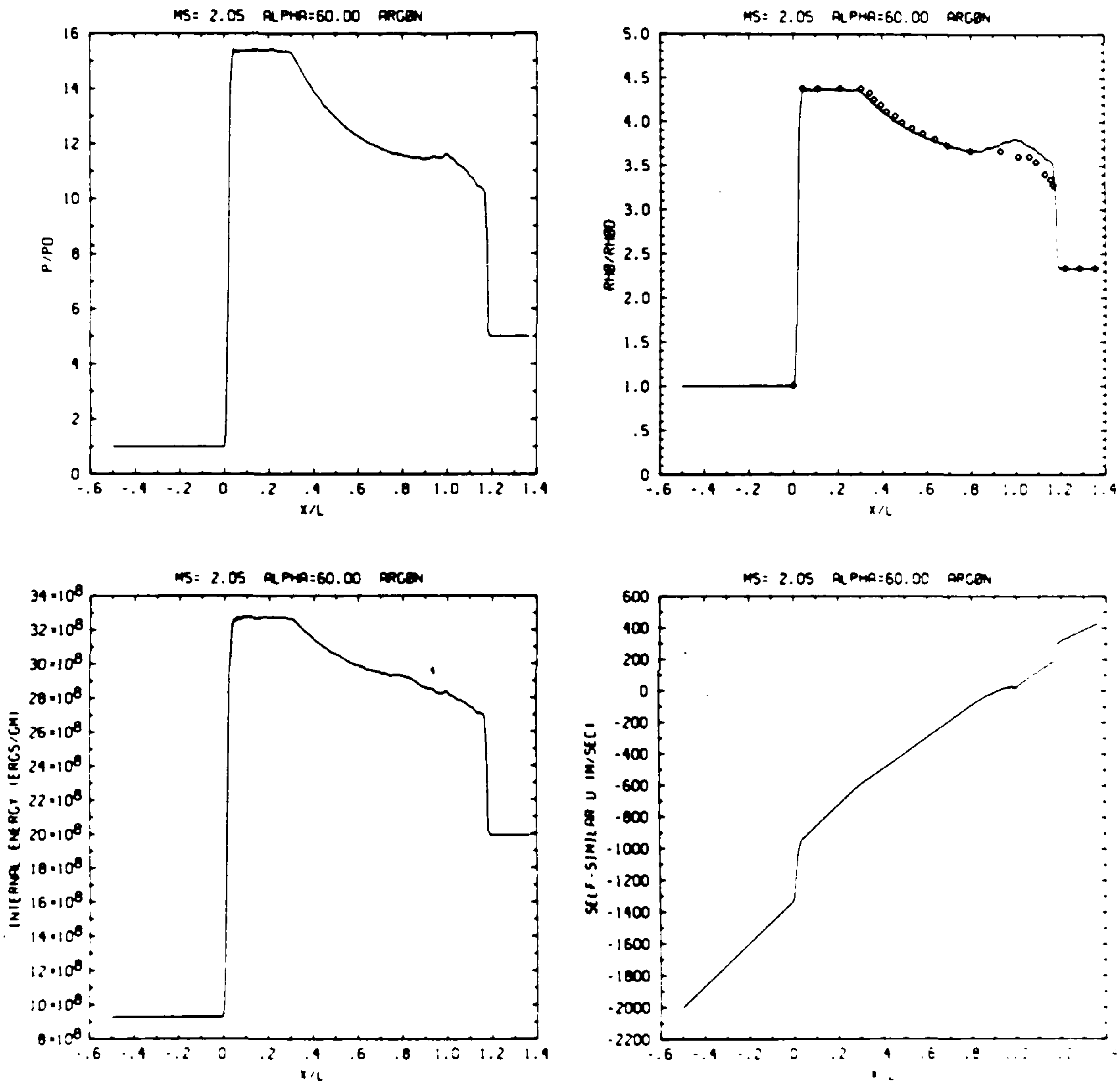

Figure 4c. Wall plots for p/p_0, ρ/ρ_0 with experimental data included, e, $\bar{u}$

Figure 4. Case 1, $M_s = 2.05$, $\theta_w = 60°$, Argon, $\gamma = 5/3$, RR - Continued.

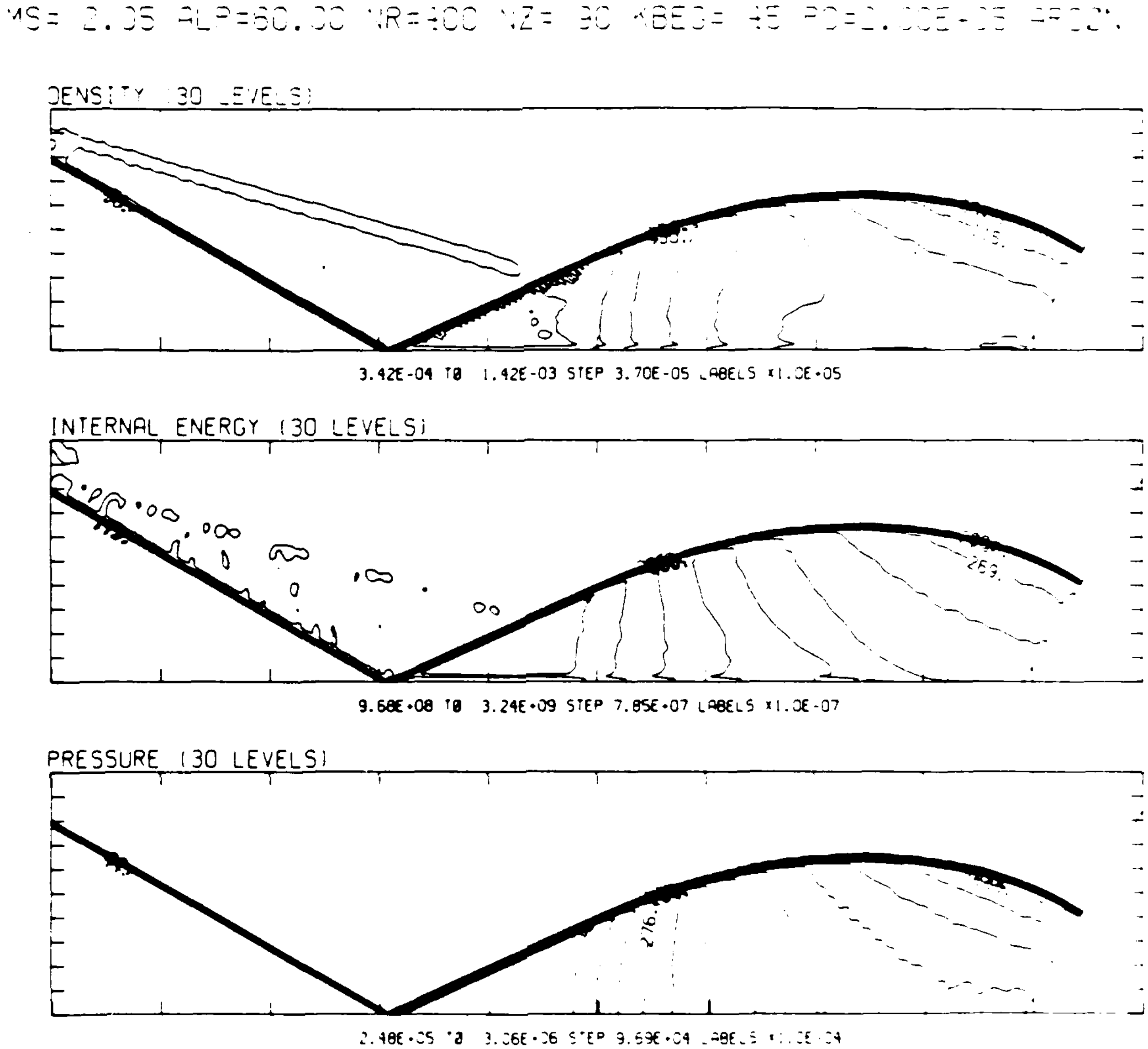

Figure 4d. Whole-flowfield contour-plots

Figure 4. Case 1, M_s = 2.05, θ_w = 60°, Argon, γ = 5/3, RR - Continued.

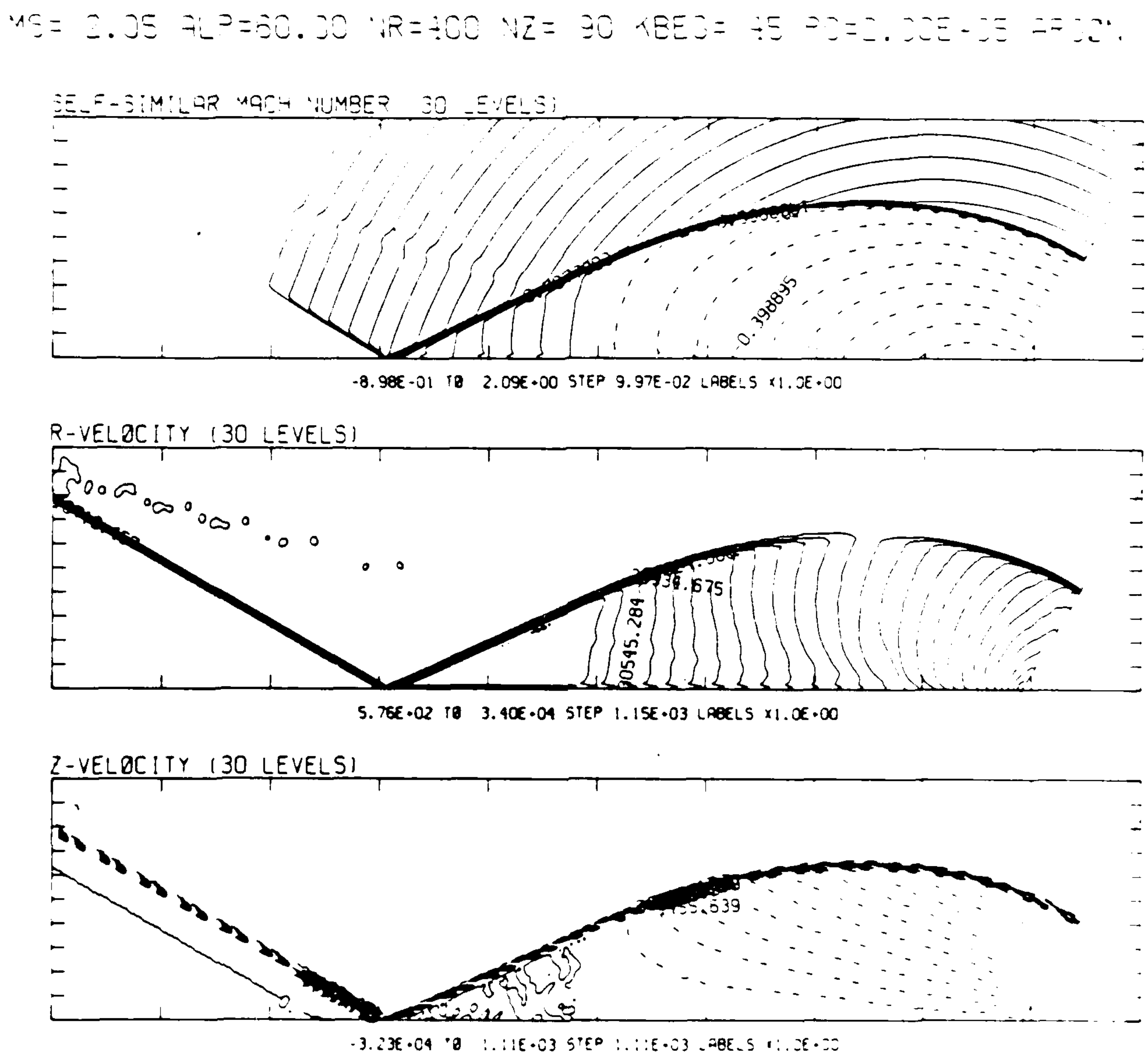

Figure 4d. Whole-flowfield contour-plots - continued.

Figure 4. Case 1, M_S = 2.05, θ_W = 60°, Argon, γ = 5/3, RR - Continued.

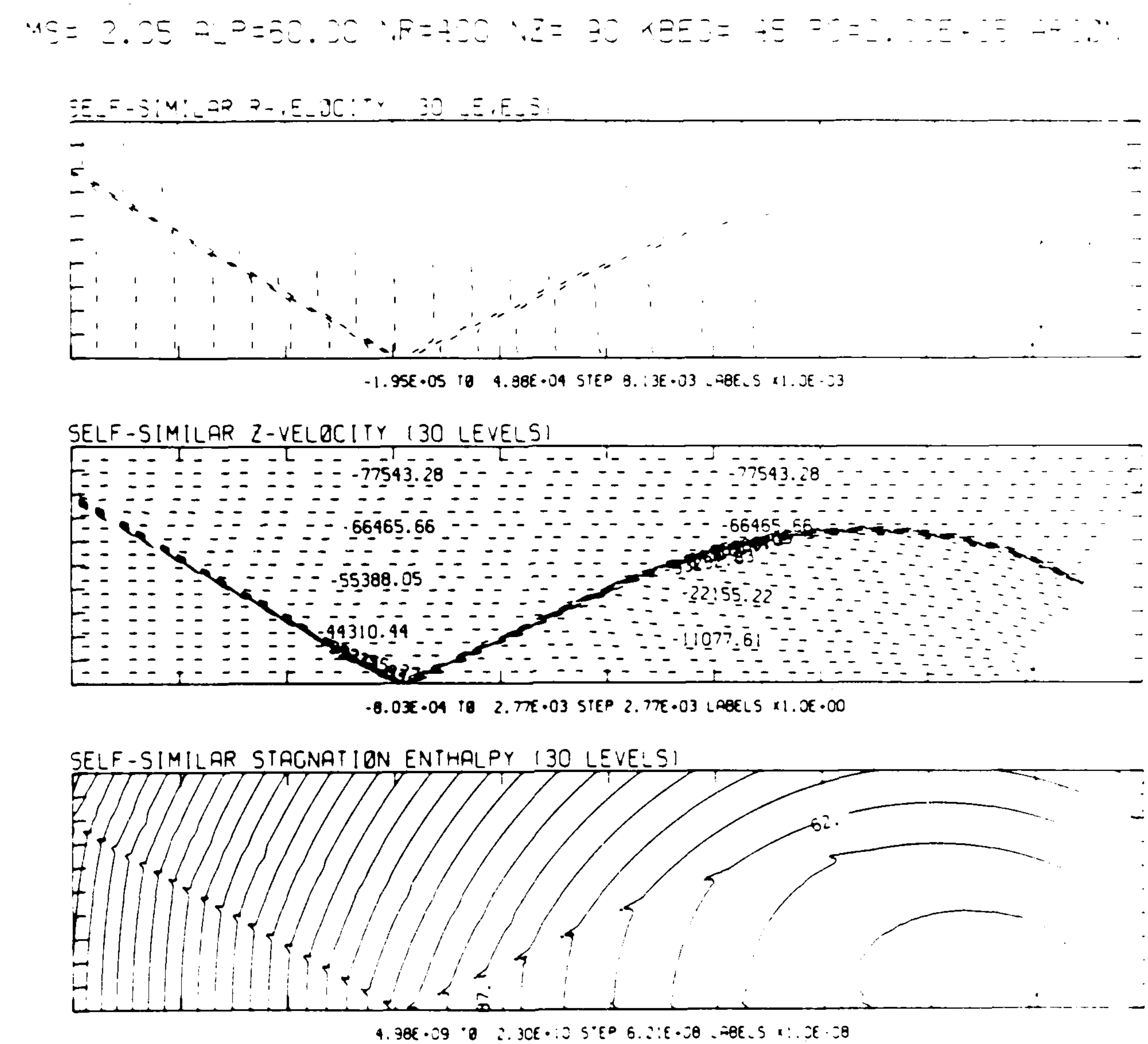

Figure 4d. Whole-flowfield contour-plots - continued.

Figure 4. Case 1, M_s = 2.05, θ_w = 60°, Argon, γ = 5/3, RR - Continued.

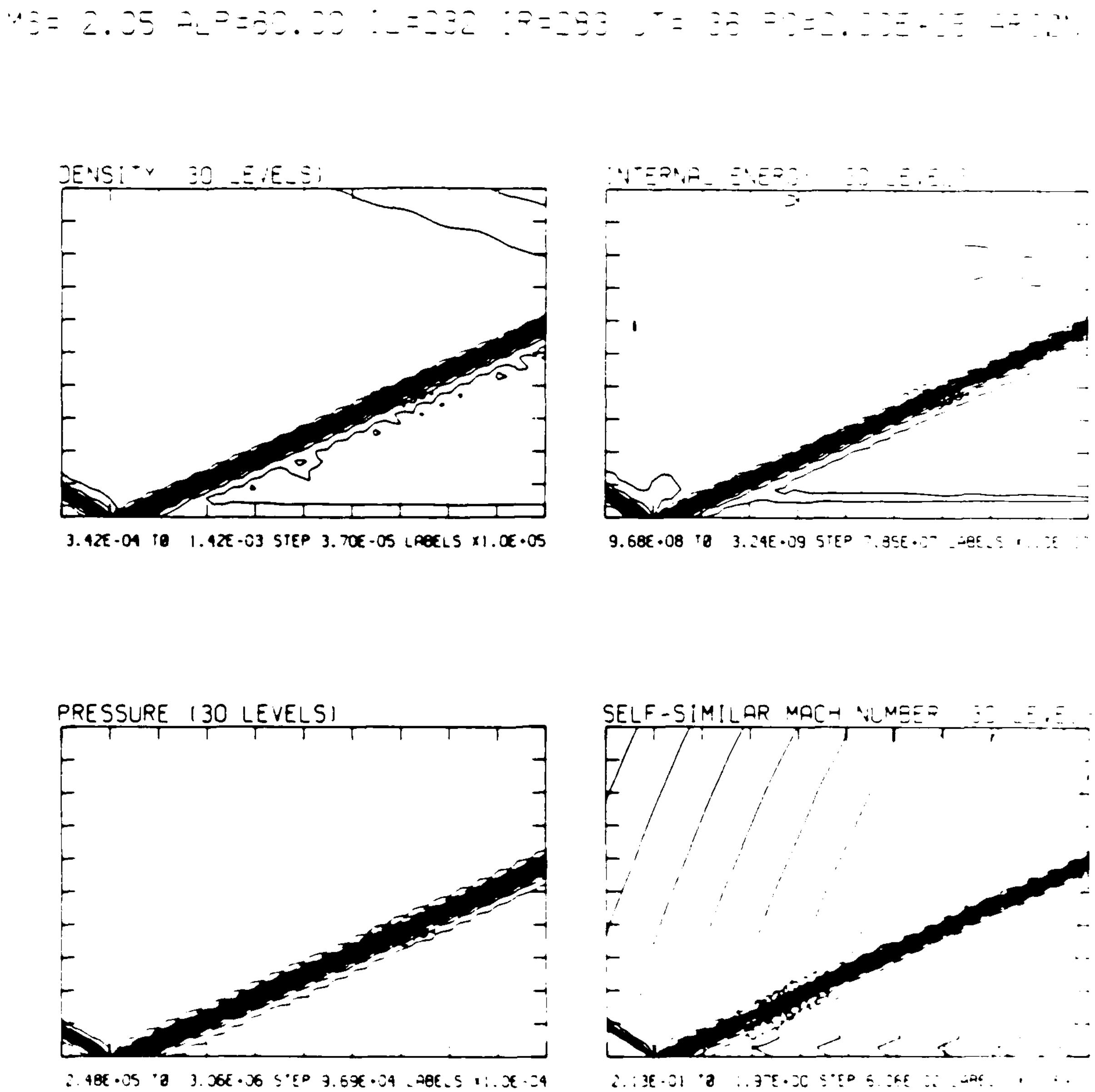

Figure 4e - Blowup-frame plots

Figure 4. Case 1, M_s = 2.05, θ_w = 60°, Argon, γ = 5/3, RR - Continued.

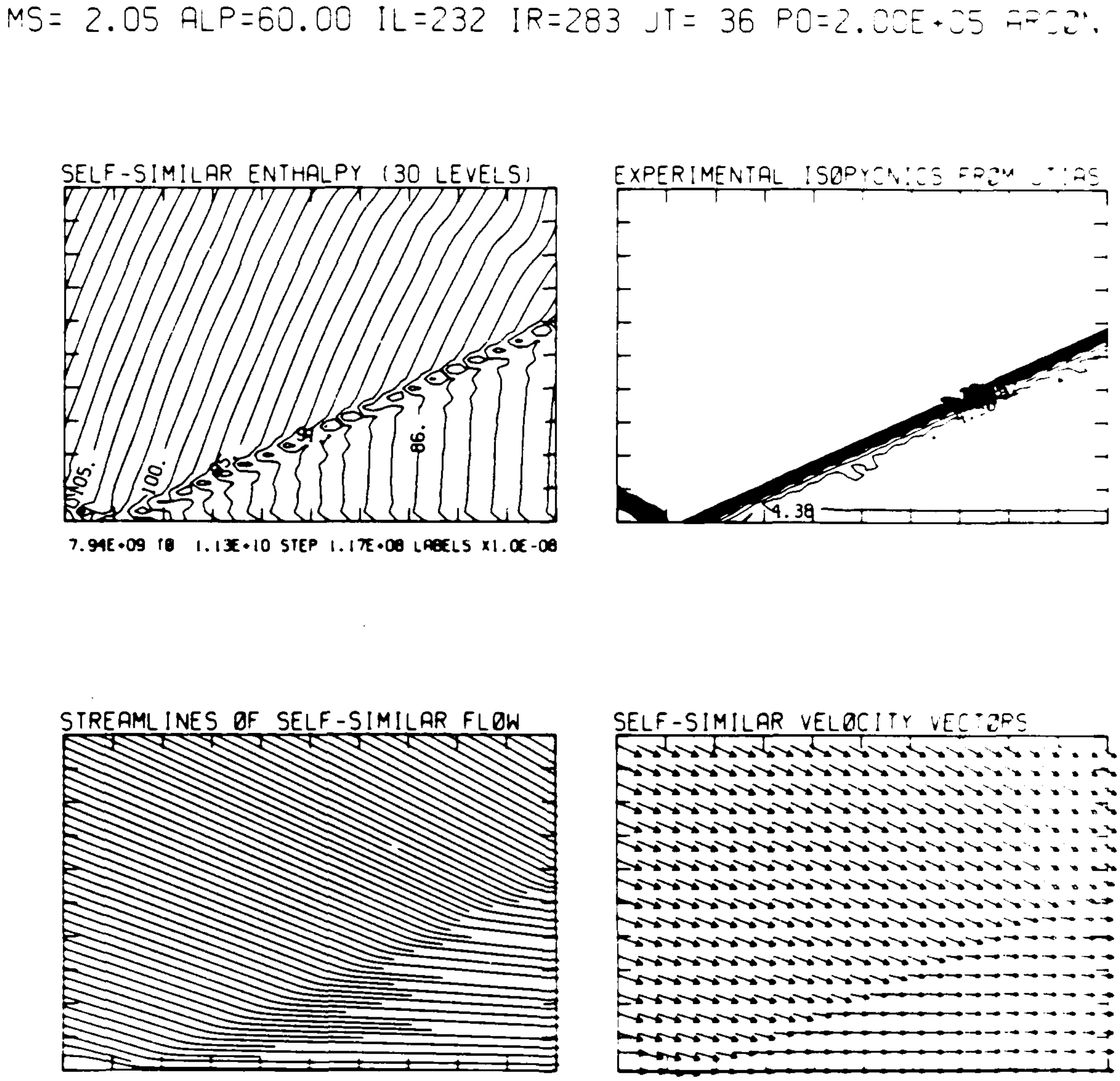

Figure 4e. Blowup-frame plots - continued.

Figure 4. Case 1, M_s = 2.05, θ_w = 60°, Argon, γ = 5/3, RR - Continued.

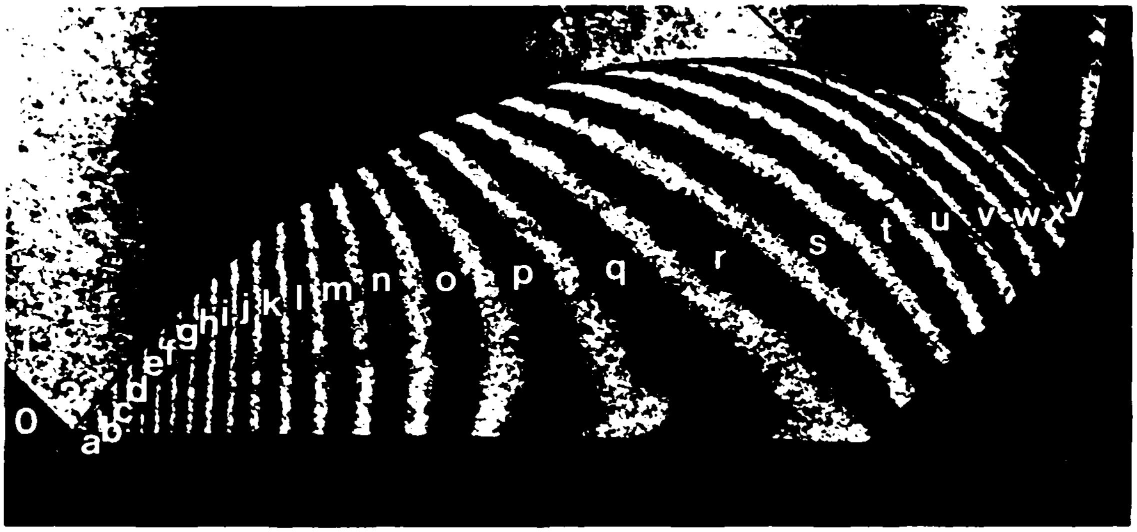

Region	ρ/ρ_c	Region	ρ/ρ_c	Region	ρ/ρ_c
0	1.00	h	2.29	r	2.03
1	1.45	i	2.26	s	2.00
2	2.49	j	2.23	t	1.97
a	2.47	k	2.21	u	1.95
b	2.44	l	2.18	v	1.92
c	2.42	m	2.16	w	1.89
d	2.39	n	2.13	x	1.87
e	2.36	o	2.10	y	1.84
f	2.34	p	2.08		
g	2.31	q	2.05		

Figure 5a. Interferogram

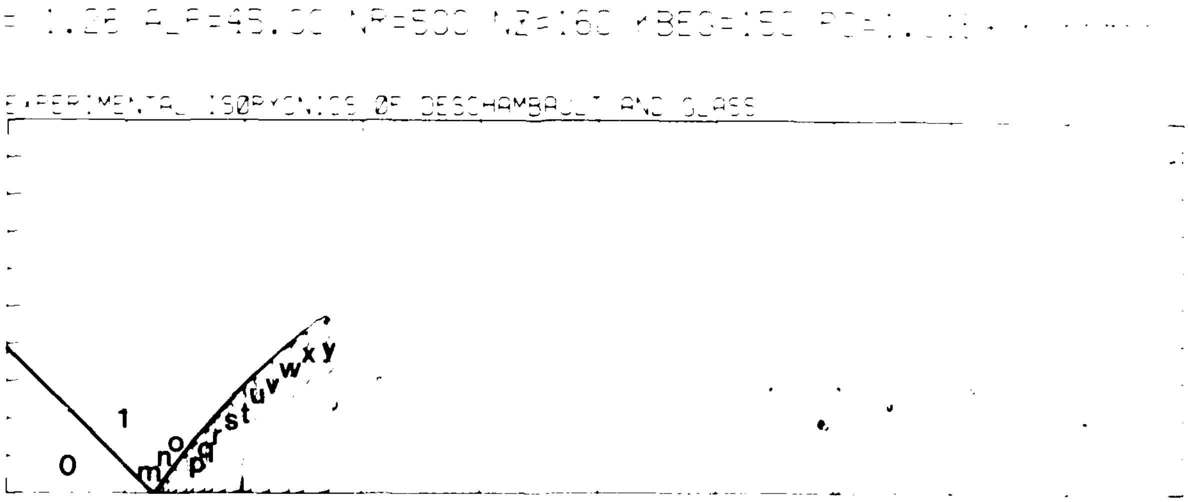

XBB 859-7194

Figure $5b_P$. Calculated isopycnics (γ=1.4) using the experimental fringes

Figure 5. Case 2, M_s = 1.26, θ_w = 45°, Air, γ = 1.4 and Hansen EOS, RP.

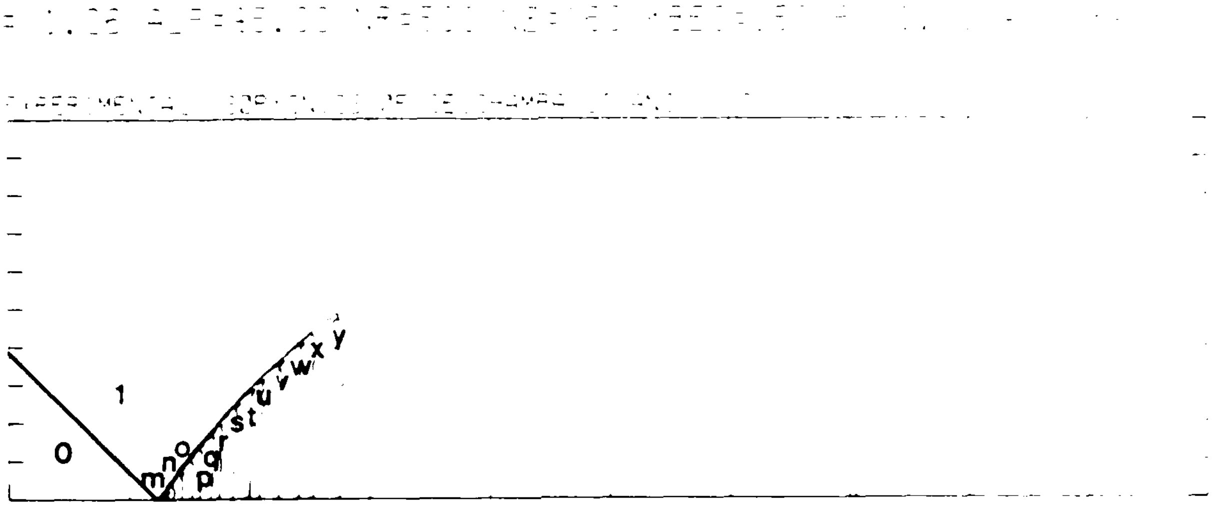

Figure $5b_H$. Calculated isopycnics (Hansen) using the experimental fringes

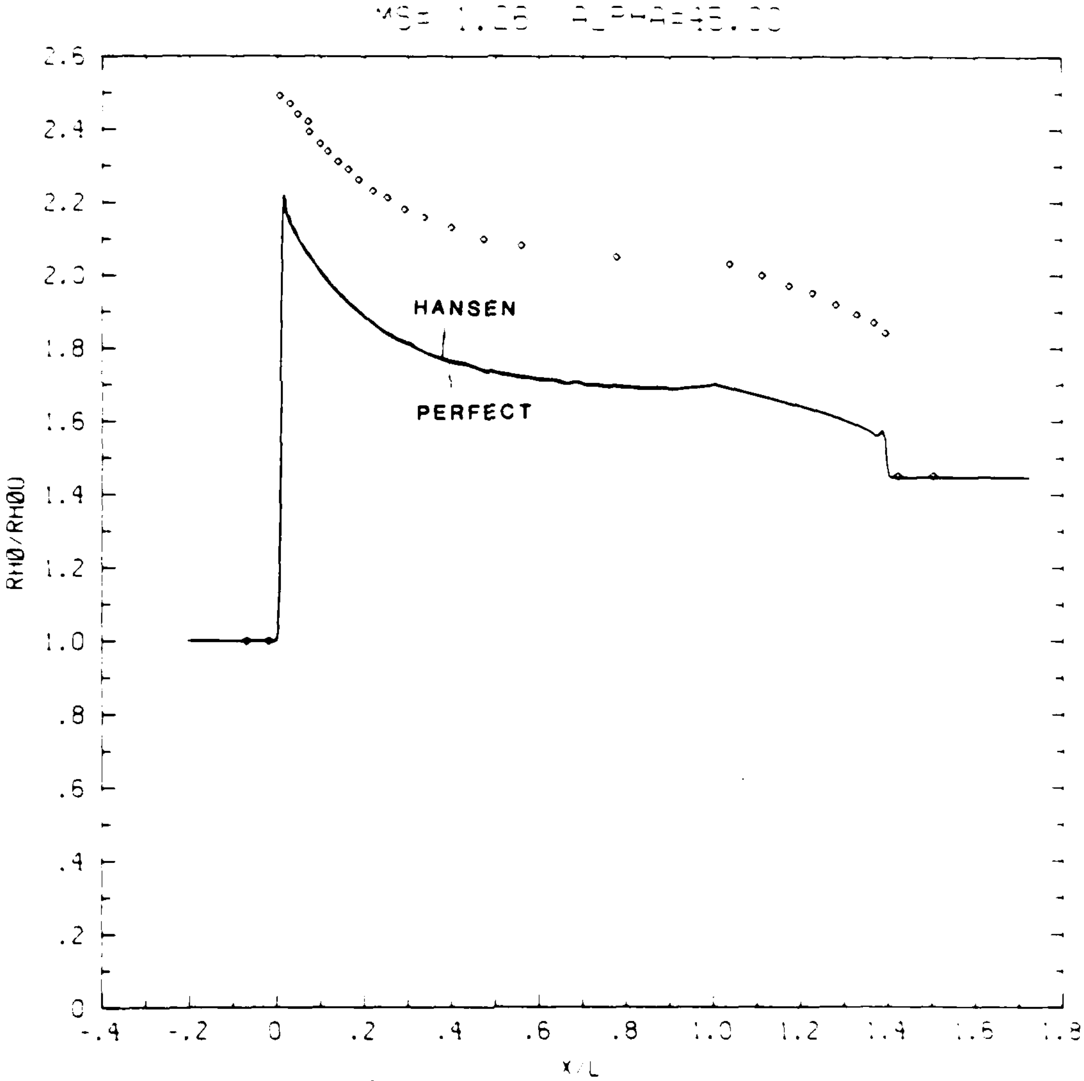

Figure 5c. Wall plot for ρ/ρ_0, γ = 1.4 and Hansen calculations, with experimental data

Figure 5. Case 2, M_s = 1.26, θ = 45°, Air, γ = 1.4 and Hansen EOS, RR - continued.

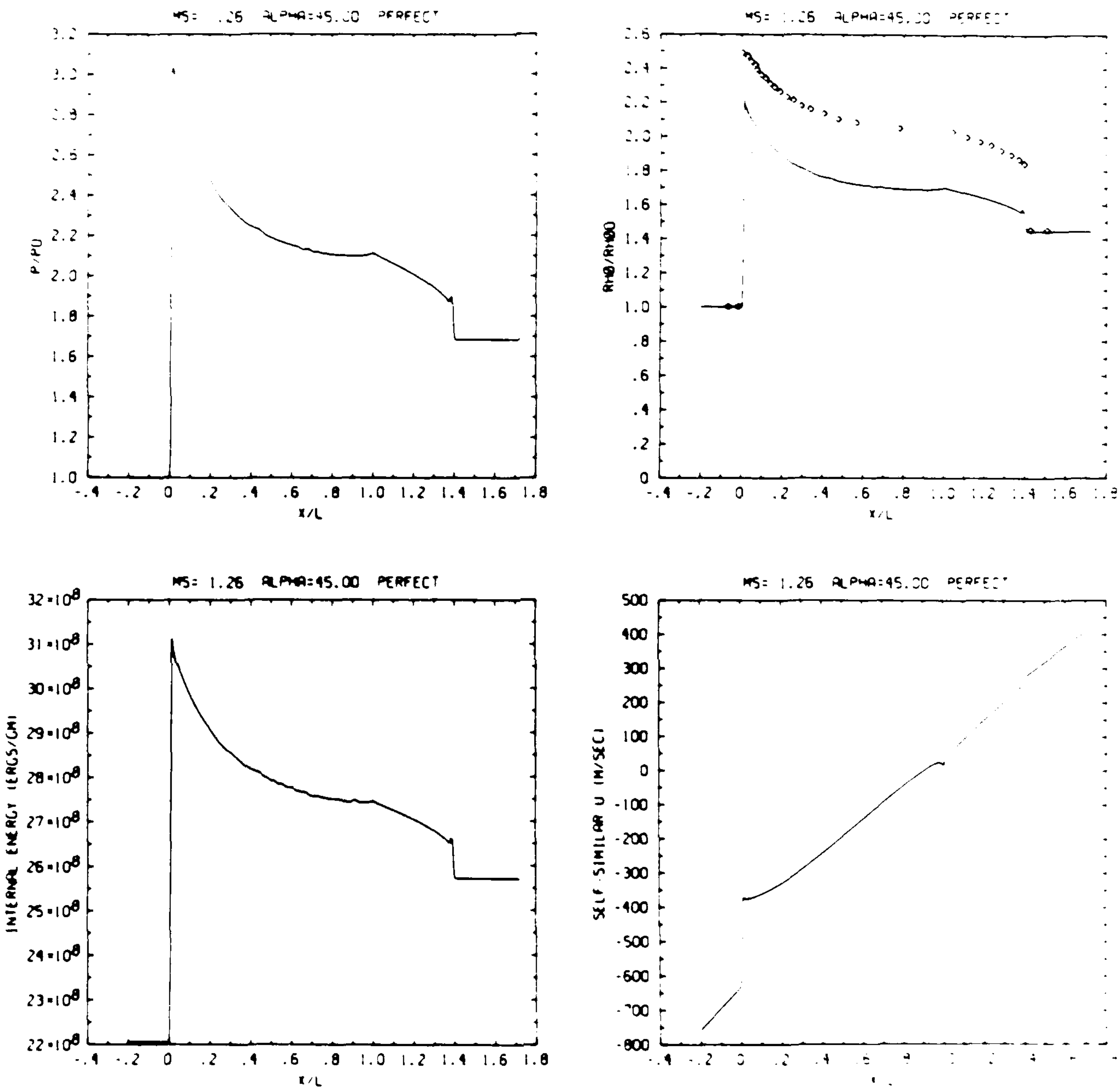

Figure $5c_p$. Wall plot for p/p_0, ρ/ρ_0 with experimental data included, e, u; γ = 1.4.

Figure 5. Case 2, M_s = 1.26, θ = 45°, Air, γ = 1.4 and Hansen EOS, RR - continued.

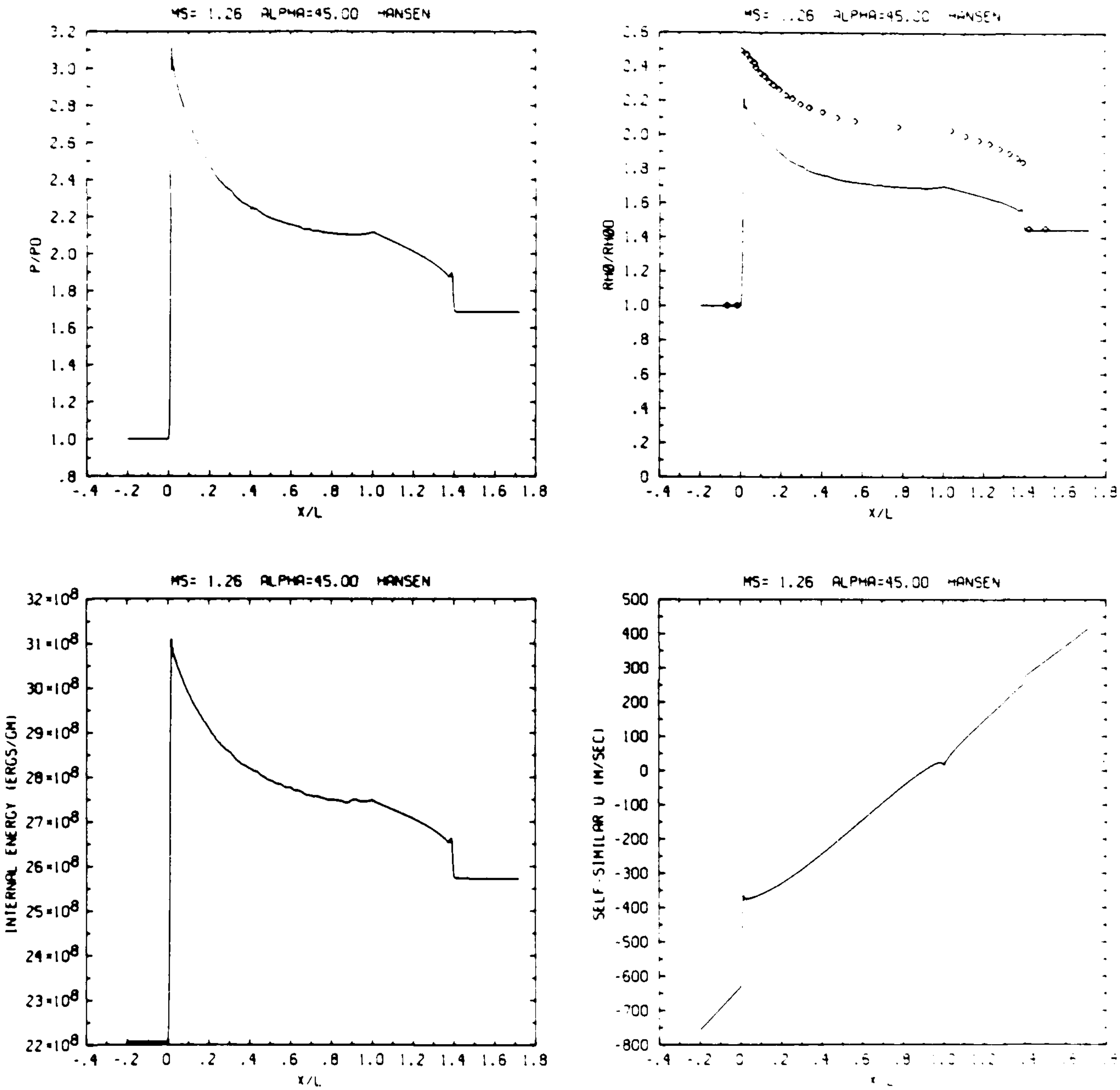

Figure $5c_H$. Wall plot for p/p_0, ρ/ρ_0 with experimental data included, e, u; Hansen.

Figure 5. Case 2, M_s = 1.26, θ = 45°, Air, γ = 1.4 and Hansen EOS, RR - continued.

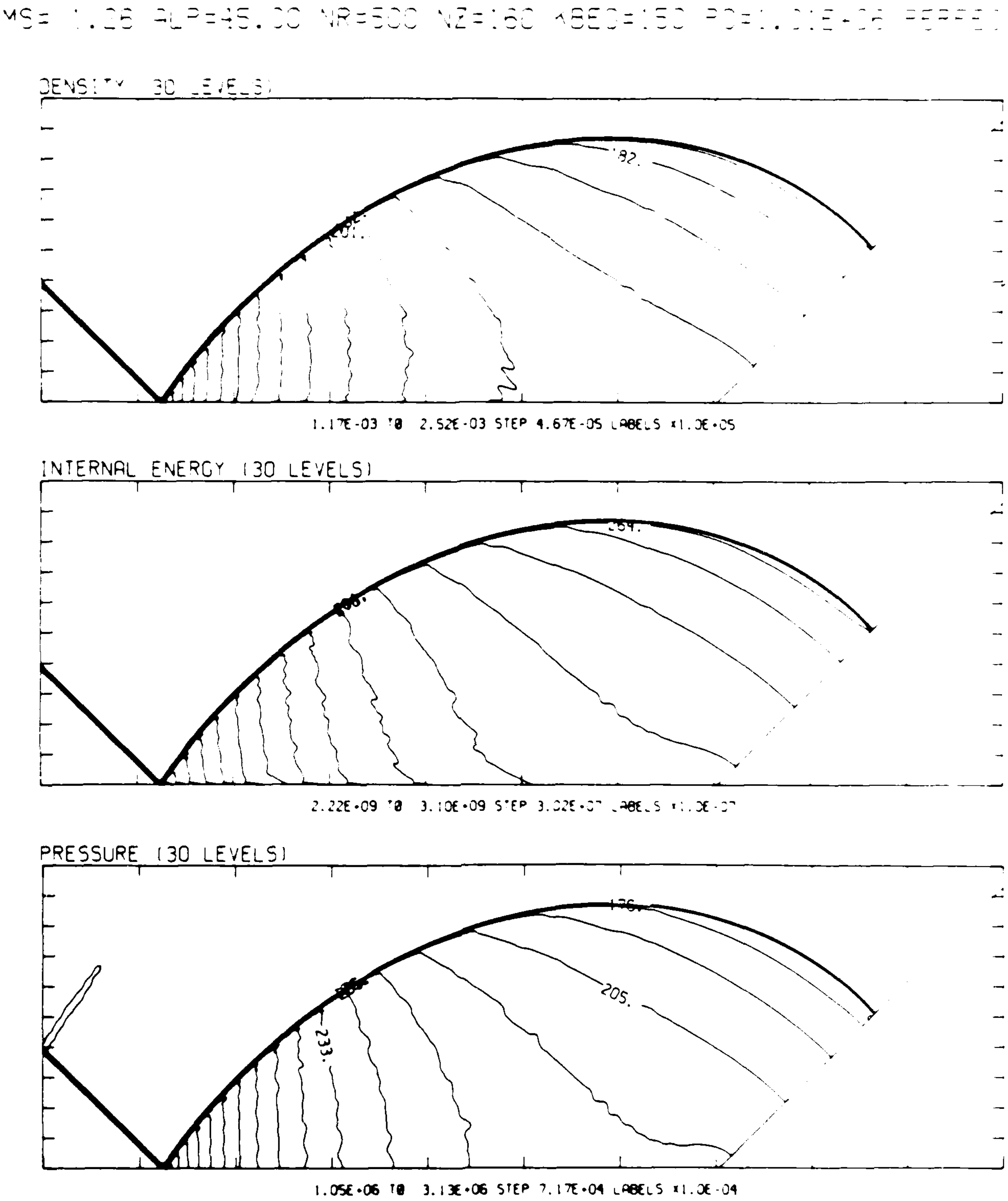

Figure $5d_p$. Whole-flowfield contour-plots; γ = 1.4.

Figure 5. Case 2, M_s = 1.26, θ = 45°, Air, γ = 1.4 and Hansen EOS, RR - continued.

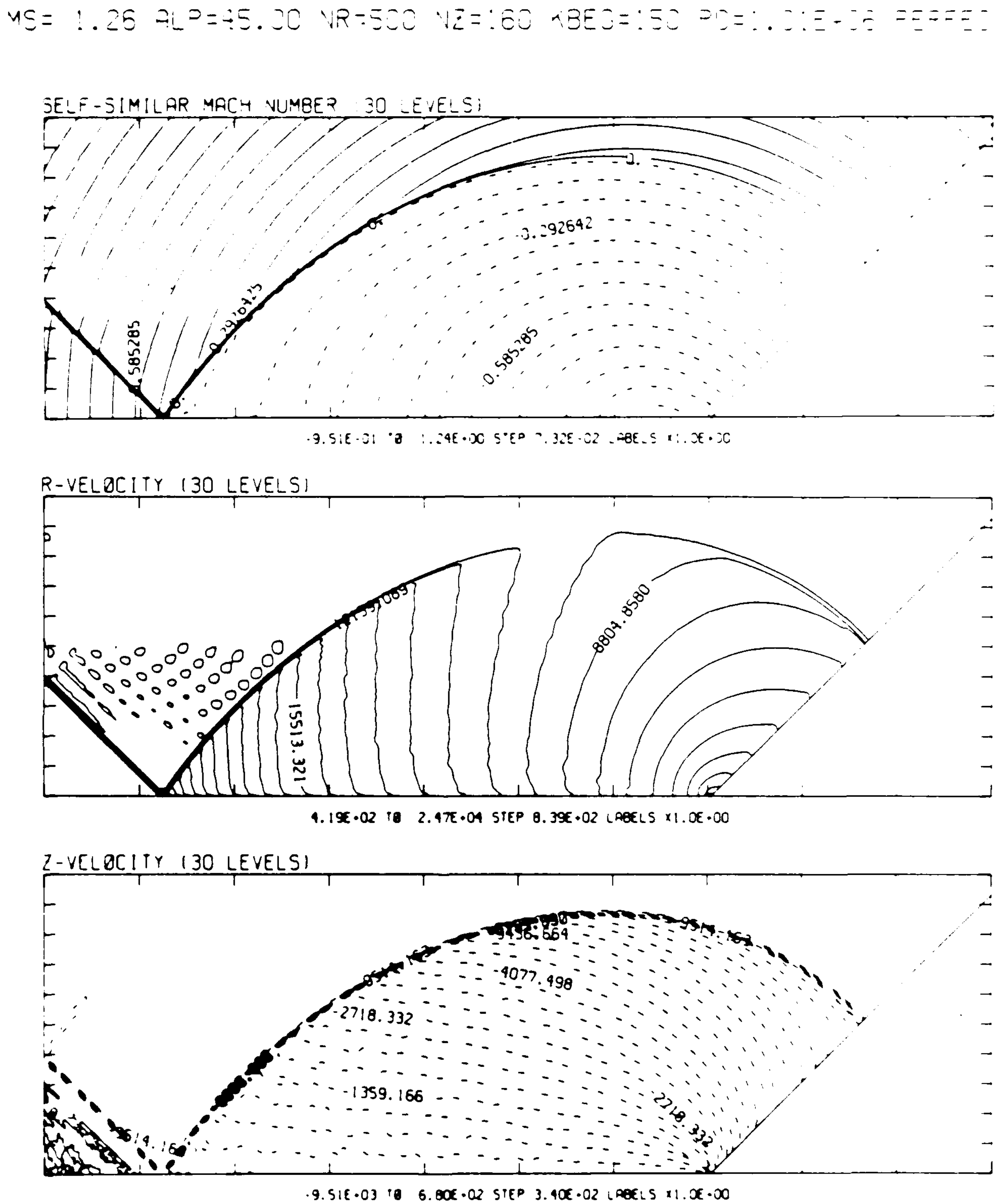

Figure 5d$_p$. Whole-flowfield contour-plots; γ = 1.4 - continued.

Figure 5. Case 2, M_s = 1.26, θ = 45°, Air, γ = 1.4 and Hansen EOS, RR - continued.

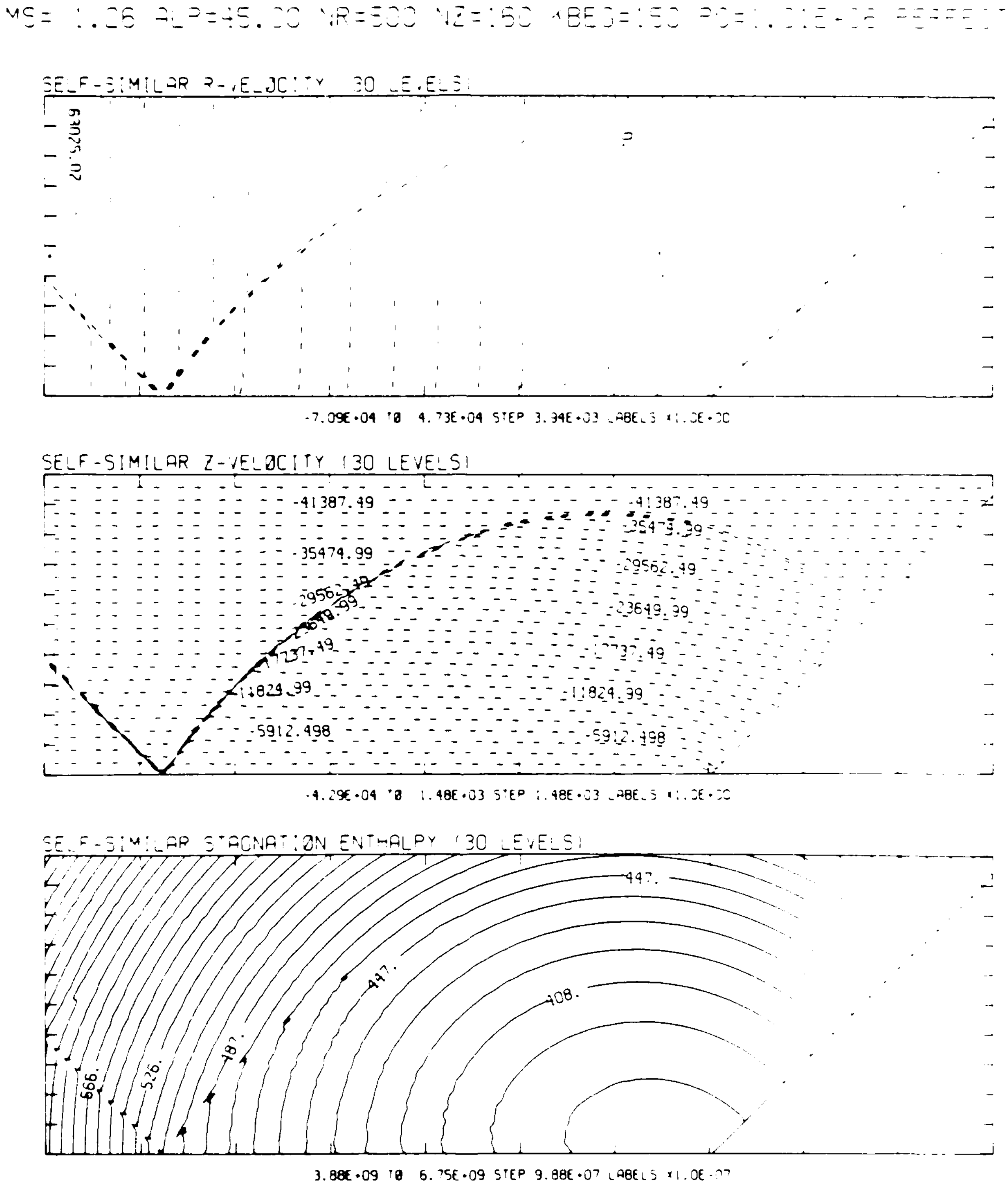

Figure $5d_p$. Whole-flowfield contour-plots; γ = 1.4 - continued.

Figure 5. Case 2, M_s = 1.26, θ = 45°, Air, γ = 1.4 and Hansen EOS, RR - continued.

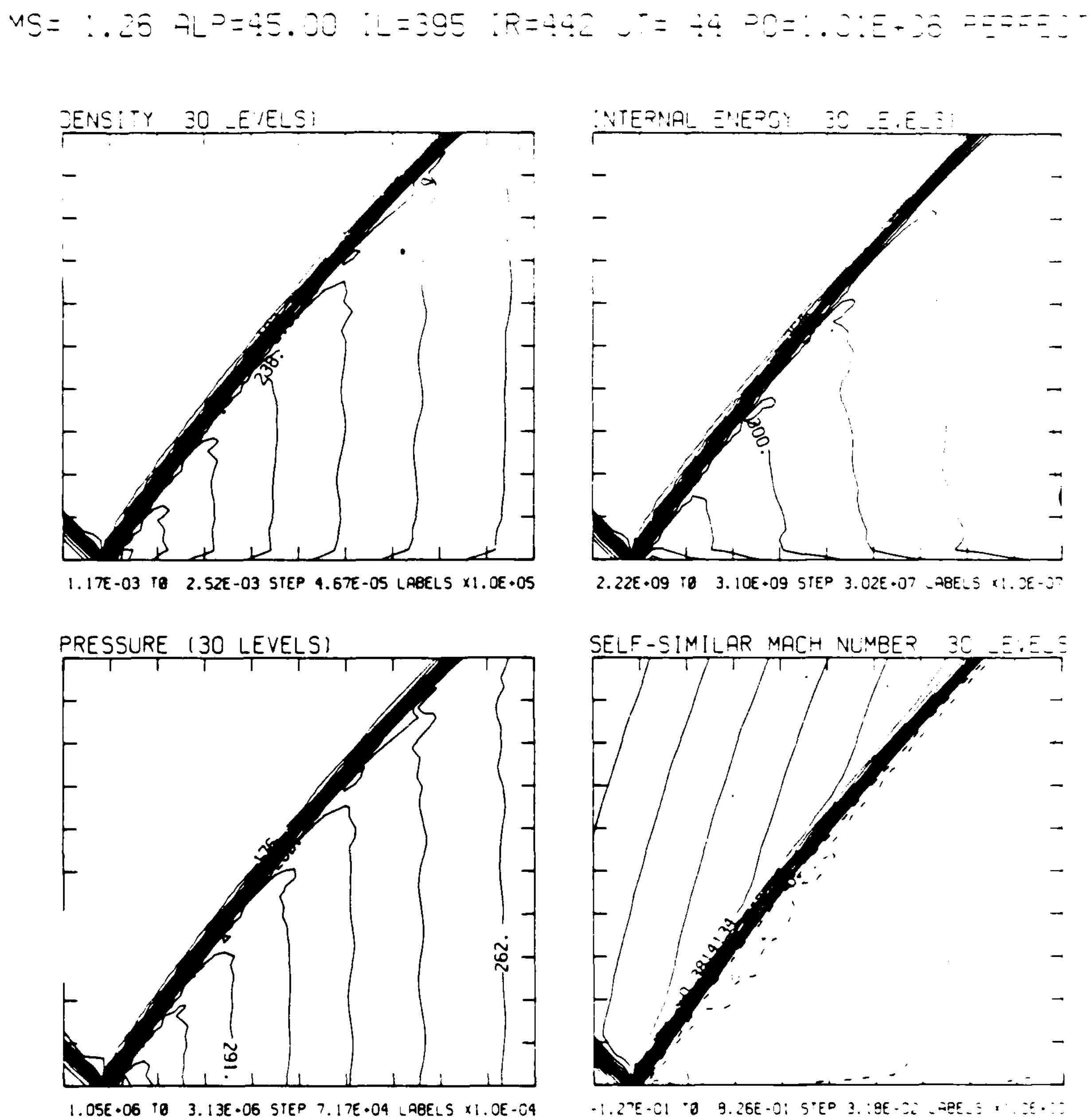

Figure $5e_p$. Blowup-frame plots; $\gamma = 1.4$

Figure 5. Case 2, $M_s = 1.26$, $\theta = 45°$, Air, $\gamma = 1.4$ and Hansen EOS, RR - continued.

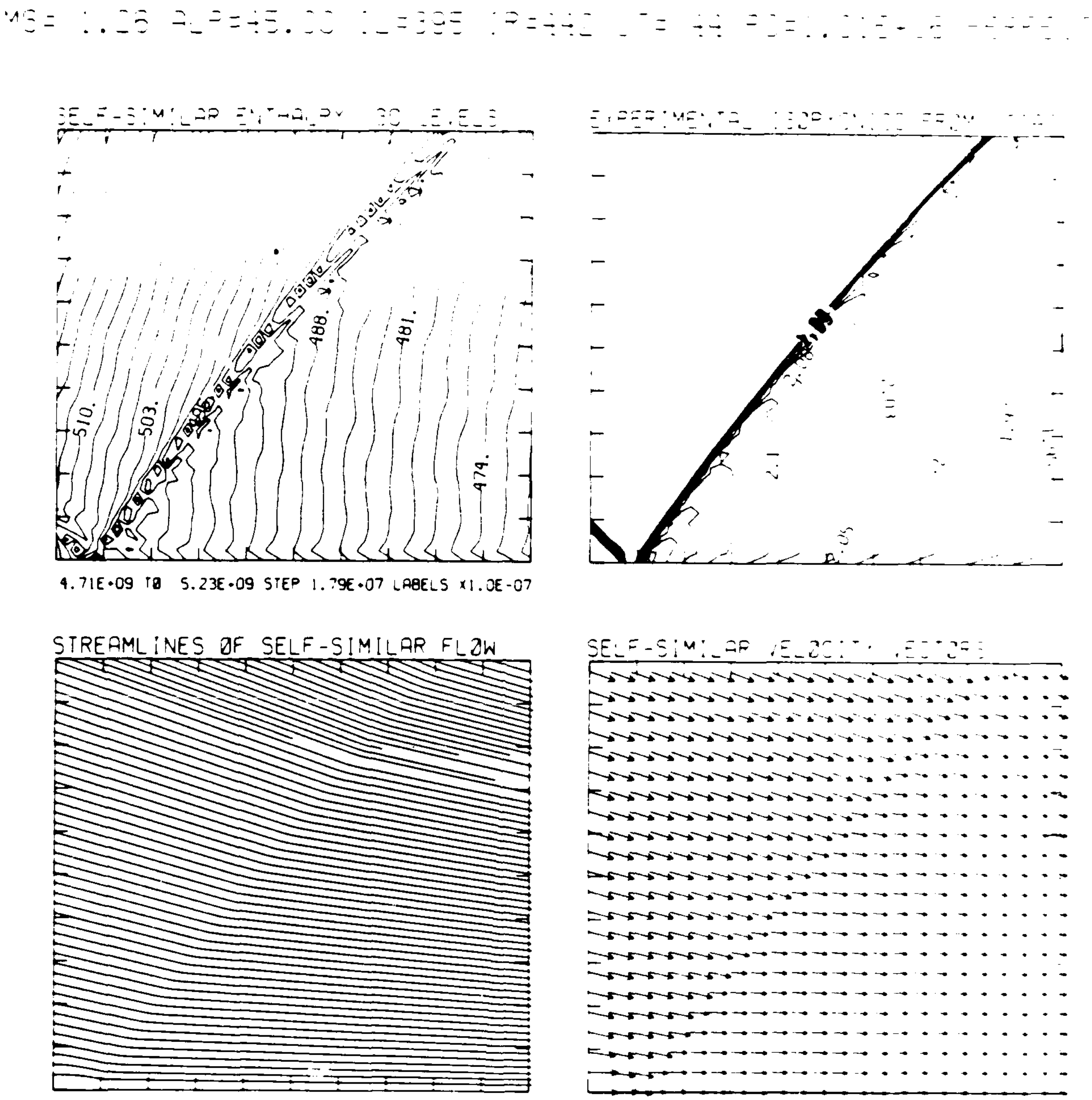

Figure $5e_p$. Blowup-frame plots; γ = 1.4 - continued

Figure 5. Case 2, M_s = 1.26, θ = 45°, Air, γ = 1.4 and Hansen EOS, RR - continued.

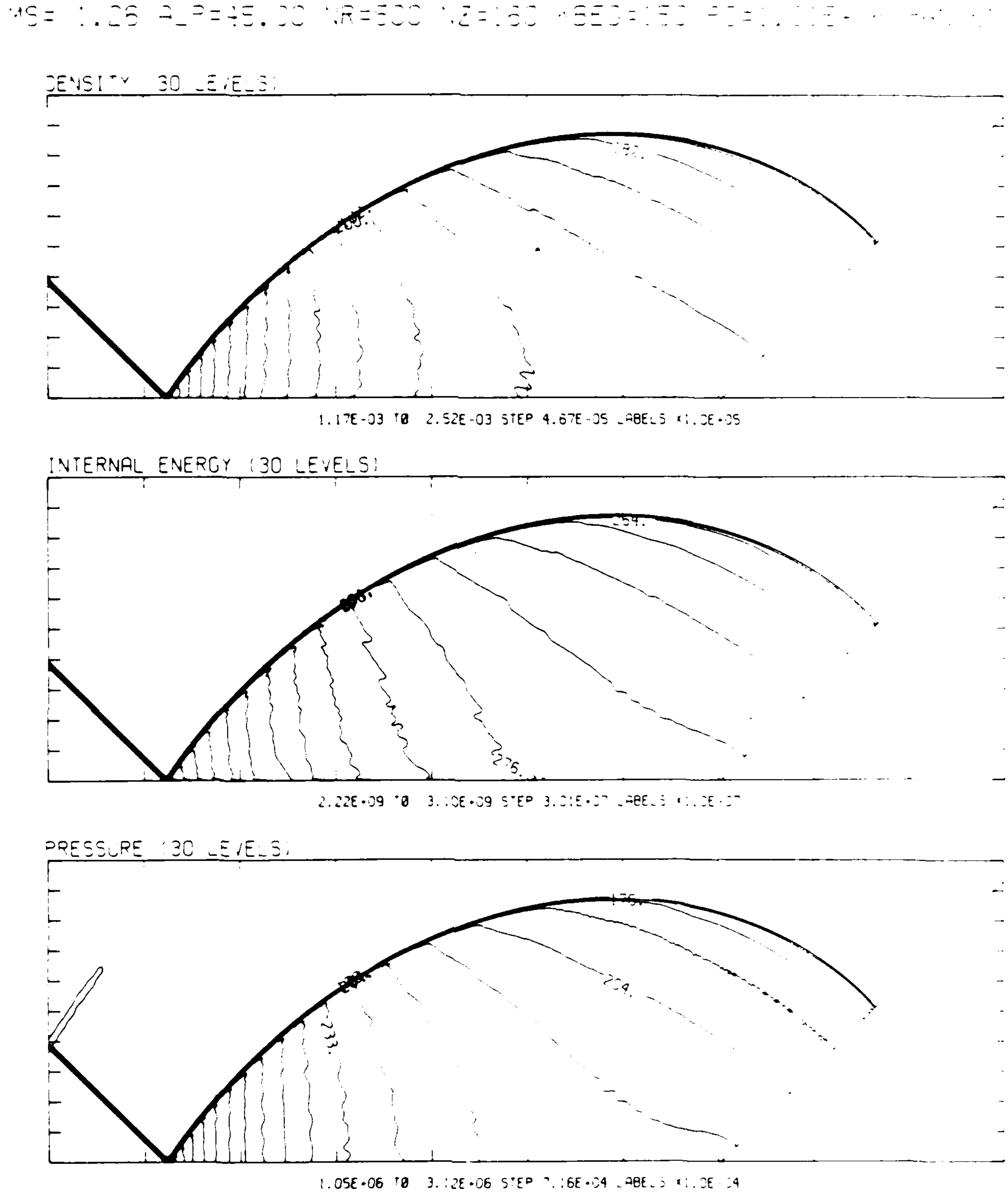

Figure $5d_H$. Whole-flowfield contour-plots; Hansen

Figure 5. Case 2, M_s = 1.26, θ = 45°, Air, γ = 1.4 and Hansen EOS, RR - continued.

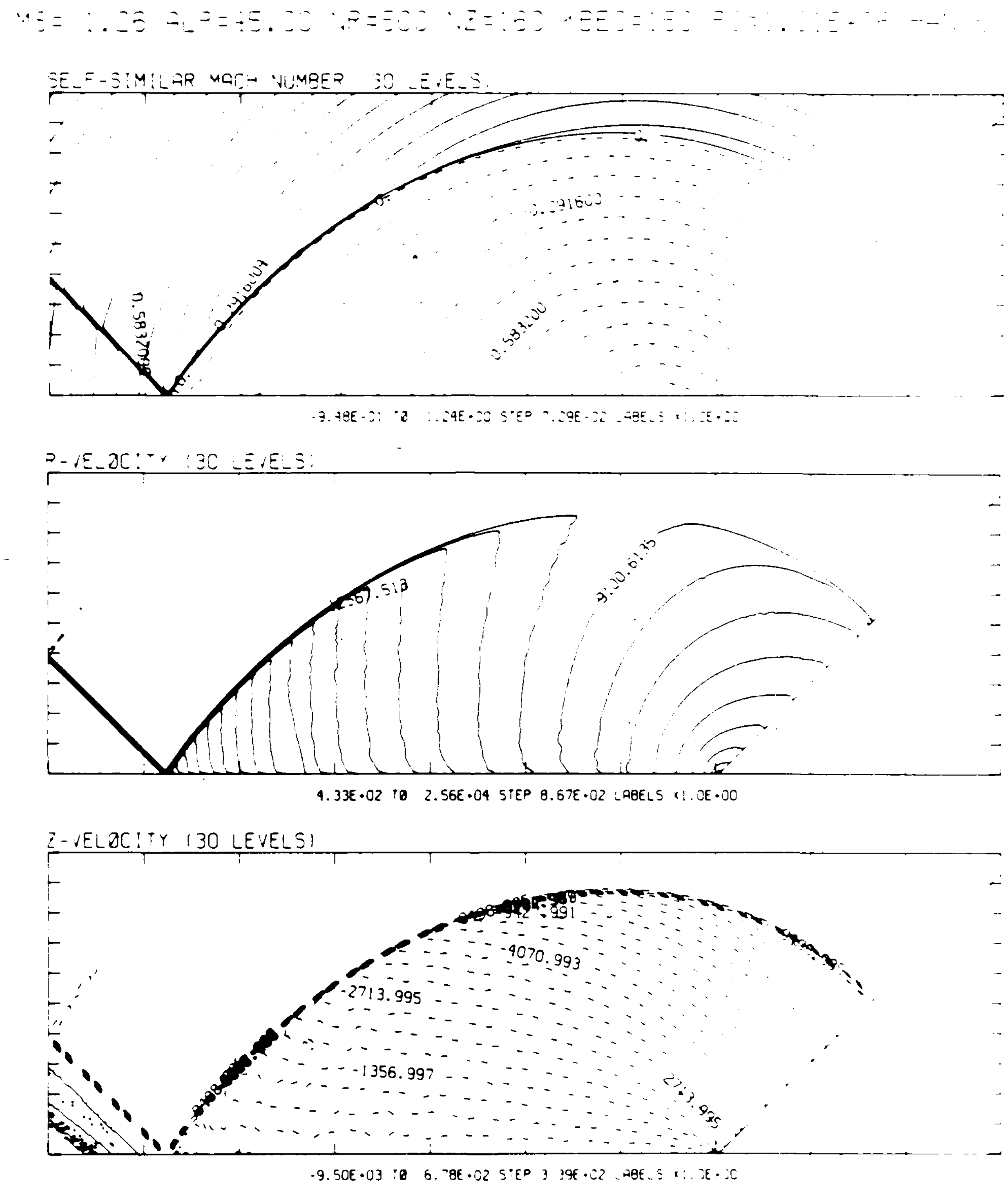

Figure $5d_H$. Whole-flowfield contour-plots; Hansen - continued

Figure 5. Case 2, M_S = 1.26, θ = 45°, Air, γ = 1.4 and Hansen EOS, RR - continued.

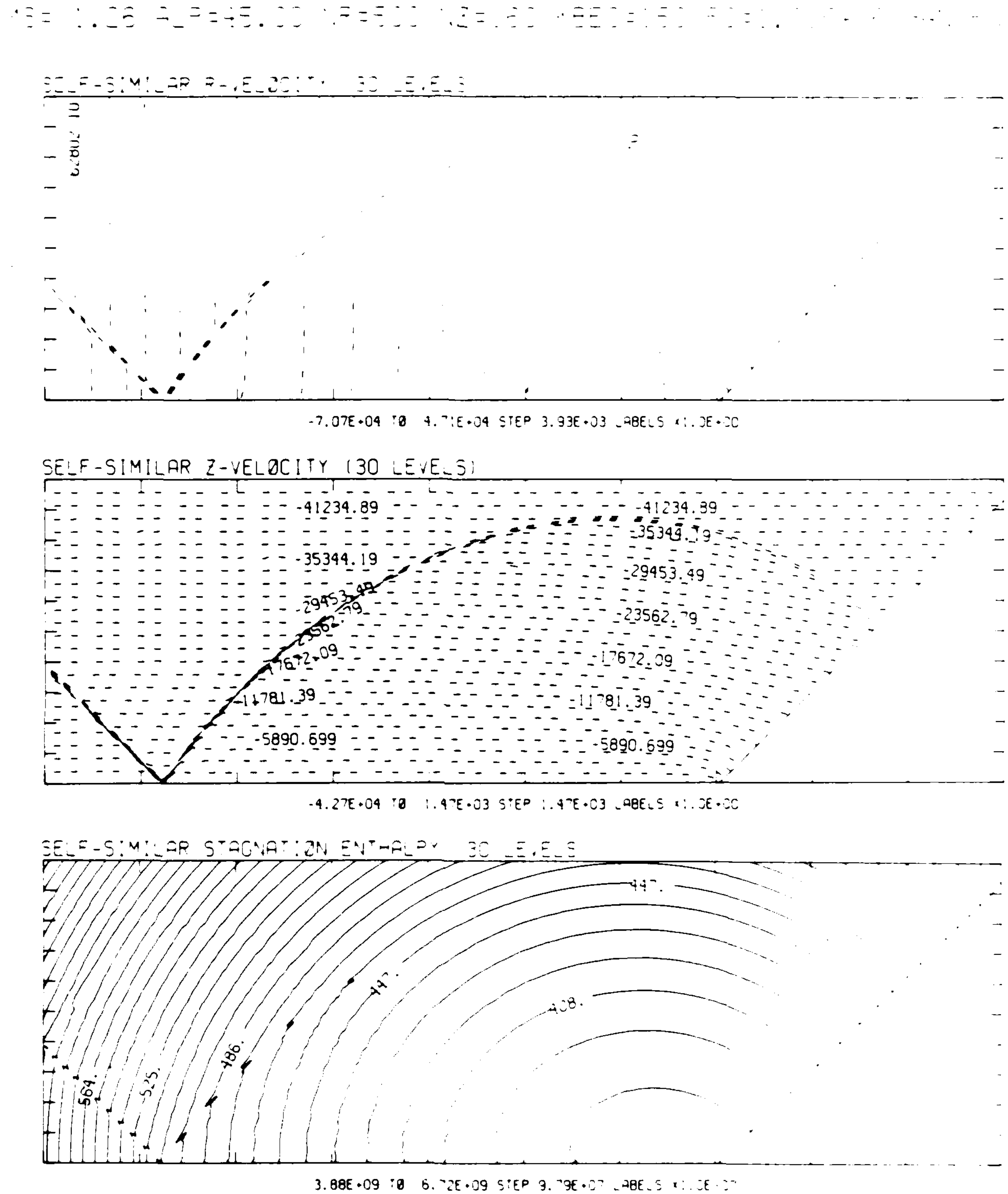

Figure 5d$_H$. Whole-flowfield contour-plots; Hansen - continued

Figure 5. Case 2, M_s = 1.26, θ = 45°, Air, γ = 1.4 and Hansen EOS, RR - continued.

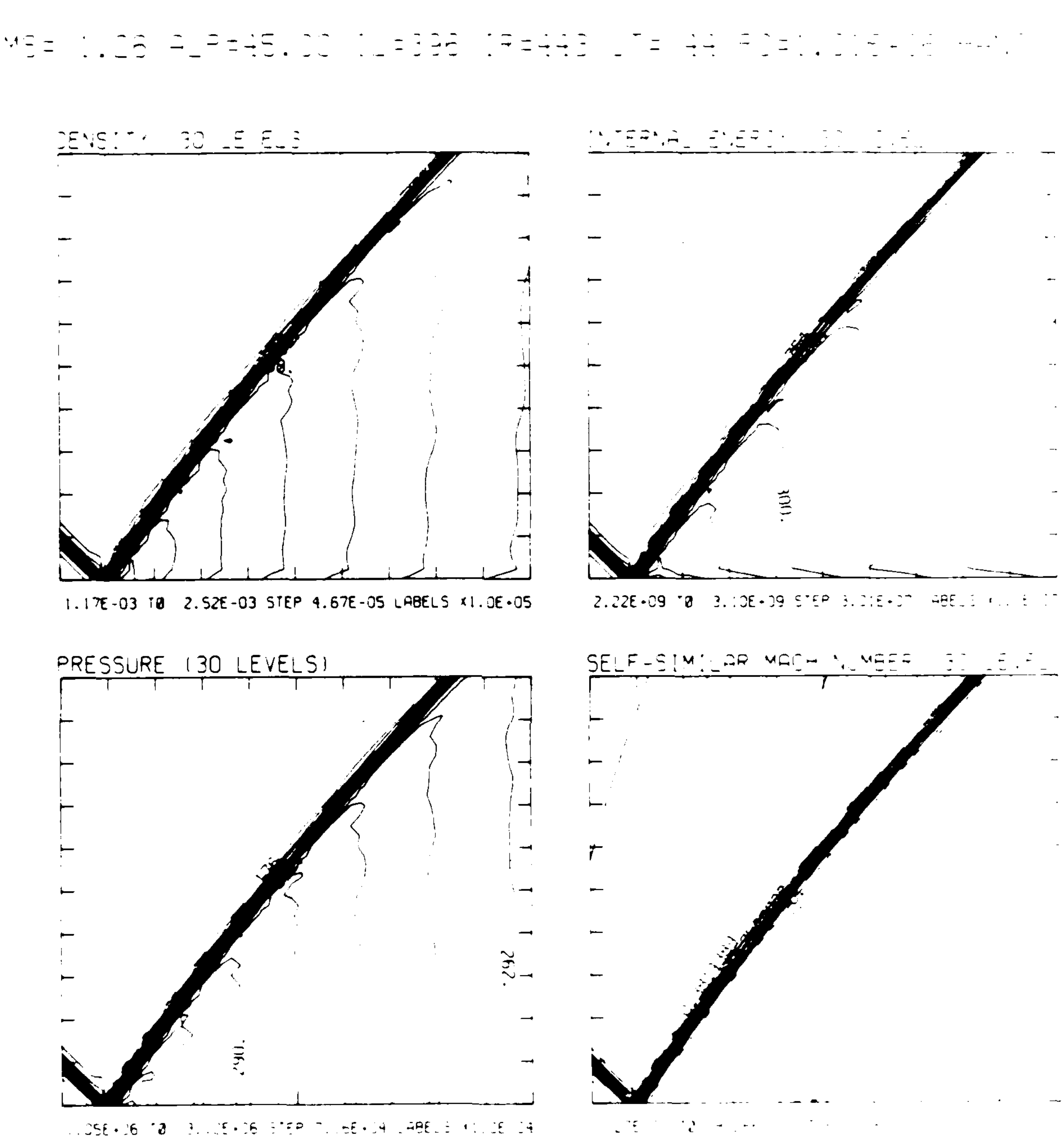

Figure $5e_H$. Blowup-frame plots; Hansen

Figure 5. Case 2, M_s = 1.26, θ = 45°, Air, γ = 1.4 and Hansen EOS, RR - continued.

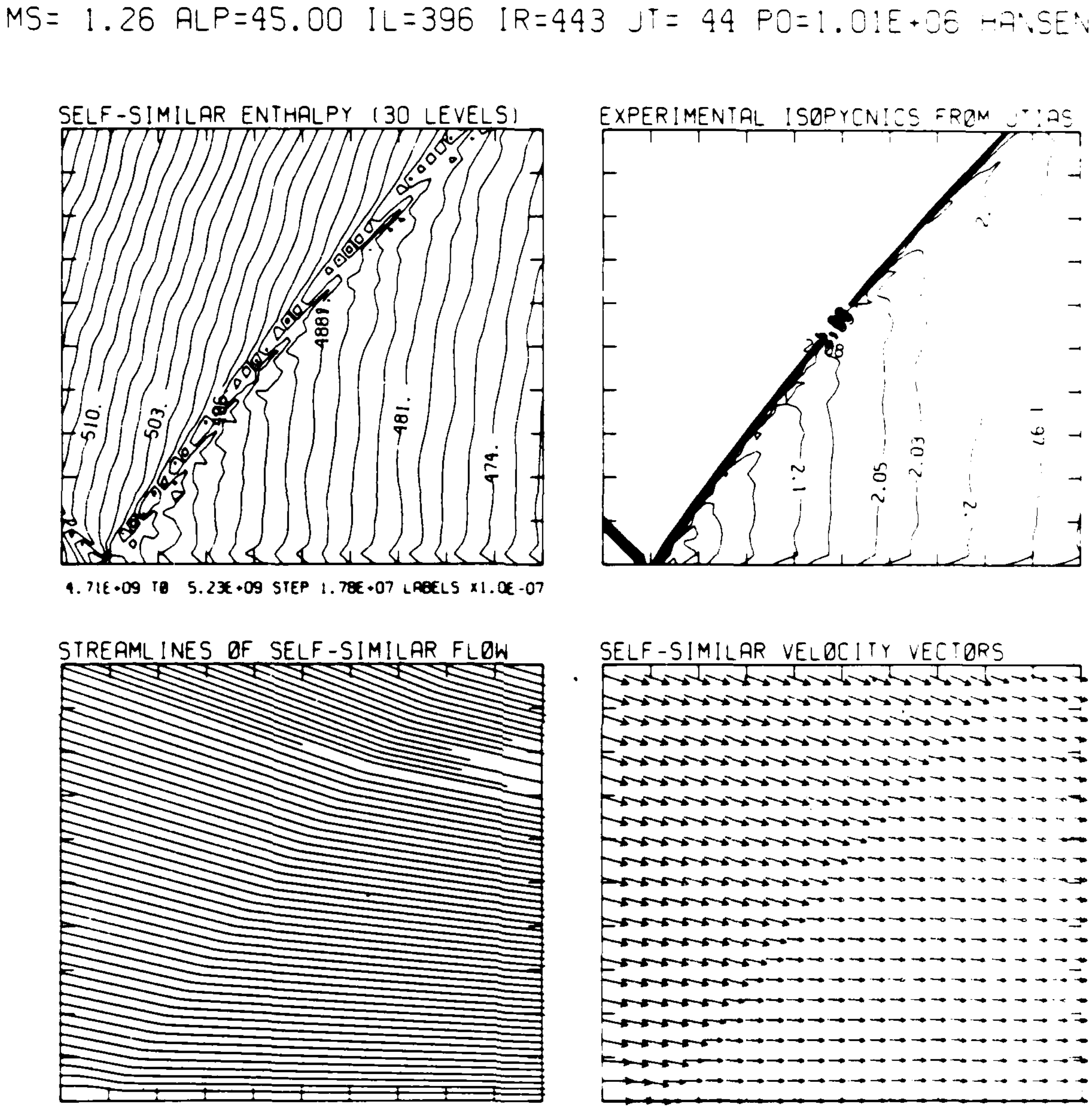

Figure $5e_H$. Blowup-frame plots; Hansen - continued

Figure 5. Case 2, M_S = 1.26, θ = 45°, Air, γ = 1.4 and Hansen EOS, RR - continued.

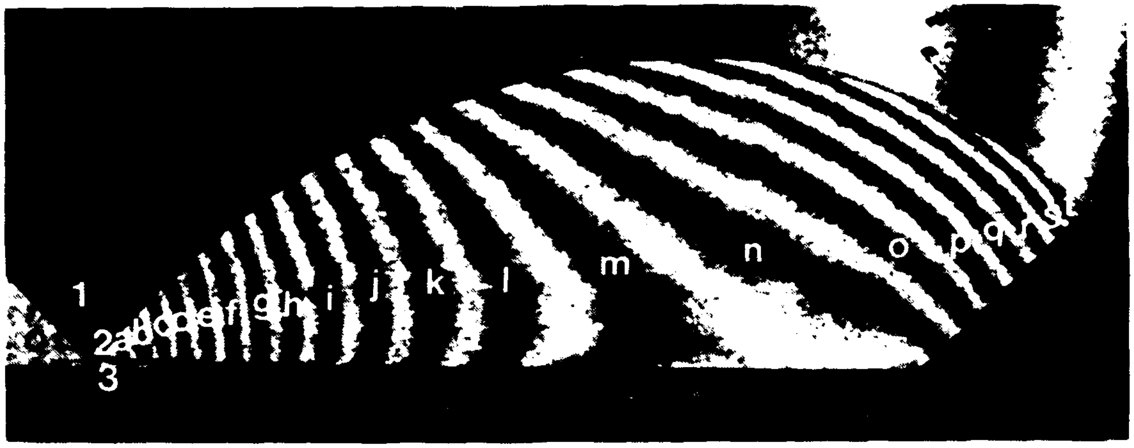

Region	ρ/ρ_0	Region	ρ/ρ_0
0	1.00	i	2.75
1	1.86	j	2.69
2	3.22	k	2.64
3	2.93	l	2.59
a	3.17	m	2.54
b	3.11	n	2.48
c	3.06	o	2.43
d	3.01	p	2.38
e	2.96	q	2.33
f	2.90	r	2.28
g	2.85	s	2.22
h	2.80	t	2.17

Figure 6a. Interferogram

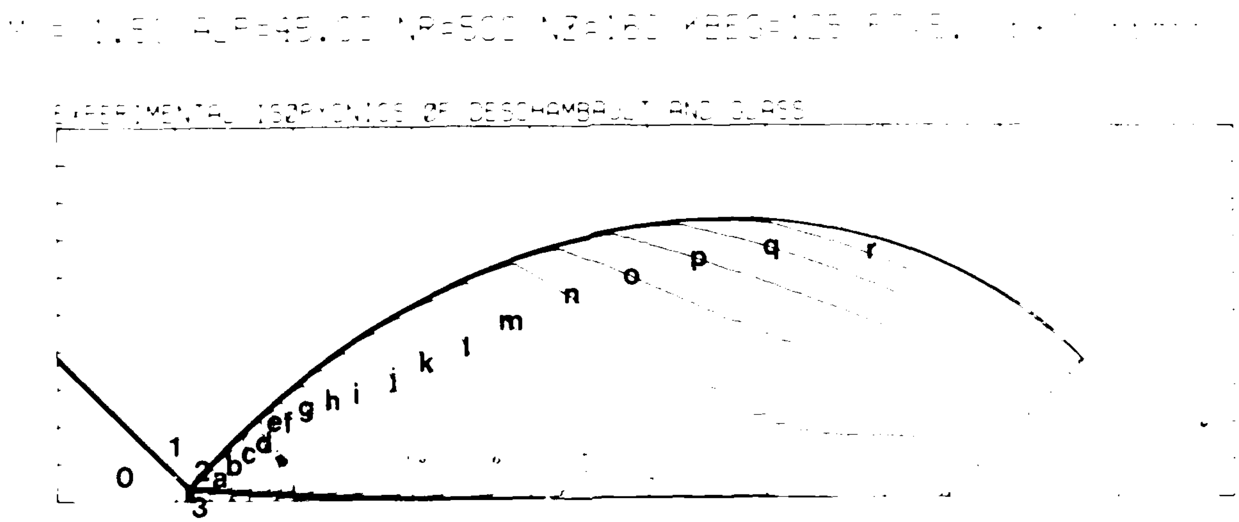

XBB 859-7195

Figure 6b. Calculated isopycnics (γ=1.4) using the experimental fringes.

Figure 6. Case 3, M_S = 1.50, θ_w = 45°, Air, γ = 1.4 and Hansen EOS, SMR - continued

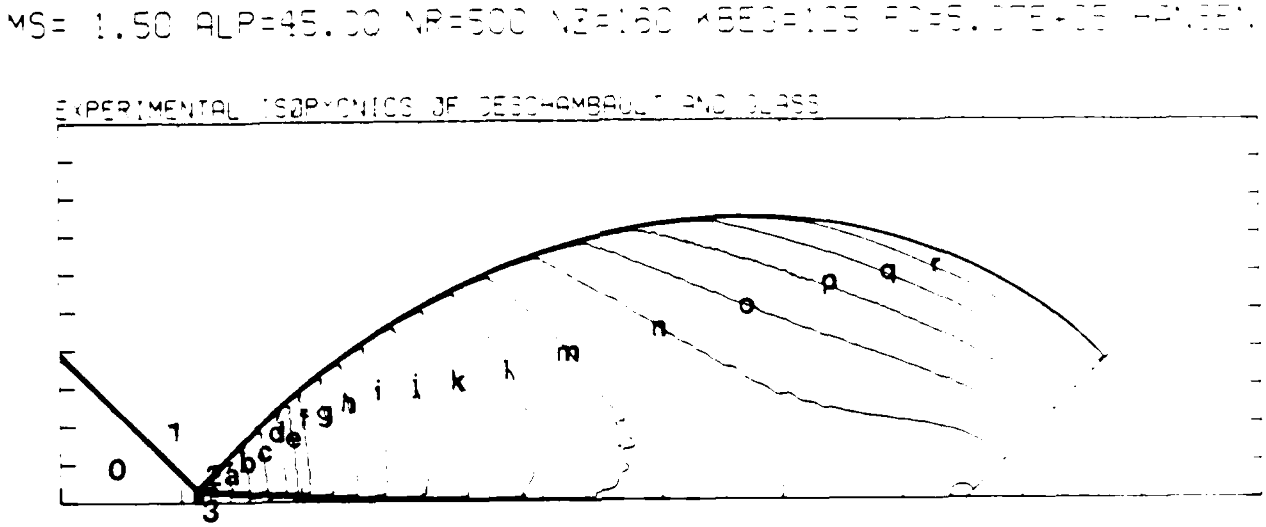

Figure 6b$_H$. Calculated isopycnics (Hansen) using the experimental fringes

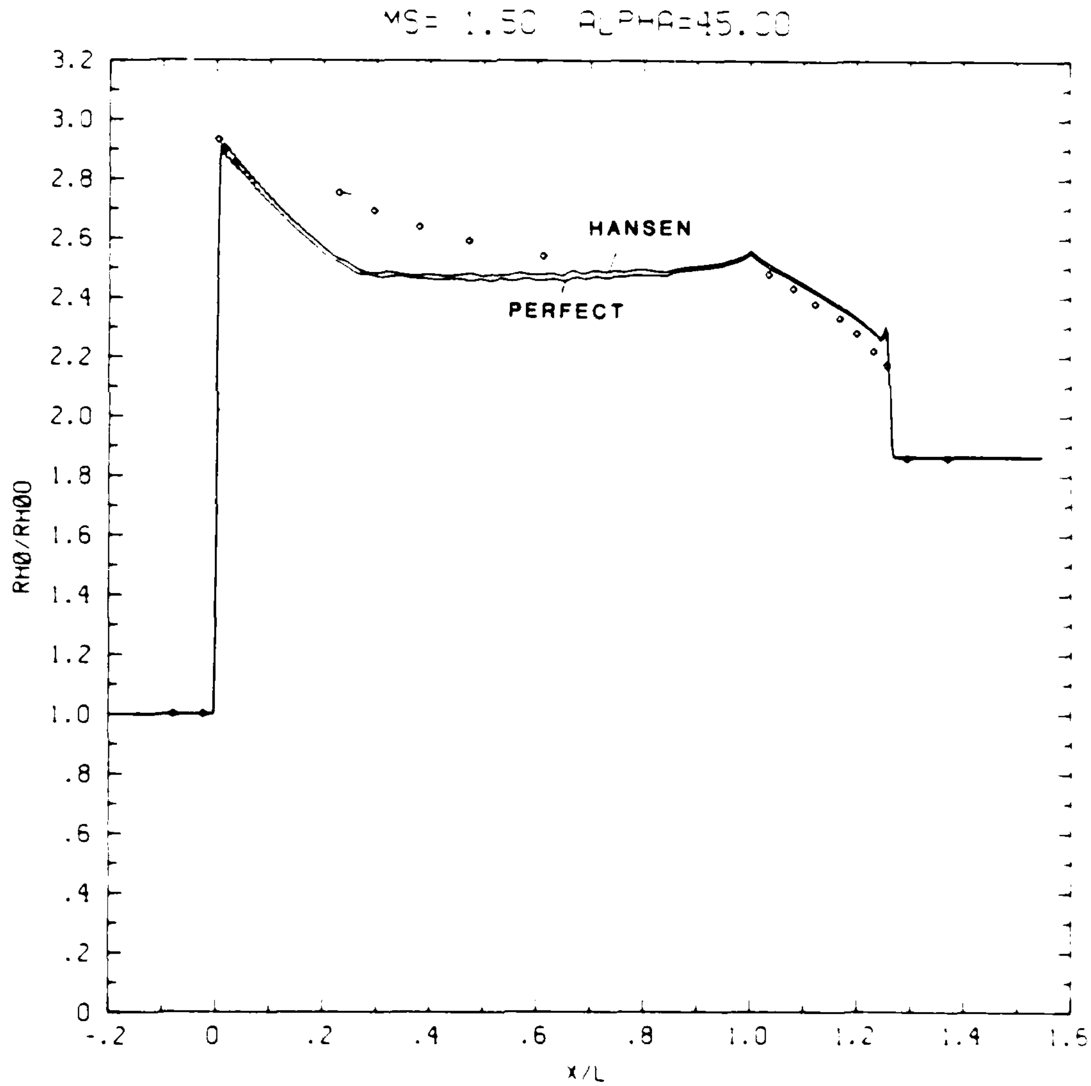

Figure 6c. Wall plot for ρ/ρ_0, γ = 1.4 and Hansen calculations, with experimental data.

Figure 6. Case 3, M_s = 1.50, θ_w = 45°, Air, γ = 1.4 and Hansen EOS, SMR - continued

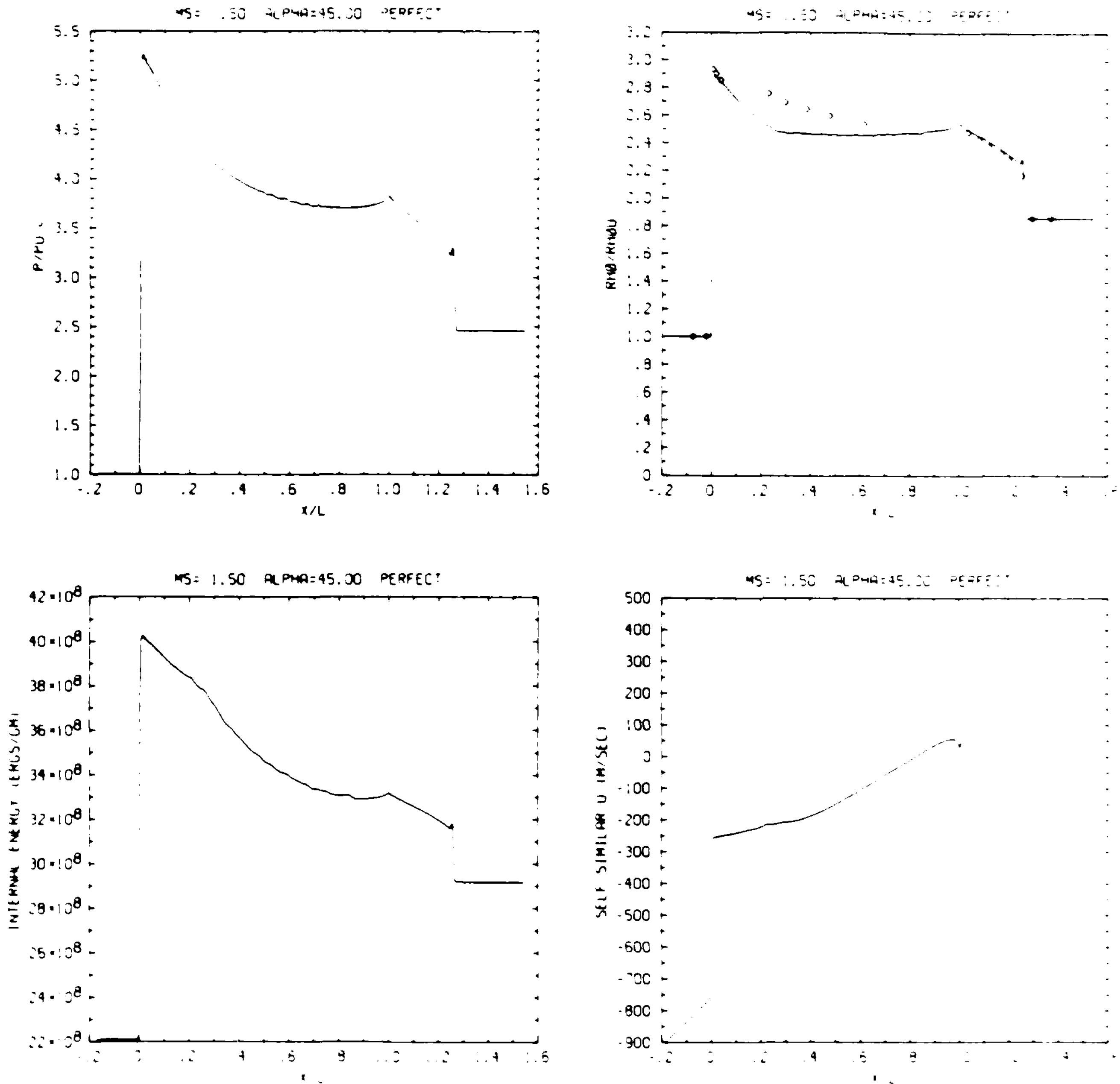

Figure $6c_p$. Wall plot for p/p_0, ρ/ρ_0 with experimental data included, e, u; $\gamma = 1.4$.

Figure 6. Case 3, $M_s = 1.50$, $\theta_w = 45°$, Air, $\gamma = 1.4$ and Hansen EOS, SMR - continued

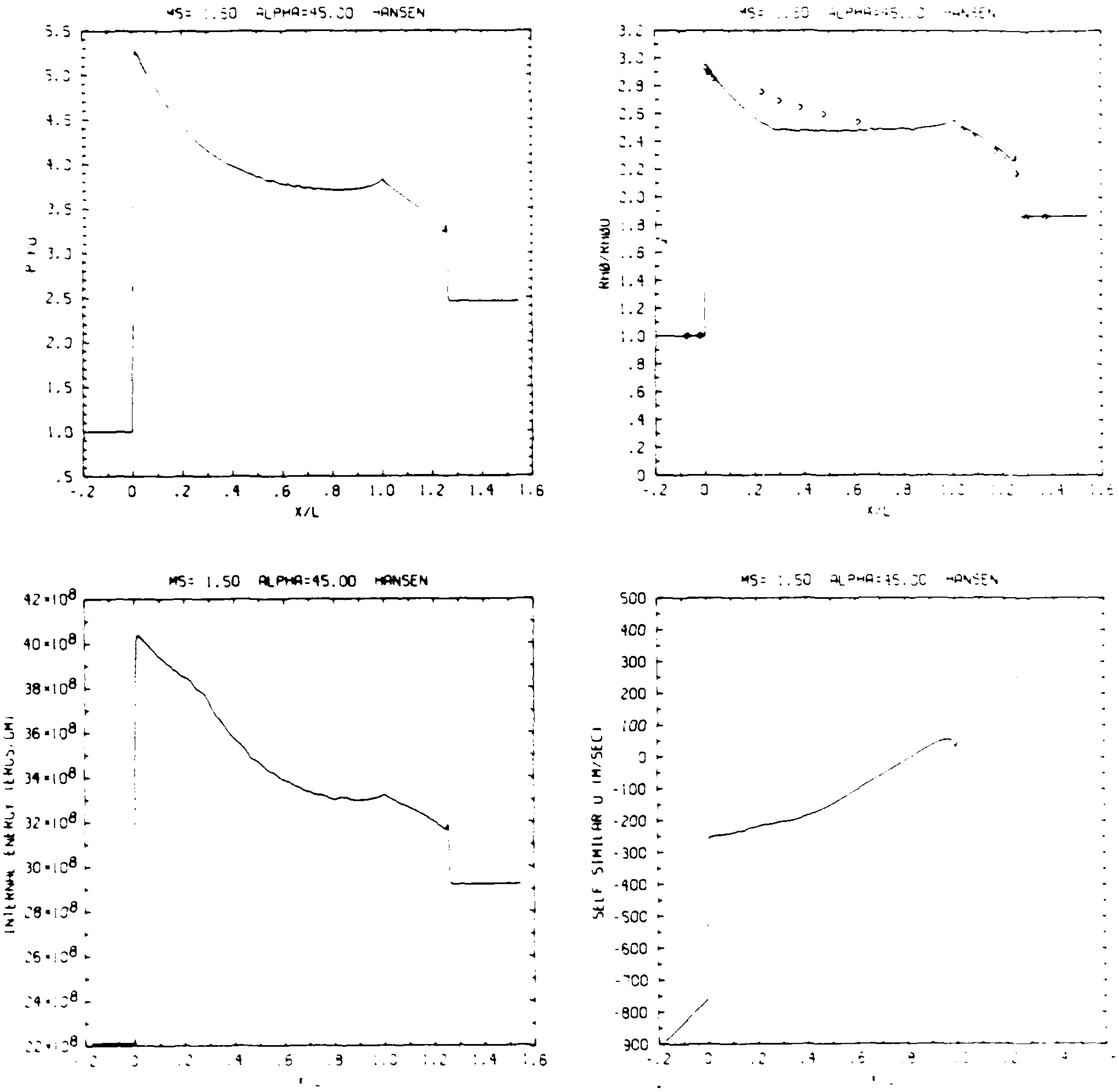

Figure $6c_H$. Wall plot for p/p_0, ρ/ρ_0 with experimental data included, e, u; Hansen

Figure 6. Case 3, M_s = 1.50, θ_w = 45°, Air, γ = 1.4 and Hansen EOS, SMR - continued

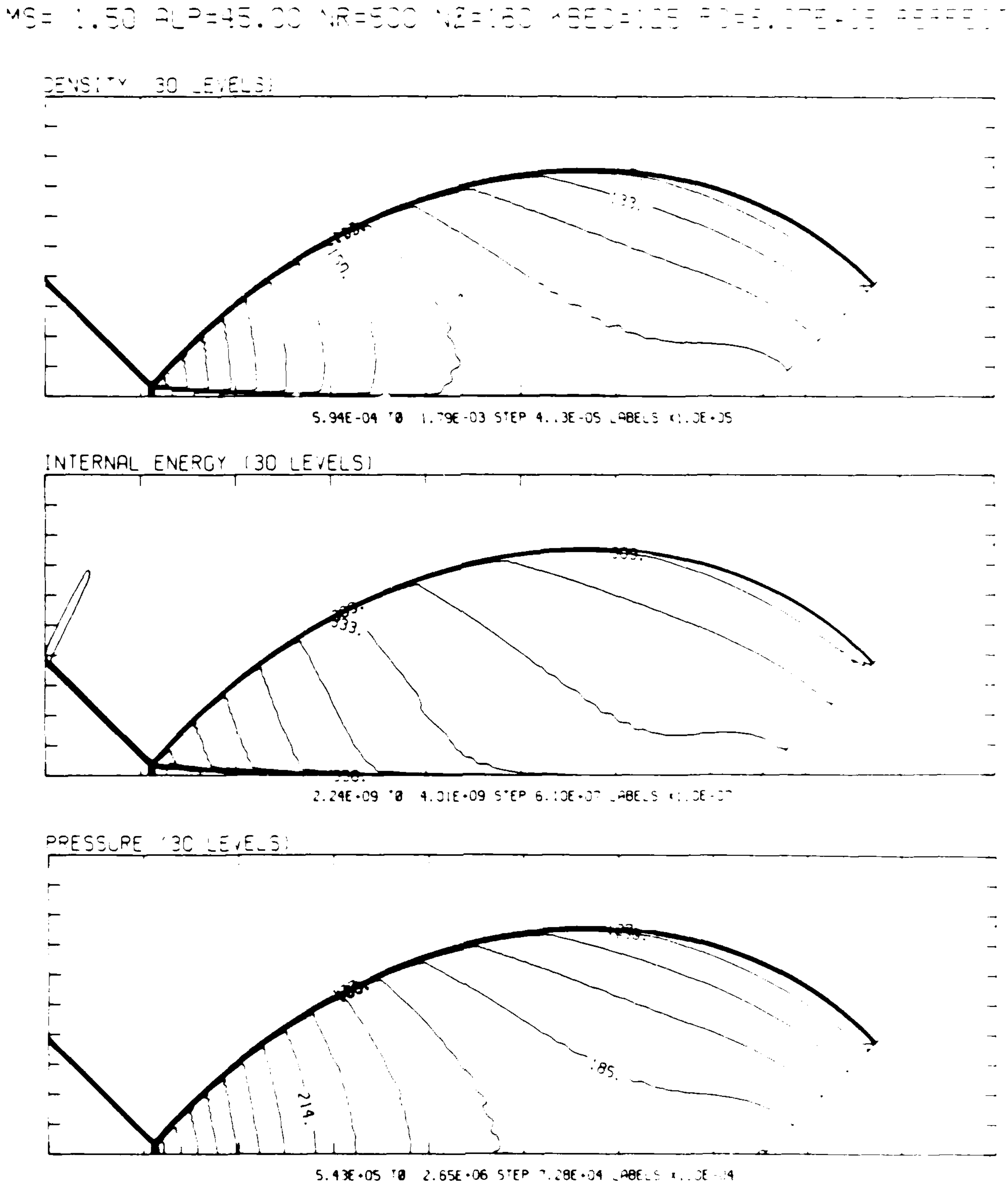

Figure 6dp. Whole-flowfield contour-plots; γ = 1.4

Figure 6. Case 3, M_s = 1.50, θ_w = 45°, Air, γ = 1.4 and Hansen EOS, SMR - continued

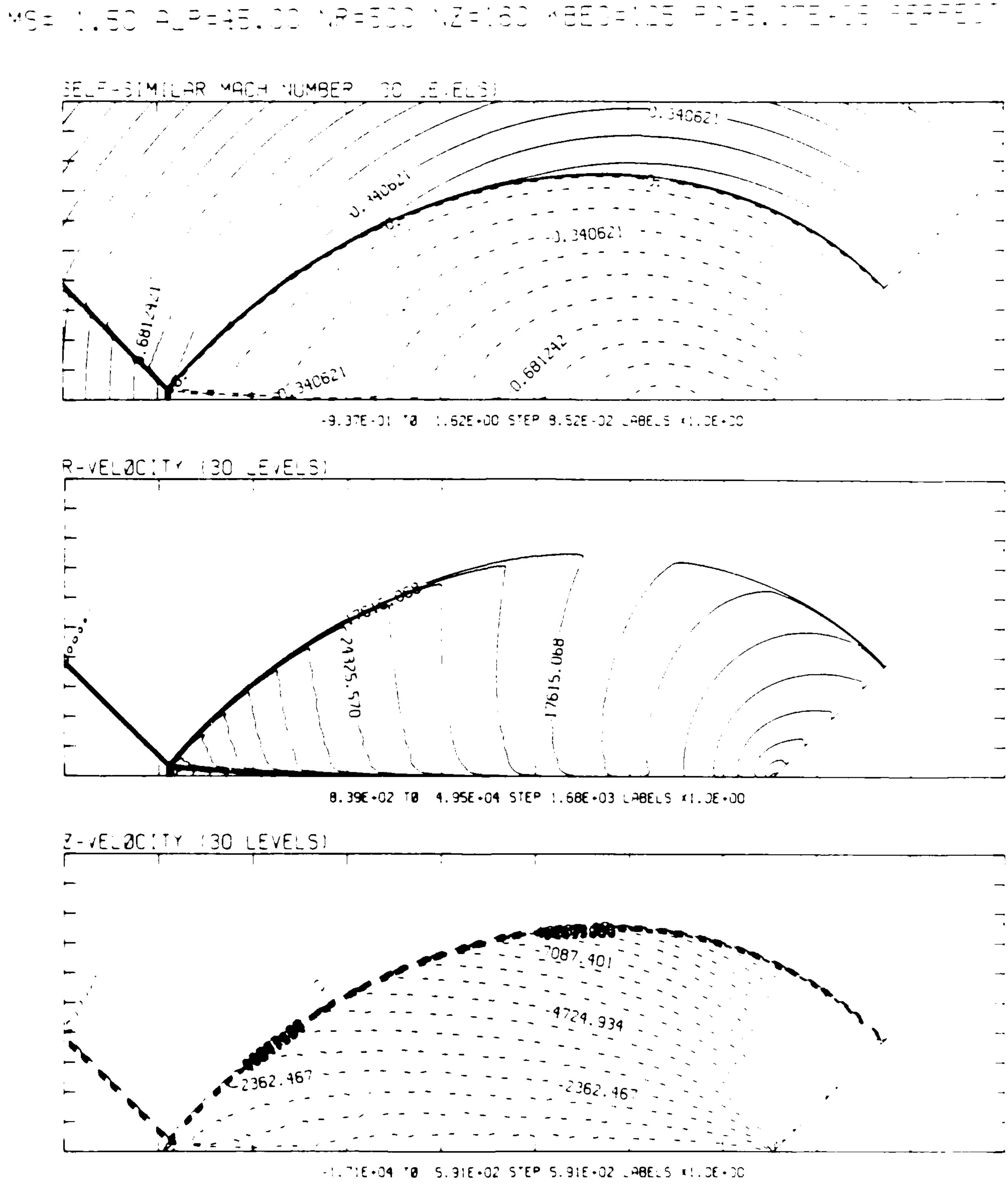

Figure $6d_p$. Whole-flowfield contour-plots; γ = 1.4 - continued

Figure 6. Case 3, M_s = 1.50, θ_w = 45°, Air, γ = 1.4 and Hansen EOS, SMR - continued

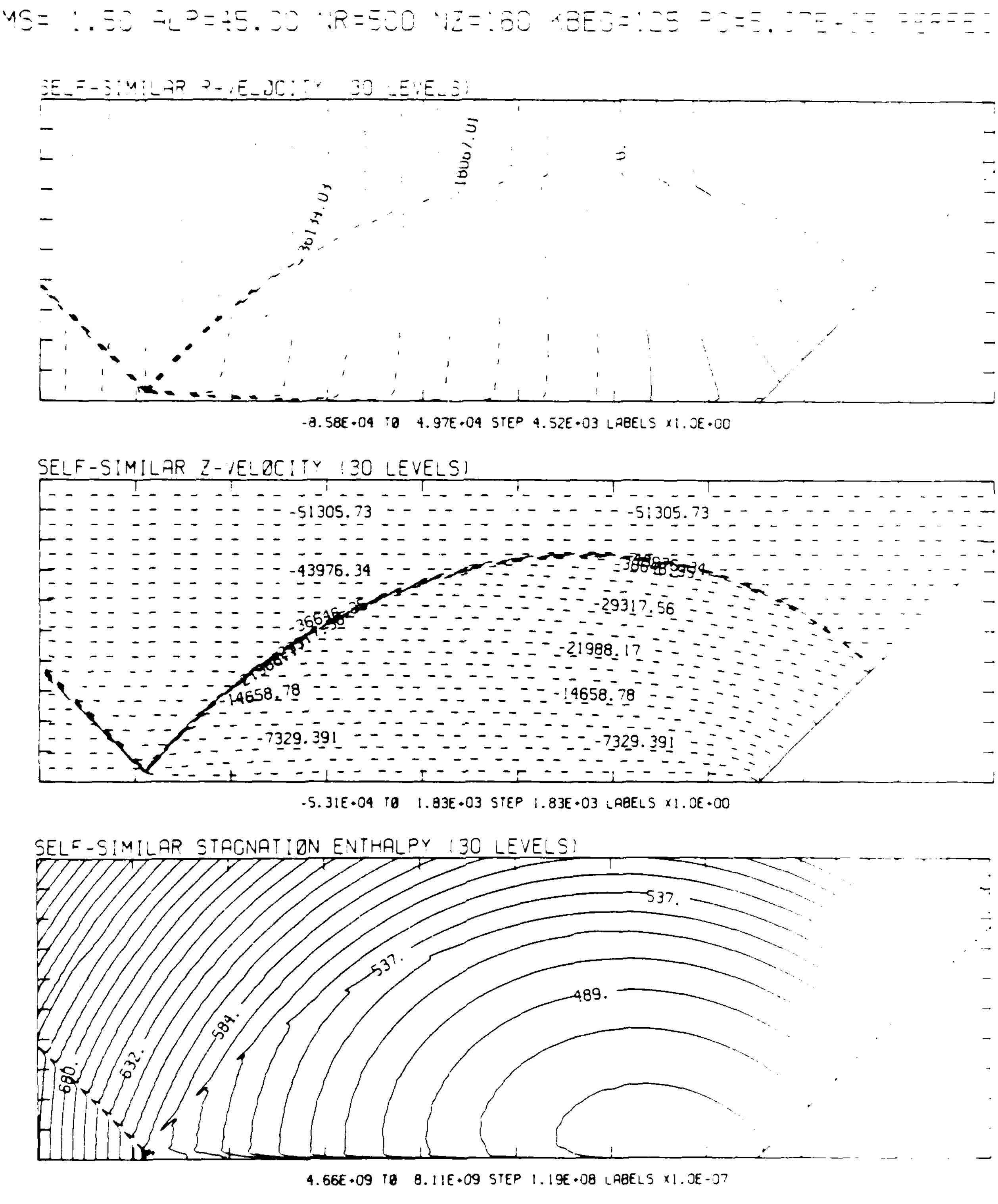

Figure $6d_P$. Whole-flowfield contour-plots; $\gamma = 1.4$ - continued

Figure 6. Case 3, $M_S = 1.50$, $\theta_W = 45°$, Air, $\gamma = 1.4$ and Hansen EOS, SMR - continued

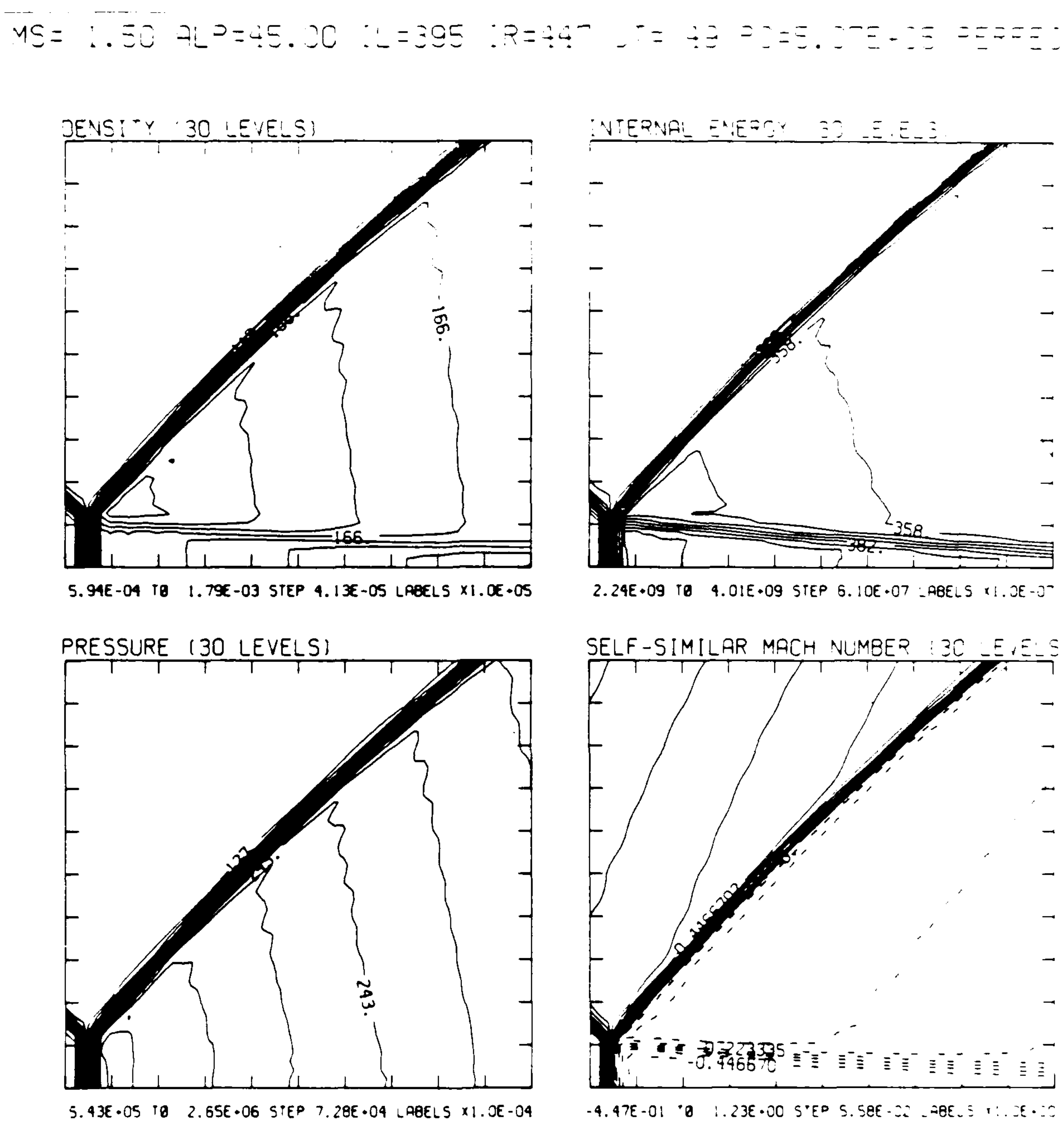

Figure 6e$_p$. Blowup-frame plots; γ = 1.4

Figure 6. Case 3, M_s = 1.50, θ_w = 45°, Air, γ = 1.4 and Hansen EOS, SMR - continued

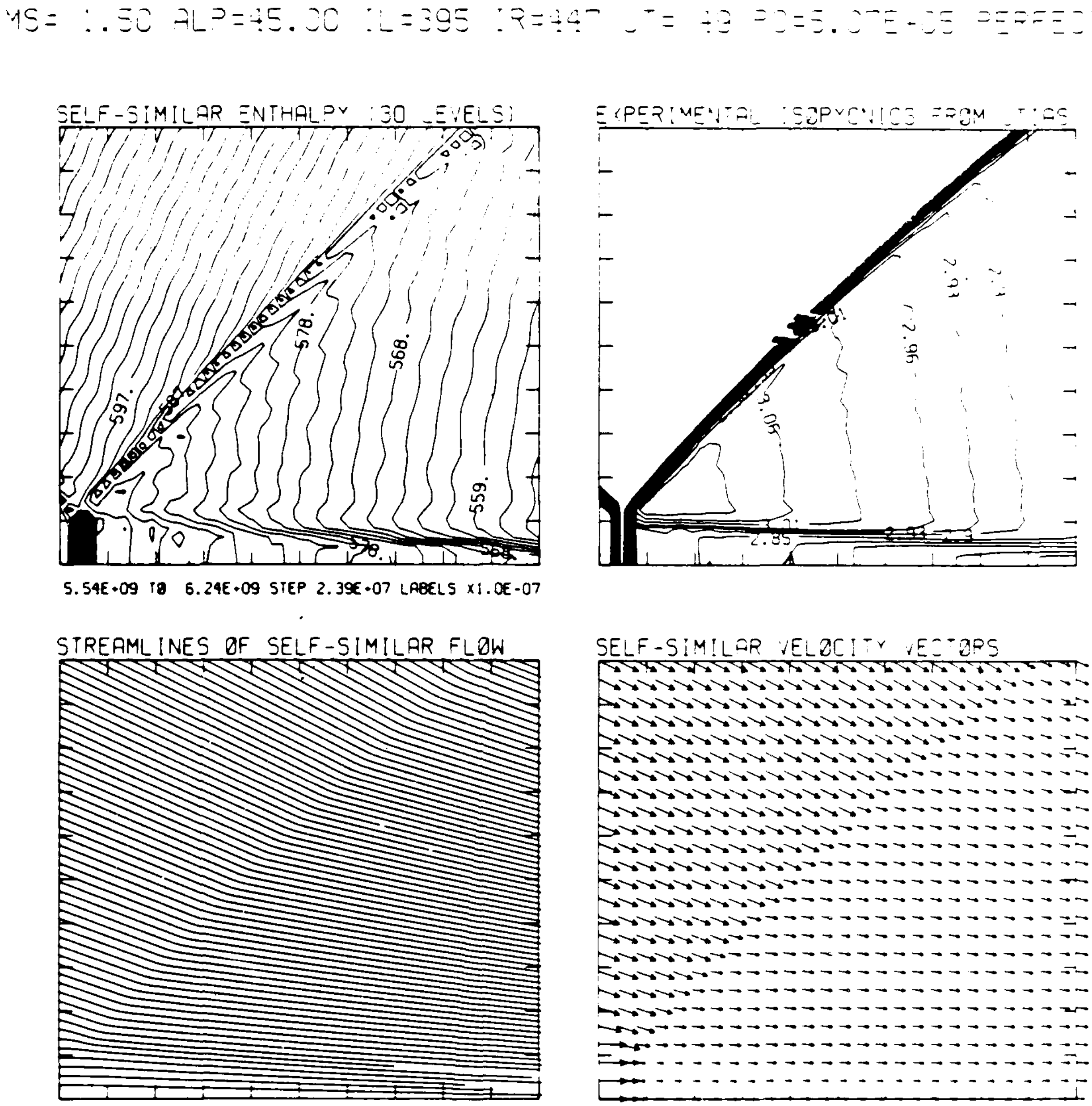

Figure $6e_p$. Blowup-frame plots; γ = 1.4 - continued

Figure 6. Case 3, M_s = 1.50, θ_w = 45°, Air, γ = 1.4 and Hansen EOS, SMR - continued

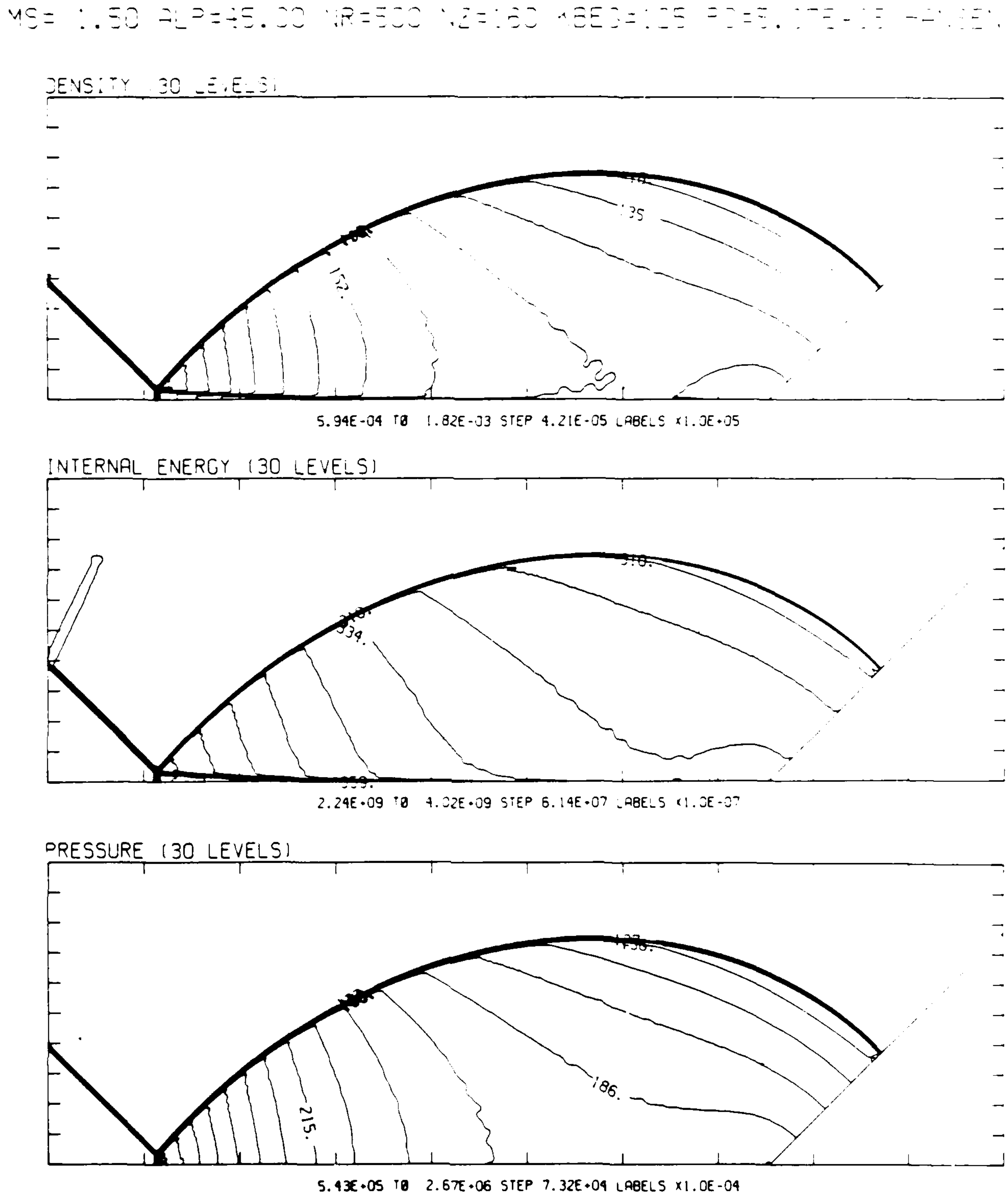

Figure 6d$_H$ - Whole-flowfield contour-plots; Hansen

Figure 6. Case 3, M_S = 1.50, θ_w = 45°, Air, γ = 1.4 and Hansen EOS, SMR - continued

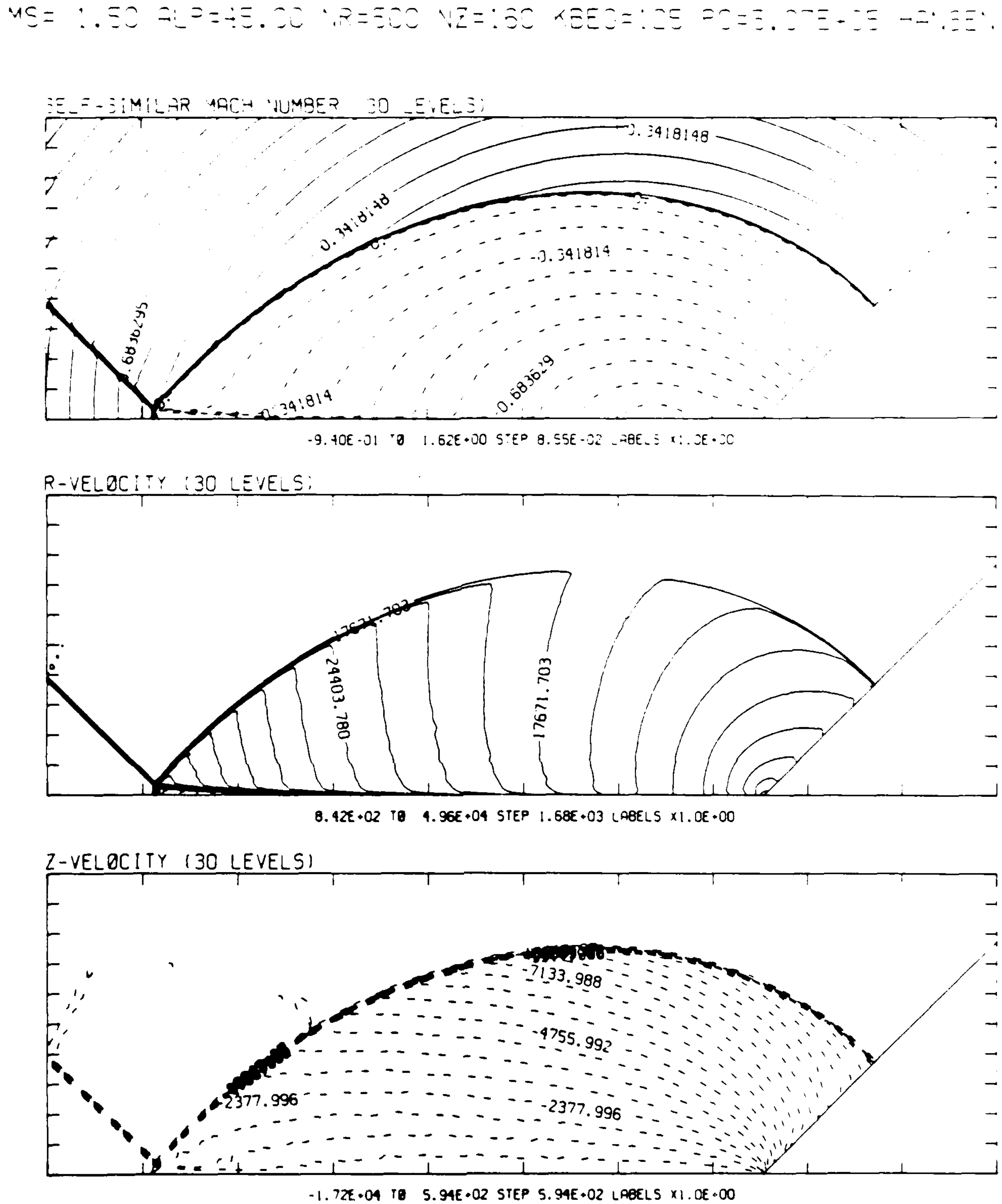

Figure $6d_H$. Whole-flowfield contour-plots; Hansen - continued.

Figure 6. Case 3, $M_S = 1.50$, $\theta_w = 45°$, Air, $\gamma = 1.4$ and Hansen EOS, SMR - continued.

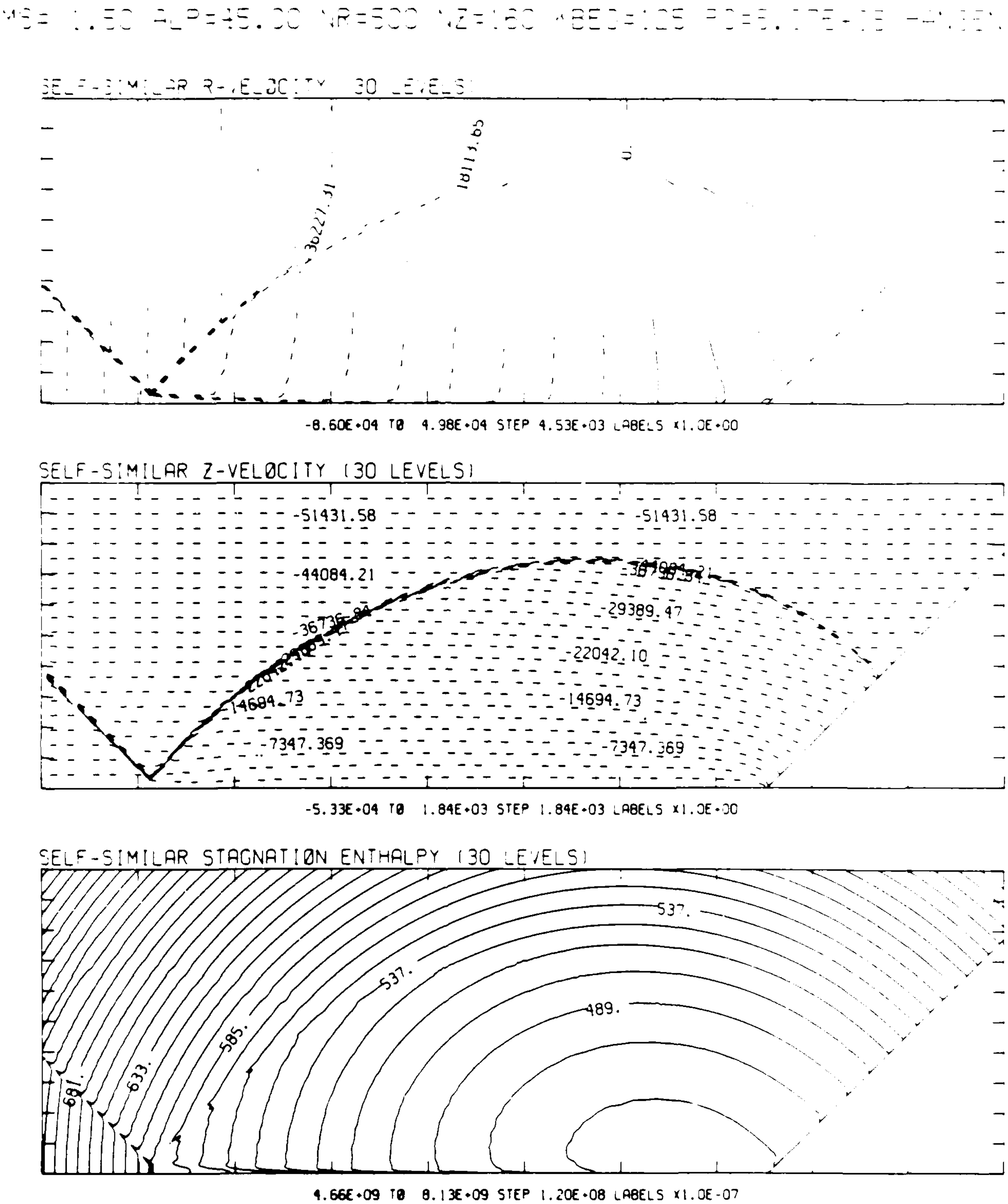

Figure 6d$_H$. Whole-flowfield contour-plots; Hansen - continued.

Figure 6. Case 3, M_s = 1.50, θ_w = 45°, Air, γ = 1.4 and Hansen EOS, SMR - continued.

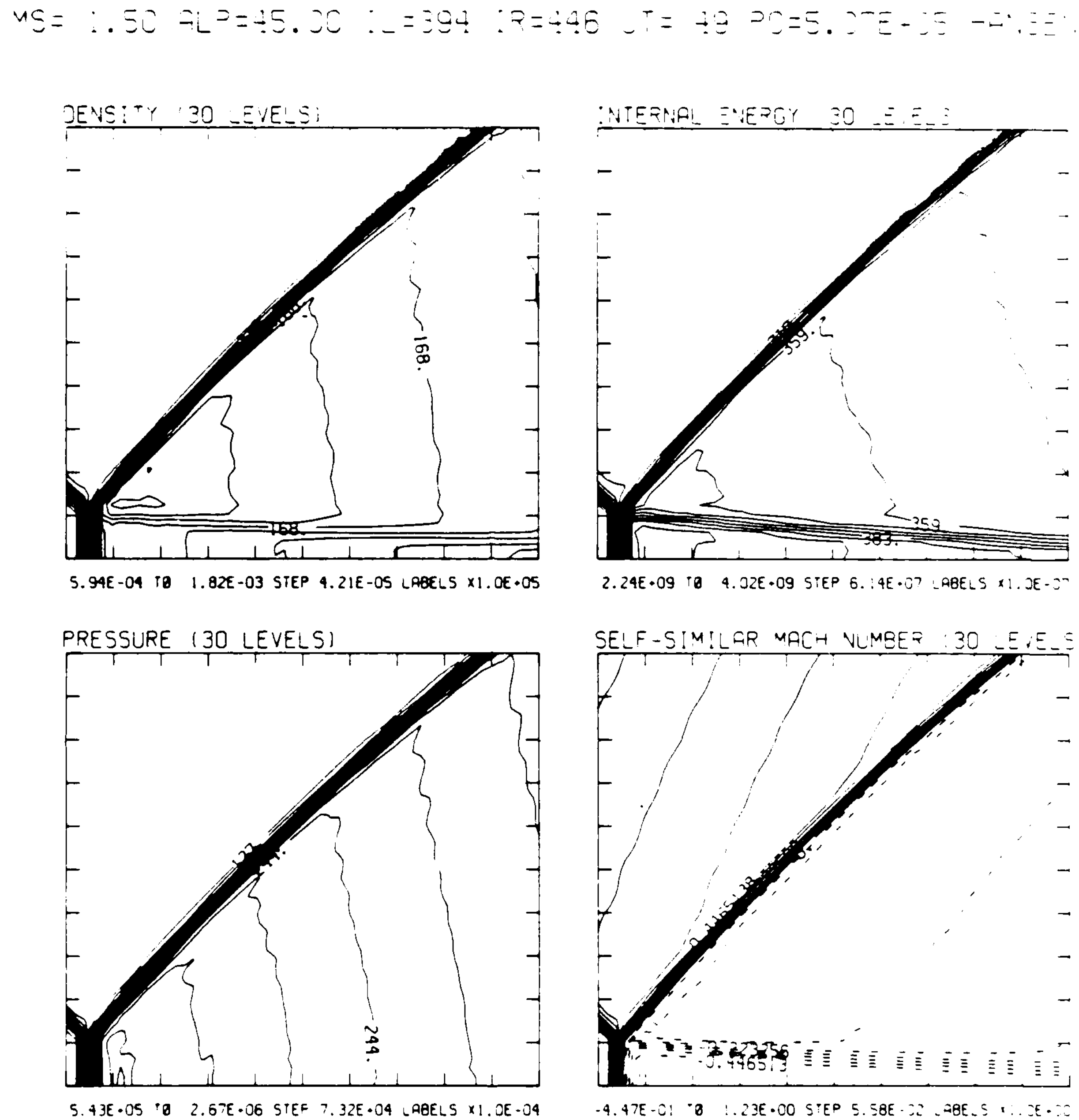

Figure 6e$_H$. Blowup-frame plots; Hansen.

Figure 6. Case 3, M_s = 1.50, θ_w = 45°, Air, γ = 1.4 and Hansen EOS, SMR - continued.

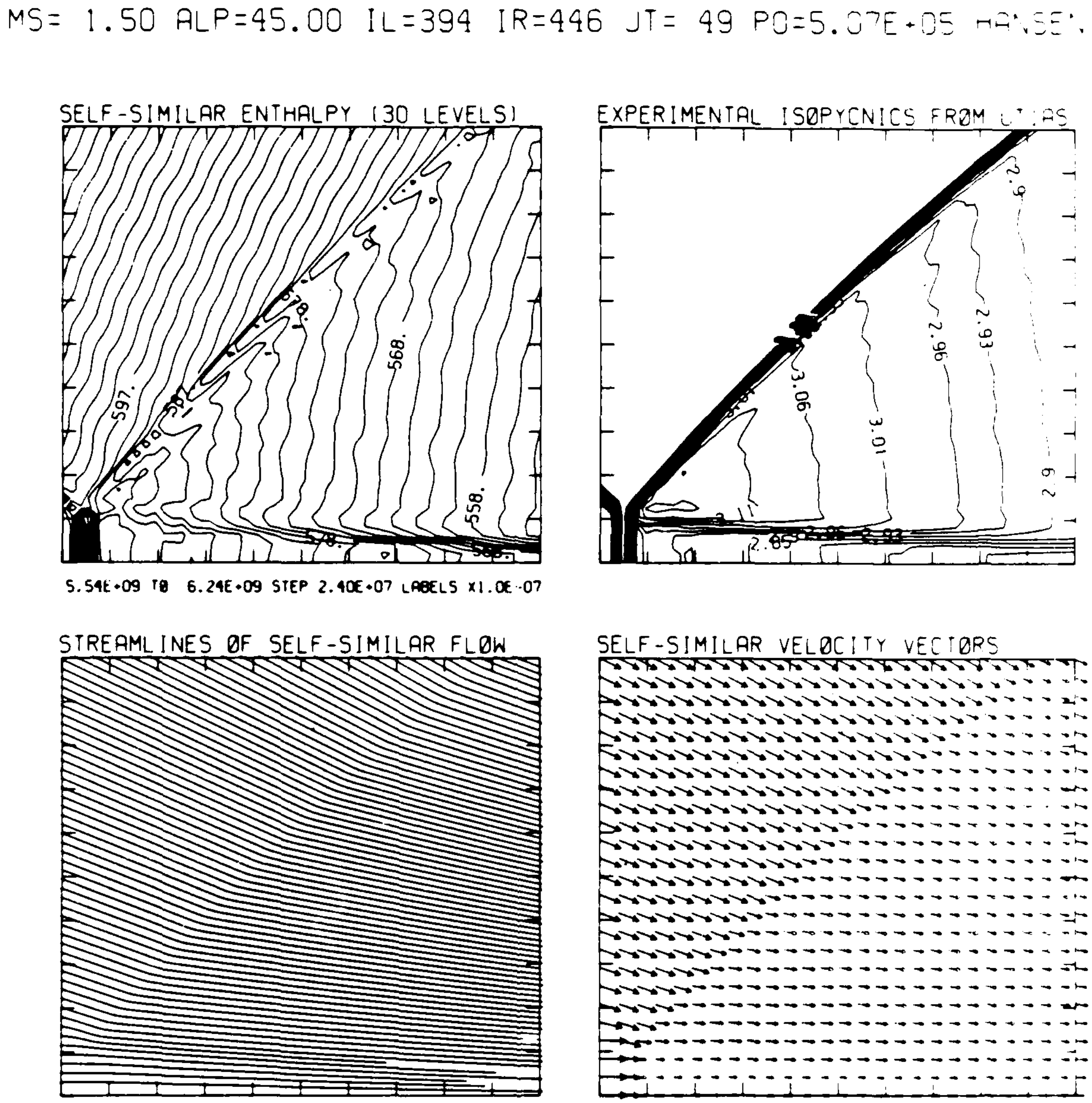

Figure $6e_H$. Blowup-frame plots; Hansen - continued.

Figure 6. Case 3, M_S = 1.50, θ_W = 45°, Air, γ = 1.4 and Hansen EOS, SMR - continued.

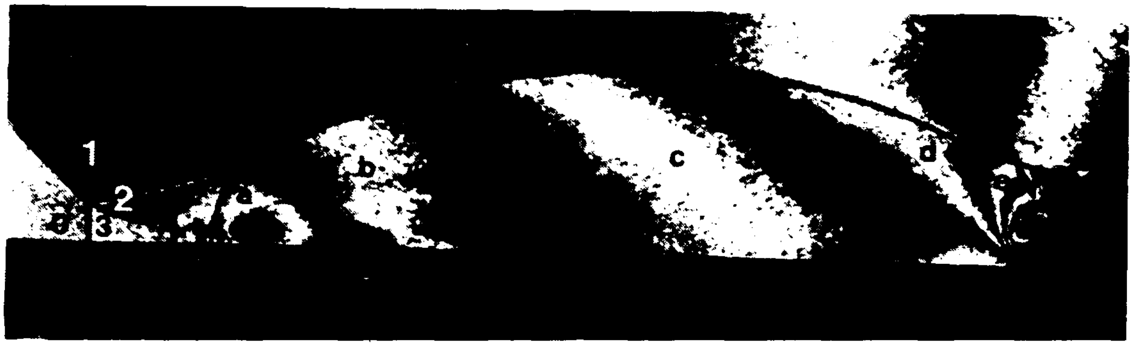

Region	ρ/ρ_0	Region	ρ/ρ_0
0	1.00	c	8.00
1	3.88	d	7.21
2	7.21	e	6.41
3	4.90	f	5.61
a	9.60	g	4.82
b	8.80		

Figure 7a. Interferogram

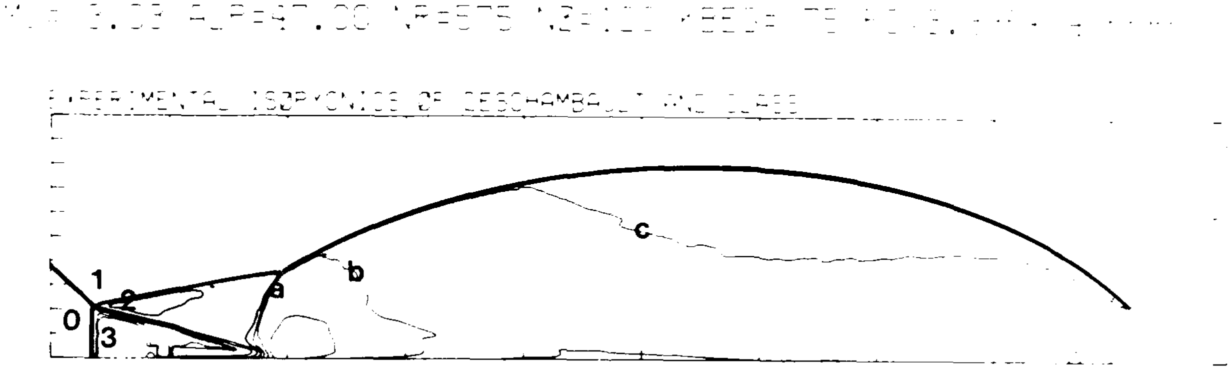

Figure $7b_P$. Calculated isopycnics (γ = 1.4) using the experimental fringes

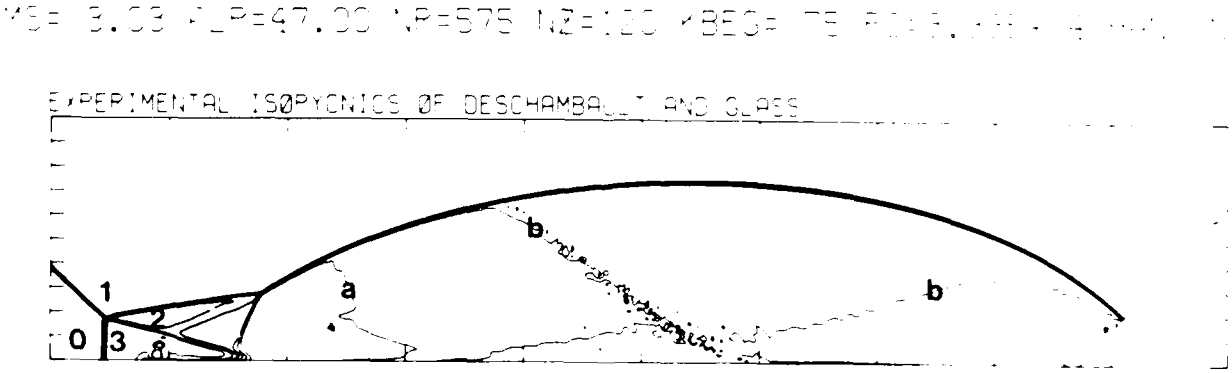

Figure $7b_H$. Calculated isopycnics (Hansen) using the experimental fringes

XBB 859-7196

Figure 7. Case 4, M_S = 3.03, θ_W = 47°, Air, γ = 1.4 and Hansen EOS, DMR.

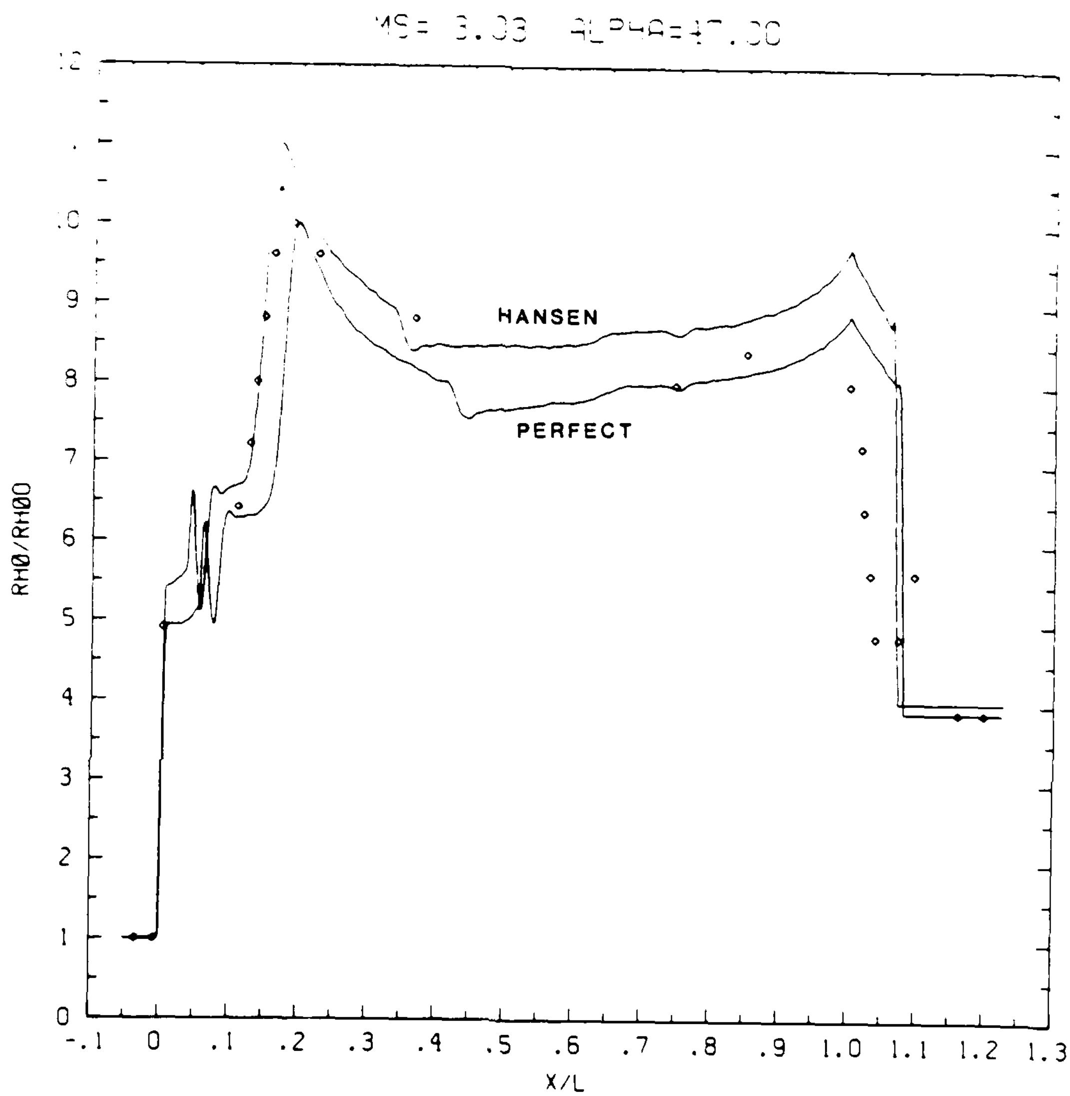

Figure 7c. Wall plot for p/p_0, γ = 1.4 and Hansen calculations, with experimental data.

Figure 7. Case 4, M_s = 3.03, θ_w = 47°, Air, γ = 1.4 and Hansen EOS, DMR - continued.

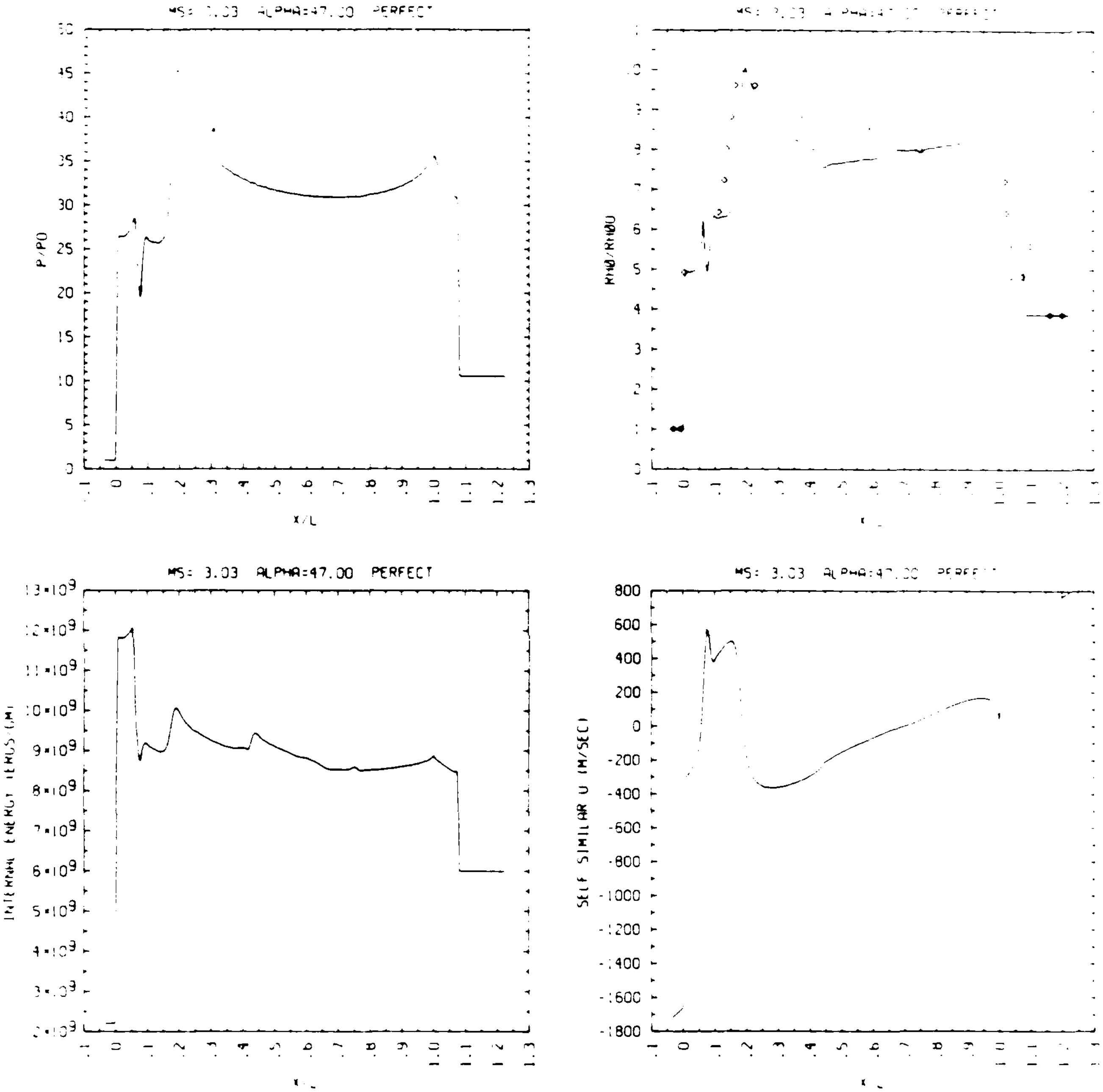

Figure $7c_p$. Wall plot for p/p_0, ρ/ρ_0 with experimental data included, e, u; γ = 1.4

Figure 7. Case 4, M_s = 3.03, θ_w = 47°, Air, γ = 1.4 and Hansen EOS, DMR - continued.

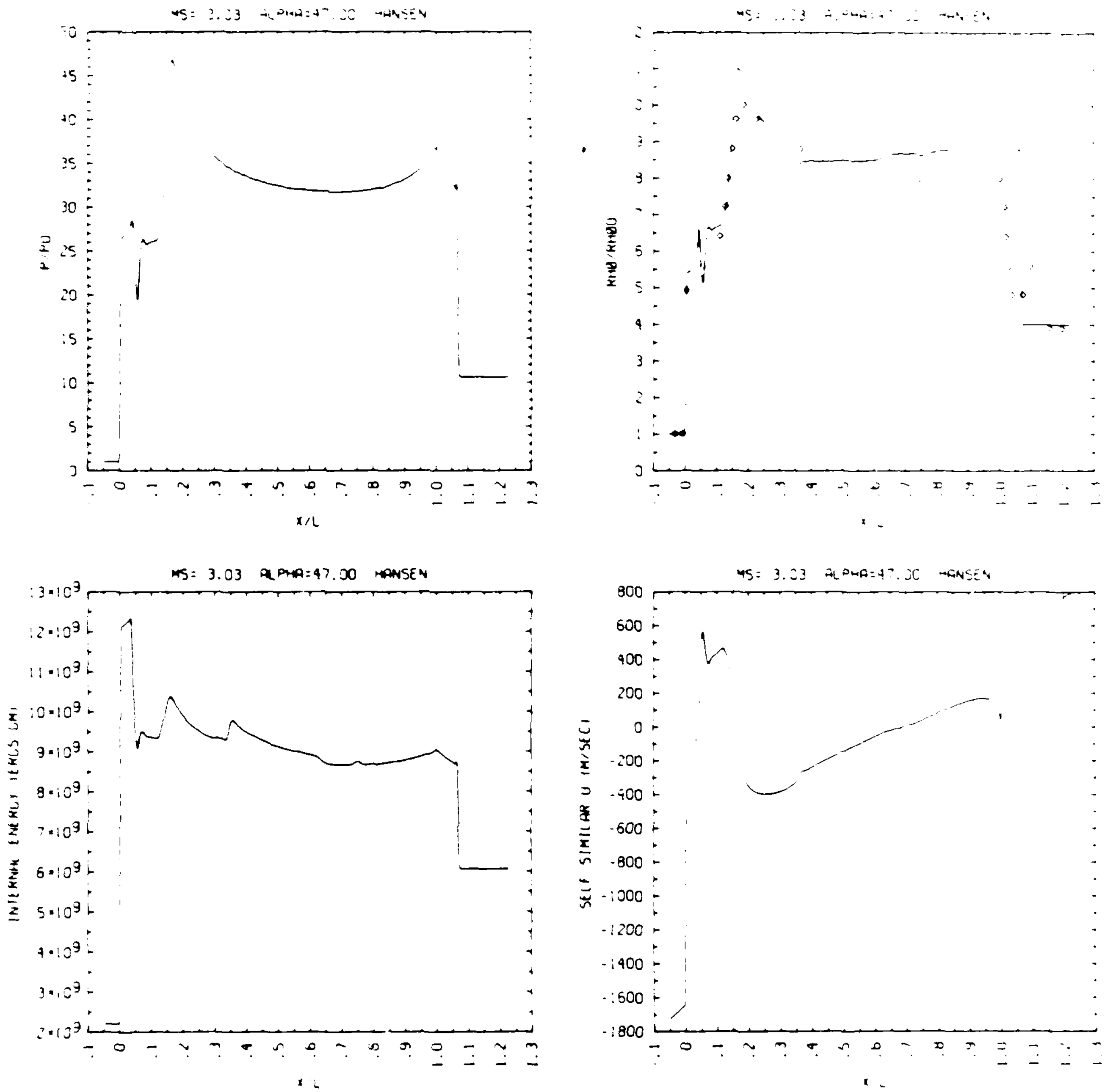

Figure $7c_H$. Wall plots for p/p_0, ρ/ρ_0 with experimental data included, e, u; Hansen.

Figure 7. Case 4, M_s = 3.03, θ_w = 47°, Air, γ = 1.4 and Hansen EOS, DMR - continued.

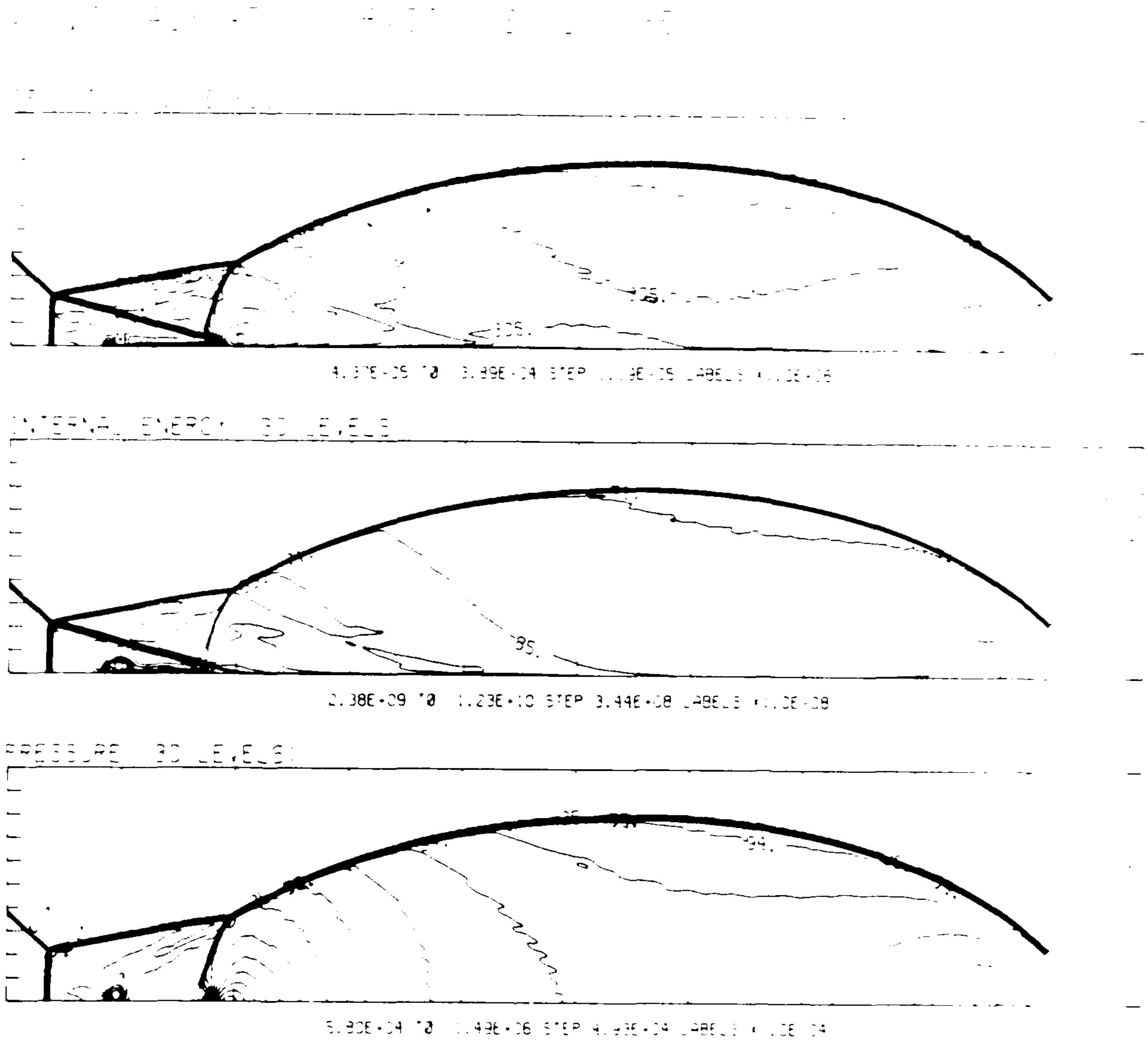

Figure $7d_p$. Whole-flowfield contour-plots; $\gamma = 1.4$

Figure 7. Case 4, $M_s = 3.03$, $\theta_w = 47°$, Air, $\gamma = 1.4$ and Hansen EOS, DMR - continued.

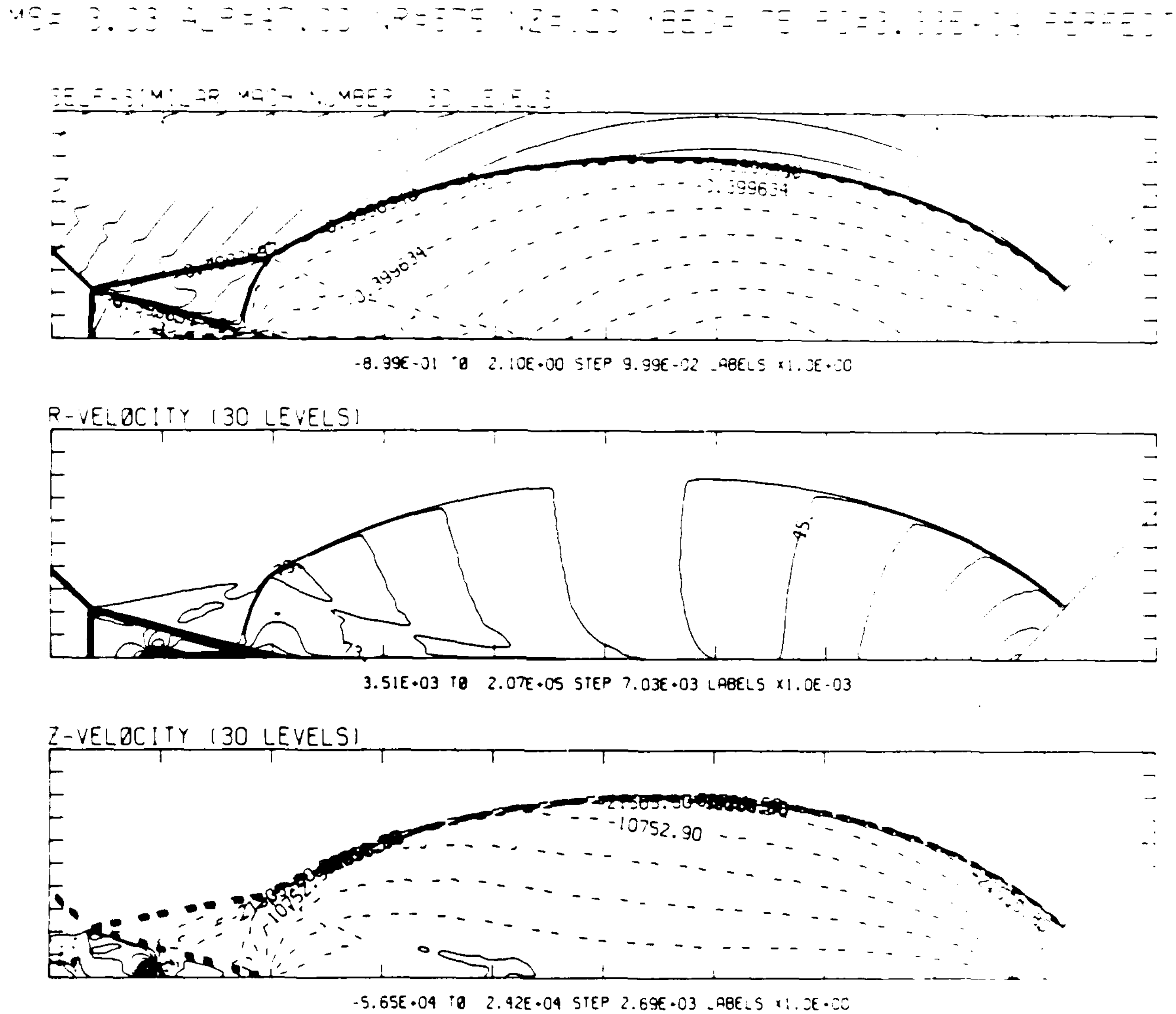

Figure $7d_p$. Whole-flowfield contour-plots; γ = 1.4 -

Figure 7. Case 4, M_s = 3.03, θ_w = 47°, Air, ... continued.

AD-A186 440   A DETAILED NUMERICAL GRAPHICAL AND EXPERIMENTAL STUDY   2/5
OF OBLIQUE SHOCK WA (U) TORONTO UNIV DOWNSVIEW
(ONTARIO) INST FOR AEROSPACE STUDIES   H M GLAZ ET AL
UNCLASSIFIED 01 AUG 86 UTIAS-285 DNA-TR-86-365   F/G 20/4   NL

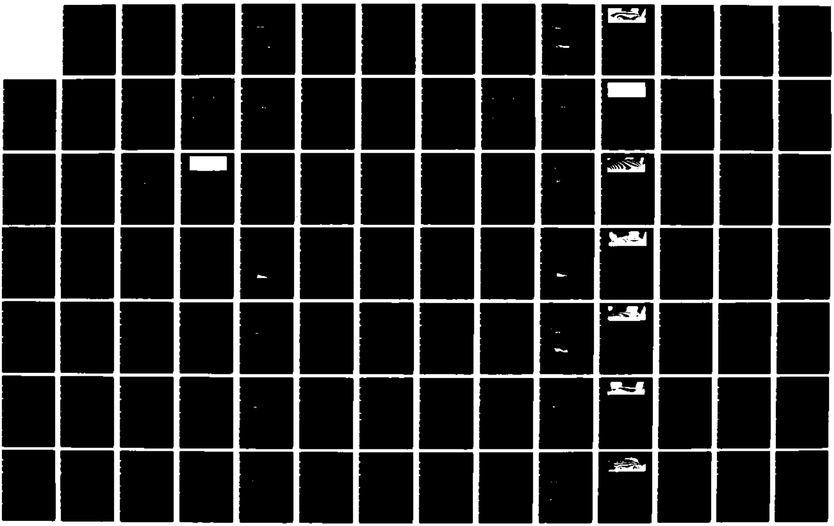

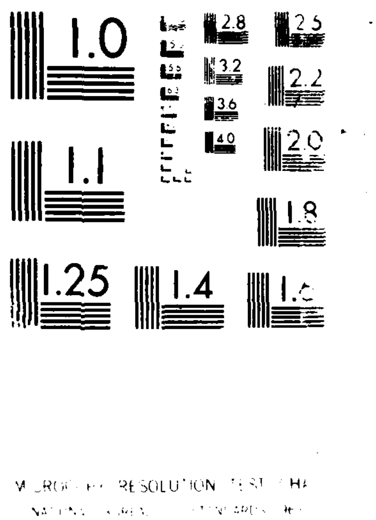
1.0
2.8
2.5
3.2
2.2
3.6
4.0
2.0
1.1
1.8
1.25
1.4
RESOLUTION

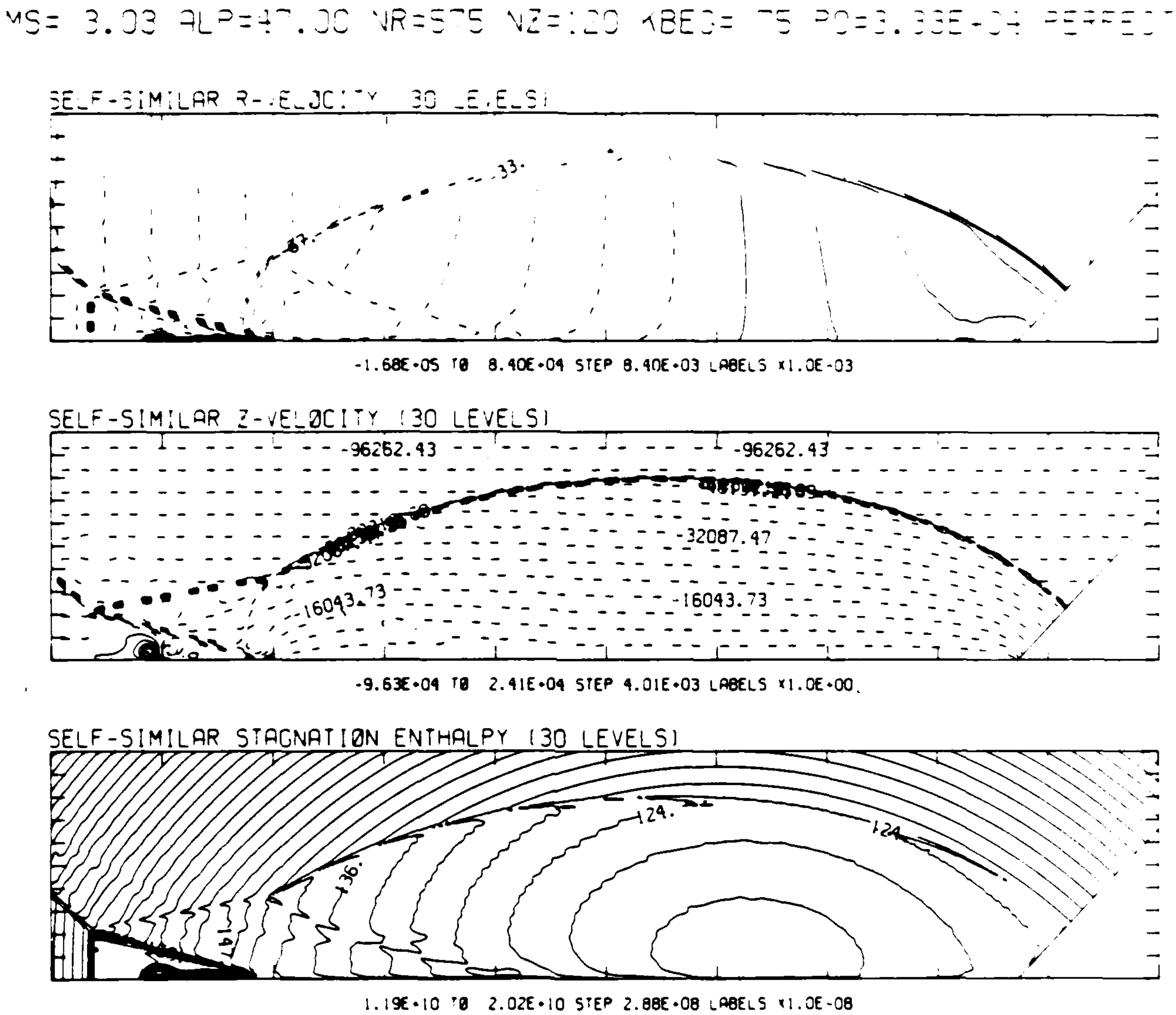

Figure $7d_p$. Whole-flowfield contour-plots; $\gamma = 1.4$ - continued.

Figure 7. Case 4, $M_S = 3.03$, $\theta_w = 47°$, Air, $\gamma = 1.4$ and Hansen EOS, DMR - continued.

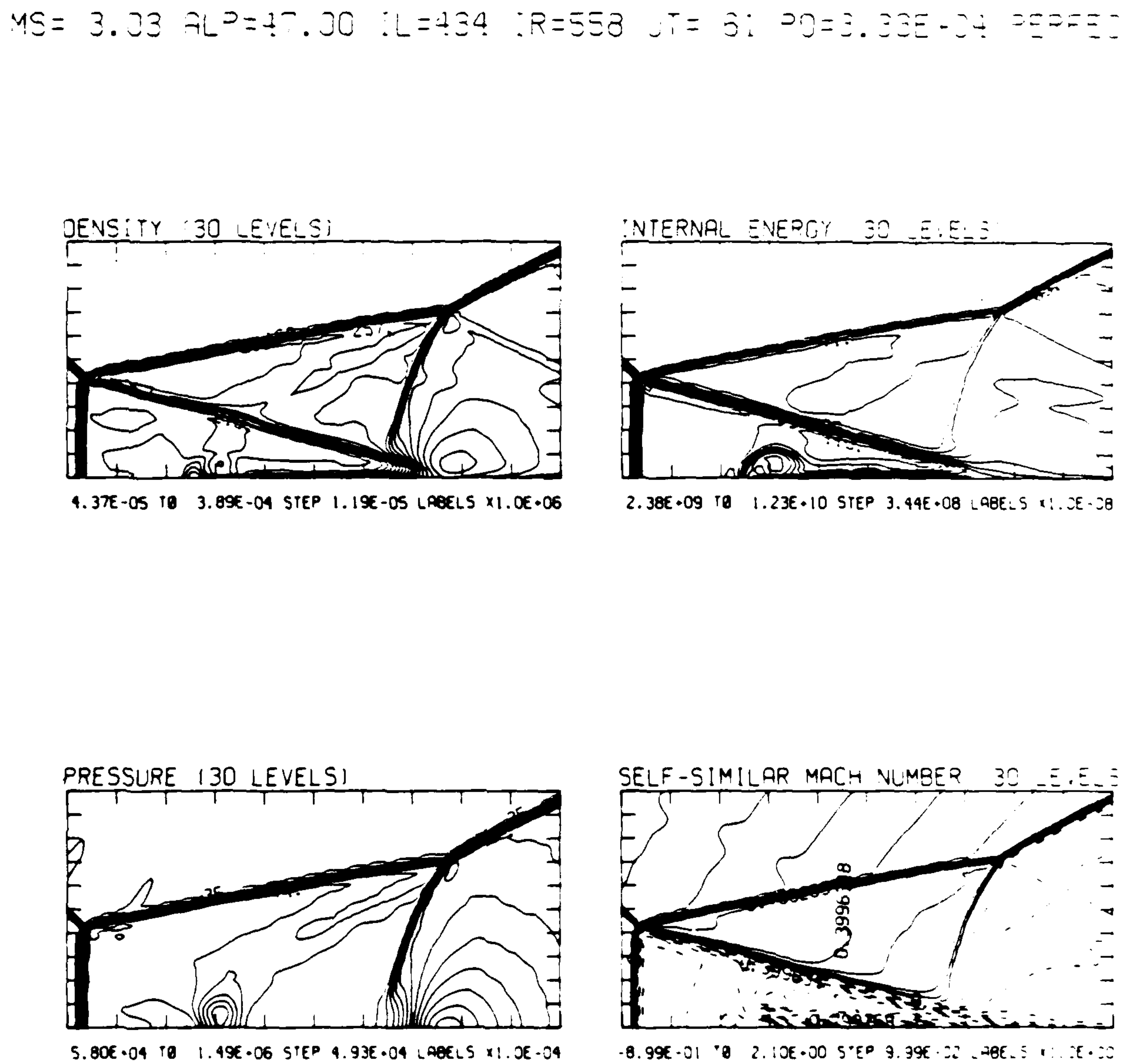

Figure $7e_p$. Blowup-frame plots; $\gamma = 1.4$

Figure 7. Case 4, $M_s = 3.03$, $\theta_w = 47°$, Air, $\gamma = 1.4$ and Hansen EOS, DMR - continued.

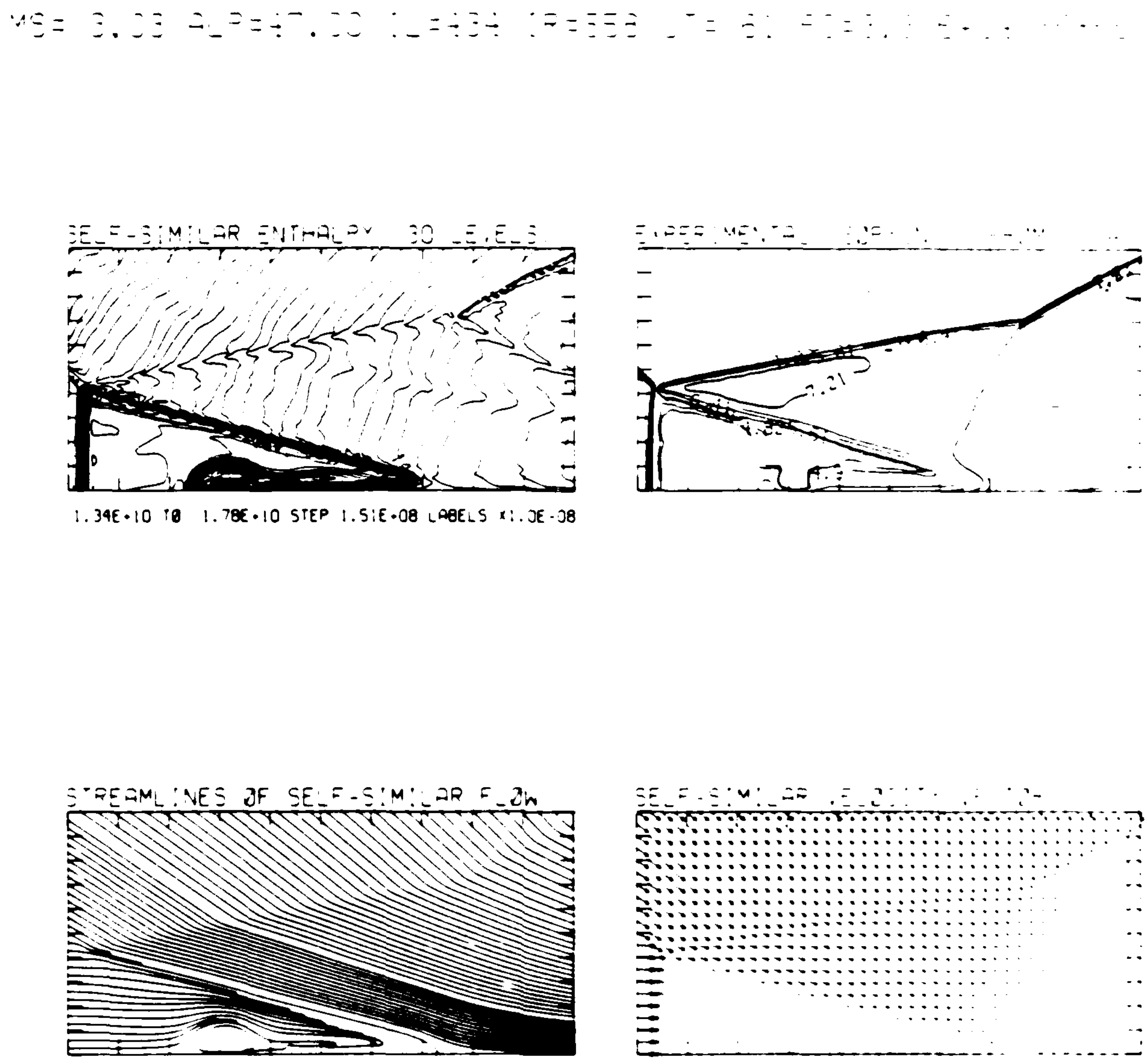

Figure $7e_p$. Blowup-frame plots; γ = 1.4 - continued.

Figure 7. Case 4, M_s = 3.03, θ_w = 47°, Air, γ = 1.4 and Hansen EOS, DMR - continued.

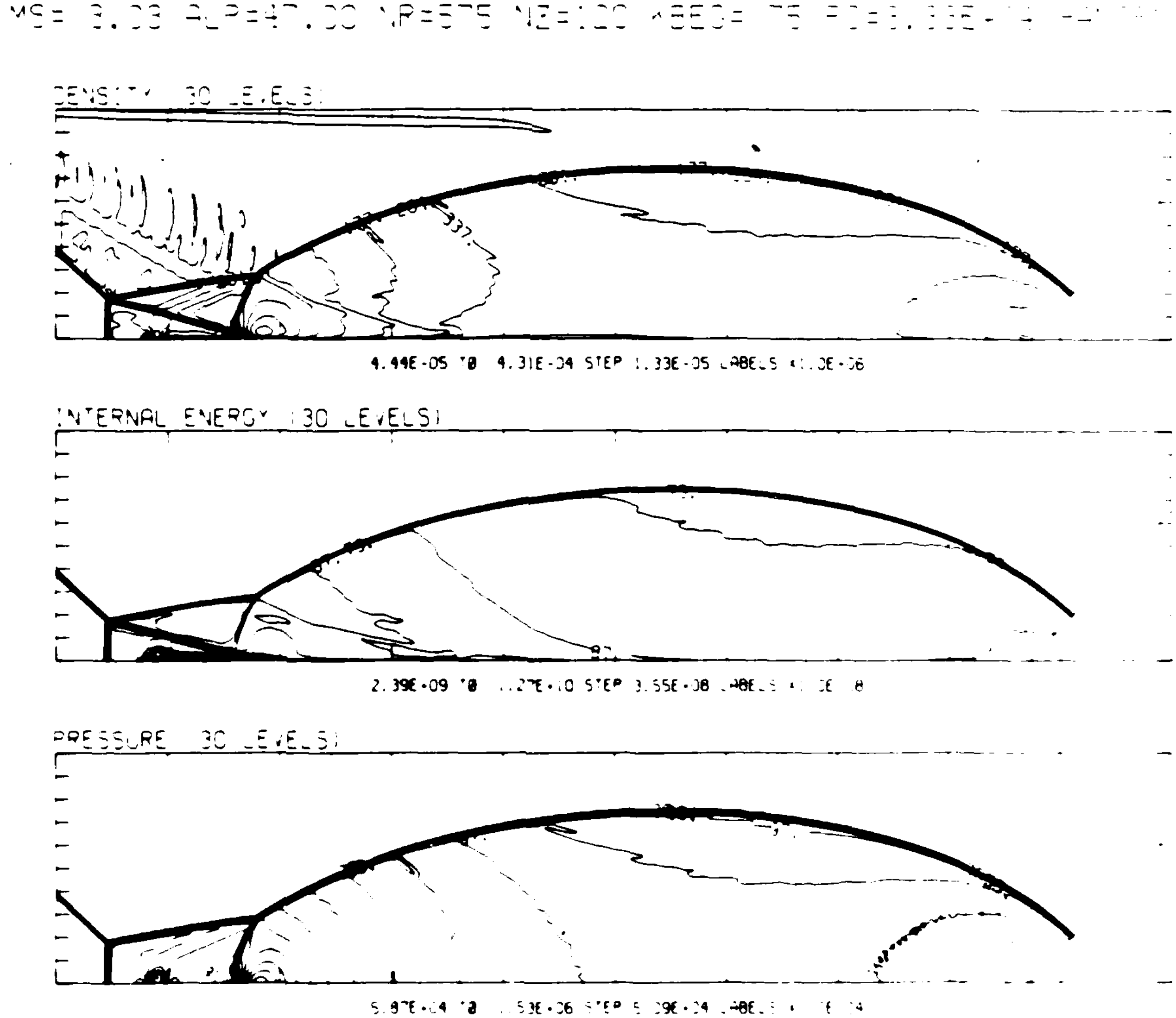

Figure $7d_H$. Whole-flowfield contour-plots; Hansen

Figure 7. Case 4, M_s = 3.03, θ_w = 47°, Air, γ = 1.4 and Hansen EOS, DMR - continued.

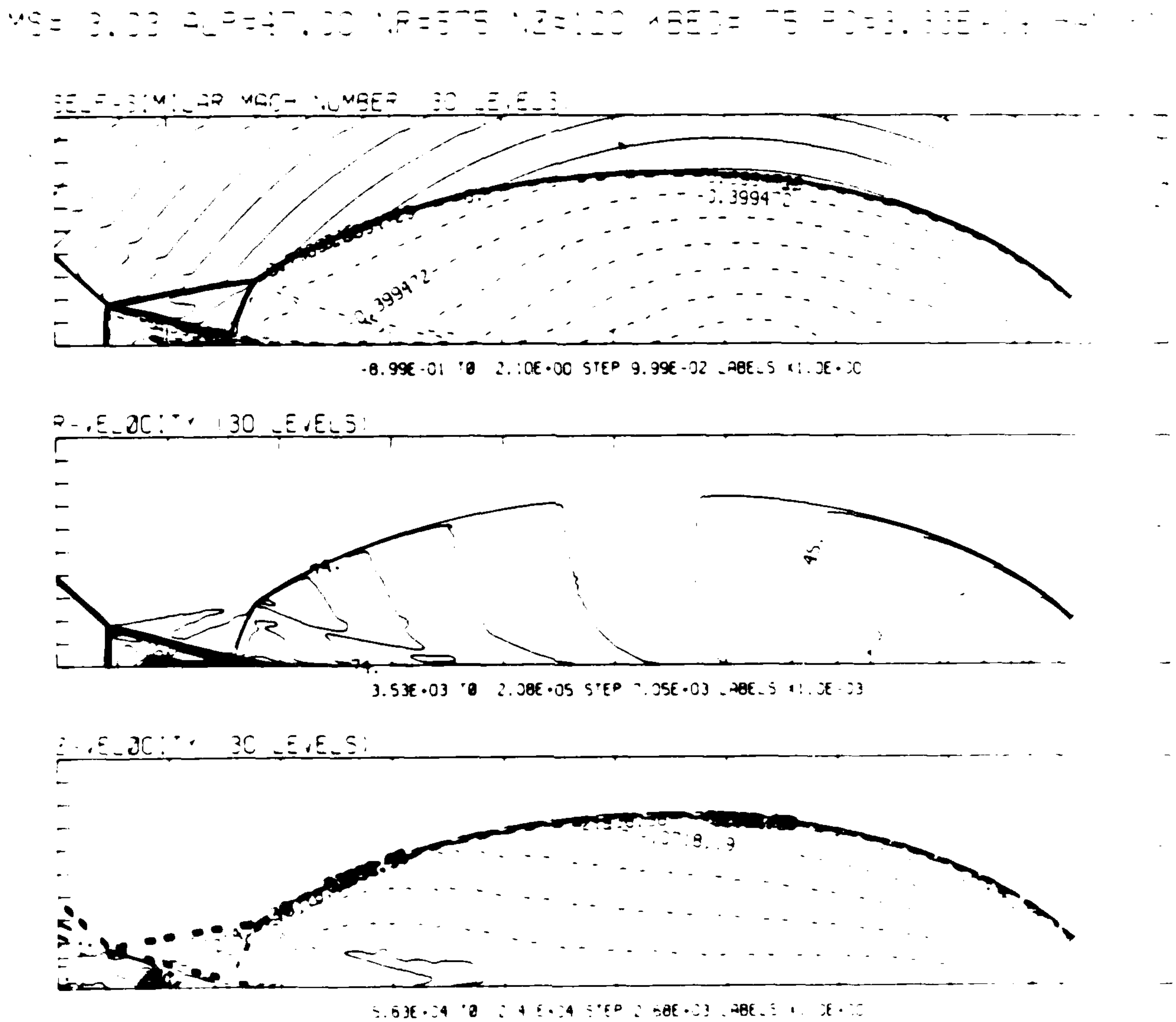

Figure $7d_H$. Whole-flowfield contour-plots; Hansen - continued.

Figure 7. Case 4, M_s = 3.03, θ_w = 47°, Air, γ = 1.4 and Hansen EOS, DMR - continued.

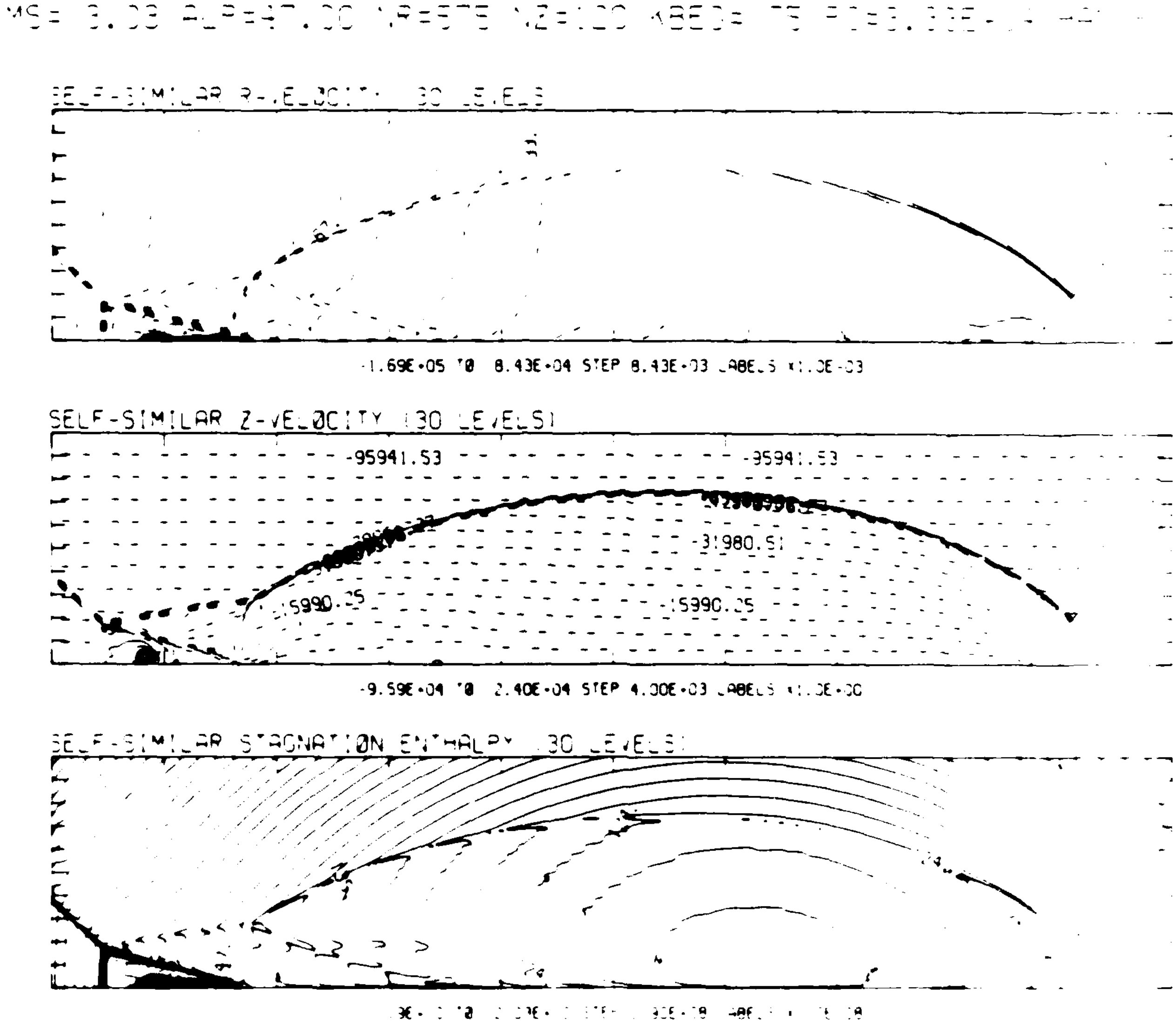

Figure 7d$_4$. Whole-flowfield contour-plots; Hansen - continued.

Figure 7. Case 4, M_s = 3.03, θ_w = 47°, Air, γ = 1.4 and Hansen EOS, DMR - continued.

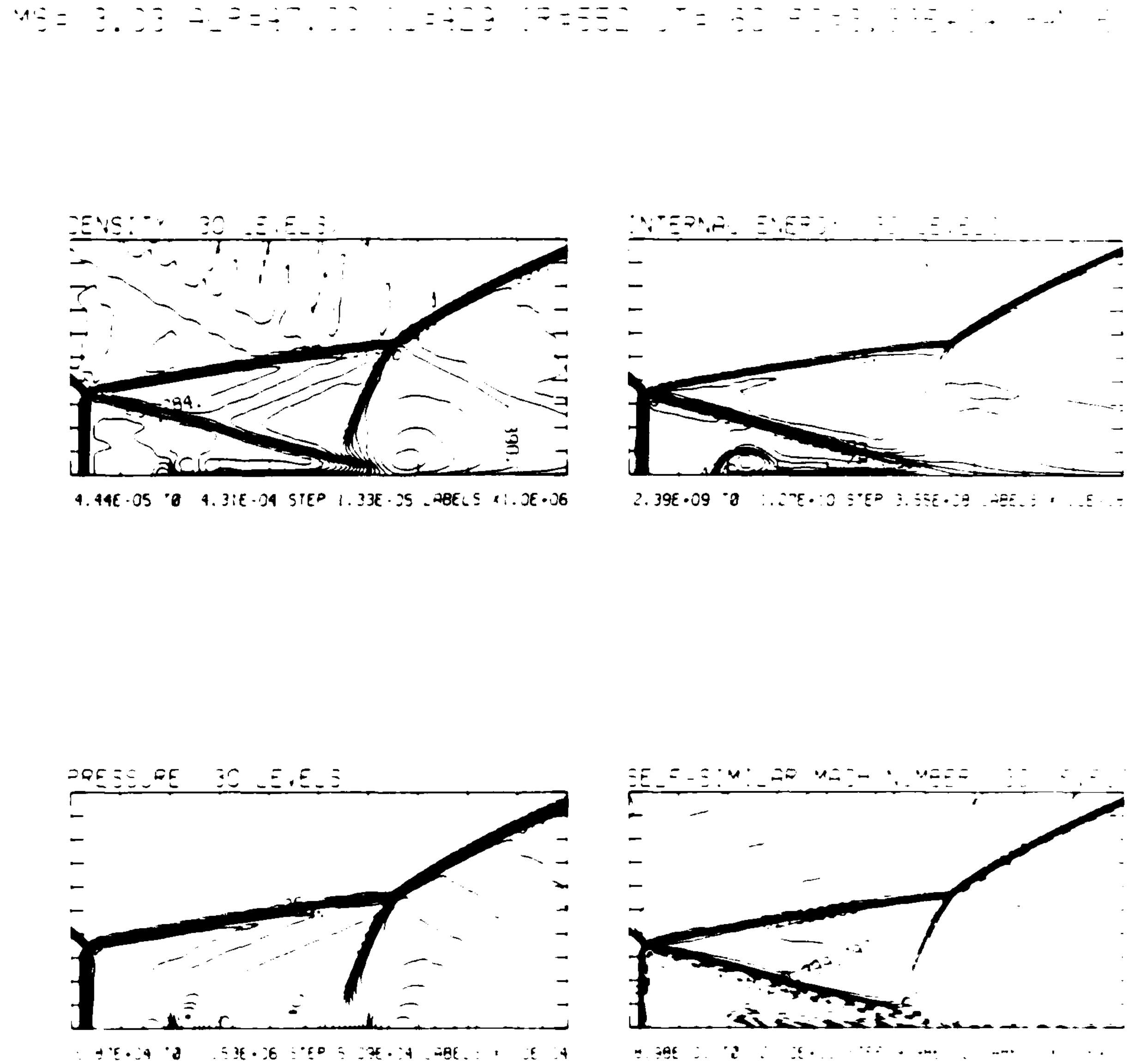

Figure $7e_H$. Blowup-frame plots; Hansen

Figure 7. Case 4, M_s = 3.03, θ_w = 47°, Air, γ = 1.4 and Hansen EOS, DMR - continued.

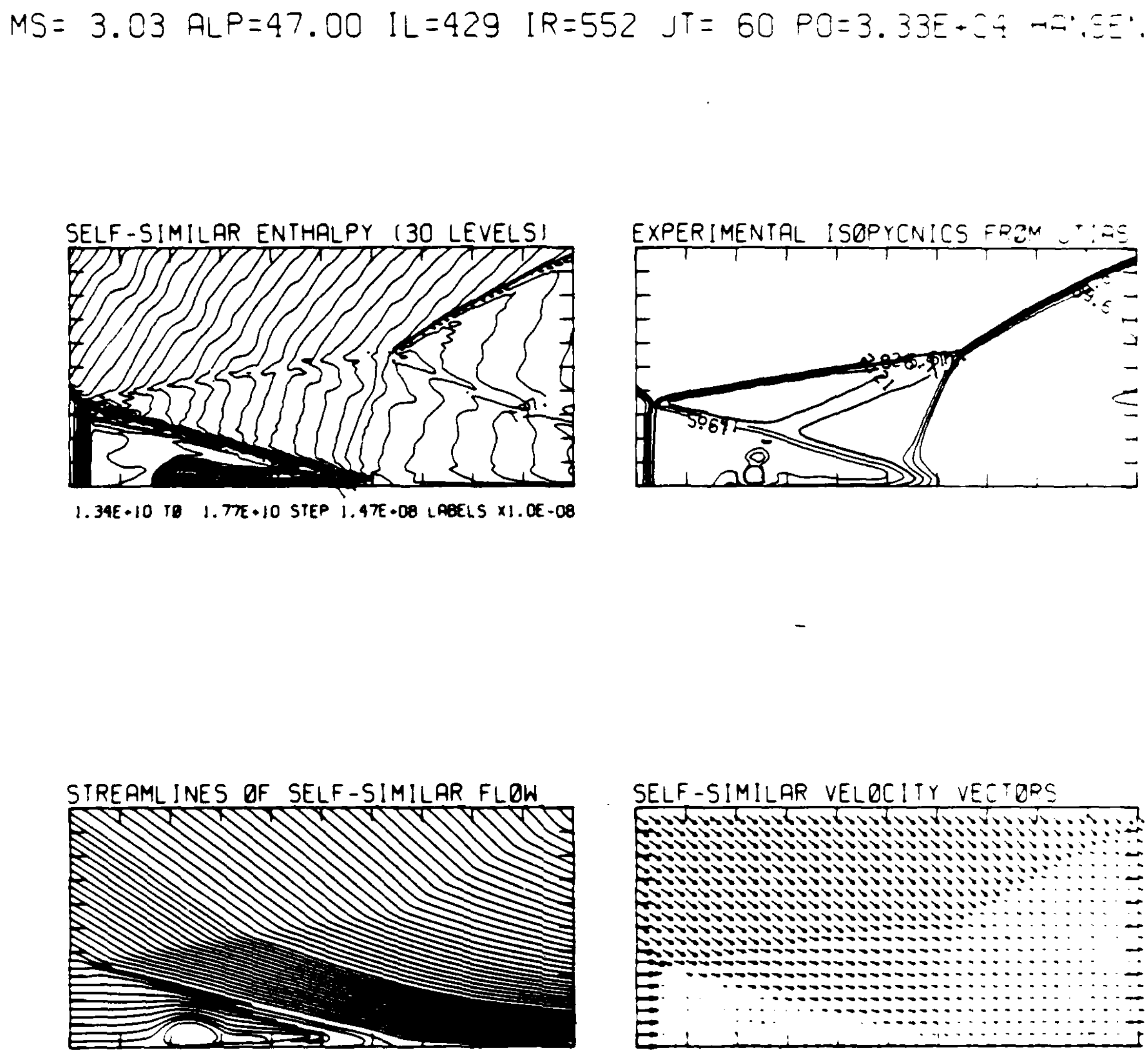

Figure $7e_H$. Blowup-frame plots; Hansen - continued.

Figure 7. Case 4, M_S = 3.03, θ_w = 47°, Air, γ = 1.4 and Hansen EOS, DMR - continued.

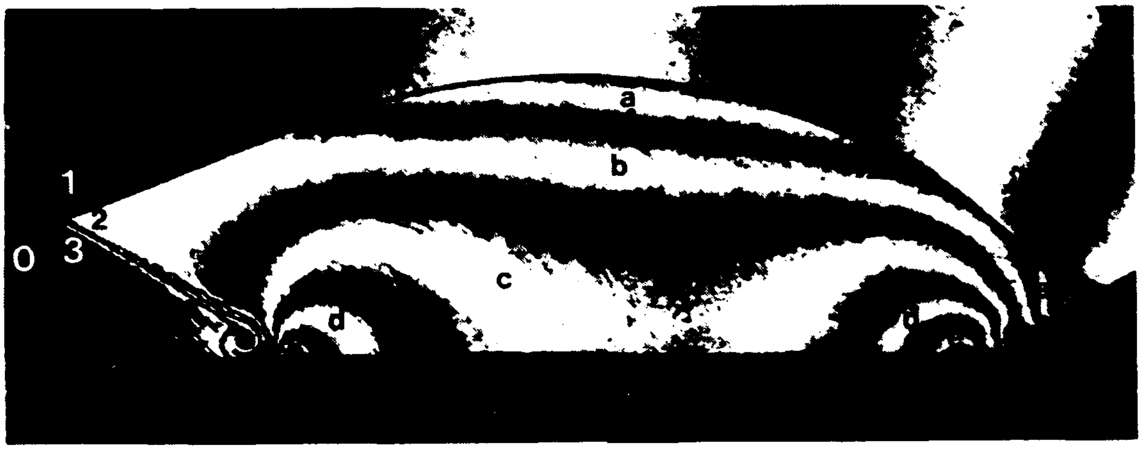

Region	ρ/ρ_0
0	1.00
1	3.51
2	4.89
3	4.14
a	4.69
b	4.89
c	5.09
d	5.28
e	5.48
f	4.49

Figure 8a. Interferogram

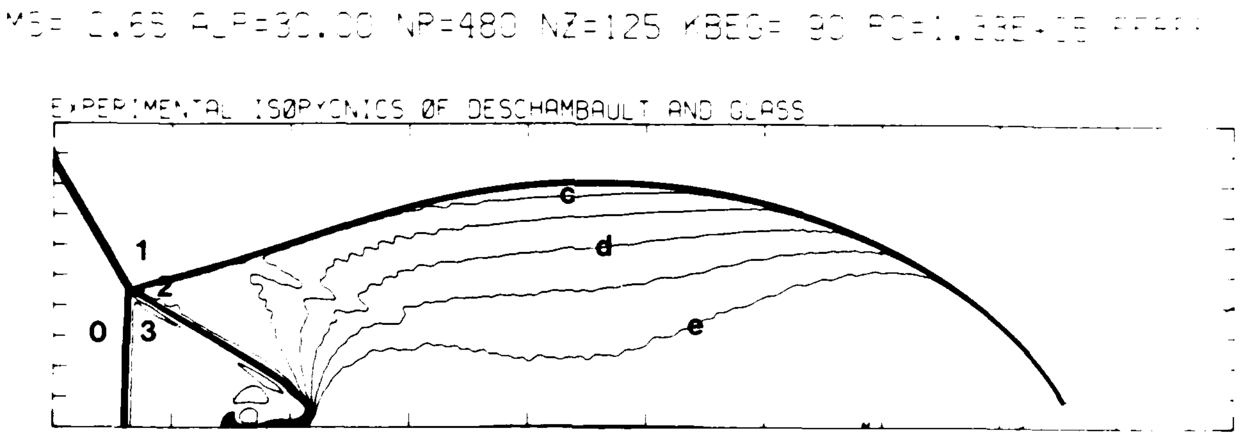

XBB 859-7197

Figure $8b_p$. Calculated isopycnics (γ = 1.4) using the experimental fringes

Figure 8. Case 5, M_s = 2.65, θ_w = 30°, Air, γ = 1.4 and Hansen EOS, CMR.

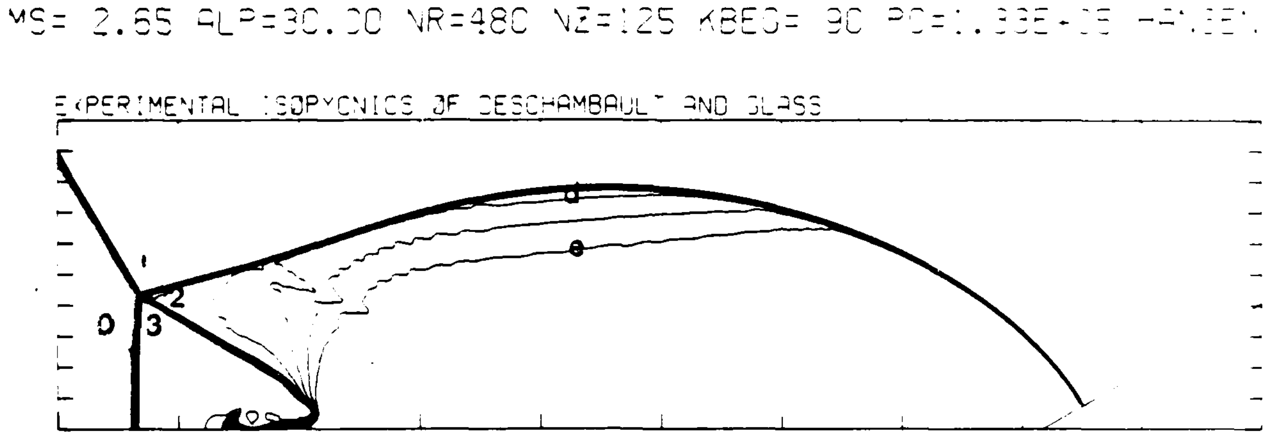

Figure $8b_H$. Calculated isopycnics (Hansen) using the experimental fringes.

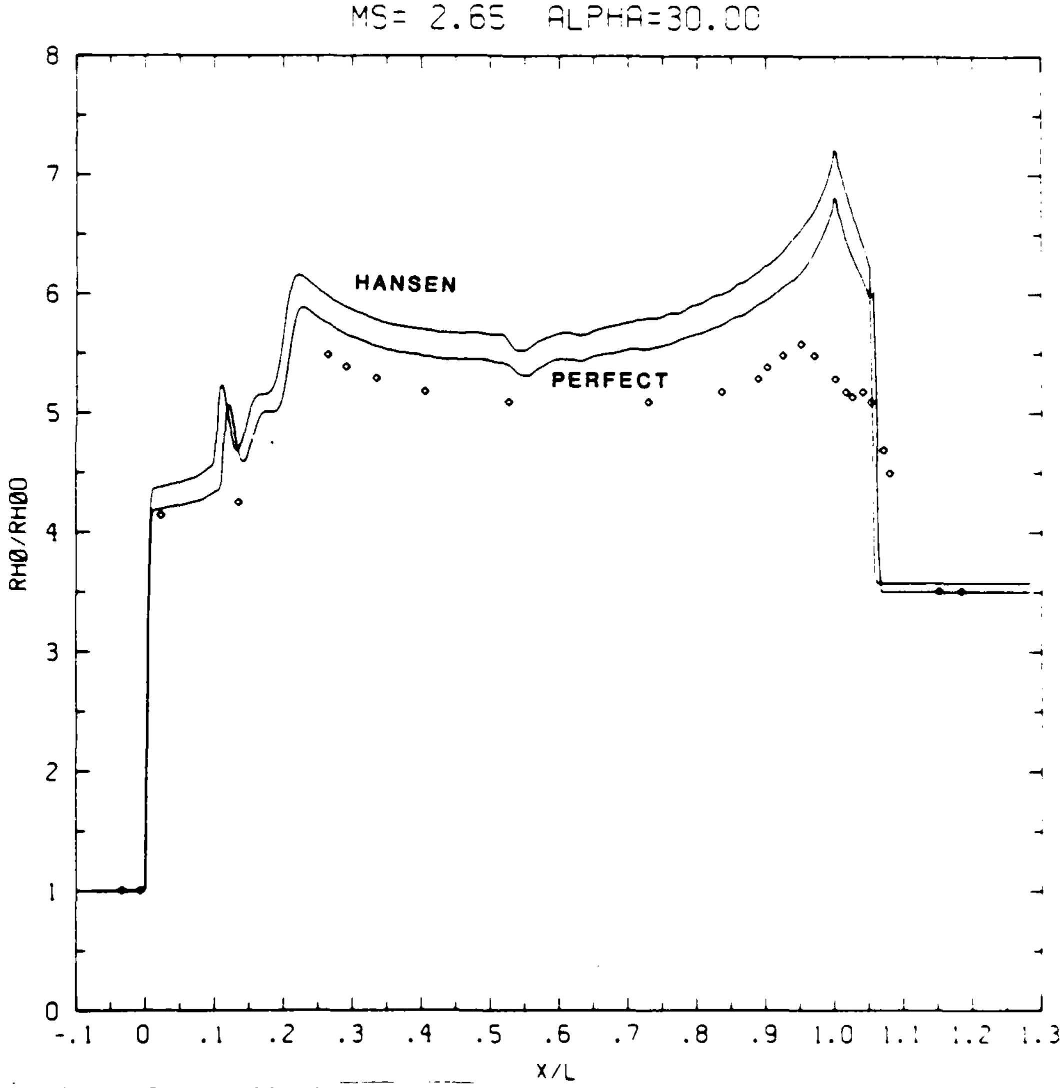

Figure 8c. Wall plot for $\overline{p}/\overline{p}_0$, γ = 1.4 and Hansen calculations with experimental data.

Figure 8. Case 5, M_s = 2.65, θ_w = 30°, Air, γ = 1.4 and Hansen EOS, CMR - continued.

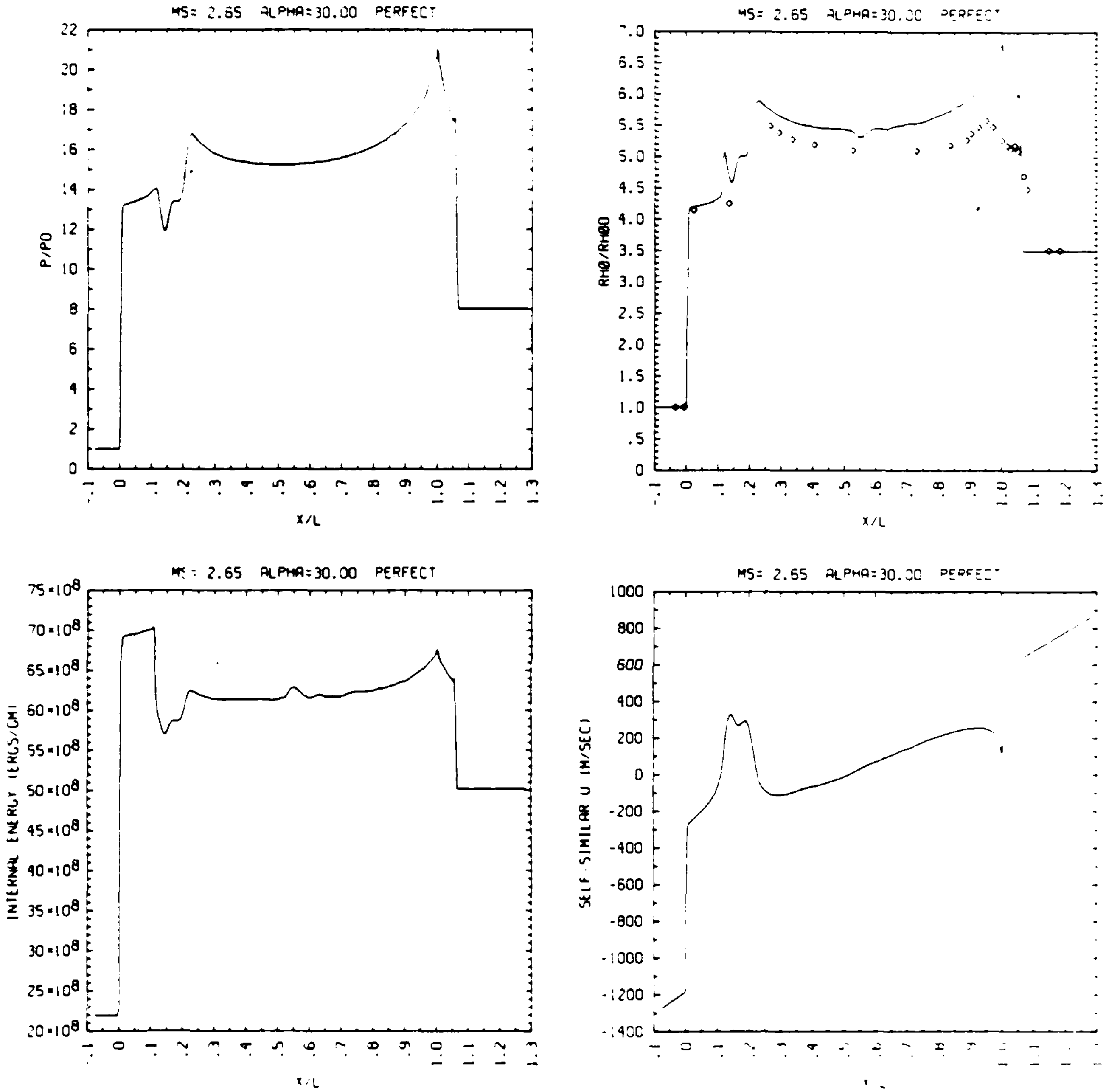

Figure $8c_p$. Wall plot for p/p_0, ρ/ρ_0 with experimental data included, e, u; γ = 1.4.

Figure 8. Case 5, M_s = 2.65, θ_w = 30°, Air, γ = 1.4 and Hansen EOS, CMR - continued.

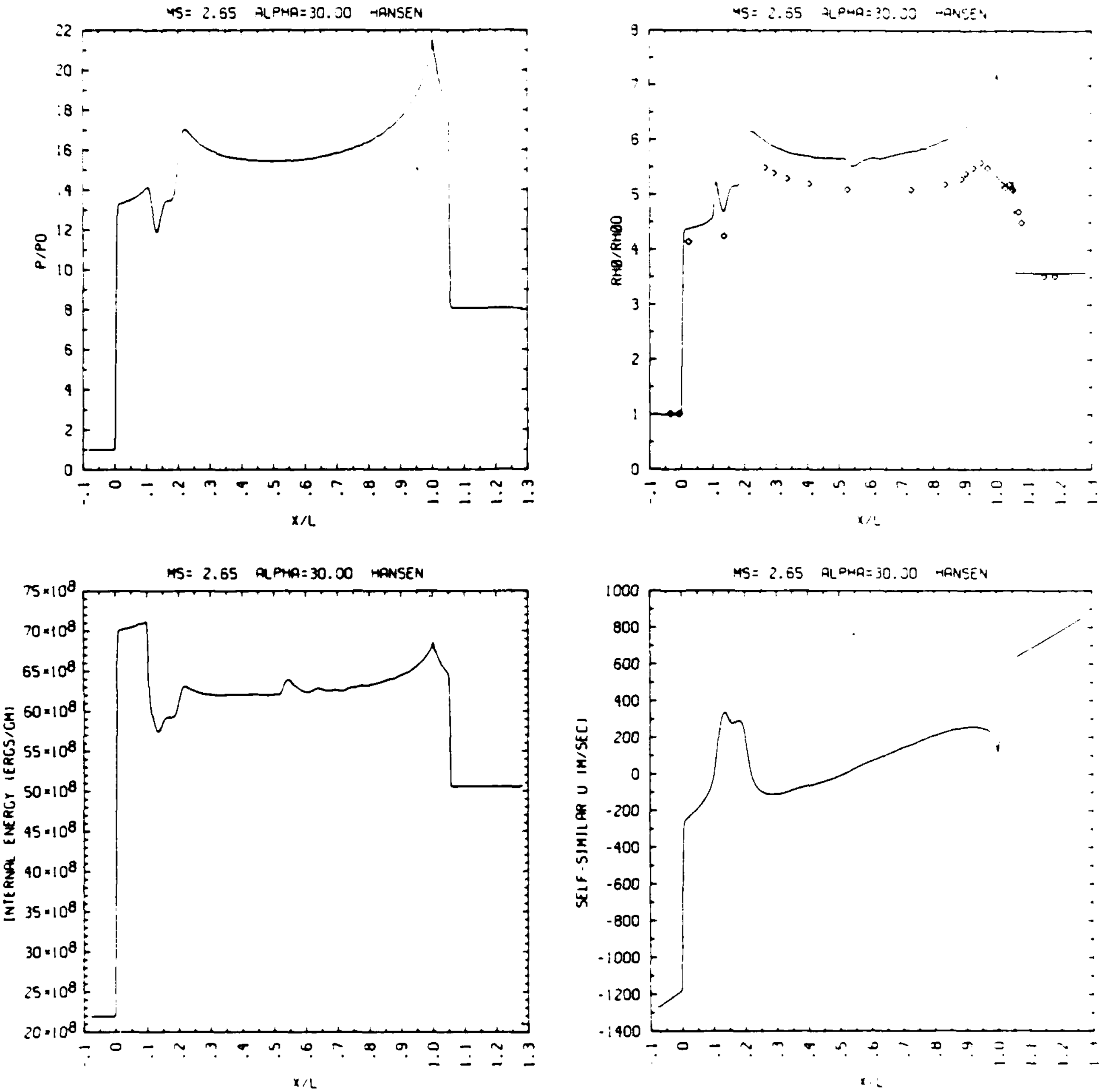

Figure $8c_H$. Wall plot for p/p_0, ρ/ρ_0 with experimental data included, e, u; Hansen

Figure 8. Case 5, $M_s = 2.65$, $\theta_w = 30°$, Air, $\gamma = 1.4$ and Hansen EOS, CMR - continued.

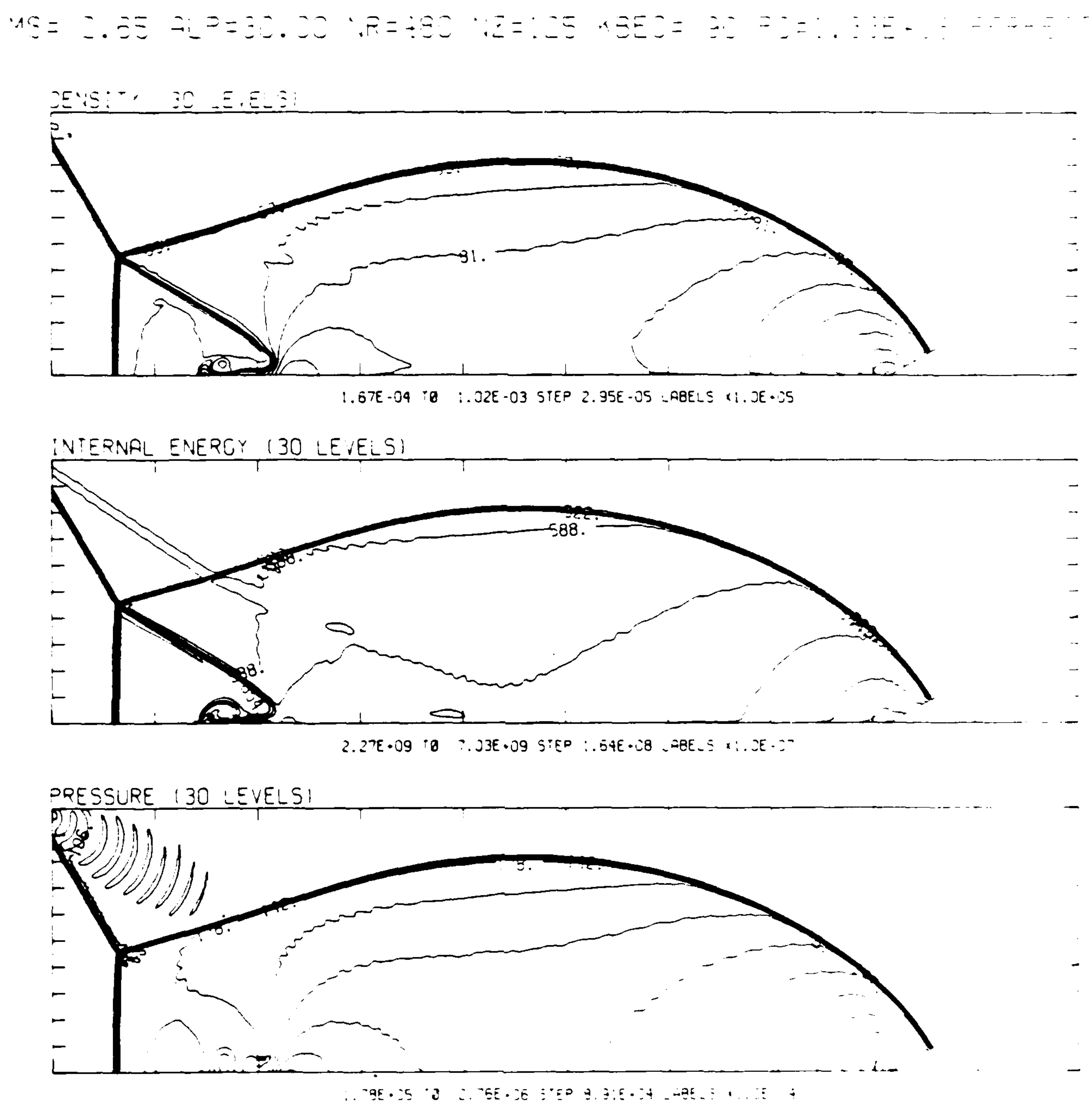

Figure $8d_p$. Whole-flowfield contour-plots; γ = 1.4

Figure 8. Case 5, M_s = 2.65, θ_w = 30°, Air, γ = 1.4 and Hansen EOS, CMR - continued.

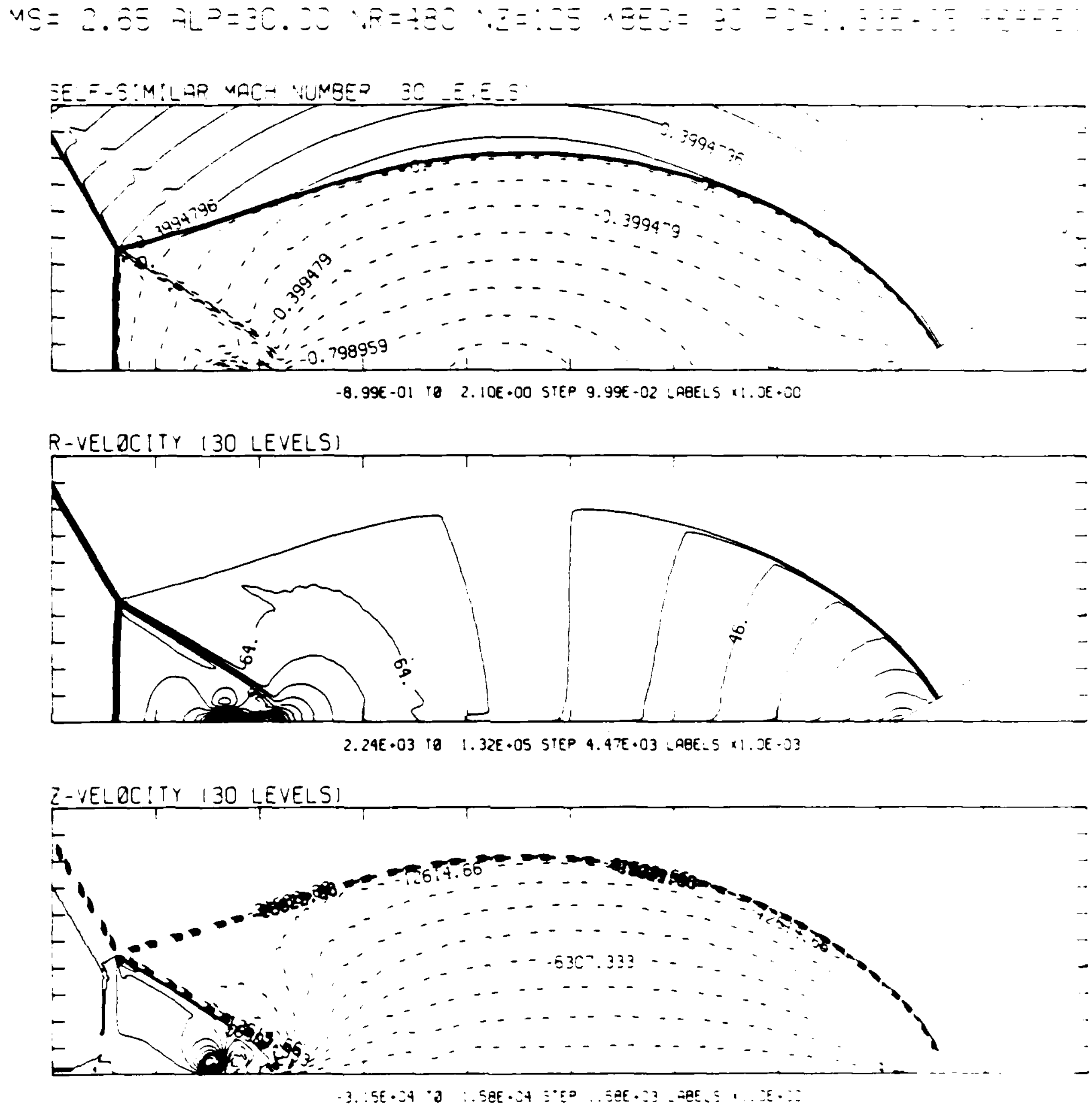

Figure $8d_p$. Whole-flowfield contour-plots; γ = 1.4 - continued.

Figure 8. Case 5, M_s = 2.65, θ_w = 30°, Air, γ = 1.4 and Hansen EOS, CMR - continued.

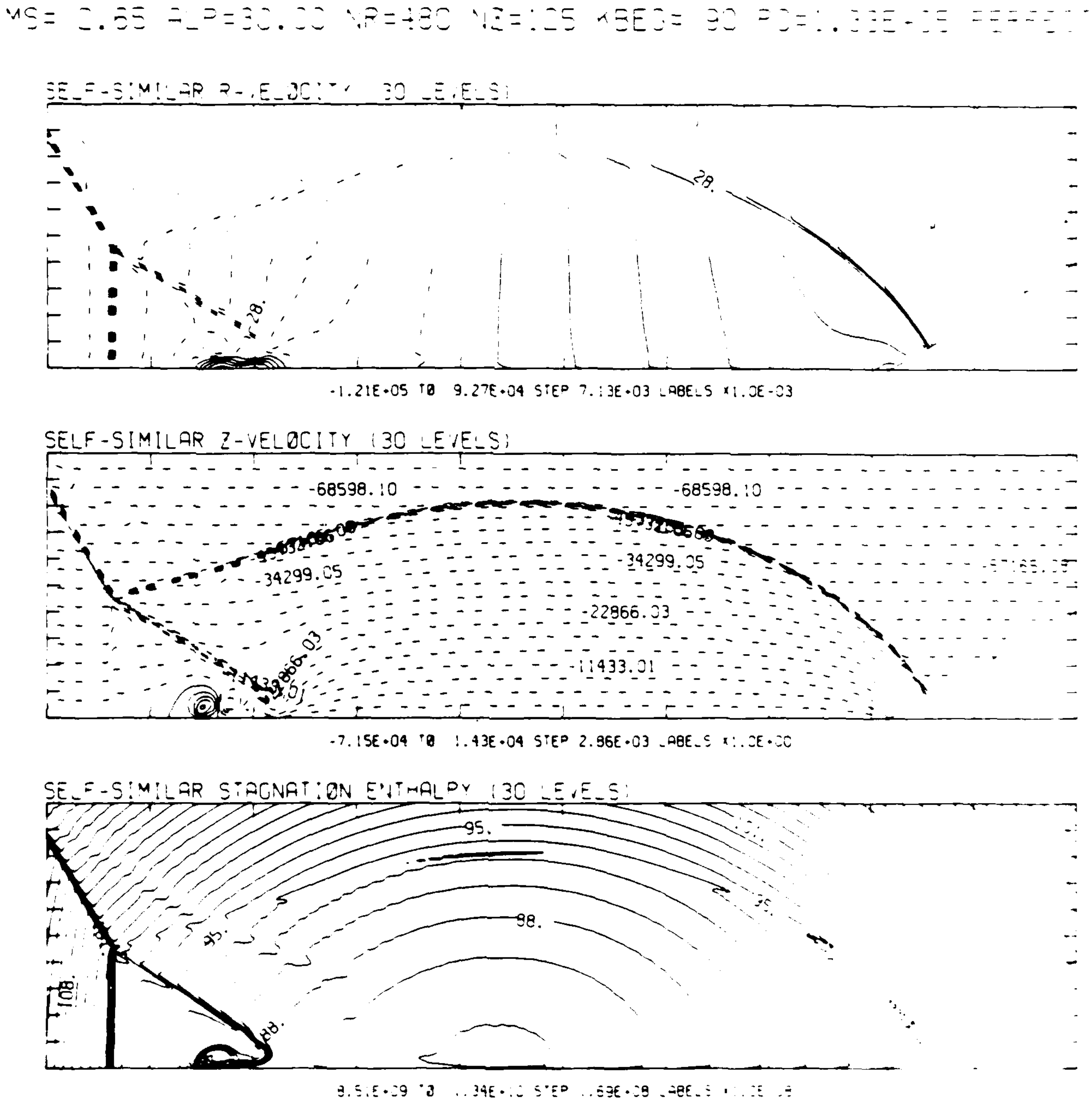

Figure 8d$_p$. Whole-flowfield contour-plots; γ = 1.4 - continued.

Figure 8. Case 5, M_s = 2.65, θ_w = 30°, Air, γ = 1.4 and Hansen EOS, CMR - continued.

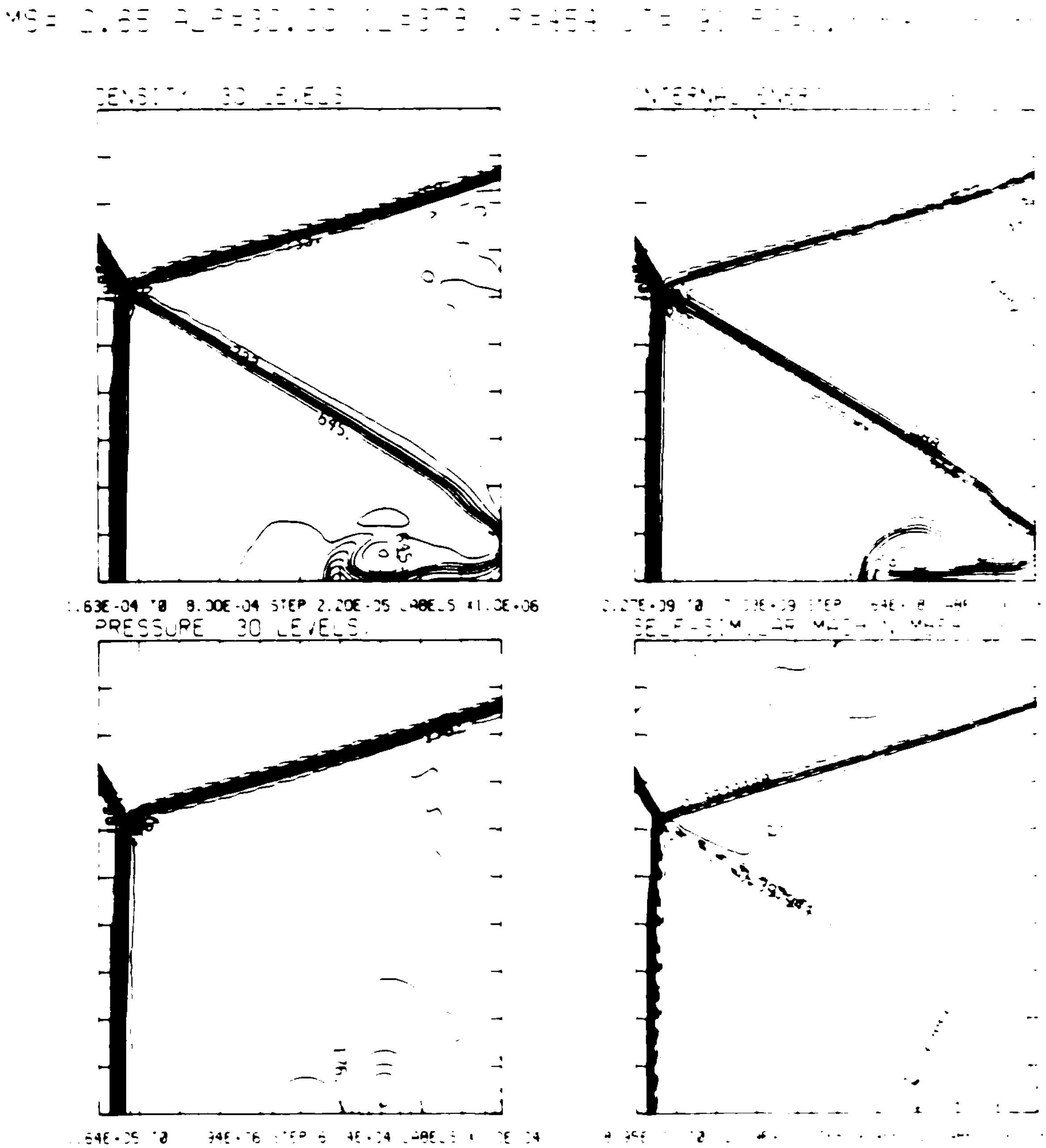

Figure $8e_p$. Blowup-frame plots; $\gamma = 1.4$

Figure 8. Case 5, $M_s = 2.65$, $\theta_w = 30°$, Air, $\gamma = 1.4$ and Hansen EOS, CMR - continued.

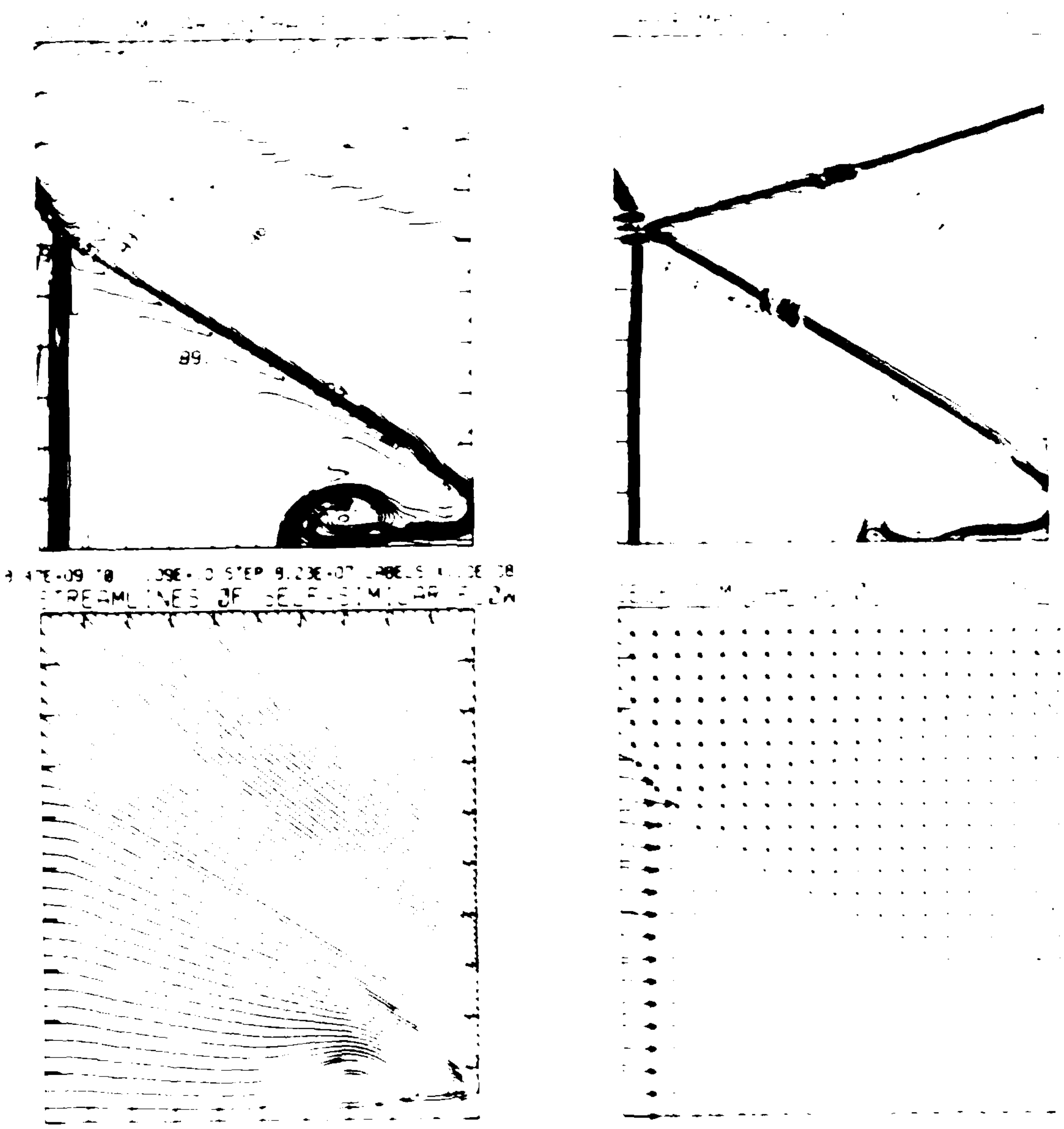

Figure 8e$_p$. Blowup-frame plots; γ = 1.4 - continued.

Figure 8. Case 5, M_s = 2.65, θ_w = 30°, Air, γ = 1.4 and Hansen EOS, CMR - continued.

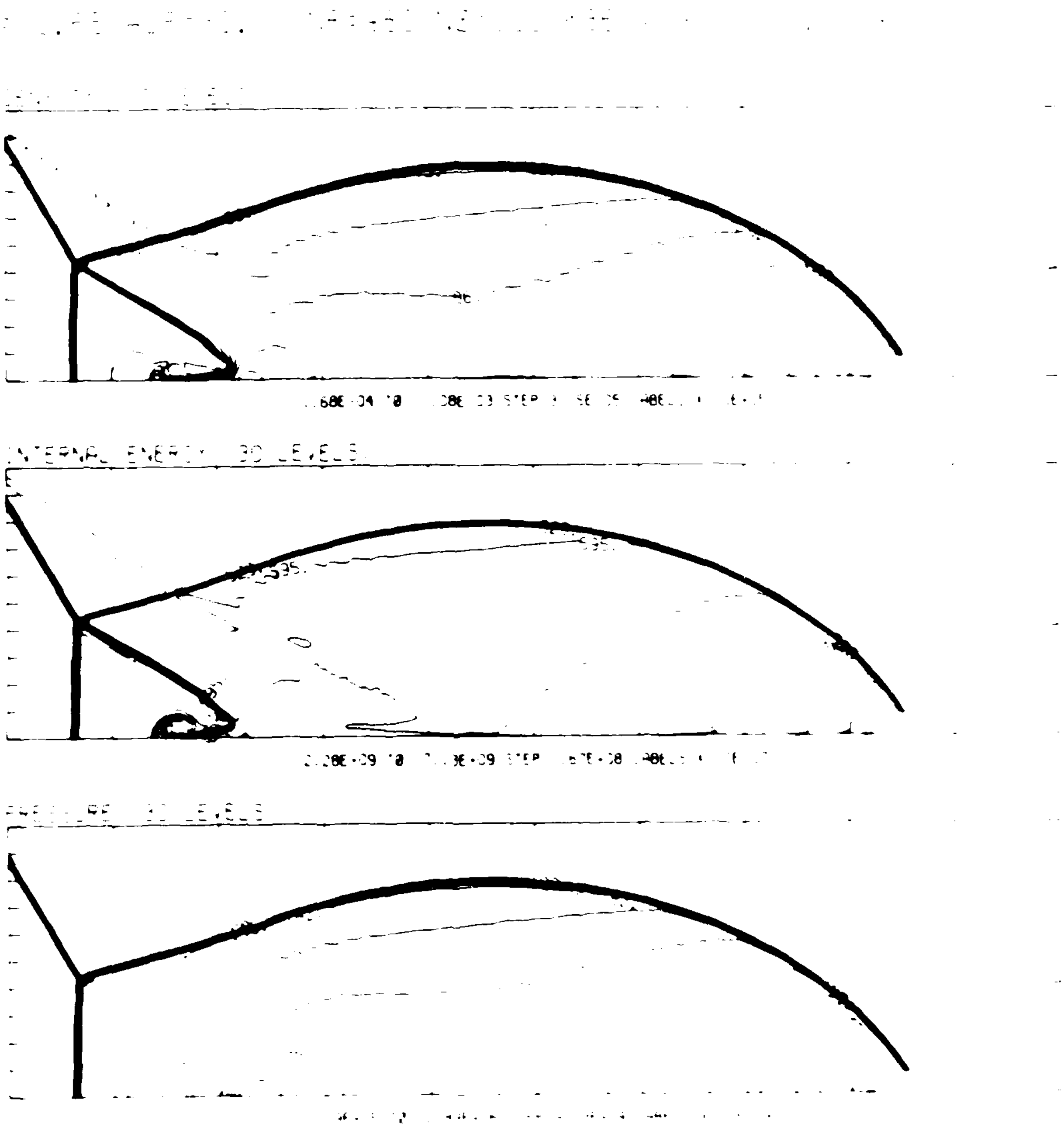

Figure 8d$_H$. Whole-flowfield contour-plots, Hansen

Figure 8. Case 5, M_s = 2.65, θ_w = 30°, Air, γ = 1.4 and Hansen EOS, CMR - continued.

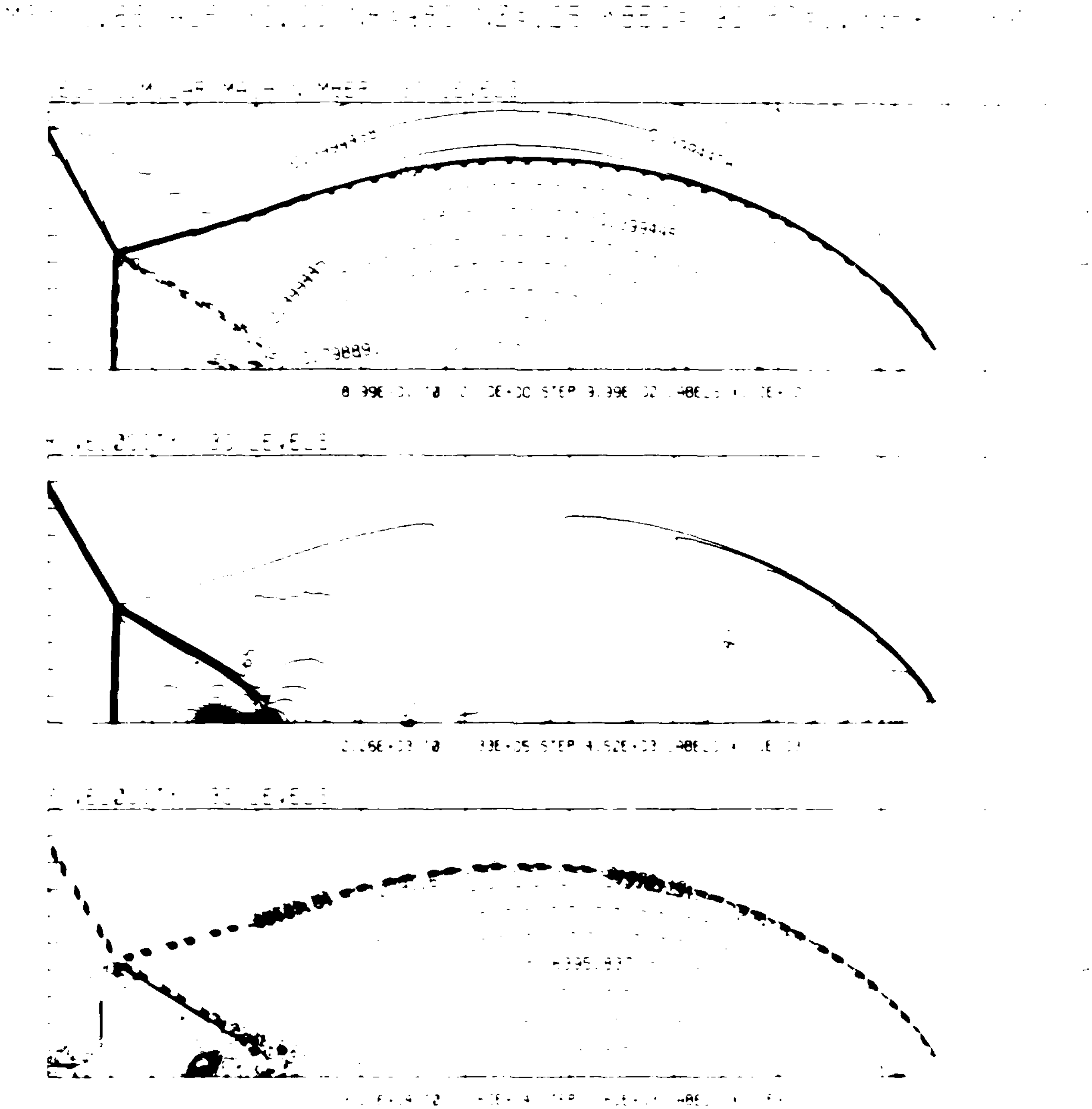

Figure 8d$_H$. Whole-flowfield contour-plots; Hansen - continued.

Figure 8. Case 5, M_s = 2.65, θ_w = 30°, Air, γ = 1.4 and Hansen EOS, CMR - continued.

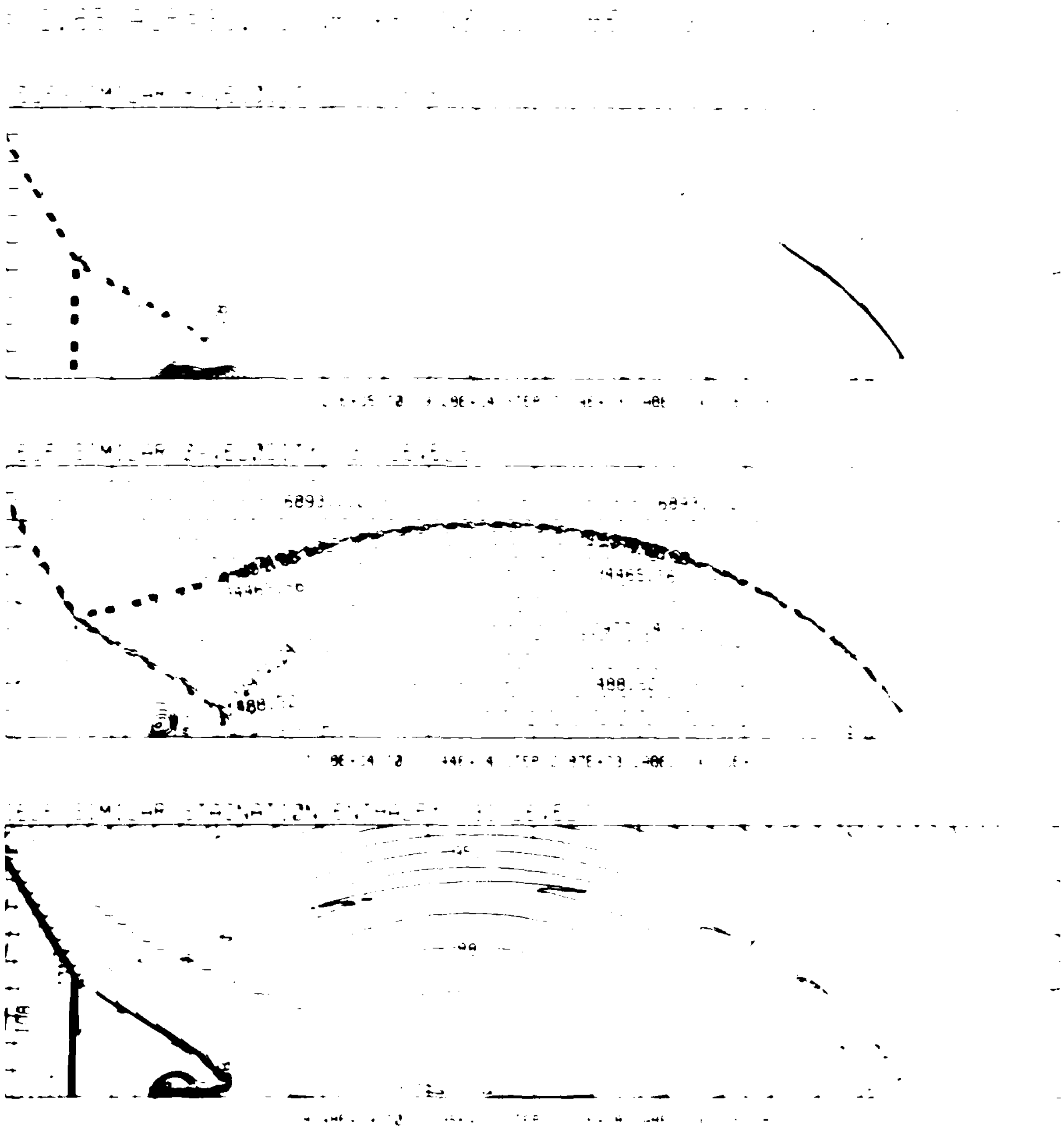

Figure $8d_H$. Whole-flowfield contour-plots; Hansen - continued.

Figure 8. Case 5, M_s = 2.65, θ_w = 30°, Air, γ = 1.4 and Hansen EOS, CMR - continued.

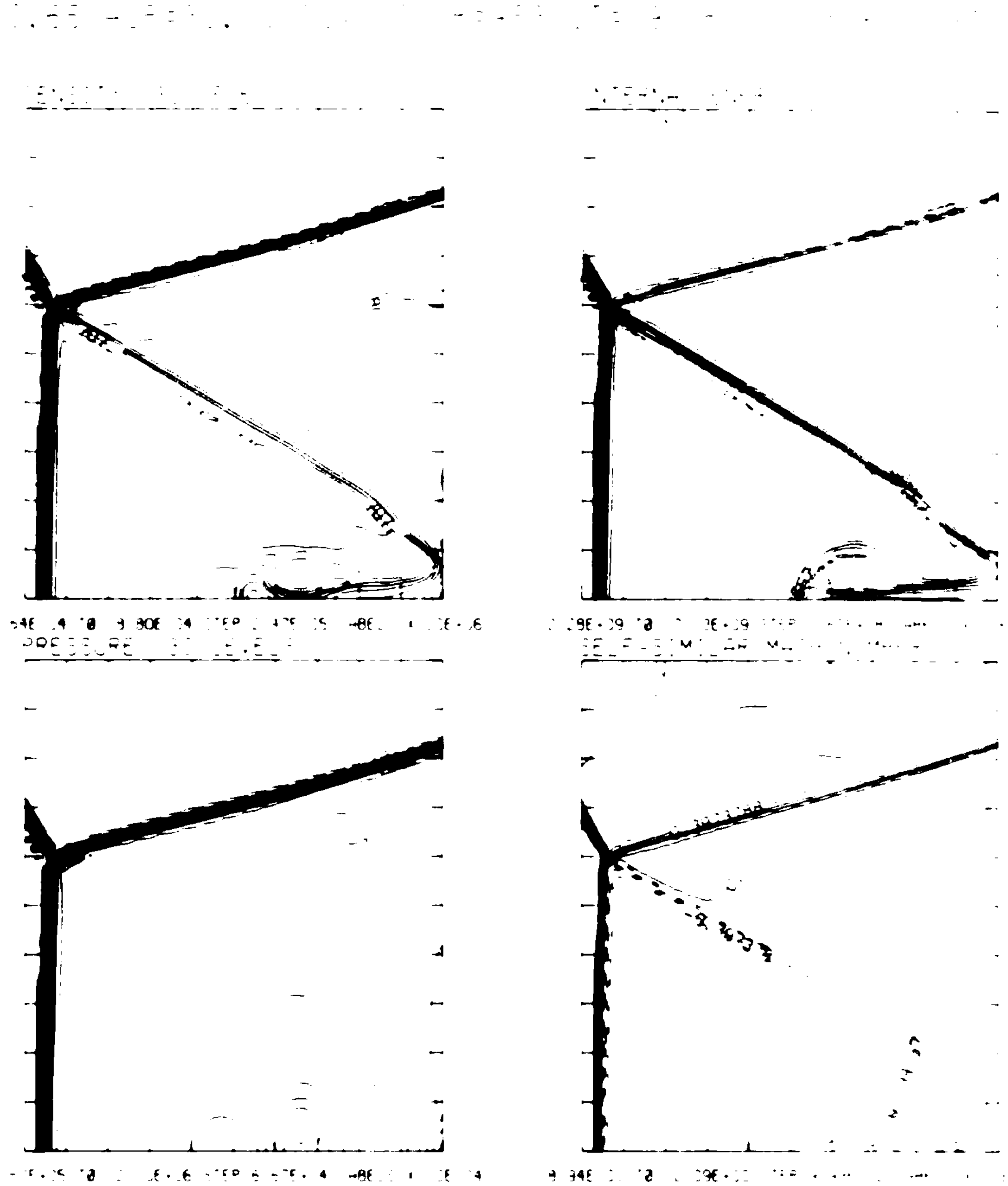

Figure 8e$_{u}$. Blowup-frame plots; Hansen

Figure 8. Case 5, M_S = 2.65, θ_w = 30°, Air, γ = 1.4 and Hansen EOS, CMR - continued.

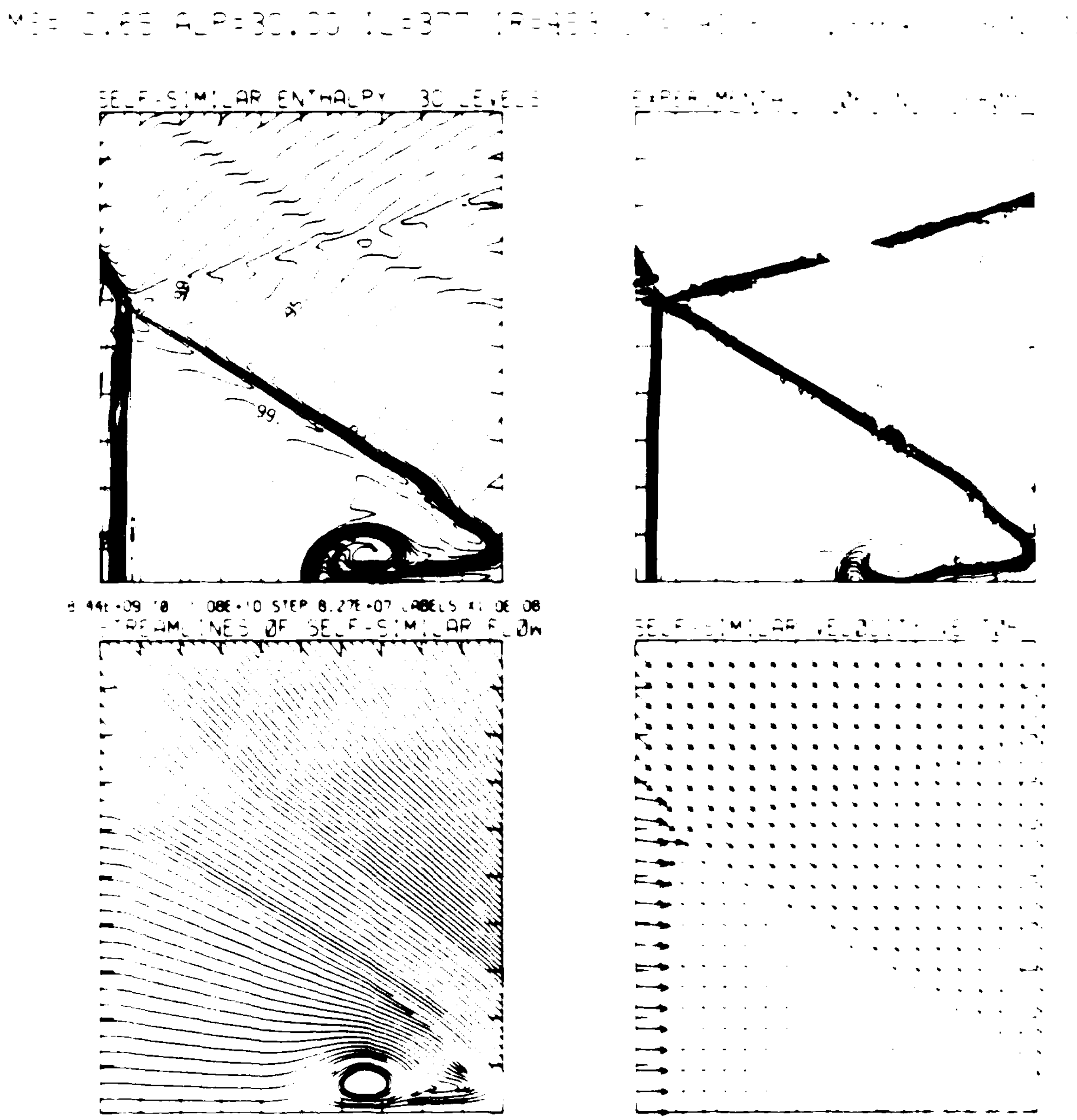

Figure 8e$_H$. Blowup-frame plots; Hansen - continued.

Figure 8. Case 5, M_s = 2.65, θ_w = 30°, Air, γ = 1.4 and Hansen EOS, CMR - continued.

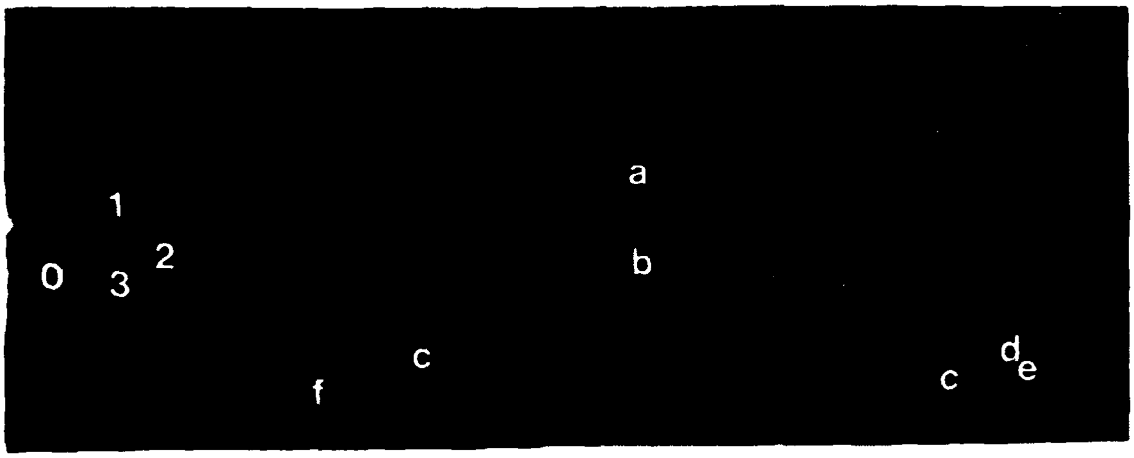

Region	ρ/ρ_0
0	1.00
1	3.59
2	4.83
3	3.74
a	4.83
b	5.16
c	5.48
d	4.50
e	4.18
f	5.80

Figure 9a. Interferogram

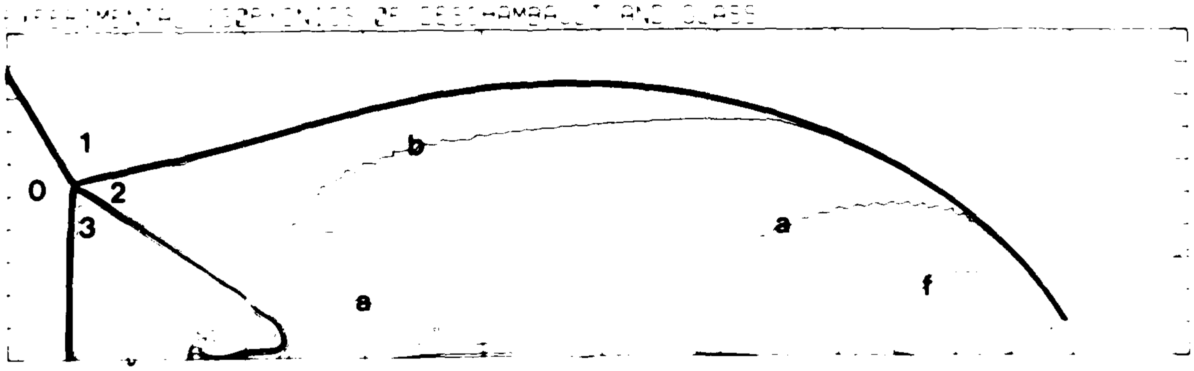

XBB 859-7198

Figure 9b. Calculated isopycnics using the experimental fringes.

Figure 9. Case 6, M_s = 5.07, θ_w = 30°, Argon, γ = 5/3, CMR.

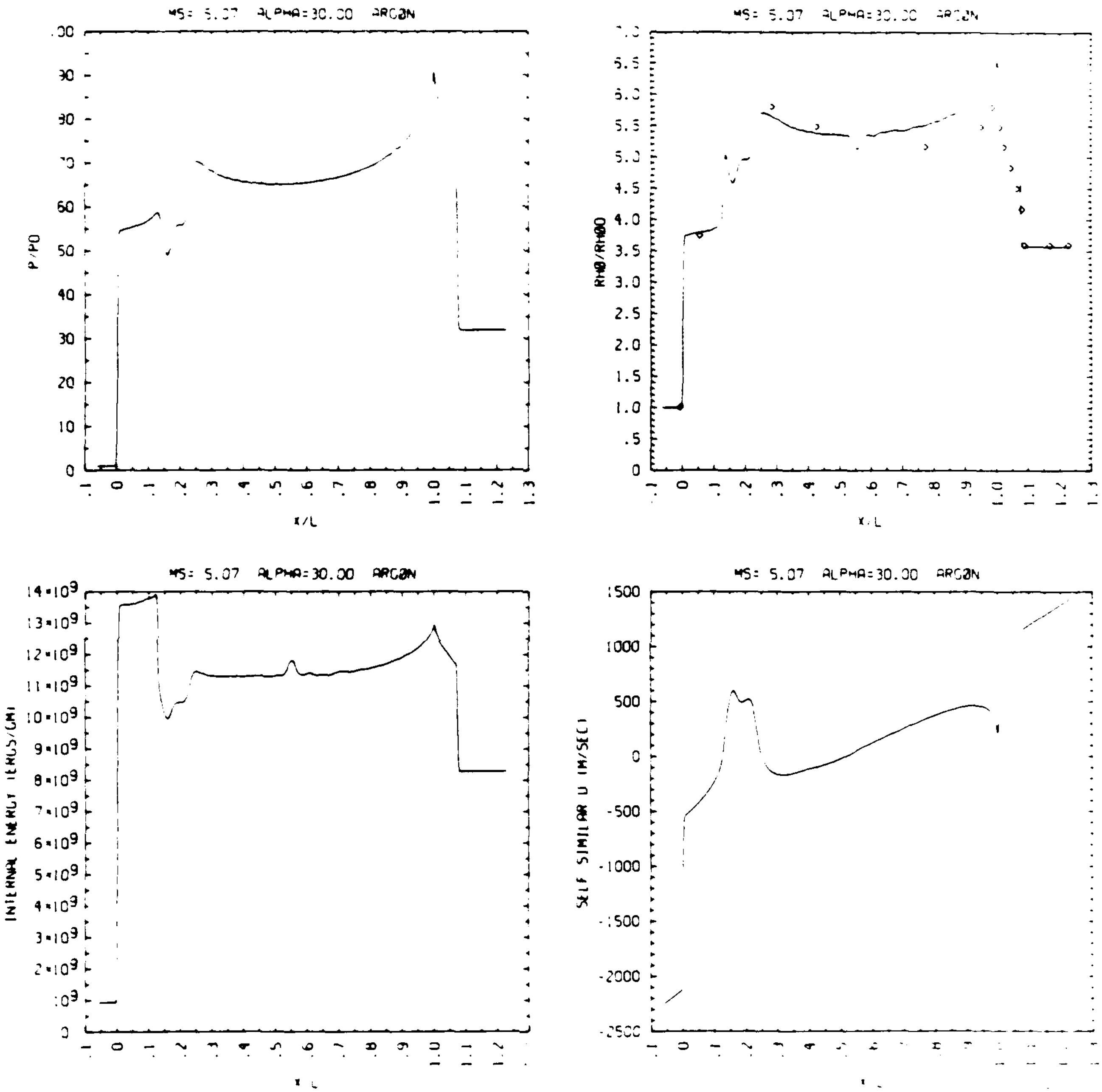

Figure 9c. Wall plots for p/p_0, ρ/ρ_0 with experimental data included, e, $\bar{u}$.

Figure 9. Case 6, M_s = 5.07, θ_w = 30°, Argon, γ = 5/3, CMR - continued.

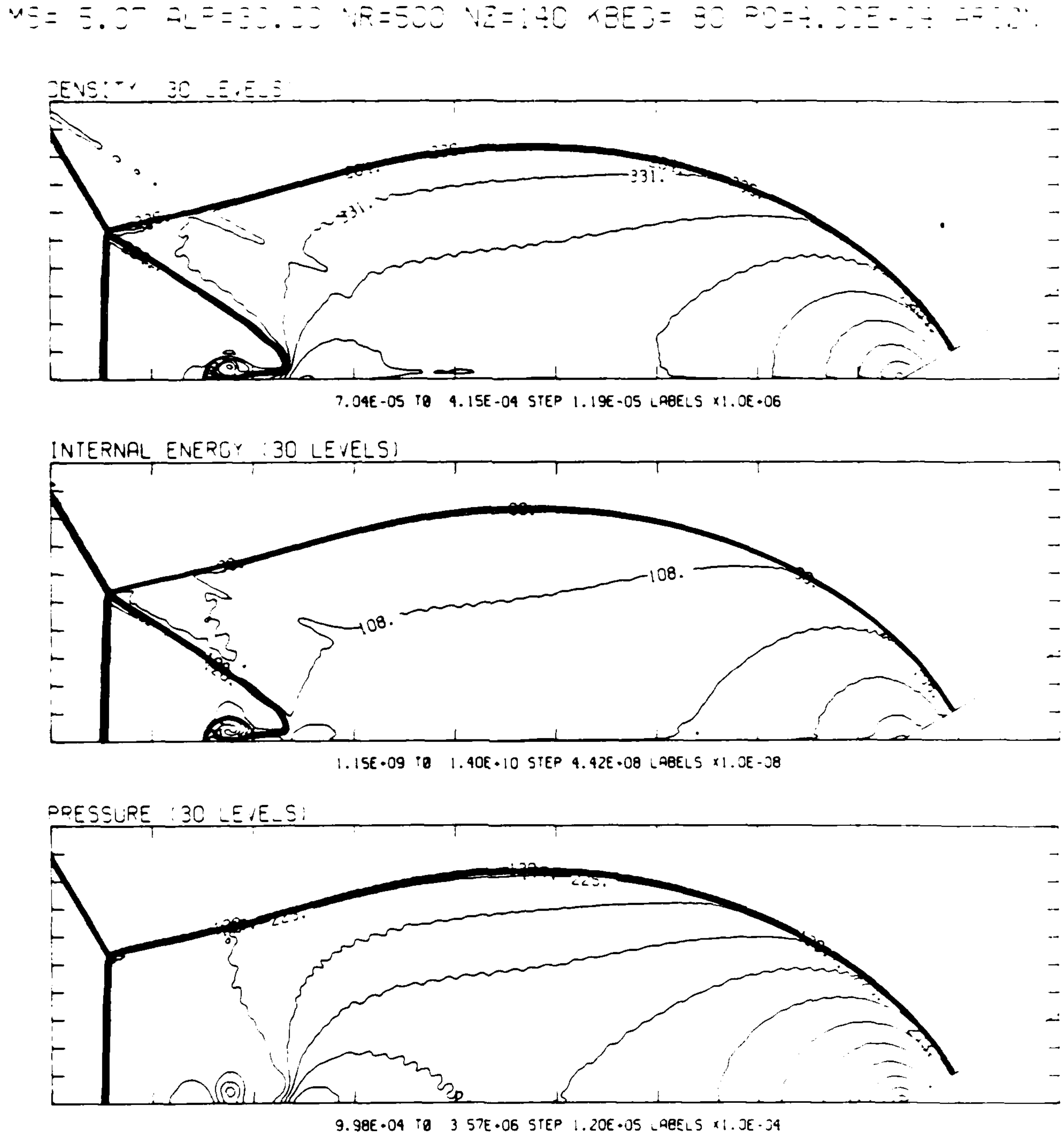

Figure 9d. Whole-flowfield contour-plots.

Figure 9. Case 6, M_s = 5.07, θ_w = 30°, Argon, γ = 5/3, CMR - continued.

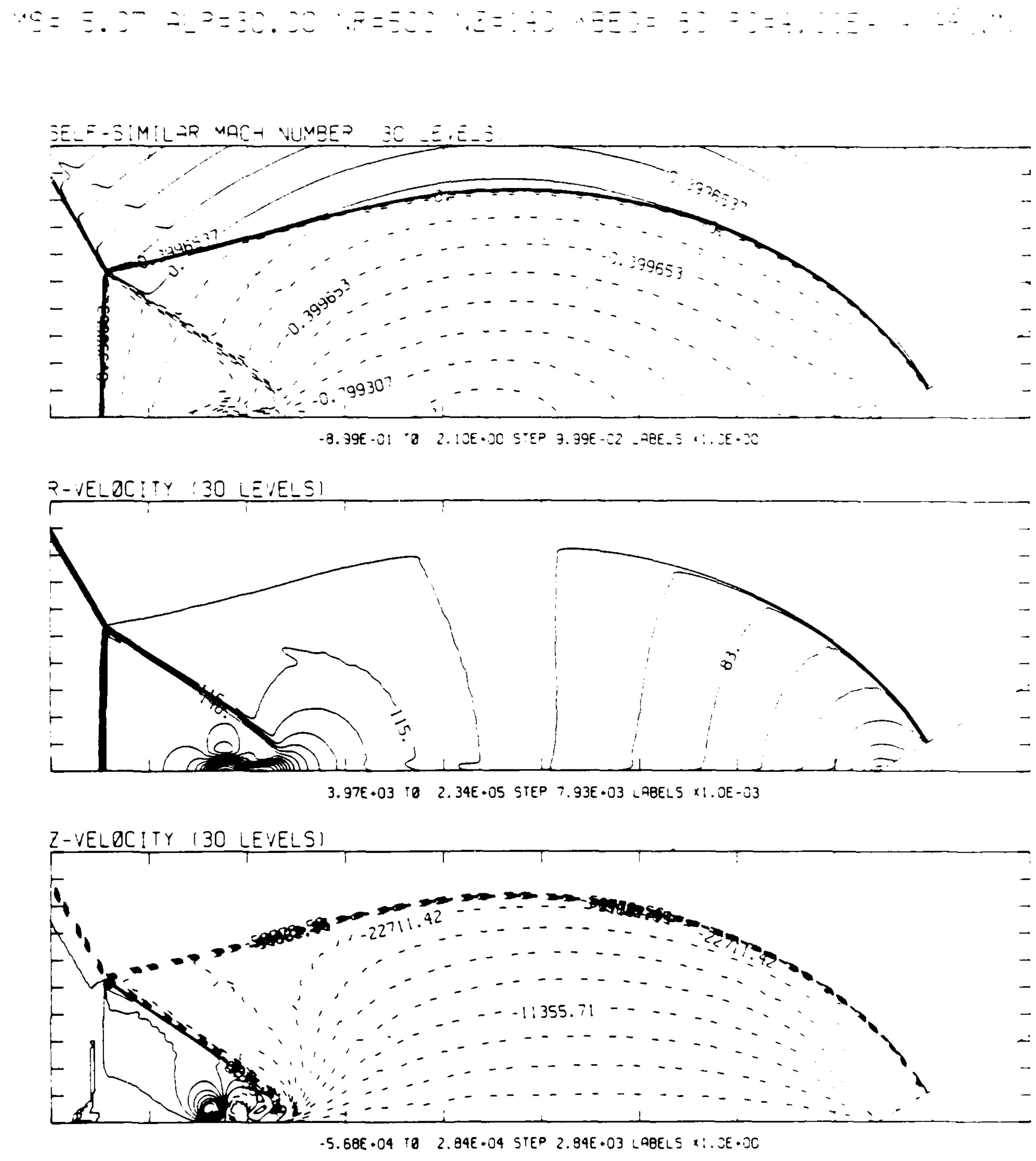

Figure 9d. Whole-flowfield contour-plots - continued.

Figure 9. Case 6, M_s = 5.07, θ_w = 30°, Argon, γ = 5/3, CMR - continued.

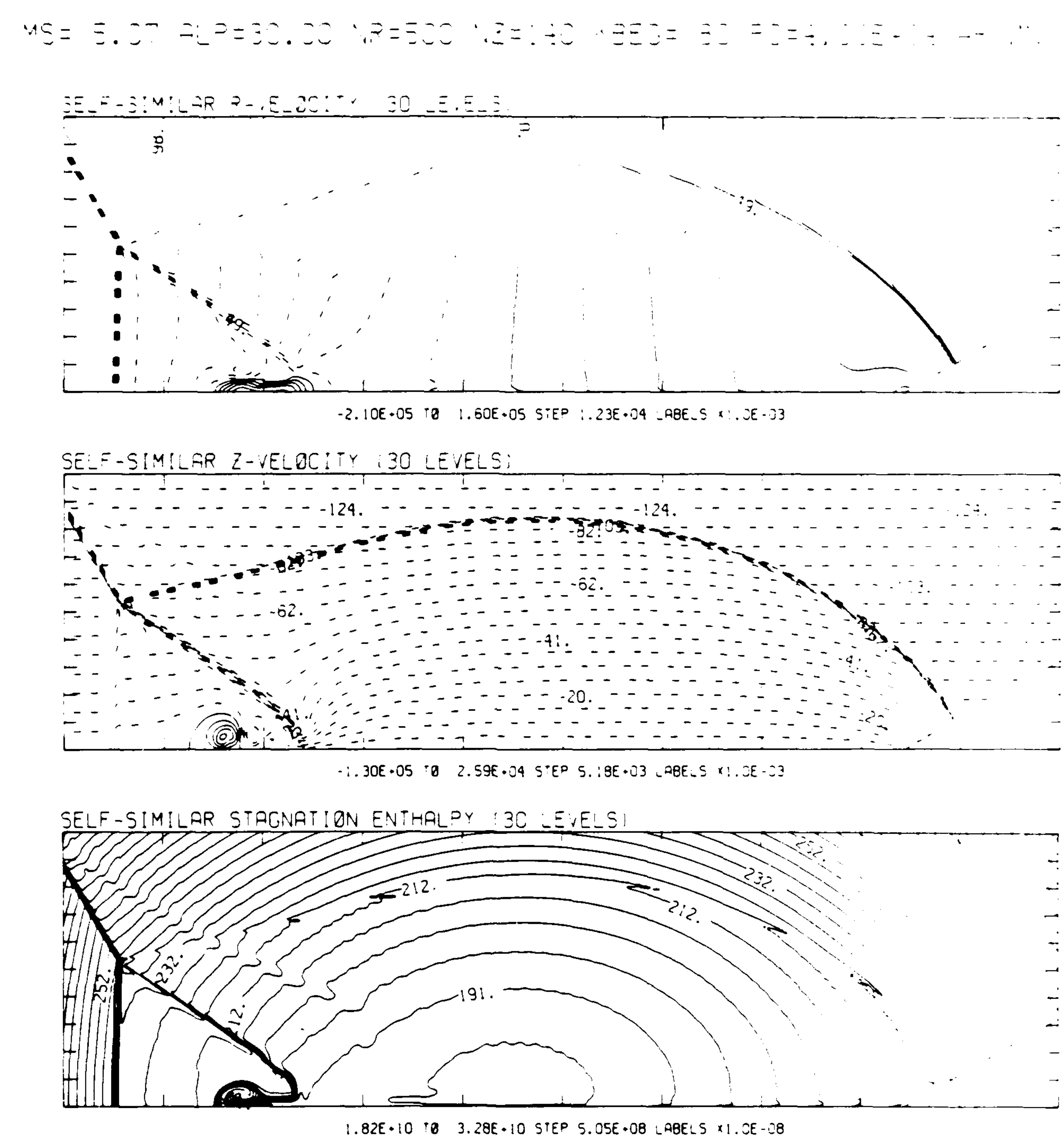

Figure 9d. Whole-flowfield contour-plots - continued.

Figure 9. Case 6, M_s = 5.07, θ_w = 30°, Argon, γ = 5/3, CMR - continued.

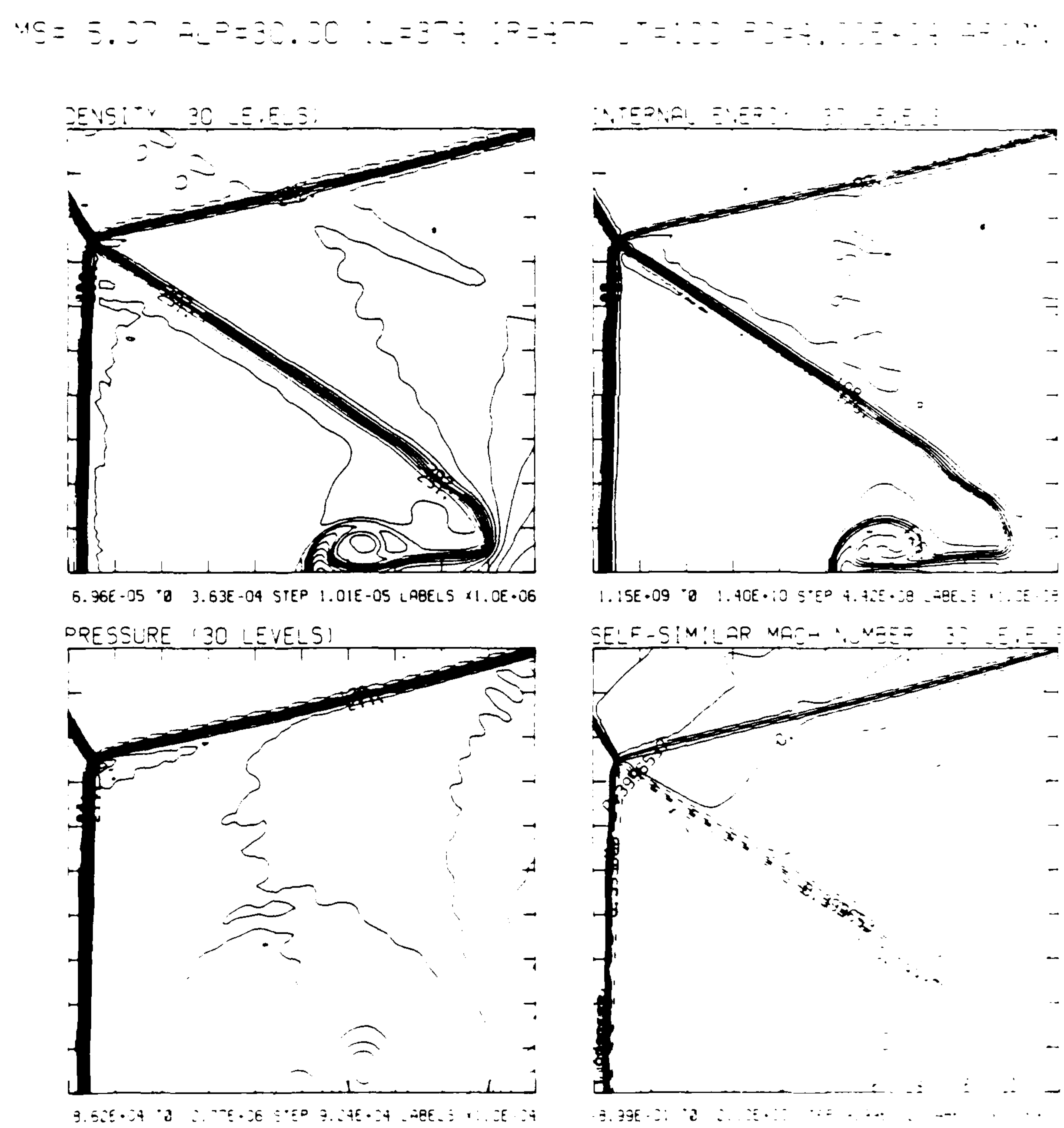

Figure 9e. Blowup-frame plots.

Figure 9. Case 6, M_s = 5.07, θ_w = 30°, Argon, γ = 5/3, CMR - continued.

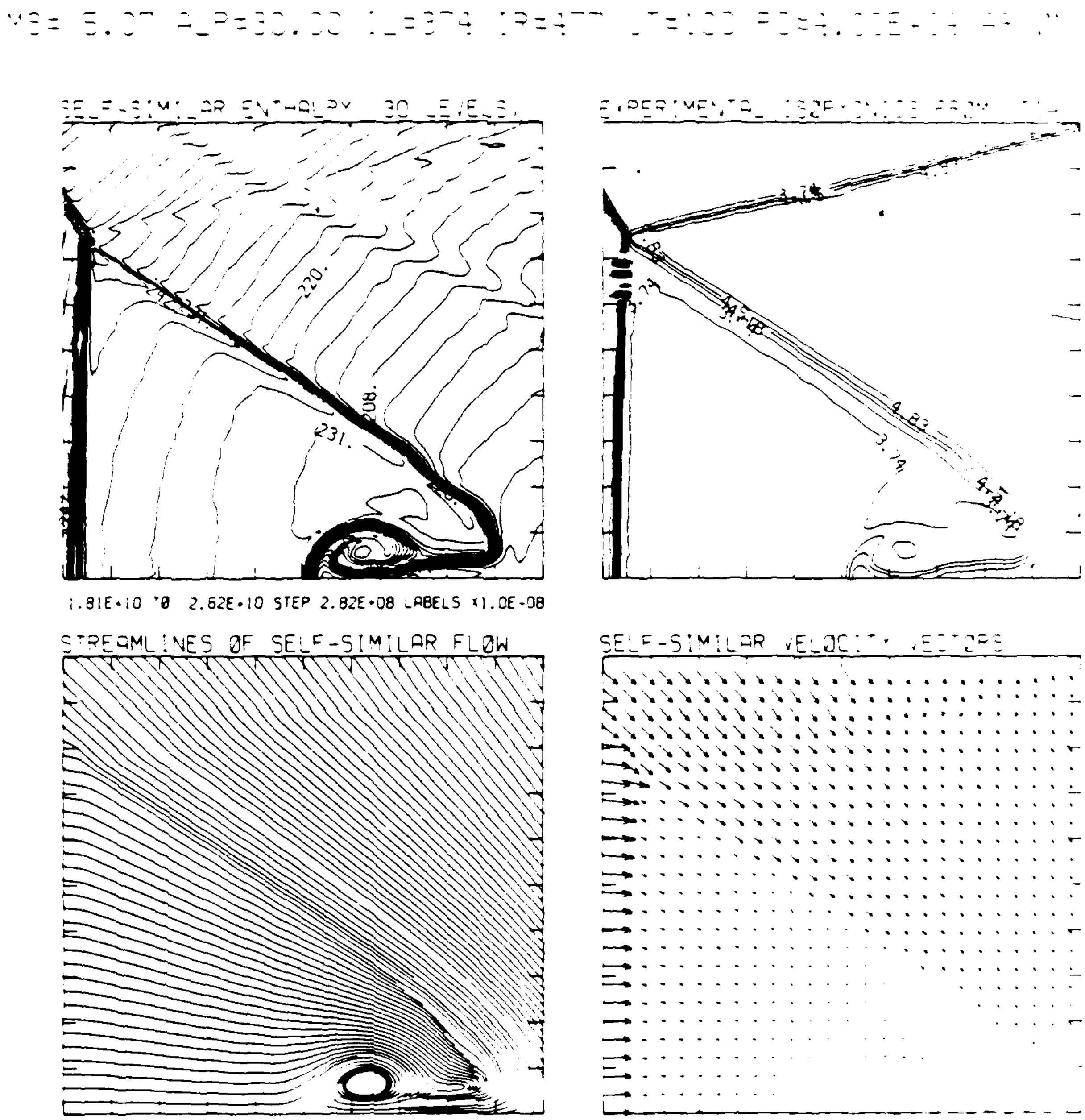

Figure 9e. Blowup-frame plots - continued.

Figure 9. Case 6, M_s = 5.07, θ_w = 30°, Argon, γ = 5/3, CMR - continued.

Region	ρ/ρ_0
0	1.00
1	5.73
1'	6.33
2	6.30
3	5.77
a	6.70
b	7.10
c	7.50
d	7.90
e	8.29
f	8.69
g	9.09
h	9.49
i	9.89
j	10.29

Figure 10a. Interferogram.

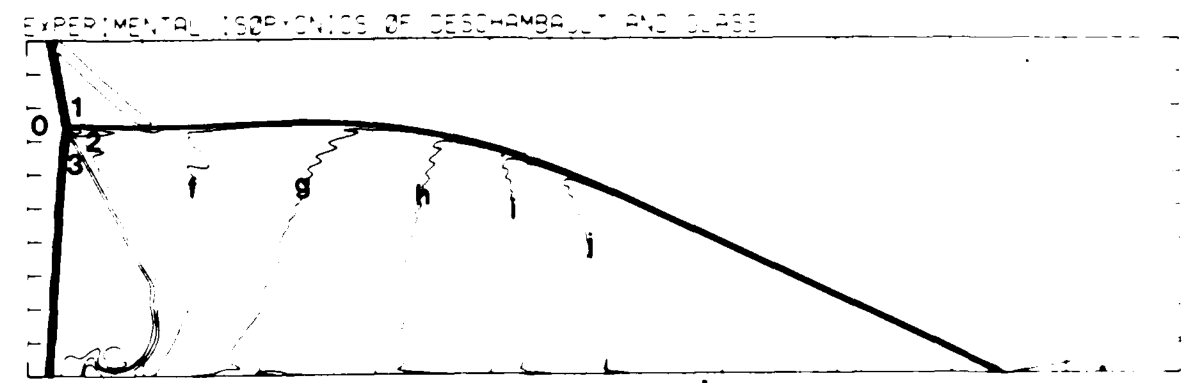

XBB 859-7199

Figure 10b. Calculated isopycnics using the experimental fringes.

Figure 10. Case 7, M_s = 10.37, θ_w = 10°, Air, Hansen EOS, CMR.

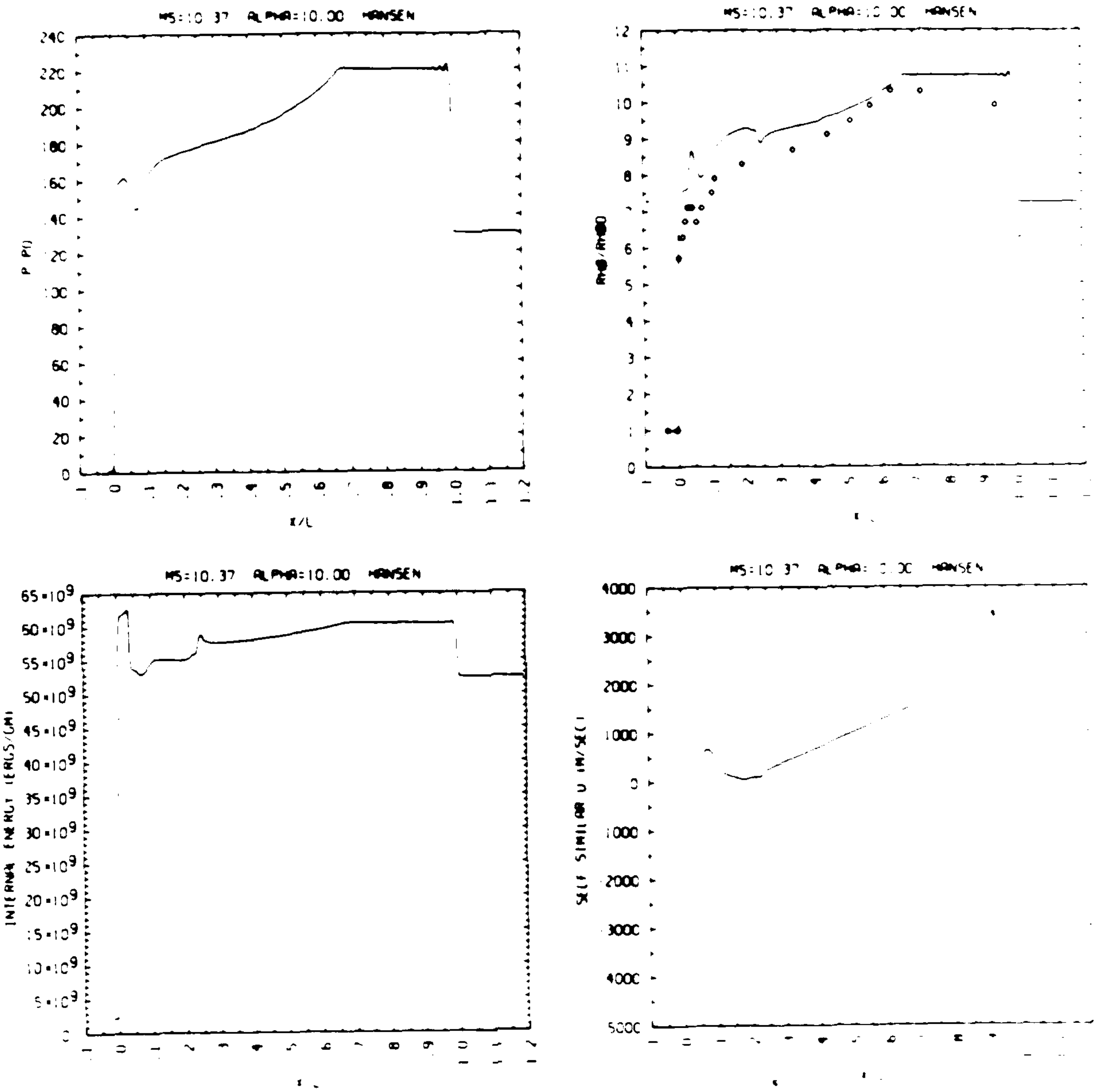

Figure 10c. Wall plots for p/p_0, ρ/ρ_0 with experimental data included, e, $\bar{u}$.

Figure 10. Case 7, M_s = 10.37, θ_w = 10°, Air, Hansen EOS, CMR - continued.

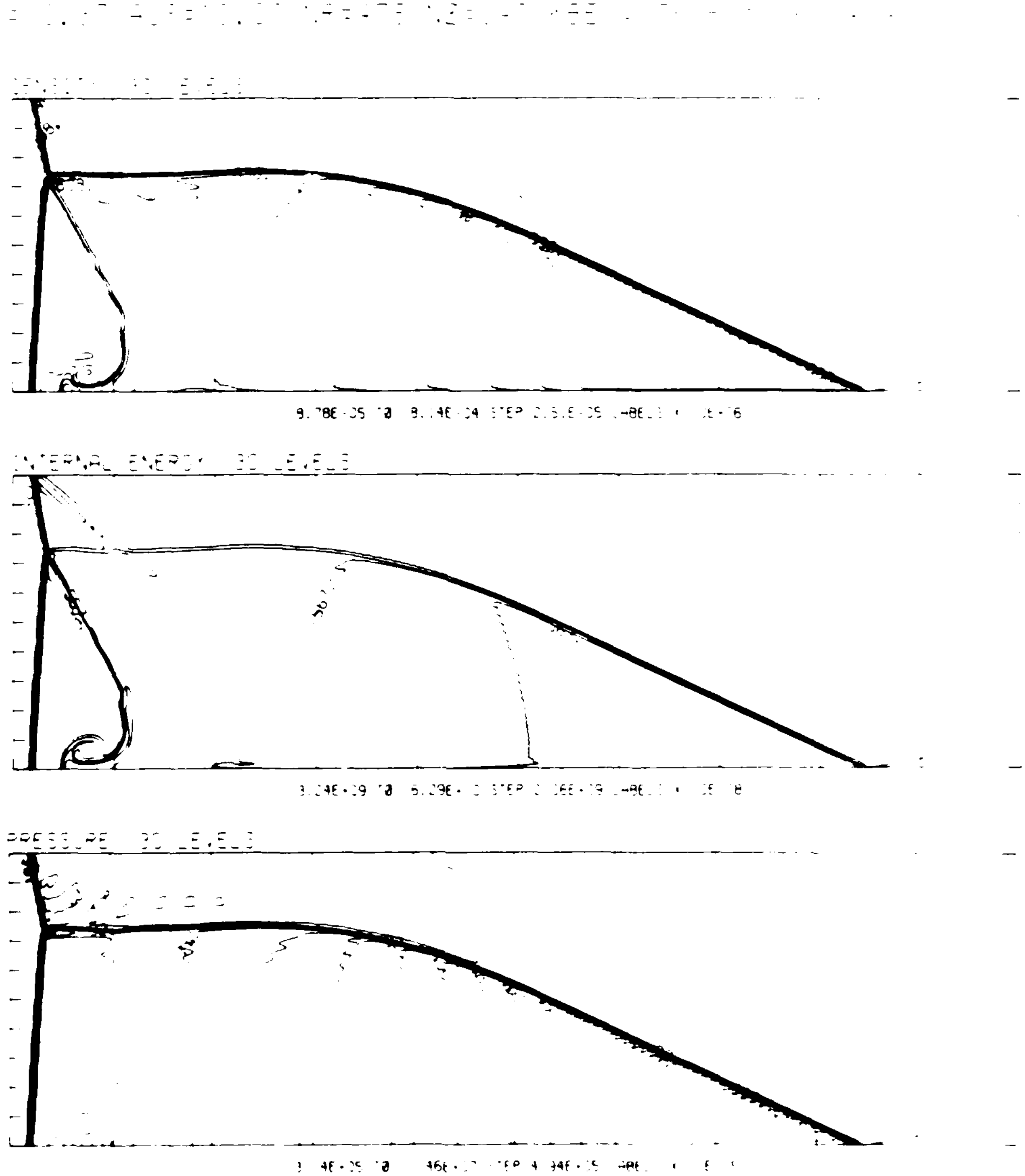

Figure 10d. Whole-flowfield contour-plots.

Figure 10. Case 7, M_s = 10.37, θ_w = 10°, Air, Hansen EOS, CMR - Continued.

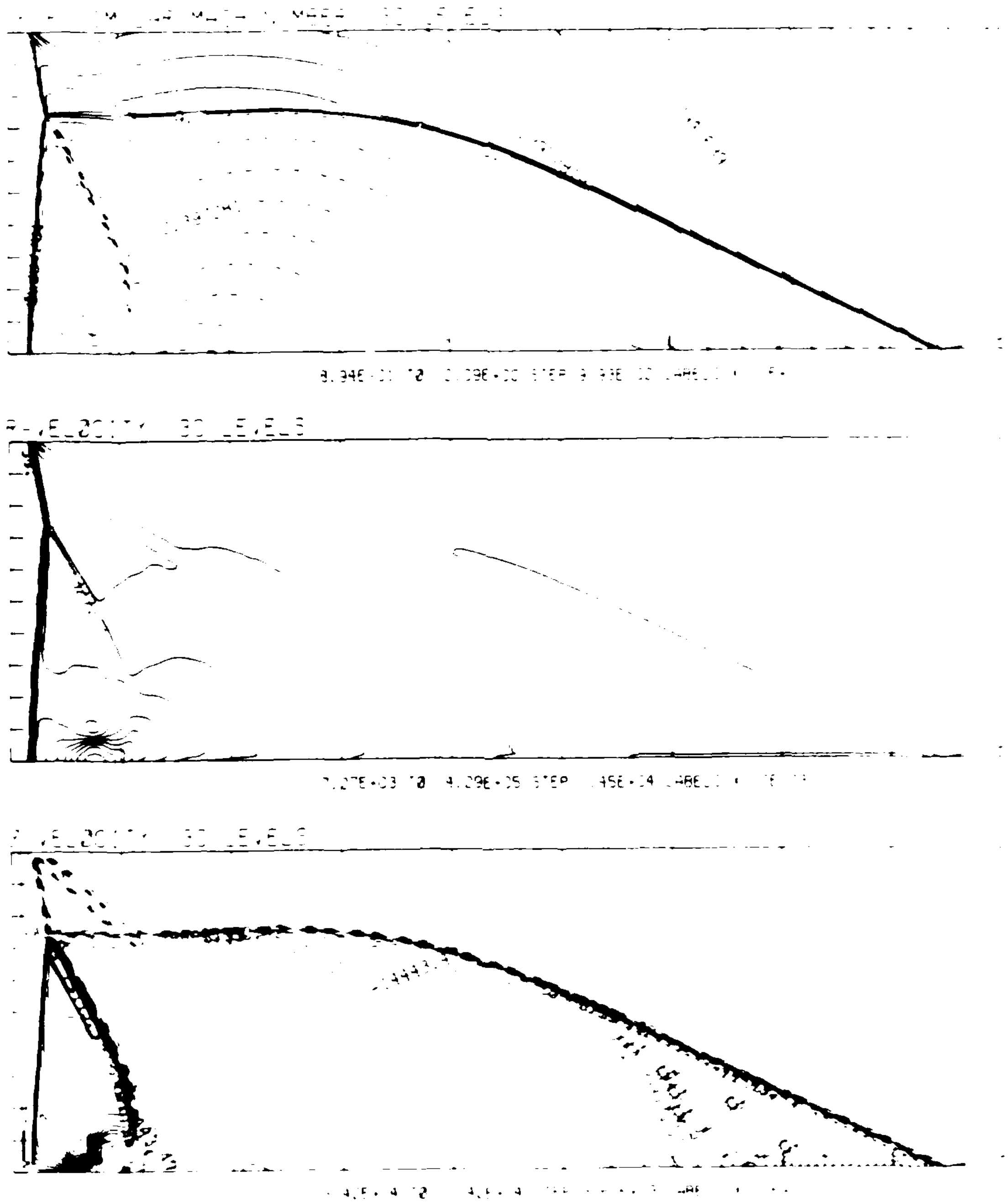

Figure 10d. Whole-flowfield contour-plots - continued.

Figure 10. Case 7, M_s = 10.37, θ_w = 10°, Air, Hansen EOS, CMR - continued.

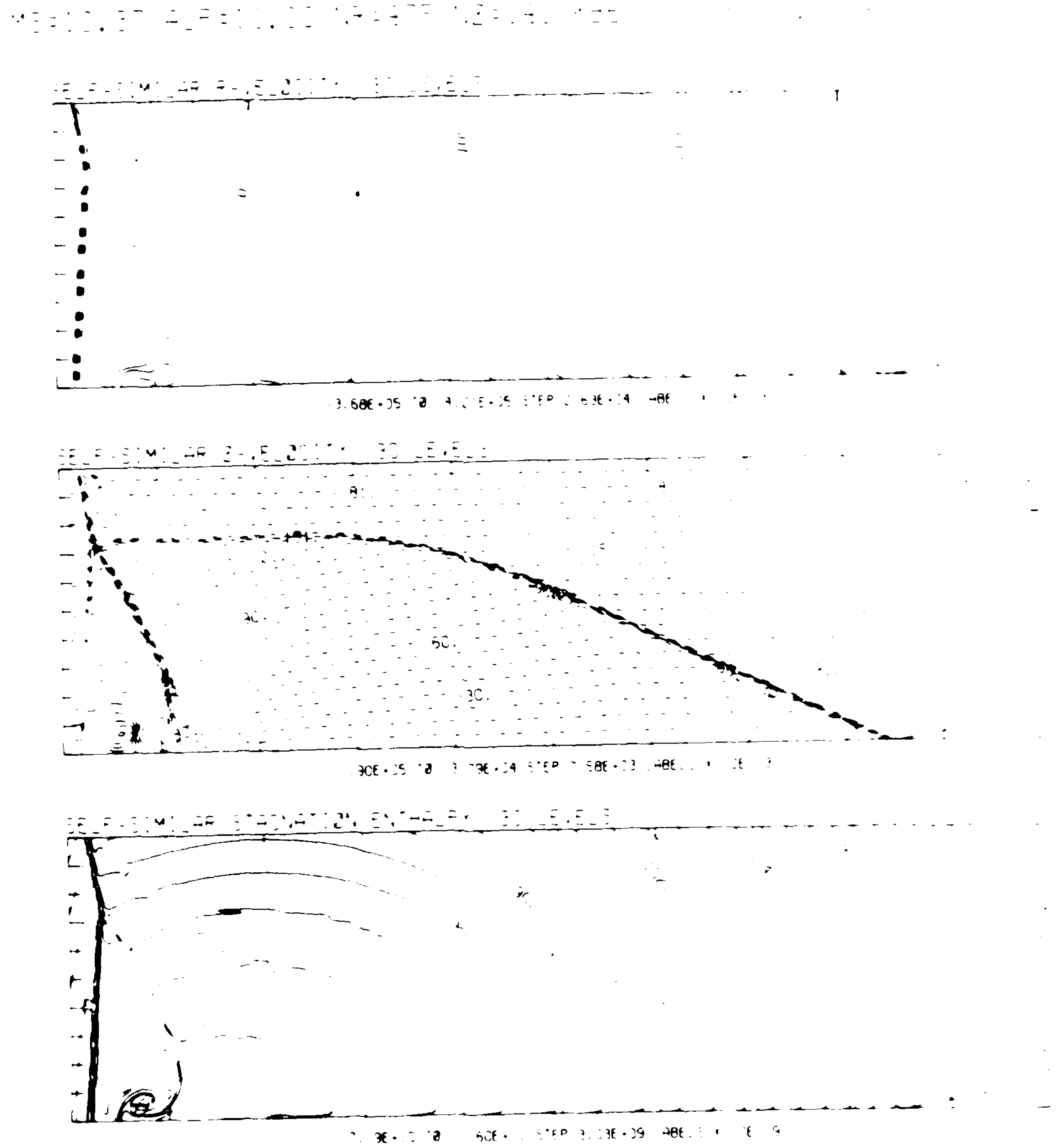

Figure 10d. Whole-flowfield contour-plots - continued.

Figure 10. Case 7, M_s = 10.37, θ_w = 10°, Air, Hansen EOS, CMR - continued.

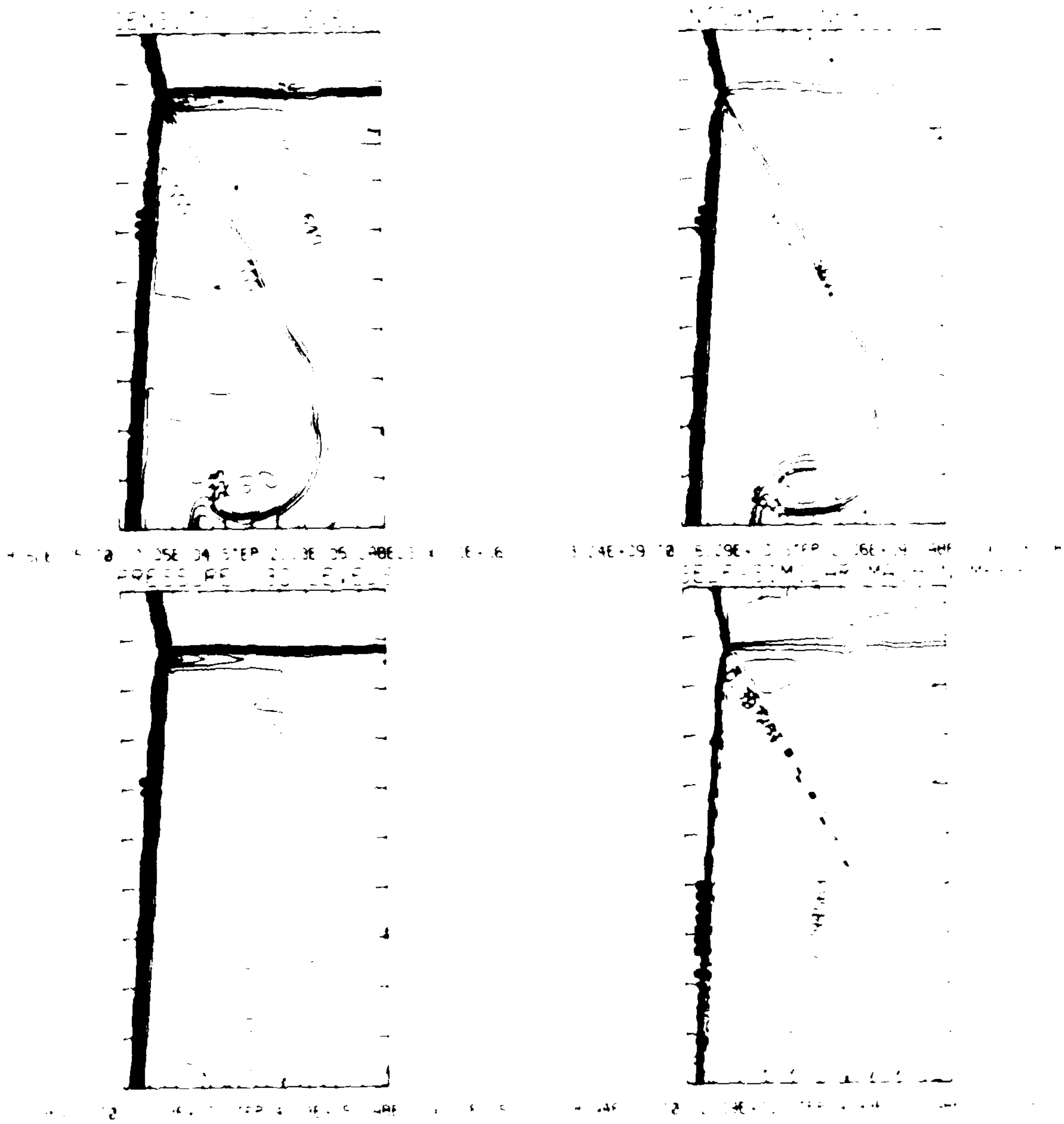

Figure 10e. Blowup-frame plots.

Figure 10. Case 7, M_s = 10.37, θ_w = 10°, Air, Hansen EOS, CMR - continued.

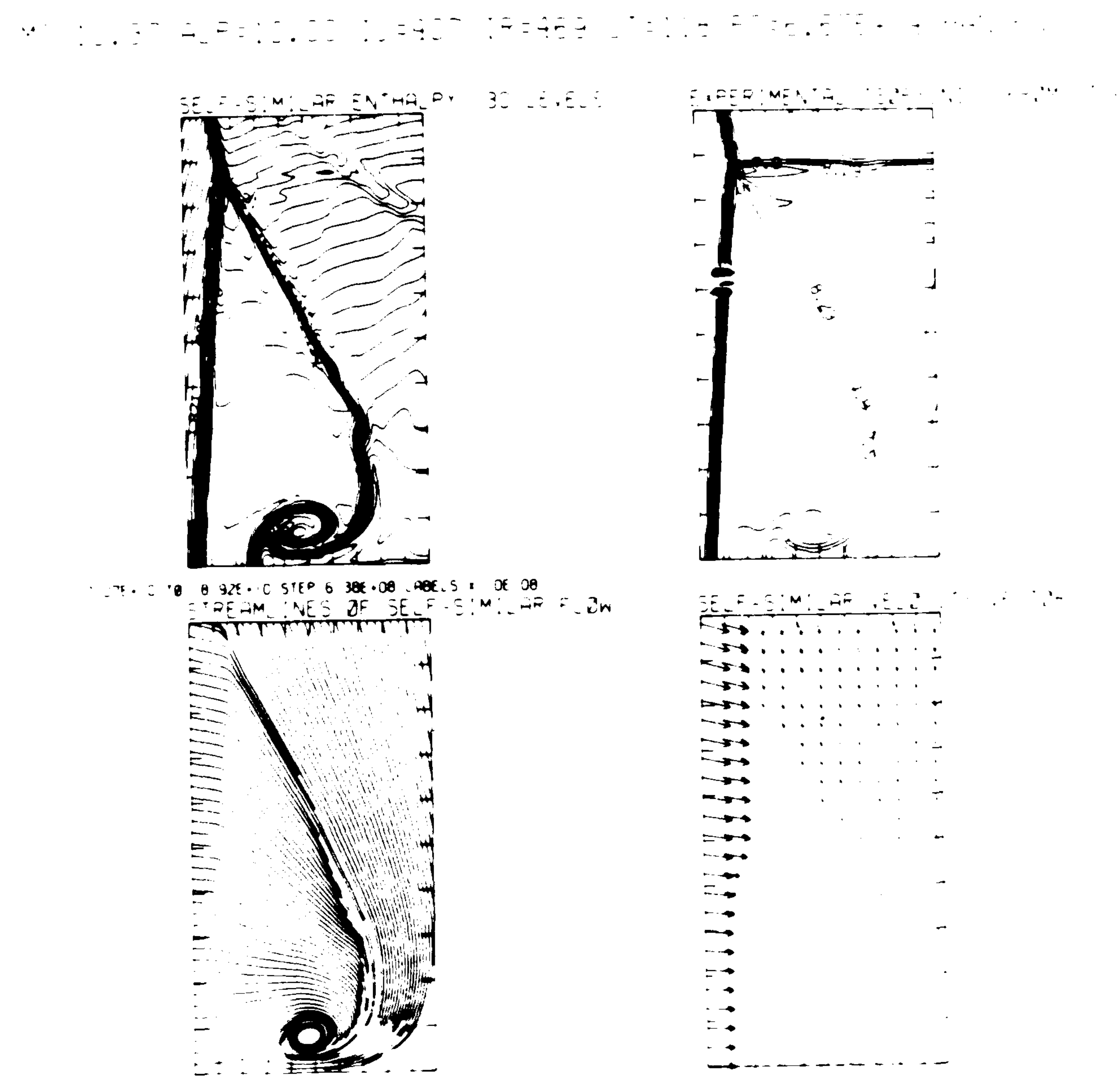

Figure 10e. Blowup-frame plots - continued.

Figure 10. Case 7, M_s = 10.37, θ_w = 10°, Air, Hansen EOS, CMR - continued.

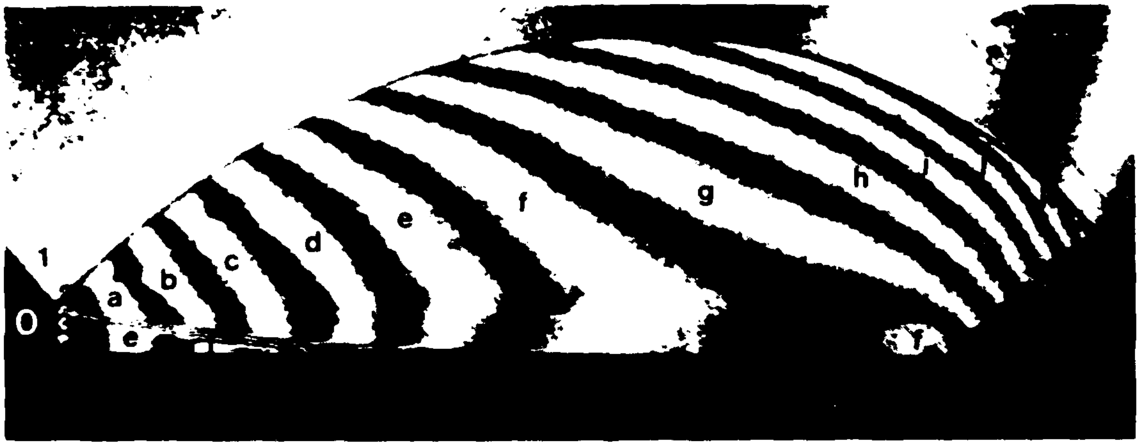

Region	ρ/ρ_c	Region	ρ/ρ_c
0	1.00	e	3.04
1	2.13	f	2.96
2	3.44	g	2.88
3	3.09	h	2.80
a	3.36	i	2.72
b	3.28	j	2.65
c	3.20	k	2.57
d	3.12	l	2.49

Figure 11a. Interferogram.

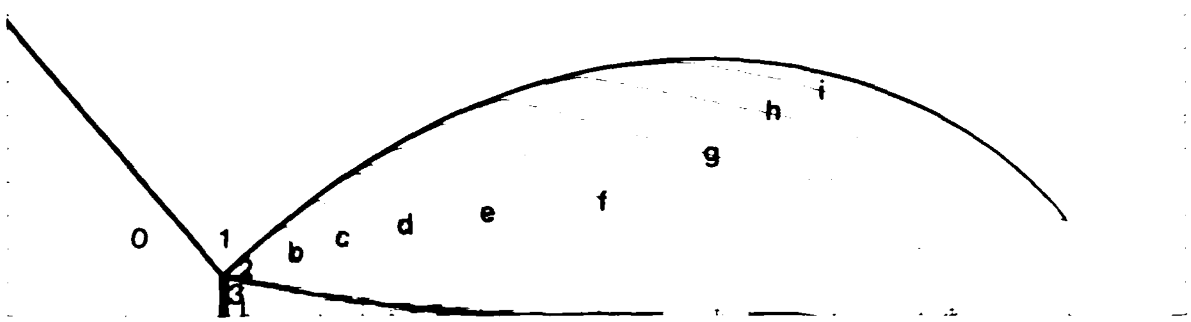

XBB 859-7200

Figure 11b. Calculated isopycnics (γ = 1.4) using the experimental fringes.

Figure 11. Case 3, M_s = 1.66, θ_w = 40°, Air, γ = 1.4 and Hansen EOS, SMR.

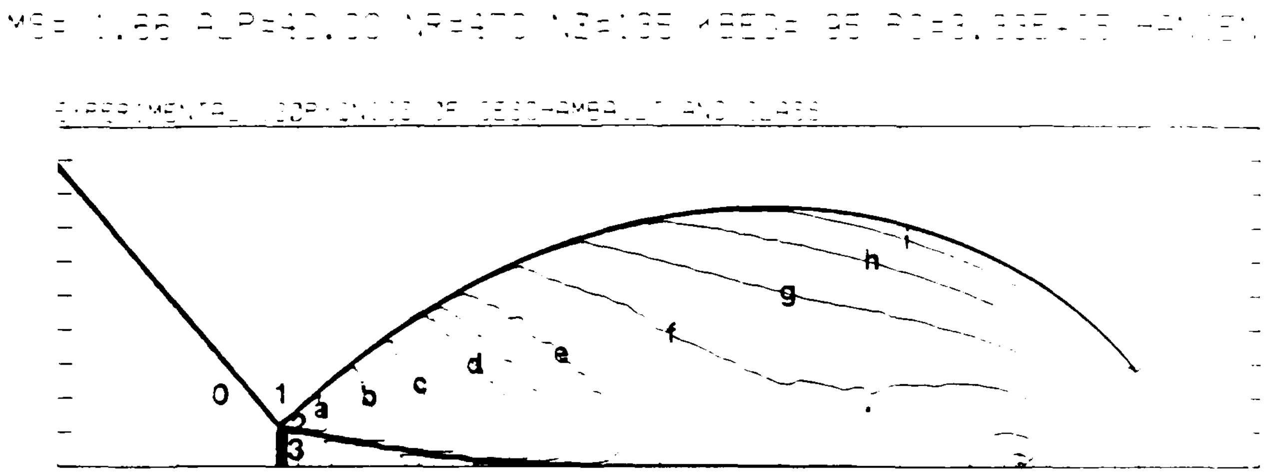

Figure $11b_H$. Calculated isopycnics (Hansen) using the experimental fringes.

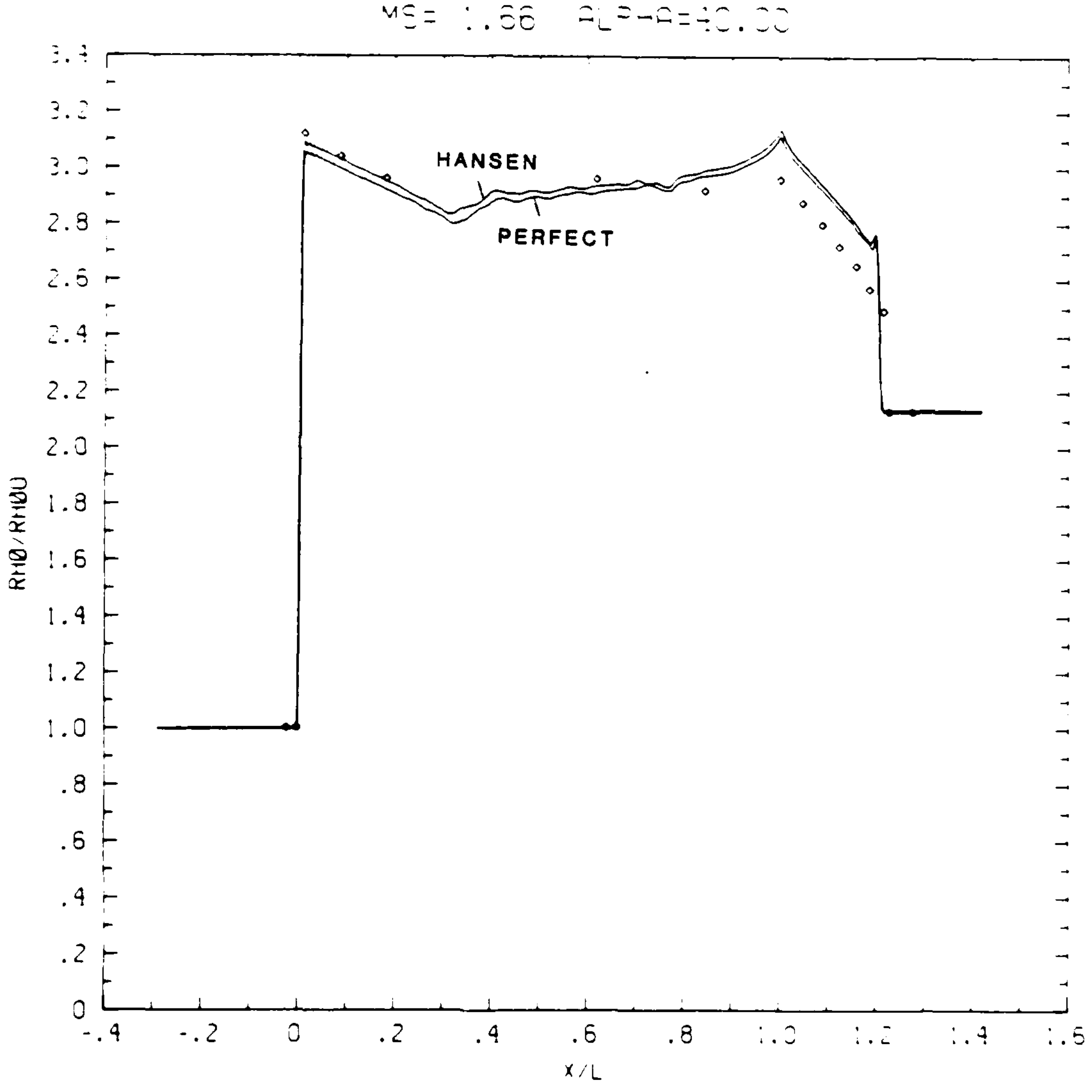

Figure 11c. Wall plot for p/p_0, γ = 1.4 and Hansen calculations, with experimental data.

Figure 11. Case 8, M_s = 1.66, θ_w = 40°, Air, γ = 1.4 and Hansen EOS, SMR - continued.

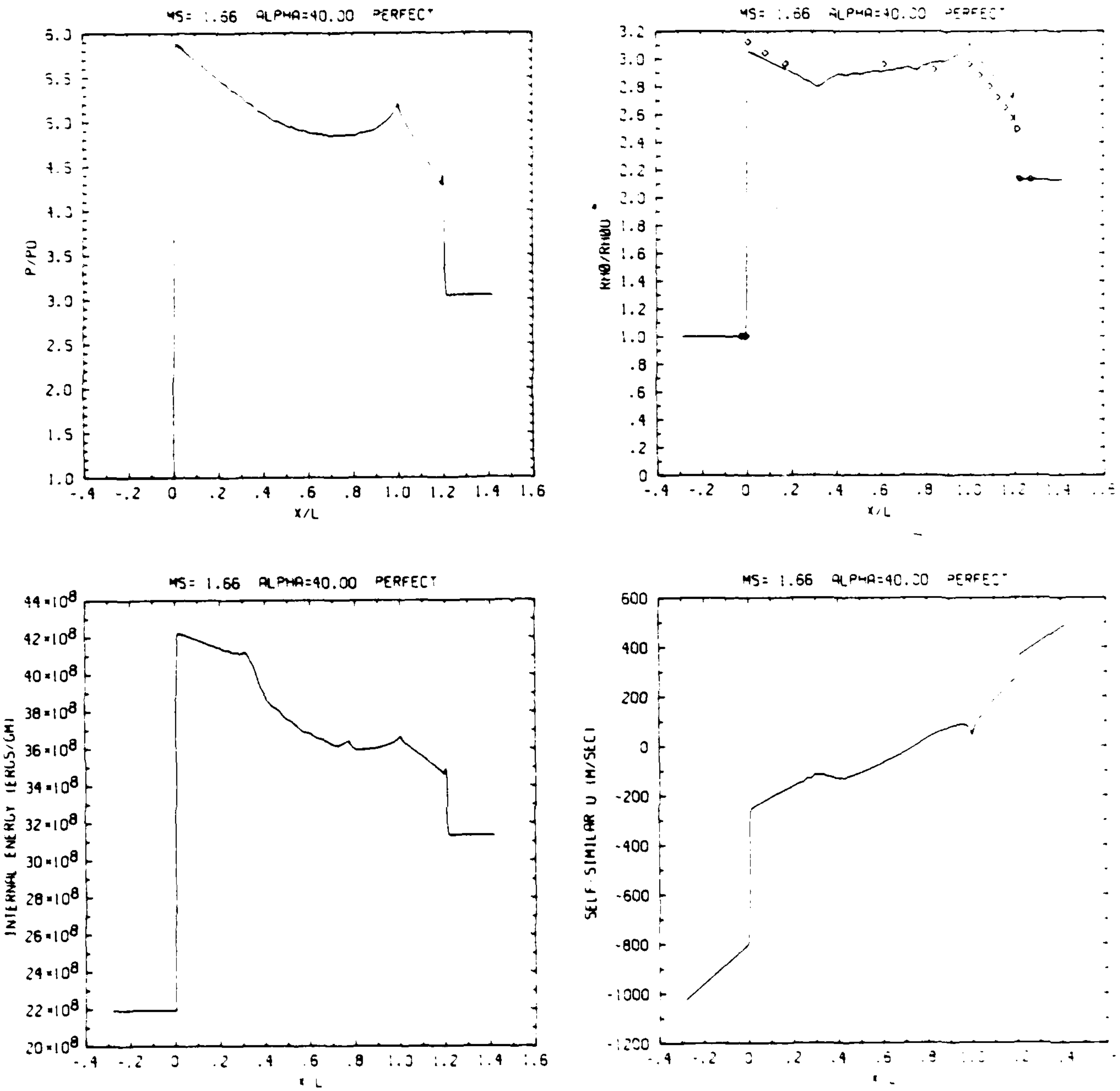

Figure 11c$_p$. Wall plots for p/p_0, ρ/ρ_0 with experimental data included, e, u; γ = 1.4.

Figure 11. Case 8, M_s = 1.66, θ_w= 40°, Air, γ = 1.4 and Hansen EOS, SMR - continued.

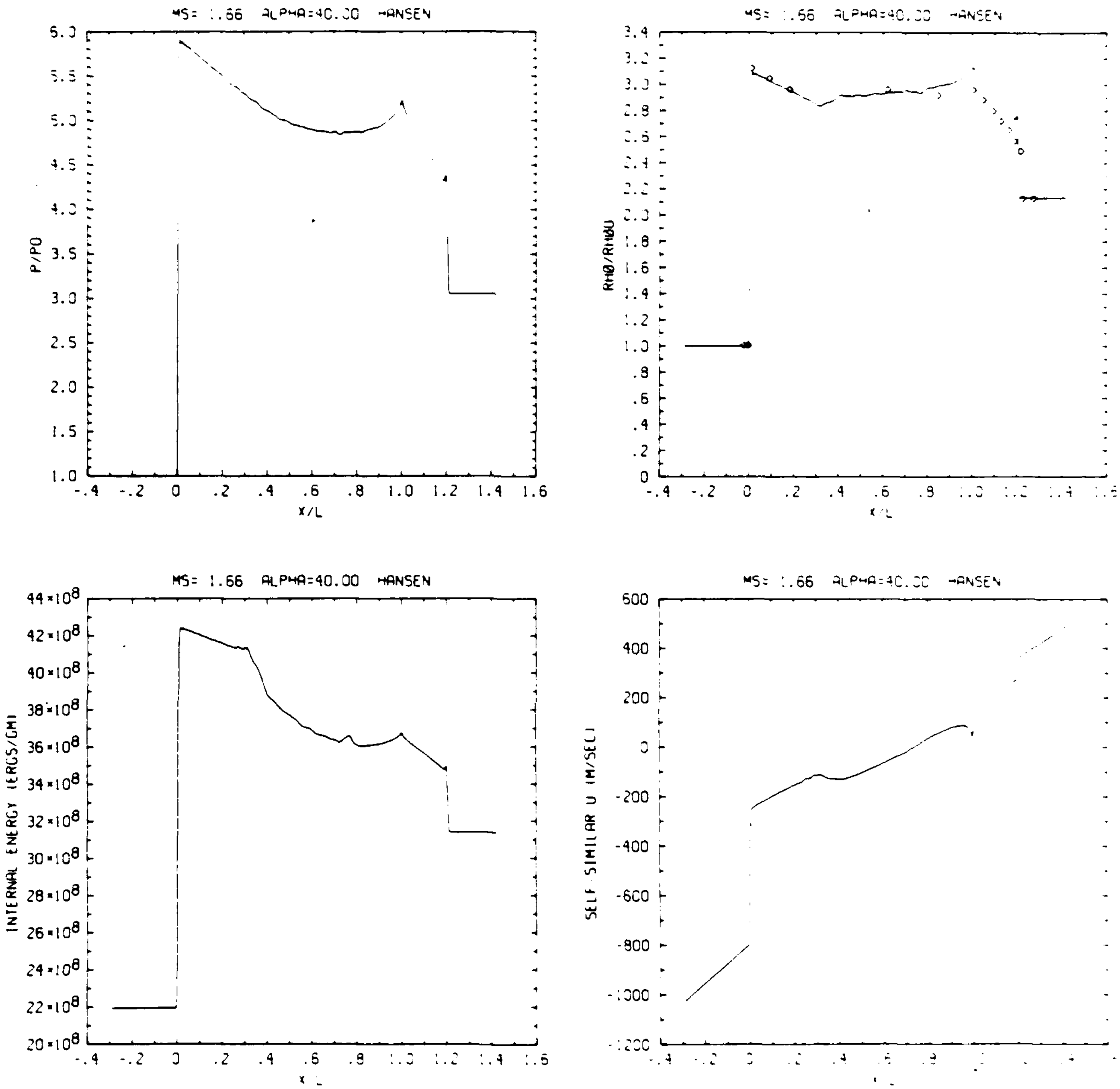

Figure $11c_H$. Wall plots for p/p_0, ρ/ρ_0 with experimental data included, e, u; Hansen.

Figure 11. Case 8, M_s = 1.66, θ_w = 40°, Air, γ = 1.4 and Hansen EOS, SMR - continued.

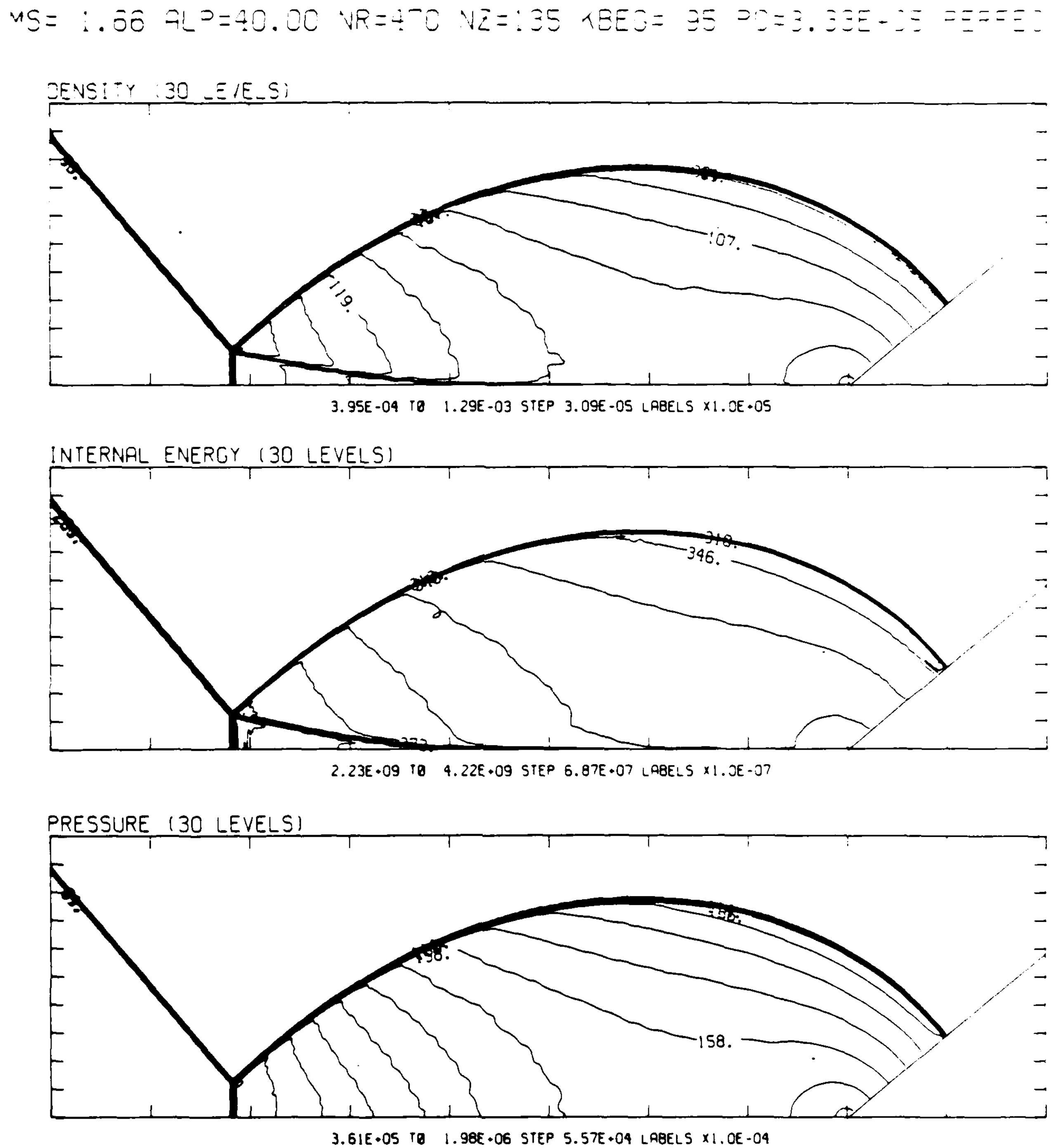

Figure 11d$_p$. Whole-flowfield contour-plots; $\gamma = 1.4$.

Figure 11. Case 8, $M_s = 1.66$, $\theta_w = 40°$, Air, $\gamma = 1.4$ and Hansen EOS, SMR - continued.

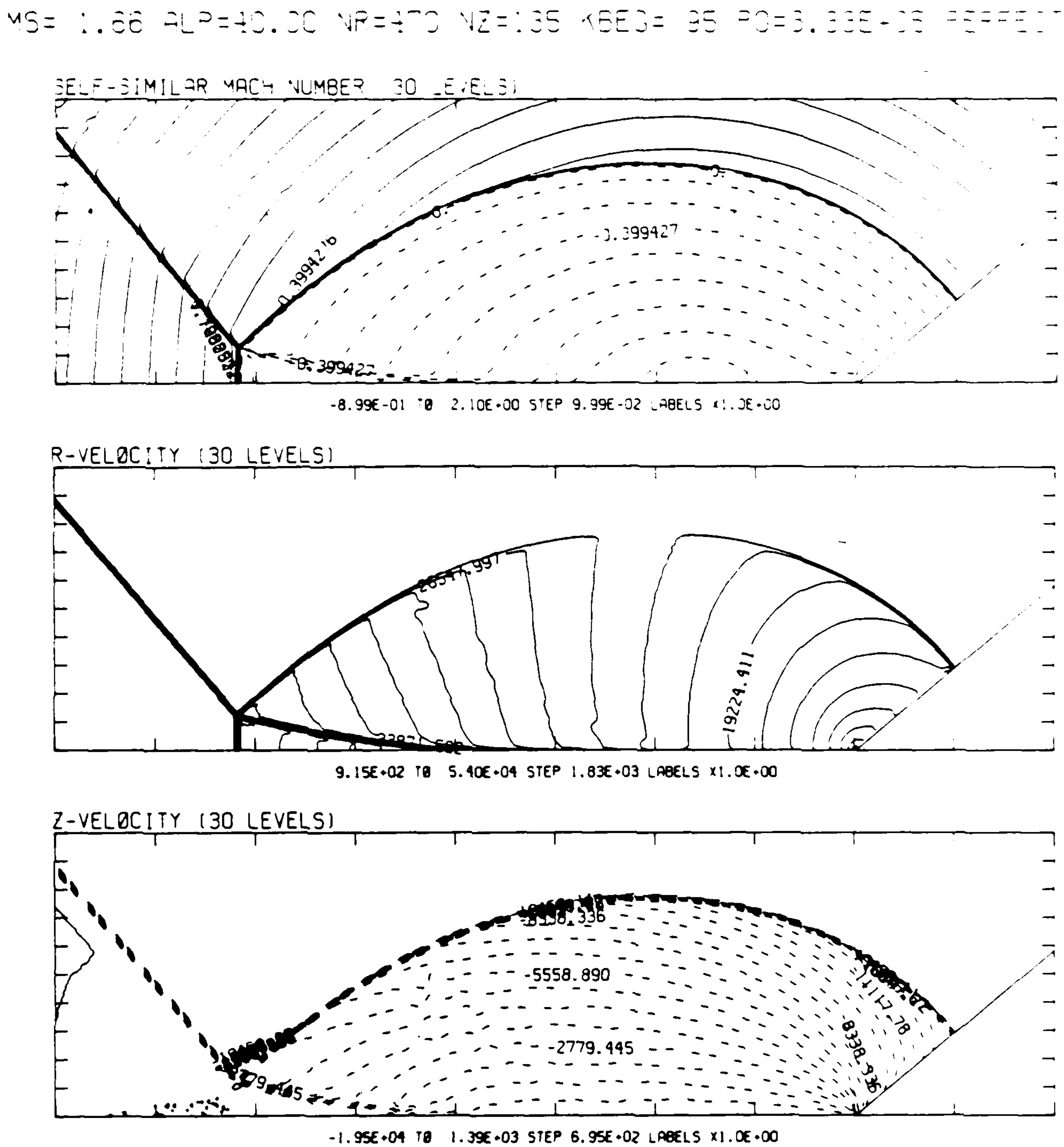

Figure $11d_p$. Whole-flowfield contour-plots; γ = 1.4 - continued.

Figure 11. Case 8, M_s = 1.66, θ_w= 40°, Air, γ = 1.4 and Hansen EOS, SMR - continued.

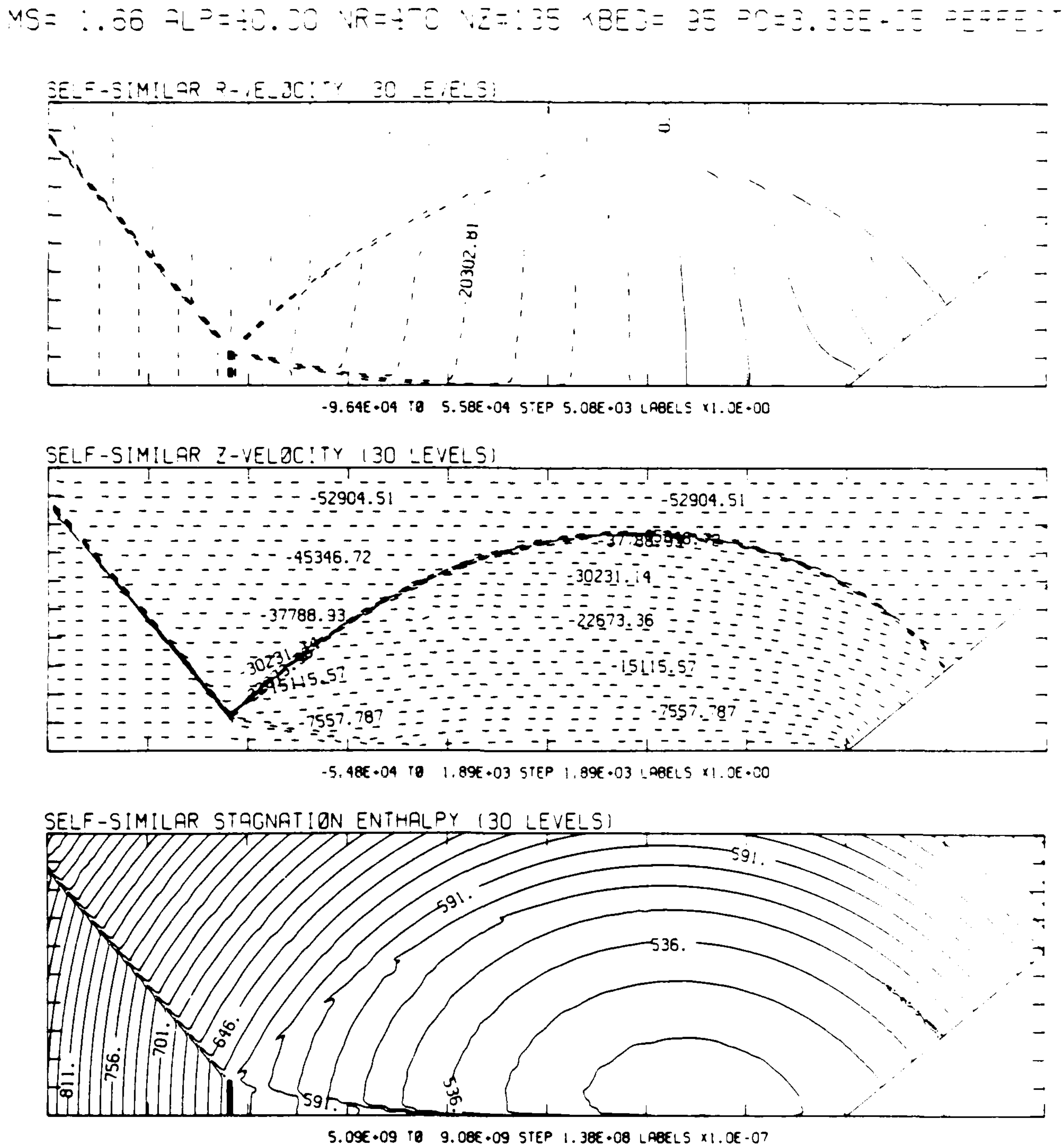

Figure 11d$_P$. Whole-flowfield contour-plots; γ = 1.4 - continued.

Figure 11. Case 8, M_s = 1.66, θ_w= 40°, Air, γ = 1.4 and Hansen EOS, SMR - continued.

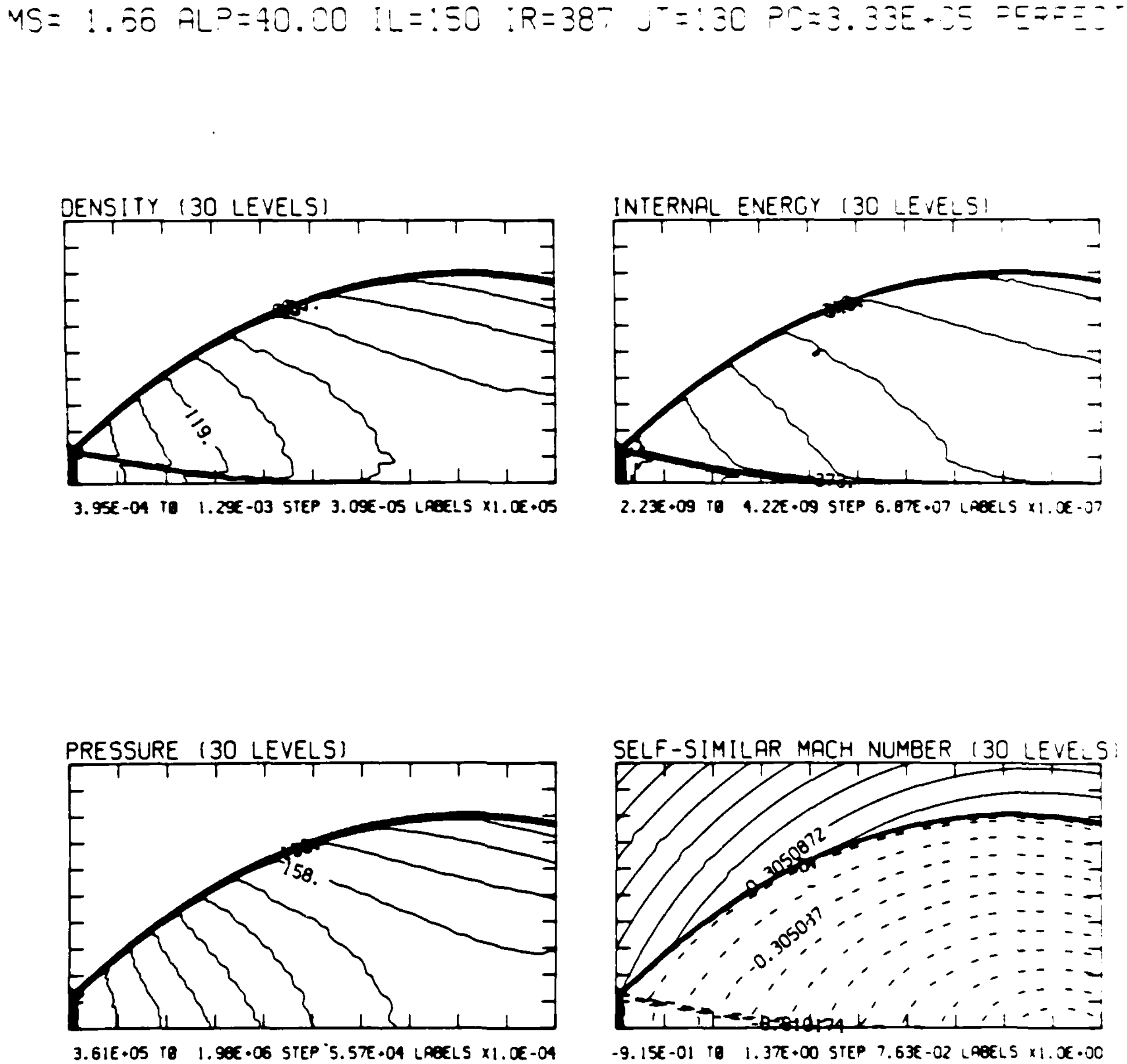

Figure 11e$_p$. Blowup-frame plots; γ = 1.4.

Figure 11. Case 8, M_s = 1.66, θ_w= 40°, Air, γ = 1.4 and Hansen EOS, SMR - continued.

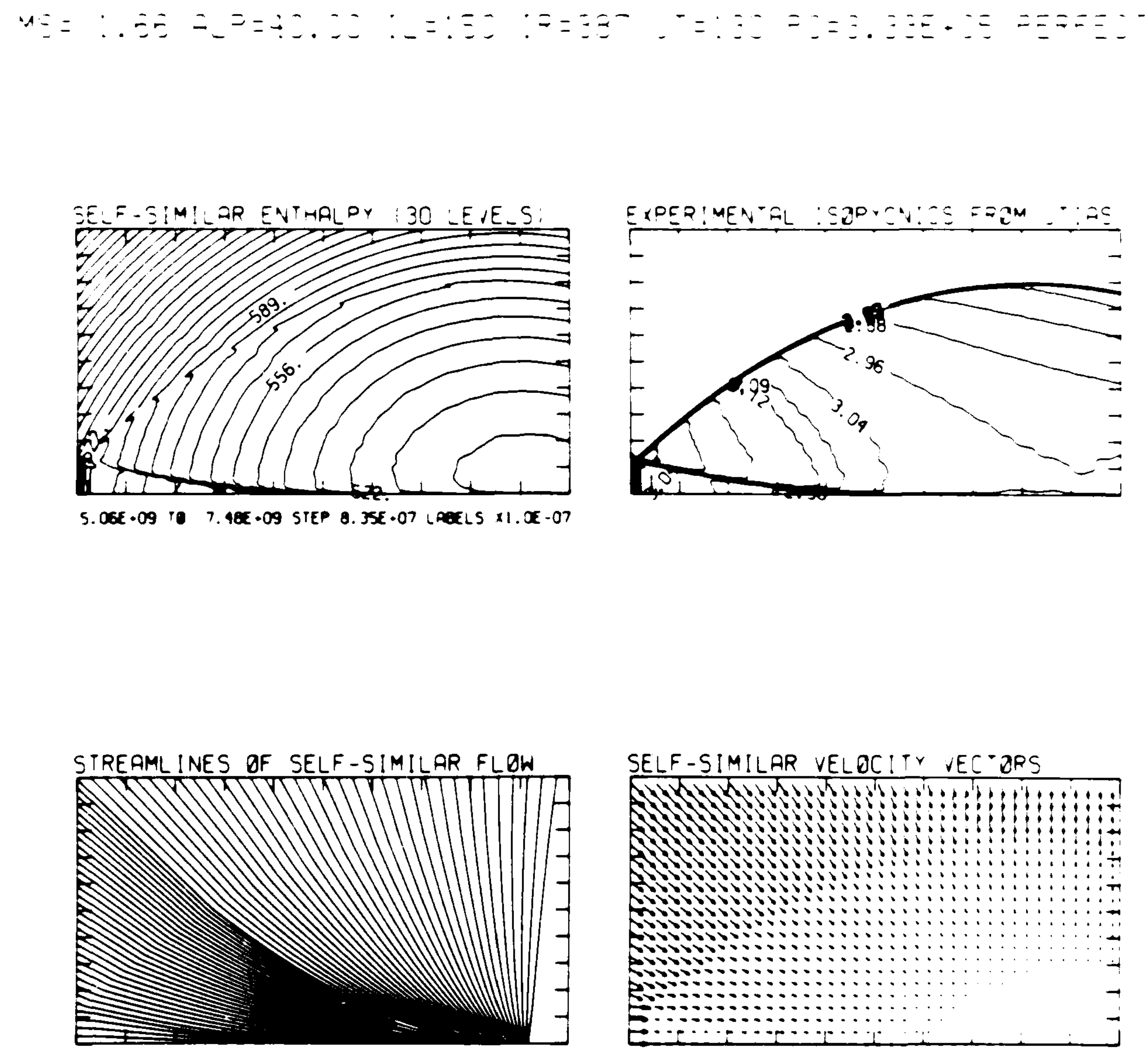

Figure 11e$_p$. Blowup-frame plots; γ = 1.4 - continued.

Figure 11. Case 8, M_s = 1.66, θ_w = 40°, Air, γ = 1.4 and Hansen EOS, SMR - continued.

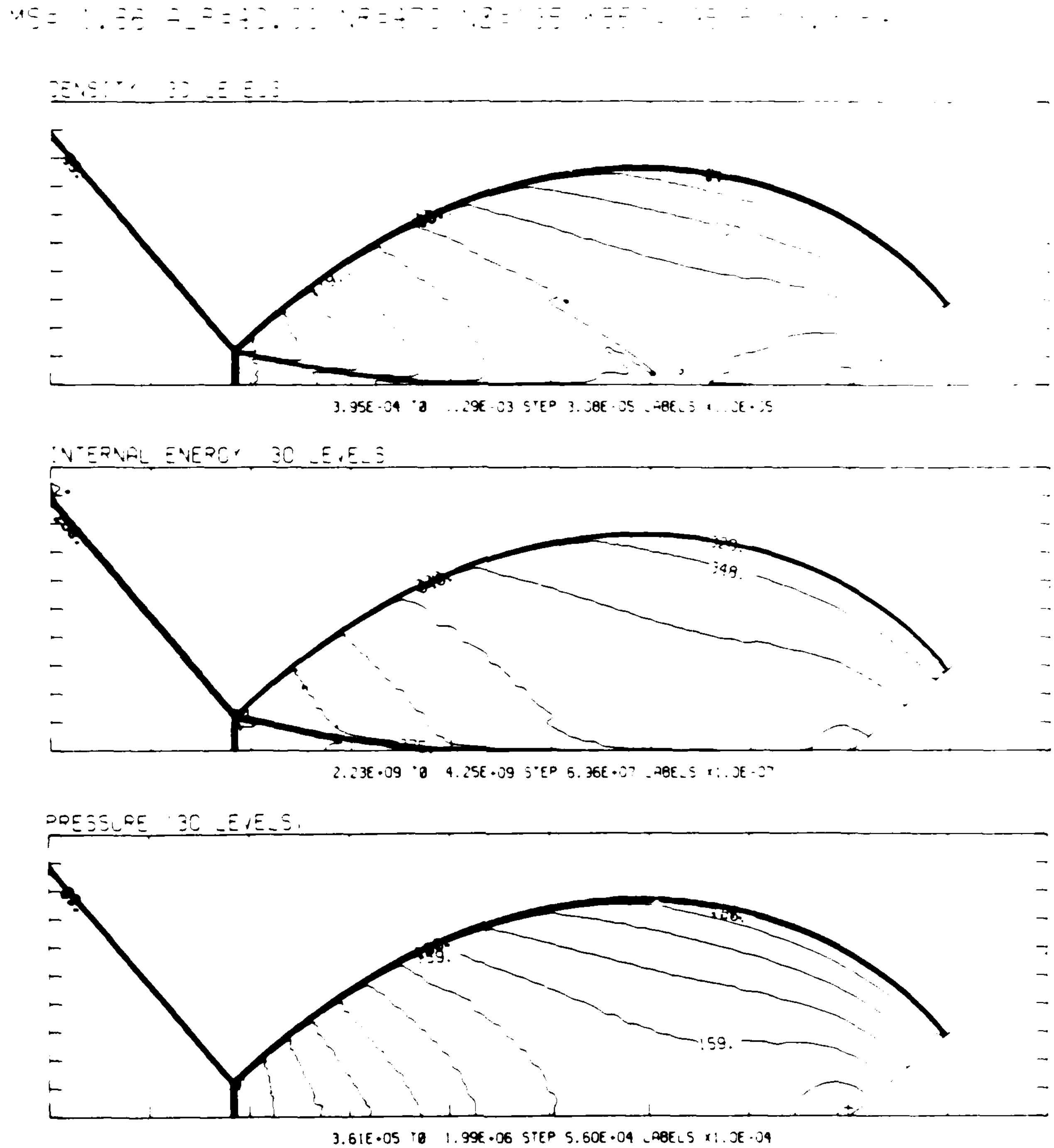

Figure $11d_H$. Whole-flowfield contour-plots; Hansen.

Figure 11. Case 8, M_S = 1.66, θ_w = 40°, Air, γ = 1.4 and Hansen EQS, SMR - continued.

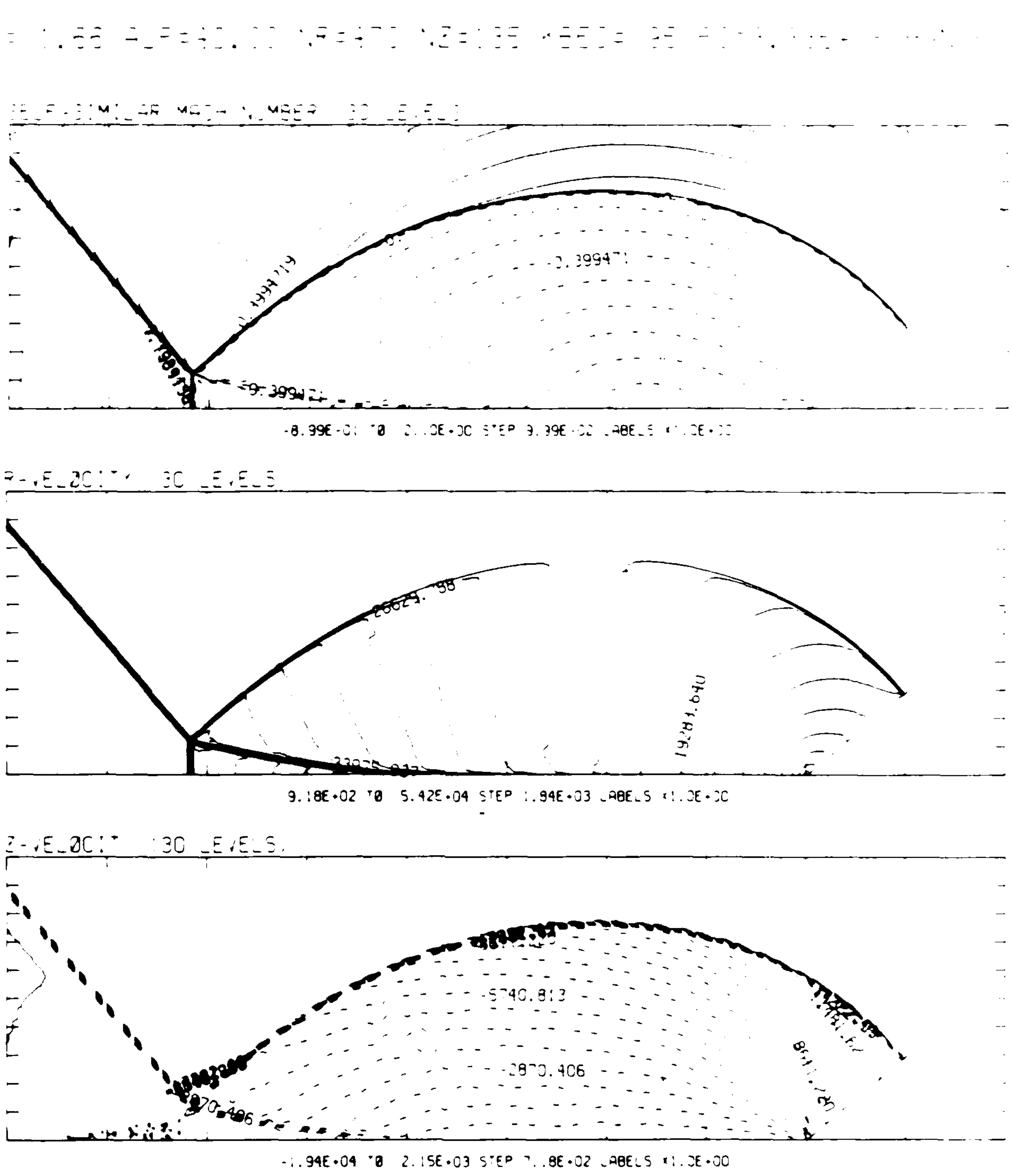

Figure 11d$_H$. Whole-flowfield contour-plots; Hansen - continued.

Figure 11. Case 8, M_s = 1.66, θ_w = 40°, Air, γ = 1.4 and Hansen EOS, SMR - continued.

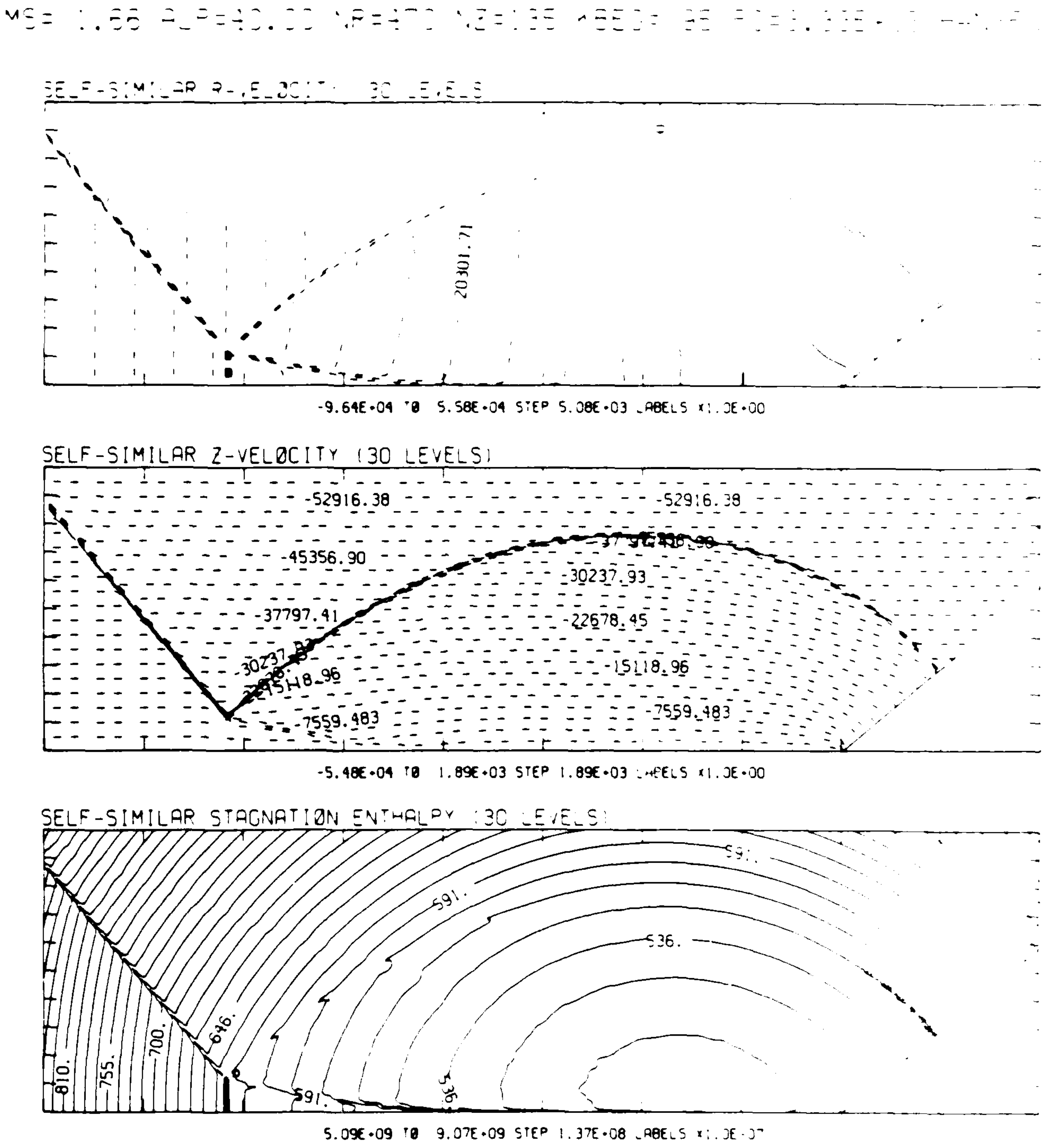

Figure 11d$_H$. Whole-flowfield contour-plots; Hansen - continued.

Figure 11. Case 8, M_s = 1.66, θ_w= 40°, Air, γ = 1.4 and Hansen EOS, SMR - continued.

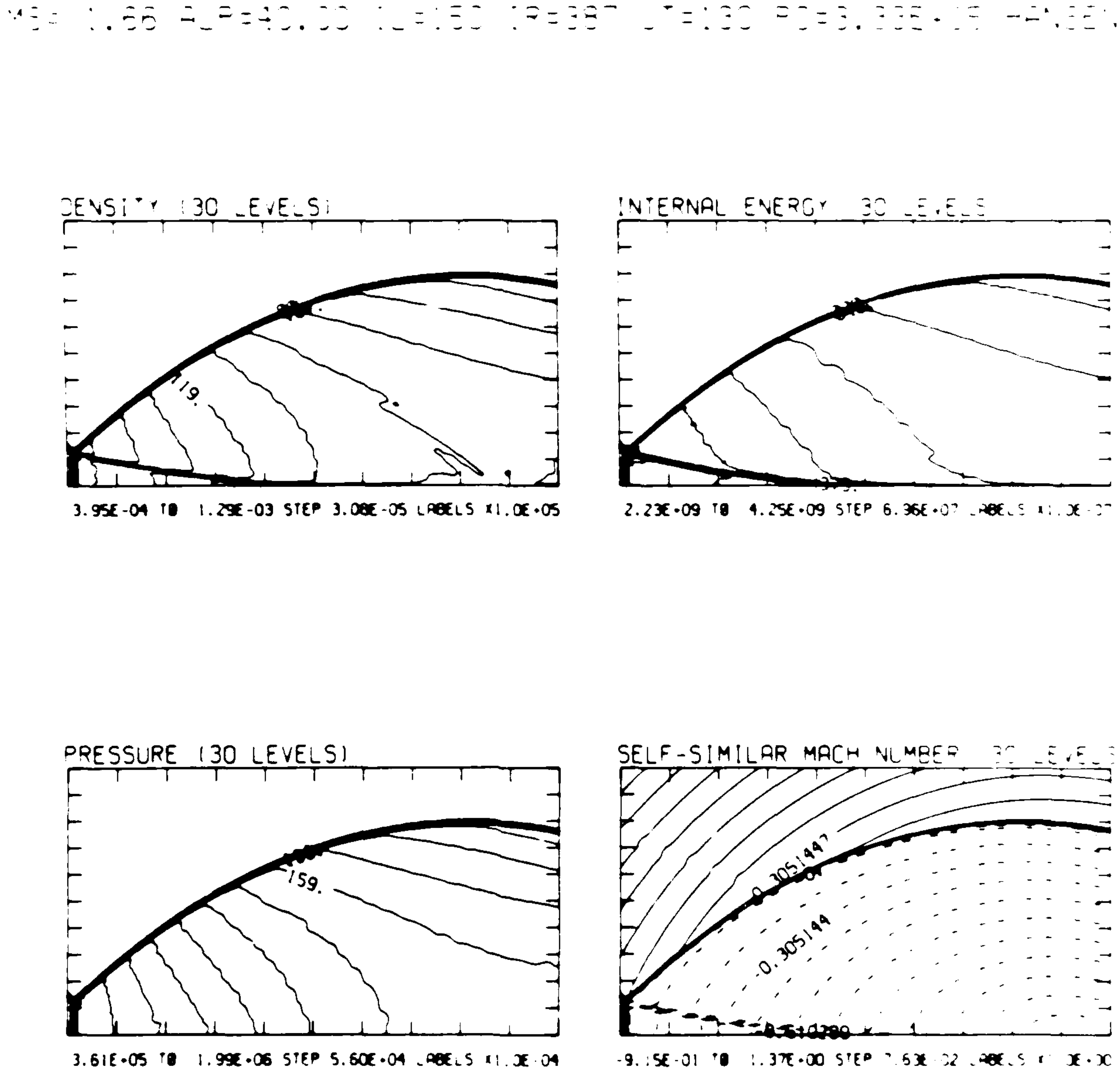

Figure 11e$_H$. Blow-up frame plots; Hansen.

Figure 11. Case 8, M_s = 1.66, θ_w = 40°, Air, γ = 1.4 and Hansen EOS, SMR - continued.

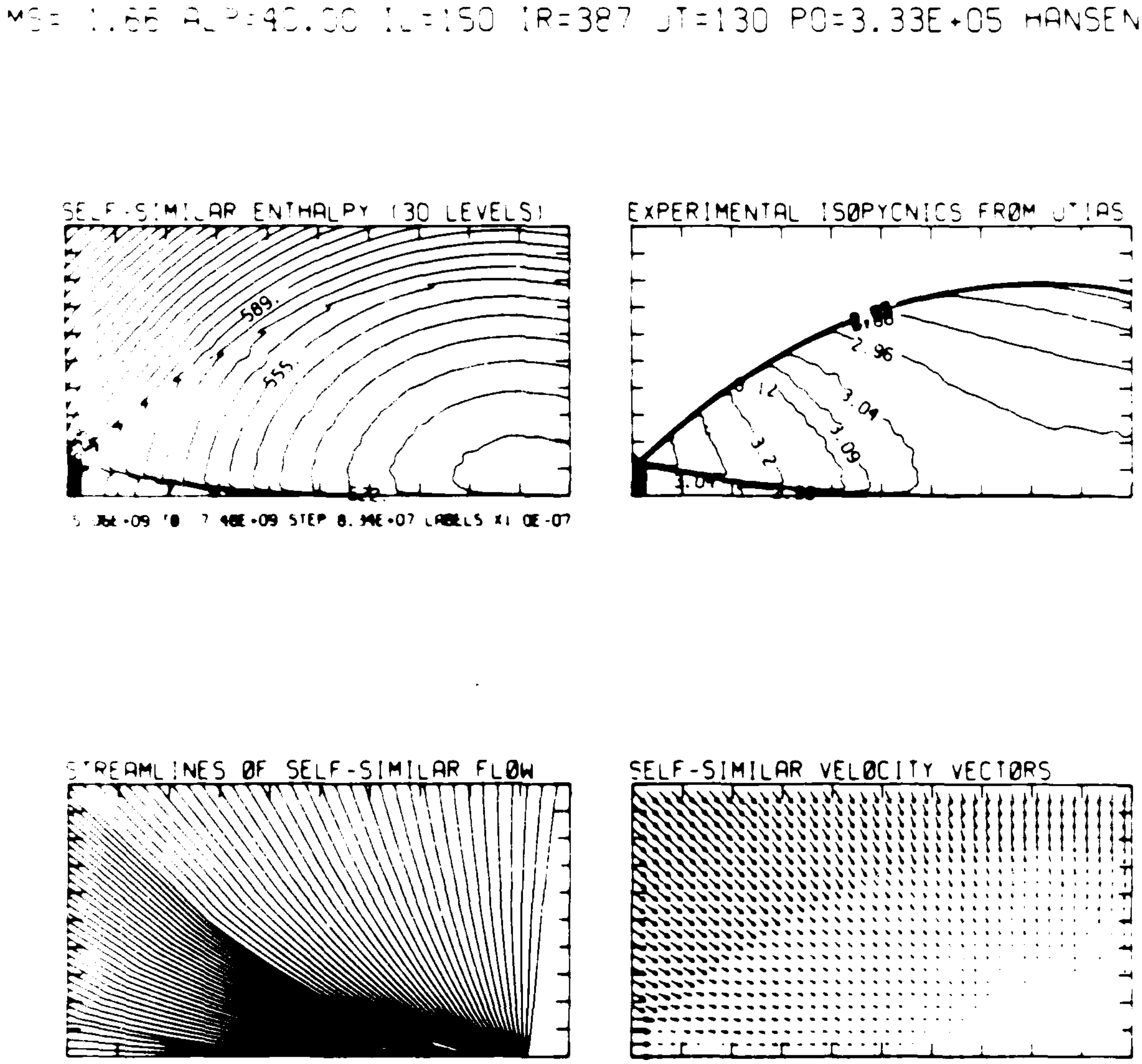

Figure 11e$_H$. Blow-up frame plots;. Hansen - continued.

Figure 11. Case 8, M_s = 1.66, θ_w = 40°, Air, γ = 1.4 and Hansen EOS, SMR - continued.

Region	ρ/ρ_0
0	1.00
1	3.73
2	6.06
3	4.59
a	6.21
b	6.37
c	6.53
d	6.69
e	6.85
f	7.00
g	7.16
h	7.32
i	6.06
j	5.90

Figure 12a. Interferogram.

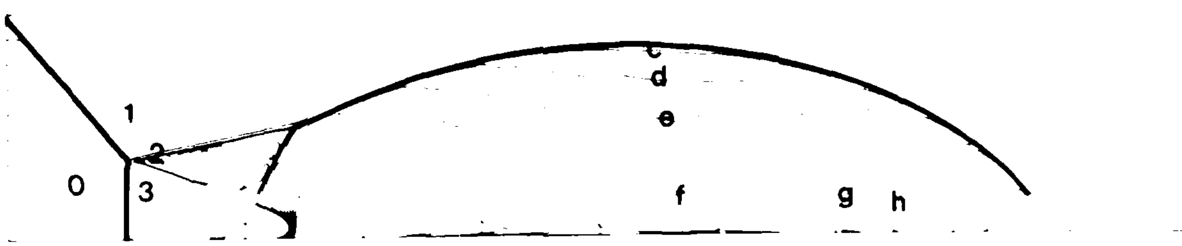

XBB 859-7201

Figure 12b. Calculated isopycnics (γ = 1.4) using the experimental fringes.

Figure 12. Case 9, M_s = 2.87, θ_w = 40°, Air, γ = 1.4 and Hansen EOS, DMR.

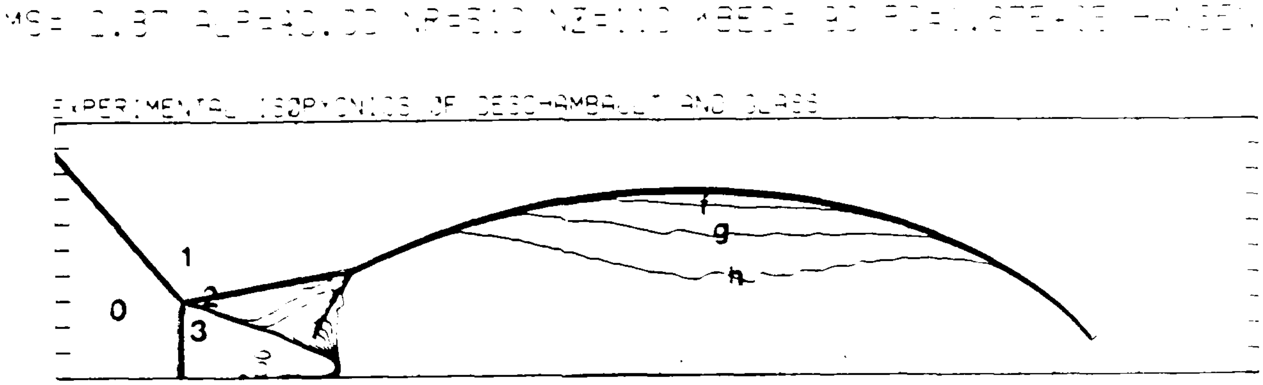

Figure $12b_H$. Calculated isopycnics (Hansen) using the experimental fringes.

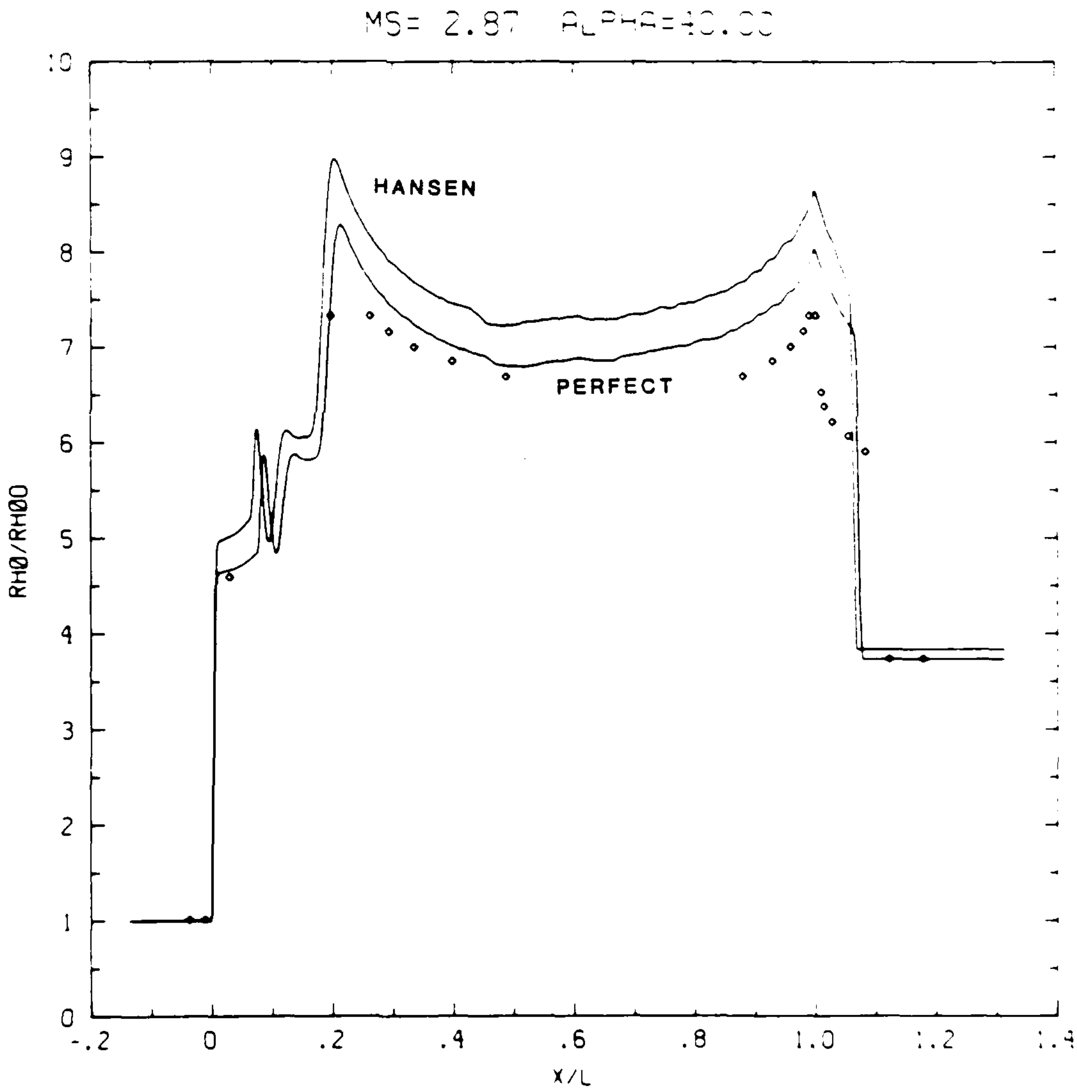

Figure 12c. Wall plots for p/p_0, ρ/ρ_0, γ = 1.4 and Hansen calculations, with experimental data.

Figure 12. Case 9, M_s = 2.87, θ_w = 40°, Air, γ = 1.4 and Hansen EOS, DMR - continued.

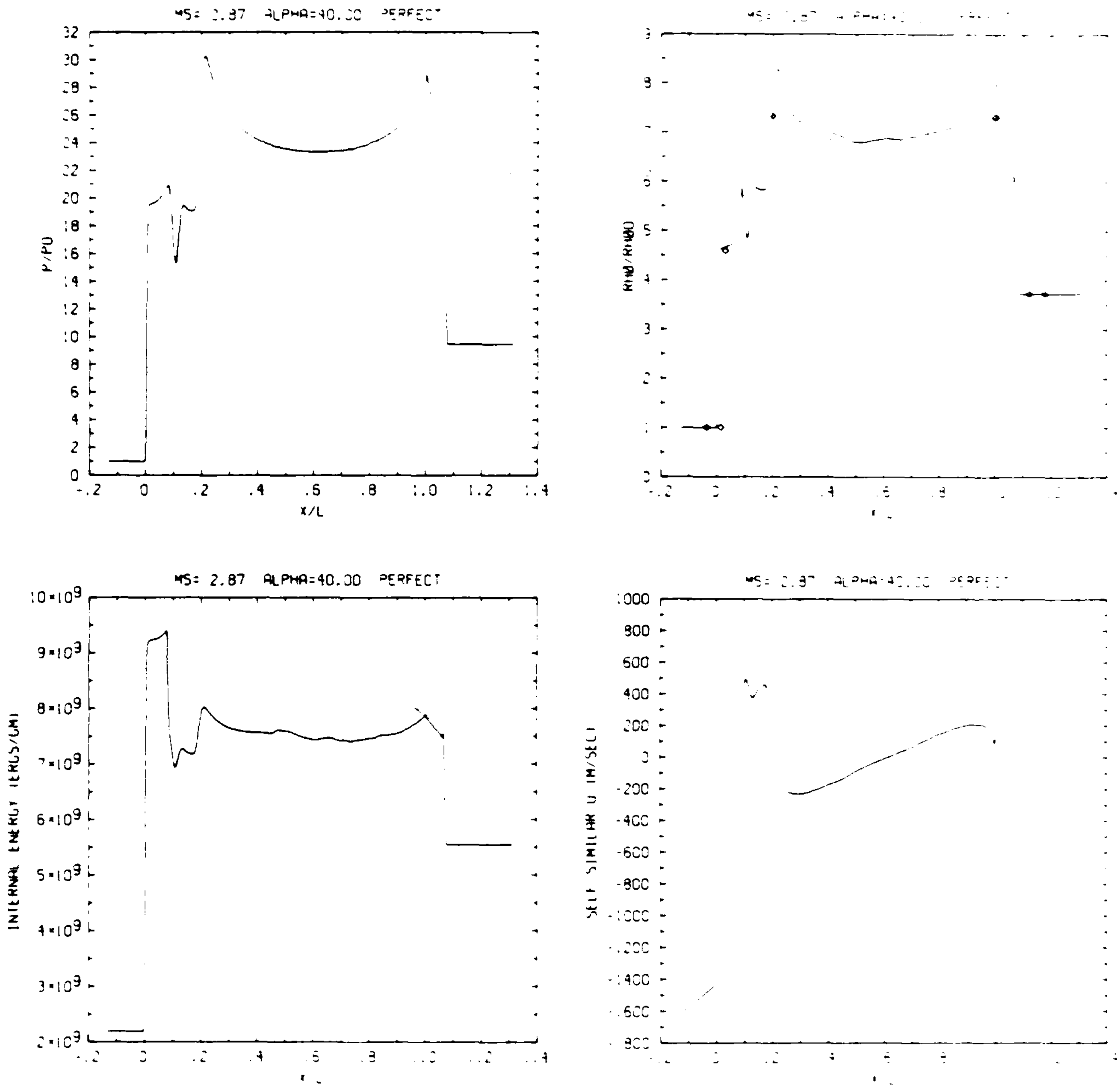

Figure 12c$_p$. Wall plots for p/p_0, ρ/ρ_0 with experimental data included, e, u; γ = 1.4.

Figure 12. Case 9, M_s = 2.87, θ_w = 40°, Air, γ = 1.4 and Hansen EOS, DMR - continued.

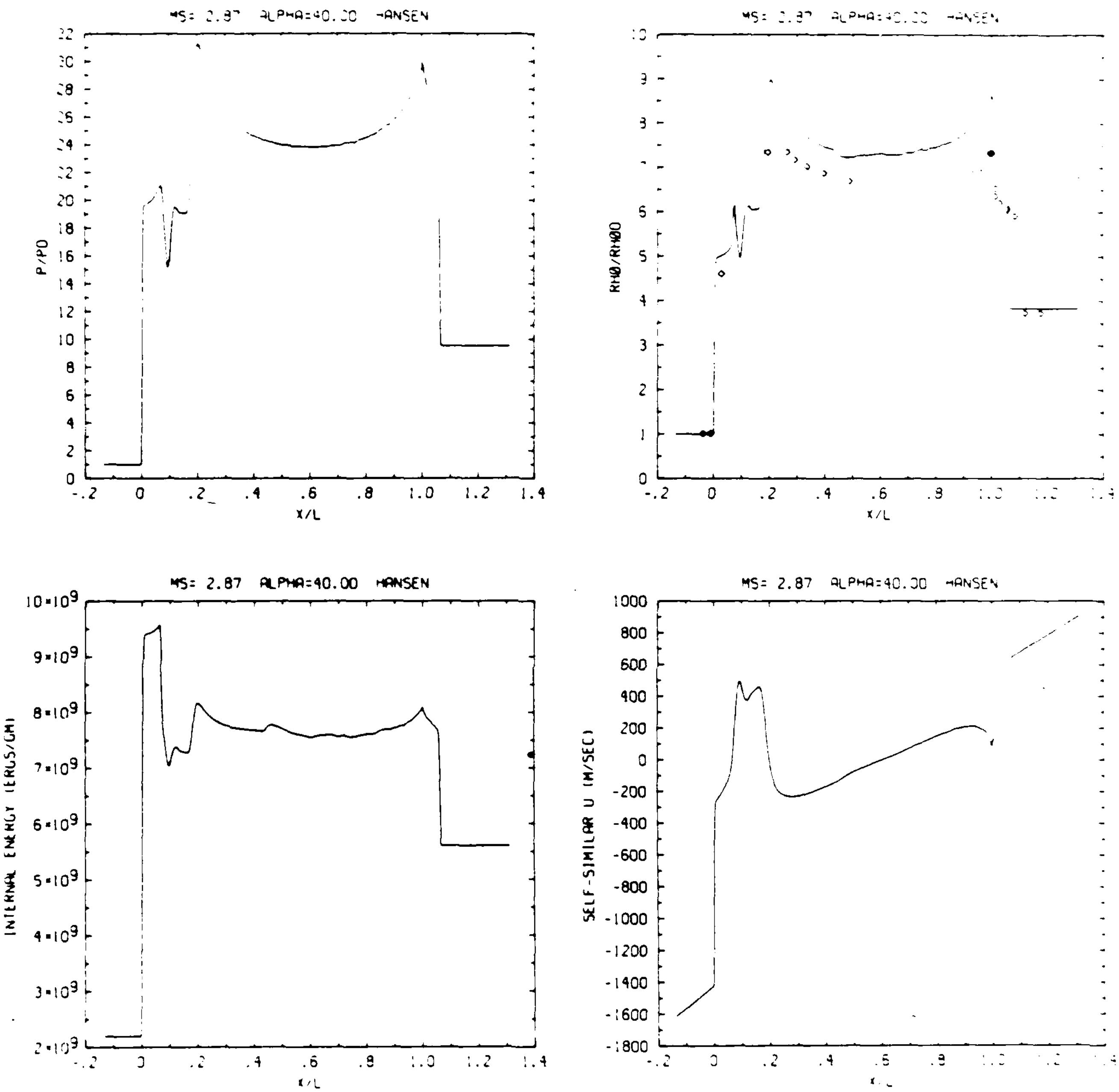

Figure $12c_H$. Wall plots for p/p_0, ρ/ρ_0 with experimental data included, e, u; Hansen.

Figure 12. Case 9, M_S = 2.87, θ_W = 40°, Air, γ = 1.4 and Hansen EOS, DMR - continued.

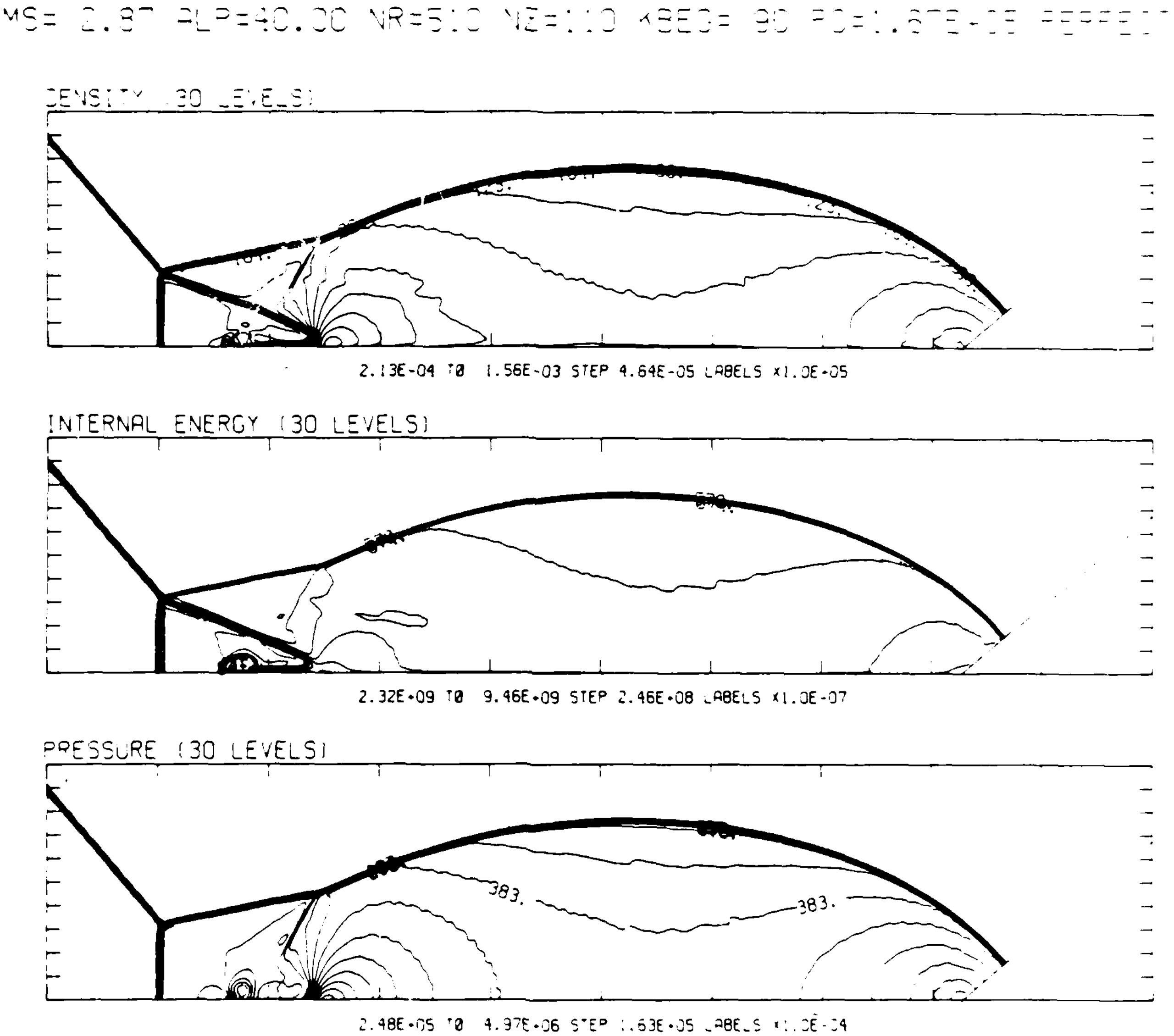

Figure $12d_p$. Whole-flowfield contour-plots; γ = 1.4.

Figure 12. Case 9, M_S = 2.87, θ_w = 40°, Air, γ = 1.4 and Hansen EOS, DMR - continued.

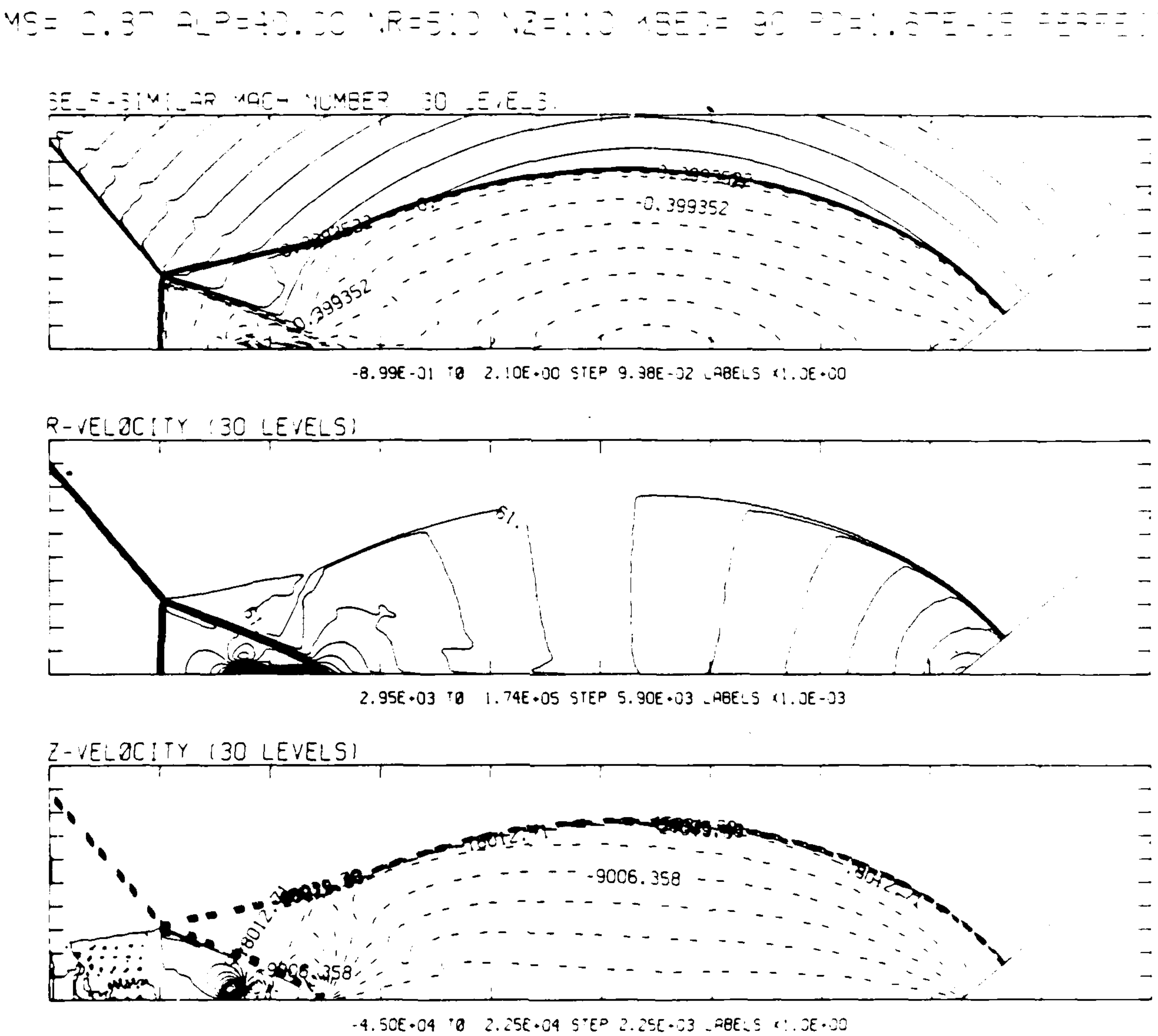

Figure $12d_p$. Whole-flowfield contour-plots; γ = 1.4 - continued.

Figure 12. Case 9, M_s = 2.87, θ_w = 40°, Air, γ = 1.4 and Hansen EOS, DMR - continued.

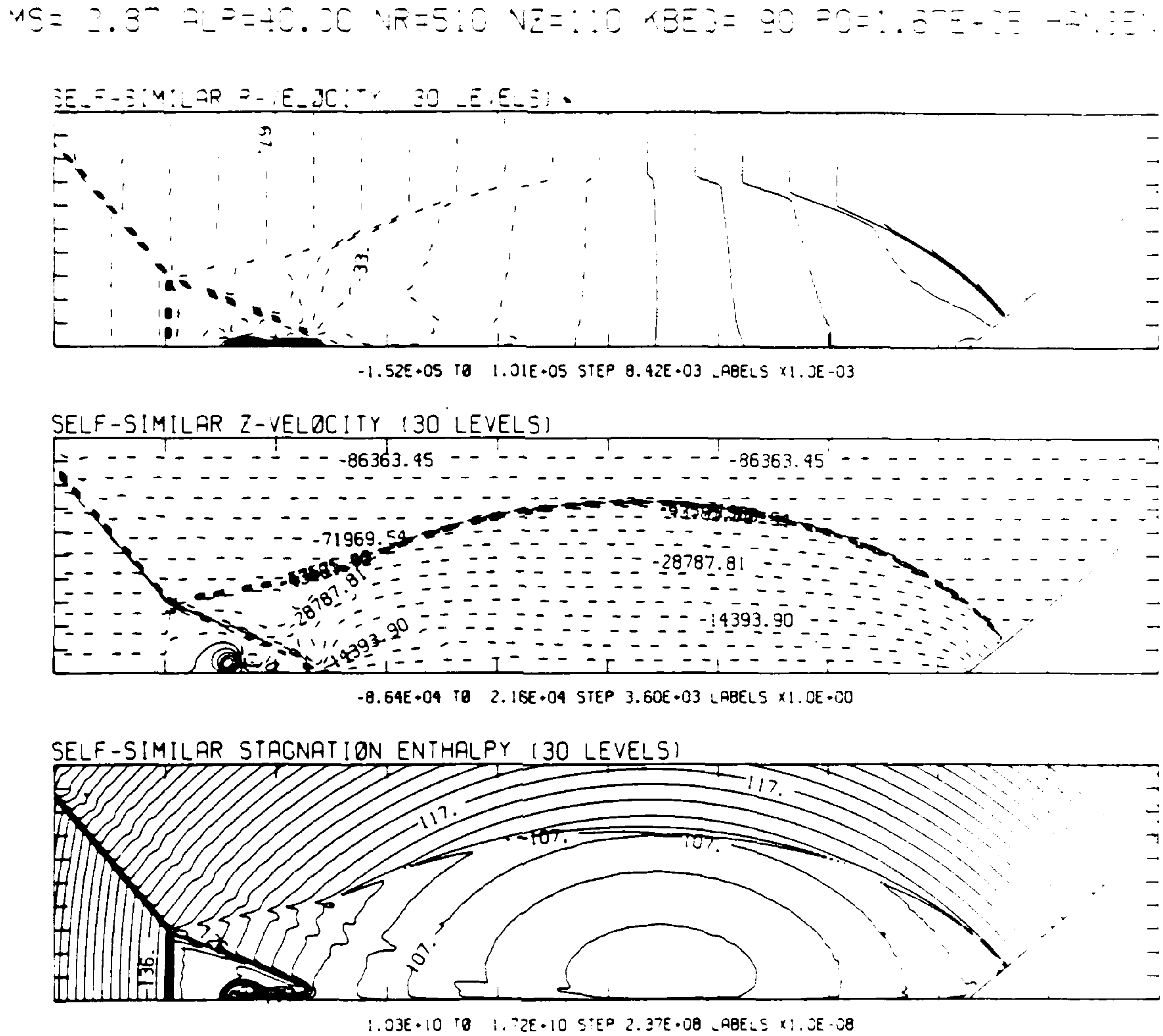

Figure $12d_p$. Whole-flowfield contour-plots; γ = 1.4 - continued.

Figure 12. Case 9, M_s = 2.87, θ_w = 40°, Air, γ = 1.4 and Hansen EOS, DMR - continued.

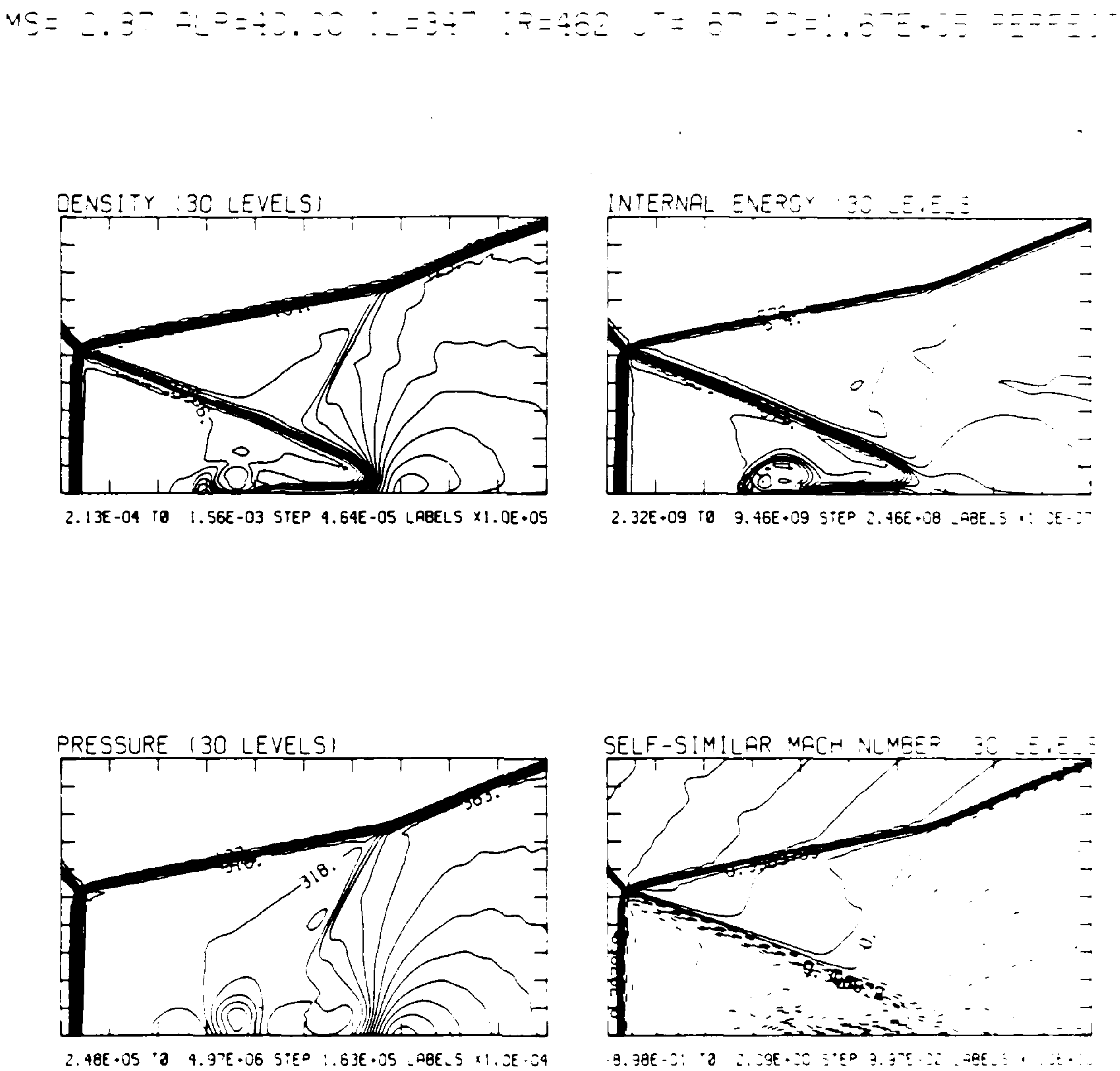

Figure $12e_p$. Blowup-frame plots; γ = 1.4.

Figure 12. Case 9, M_s = 2.87, θ_w = 40°, Air, γ = 1.4 and Hansen EOS, DMR - continued.

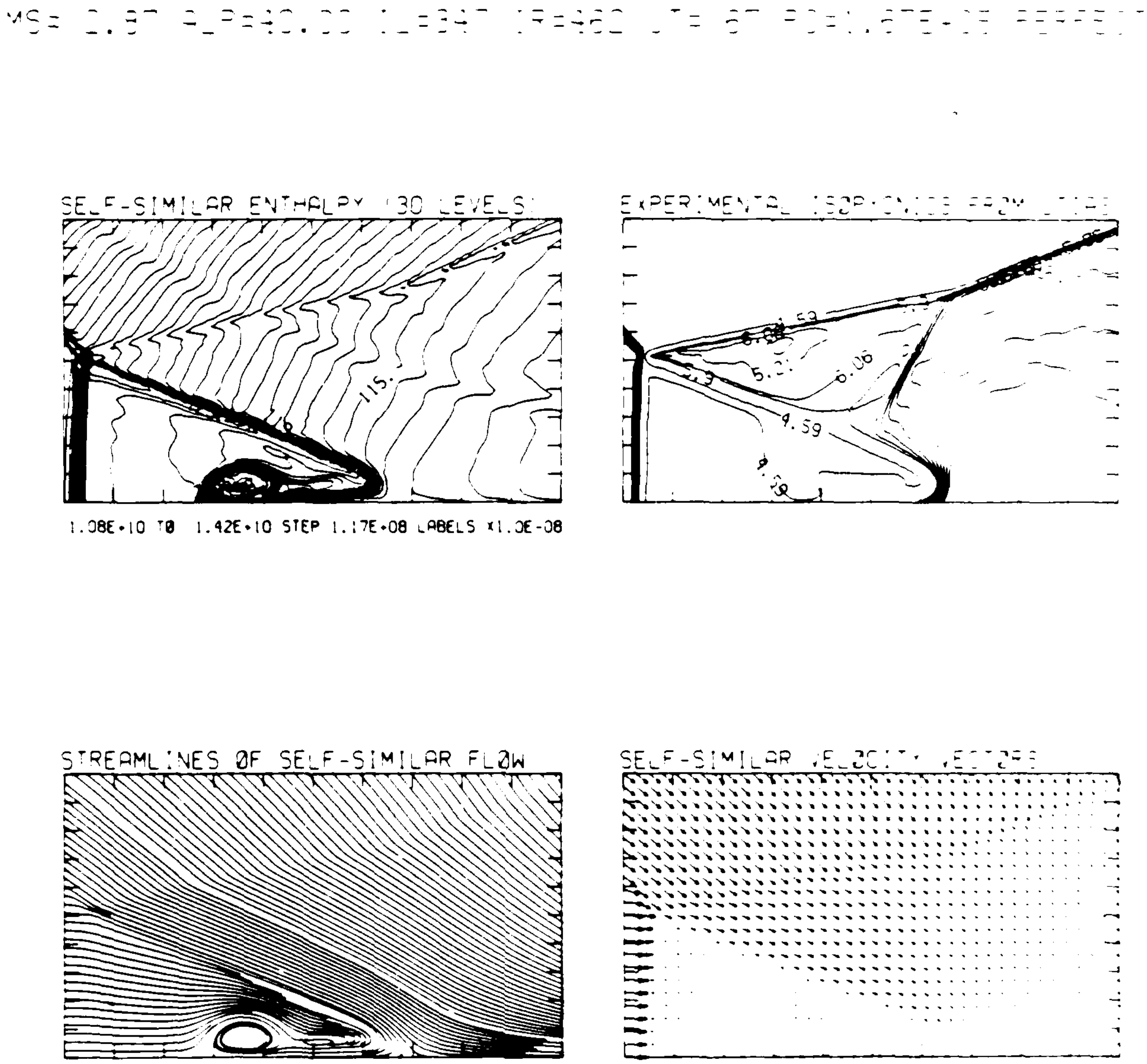

Figure $12e_p$. Blowup-frame plots; γ = 1.4 - continued.

Figure 12. Case 9, M_s = 2.87, θ_w = 40°, Air, γ = 1.4 and Hansen EOS, DMR - continued.

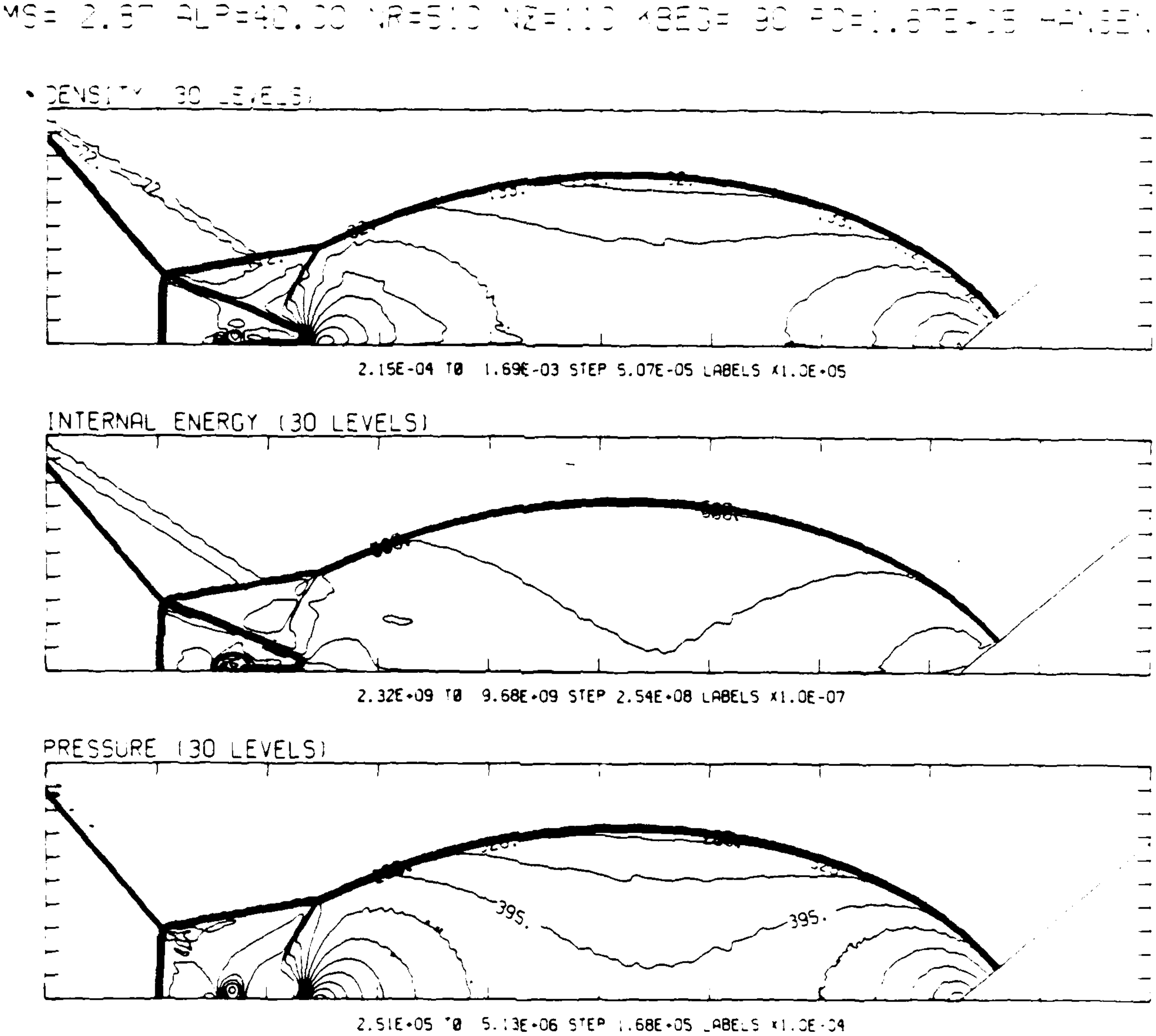

Figure $12d_H$. Whole-flowfield contour-plots; Hansen.

Figure 12. Case 9, M_s = 2.87, θ_w = 40°, Air, γ = 1.4 and Hansen EOS, DMR - continued.

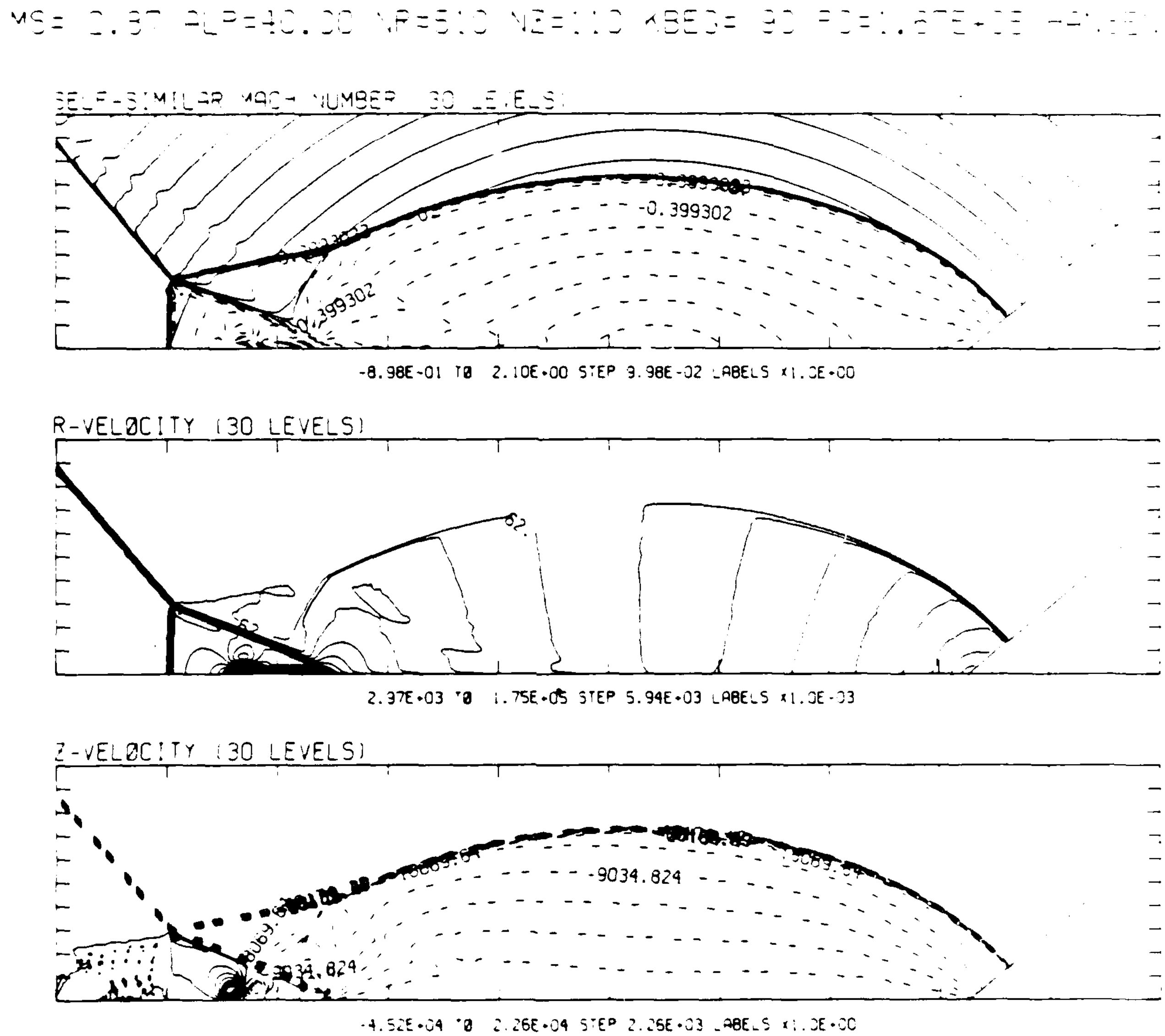

Figure $12d_4$. Whole-flowfield contour-plots; Hansen - continued.

Figure 12. Case 9, M_s = 2.87, θ_w = 40°, Air, γ = 1.4 and Hansen EOS, DMR - continued.

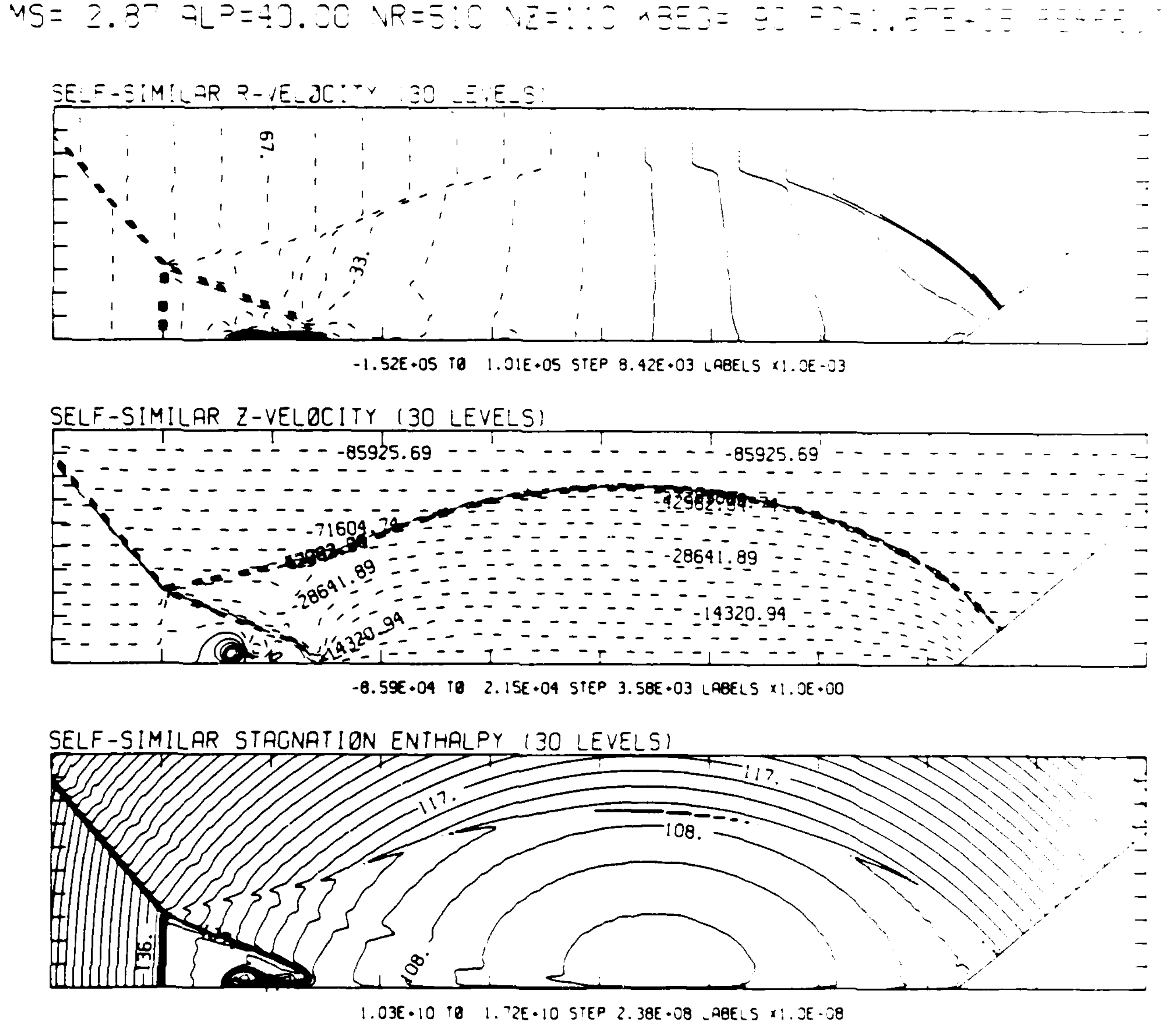

Figure 12d$_H$. Whole-flowfield contour-plots; Hansen - continued.

Figure 12. Case 9, M_S = 2.87, θ_W = 40°, Air, γ = 1.4 and Hansen EOS, DMR - continued.

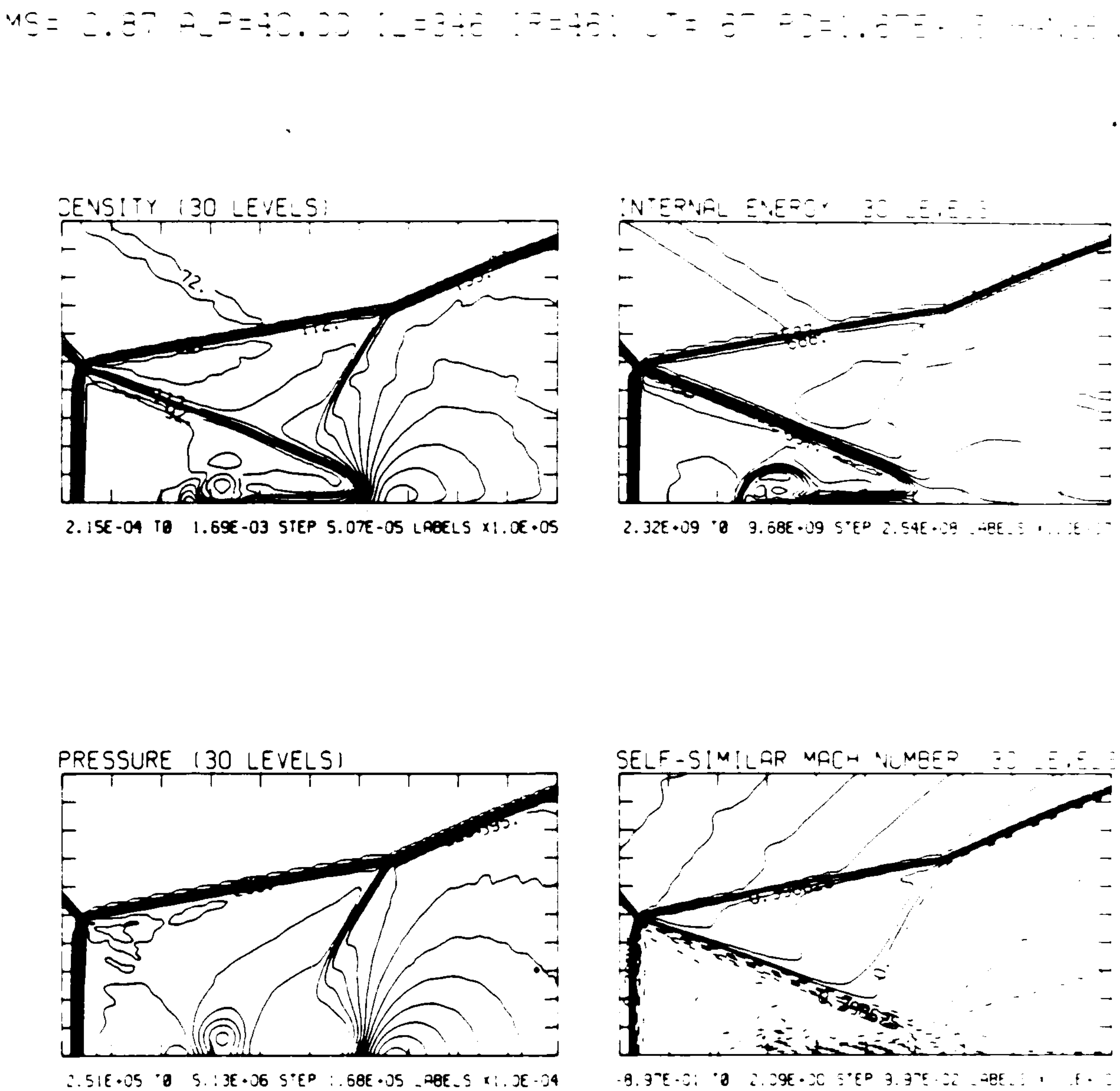

Figure $12e_H$. Blowup-frame plots; Hansen.

Figure 12. Case 9, M_S = 2.87, θ_w = 40°, Air, γ = 1.4 and Hansen EOS, DMR - continued.

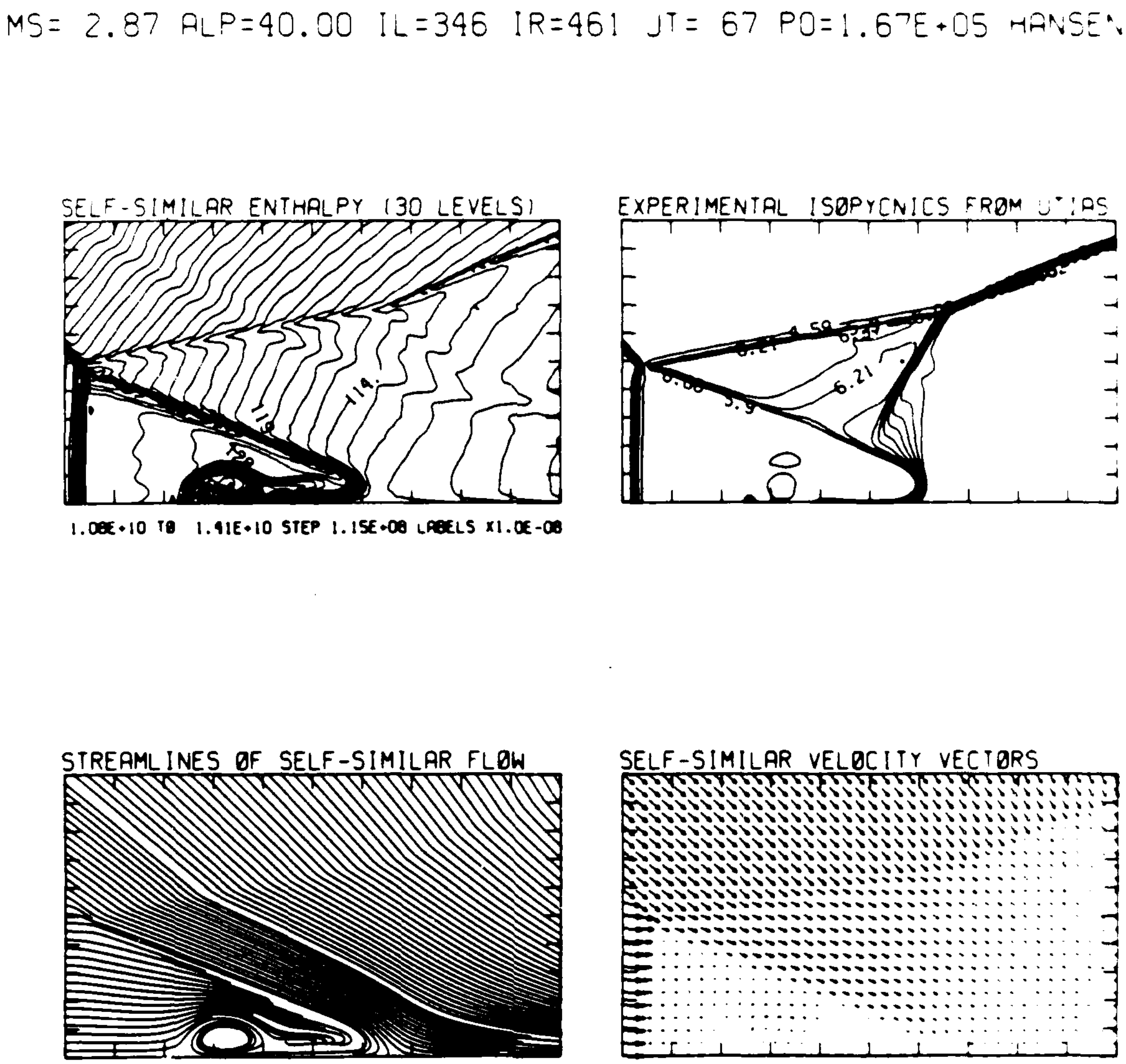

Figure $12e_H$. Blowup-frame plots; Hansen - continued.

Figure 12. Case 9, M_S = 2.87, θ_w = 40°, Air, γ = 1.4 and Hansen EOS, DMR - continued.

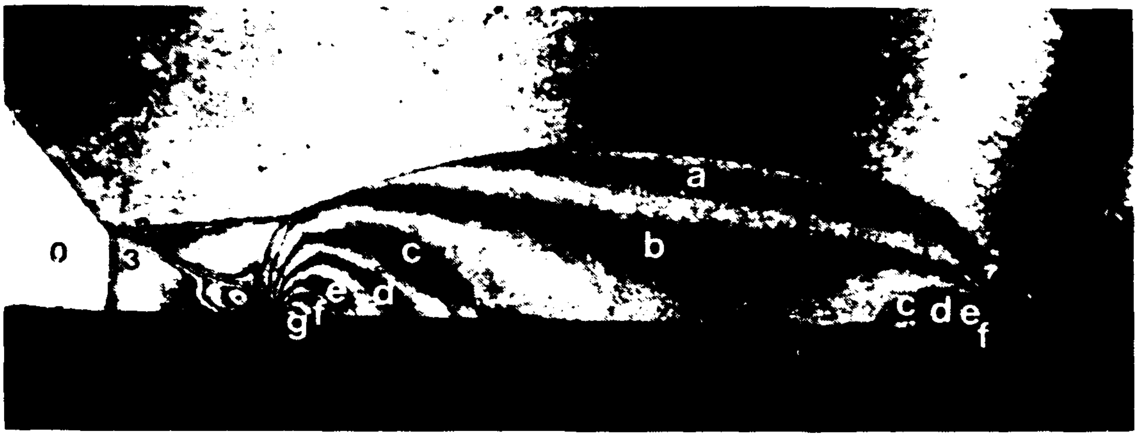

Region	ρ/ρ_0
0	1.00
1	4.41
2	7.16
3	5.08
a	7.60
b	8.03
c	8.47
d	8.91
e	9.35
f	9.78
g	10.22

Figure 13a. Interferogram.

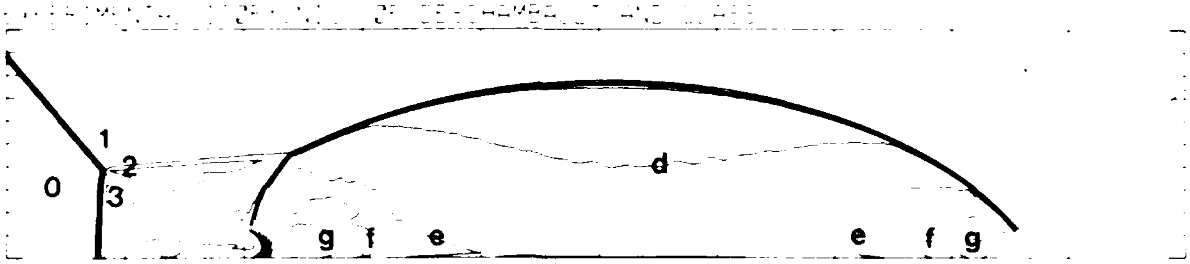

XBB 859-7202

Figure 13b. Calculated isopycnics (γ = 1.4) using the experimental fringes.

Figure 13. Case 10, M_s = 3.72, θ_w = 40°, Air, γ = 1.4 and Hansen EOS, DMR.

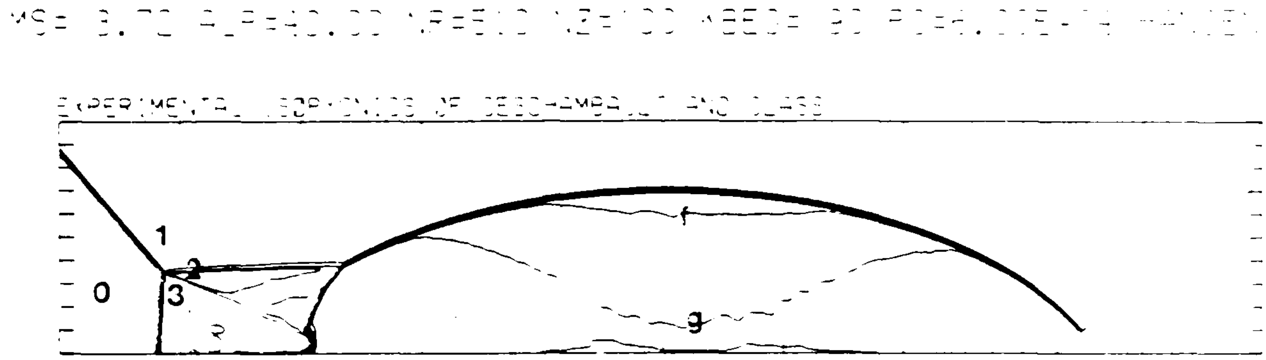

Figure 13b$_H$. Calculated isopycnics (Hansen) using the experimental fringes.

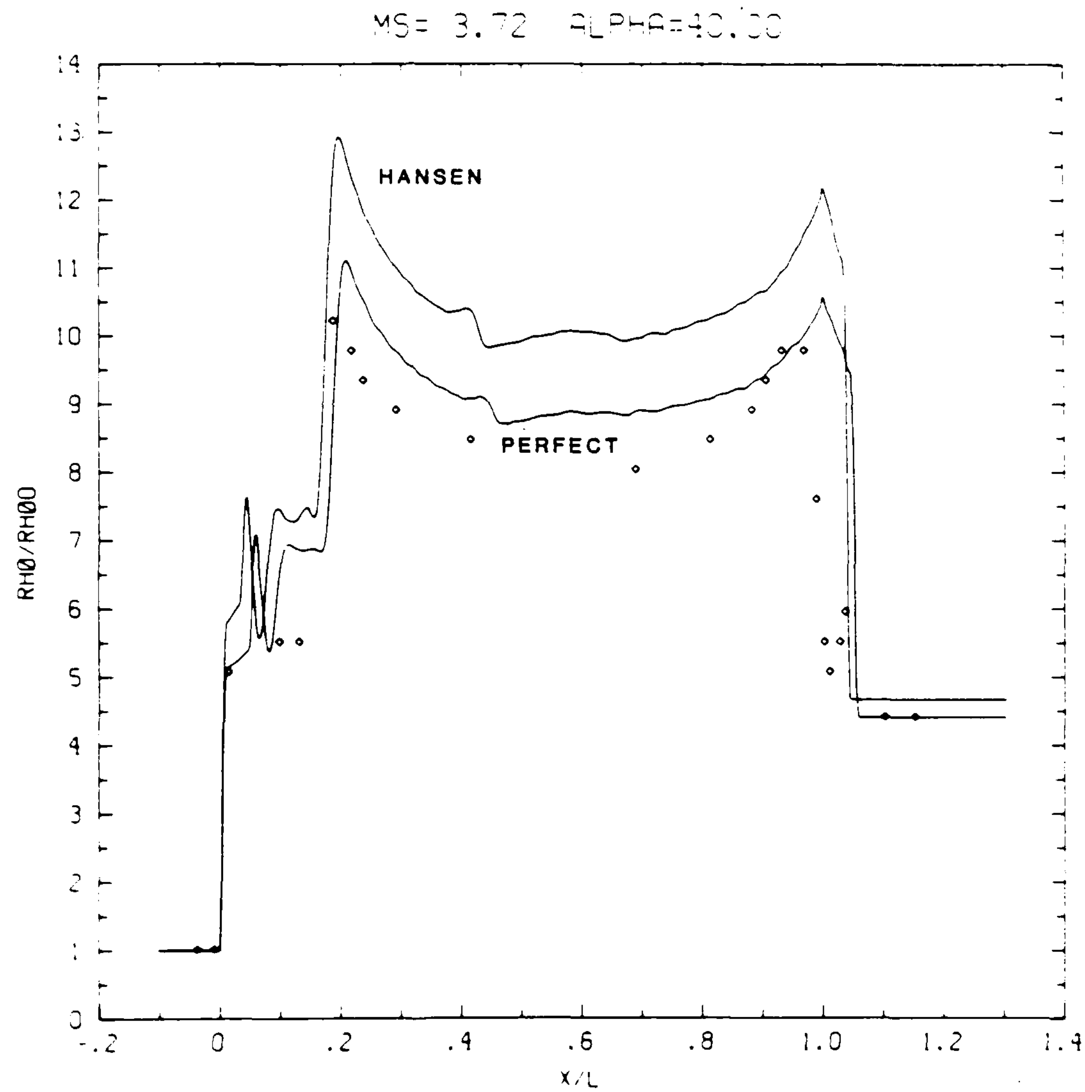

Figure 13c. Wall plot for ρ/ρ_0, γ = 1.4 and Hansen calculations, with experimental data.

Figure 13. Case 10, M_s = 3.72, θ_w = 40°, Air, γ = 1.4 and Hansen EOS, DMR - continued.

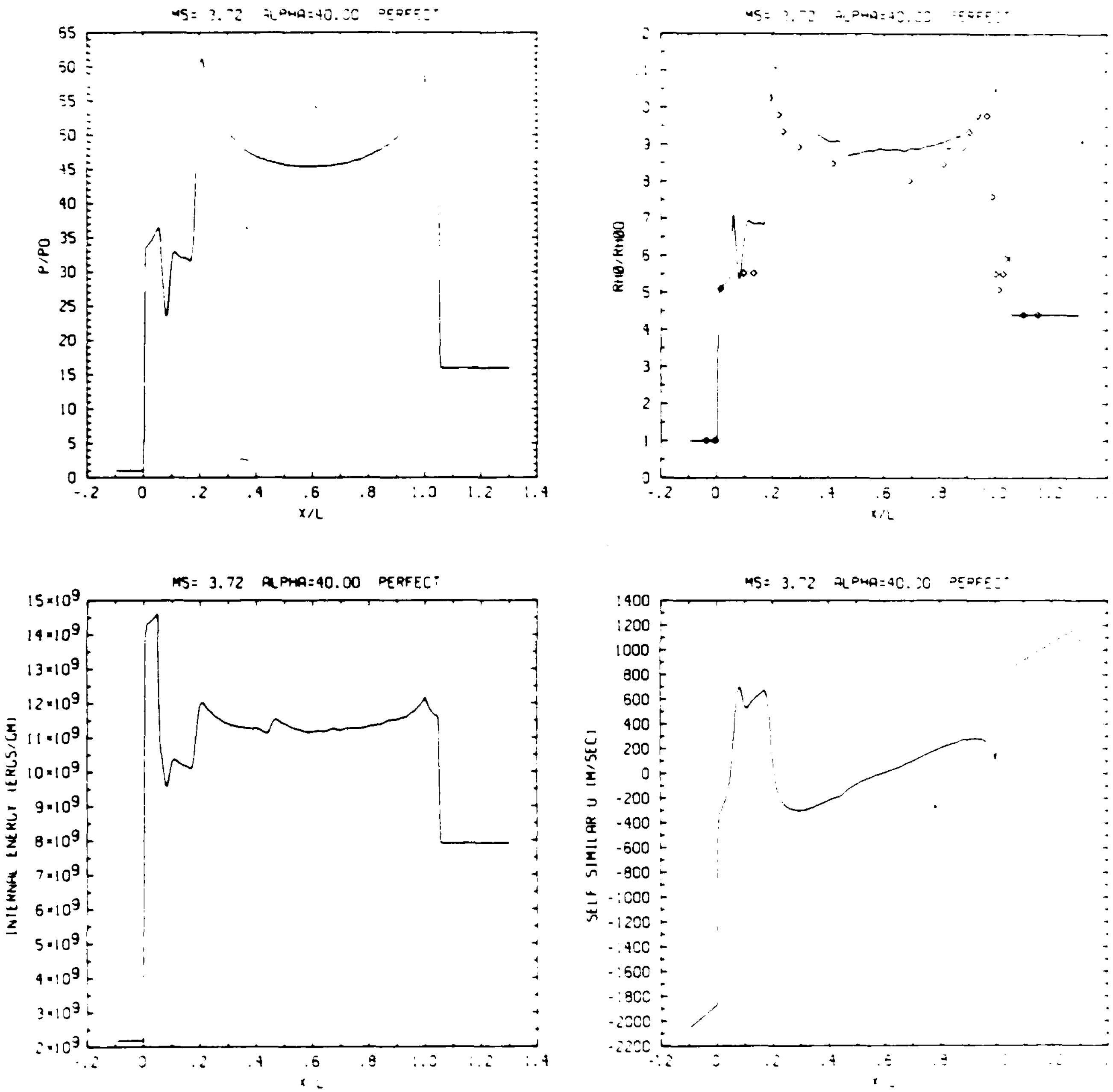

Figure 13c$_p$. Wall plots for p/p_0, ρ/ρ_0 with experimental data included, e, u; $\gamma = 1.4$.

Figure 13. Case 10, $M_s = 3.72$, $\theta_w = 40°$, Air, $\gamma = 1.4$ and Hansen EOS, DMR - continued.

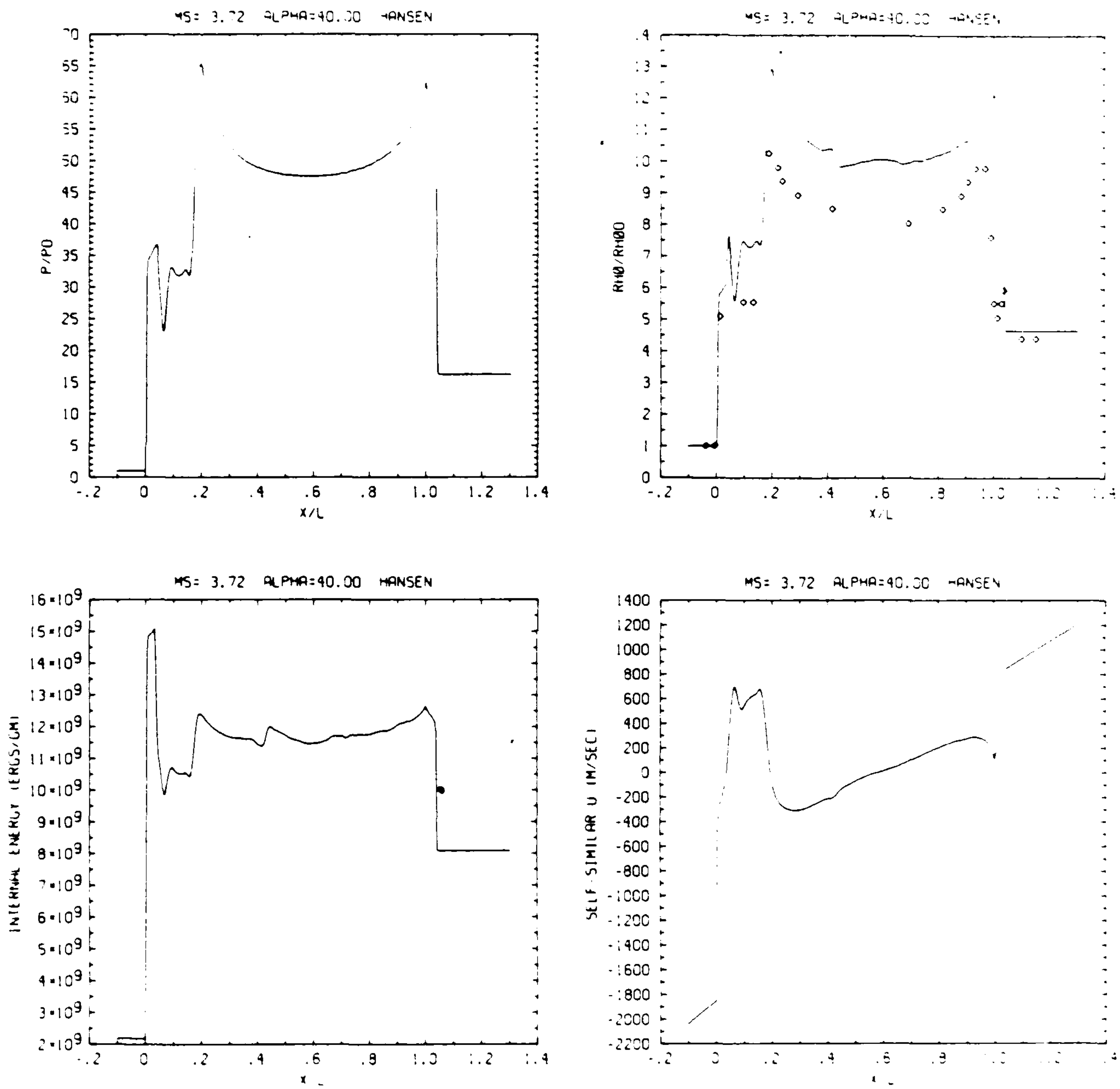

Figure 13c$_H$. Wall plots for p/p_0, ρ/ρ_0 with experimental data included, e, u; Hansen.

Figure 13. Case 10, M_s = 3.72, θ_w = 40°, Air, γ = 1.4 and Hansen EOS, DMR - continued.

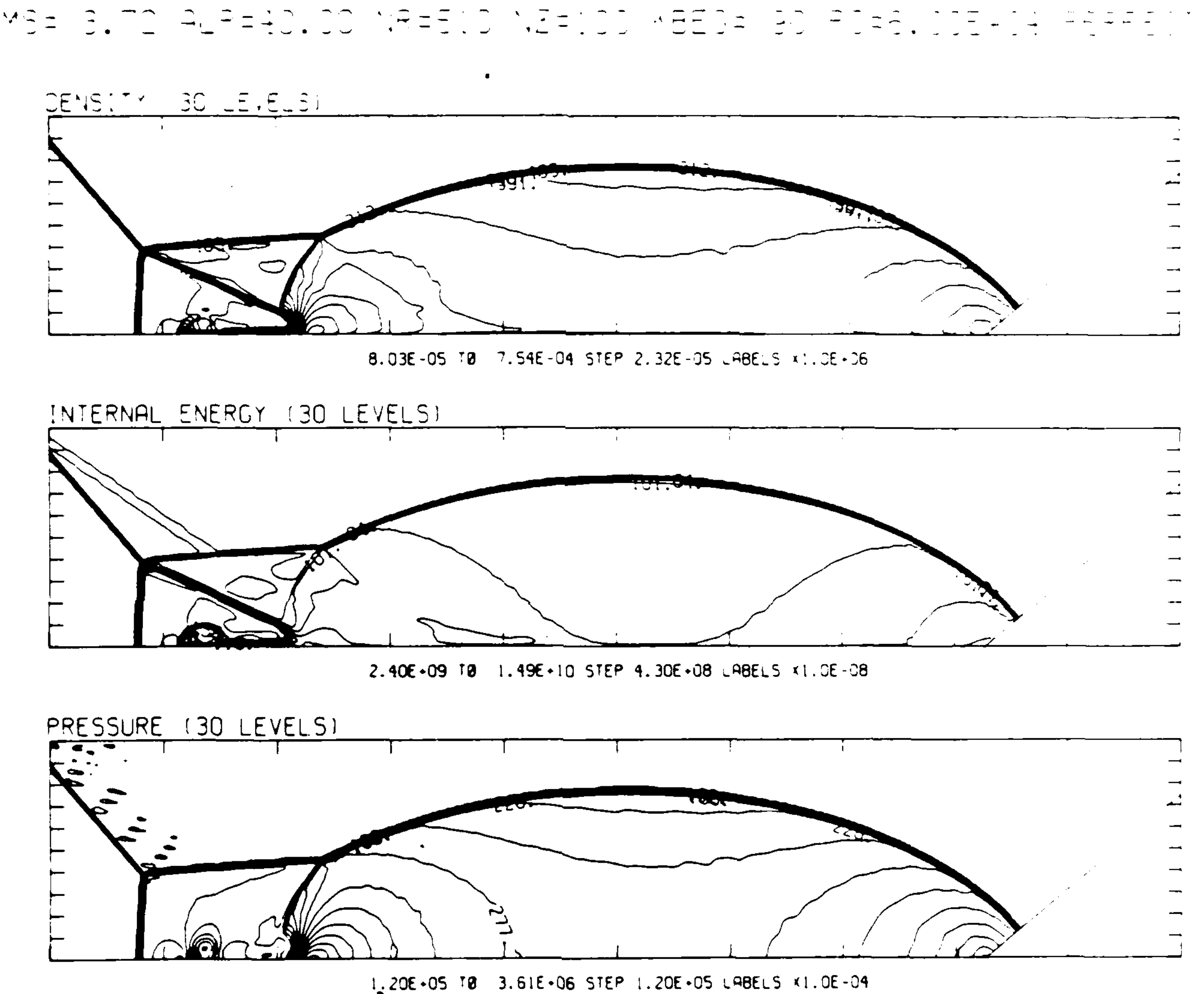

Figure $13d_p$. Whole-flowfield contour-plots; γ = 1.4.

Figure 13. Case 10, M_s = 3.72, θ_w = 40°, Air, γ = 1.4 and Hansen EOS, DMR - continued.

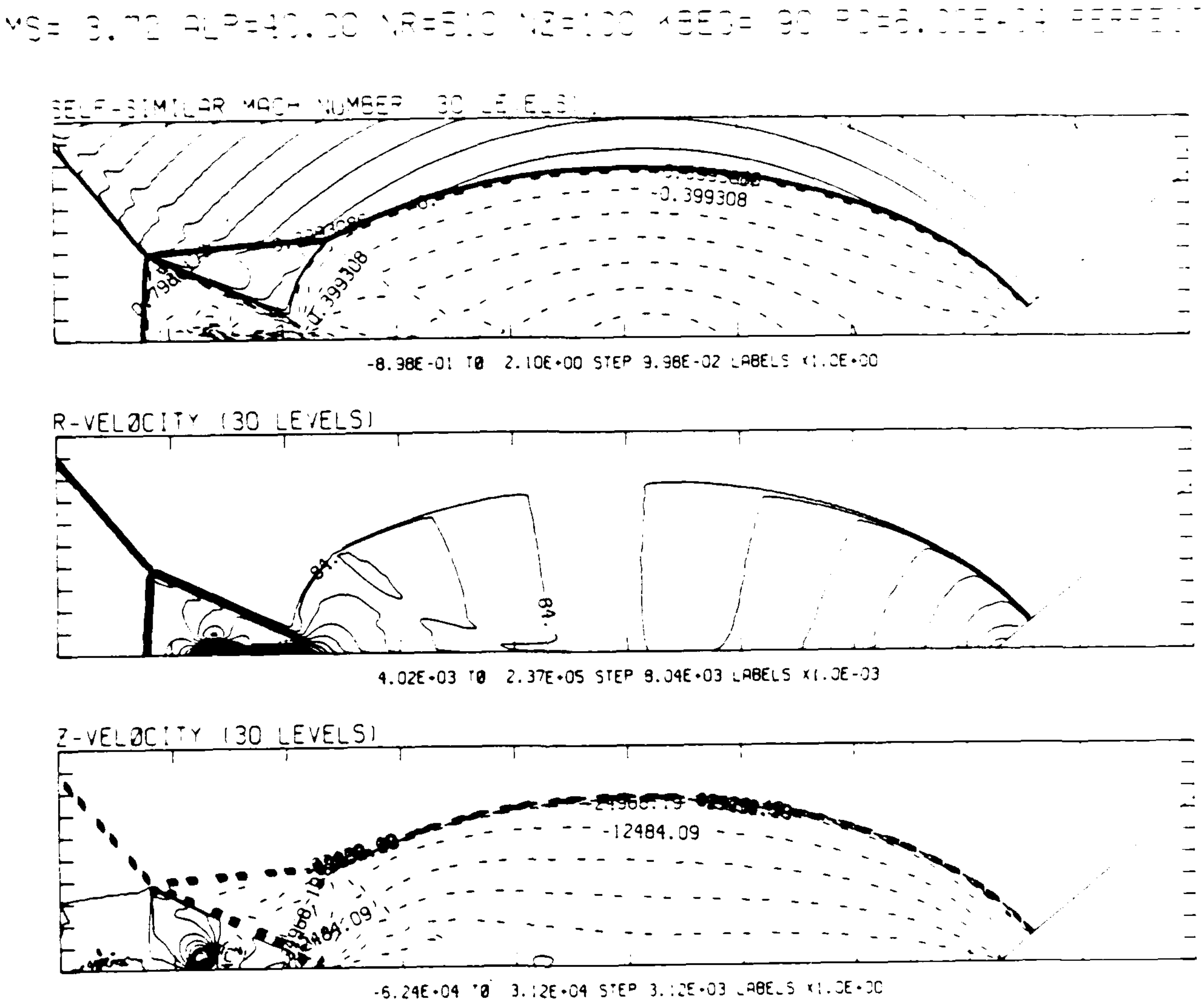

Figure 13d$_p$. Whole-flowfield contour-plots; γ = 1.4 - continued.

Figure 13. Case 10, M_s = 3.72, θ_w = 40°, Air, γ = 1.4 and Hansen EOS, DMR - continued.

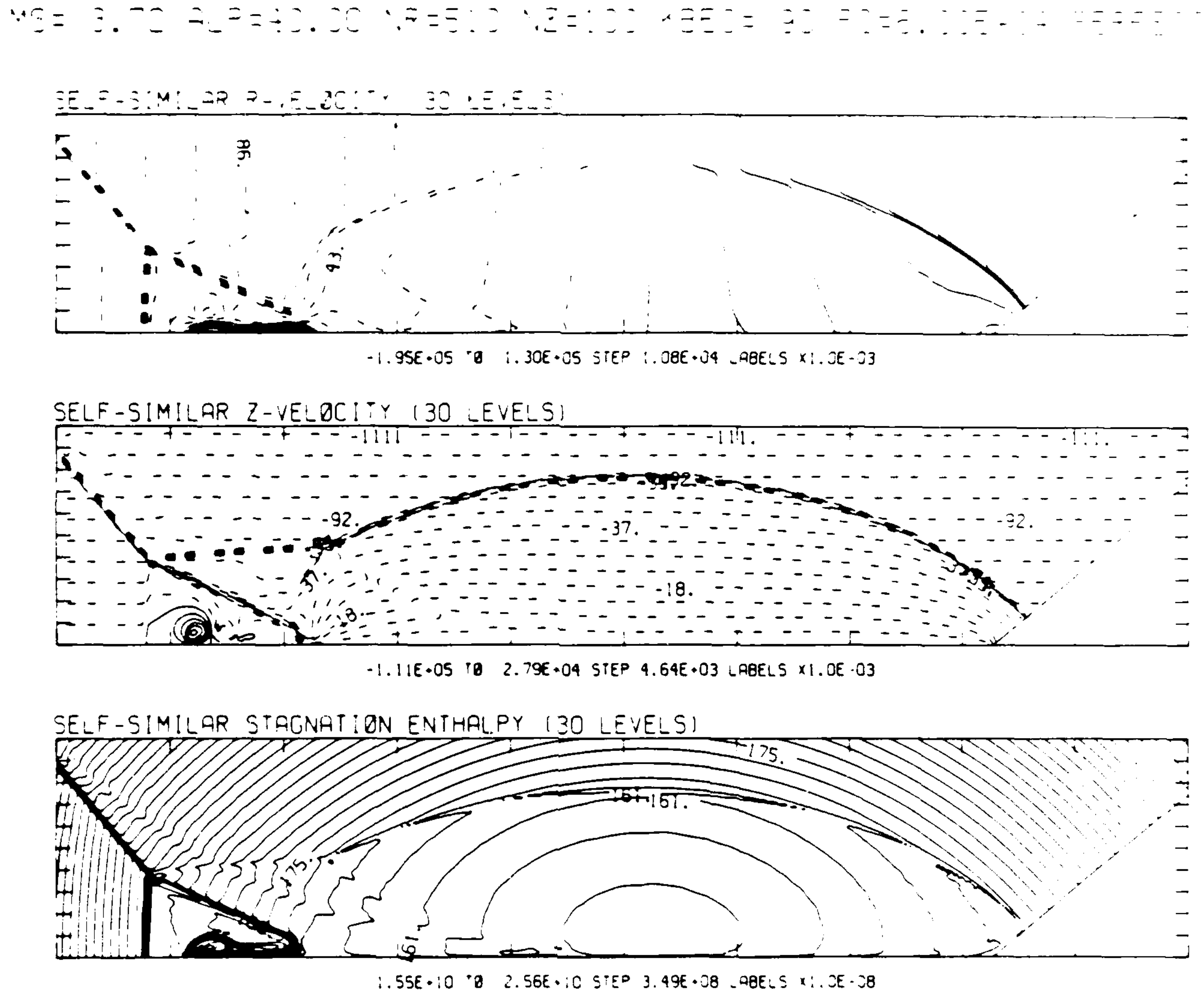

Figure 13d$_p$. Whole-flowfield contour-plots; γ = 1.4 - continued.

Figure 13. Case 10, M_s = 3.72, θ_w = 40°, Air, γ = 1.4 and Hansen EOS, DMR - continued.

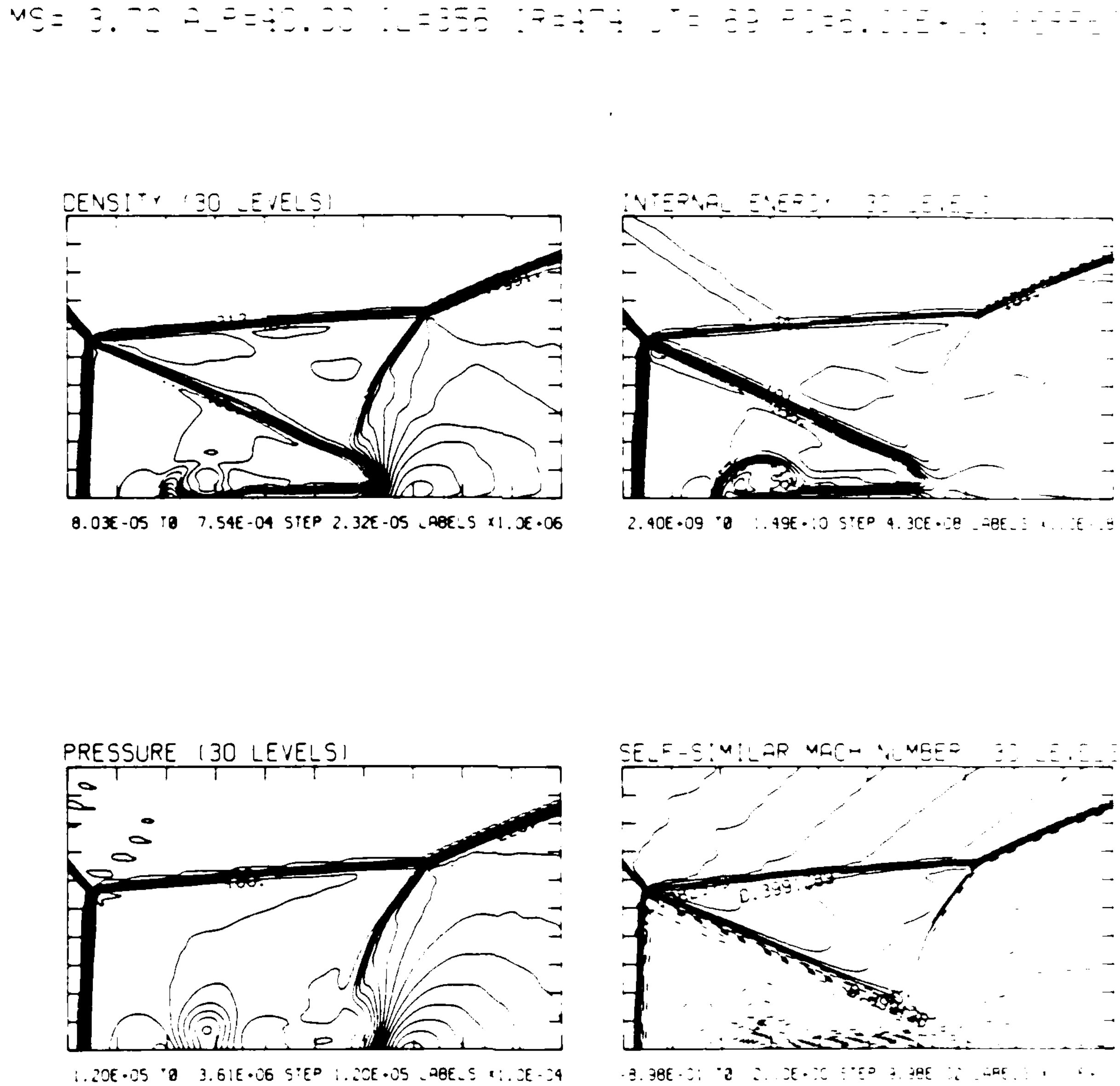

Figure 13ep. Blowup-frame plots; γ = 1.4.

Figure 13. Case 10, M_s = 3.72, θ_w = 40°, Air, γ = 1.4 and Hansen EOS, DMR - continued.

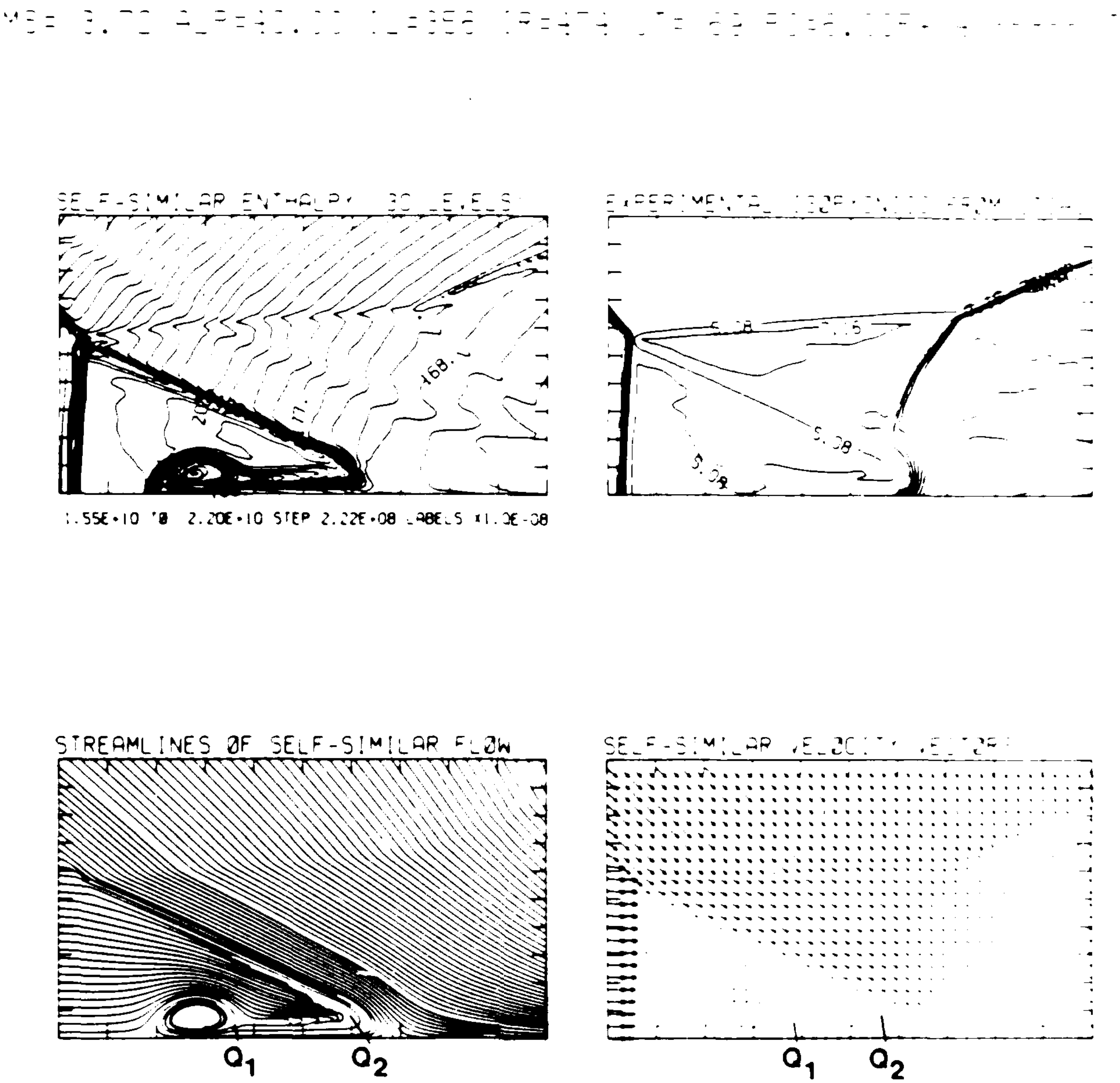

Figure 13e$_p$. Blowup-frame plots; γ = 1.4 - continued.

Figure 13. Case 10, M_s = 3.72, θ_w = 40°, Air, γ = 1.4 and Hansen EOS, DMR - continued.

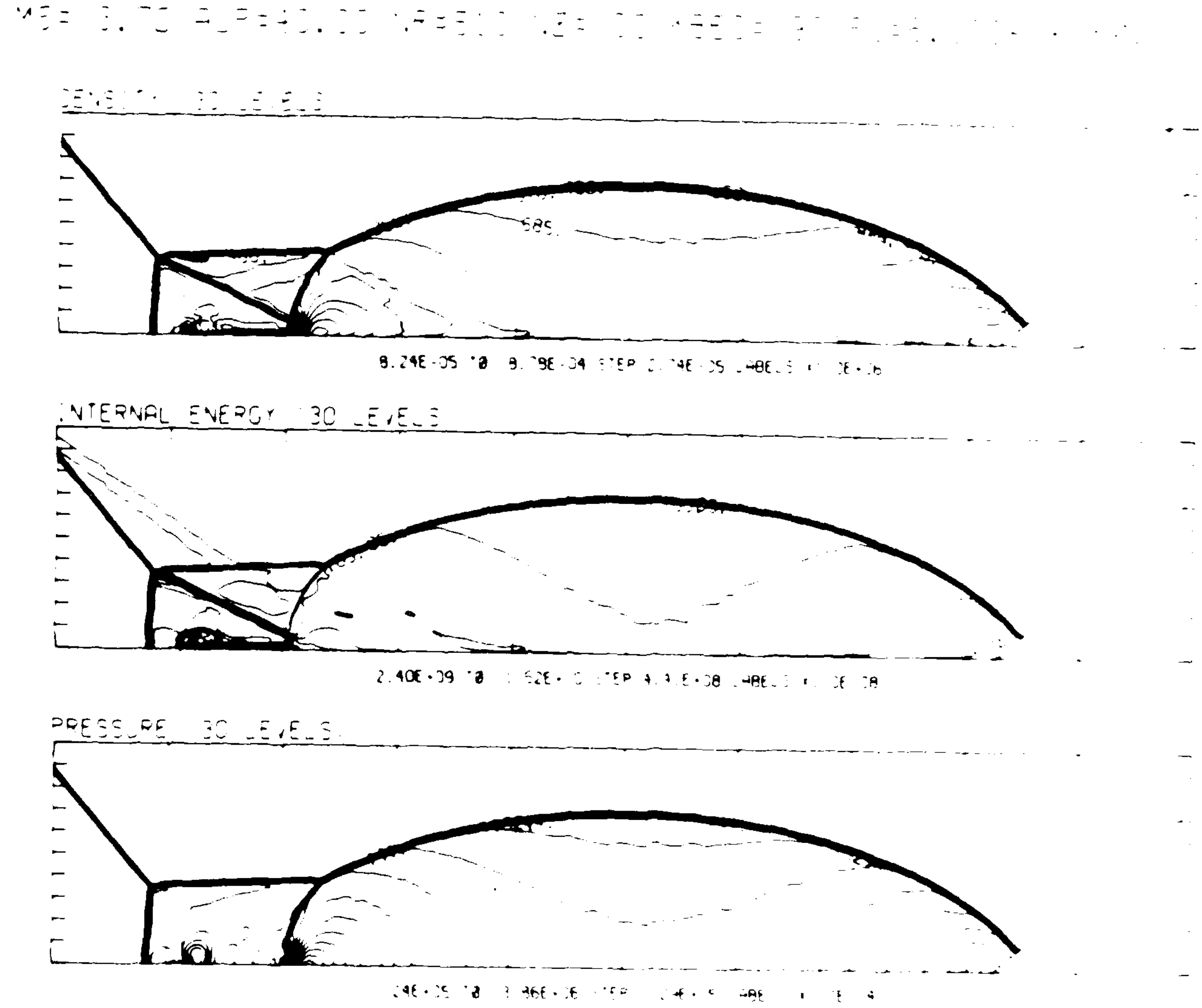

Figure $13d_H$. Whole-flowfield contour-plots; Hansen.

Figure 13. Case 10, $M_s = 3.72$, $\theta_w = 40°$, Air, $\gamma = 1.4$ and Hansen EOS, DMR - continued.

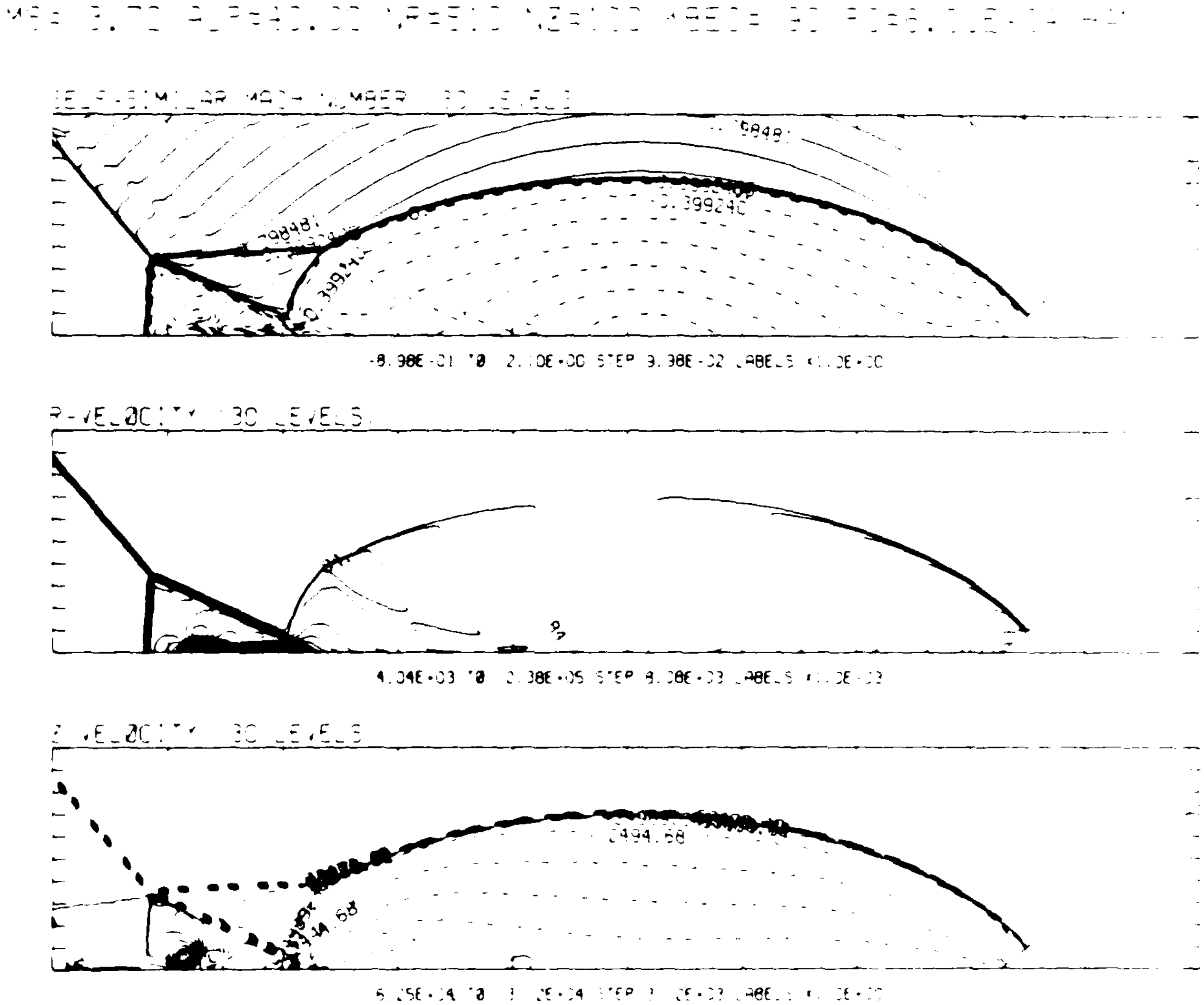

Figure 13d$_4$. Whole-flowfield contour-plots; Hansen - continued.

Figure 13. Case 10, M_s = 3.72, θ_w = 40°, Air, γ = 1.4 and Hansen EOS, DMR - continued.

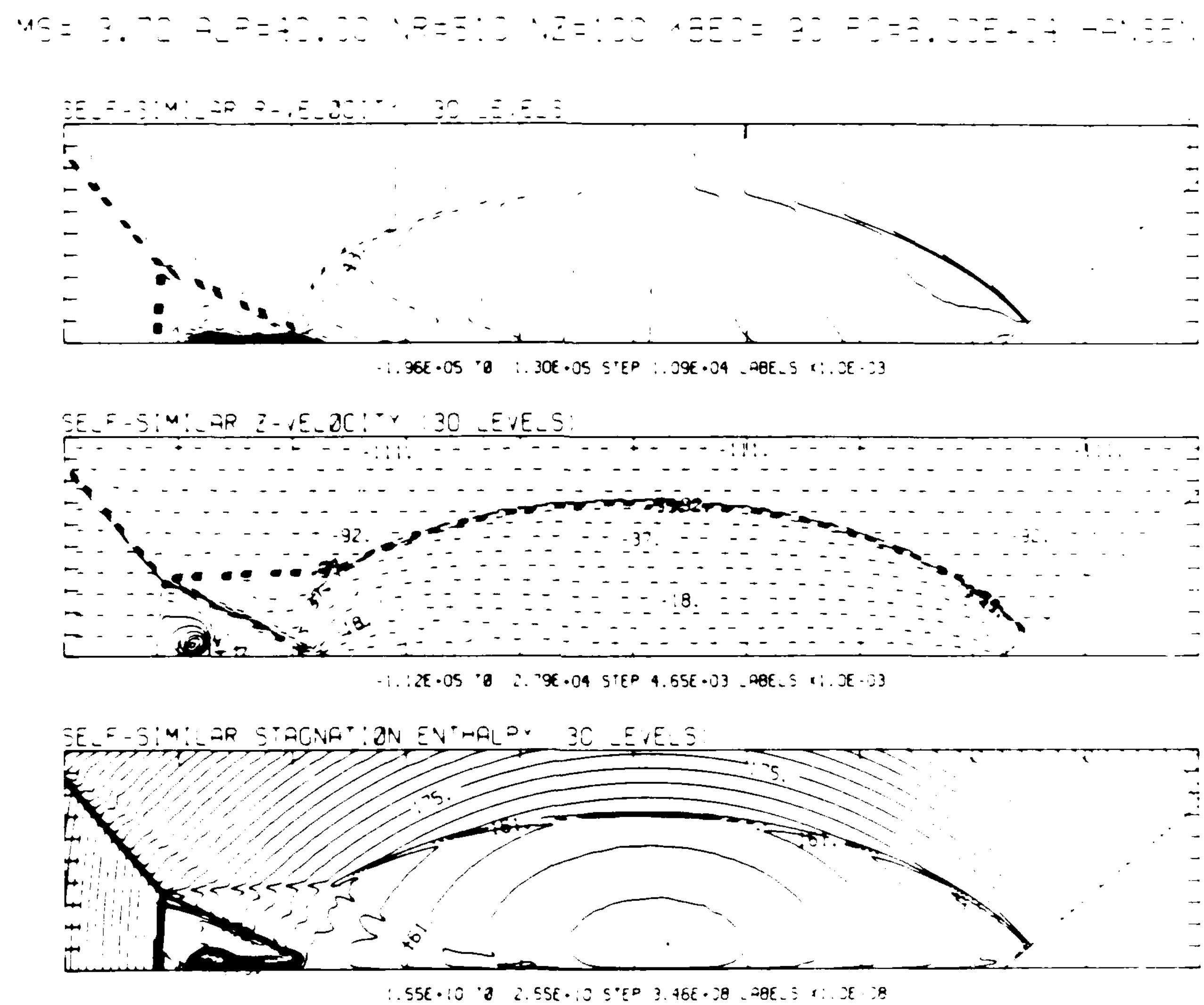

Figure 13d$_H$. Whole-flowfield contour-plots; Hansen - continued.

Figure 13. Case 10, M_s = 3.72, θ_w = 40°, Air, γ = 1.4 and Hansen EOS, DMR - continued.

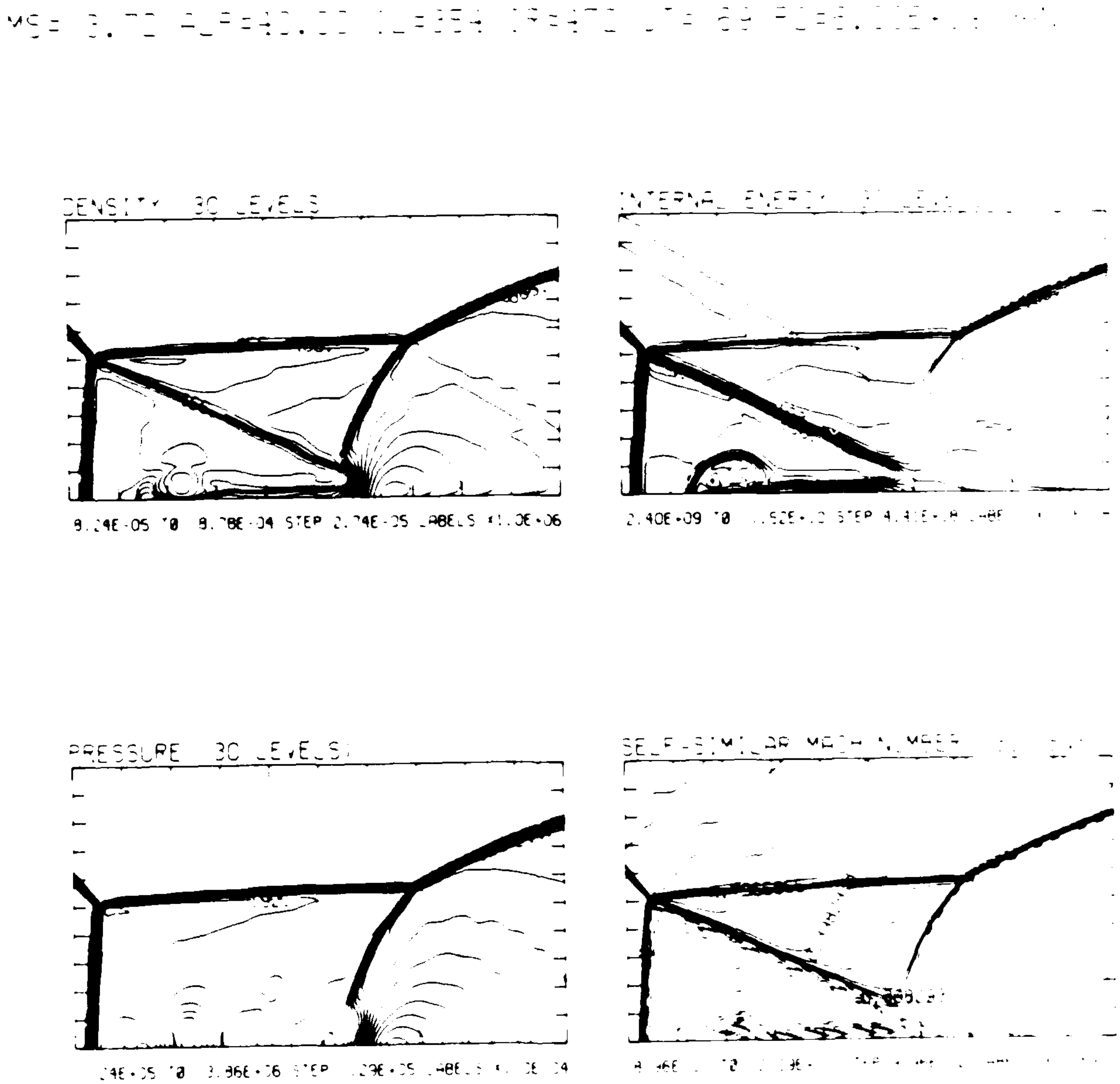

Figure $13e_H$. Blowup-frame plots; Hansen.

Figure 13. Case 10, M_s = 3.72, θ_w = 40°, Air, γ = 1.4 and Hansen EOS, DMR - continued.

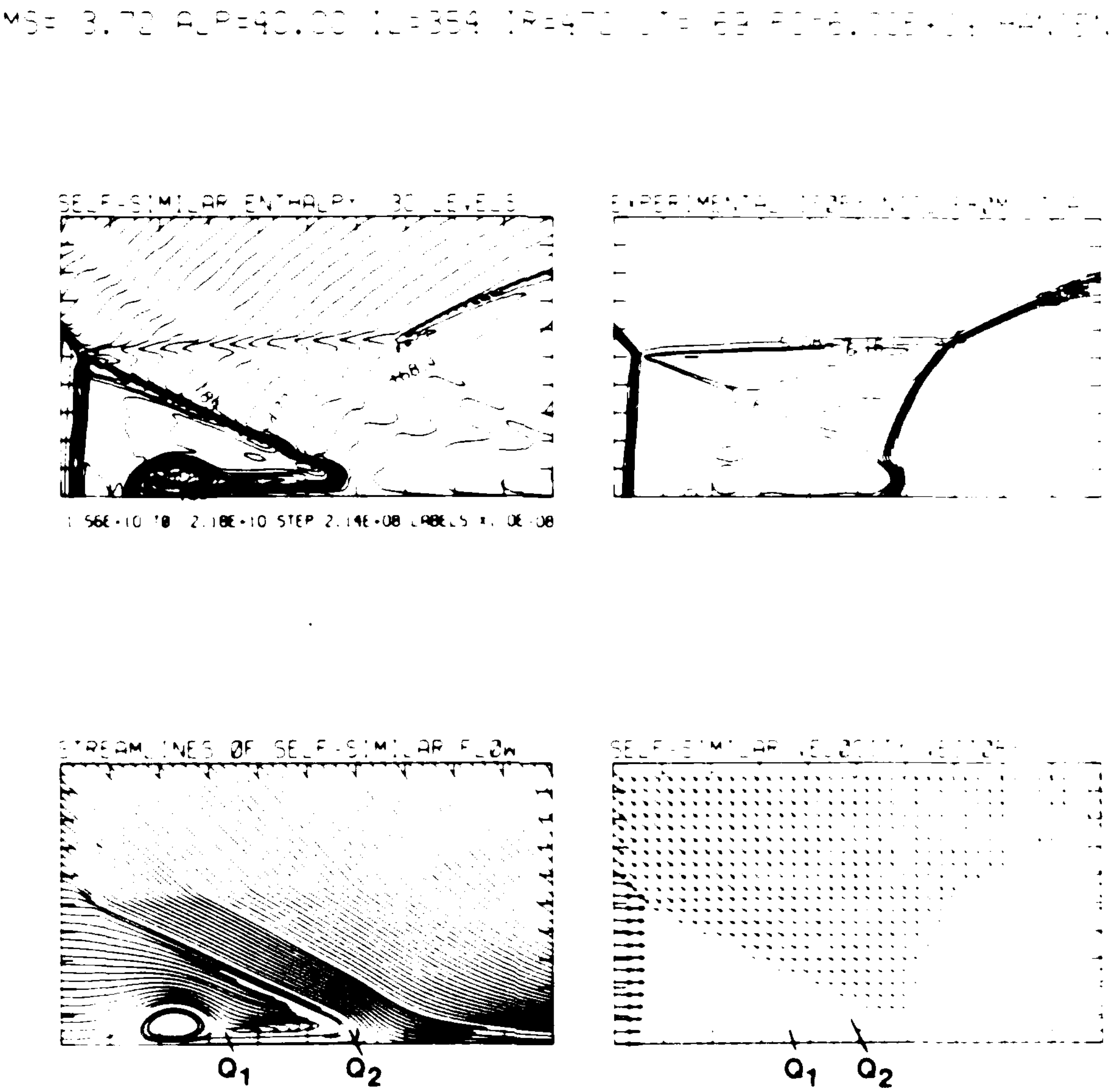

Figure 13e$_H$. Blowup-frame plots; Hansen - continued.

Figure 13. Case 10, M_s = 3.72, θ_w = 40°, Air, γ = 1.4 and Hansen EOS, DMR - continued.

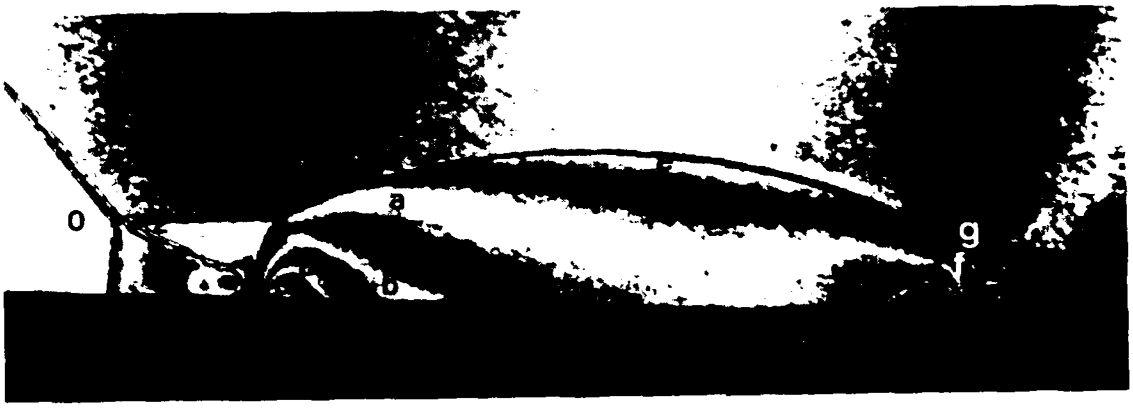

Region	ρ/ρ_0
0	1.00
1	4.86
2	7.90
3	5.37
a	9.78
b	10.72
c	11.67
d	12.61
e	8.84
f	7.90
g	6.95
h	6.01
i	5.07
j	4.13

Figure 14a. Interferogram.

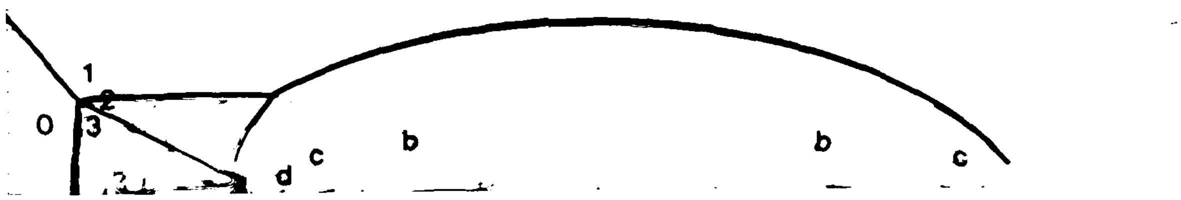

XBB 859-7203

Figure 14b. Calculated isopycnics (γ = 1.4) using the experimental fringes.

Figure 14. Case 11, M_s = 4.62, θ_w = 40°, Air, γ = 1.4 and Hansen EOS, DMR.

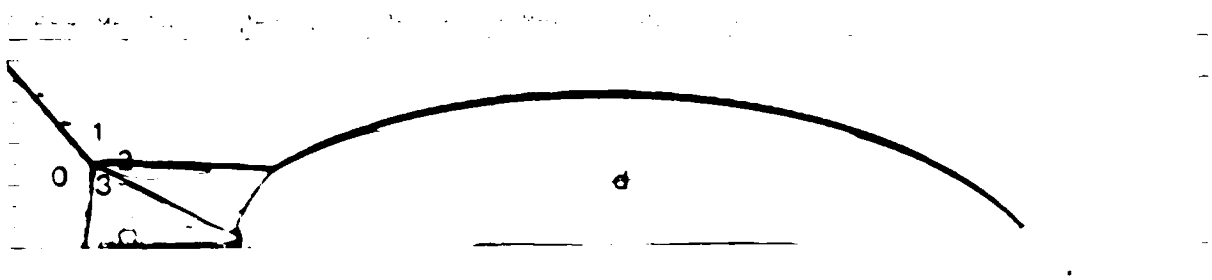

Figure 14(...) ... the experimental fringes.

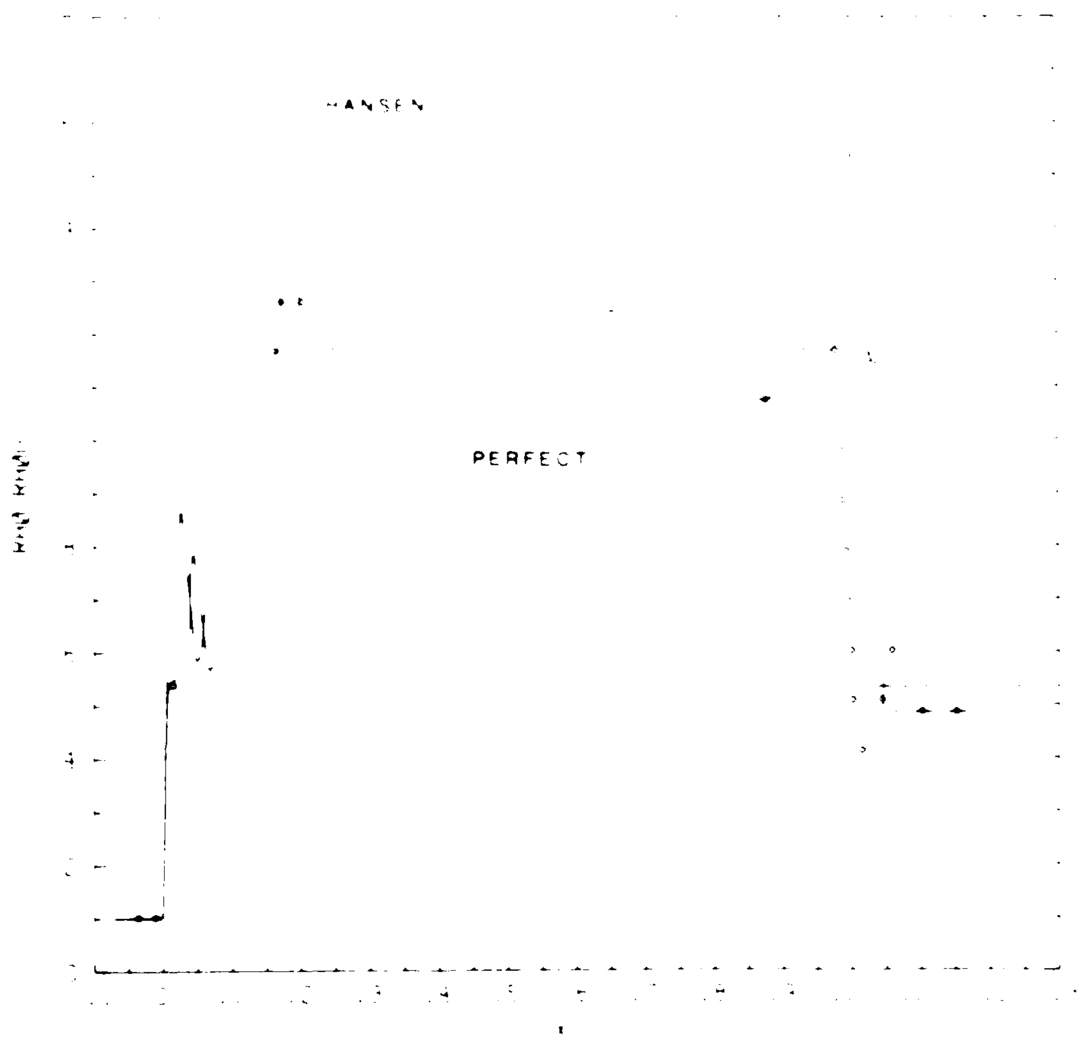

Figure 14c. Wall plot for ρ/ρ_0, γ = 1.4 and Hansen calculations, with experiment data.

Figure 14. Case 11, M_s = 4.62, θ_w = 40°, Air, γ = 1.4 and Hansen ..., DMR - continued.

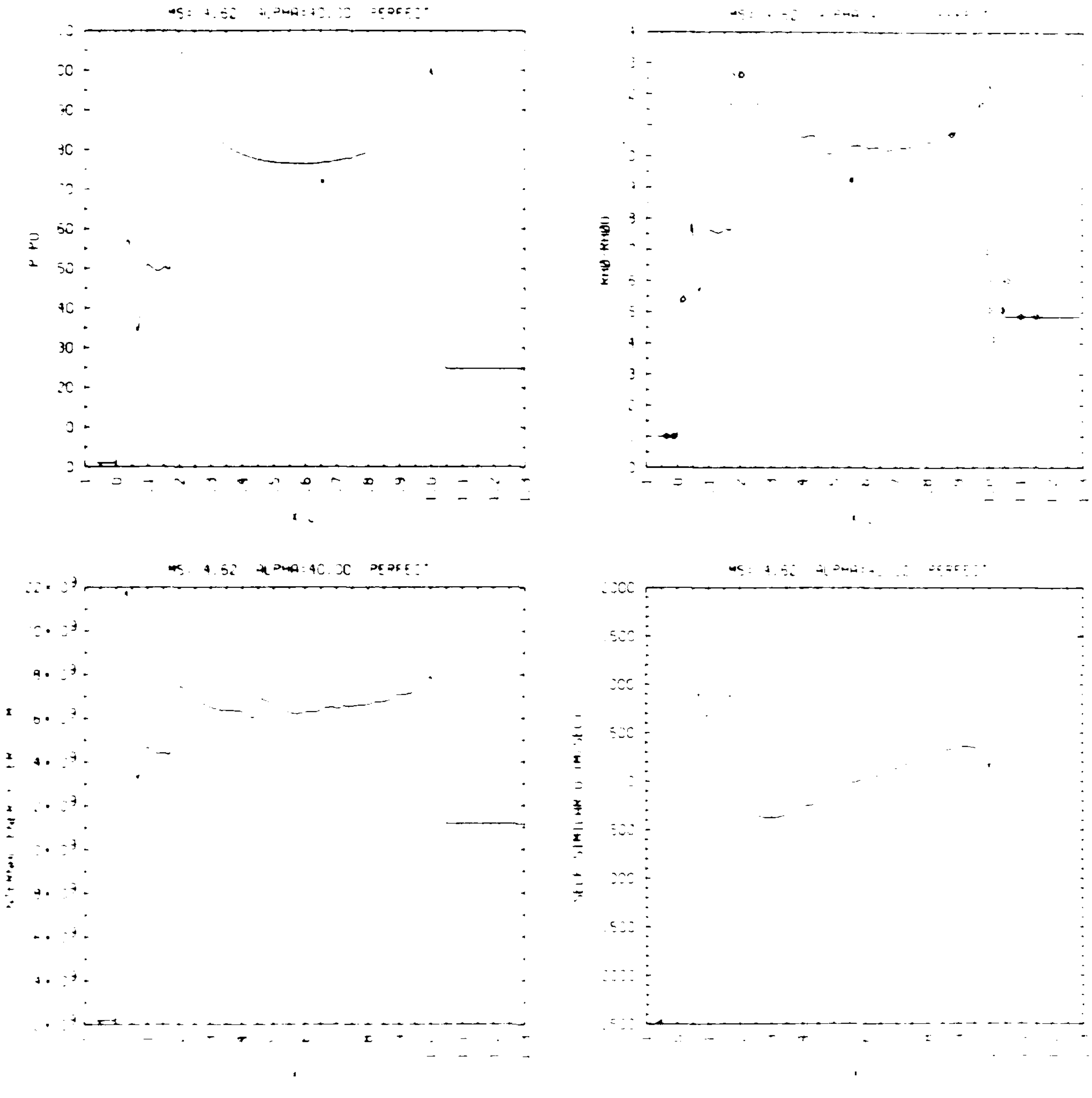

Figure 14c$_p$. Wall plots for p/p_0, ρ/ρ_0 with experimental data included, e, u; $\gamma = 1.4$.

Figure 14. Case 11, $M_s = 4.62$, $\theta_w = 40°$, Air, $\gamma = 1.4$ and Hansen EOS, DMR - continued.

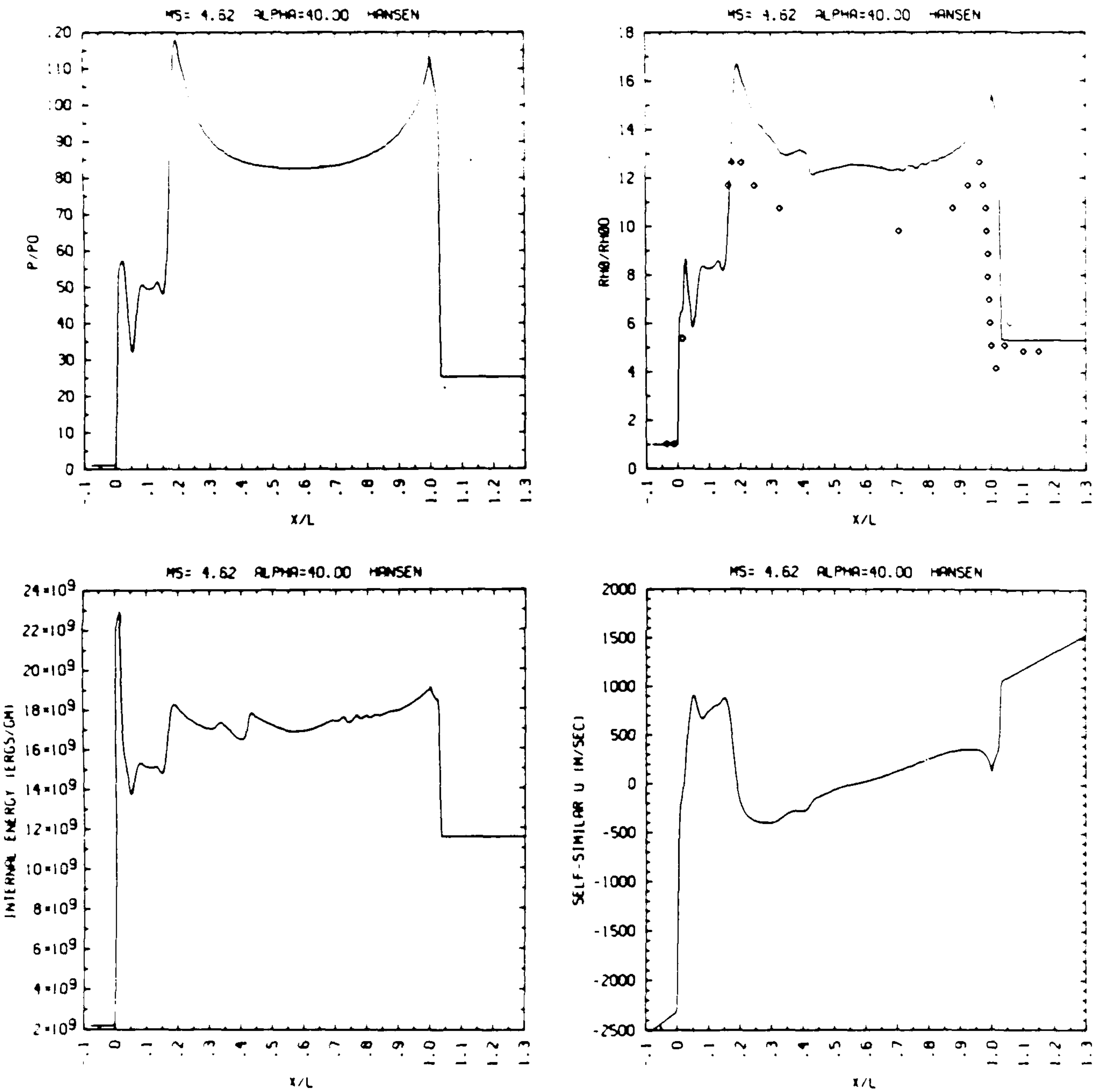

Figure $14c_H$. Wall plots for p/p_0, ρ/ρ_0 with experimental data included, e, u; Hansen.

Figure 14. Case 11, M_S = 4.62, θ_w = 40°, Air, γ = 1.4 and Hansen EOS, DMR - continued.

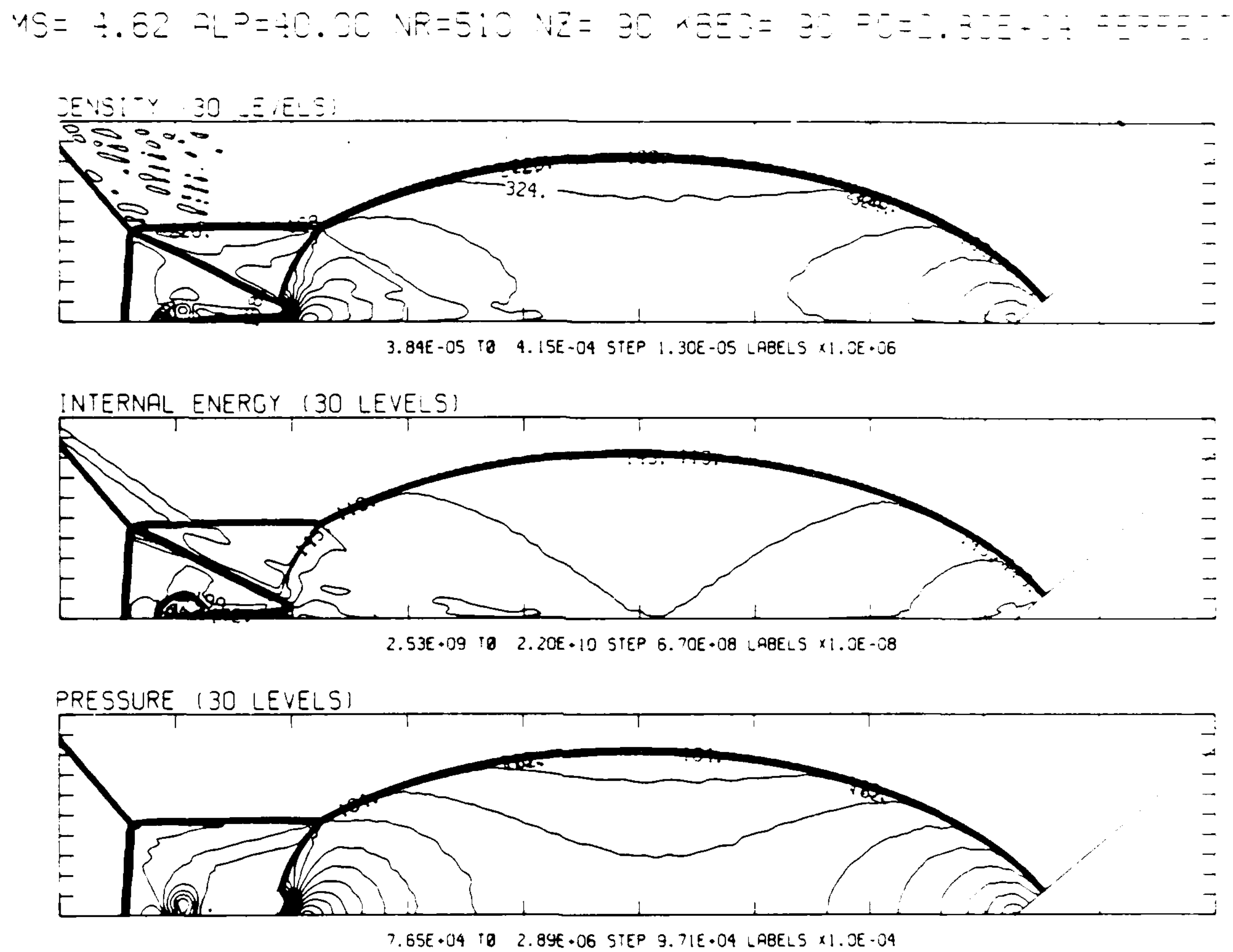

Figure 14d$_p$. Whole-flowfield contour-plots; γ = 1.4.

Figure 14. Case 11, M_s = 4.62, θ_w = 40°, Air, γ = 1.4 and Hansen EOS, DMR - continued.

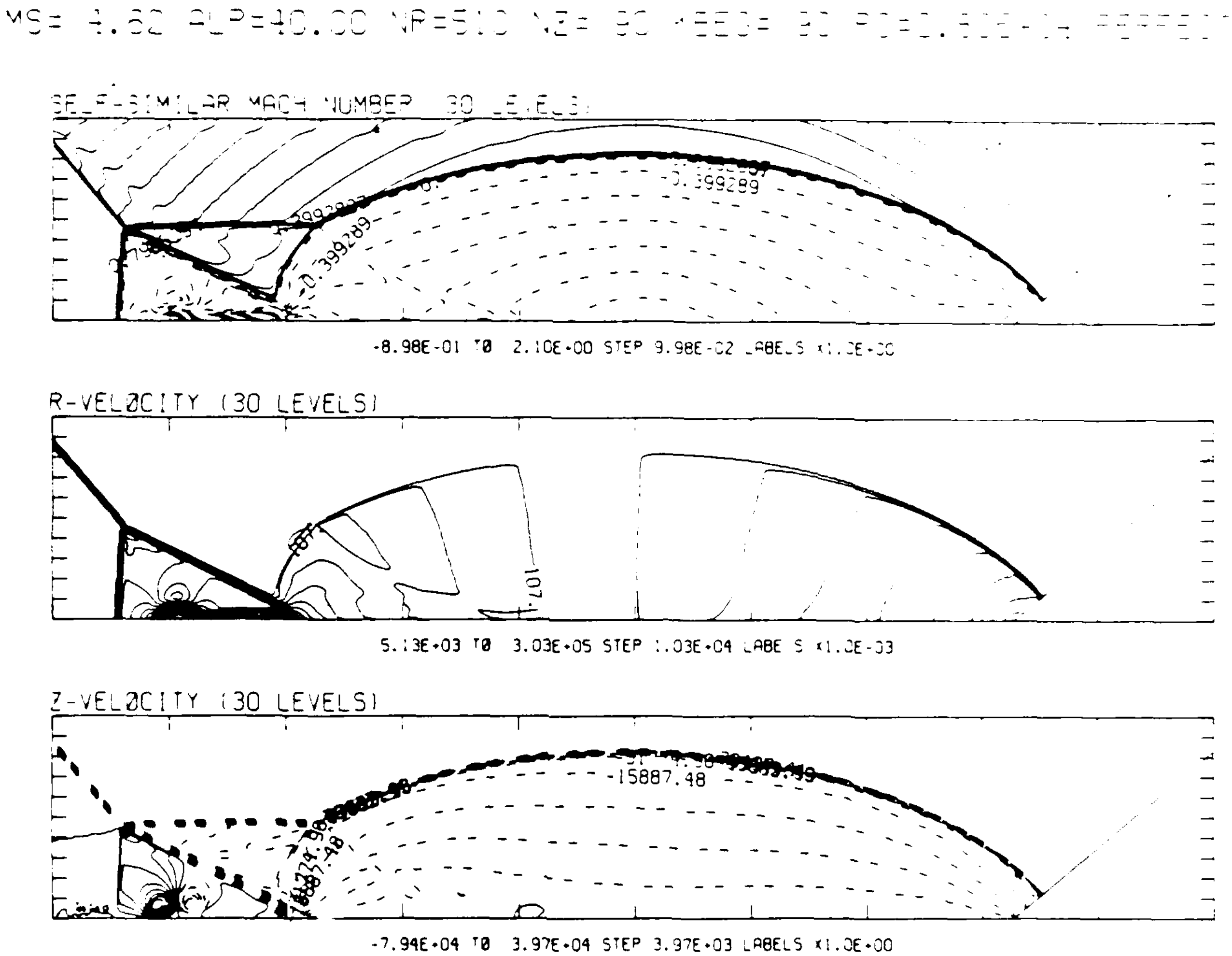

Figure $14d_p$. Whole-flowfield contour-plots; γ = 1.4 - continued.

Figure 14. Case 11, M_s = 4.62, θ_w = 40°, Air, γ = 1.4 and Hansen EOS, DMR - continued.

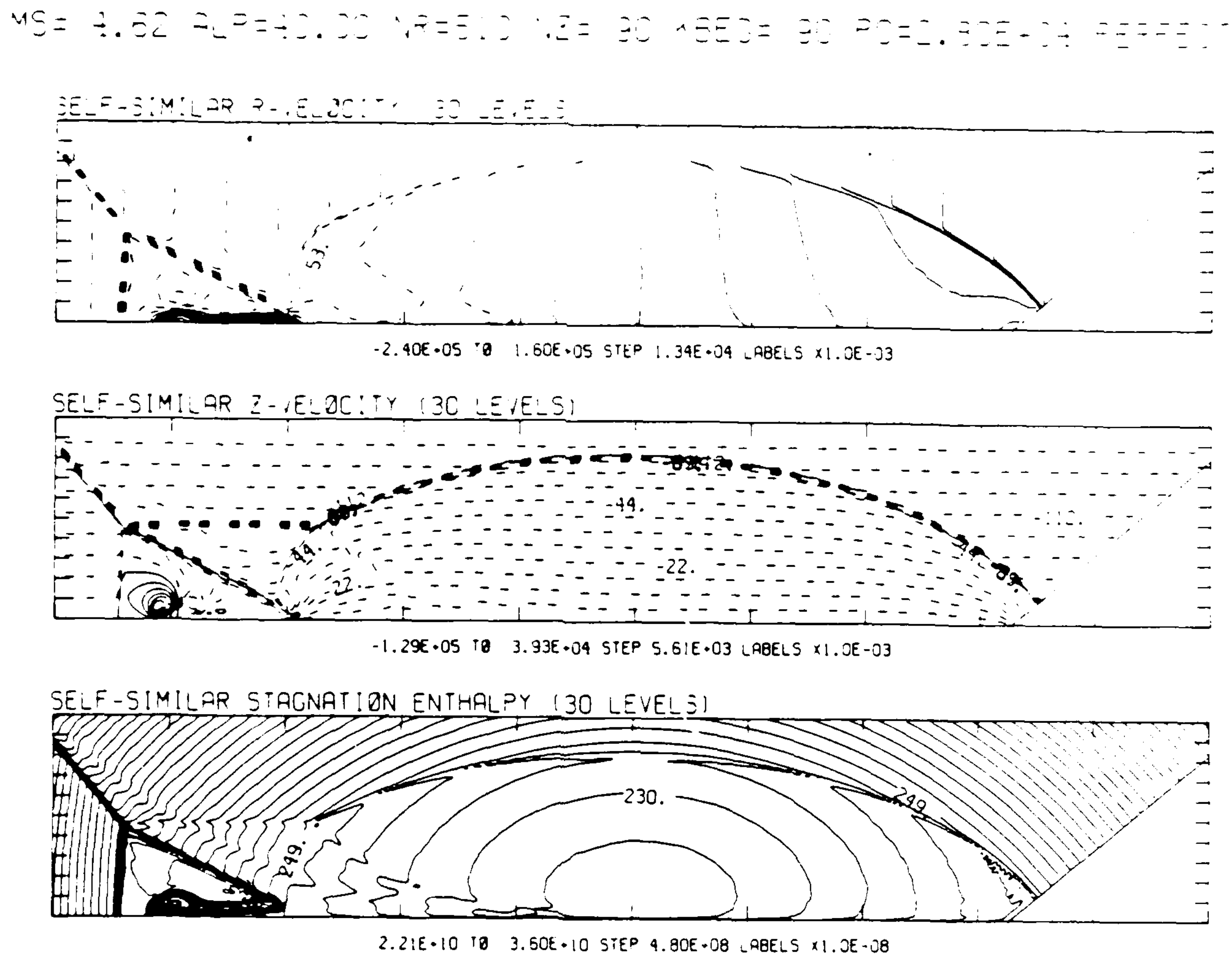

Figure 14d$_p$. Whole-flowfield contour-plots; γ = 1.4- continued.

Figure 14. Case 11, M_s = 4.62, θ_w = 40°, Air, γ = 1.4 and Hansen EOS, DMR - continued.

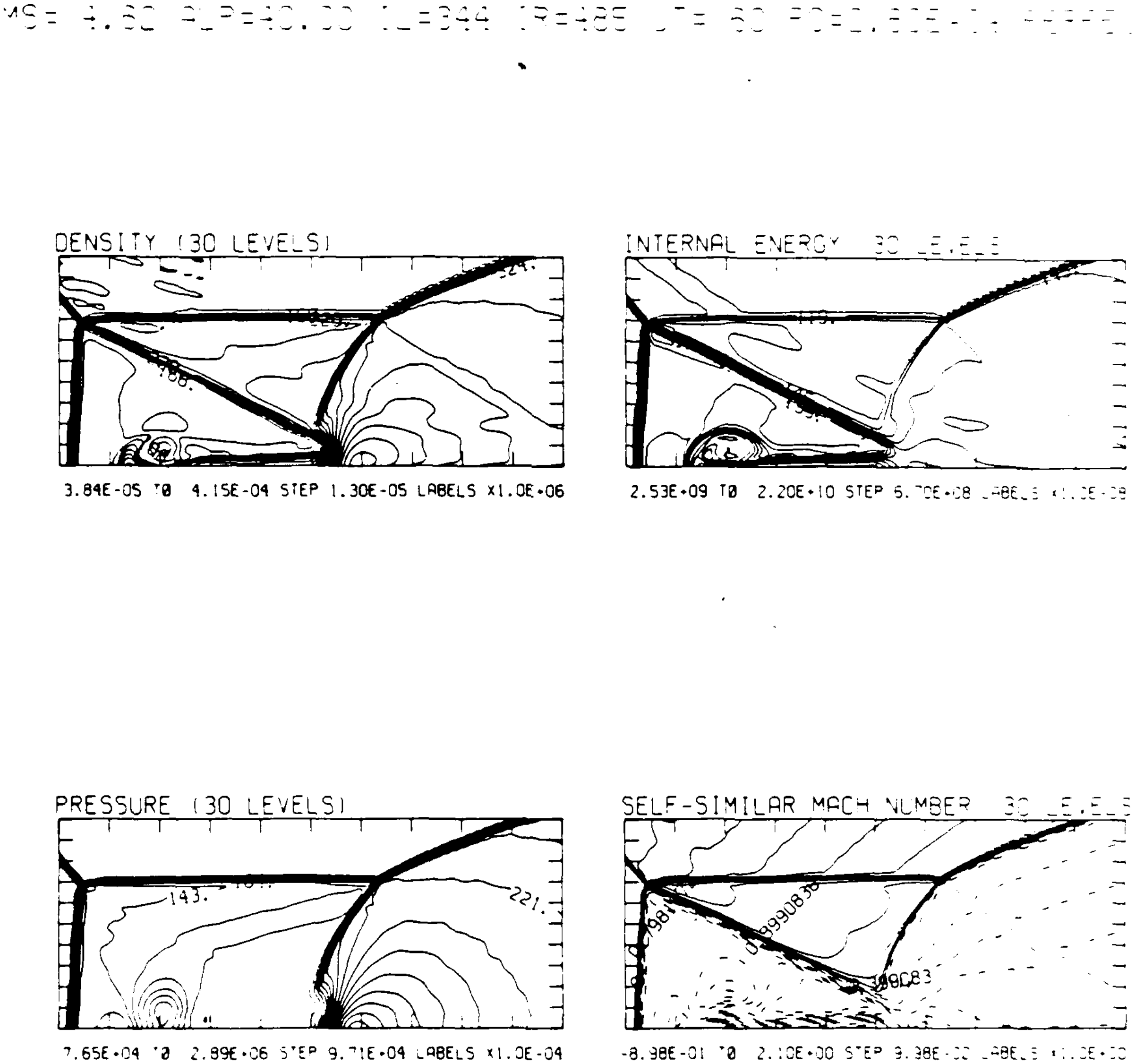

Figure 14e$_p$. Blowup-frame plots; γ = 1.4.

Figure 14. Case 11, M_s = 4.62, θ_w = 40°, Air, γ = 1.4 and Hansen EOS, DMR - continued.

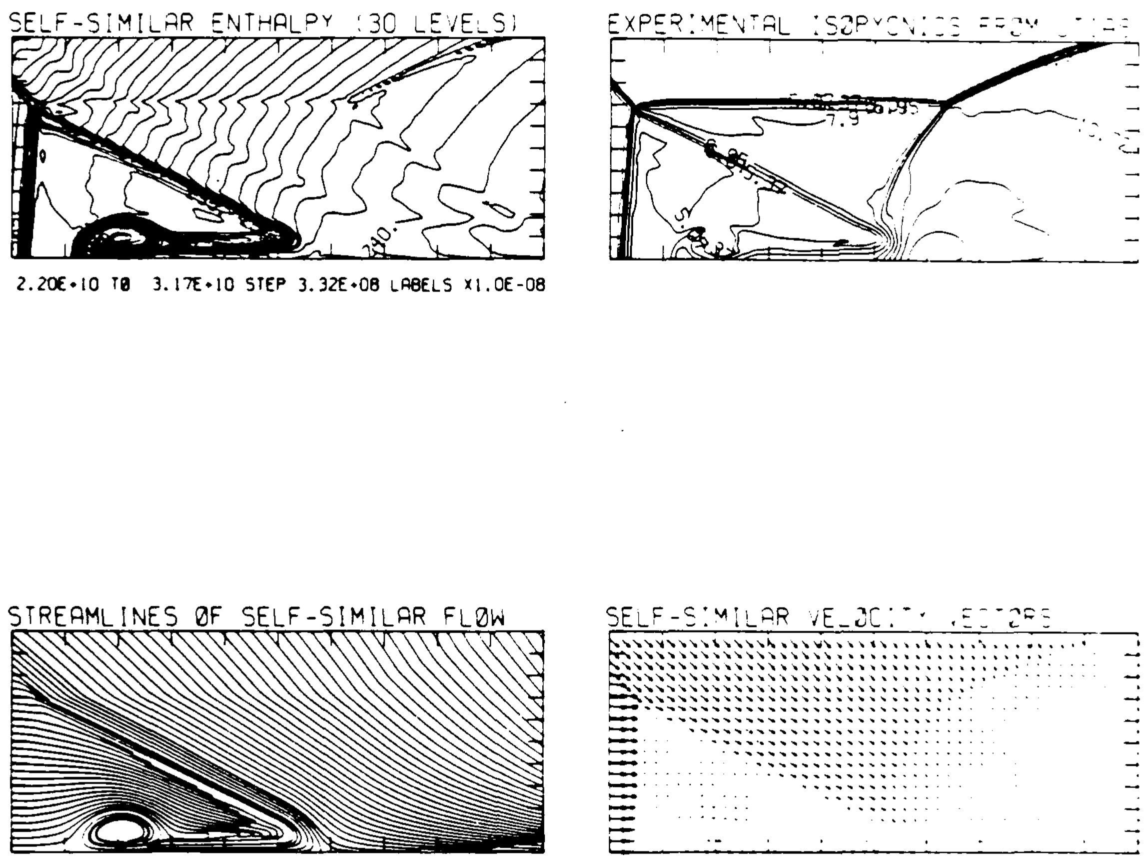

Figure $14e_p$. Blowup-frame plots; γ = 1.4 - continued.

Figure 14. Case 11, M_S = 4.62, θ_w = 40°, Air, γ = 1.4 and Hansen EOS, DMR - continued.

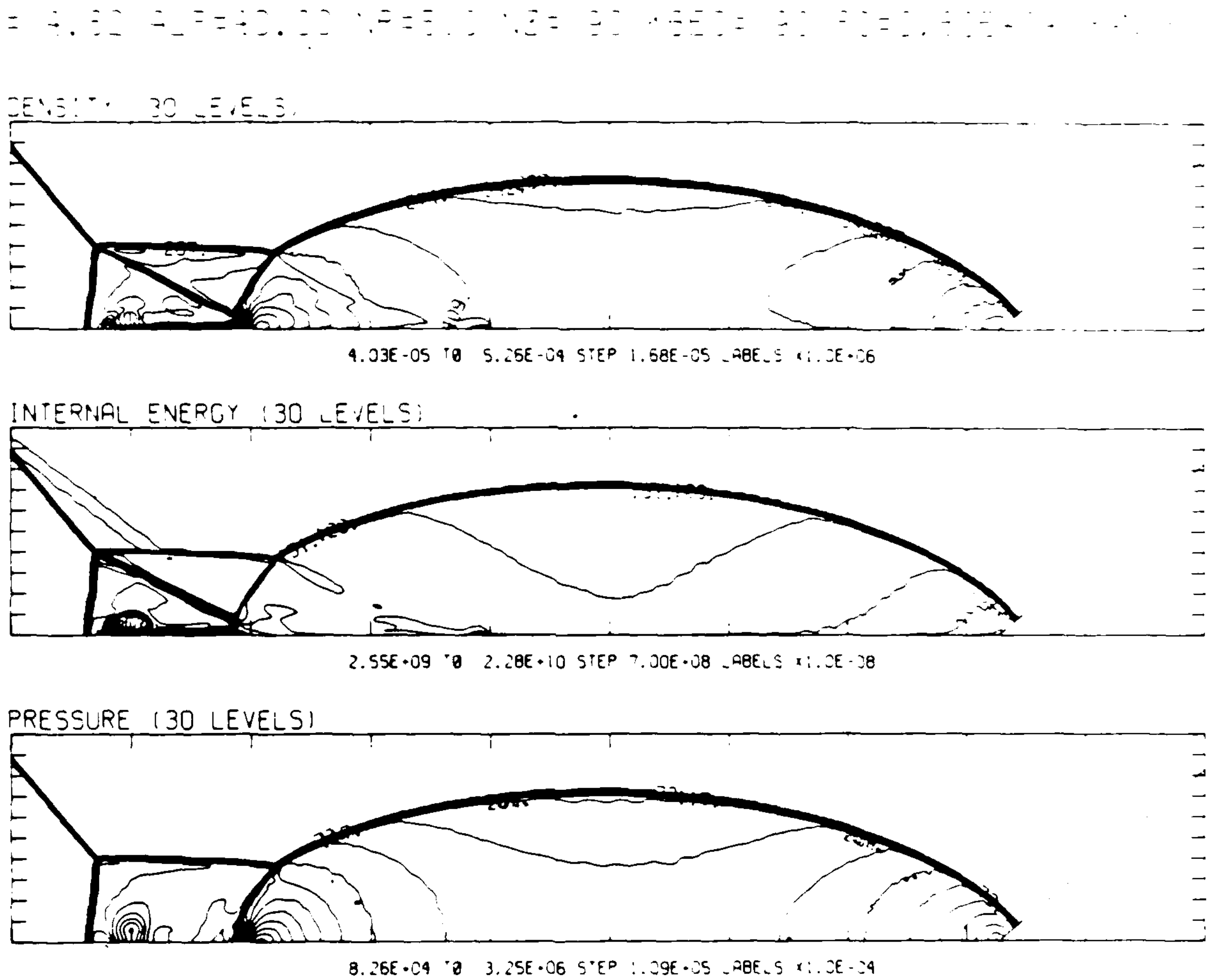

Figure $14d_H$. Whole-flowfield contour-plots; Hansen.

Figure 14. Case 11, M_s = 4.62, θ_w = 40°, Air, γ = 1.4 and Hansen EOS, DMR - continued.

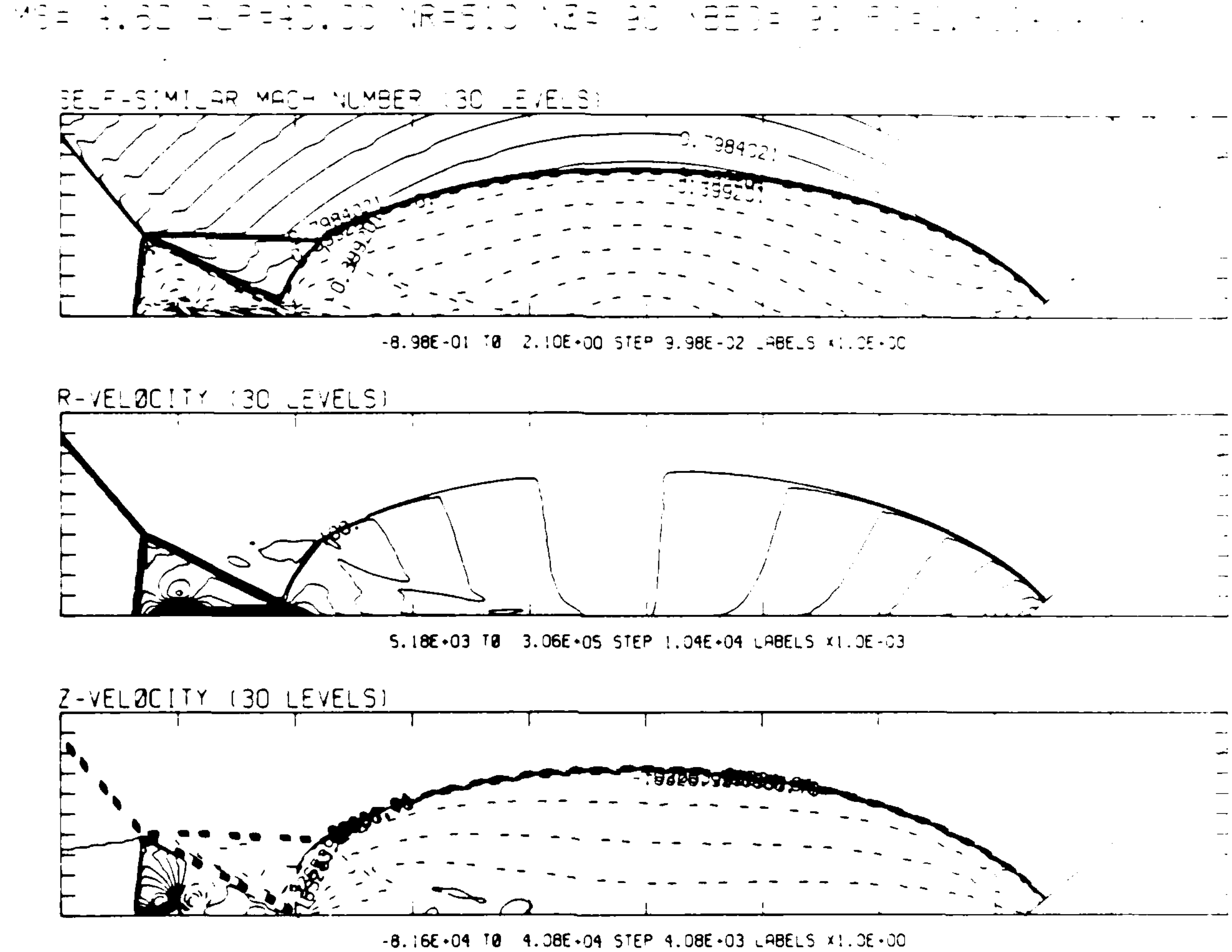

Figure $14d_H$. Whole-flowfield contour-plots; Hansen - continued.

Figure 14. Case 11, M_s = 4.62, θ_w = 40°, Air, γ = 1.4 and Hansen EOS, DMR - continued.

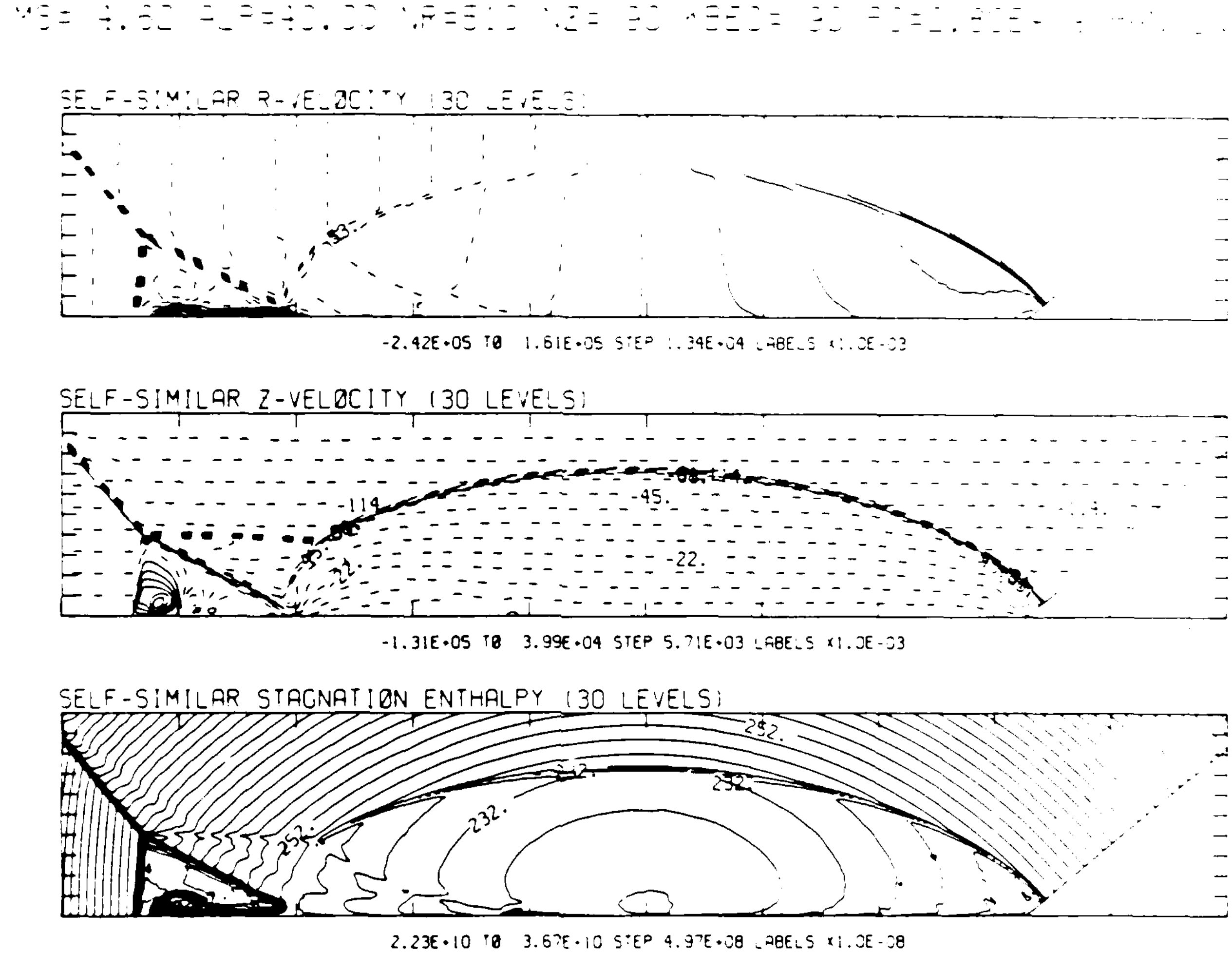

Figure $14d_H$. Whole-flowfield contour-plots; Hansen - continued.

Figure 14. Case 11, M_s = 4.62, θ_w = 40°, Air, γ = 1.4 and Hansen EOS, DMR - continued.

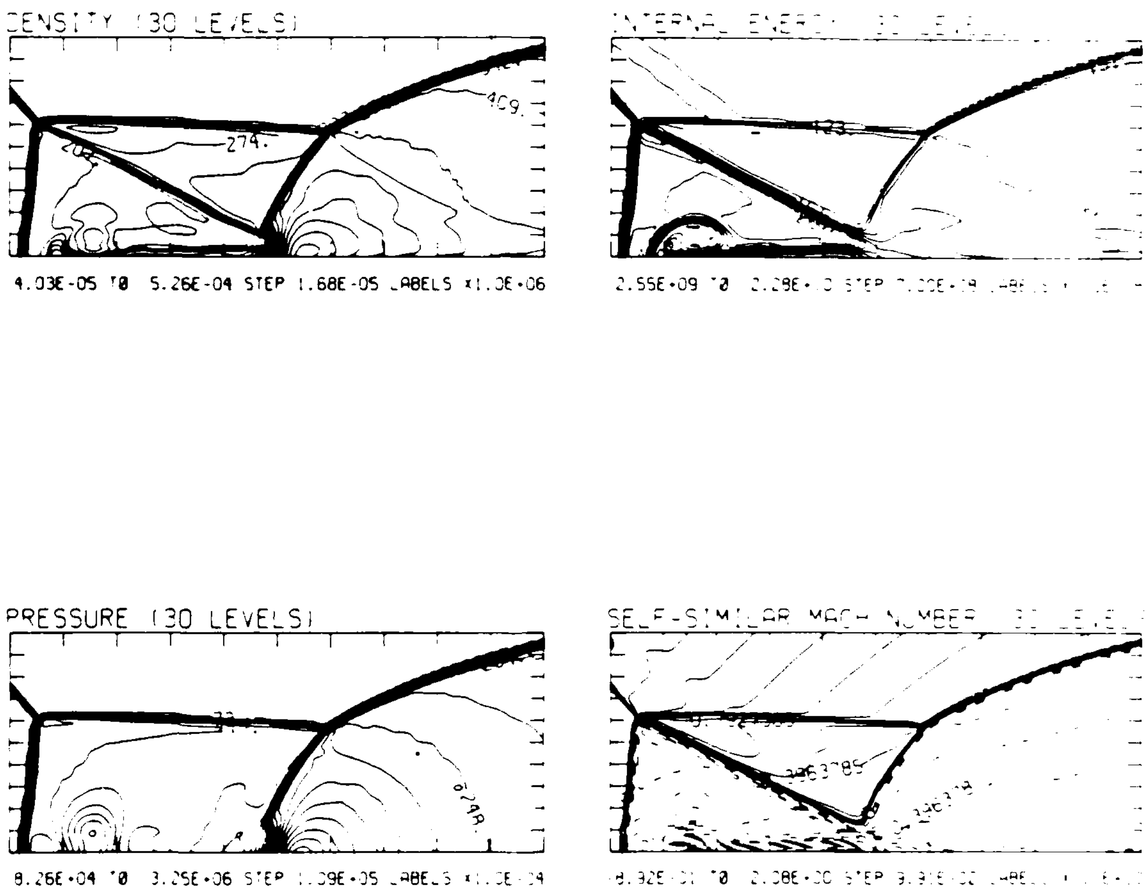

Figure 14e$_H$. Blowup-frame plots; Hansen.

Figure 14. Case 11, M_S = 4.62, θ_w = 40°, Air, γ = 1.4 and Hansen EOS, DMR - continued.

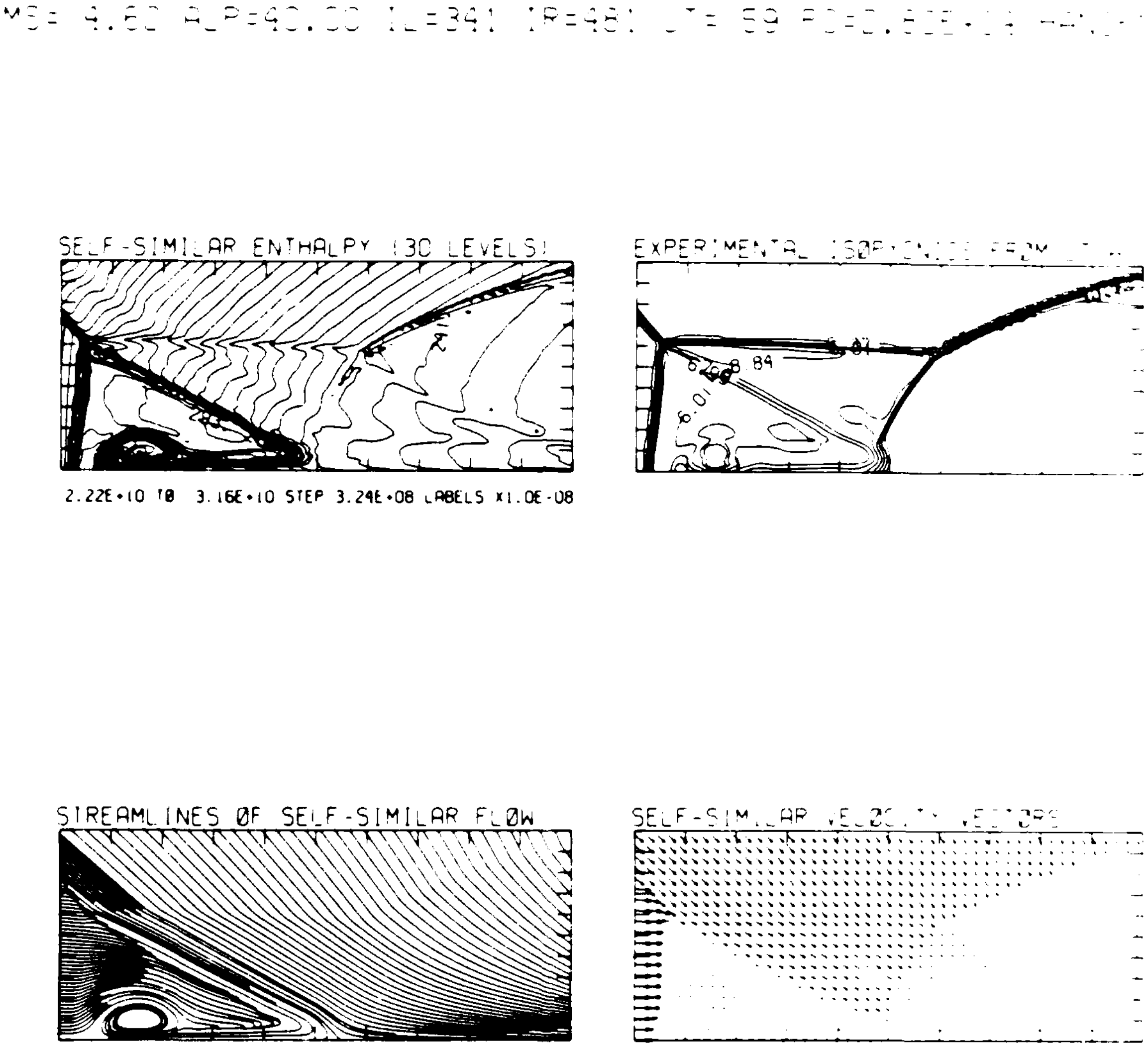

Figure $14e_H$. Blowup-frame plots; Hansen - continued.

Figure 14. Case 11, $M_s = 4.62$, $\theta_w = 40°$, Air, $\gamma = 1.4$ and Hansen EOS, DMR - continued.

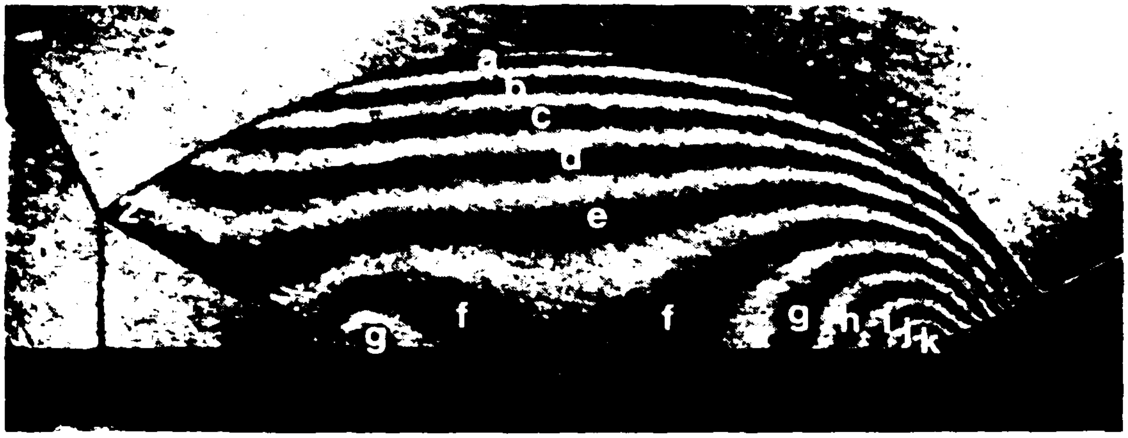
a
b
c
d
e
f
f
g
g
h
i
j
k

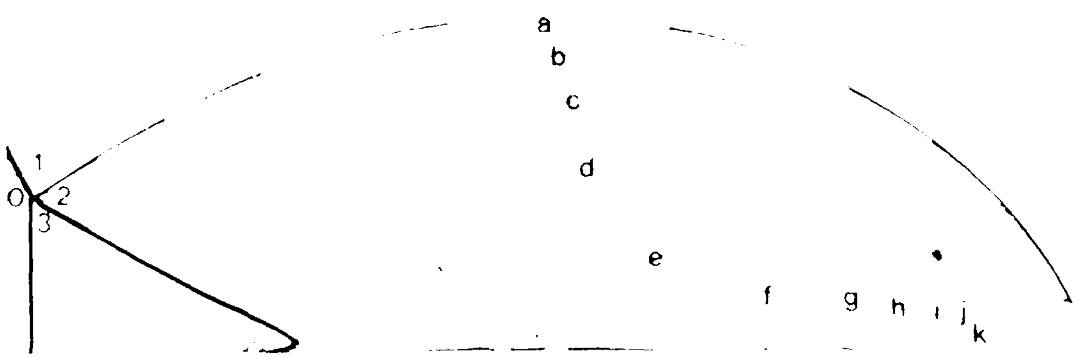
a
b
c
d
1
O
2
3
e
f
g
h
i
j
k

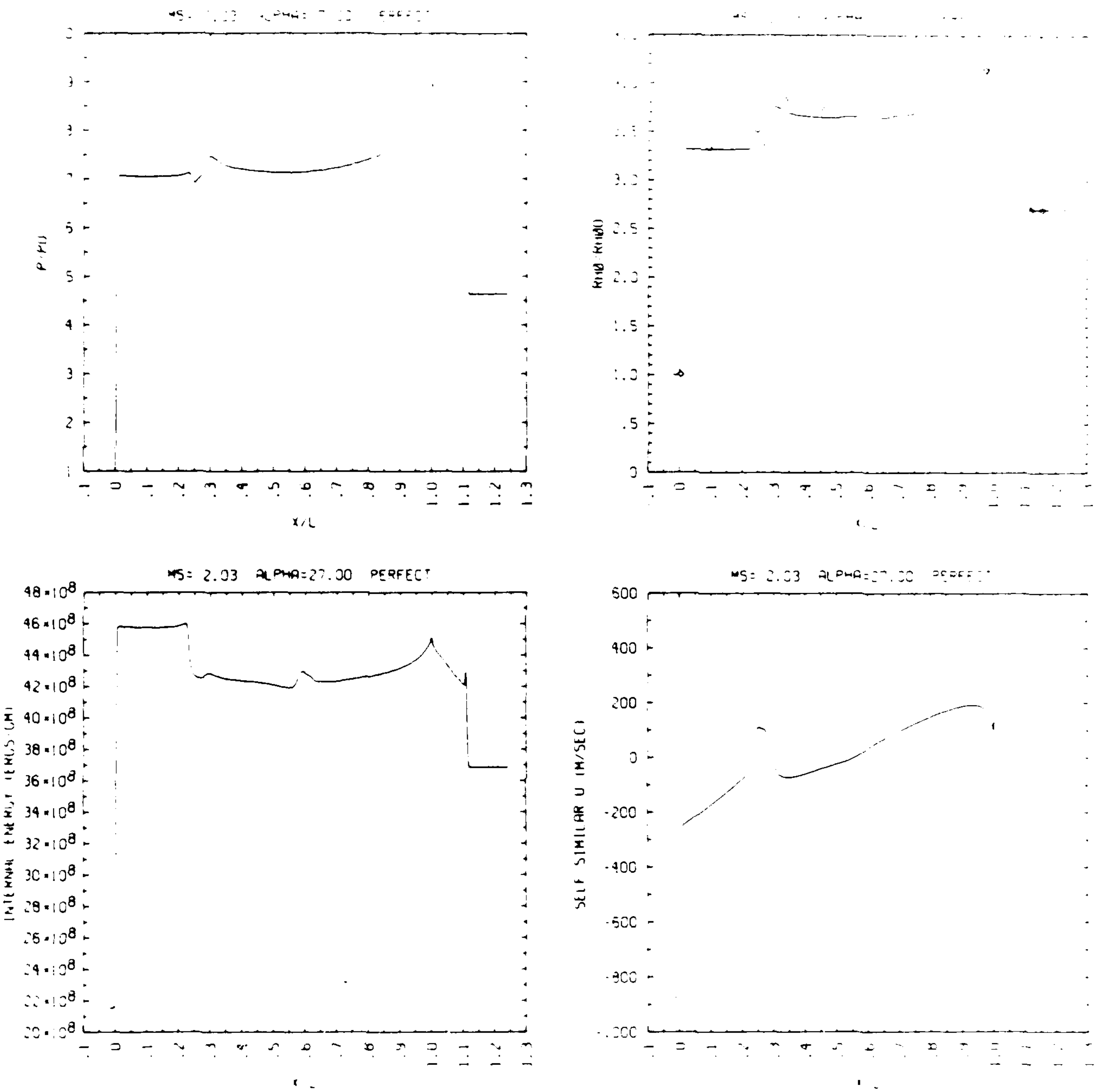

Figure 15c. Wall plots for p/p_0, ρ/ρ_0 with experimental data included, e, $\bar{u}$.

Figure 15. Case 12, M_s = 2.03, θ_w = 27°, Air, γ = 1.4, SMR - continued.

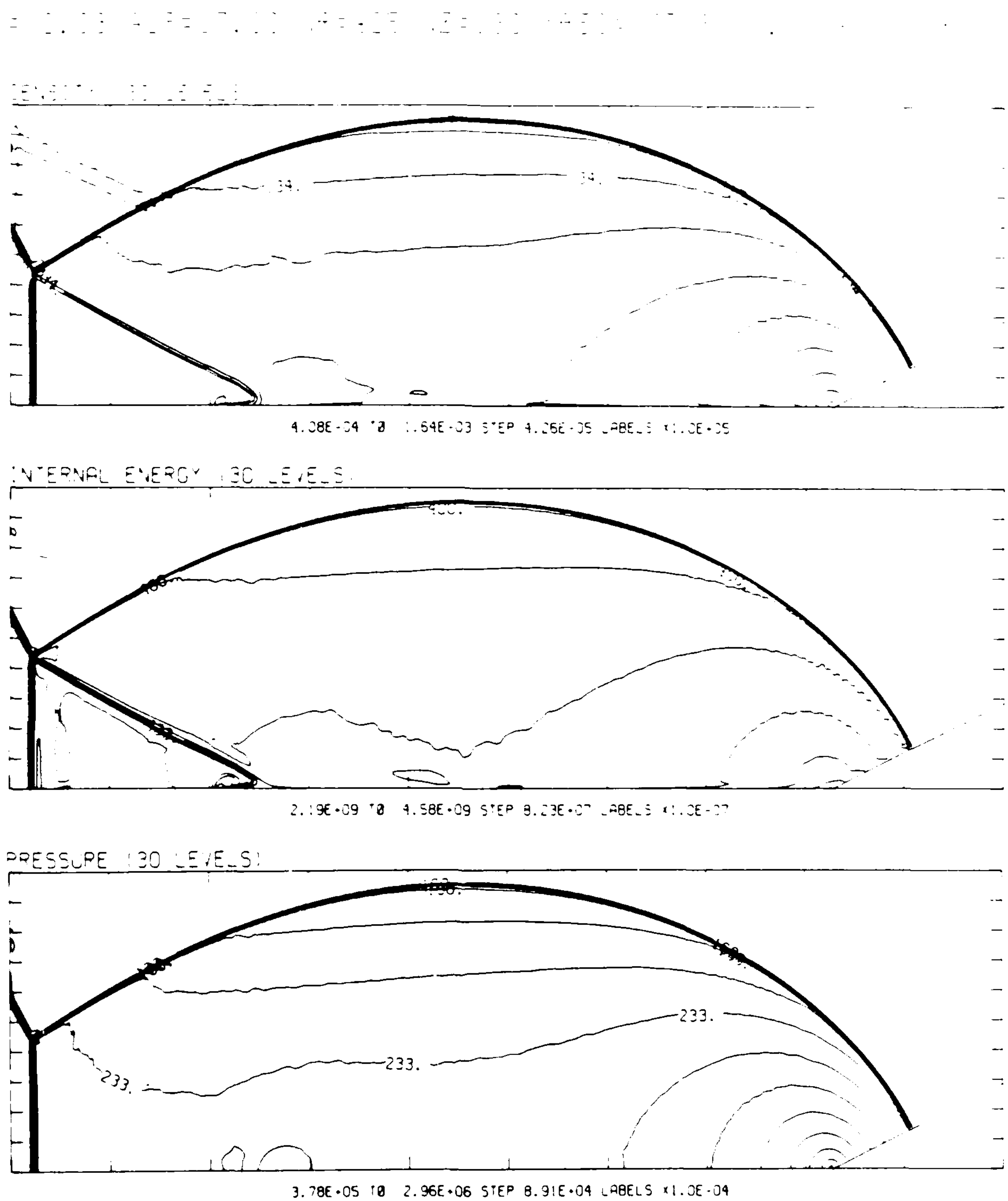

Figure 15d. Whole-flowfield contour-plots.

Figure 15. Case 12, M_s = 2.03, θ_w = 27°, Air, γ = 1.4, SMR - continued.

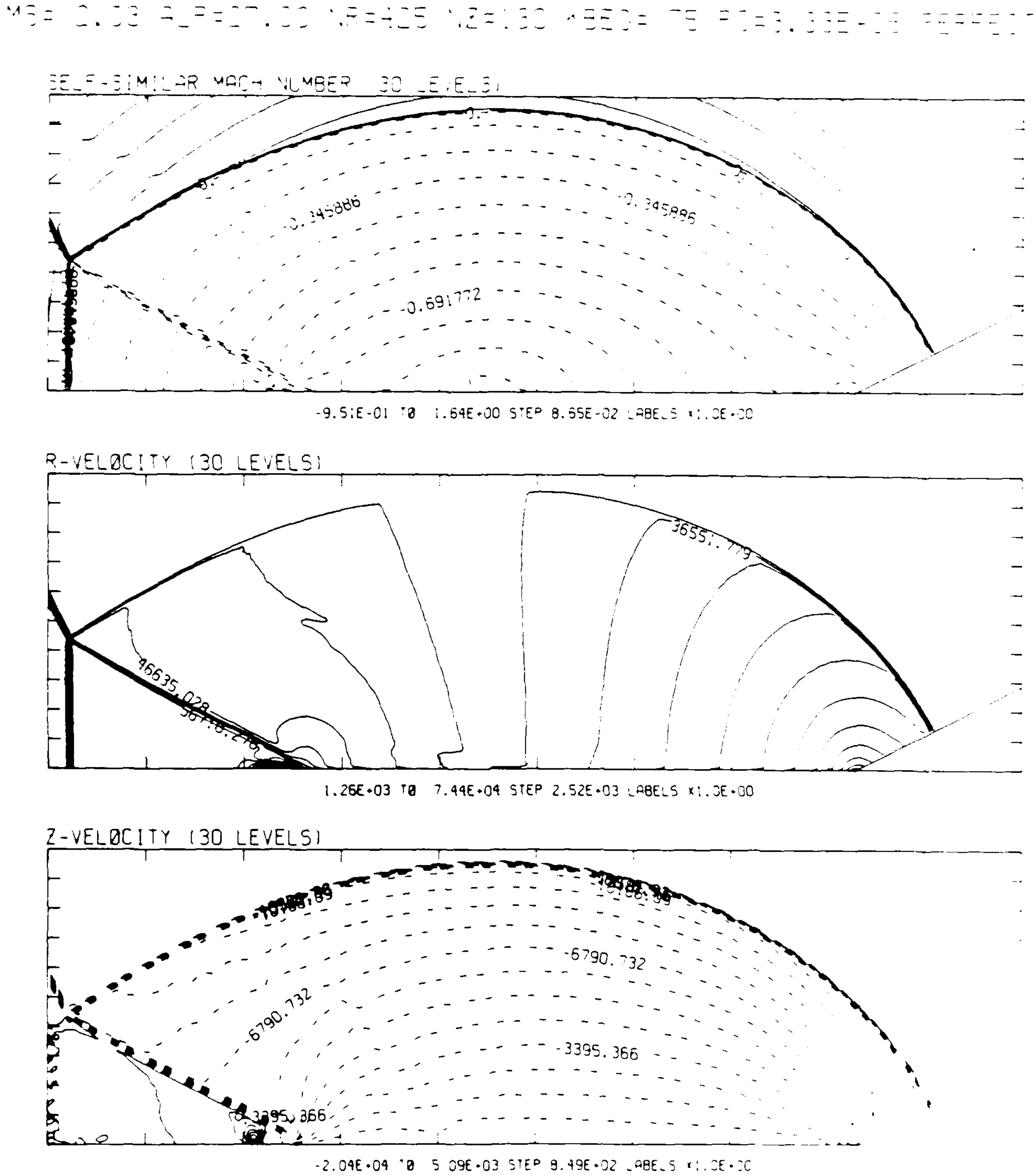

Figure 15d. Whole-flowfield contour-plots - continued.

Figure 15. Case 12, M_s = 2.03, θ_w = 27°, Air, γ = 1.4, [illegible]

AD-A186 440 A DETAILED NUMERICAL GRAPHICAL AND EXPERIMENTAL STUDY 3/5
OF OBLIQUE SHOCK WA (U) TORONTO UNIV DOWNSVIEW
(ONTRRIO) INST FOR AEROSPACE STUDIES H M GLAZ ET AL
UNCLASSIFIED 01 AUG 86 UTIAS-285 DNA-TR-86-365 F/G 20/4 NL

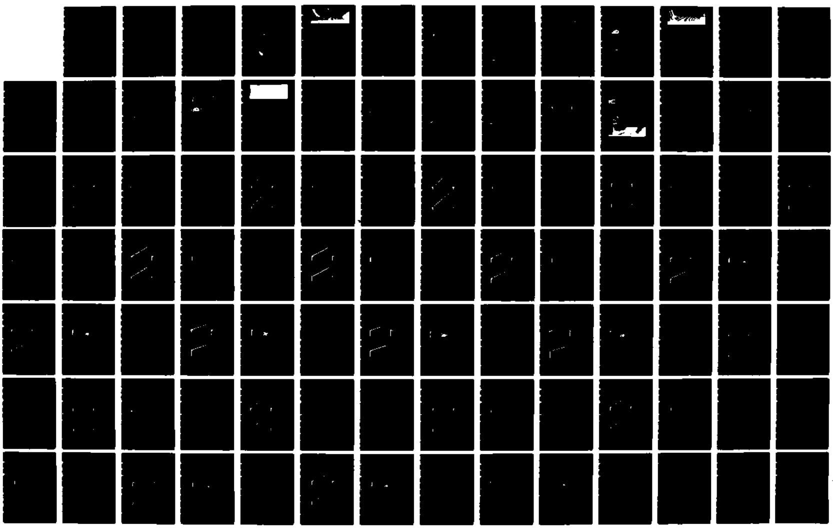

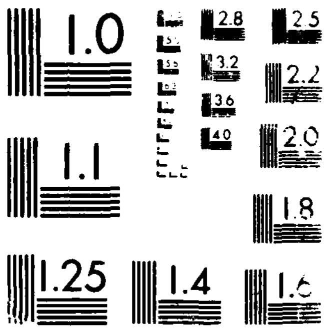

MICROCOPY RESOLUTION TEST CHART
NATIONAL BUREAU OF STANDARDS 1963-A

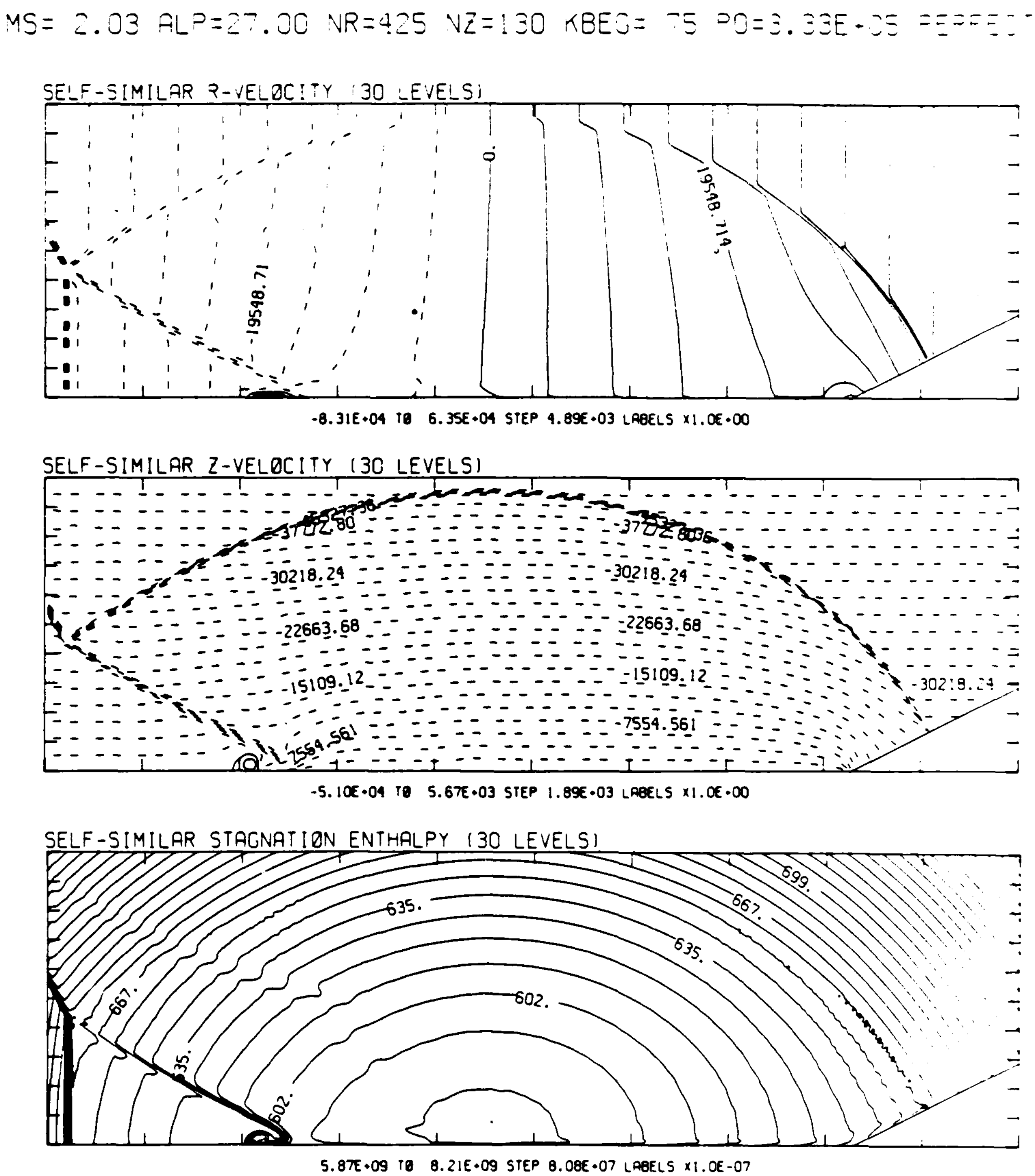

Figure 15d. Whole-flowfield contour-plots - continued.

Figure 15. Case 12, M_s = 2.03, θ_w = 27°, Air, γ = 1.4, SMR - continued.

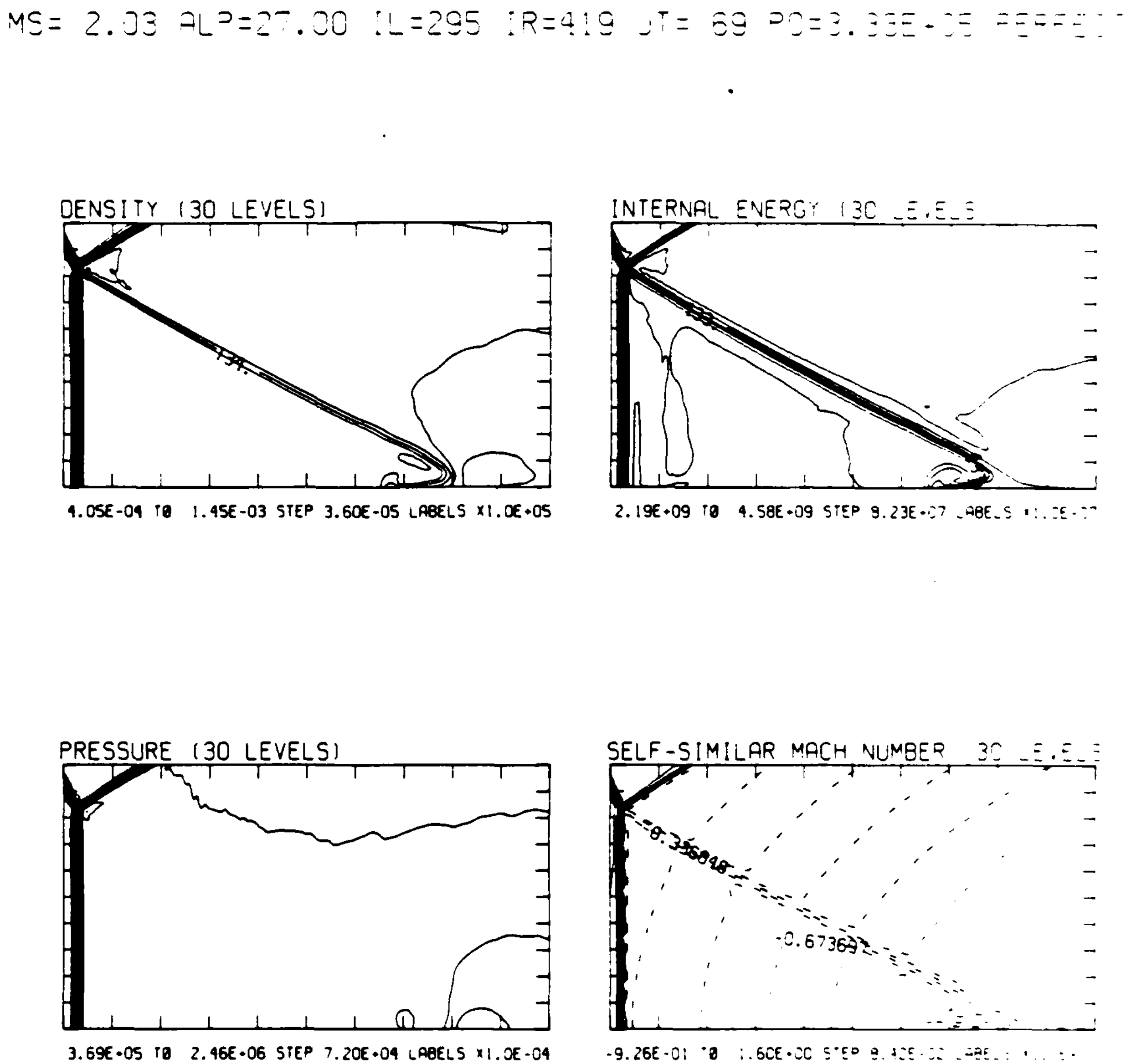

Figure 15e. Blowup-frame plots.

Figure 15. Case 12, M_s = 2.03, θ_w = 27°, Air, γ = 1.4, SMR.

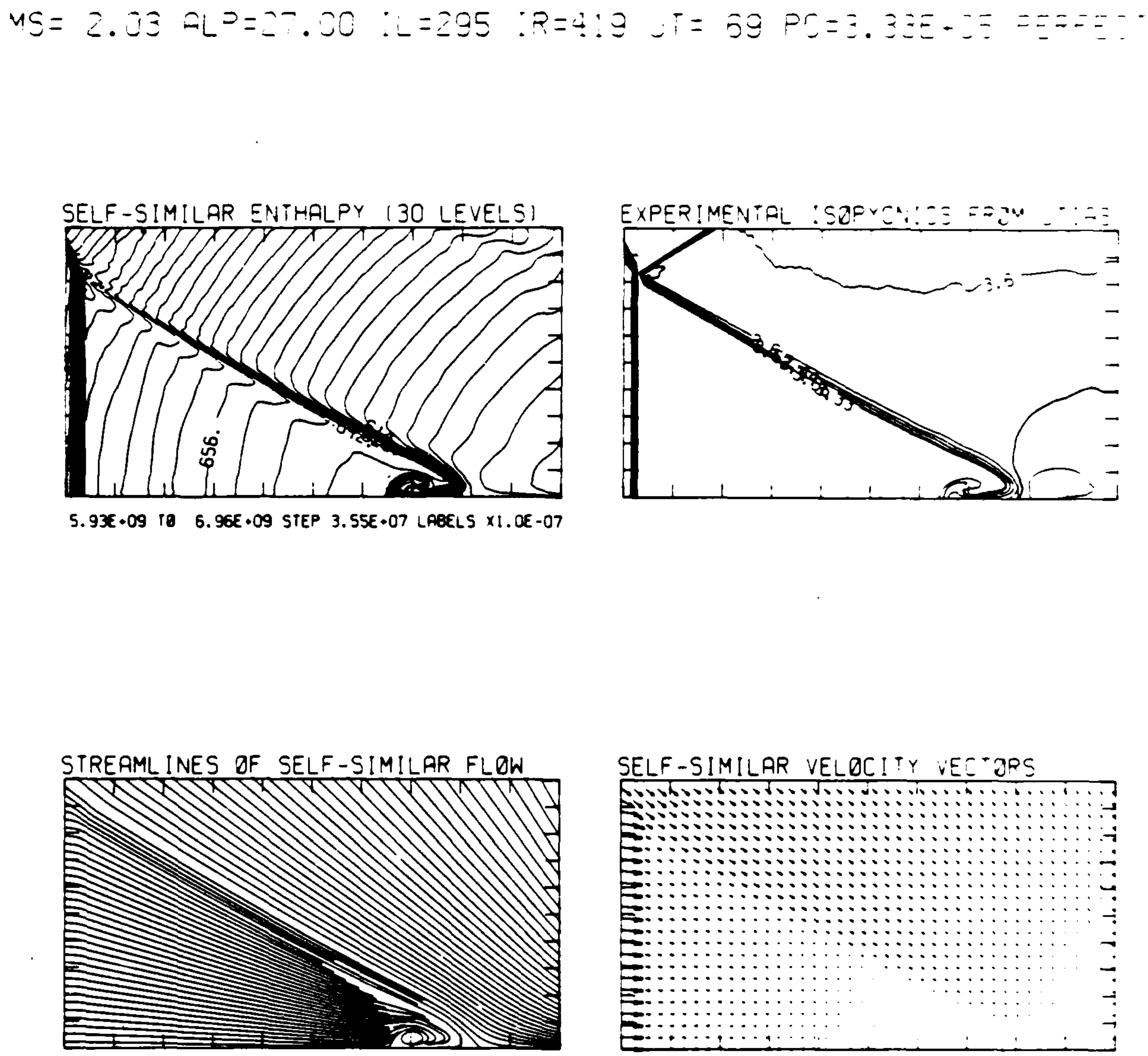

Figure 15e. Blowup-frame plots - continued.

Figure 15. Case 12, $M_s = 2.03$, $\theta_w = 27°$, Air, $\gamma = 1.4$, SMR.

Region	ρ/ρ_0	Region	ρ/ρ_0
0	1.00	g	13.32
1	5.63	h	13.95
1'	6.89	i	14.58
2	7.44	j	15.21
3	5.74	k	15.84
a	9.53	l	16.47
b	10.16	m	17.10
c	10.79	n	17.73
d	11.42	o	18.36
e	12.05	p	6.37
f	12.68	q	8.07

Figure 16a. Interferogram.

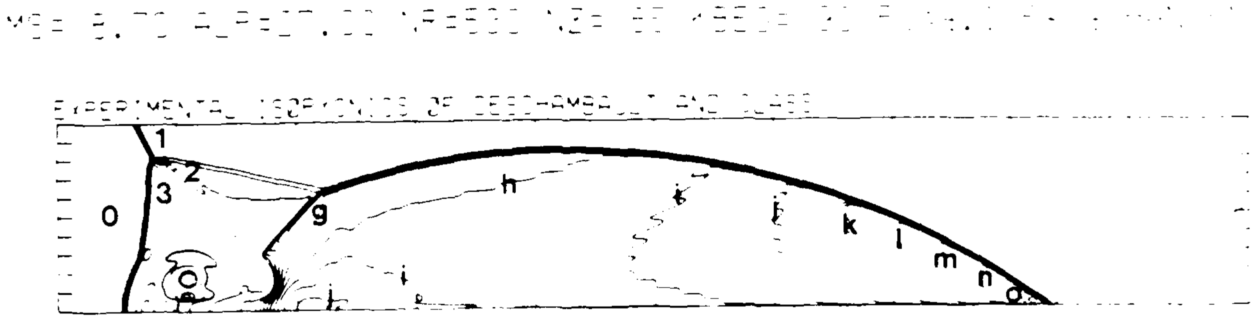

XBB 859-7205

Figure 16b. Calculated isopycnics using the experimental fringes.

Figure 16. Case 13, M_s = 8.70, θ_w = 27°, Air, Hansen, EOS, DMR.

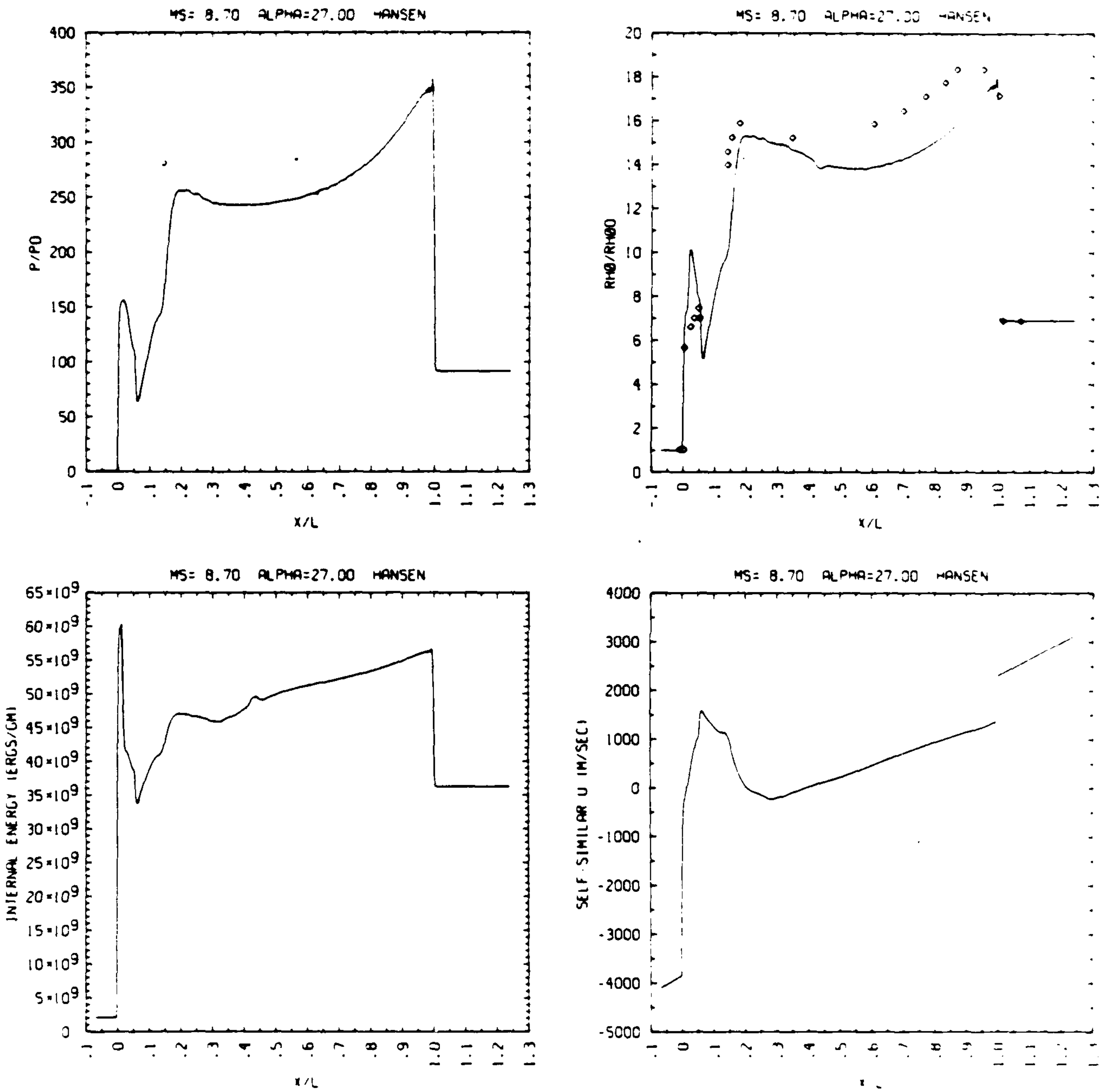

Figure 16c. Wall plots for p/p_0, ρ/ρ_0 with experimental data included, e, $\bar{u}$.

Figure 16. Case 13, M_s = 8.70, θ_w = 27°, Air, Hansen, EOS, DMR - continued.

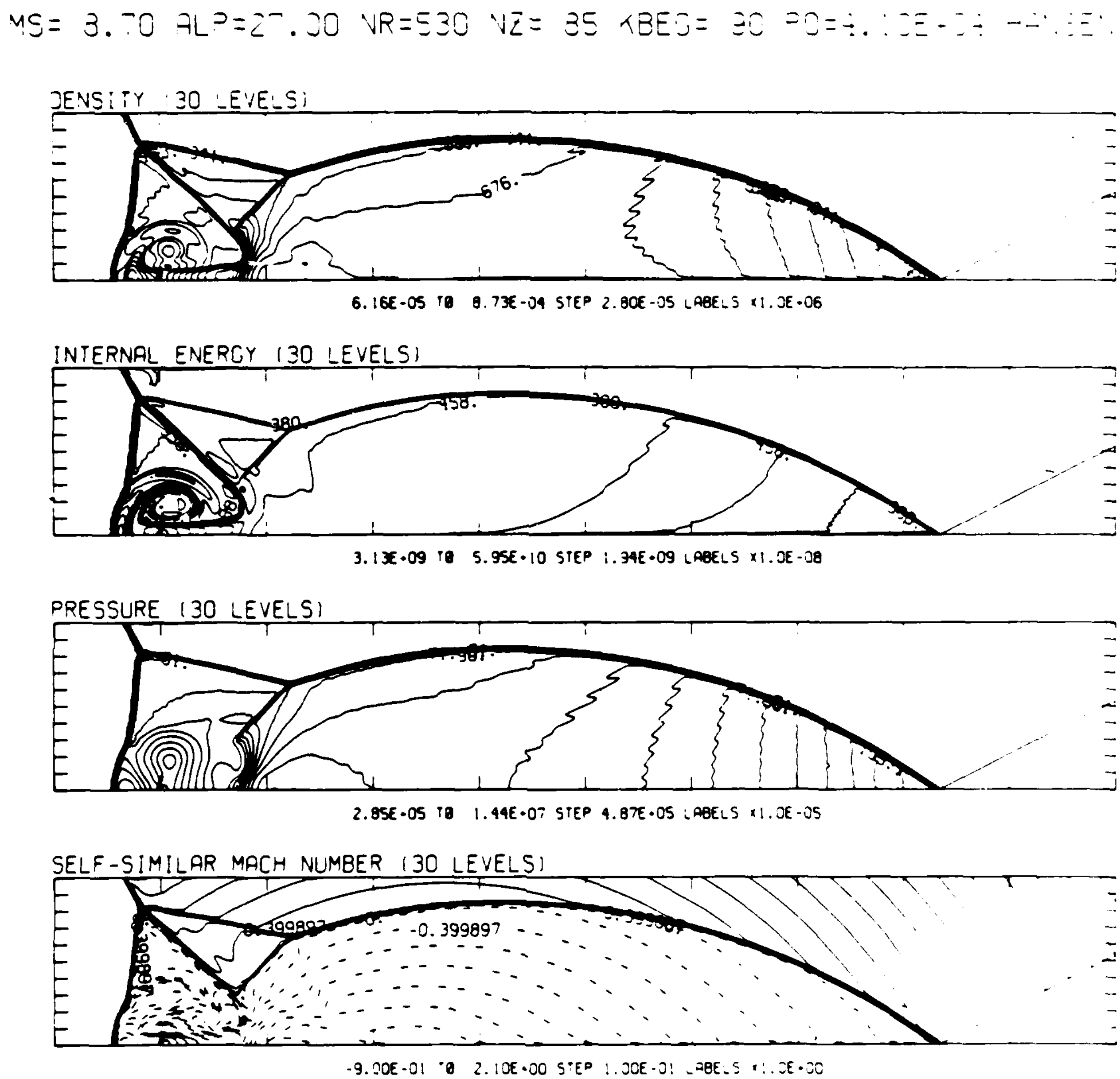

Figure 16d. Whole-flowfield contour-plots.

Figure 16. Case 13, M_S = 8.70, θ_W = 27°, Air, Hansen, EOS, DMR - continued.

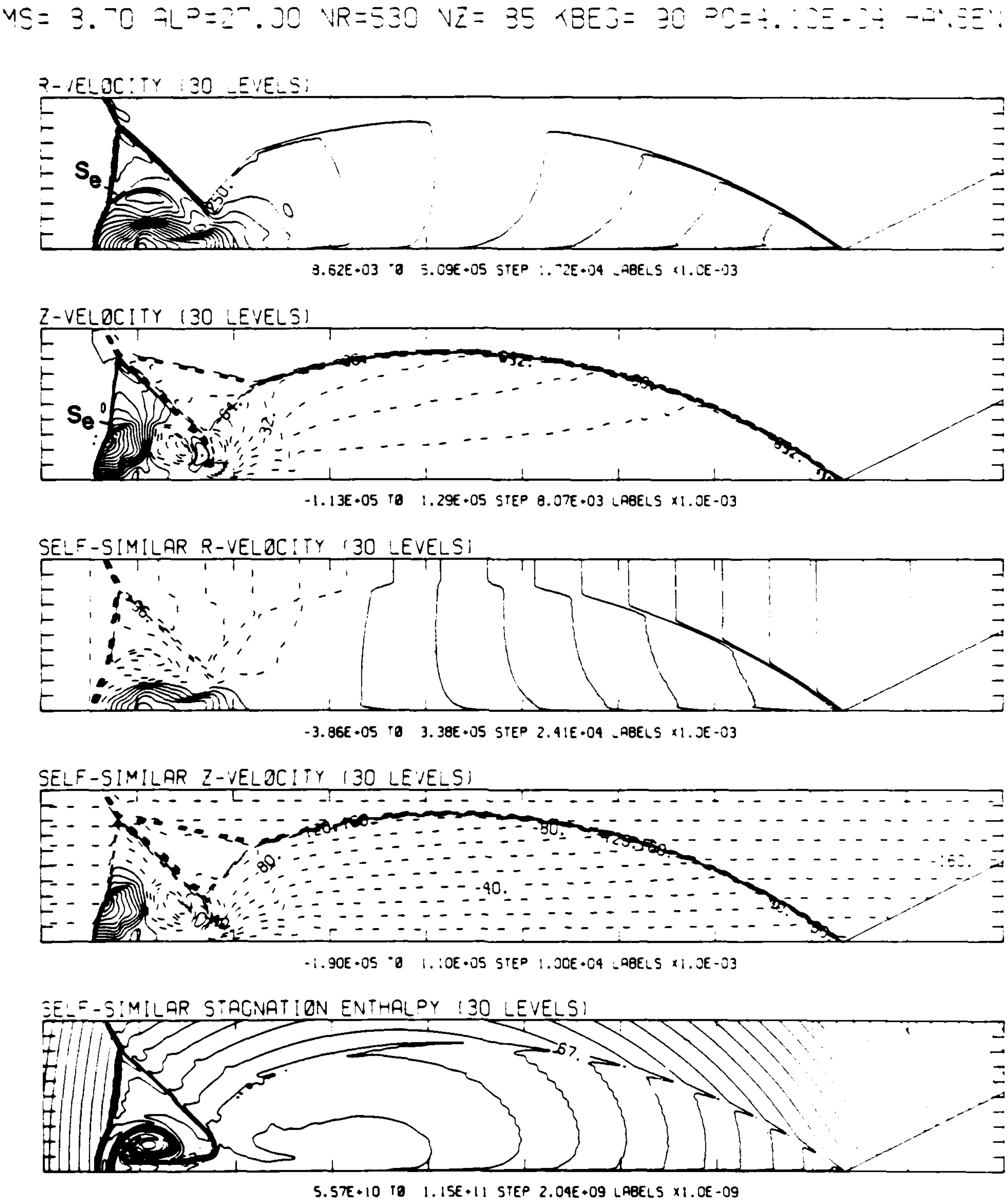

Figure 16d. Whole-flowfield contour-plots - continued.

Figure 16. Case 13, M_s = 8.70, θ_w = 27°, Air, Hansen, EOS, DMR - continued.

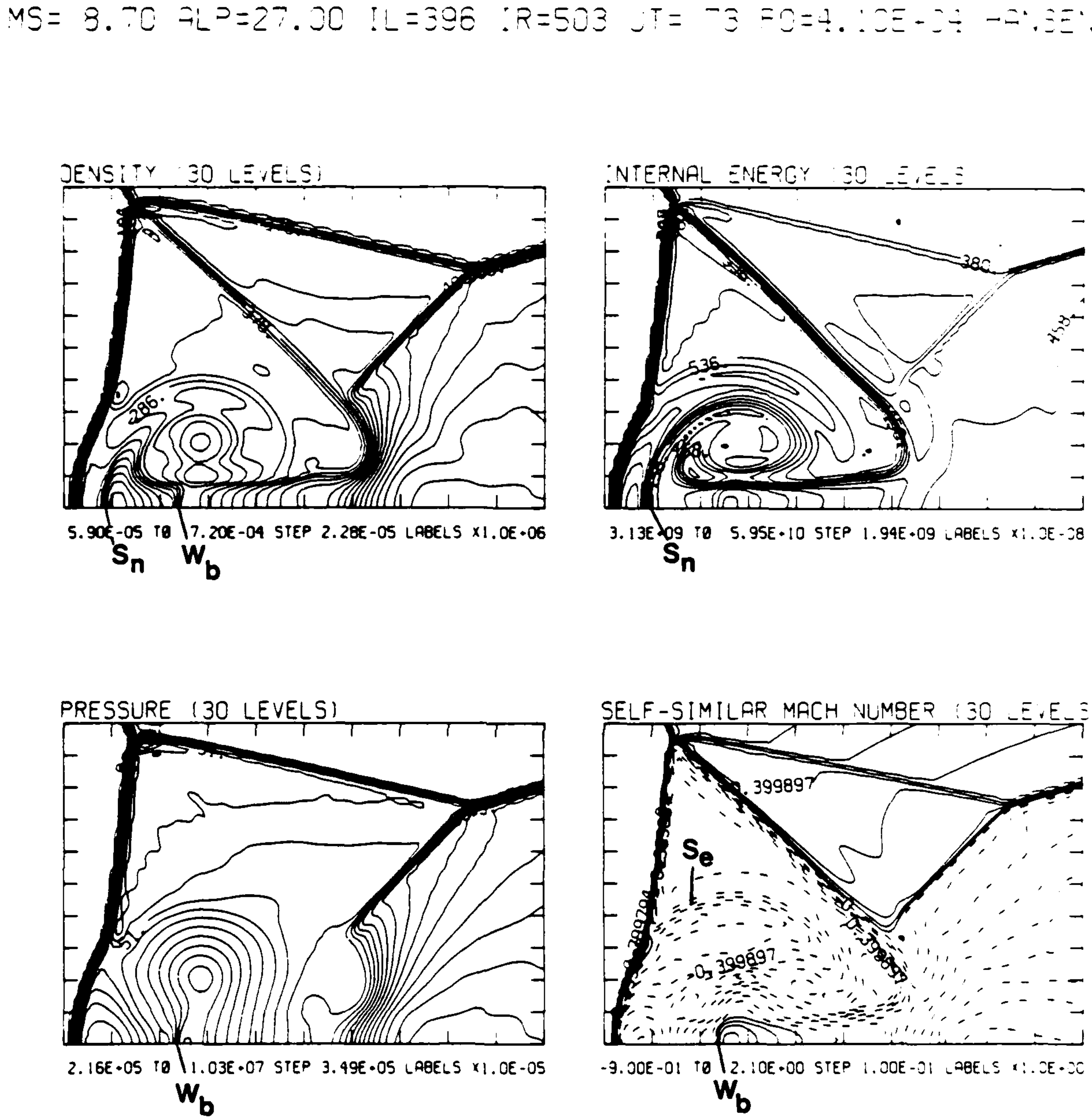

Figure 16e. Blowup-frame plots.

Figure 16. Case 13, M_s = 8.70, θ_w = 27°, Air, Hansen, EOS, DMR - continued.

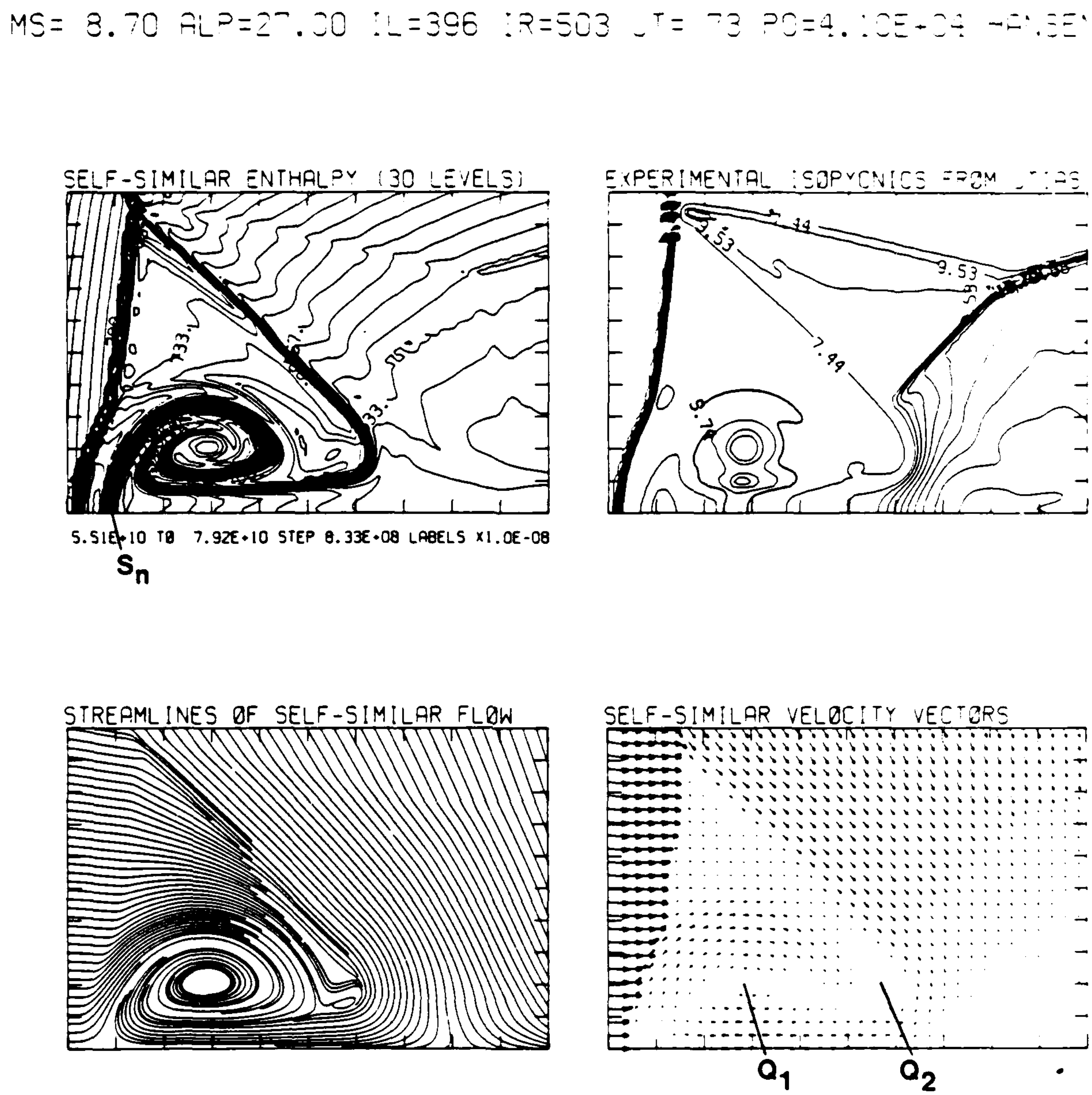

Figure 16e. Blowup-frame plots - continued.

Figure 16. Case 13, M_S = 8.70, θ_W = 27°, Air, Hansen, EOS, DMR - continued.

Region	ρ/ρ_0	Region	ρ/ρ_0
0	1.00	h	9.24
1	5.47	i	9.56
1'	6.13	j	9.88
2	6.65	k	10.21
3	5.59	l	10.53
a	6.97	m	10.85
b	7.30	n	11.18
c	7.62	o	11.50
d	7.94	p	11.82
e	8.27	q	12.15
f	8.59	r	12.47
g	8.91	s	5.91

Figure 17a. Interferogram.

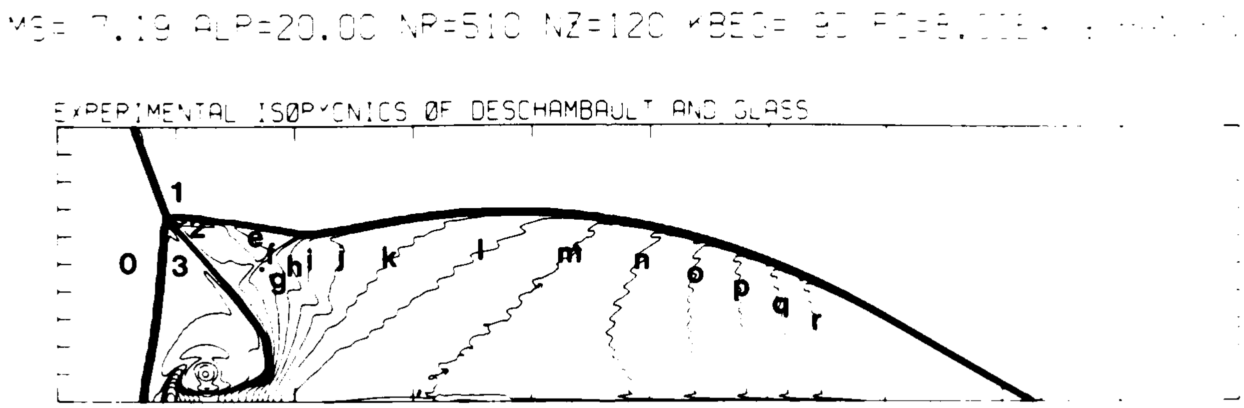

XBB 859-7206

Figure 17b. Calculated isopycnics using the experimental fringes.

Figure 17. Case 14, M_S = 7.19, θ_W = 20°, Air, Hansen EOS, C/DMR.

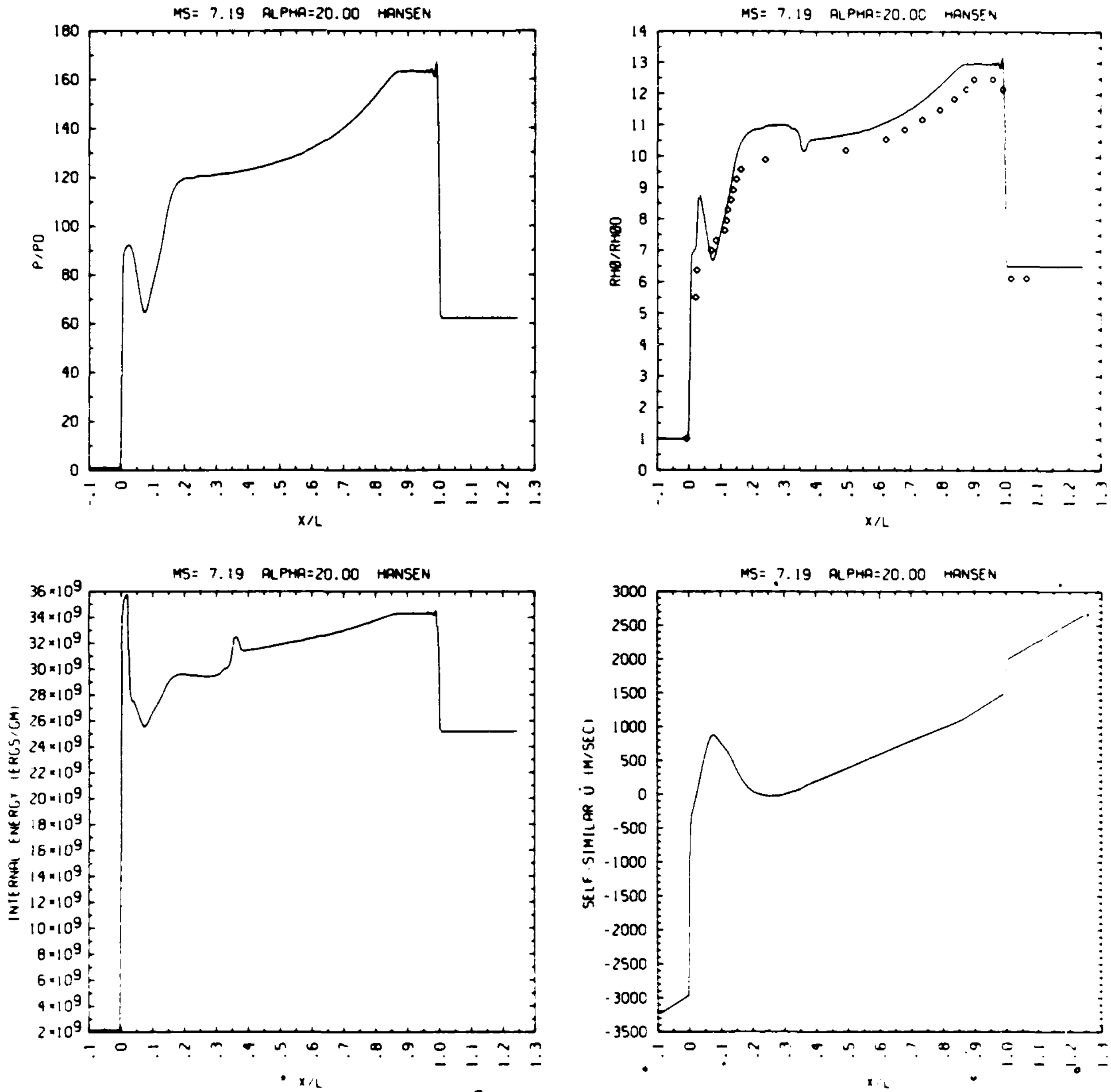

Figure 17c. Wall plots for p/p_0, ρ/ρ_0 with experimental data included, e, $\bar{u}$.

Figure 17. Case 14, M_s = 7.19, θ_w = 20°, Air, Hansen EOS, C/DMR - continued.

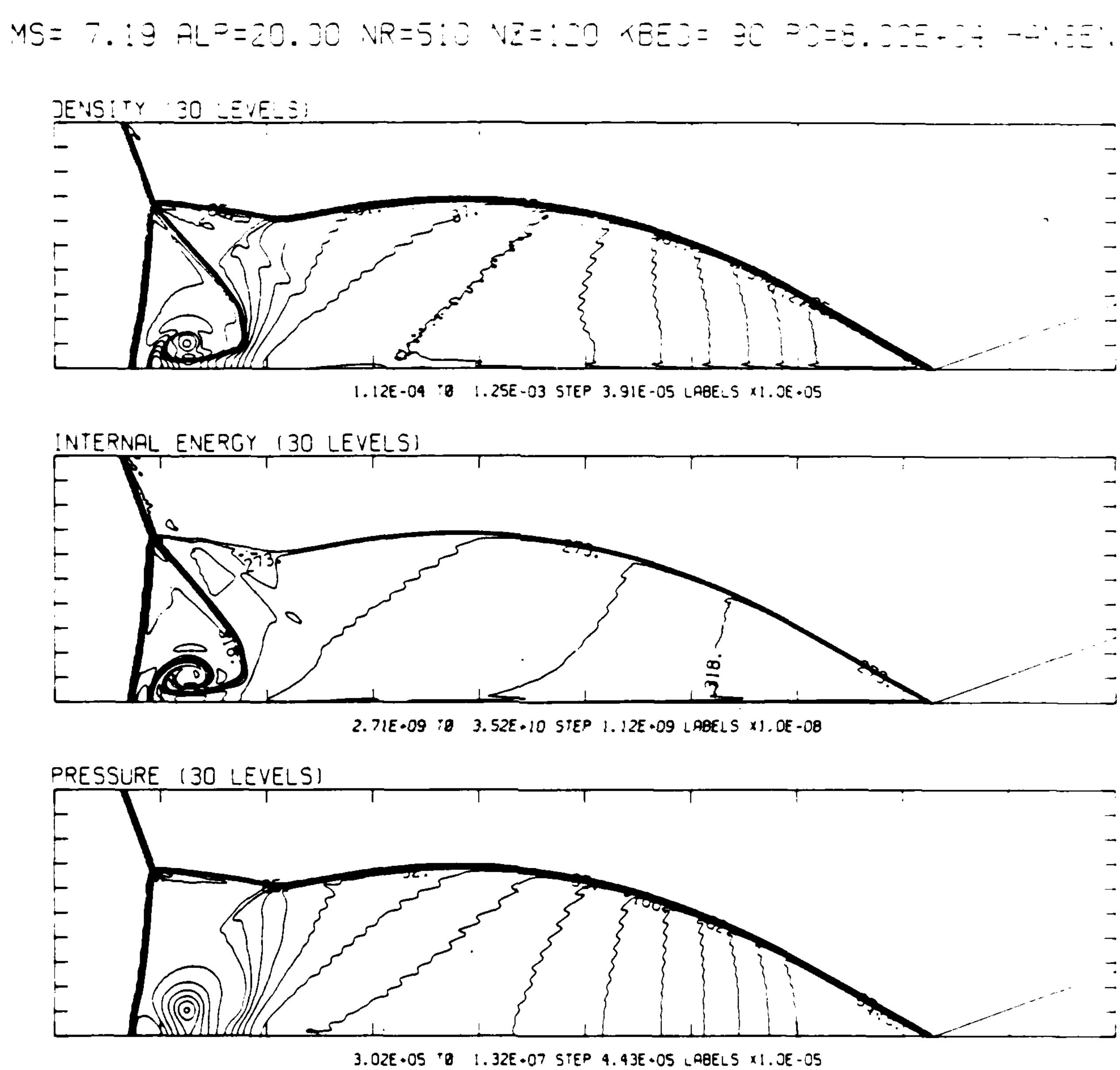

Figure 17d. Whole-flowfield contour-plots.

Figure 17. Case 14, M_s = 7.19, θ_w = 20°, Air, Hansen EOS, C/DMR - continued.

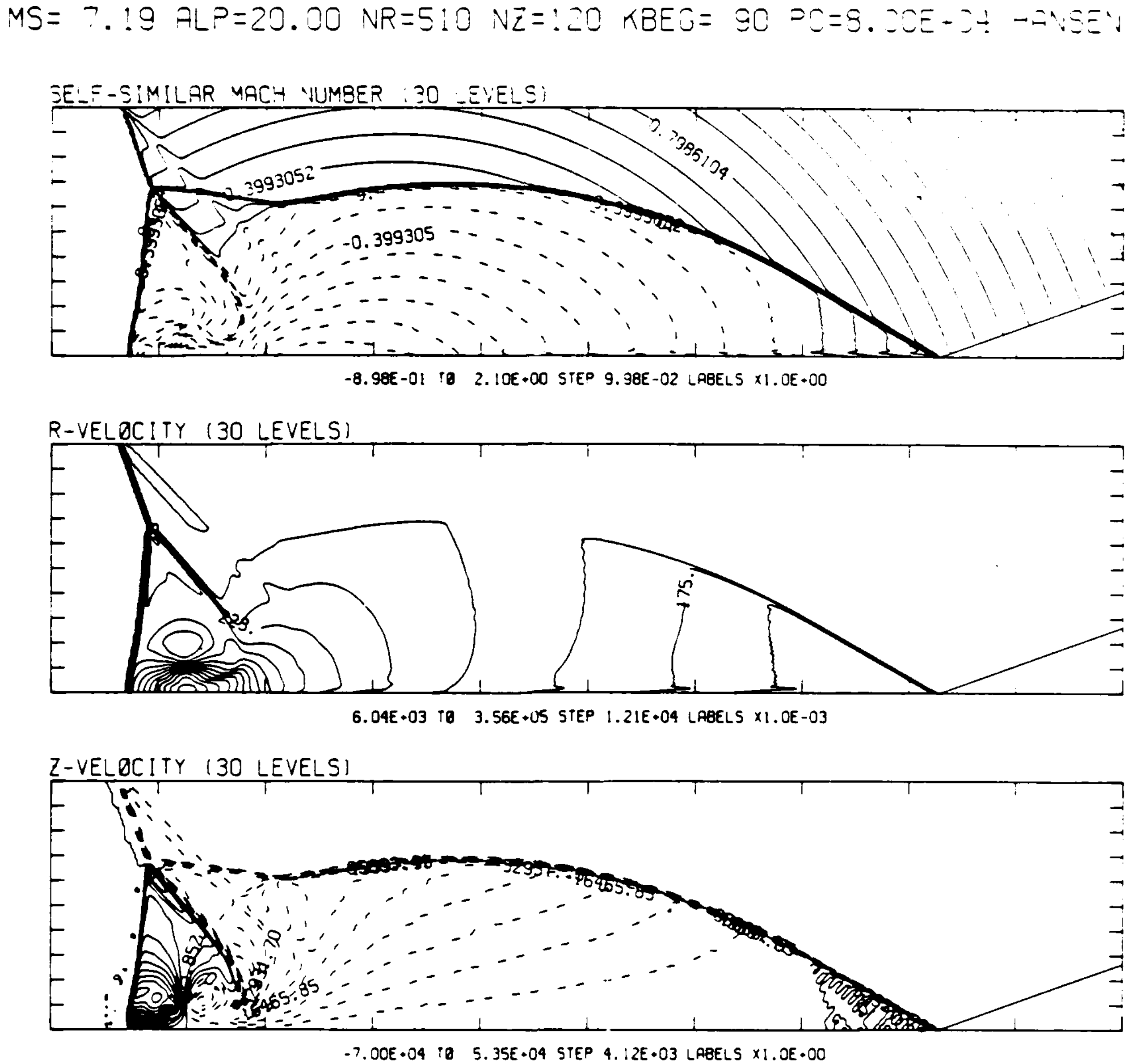

Figure 17d. Whole-flowfield contour-plots - continued.

Figure 17. Case 14, M_s = 7.19, θ_w = 20°, Air, Hansen EOS, C/DMR - continued.

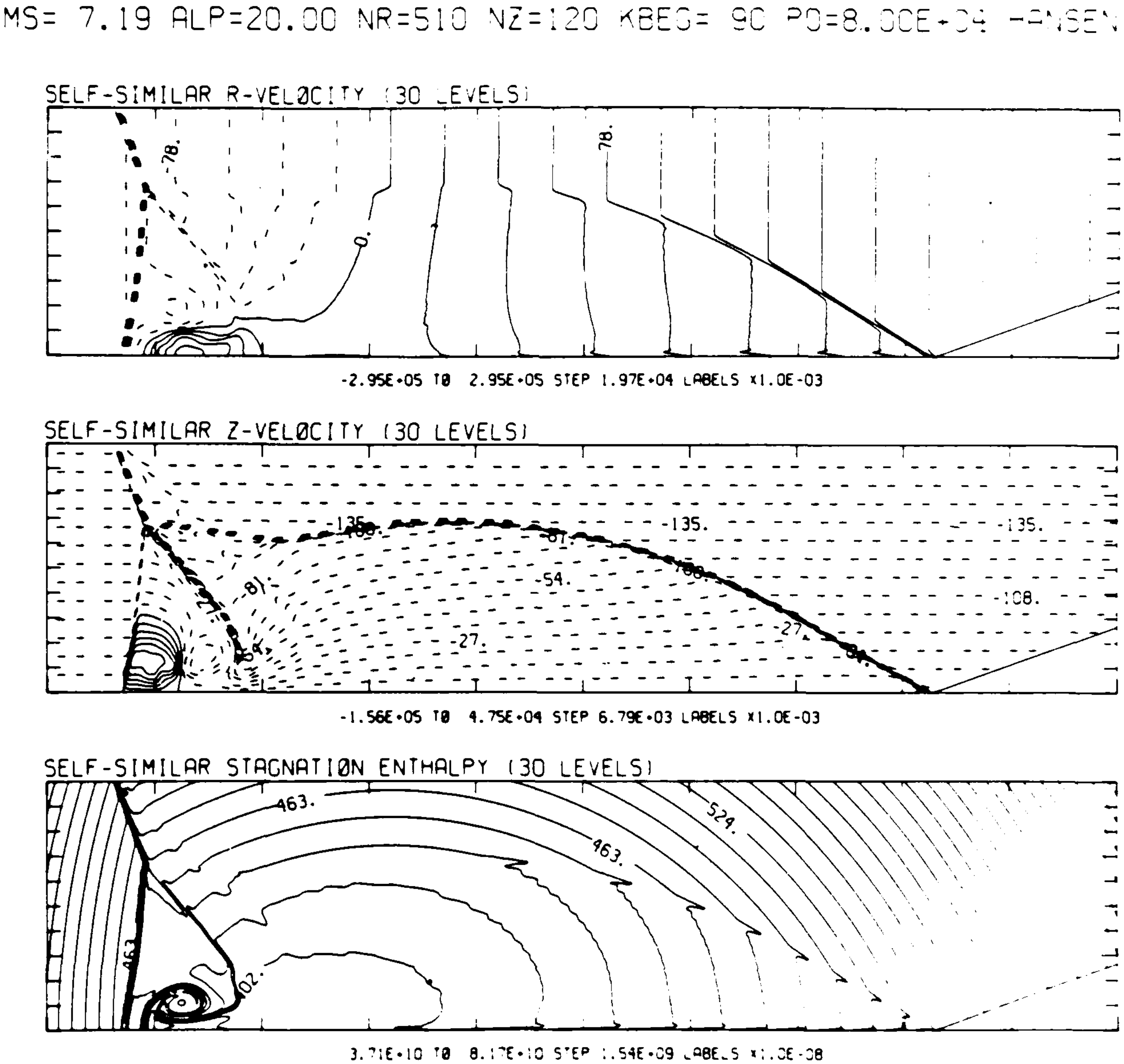

Figure 17d. Whole-flowfield contour-plots - continued.

Figure 17. Case 14, M_s = 7.19, θ_w = 20°, Air, Hansen EOS, C/DMR - continued.

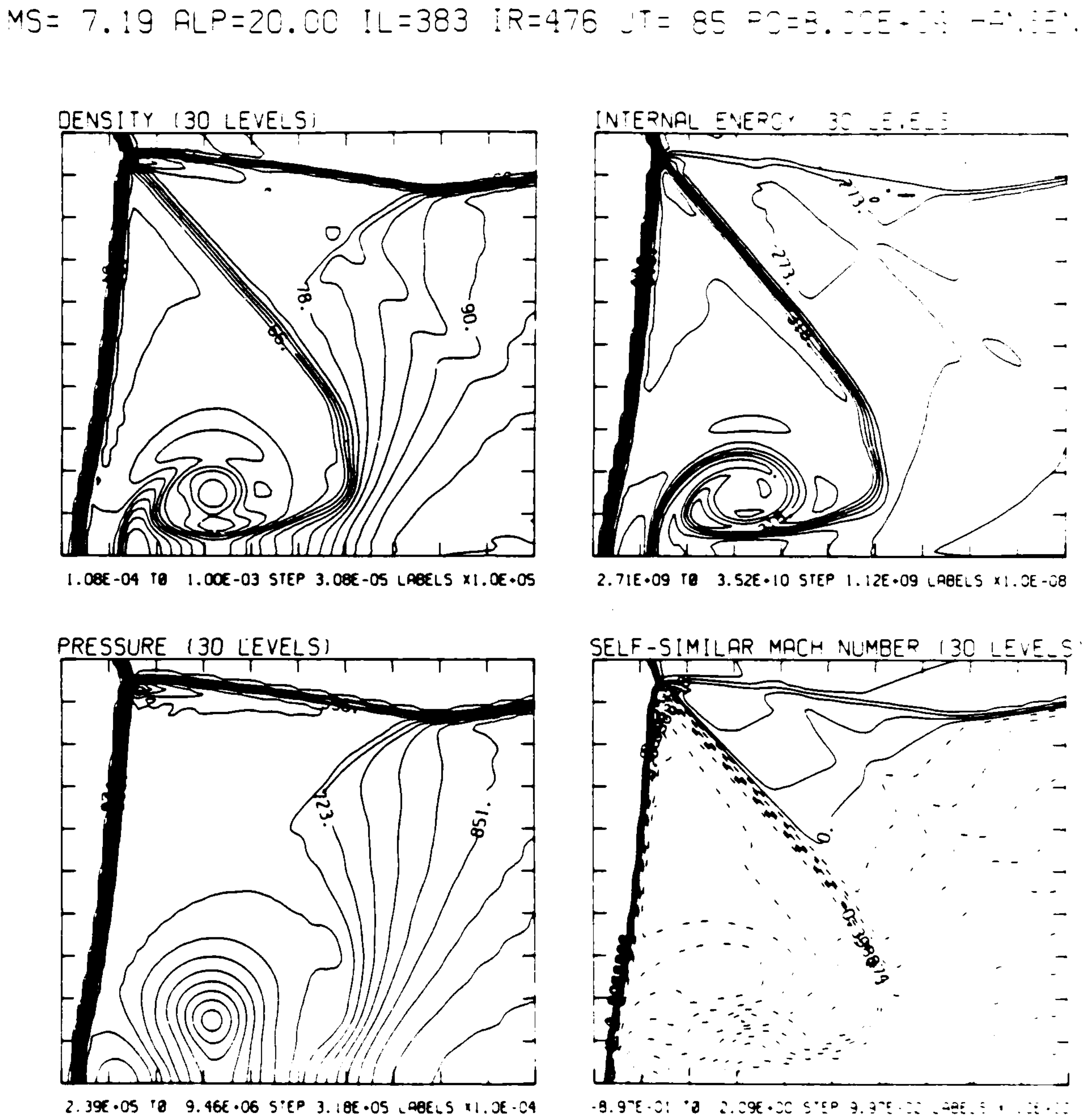

Figure 17e. Blowup-frame plots.

Figure 17. Case 14, M_s = 7.19, θ_w = 20°, Air, Hansen EOS, C/DMR - continued.

MS= 7.19 ALP=20.00 IL=383 IR=476 JT= 85 PO=8.00E+04 HANSEN

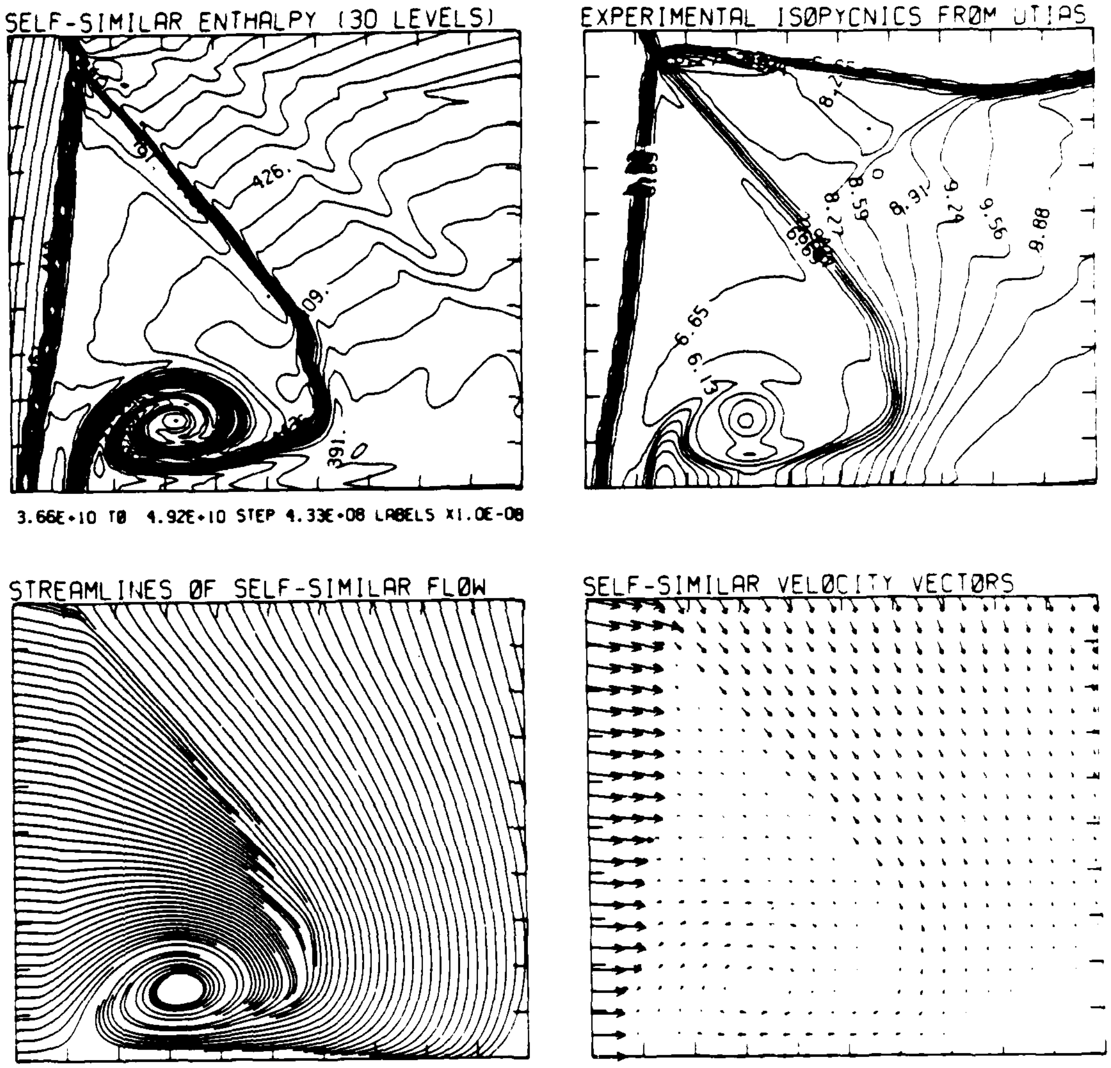

Figure 17e. Blowup-frame plots - continued.

Figure 17. Case 14, M_s = 7.19, θ_w = 20°, Air, Hansen EOS, C/DMR - continued.

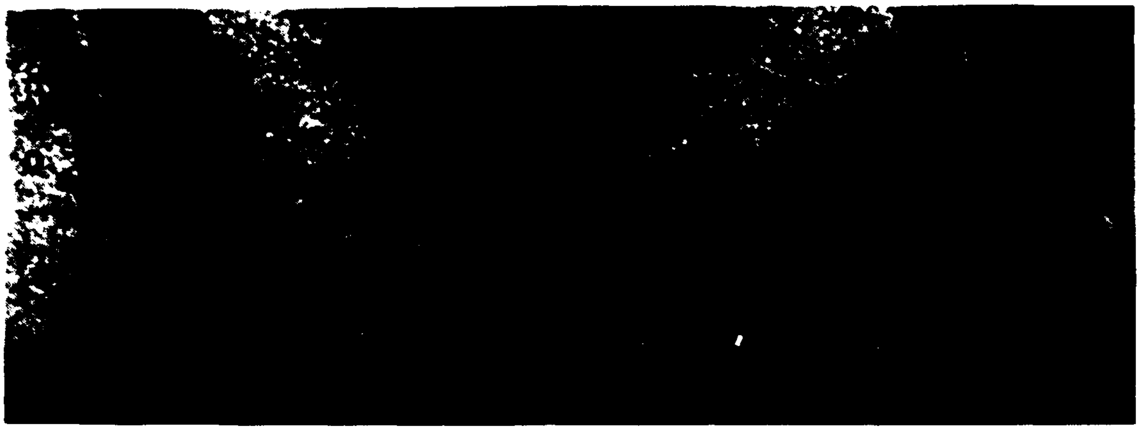

Region	ρ/ρ_0	Region	ρ/ρ_0
0	1.00	f	10.73
1	5.64	g	11.37
1'	6.93	h	12.02
2	6.85	i	12.66
3	5.72	j	13.31
a	7.50	k	13.95
b	8.14	l	14.60
c	8.79	m	15.25
d	9.43	n	15.89
e	10.08	p	6.85

Figure 18a. Interferogram.

MS= 8.86 ALP=20.00 NR=575 NZ=110 KBEG= 75 PO=4.10E+04 HANSEN

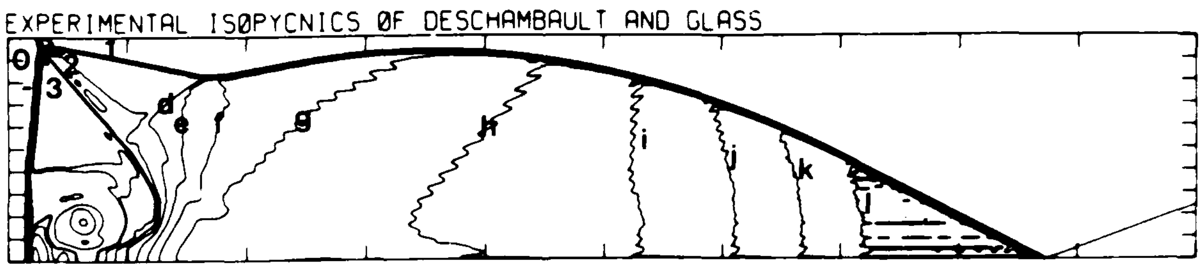

XBB 859-7207

Figure 18b. Calculated isopycnics using the experimental fringes.

Figure 18. Case 15, M_S = 8.86, θ_W = 20°, Air, Hansen EOS, DMR.

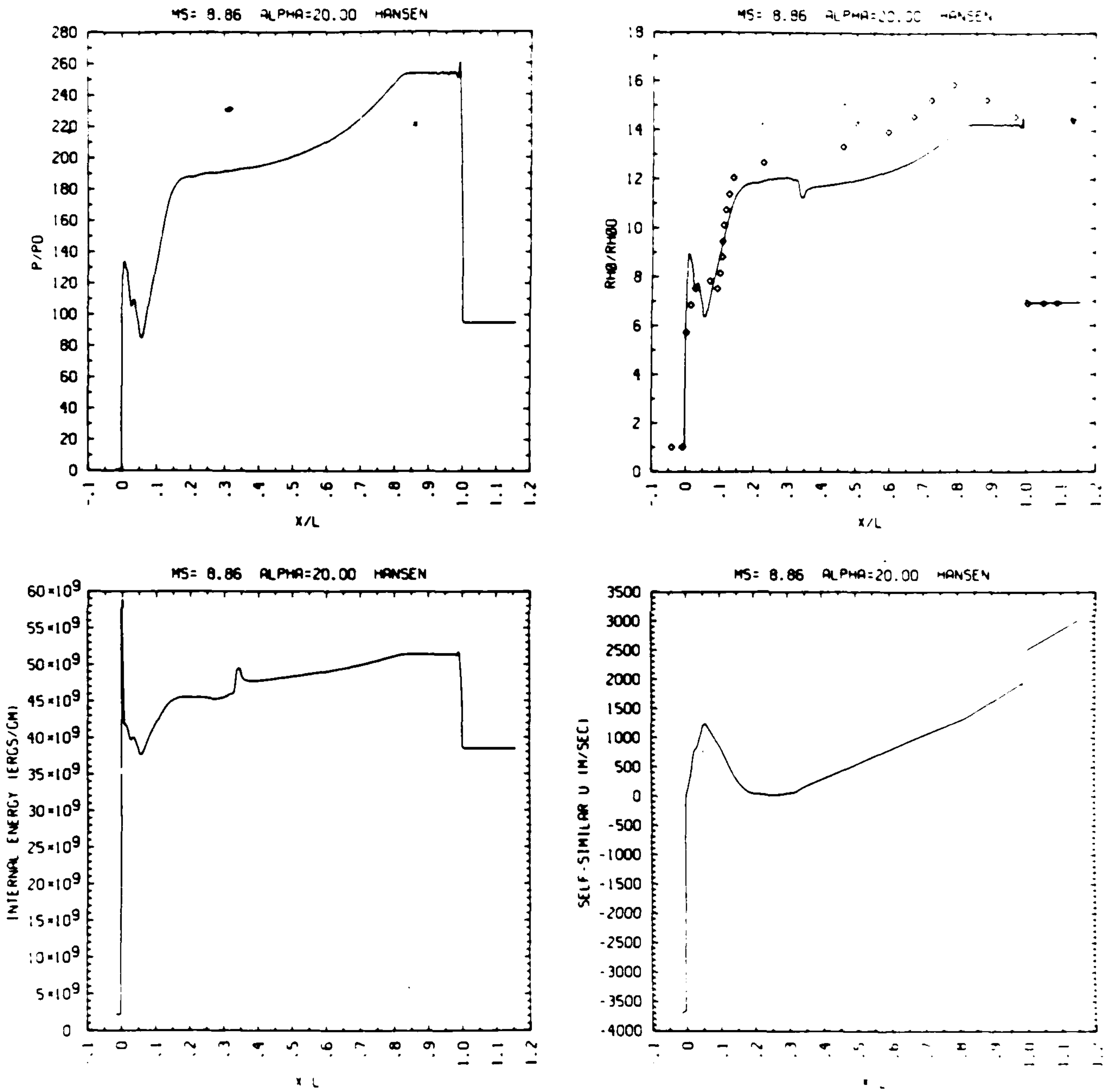

Figure 18c. Wall plots for p/p_0, ρ/ρ_0 with experimental data included, e, $\bar{u}$.

Figure 18. Case 15, $M_s = 8.86$, $\theta_w = 20°$, Air, Hansen EOS, DMR - continued.

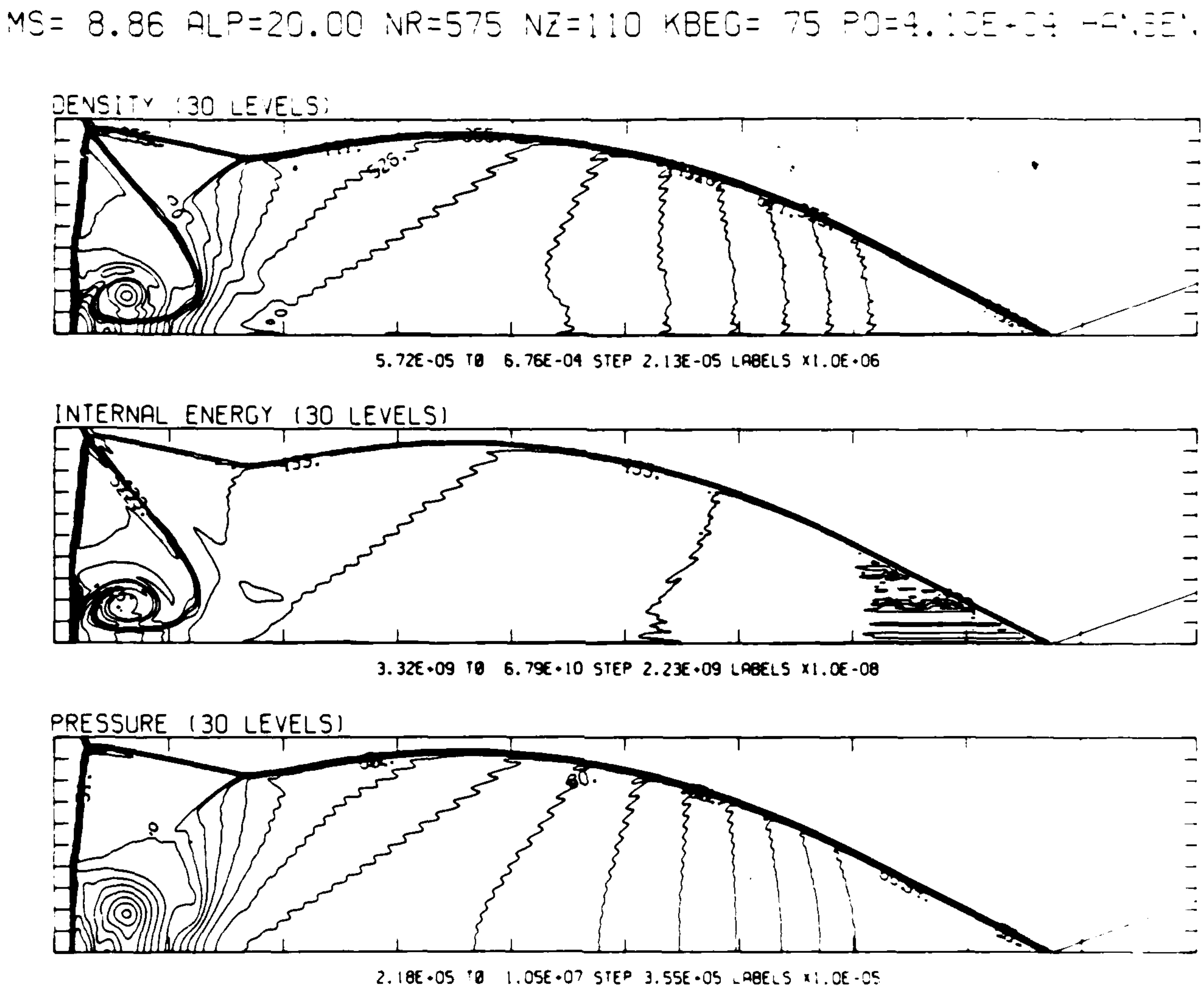

Figure 18d. Whole-flowfield contour-plots.

Figure 18. Case 15, M_s = 8.86, θ_w = 20°, Air, Hansen EOS, DMR - continued.

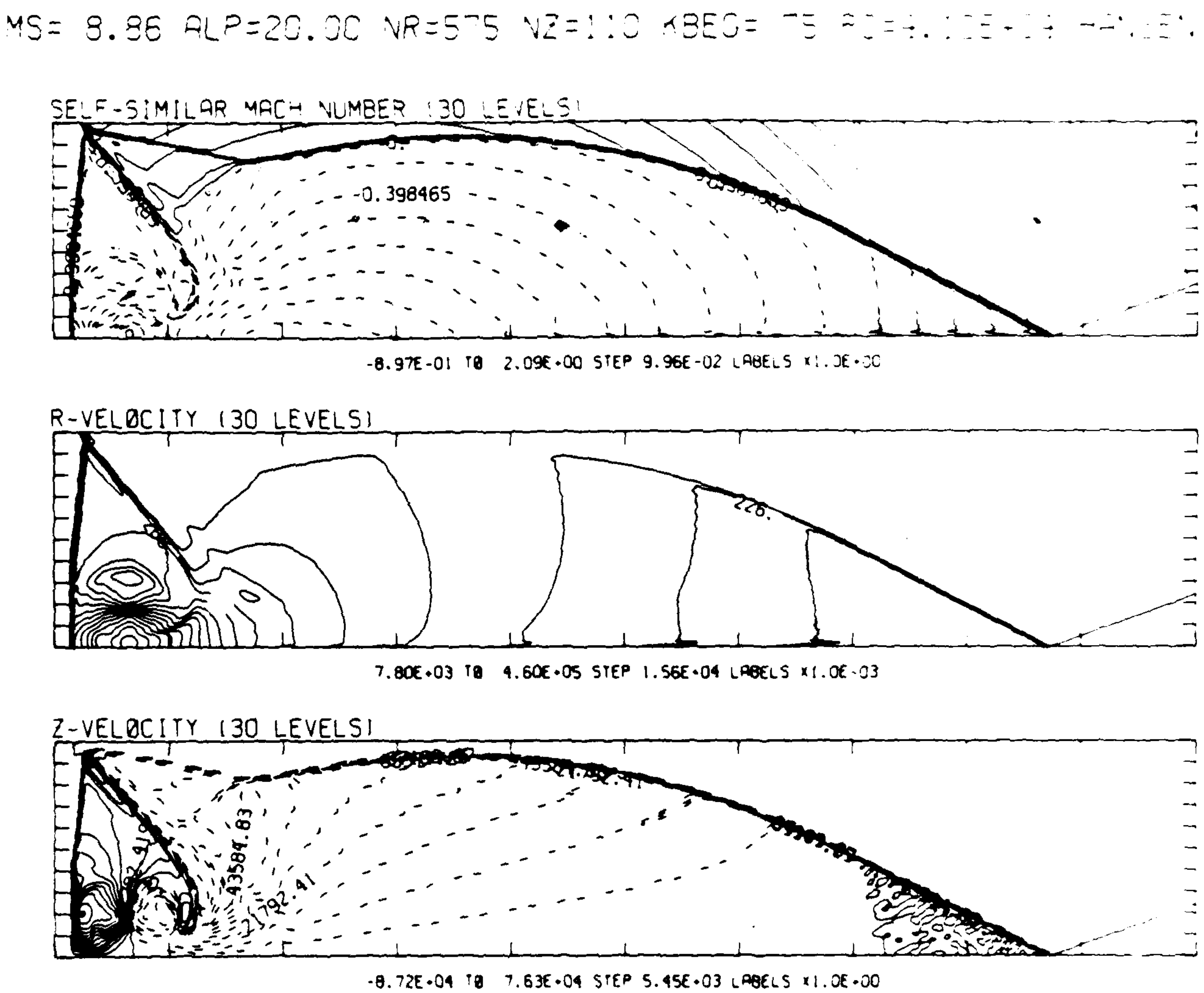

Figure 18d. Whole-flowfield contour-plots - continued.

Figure 18. Case 15, M_s = 8.86, θ_w = 20°, Air, Hansen EOS, DMR - continued.

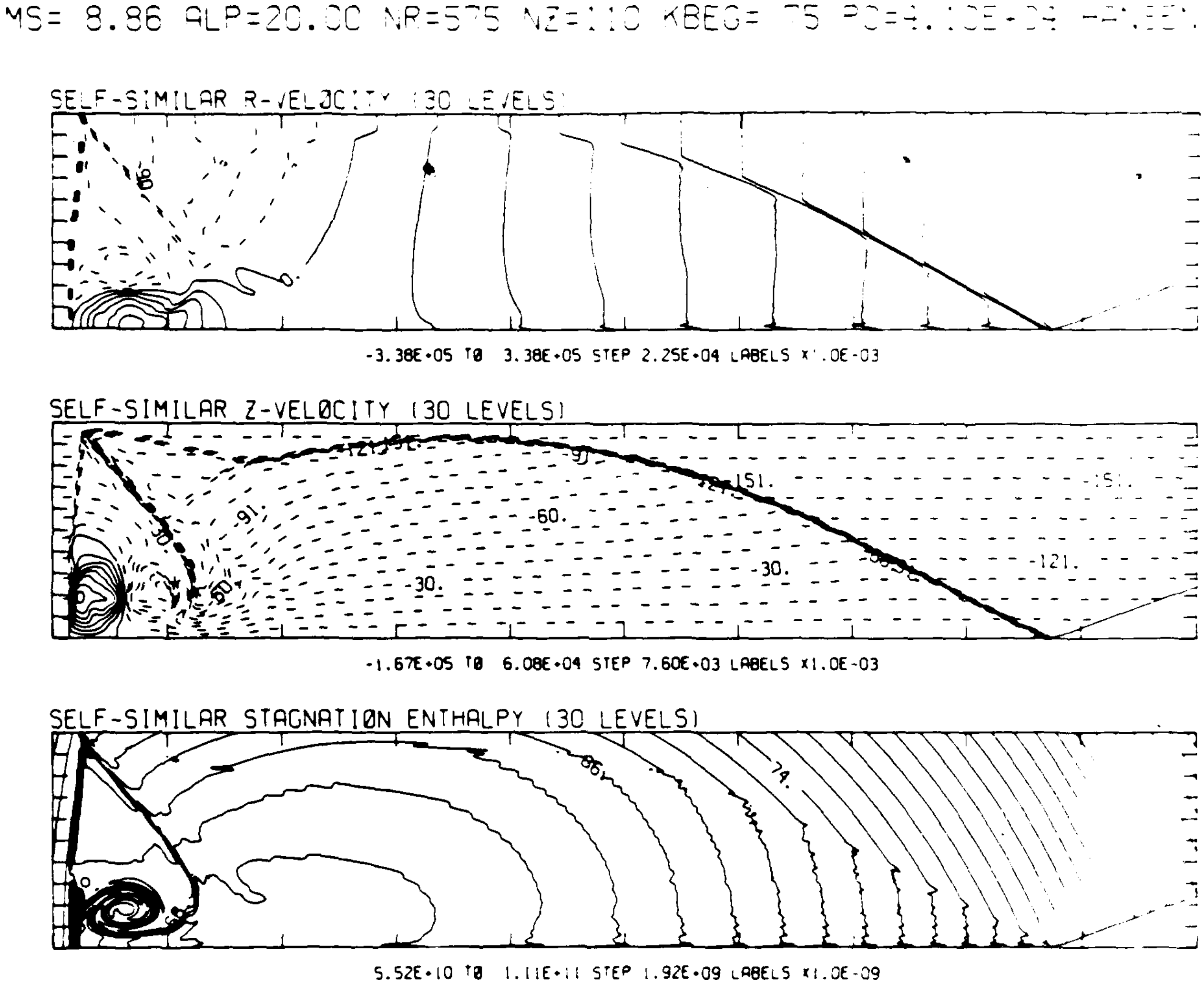

Figure 18d. Whole-flowfield contour-plots - continued.

Figure 18. Case 15, M_s = 8.86, θ_w = 20°, Air, Hansen EOS, DMR - continued.

MS= 8.86 ALP=20.00 IL=466 IR=568 JT= 99 PO=4.10E+04 HANSEN

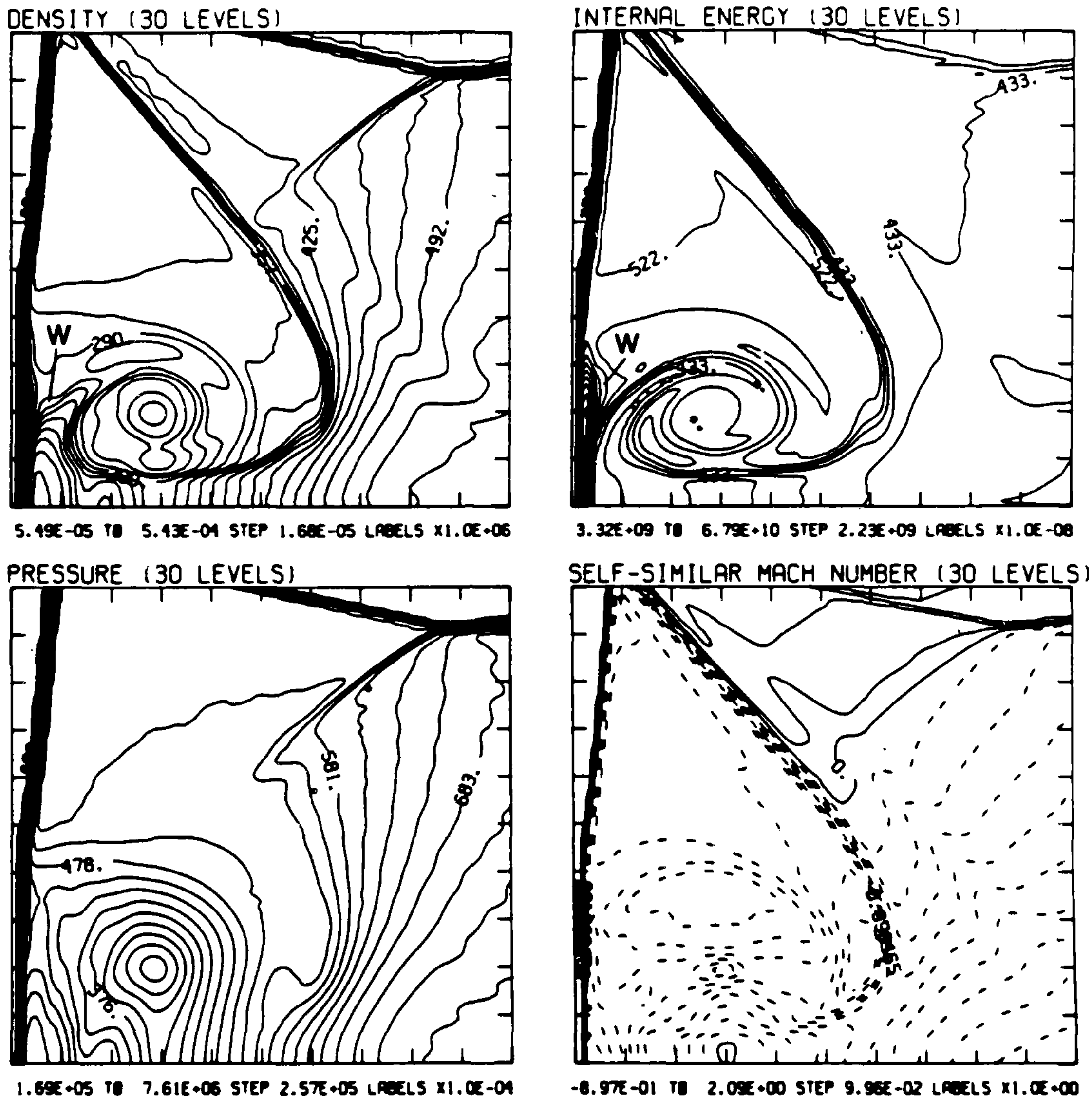

Figure 18e. Blowup-frame plots.

Figure 18. Case 15, M_S = 8.86, θ_w = 20°, Air, Hansen EOS, DMR - continued.

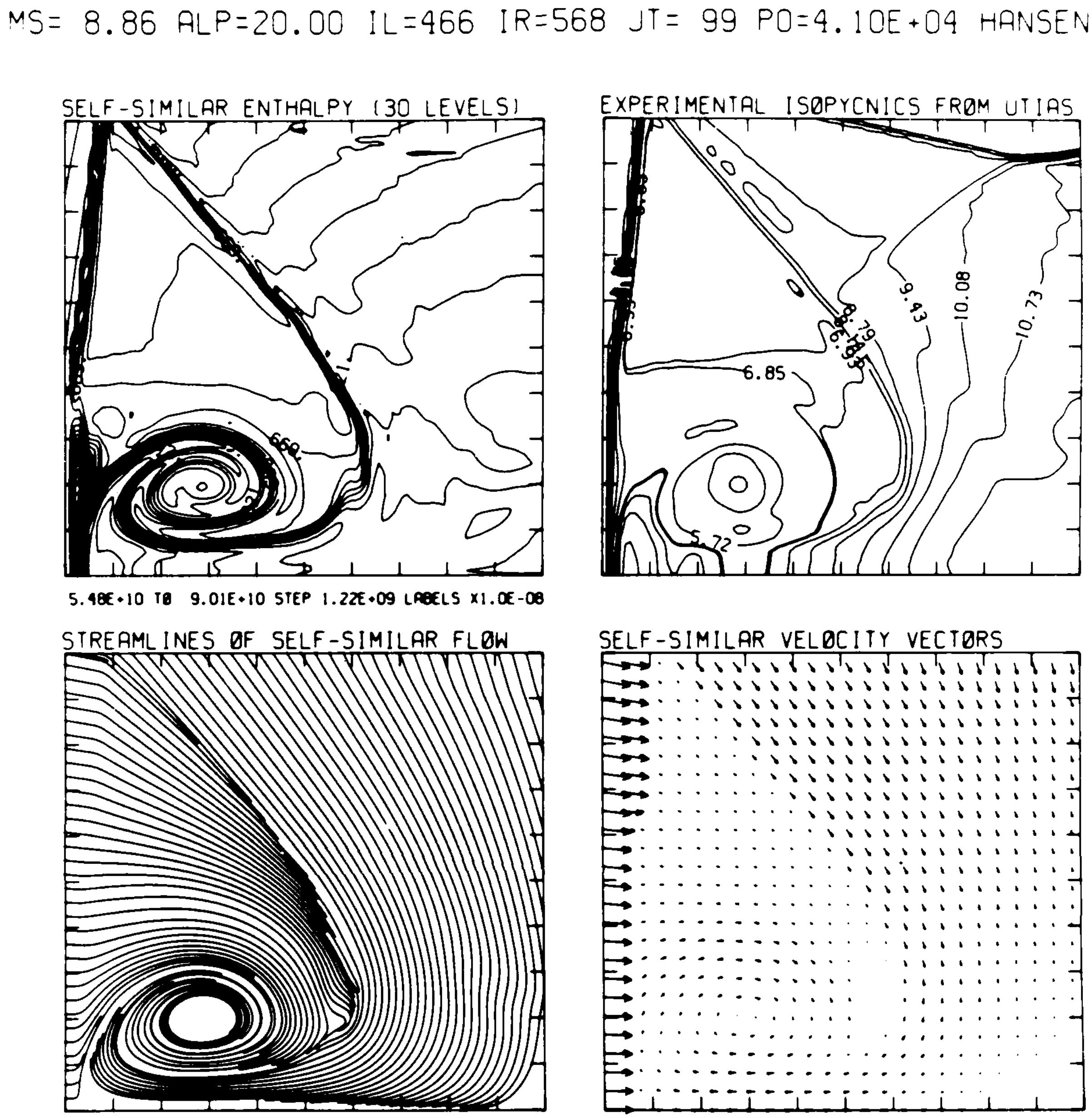

Figure 18f. Reproduction of the interferogram of Exp. 974, Ref. [14]; M_s = 10.18, θ_w = 20°, Air. XBB 859-7208

Figure 18. Case 15, M_s = 8.86, θ_w = 20°, Air, Hansen EOS, DMR - continued.

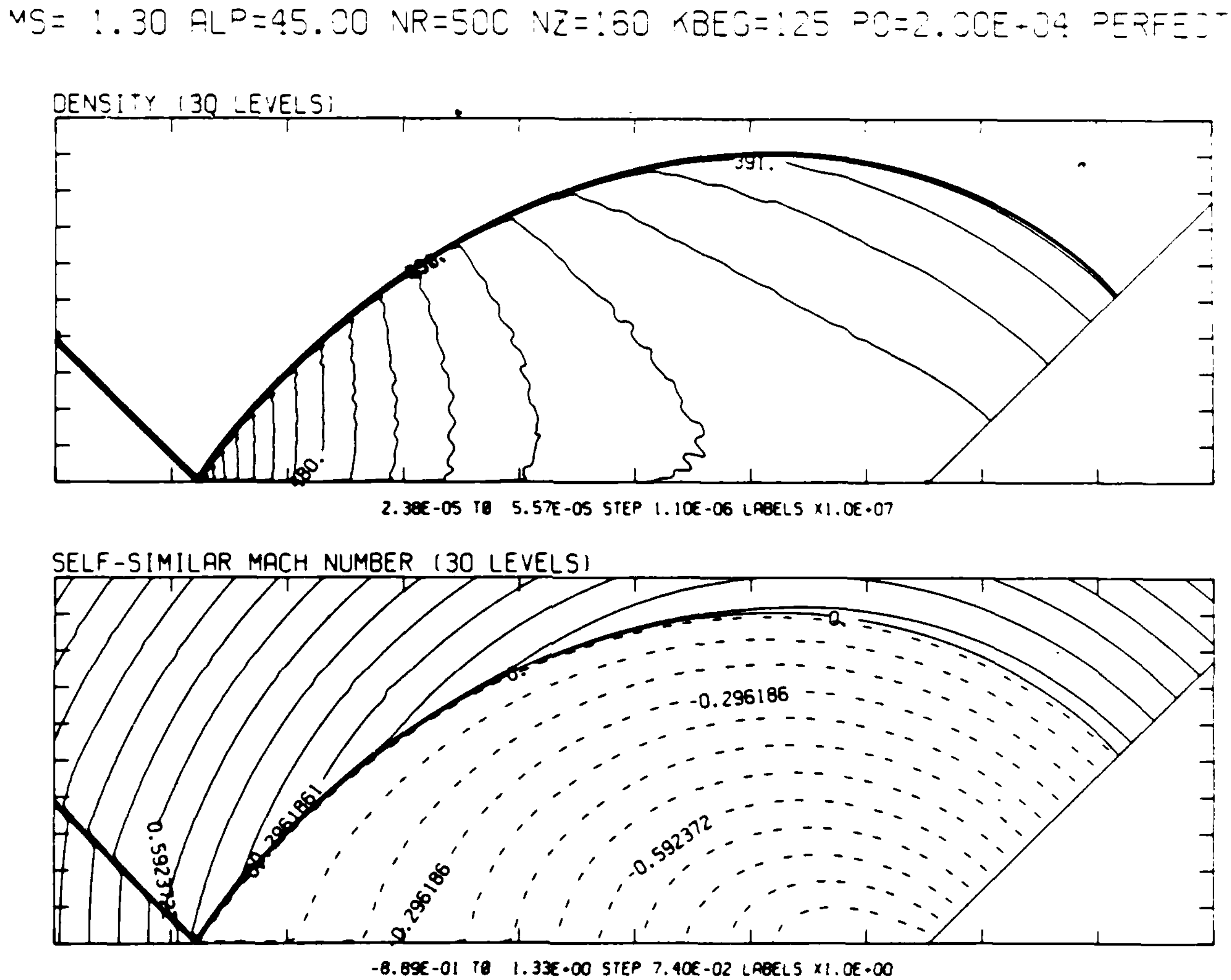

Figure 19.1a. M_s = 1.30, whole-flowfield contour plots.

Figure 19. Transition set 1, $\theta_w = 45°$, $\gamma = 1.4$.

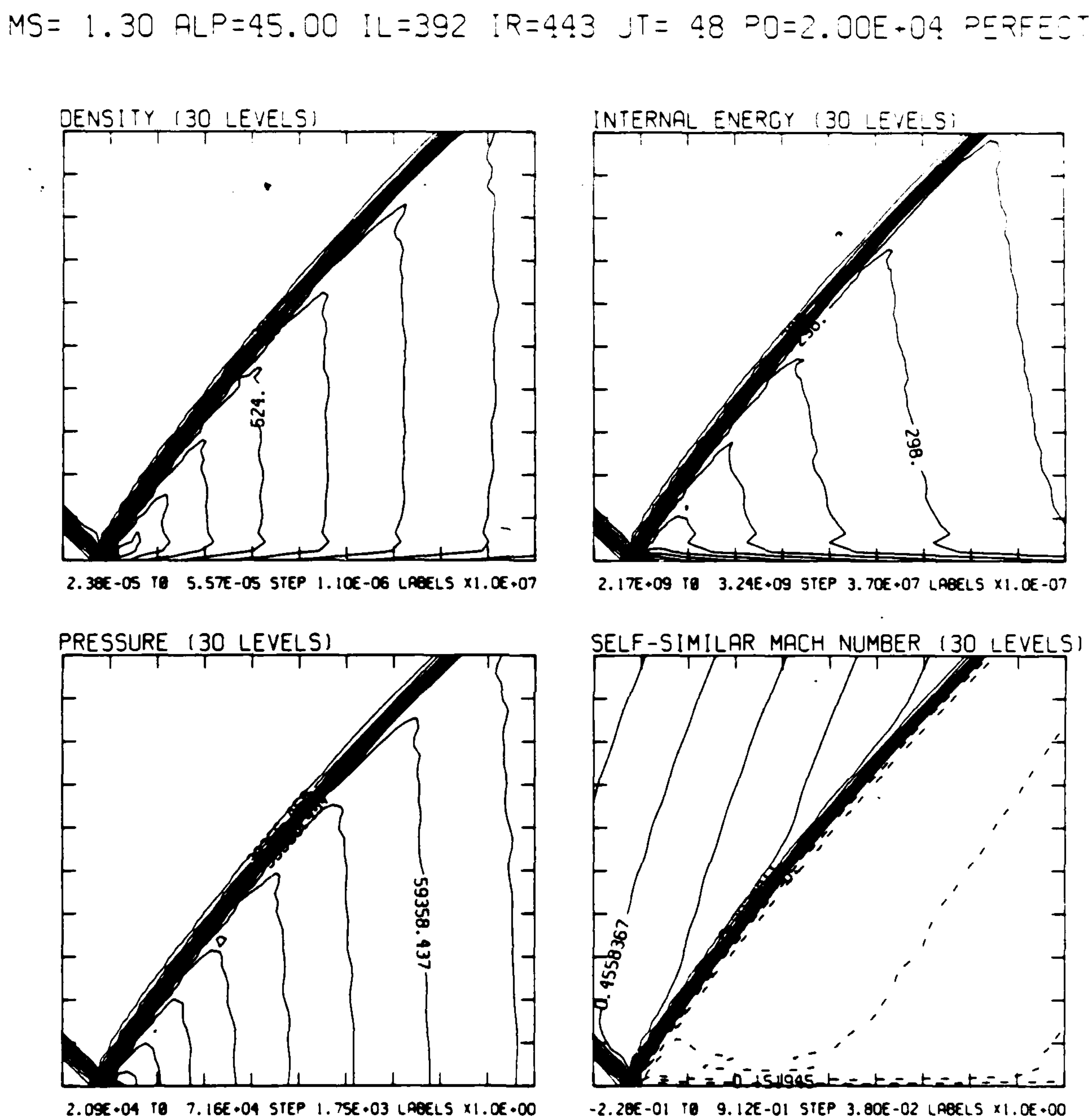

Figure 19.1b. M_S = 1.30, blowup-frame plots.

Figure 19. Transition set 1, θ_w = 45°, γ = 1.4 - continued.

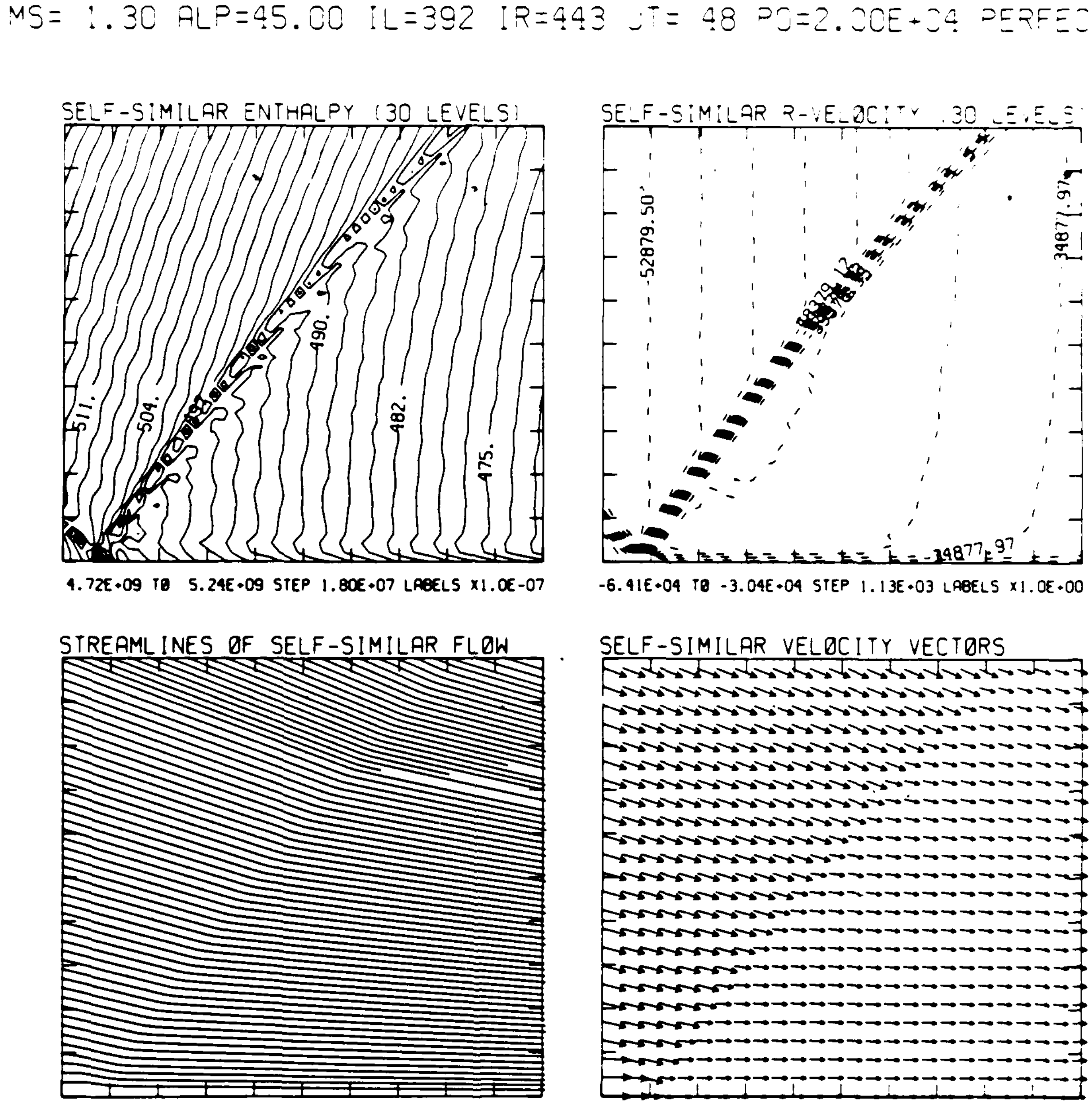

Figure 19.1b. M_s = 1.30, blowup-frame plots - continued.

Figure 19. Transition set 1, θ_w = 45°, γ = 1.4 - continued.

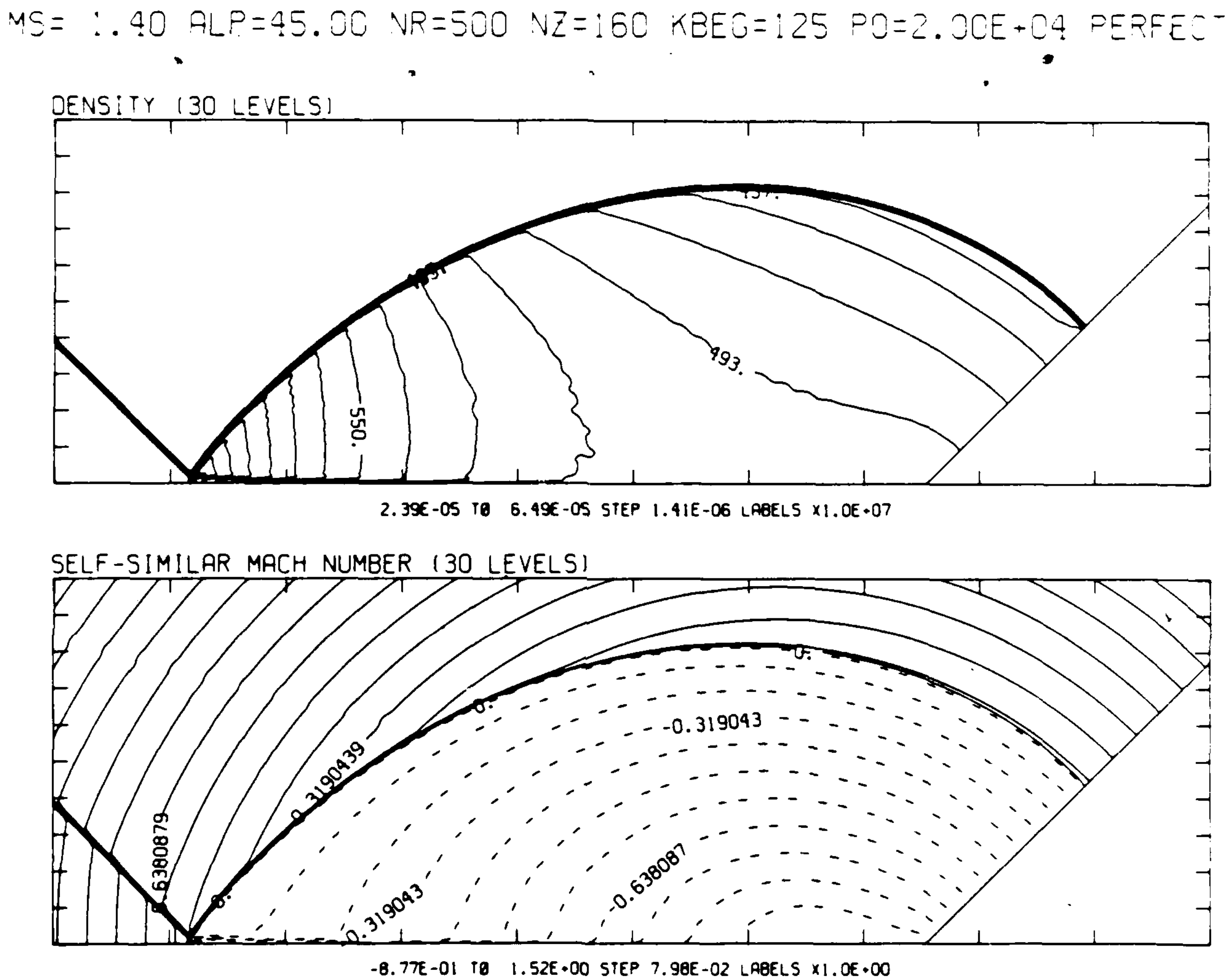

Figure 19.2a. M_S = 1.40, whole-flowfield contour-plots.

Figure 19. Transition set 1, θ_W = 45°, γ = 1.4 - continued.

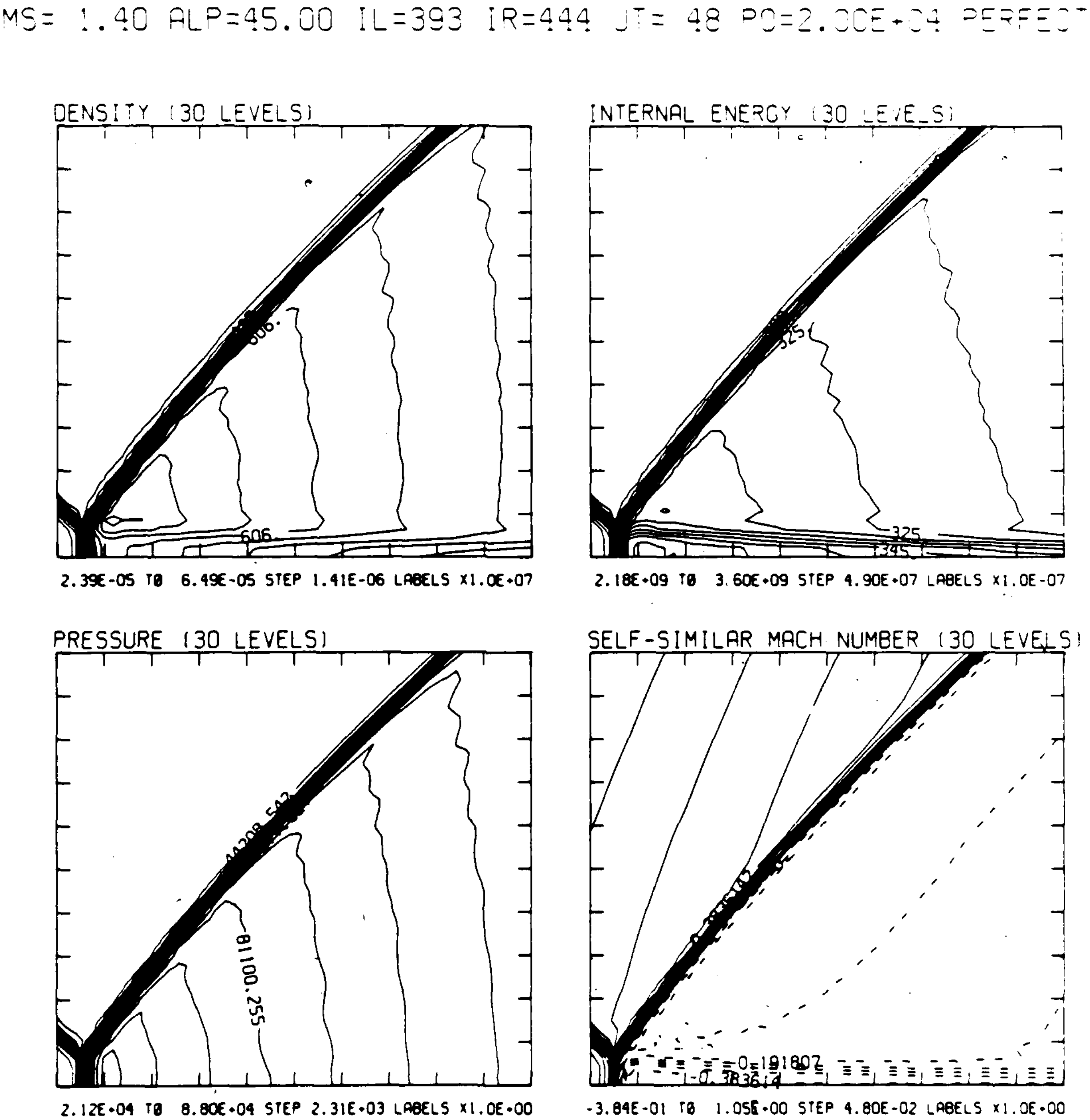

Figure 19.2b. M_s = 1.40, blowup-frame plots.

Figure 19. Transition set 1, θ_w = 45°, γ = 1.4 - continued.

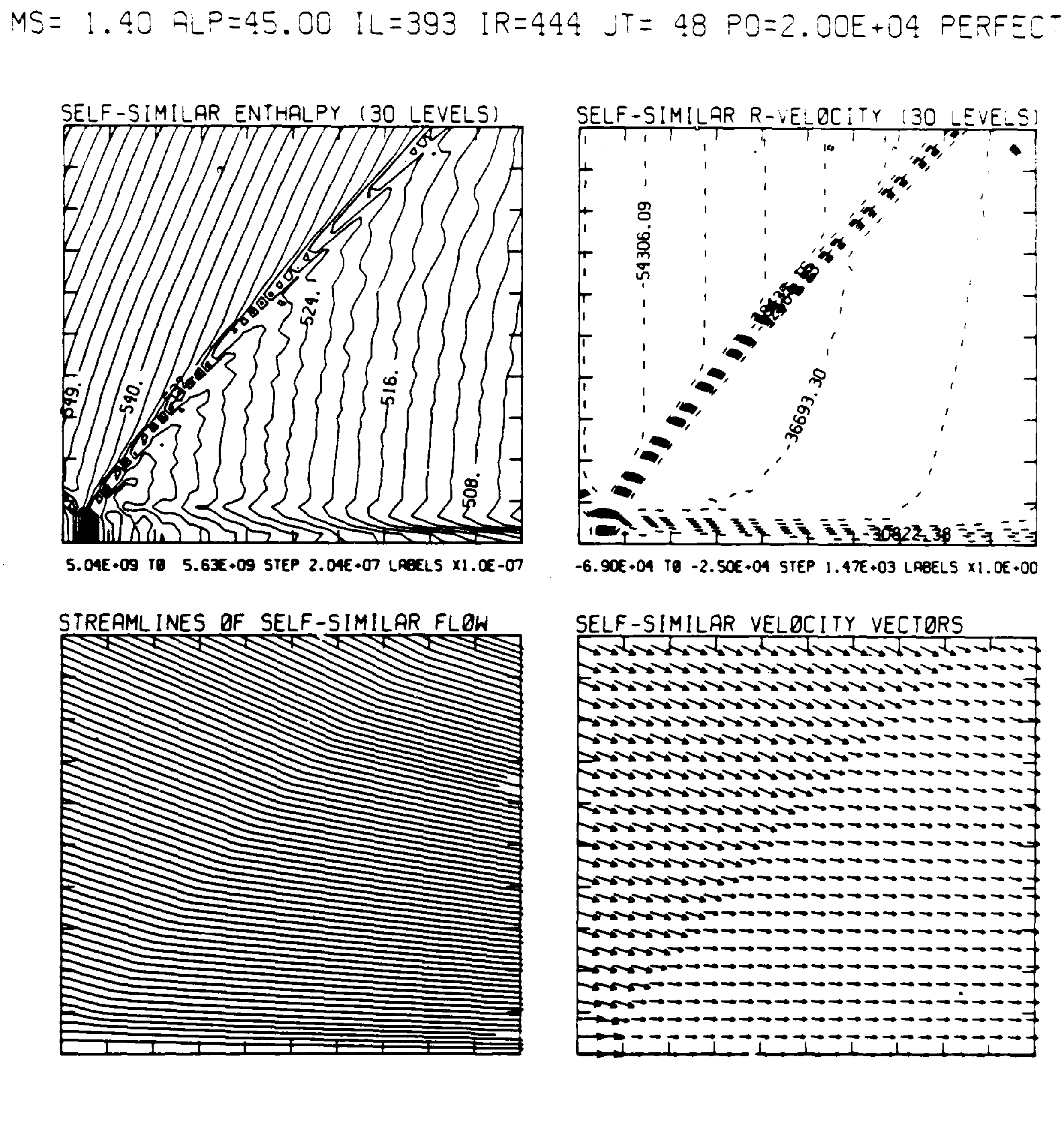

Figure 19.2b. M_s = 1.40, blowup-frame plots - continued.

Figure 19. Transition set 1, $\theta_w = 45°$, $\gamma = 1.4$ - continued.

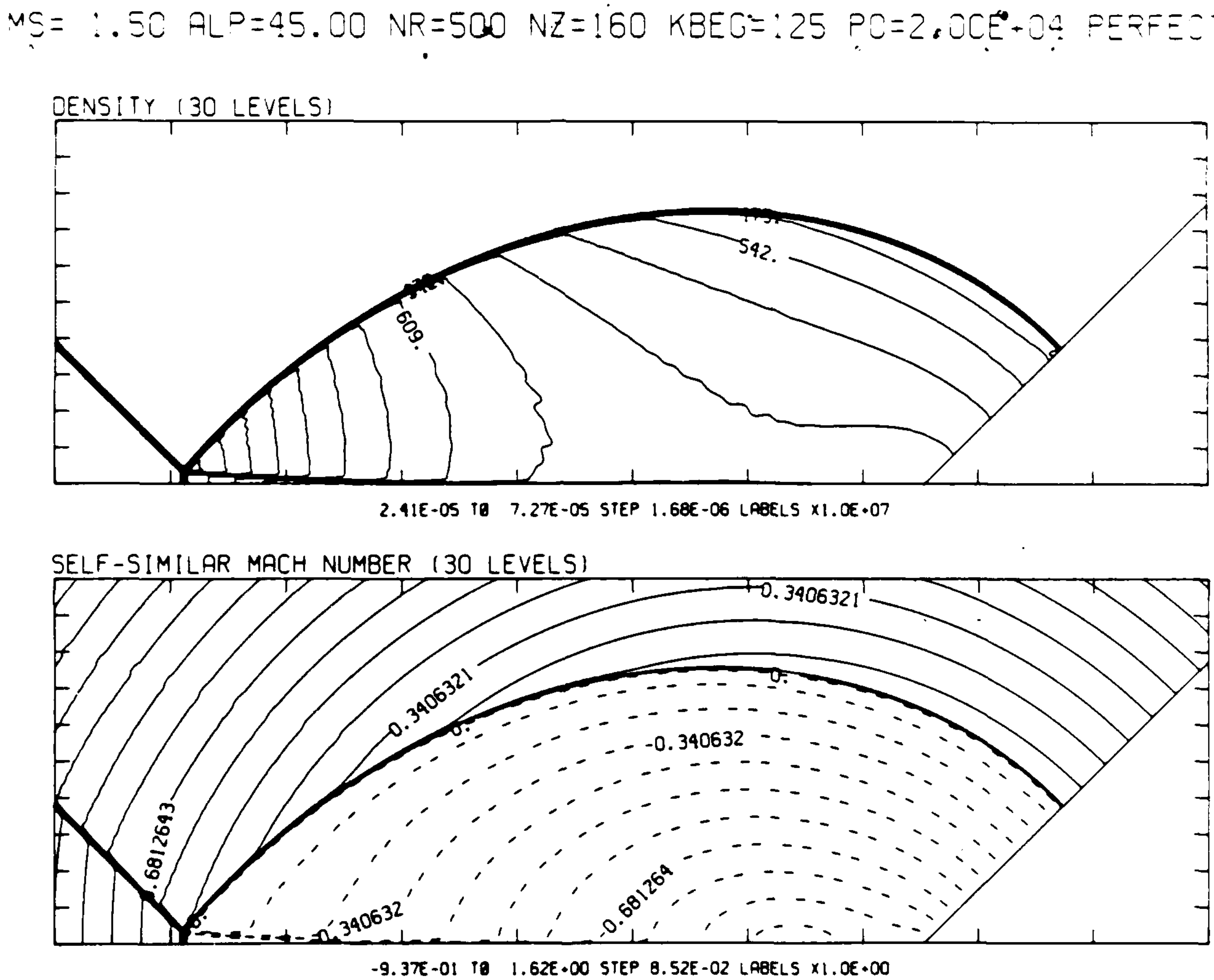

Figure 19.3a. M_S = 1.50, whole-flowfield contour-plots.

Figure 19. Transition set 1, θ_w = 45°, γ = 1.4 - continued.

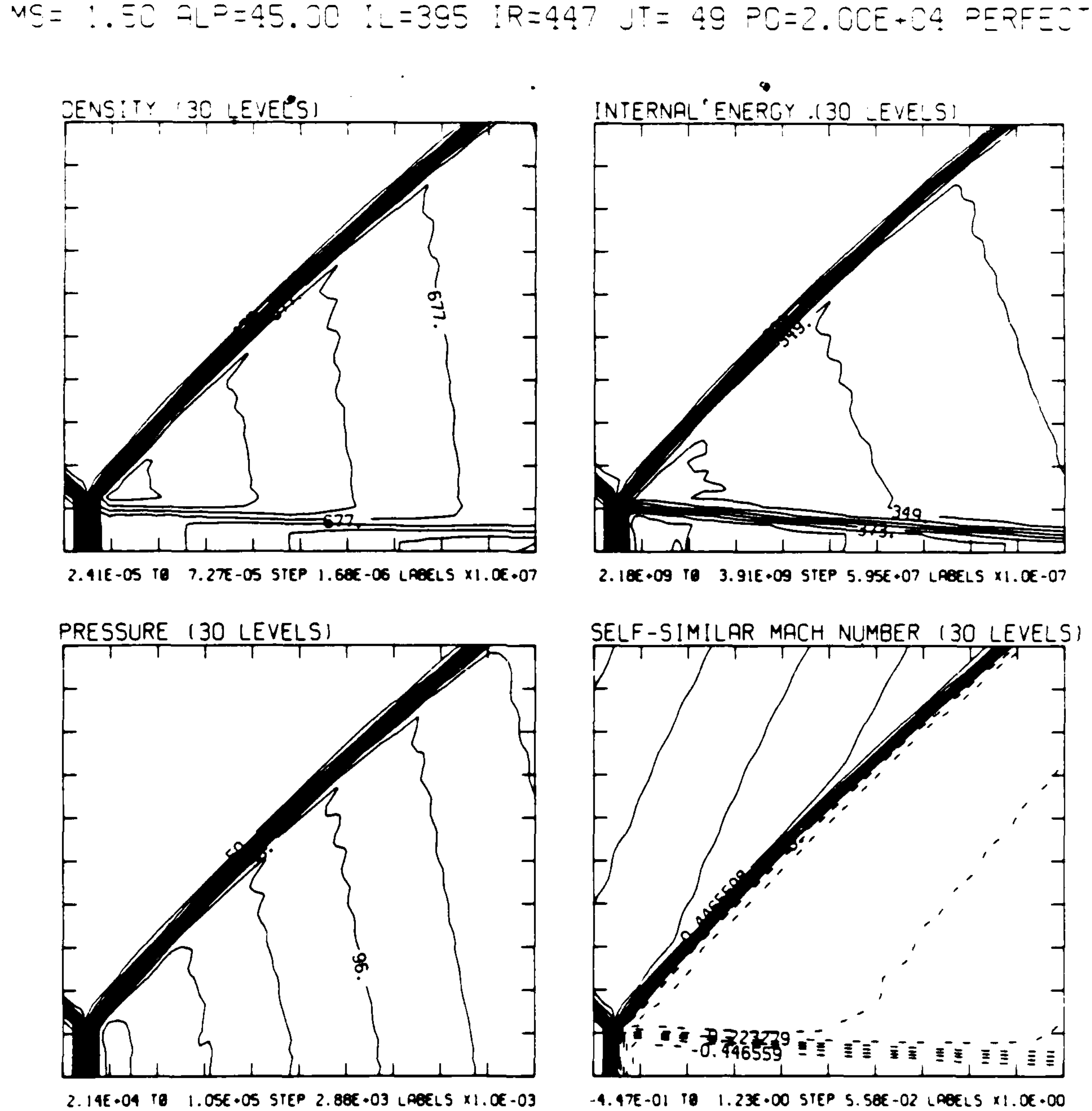

Figure 19.3b. M_s = 1.50, blowup-frame plots.

Figure 19. Transition set 1, θ_w = 45°, γ = 1.4 - continued.

MS= 1.50 ALP=45.00 IL=395 IR=447 JT= 49 PC=2.00E-04 PERFECT

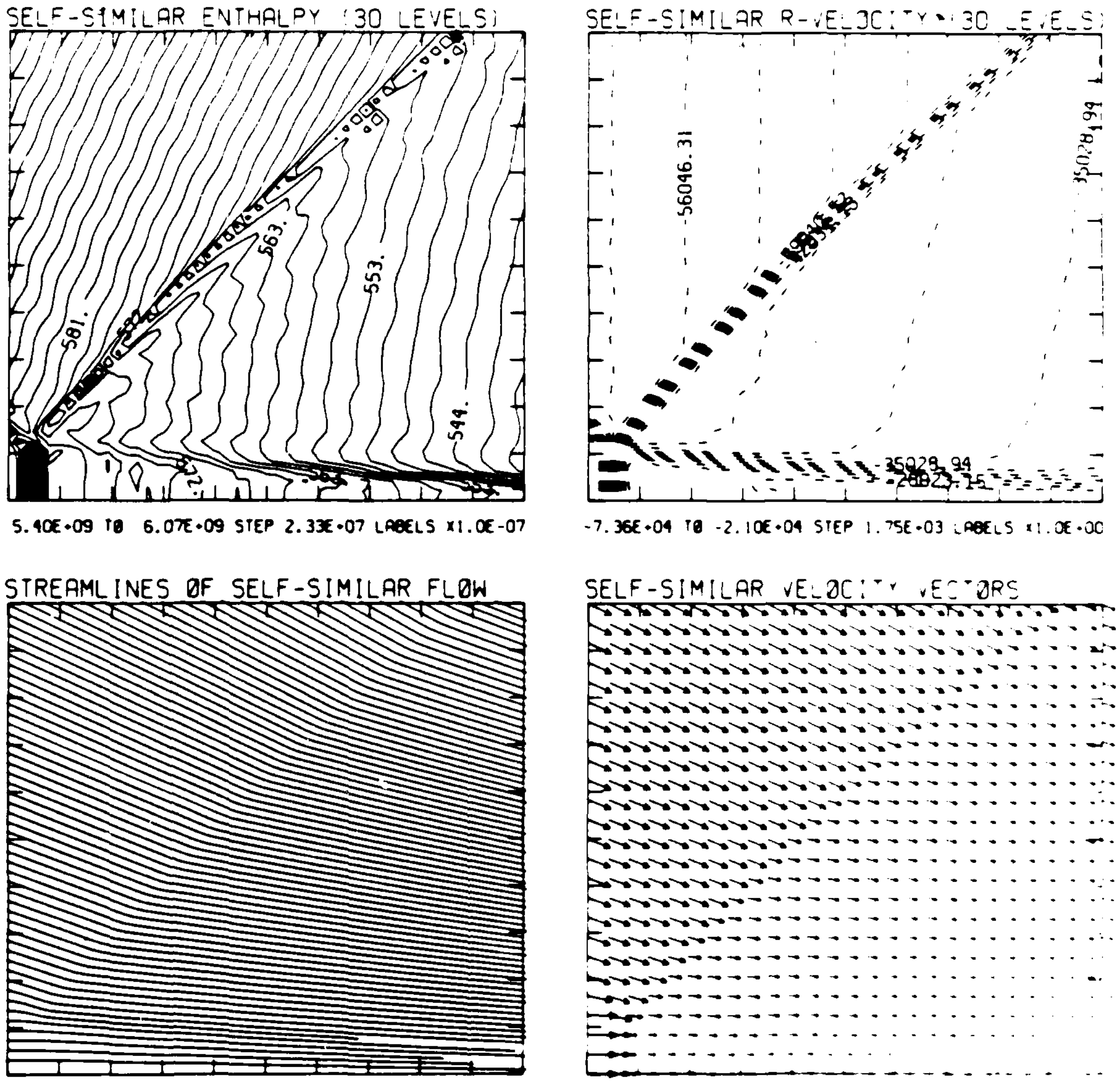

Figure 19.3b. M_s = 1.50, blowup-frame plots - continued.

Figure 19. Transition set 1, θ_w = 45°, γ = 1.4 - continued.

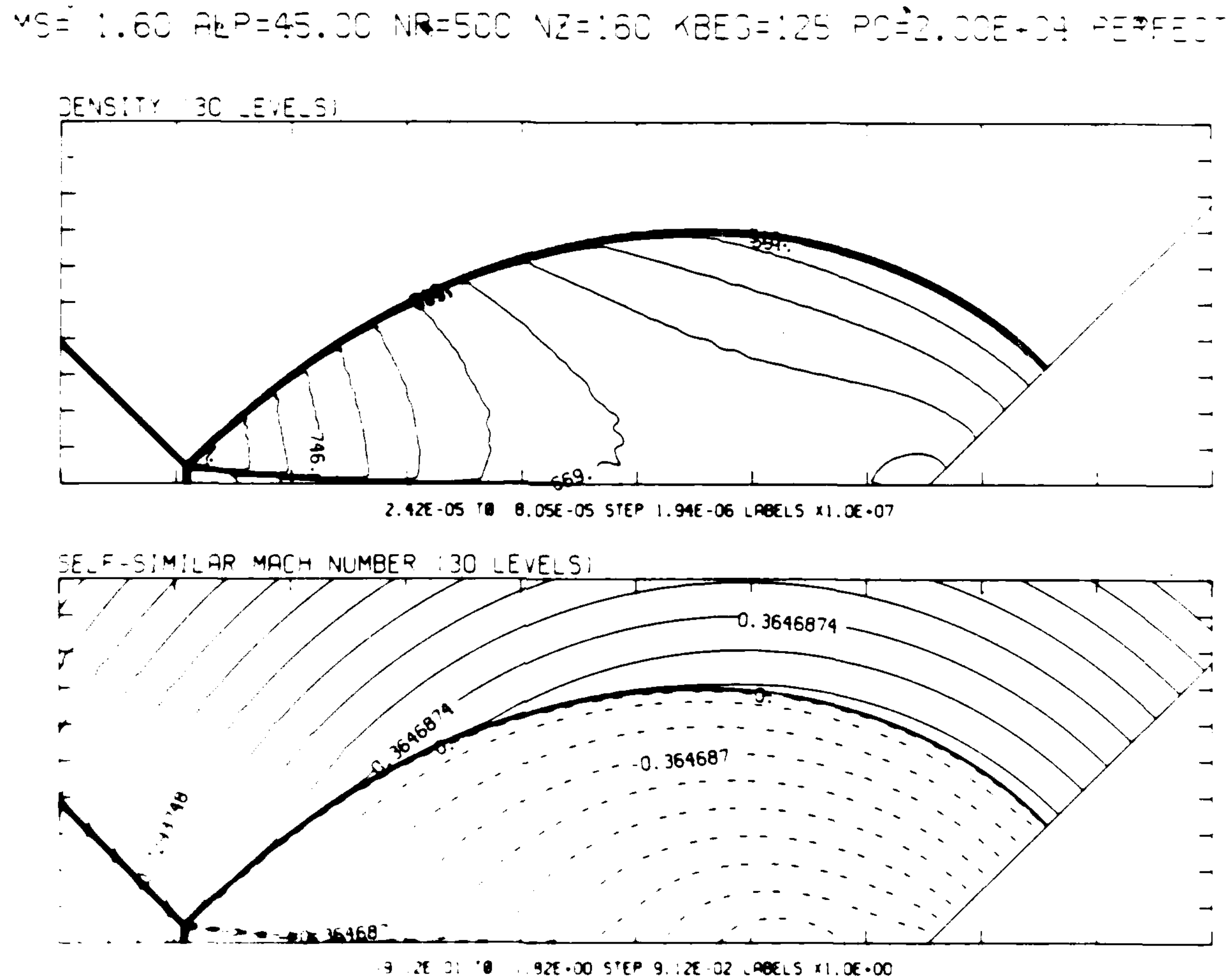

Figure 13.4a. M_s = 1.60, whole-flowfield contour-plots.

Figure 13. Transition set 1, θ_w = 45°, γ = 1.4 - continued.

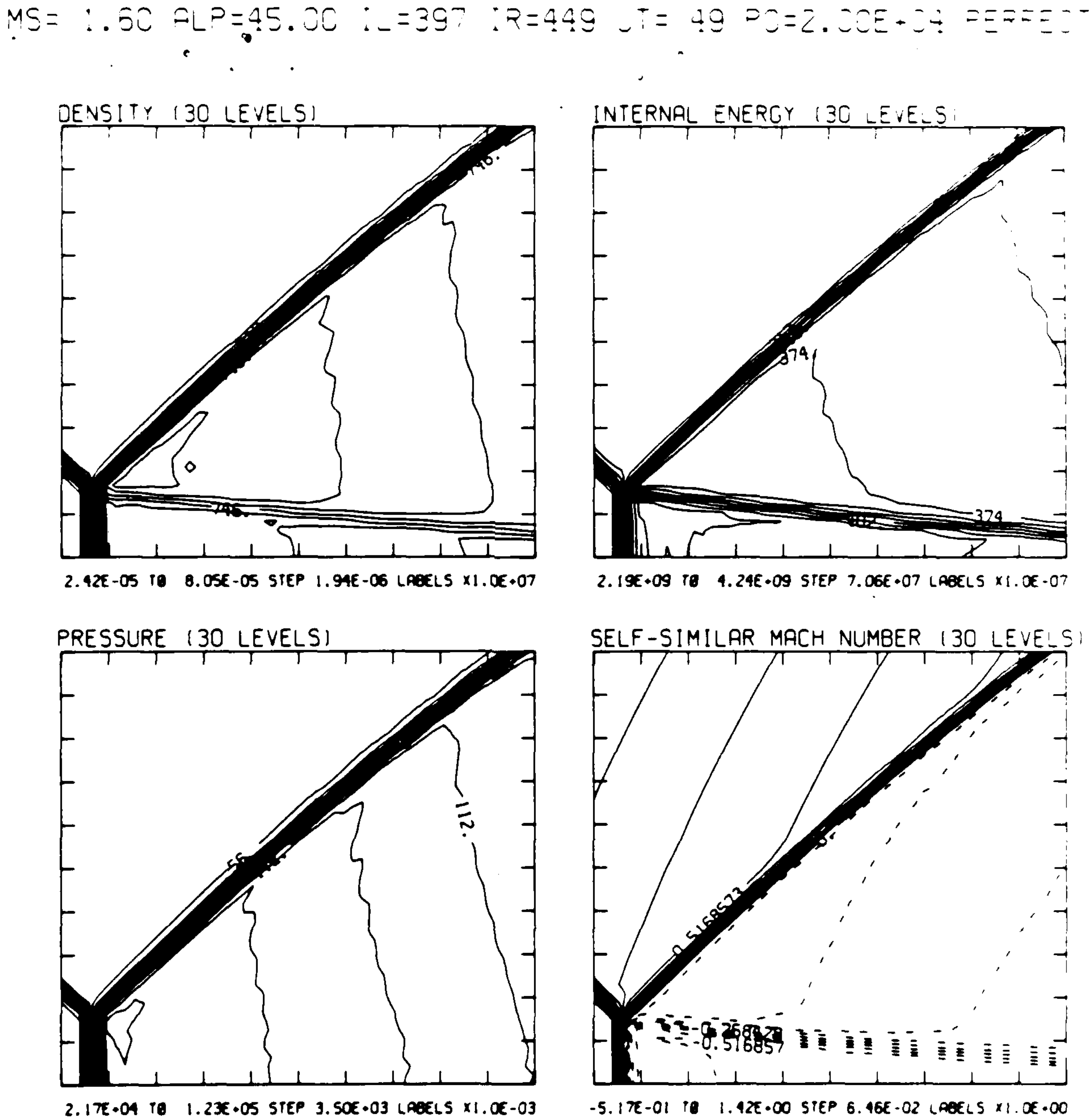

Figure 19.4b. M_S = 1.60, blowup-frame plots.

Figure 19. Transition set 1, θ_w = 45°, γ = 1.4 - continued.

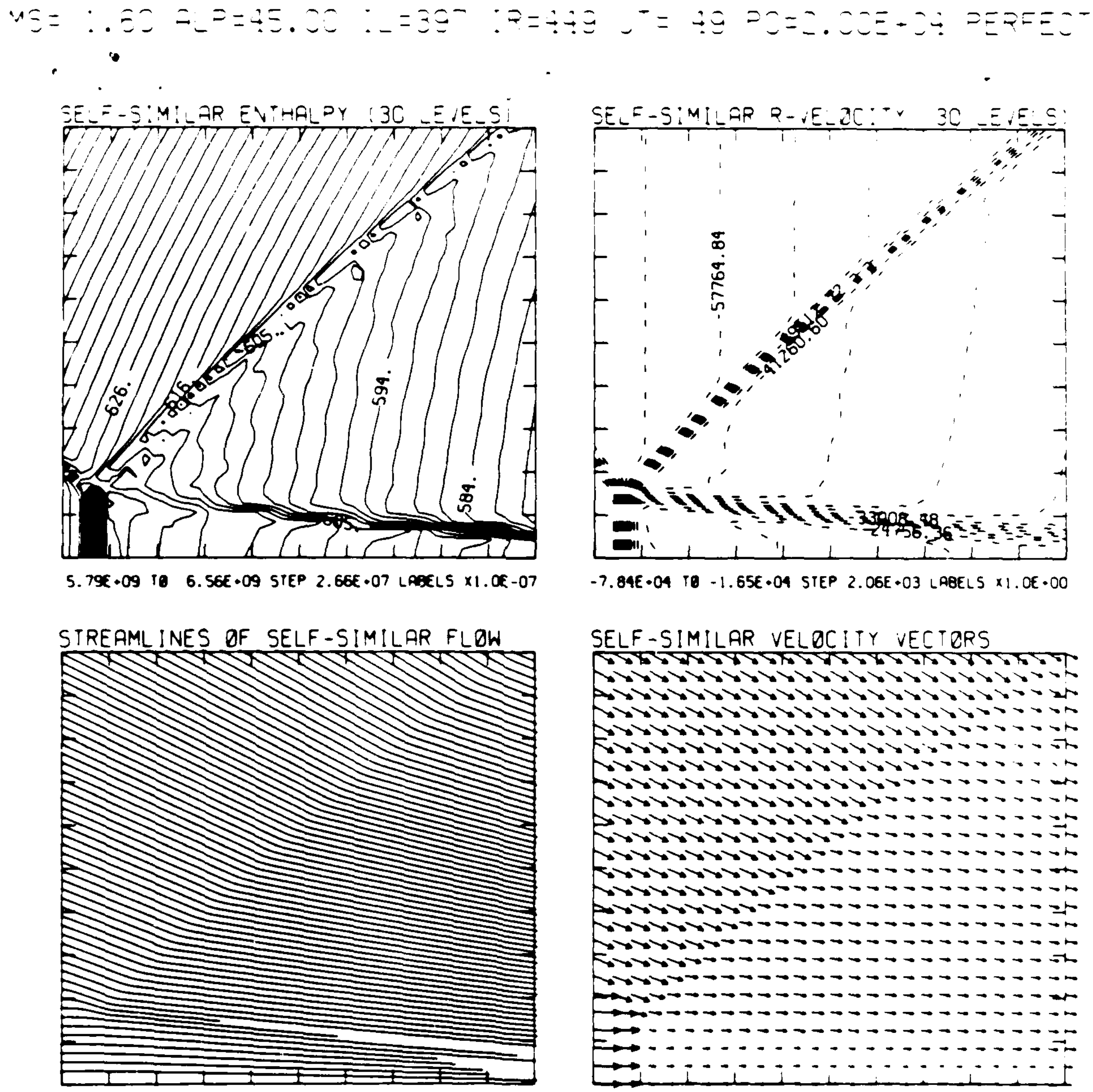

Figure 19.4b. M_s = 1.60, blowup-frame plots - continued.

Figure 19. Transition set 1, θ_w = 45°, γ = 1.4 - continued.

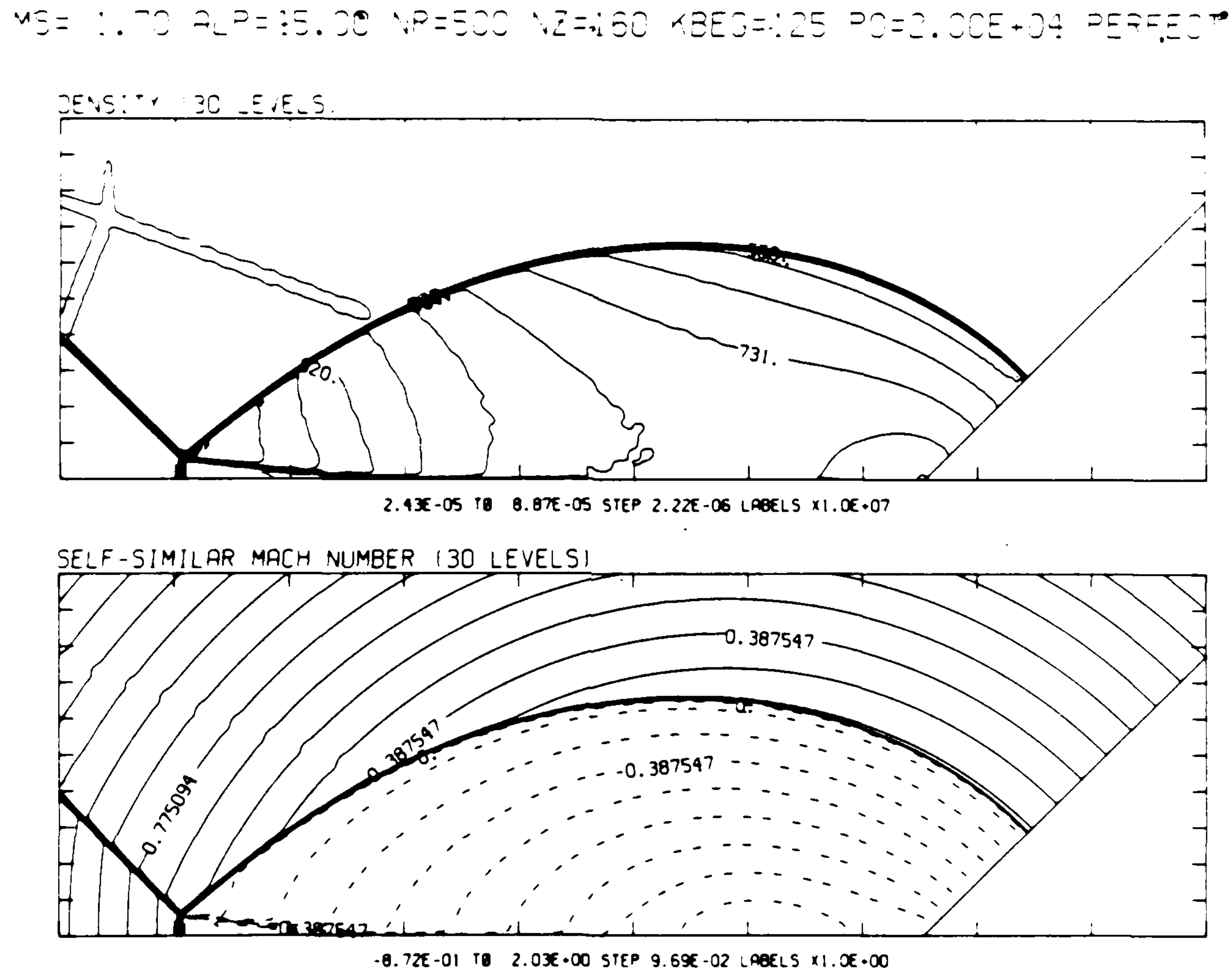

Figure 19.5a. M_S = 1.70, whole-flowfield contour-plots.

Figure 19. Transition set 1, θ_w = 45°, γ = 1.4 - continued.

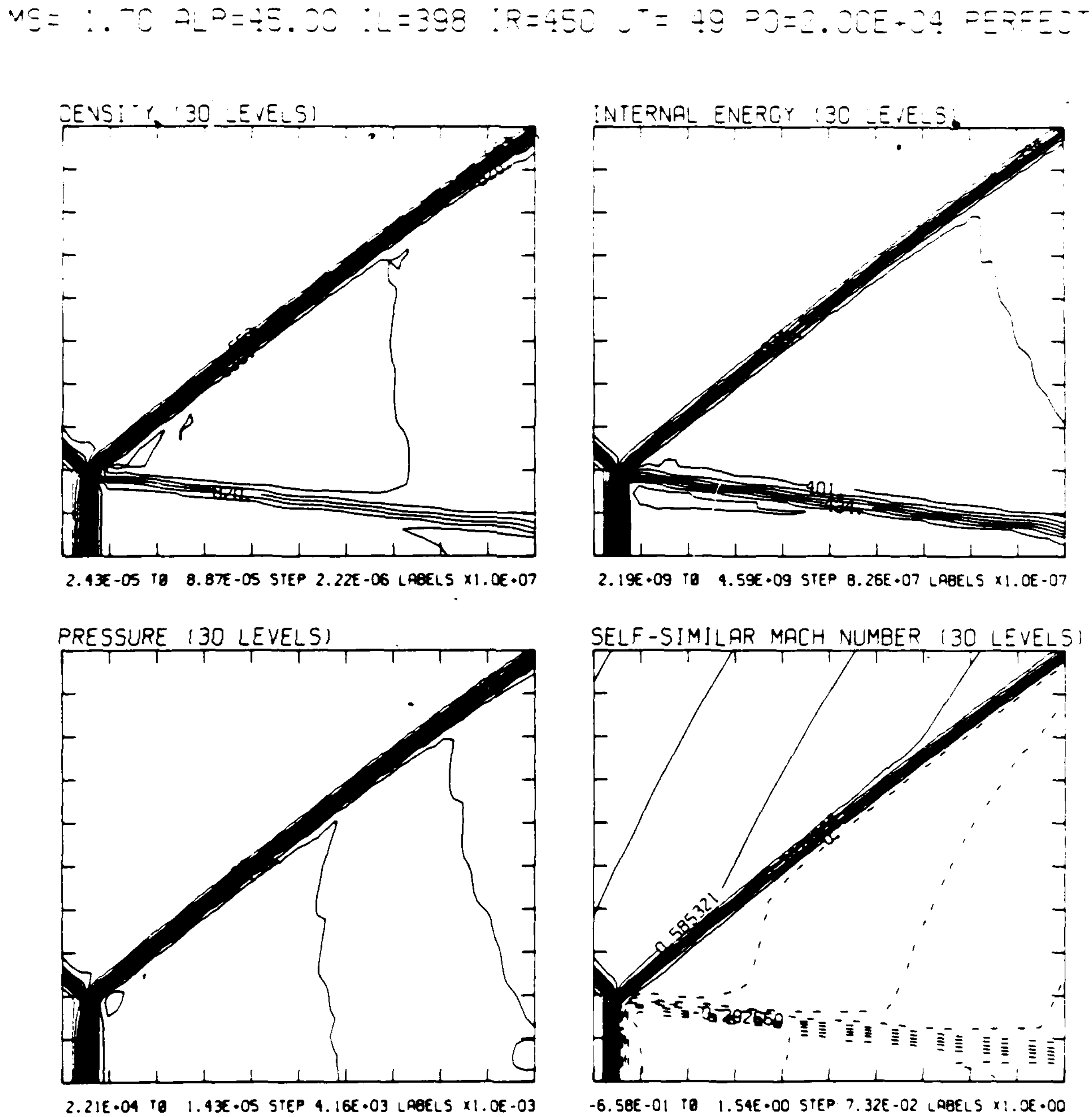

Figure 19.5b. M_s = 1.70, blowup-frame plots.

Figure 19. Transition set 1, θ_w = 45°, γ = 1.4 - continued.

MS= 1.70 ALP=45.00 IL=398 IR=450 JT= 49 PO=2.00E-04 PERFECT

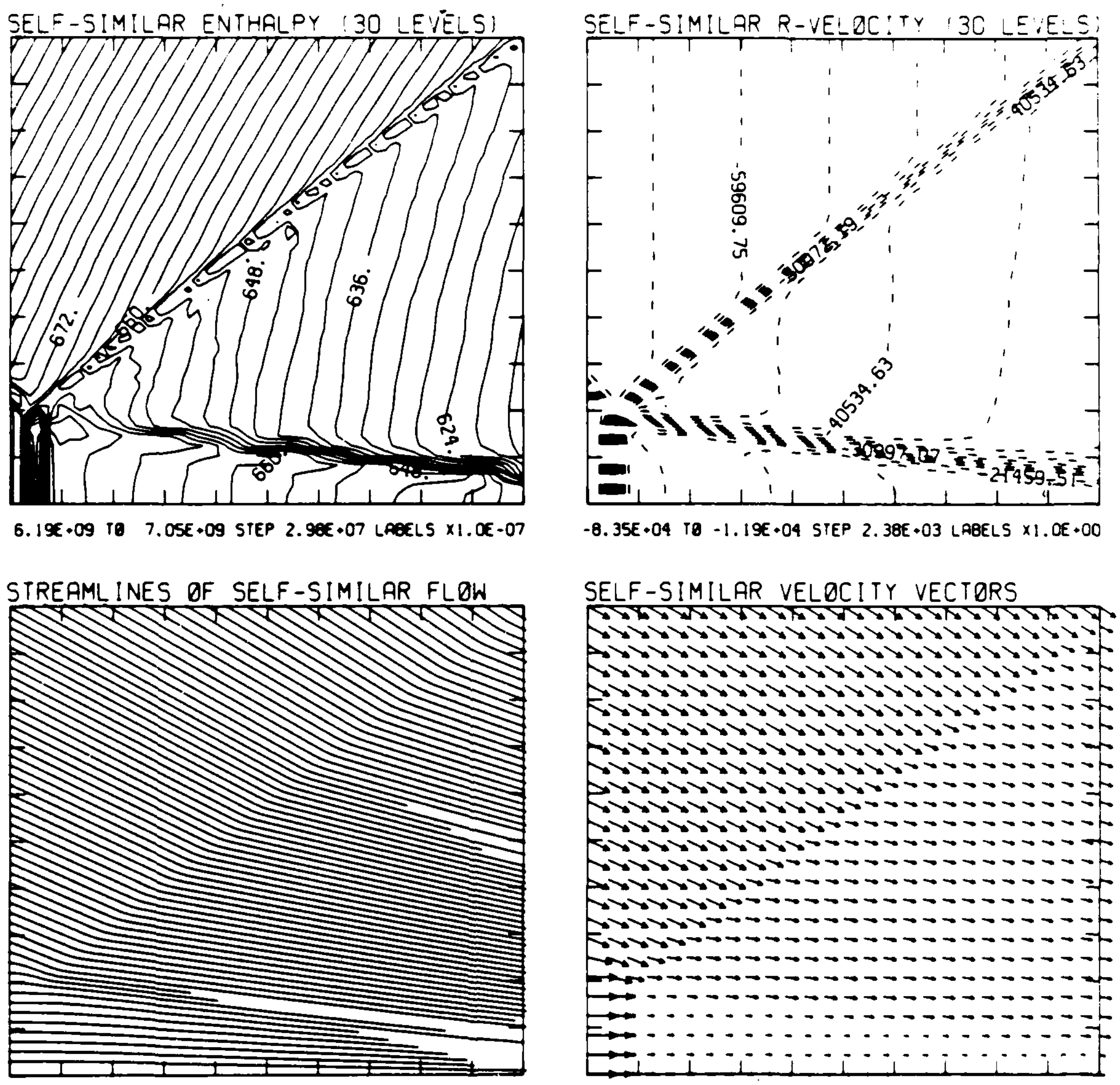

Figure 19.5b. M_S = 1.70, blowup-frame plots - continued.

Figure 19. Transition set 1, θ_w = 45°, γ = 1.4 - continued.

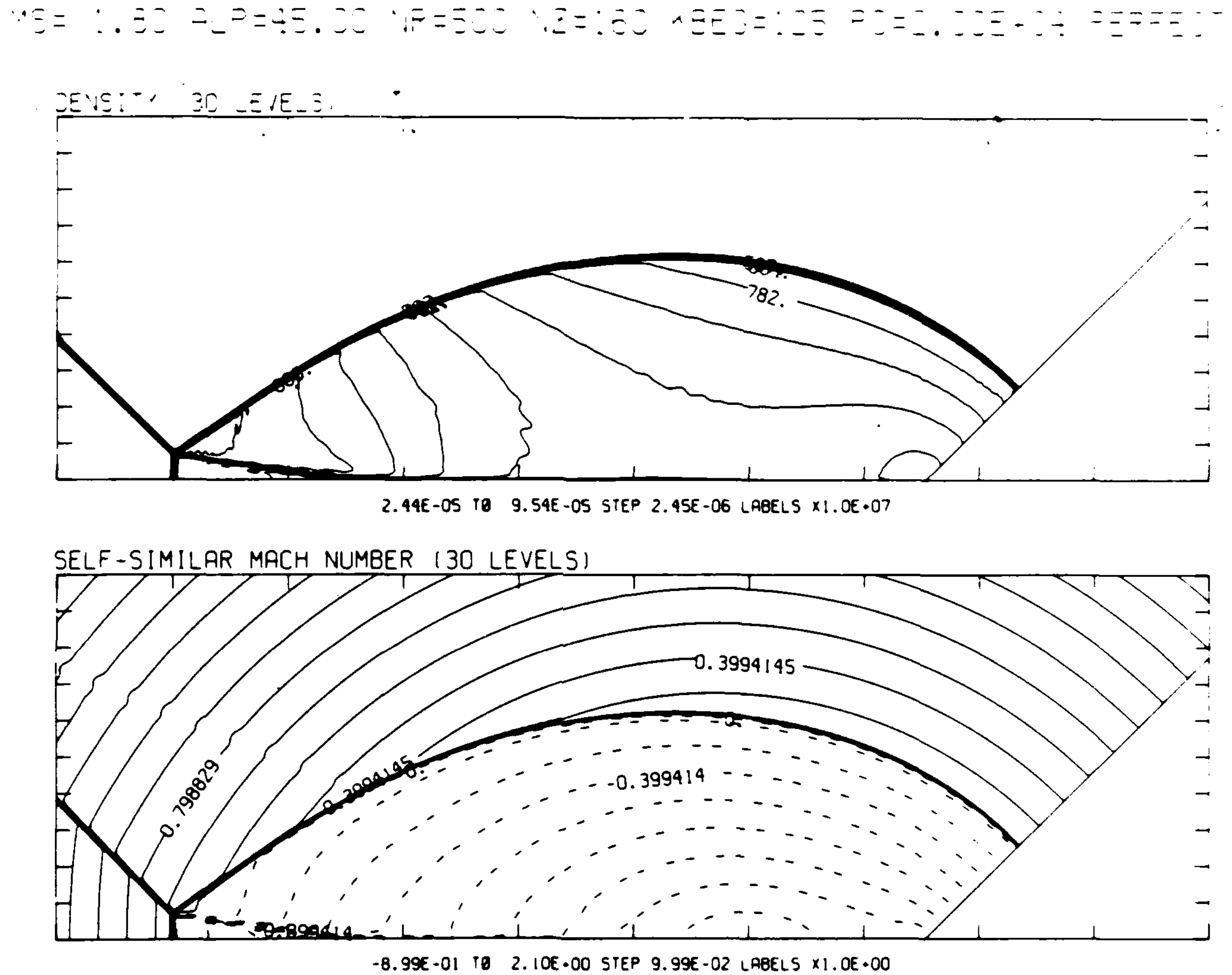

Figure 19.6a. M_s = 1.80, whole-flowfield contour-plots.

Figure 19. Transition set 1, θ_w = 45°, γ = 1.4 - continued.

MS= 1.80 ALP=45.00 IL=400 IR=453 JT= 50 PO=2.00E+04 PERFECT

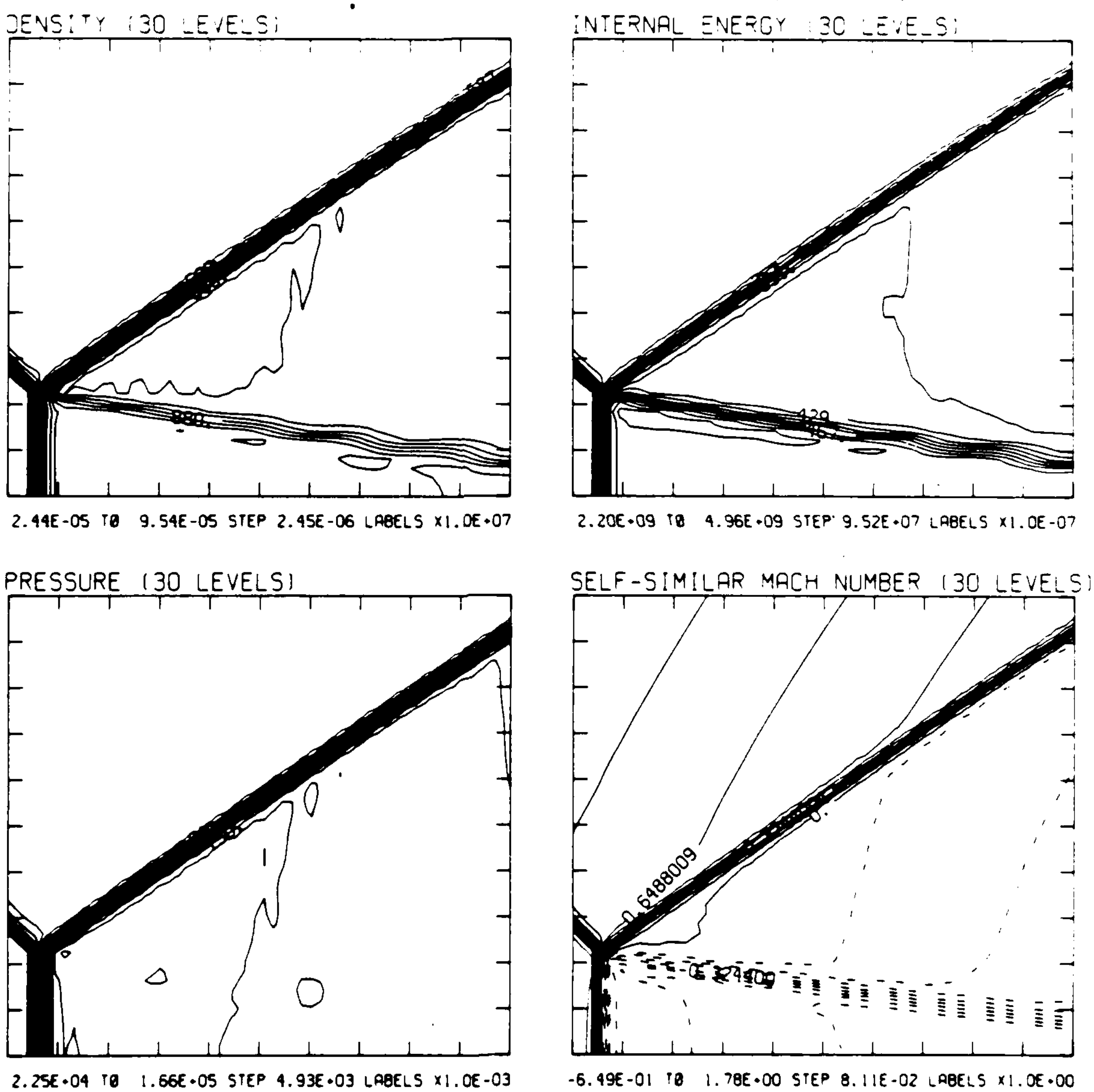

Figure 19.6b. M_s = 1.80, blowup-frame plots.

Figure 19. Transition set 1, θ_w = 45°, γ = 1.4 - continued.

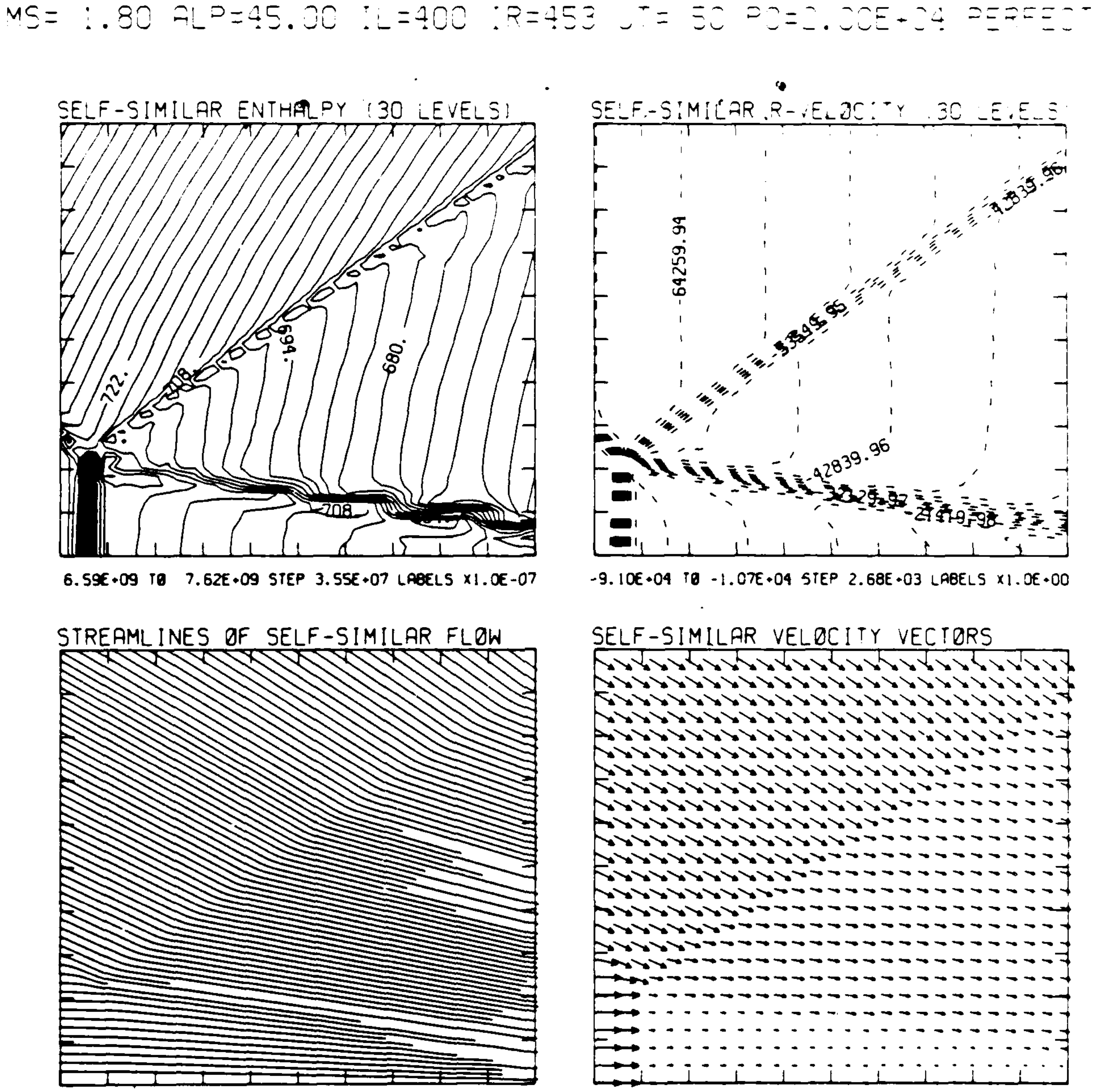

Figure 19.6b. M_S = 1.80, blowup-frame plots - continued.

Figure 19. Transition set 1, θ_w = 45°, γ = 1.4 - continued.

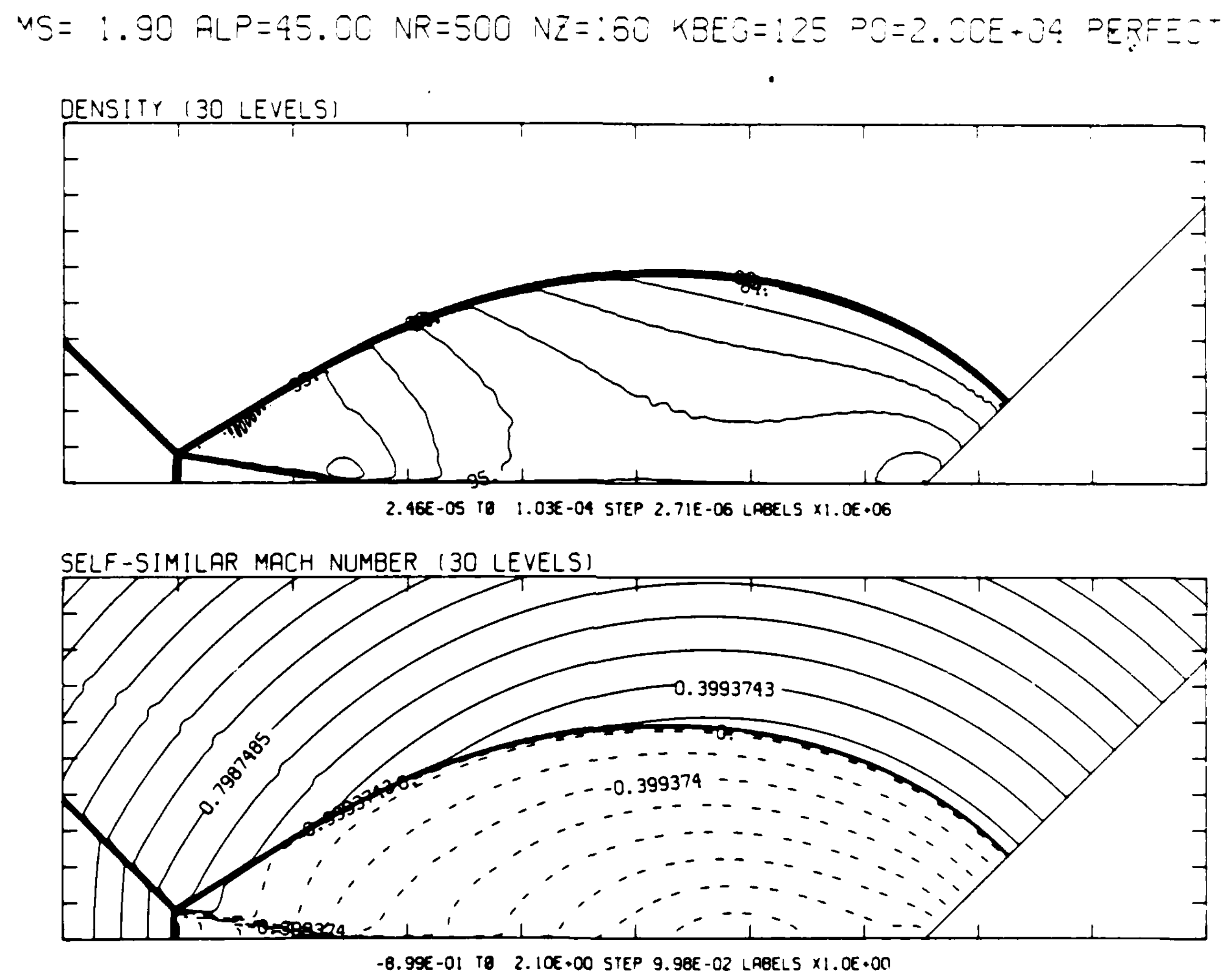

Figure 19.7a. M_s = 1.90, whole-flowfield contour-plots.

Figure 19. Transition set 1, θ_w = 45°, γ = 1.4 - continued.

MS= 1.90 ALP=45.00 IL=401 IR=454 JT= 50 PO=2.00E+04 PERFECT

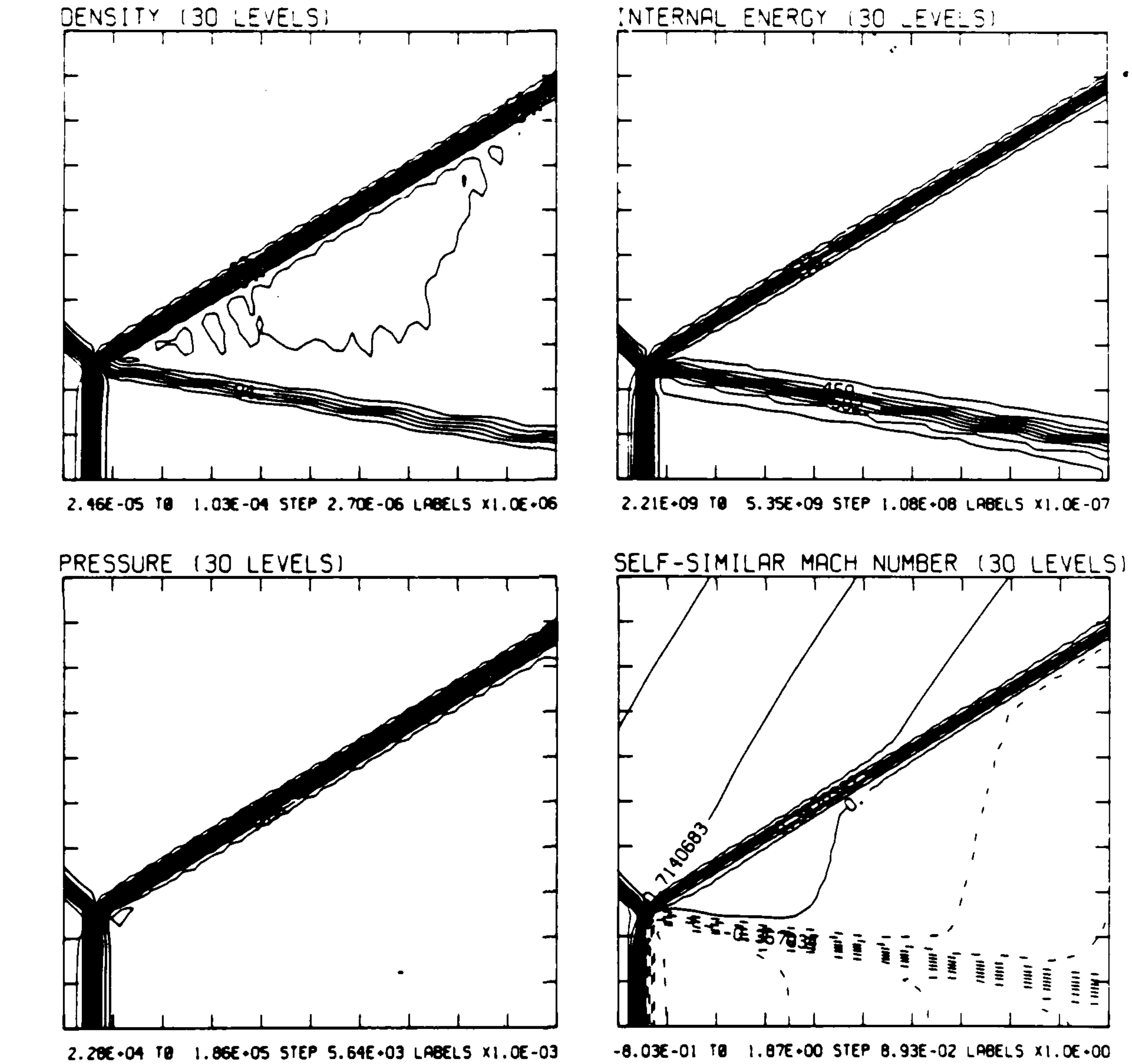

Figure 19.7b. M_s = 1.90, blowup-frame plots.

Figure 19. Transition set 1, θ_w = 45°, γ = 1.4 - continued.

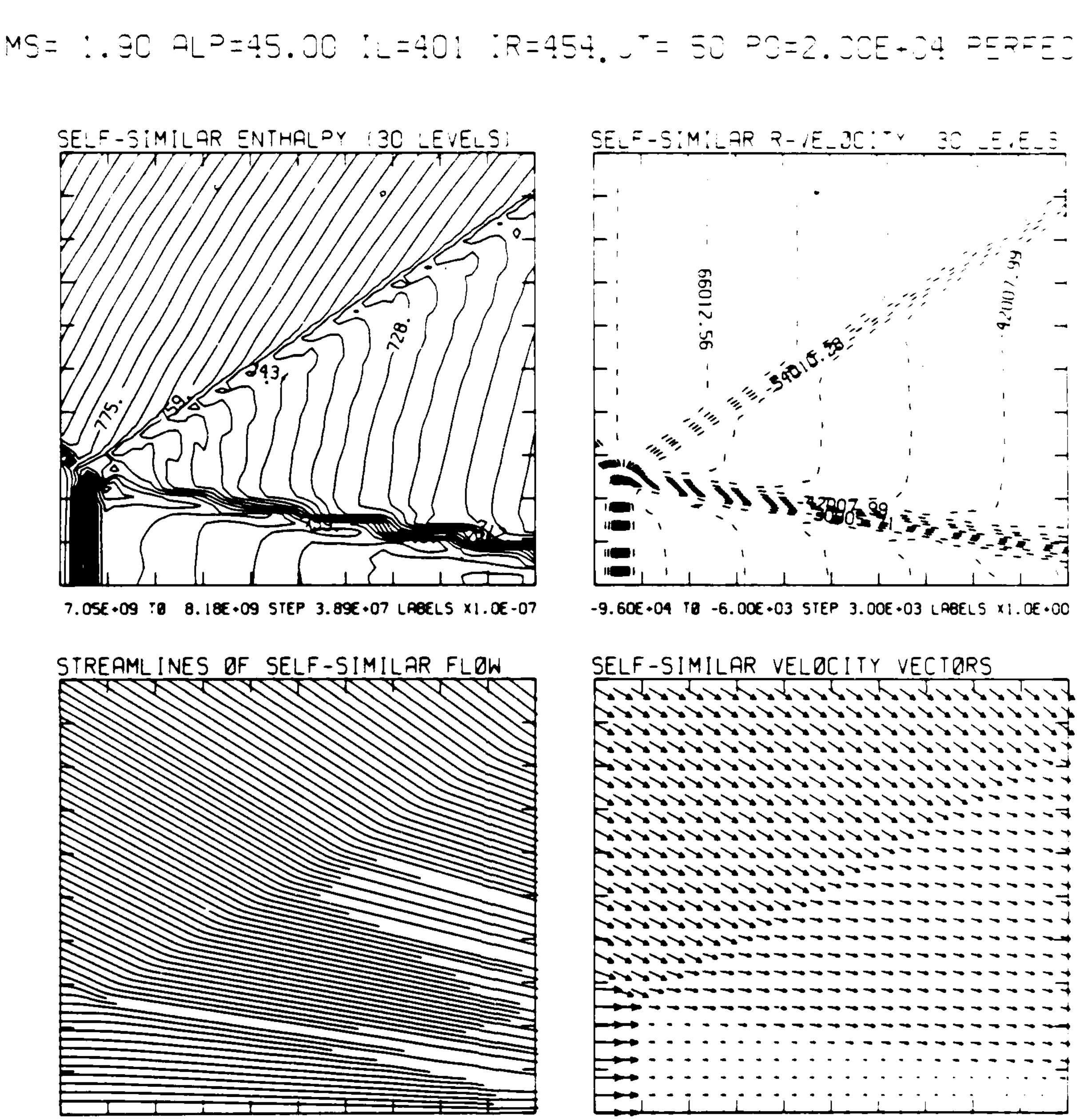

Figure 19.7b. M_S = 1.90, blowup-frame plots - continued.

Figure 19. Transition set 1, θ_w = 45°, γ = 1.4 - continued.

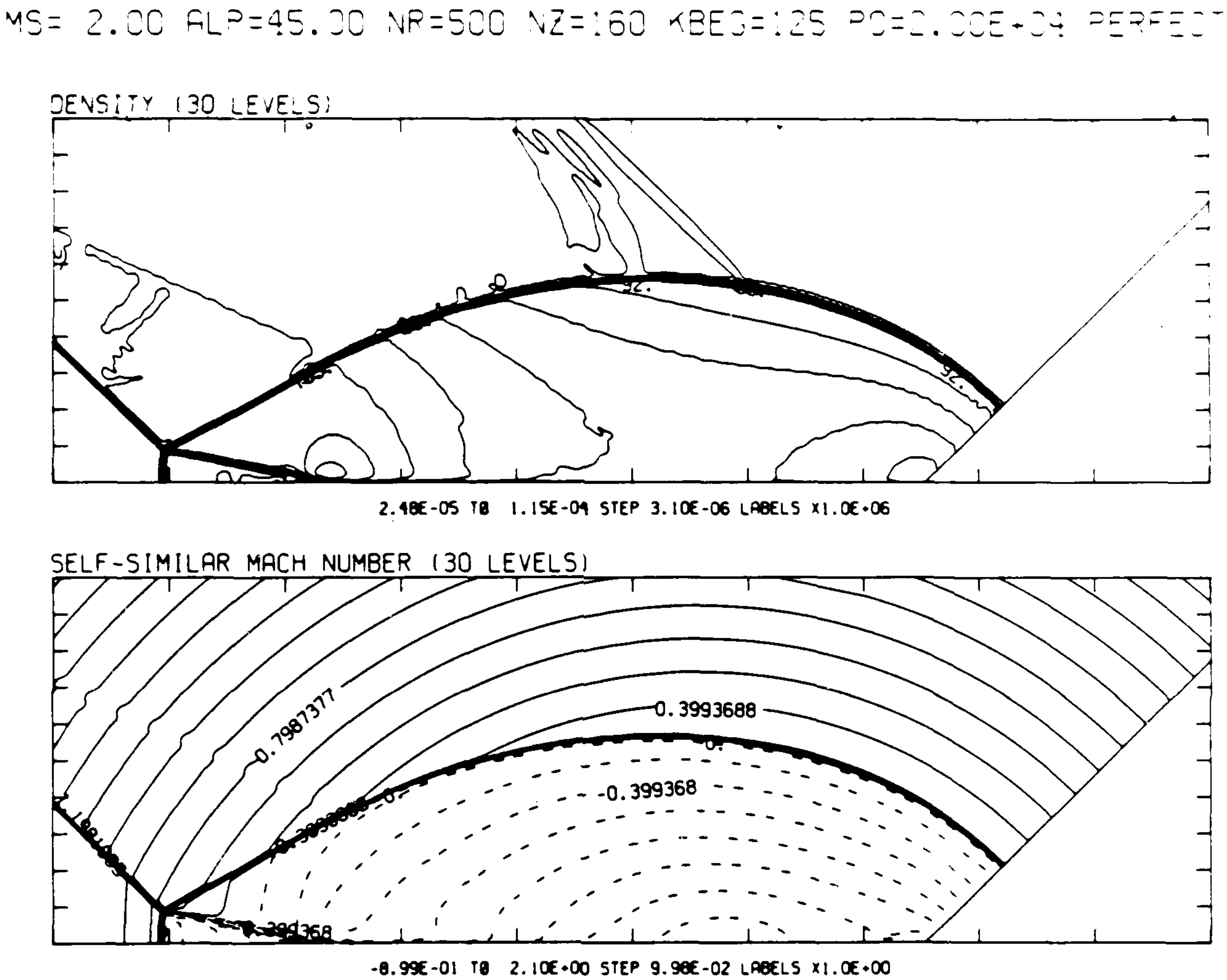

Figure 19.8a. M_s = 2.00, whole-flowfield contour-plots.

Figure 19. Transition set 1, θ_w = 45°, γ = 1.4 - continued.

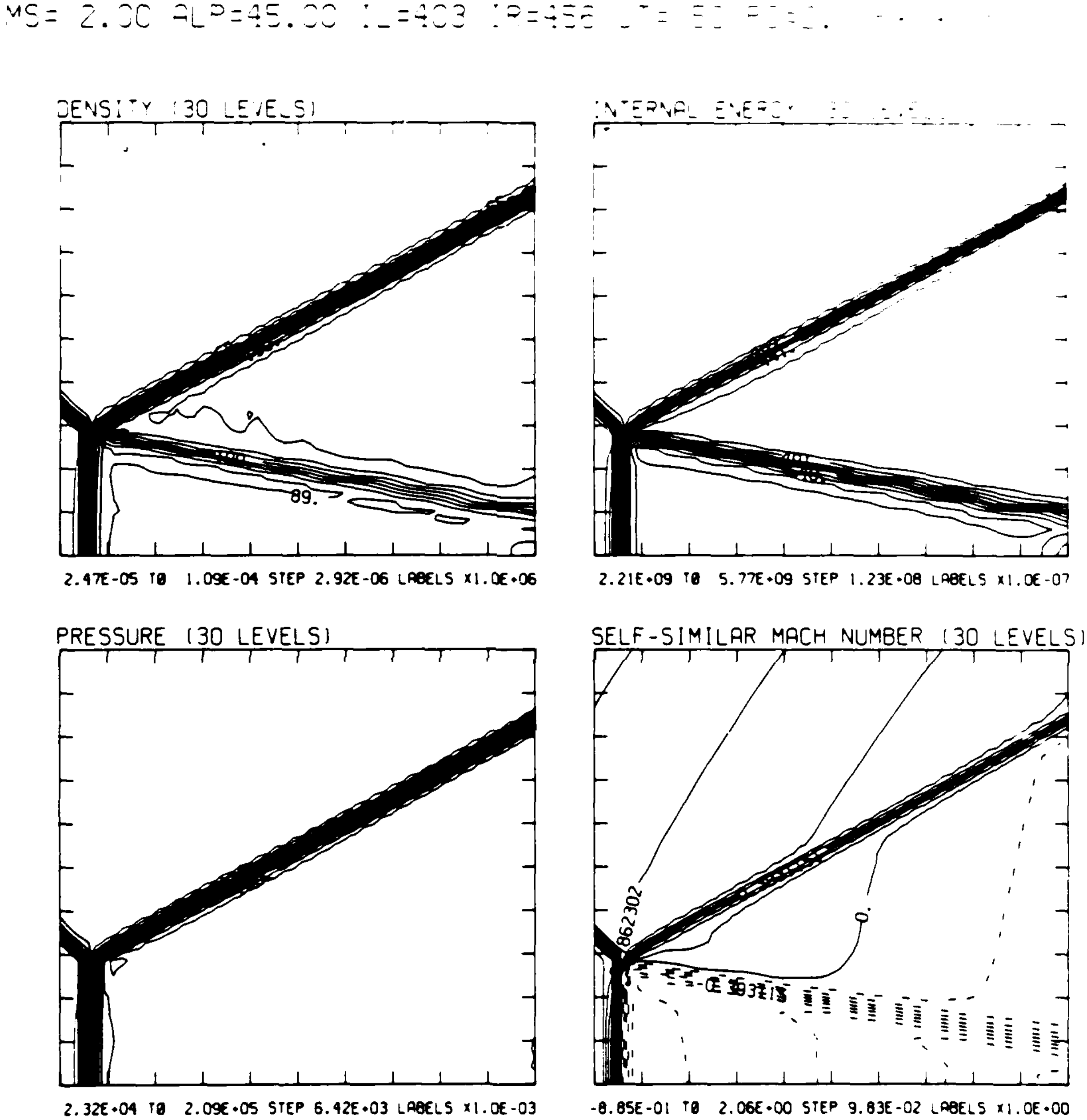

Figure 19.8b. M_s = 2.00, blowup-frame plots.

Figure 19. Transition set 1, θ_w = 45°, γ = 1.4 - continued.

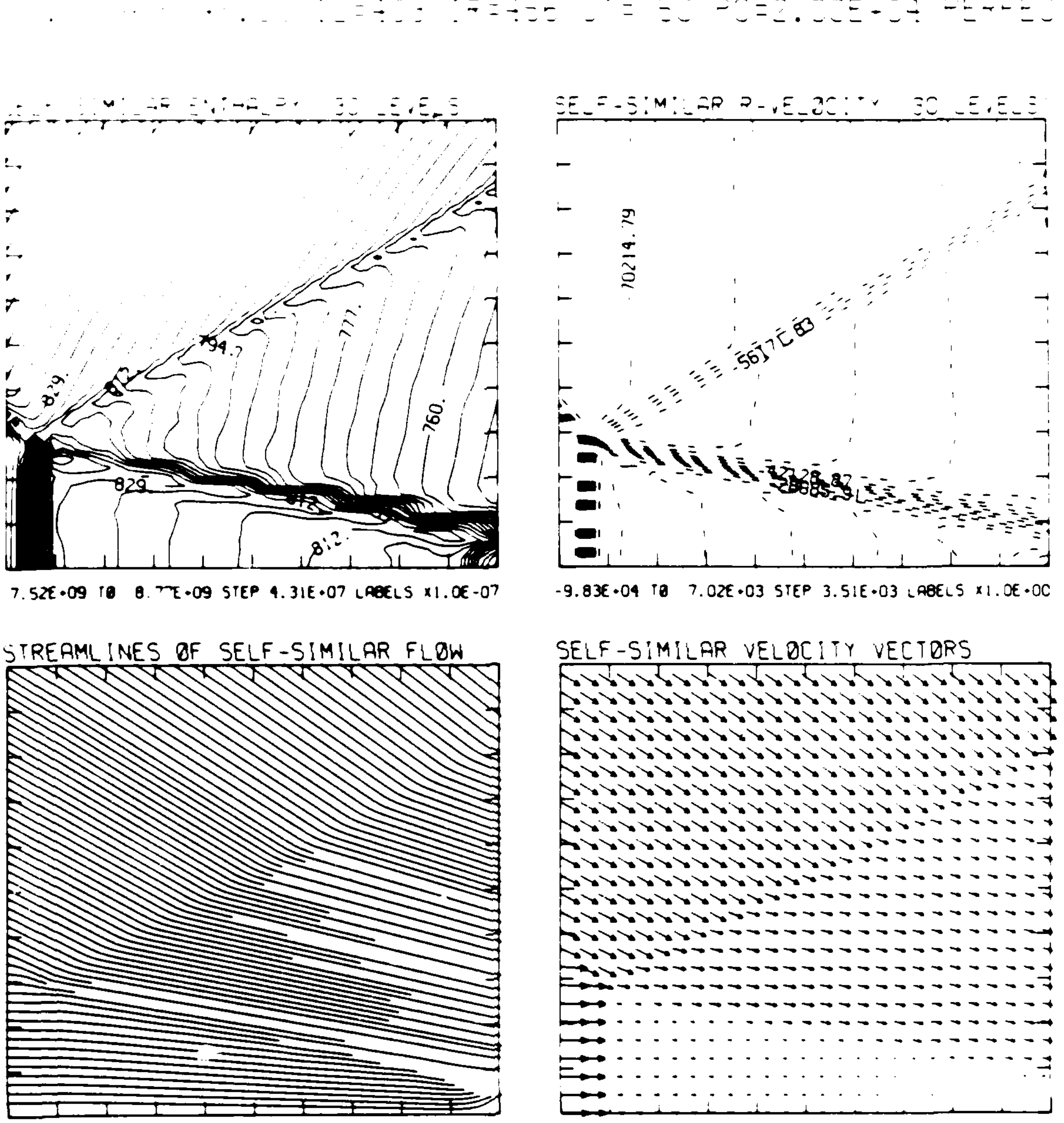

Figure 19.8b. M_s = 2.00, blowup-frame plots - continued.

Figure 19. Transition set 1, θ_w = 45°, γ = 1.4 - continued.

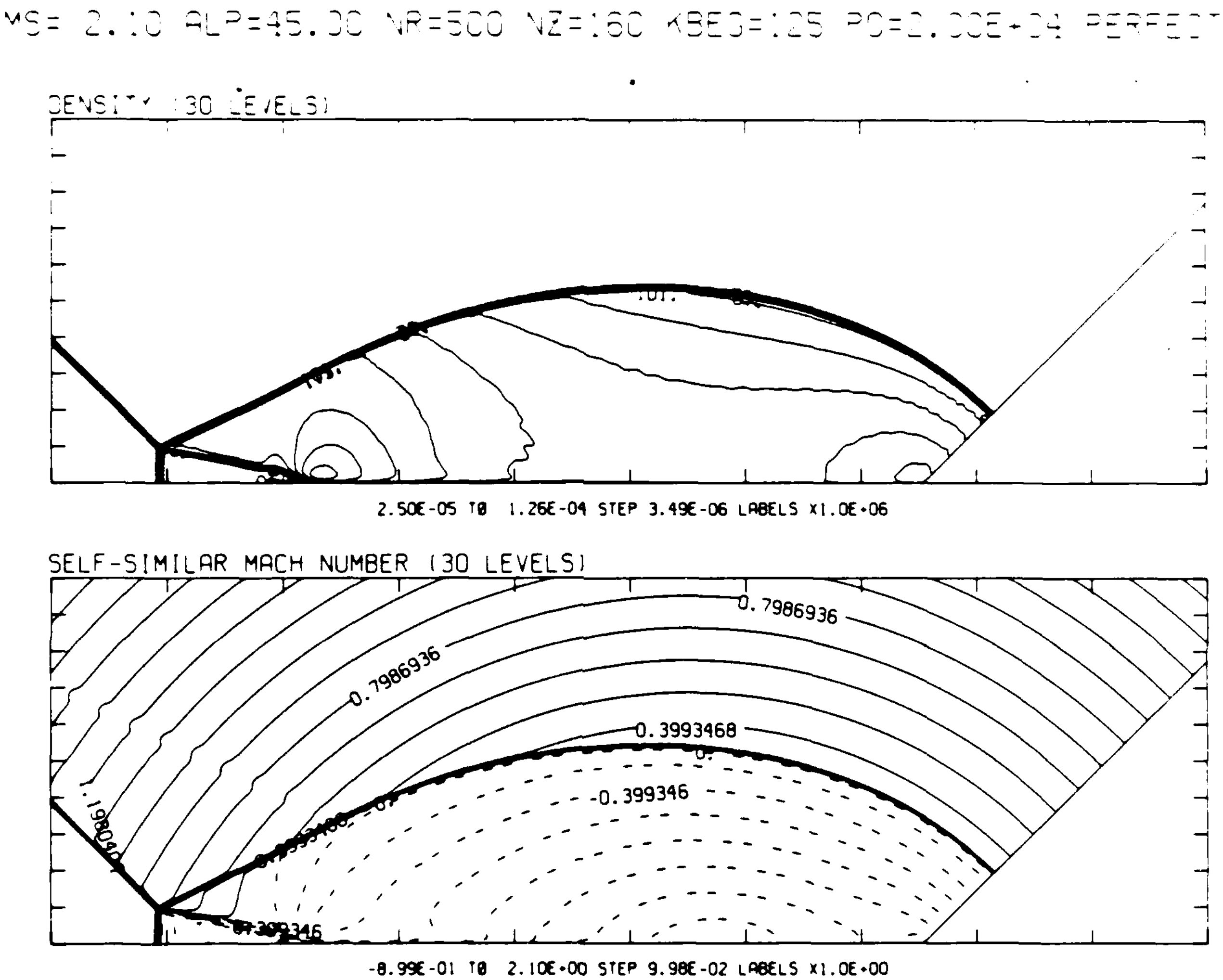

Figure 19.9a. M_s = 2.10, whole-flowfield contour-plots.

Figure 19. Transition set 1, θ_w = 45°, γ = 1.4 - continued.

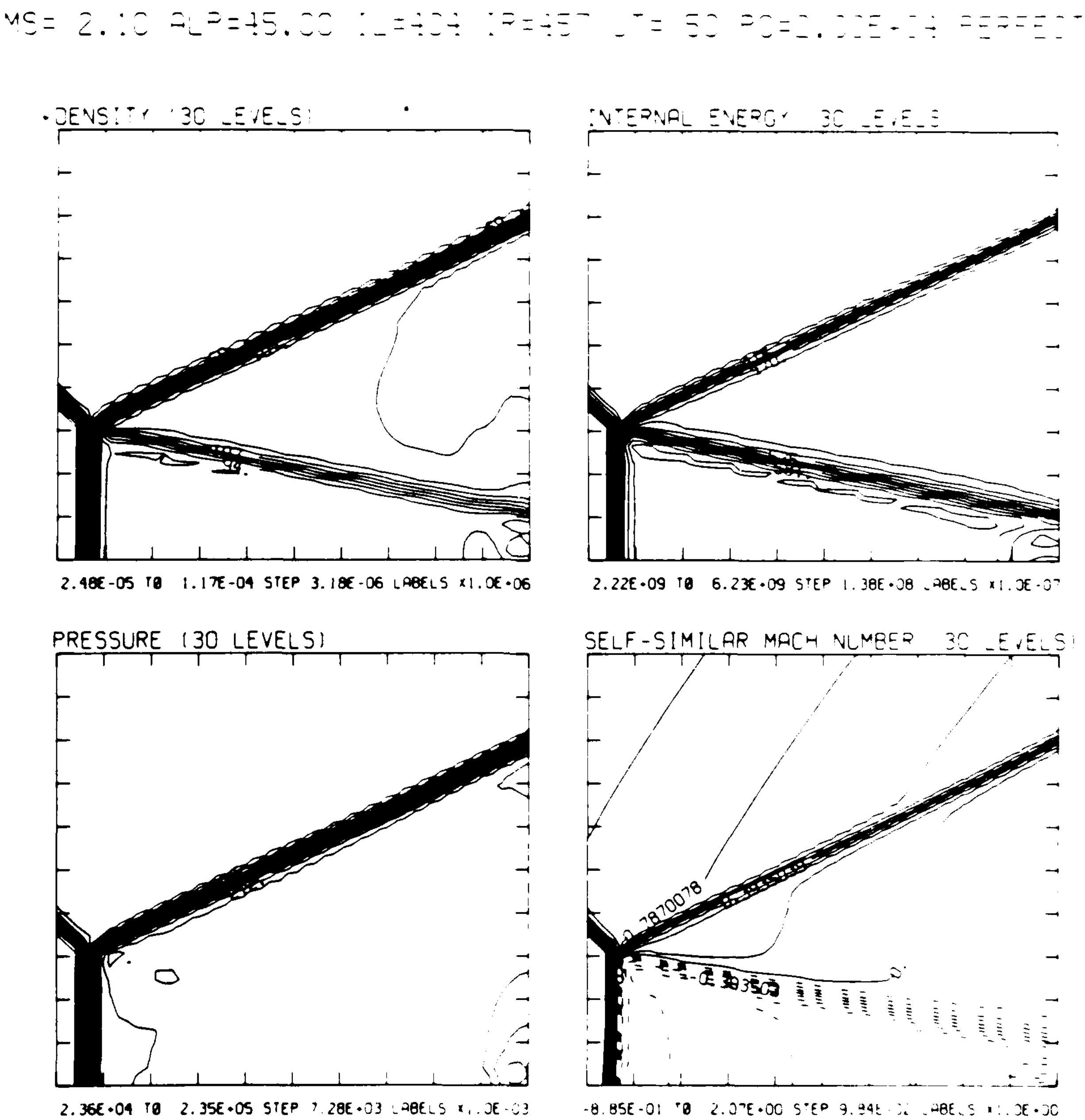

Figure 19.9b. M_s = 2.10, blowup-frame plots.

Figure 19. Transition set 1, θ_w = 45°, γ = 1.4 - continued.

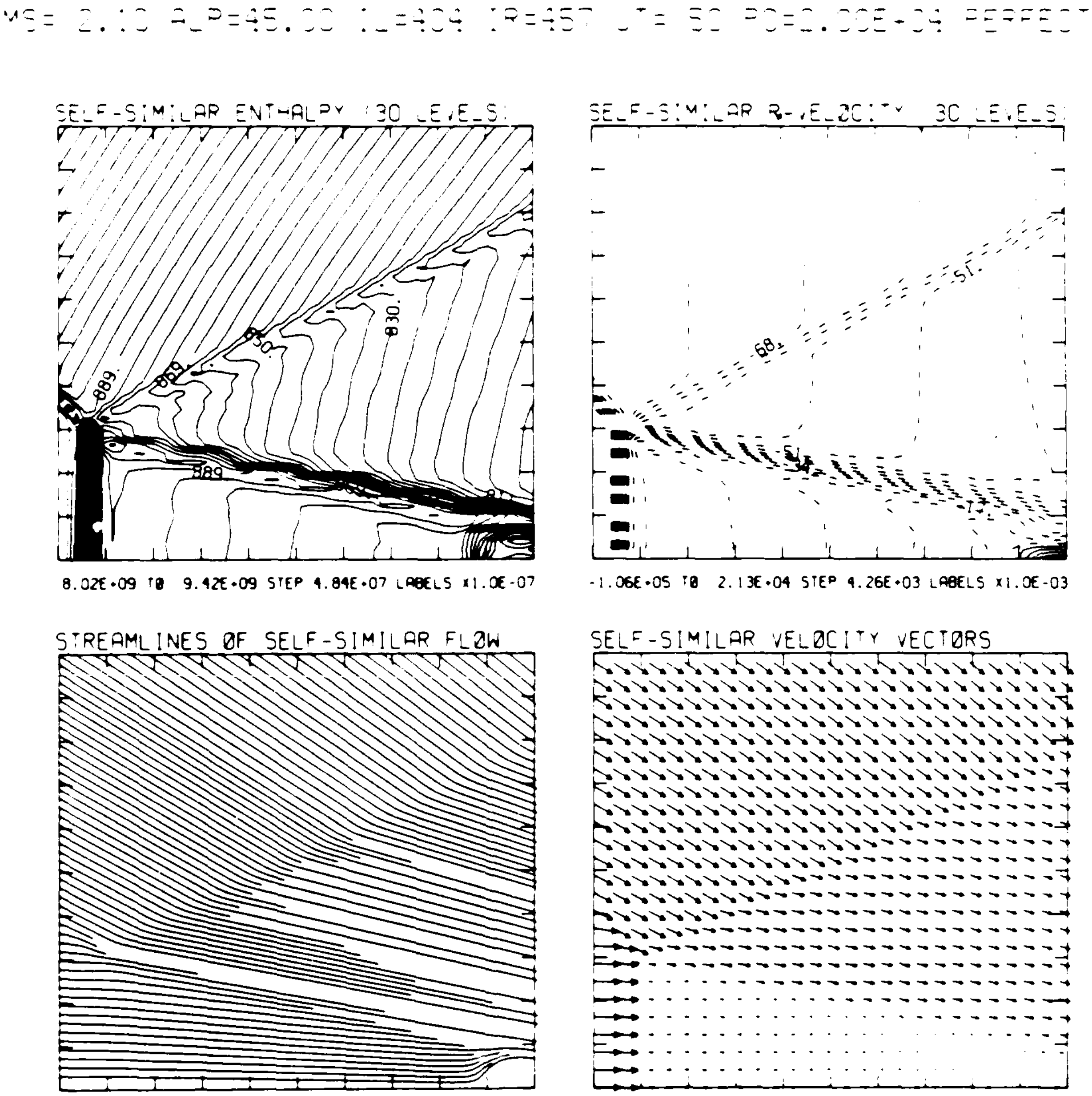

Figure 19.9b. M_s = 2.10, blowup-frame plots - continued.

Figure 19. Transition set 1, θ_w = 45°, γ = 1.4 - continued.

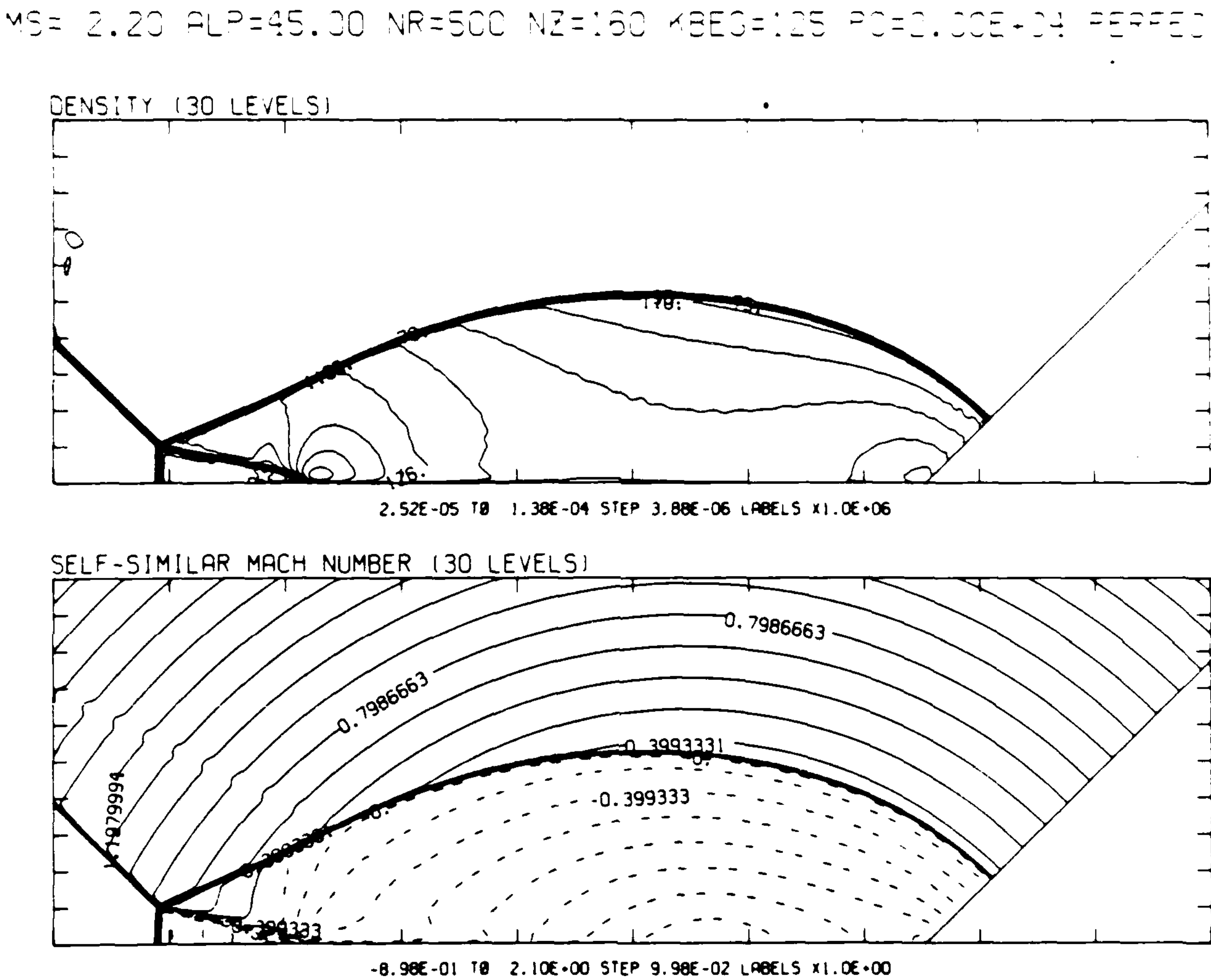

Figure 19.10a. M_s = 2.20, whole-flowfield contour-plots.

Figure 19. Transition set 1, θ_w = 45°, γ = 1.4 - continued.

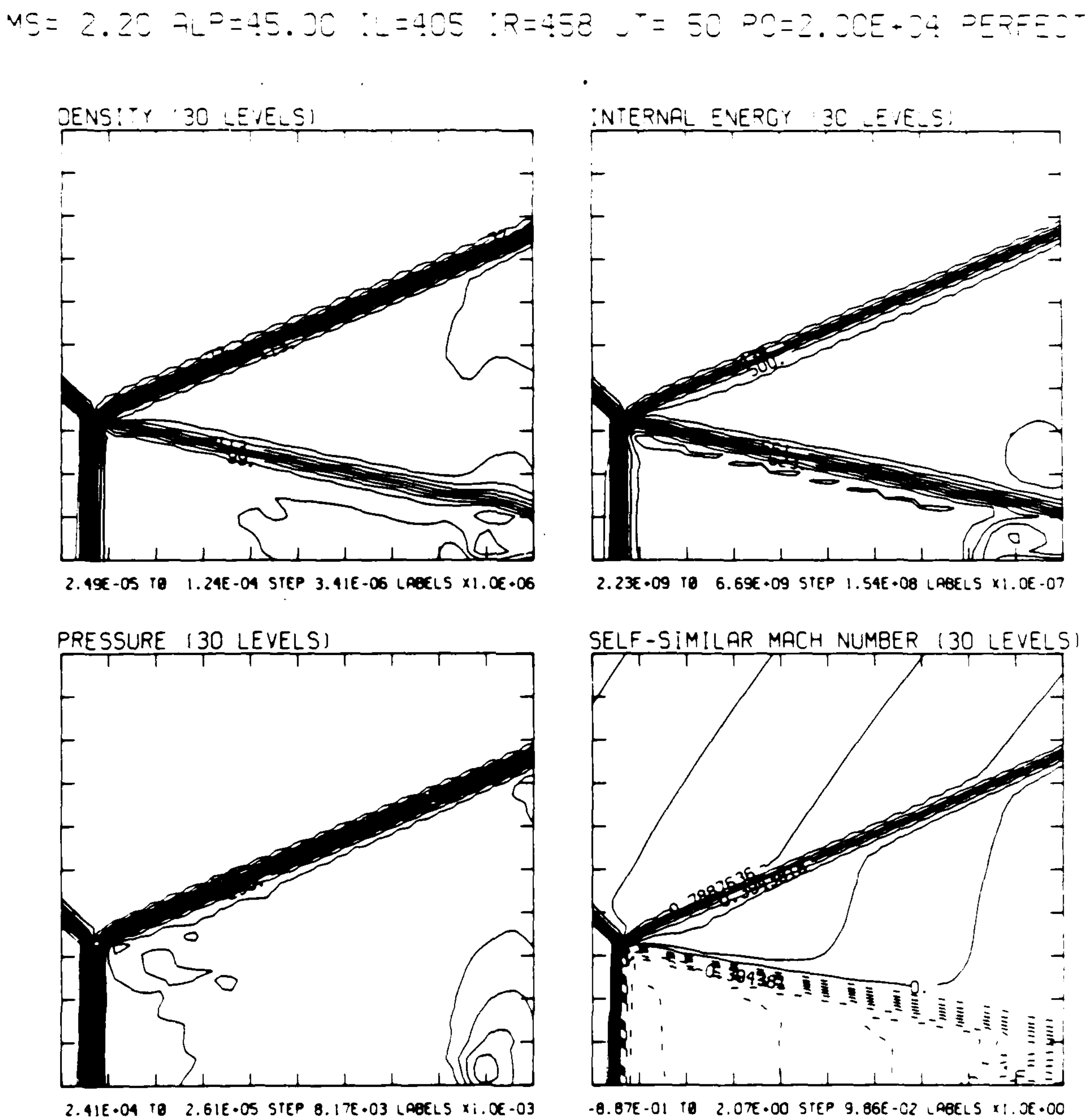

Figure 19.10b. M_s = 2.20, blowup-frame plots.

Figure 19. Transition set 1, θ_w = 45°, γ = 1.4 - continued.

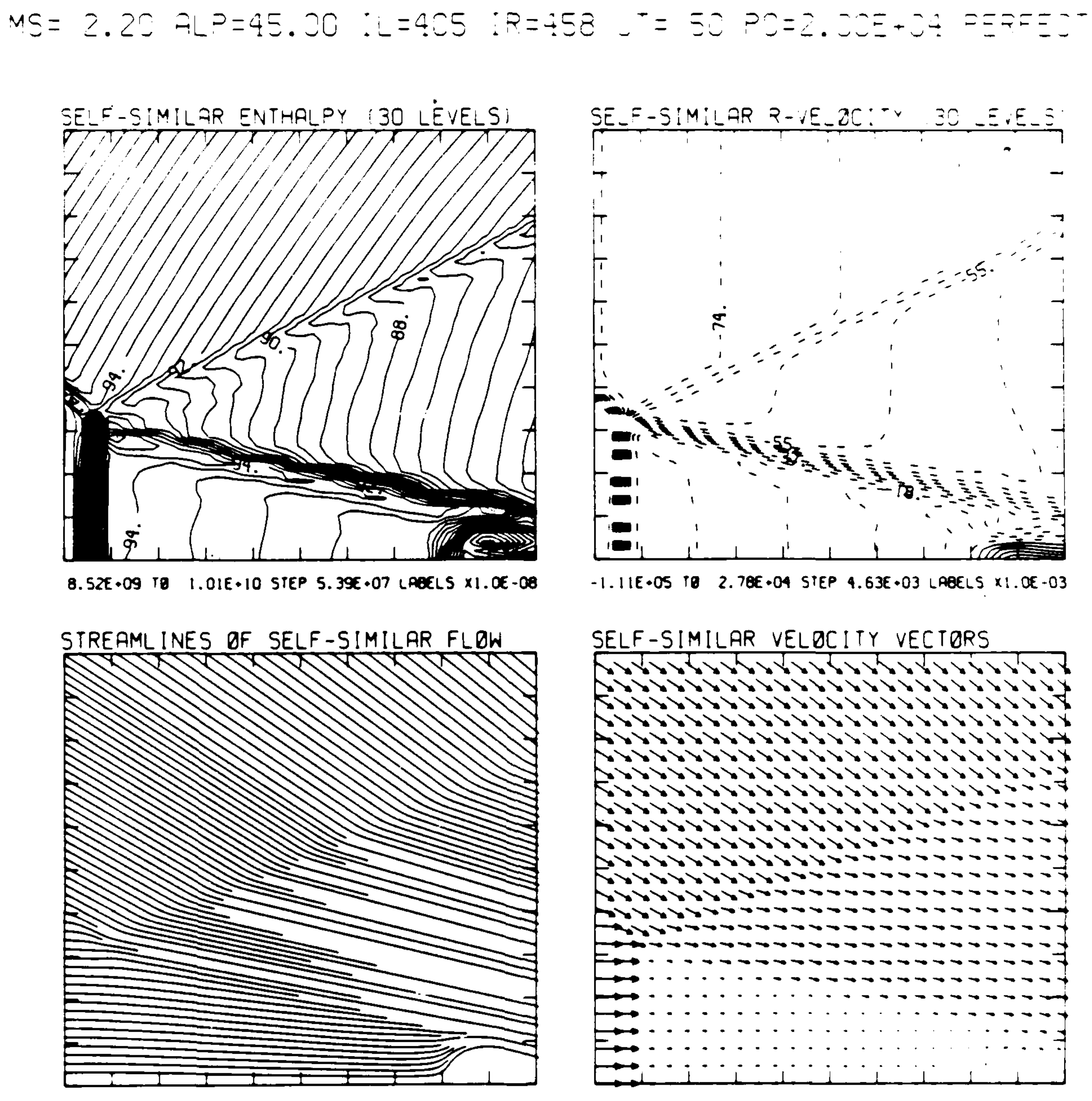

Figure 19.10b. M_S = 2.20, blowup-frame plots - continued.

Figure 19. Transition set 1, θ_W = 45°, γ = 1.4 - continued.

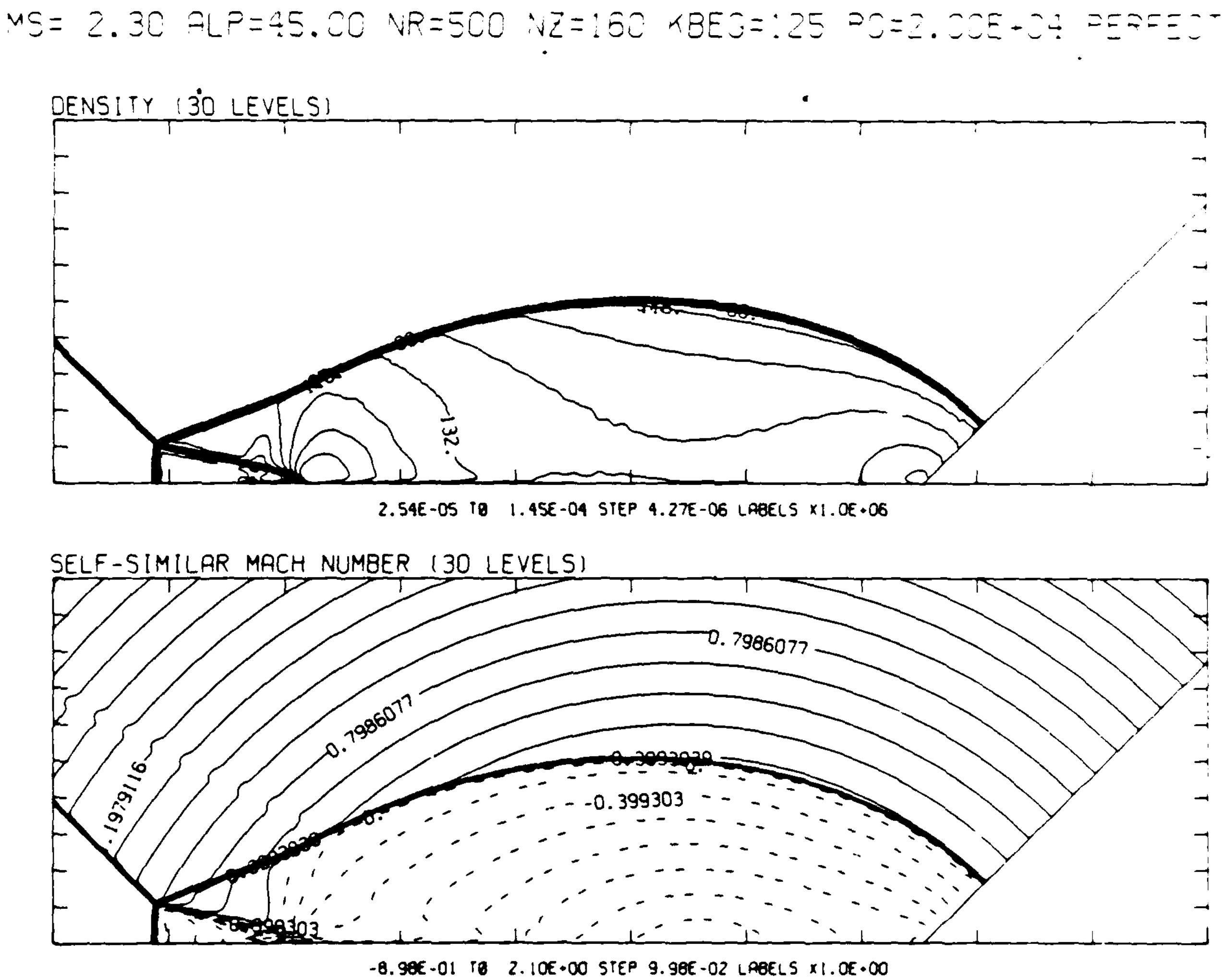

Figure 19.11a. M_s = 2.30, whole-flowfield contour-plots.

Figure 19. Transition set 1, θ_w = 45°, γ = 1.4 - continued.

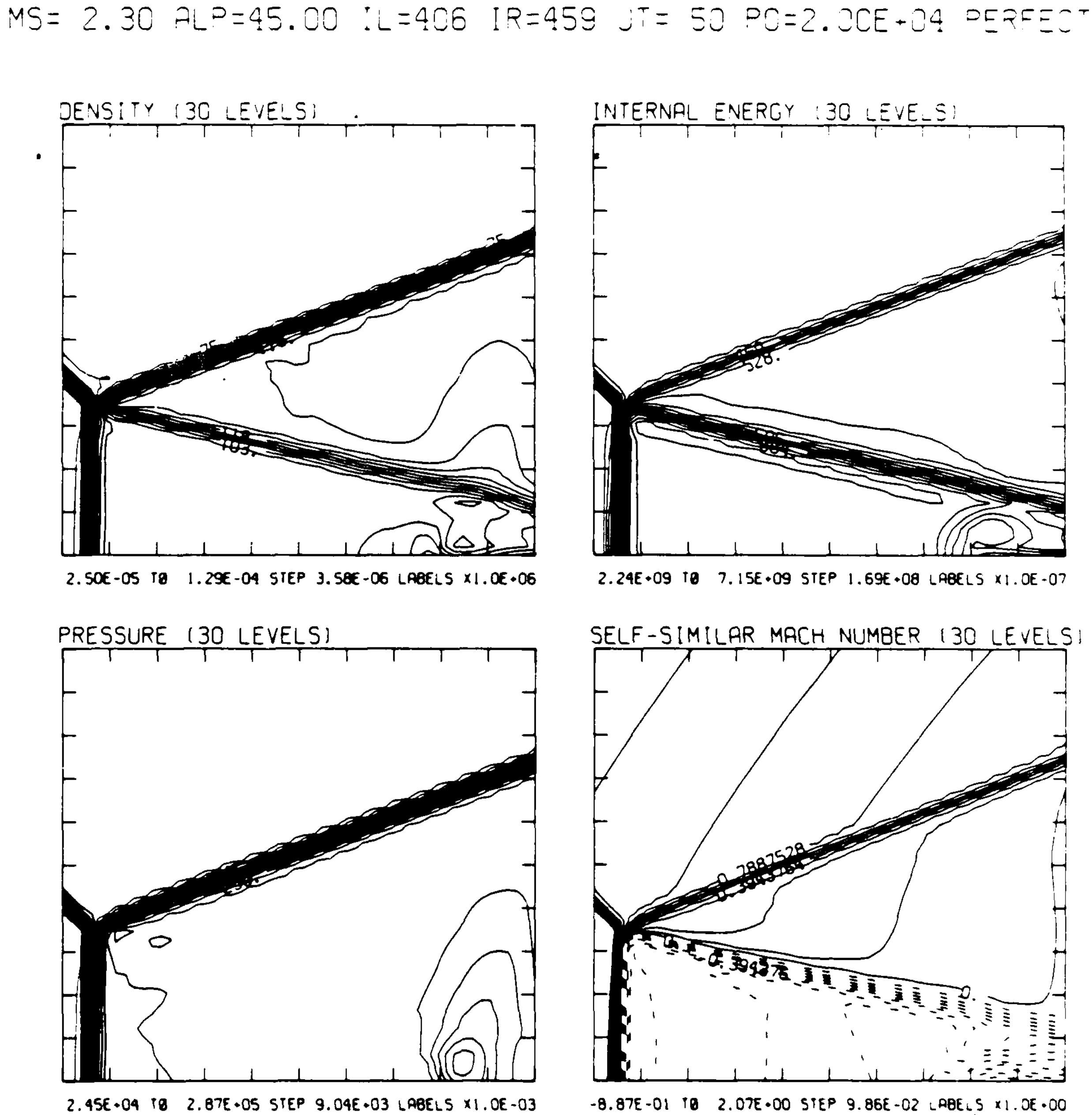

Figure 19.11b. $M_s \doteq 2.30$, blowup-frame plots.

Figure 19. Transition set 1, $\theta_w = 45°$, $\gamma = 1.4$ - continued.

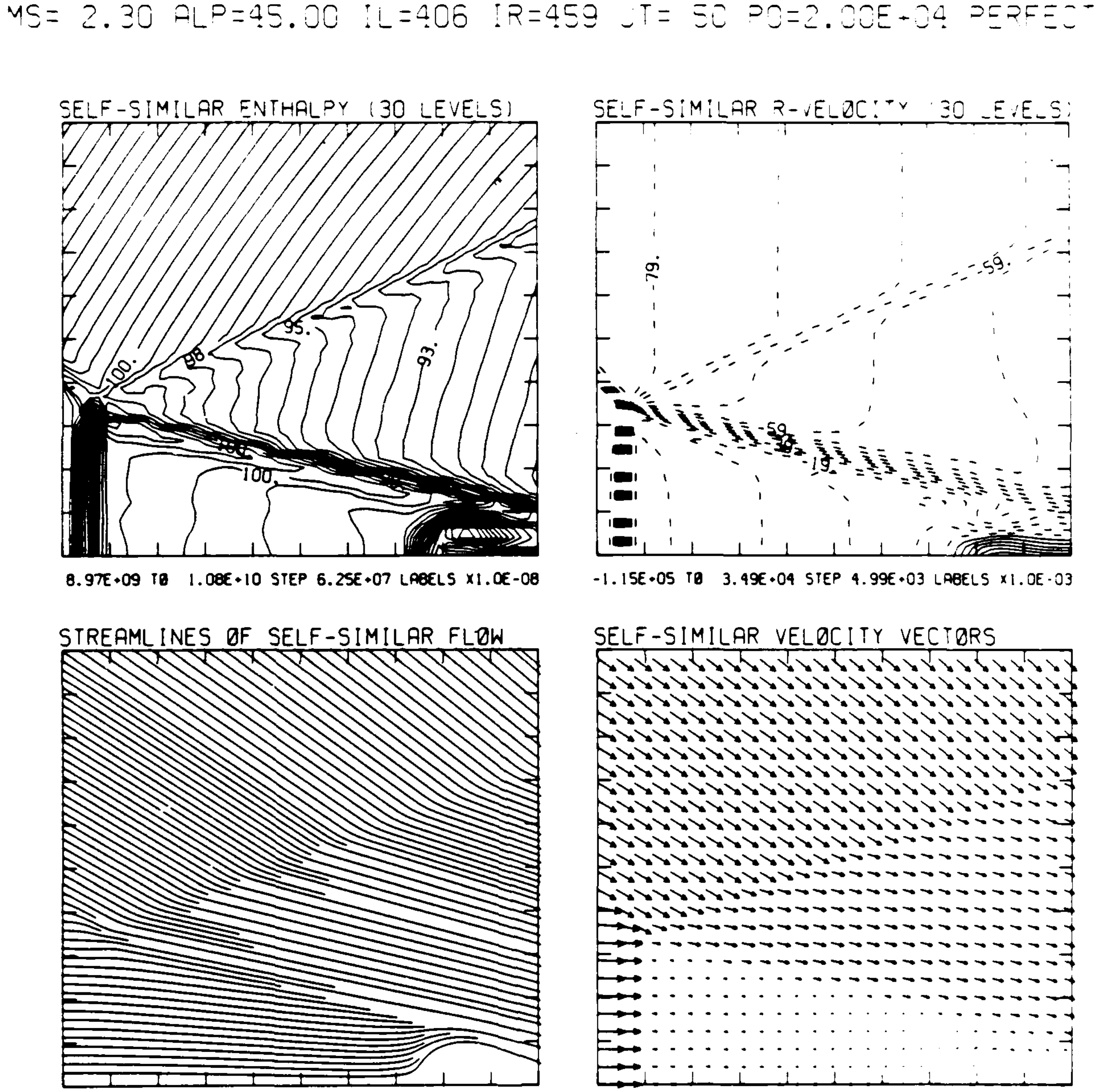

Figure 19.11b. M_s = 2.30, blowup-frame plots - continued.

Figure 19. Transition set 1, θ_w = 45°, γ = 1.4 - continued.

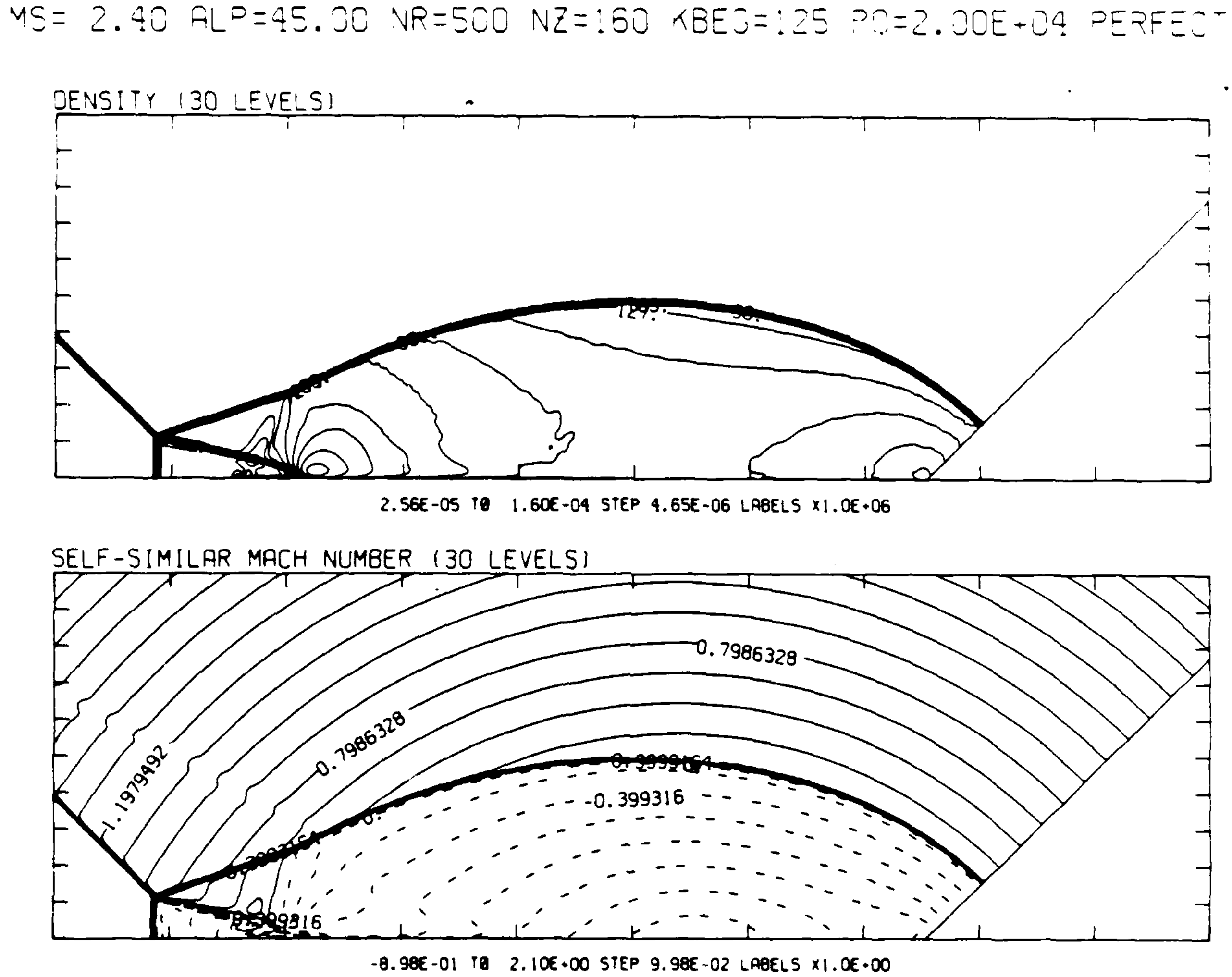

Figure 19.12a. M_s = 2.40, whole-flowfield contour-plots.

Figure 19. Transition set 1, θ_w = 45°, γ = 1.4 - continued.

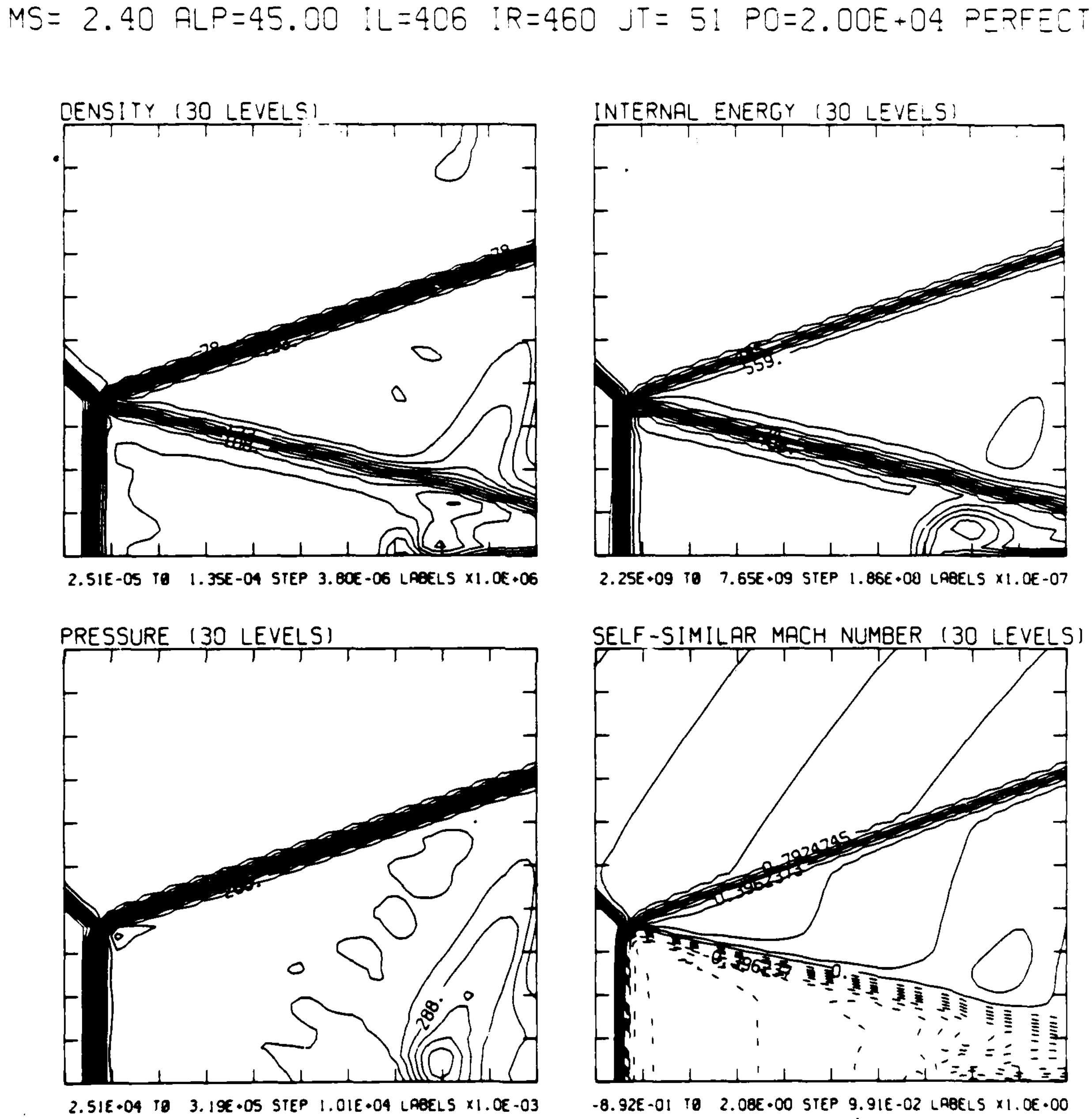

Figure 19.12b. M_s = 2.40, blowup-frame plots.

Figure 19. Transition set 1, θ_w = 45°, γ = 1.4 - continued.

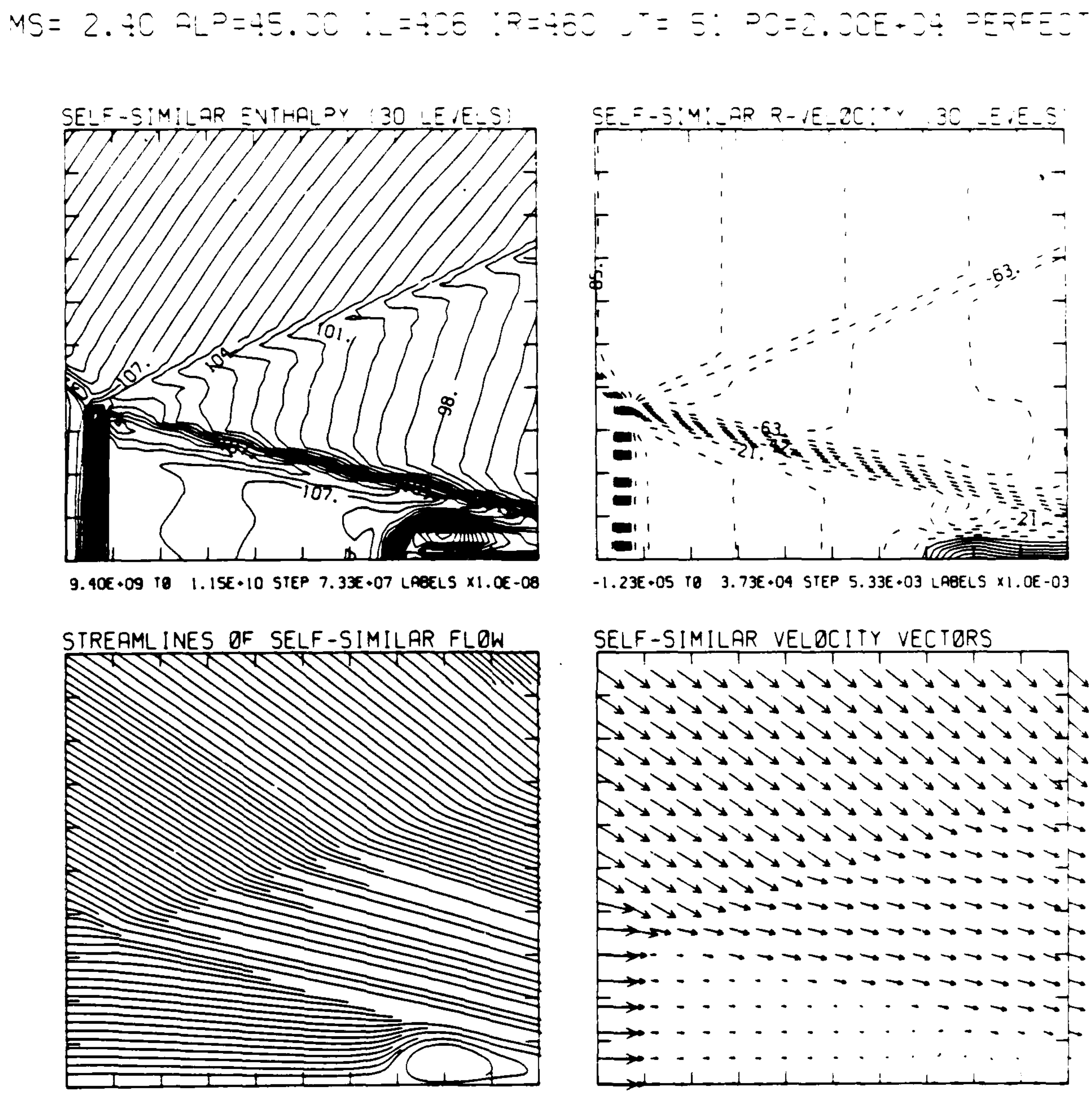

Figure 19.12b. M_s = 2.40, blowup-frame plots - continued.

Figure 19. Transition set 1, θ_w = 45°, γ = 1.4 - continued.

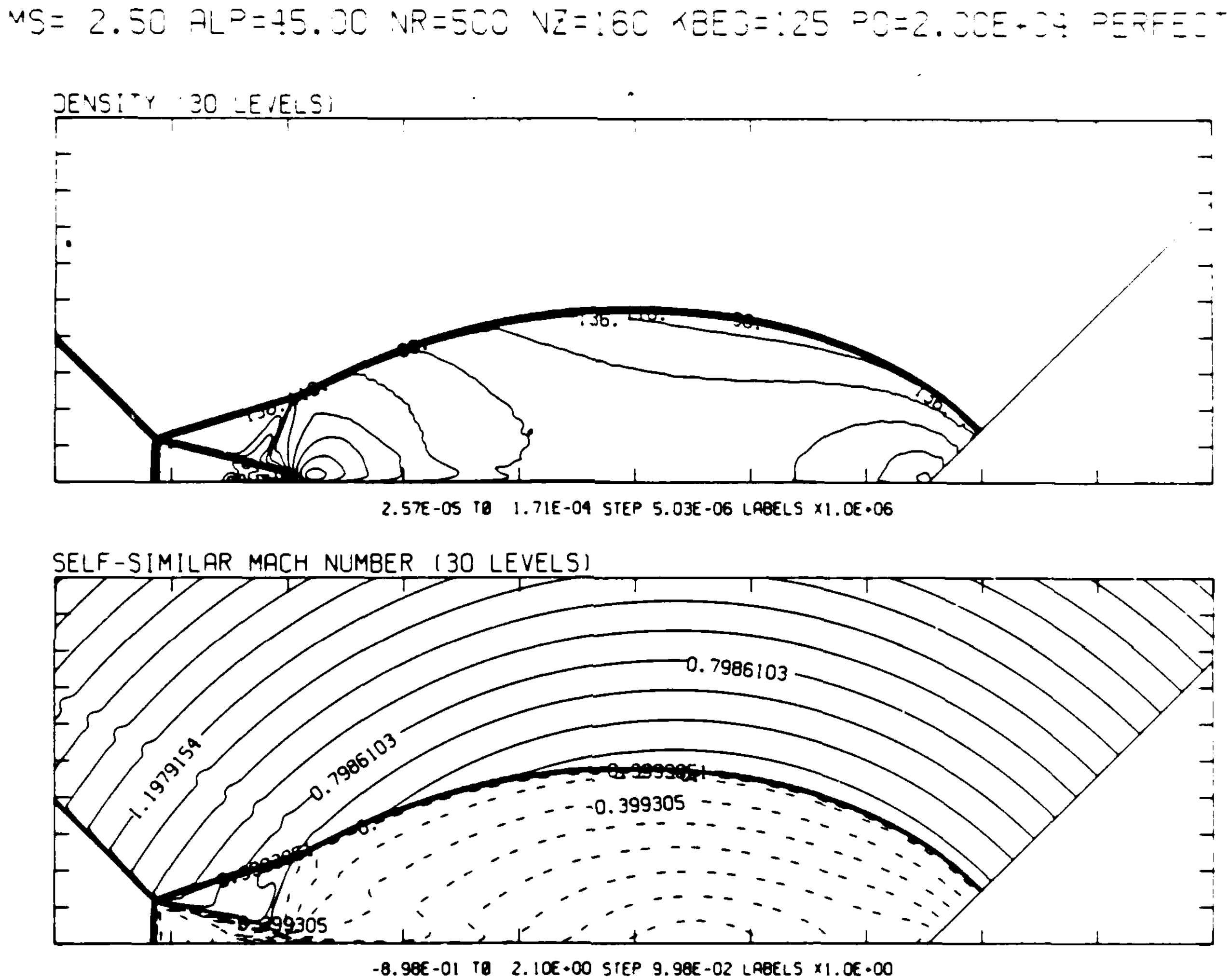

Figure 19.13a. M_s = 2.50, whole-flowfield contour-plots.

Figure 19. Transition set 1, θ_w = 45°, γ = 1.4 - continued.

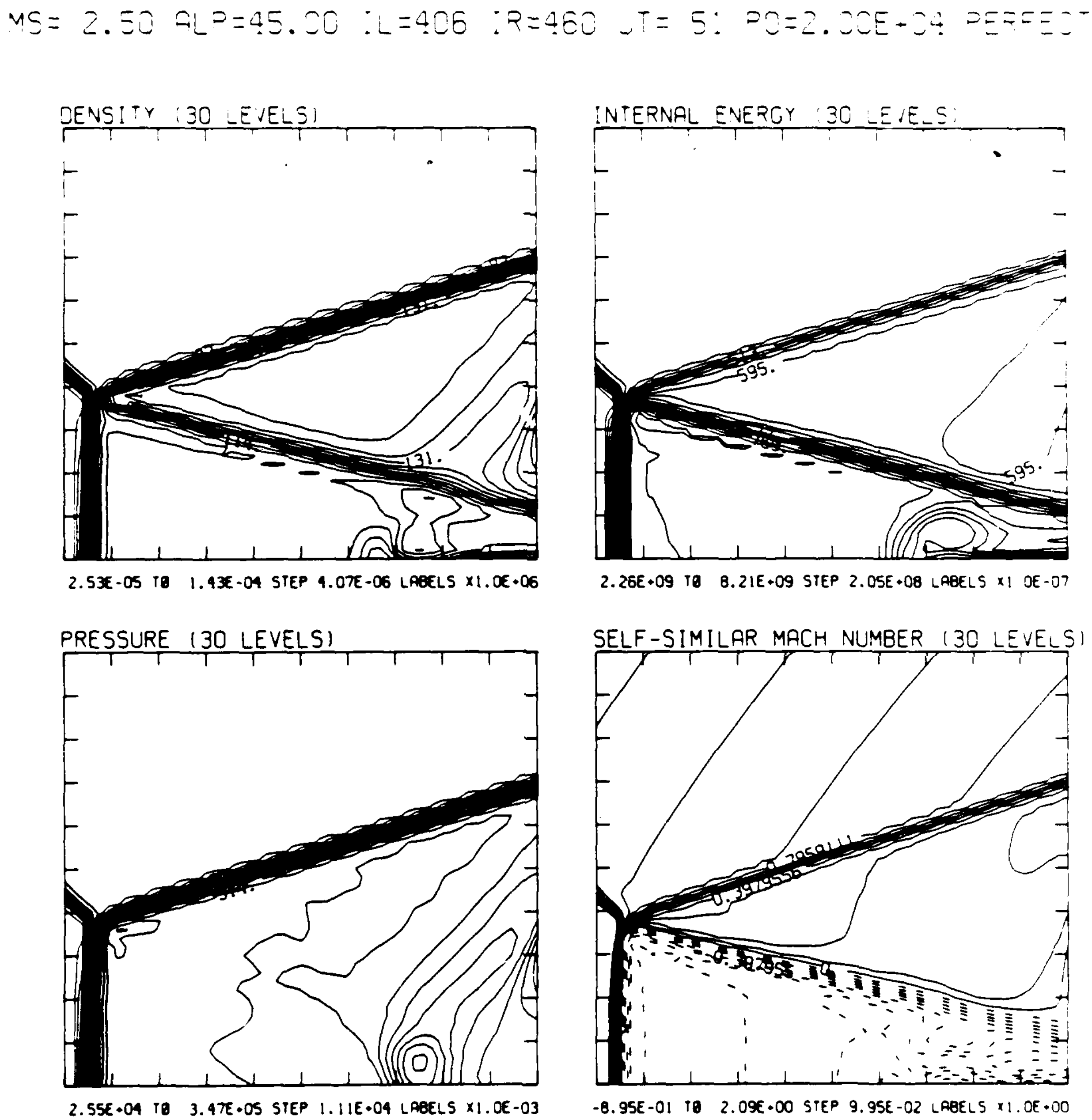

Figure 19.13b. M_S = 2.50, blowup-frame plots.

Figure 19. Transition set 1, θ_w = 45°, γ = 1.4 - continued.

MS= 2.50 ALP=45.00 IL=406 IR=460 JT= 51 PO=2.00E+04 PERFECT

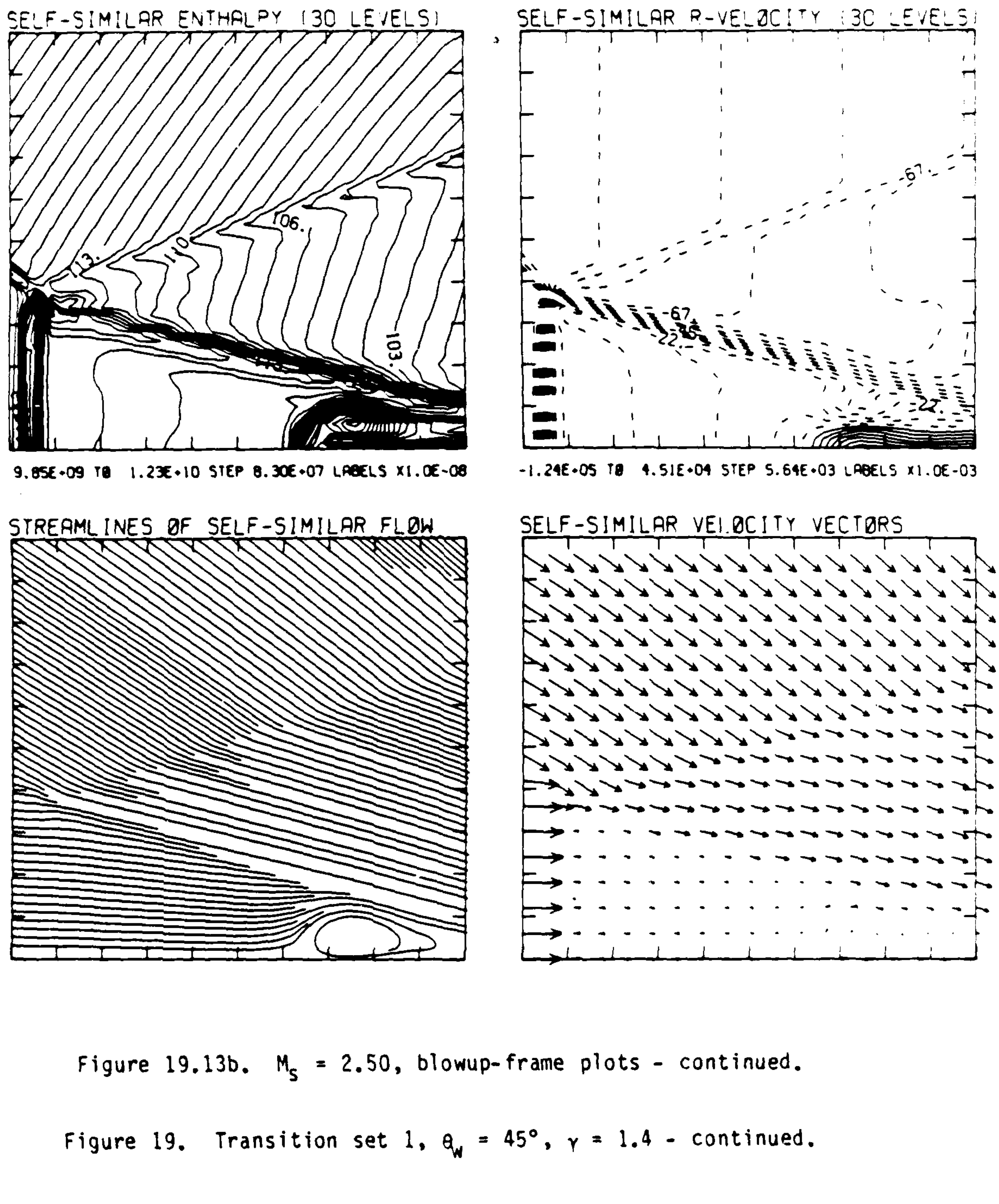

Figure 19.13b. M_s = 2.50, blowup-frame plots - continued.

Figure 19. Transition set 1, θ_w = 45°, γ = 1.4 - continued.

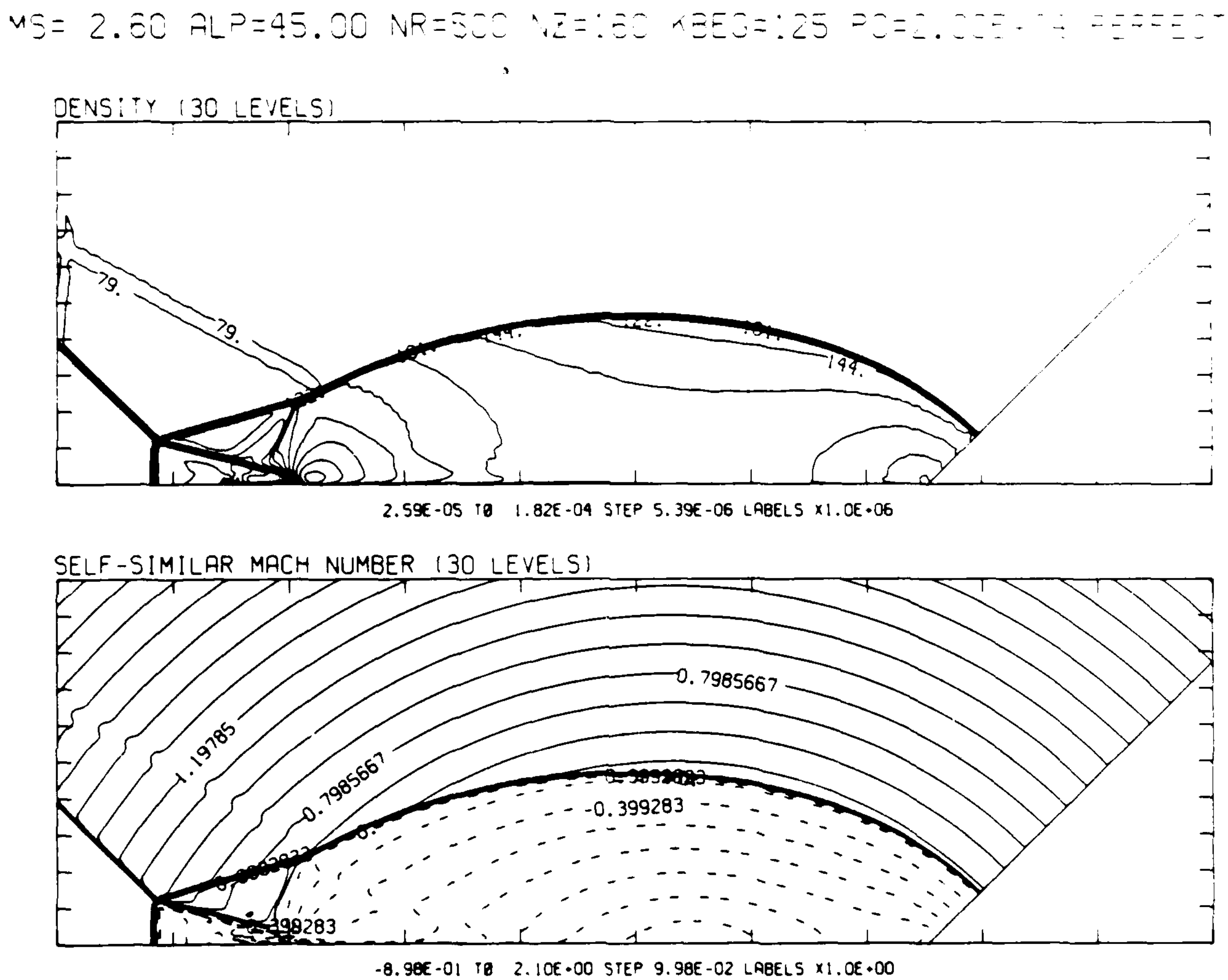

Figure 19.14a. M_s = 2.60, whole-flowfield contour-plots.

Figure 19. Transition set 1, θ_w = 45°, γ = 1.4 - continued.

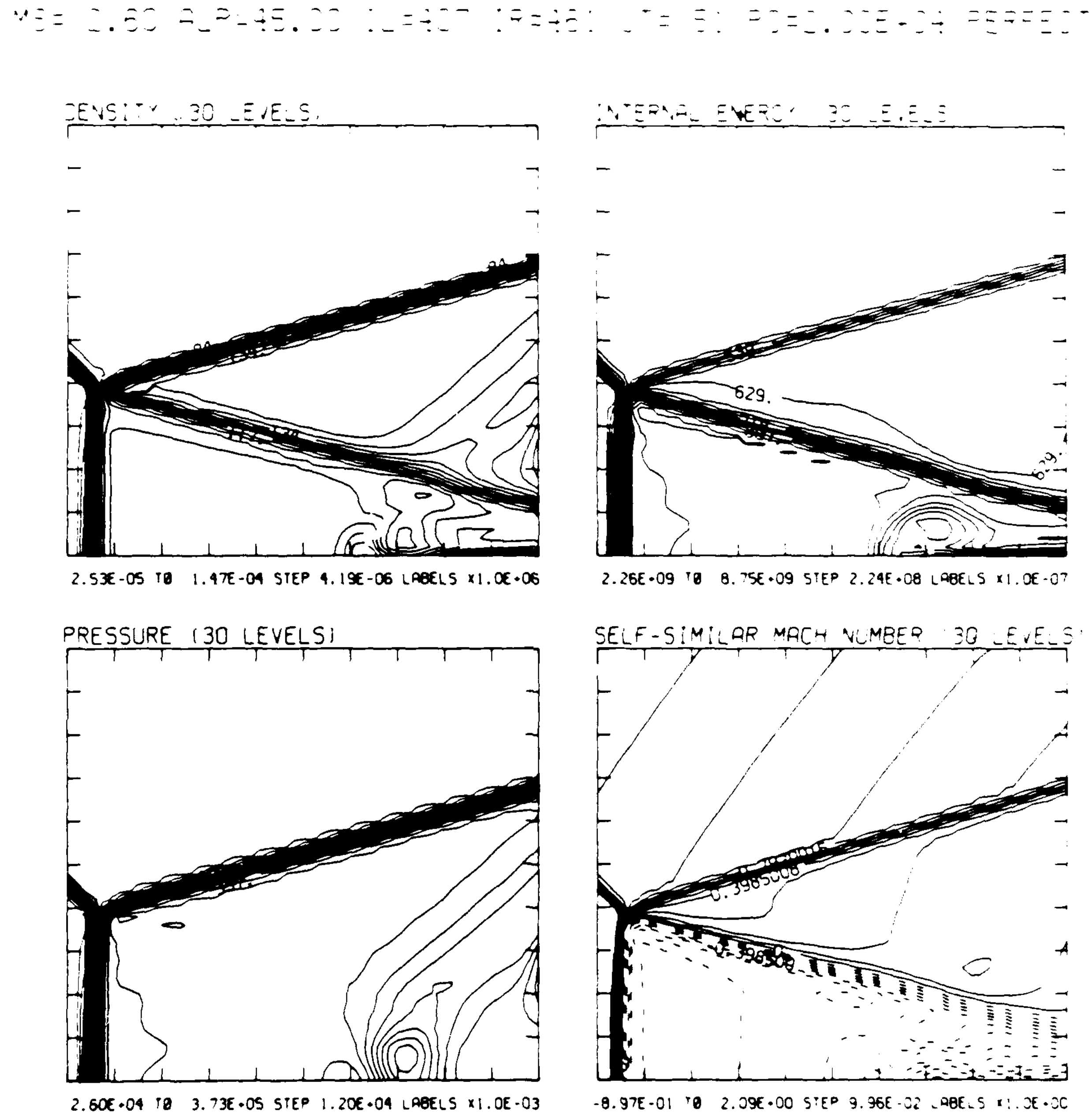

Figure 19.14b. M_s = 2.60, blowup-frame plots.

Figure 19. Transition set 1, θ_w = 45°, γ = 1.4 - continued.

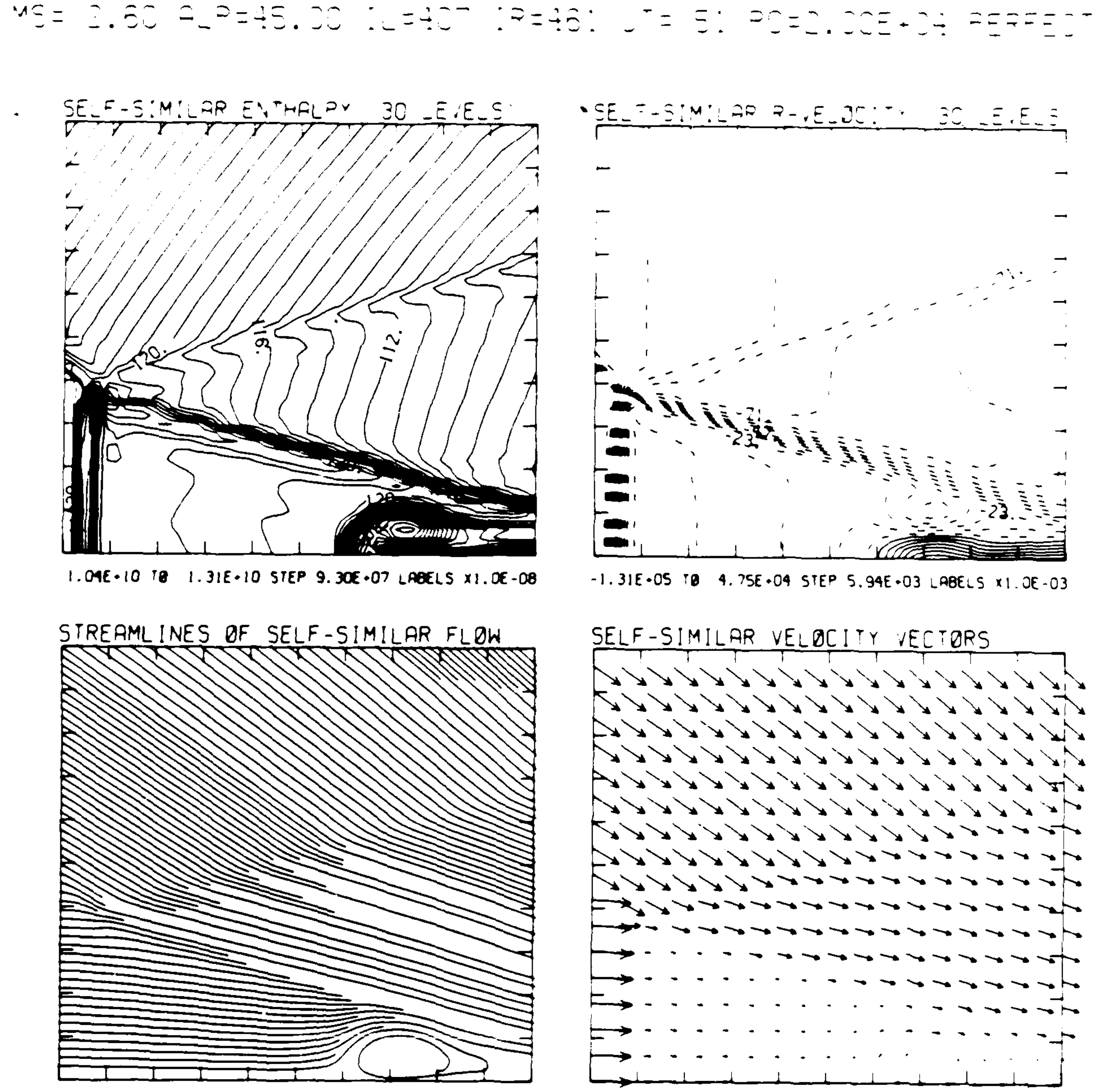

Figure 19.14b. M_s = 2.60, blowup-frame plots - continued.

Figure 19. Transition set 1, θ_w = 45°, γ = 1.4 - continued.

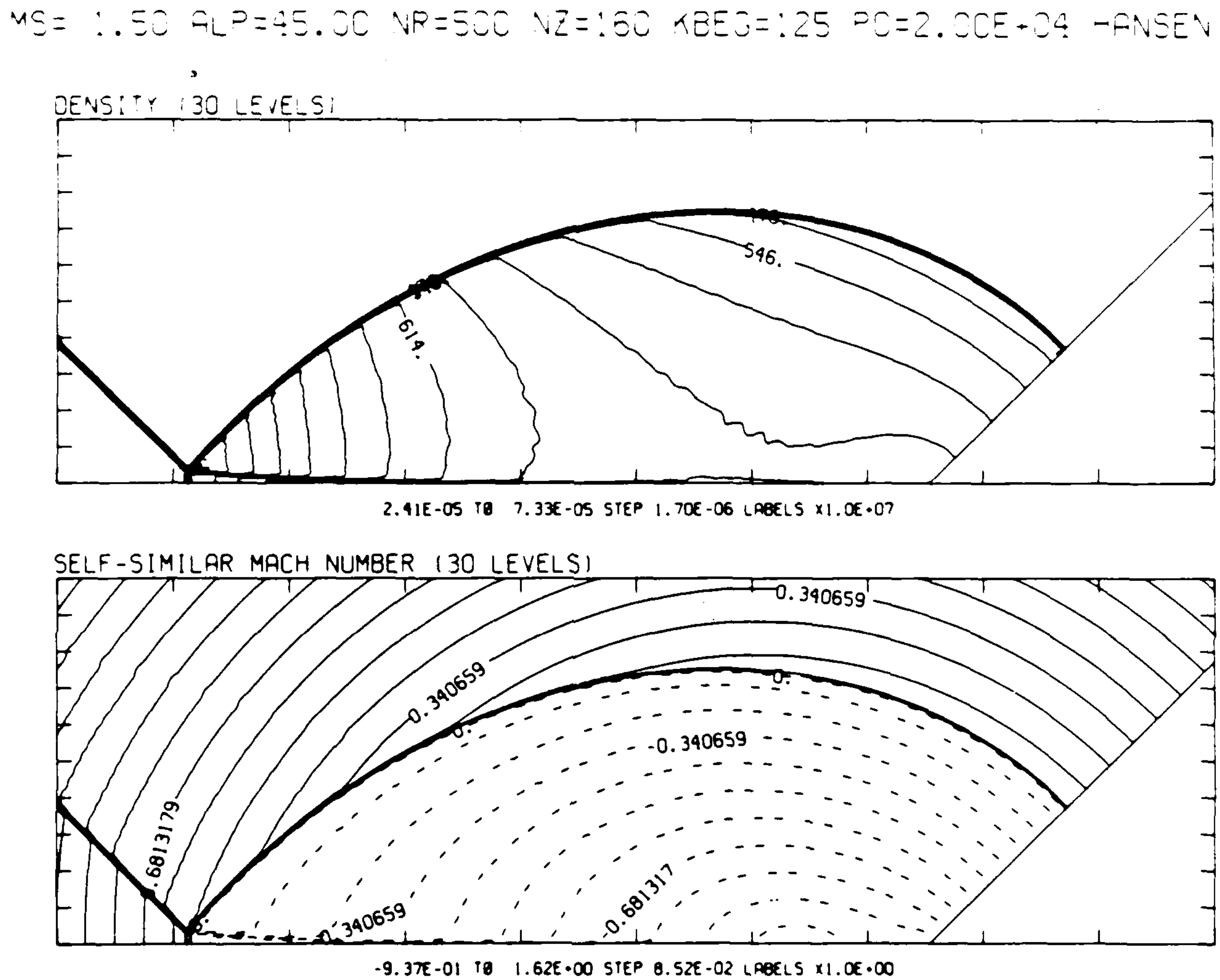

Figure 20.1a. M_s = 1.50, whole-flowfield contour-plots.

Figure 20. Transition set 1, θ_w = 45°, Hansen.

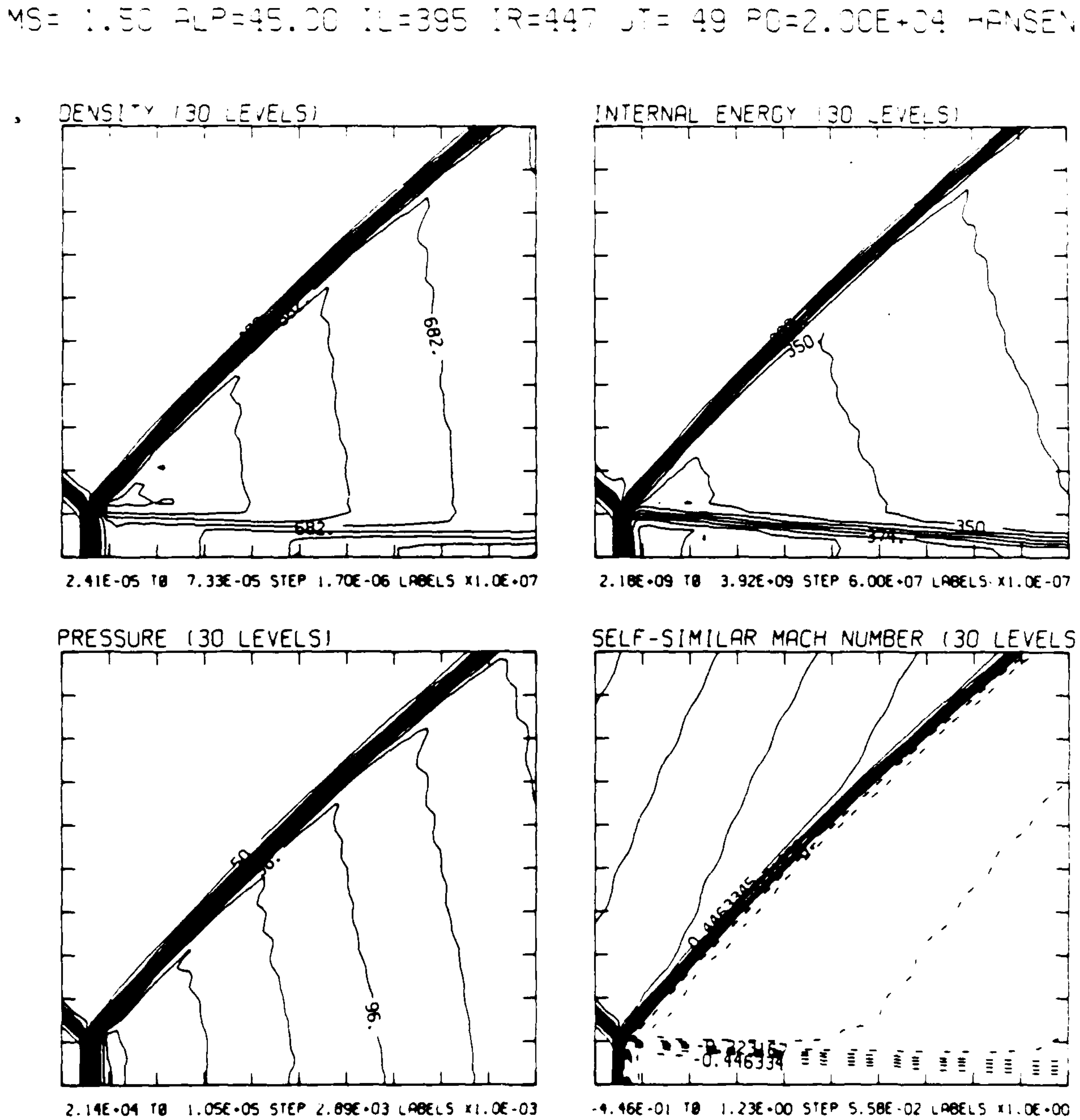

Figure 20.1b. M_s = 1.50, blowup-frame plots.

Figure 20. Transition set 1, θ_w = 45°, Hansen - continued.

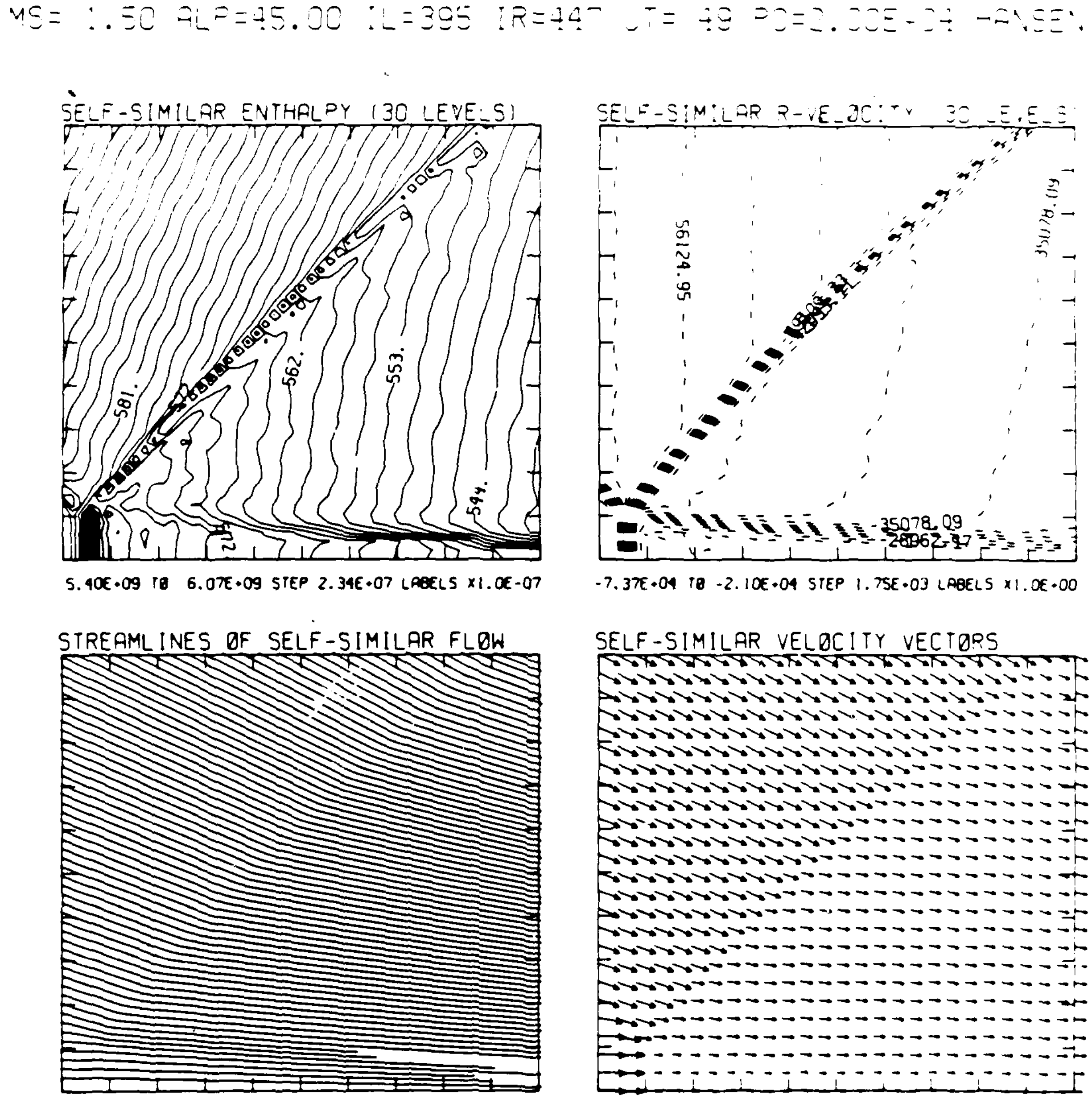

Figure 20.1b. M_s = 1.50, blowup-frame plots - continued.

Figure 20. Transition set 1, θ_w = 45°, Hansen - continued.

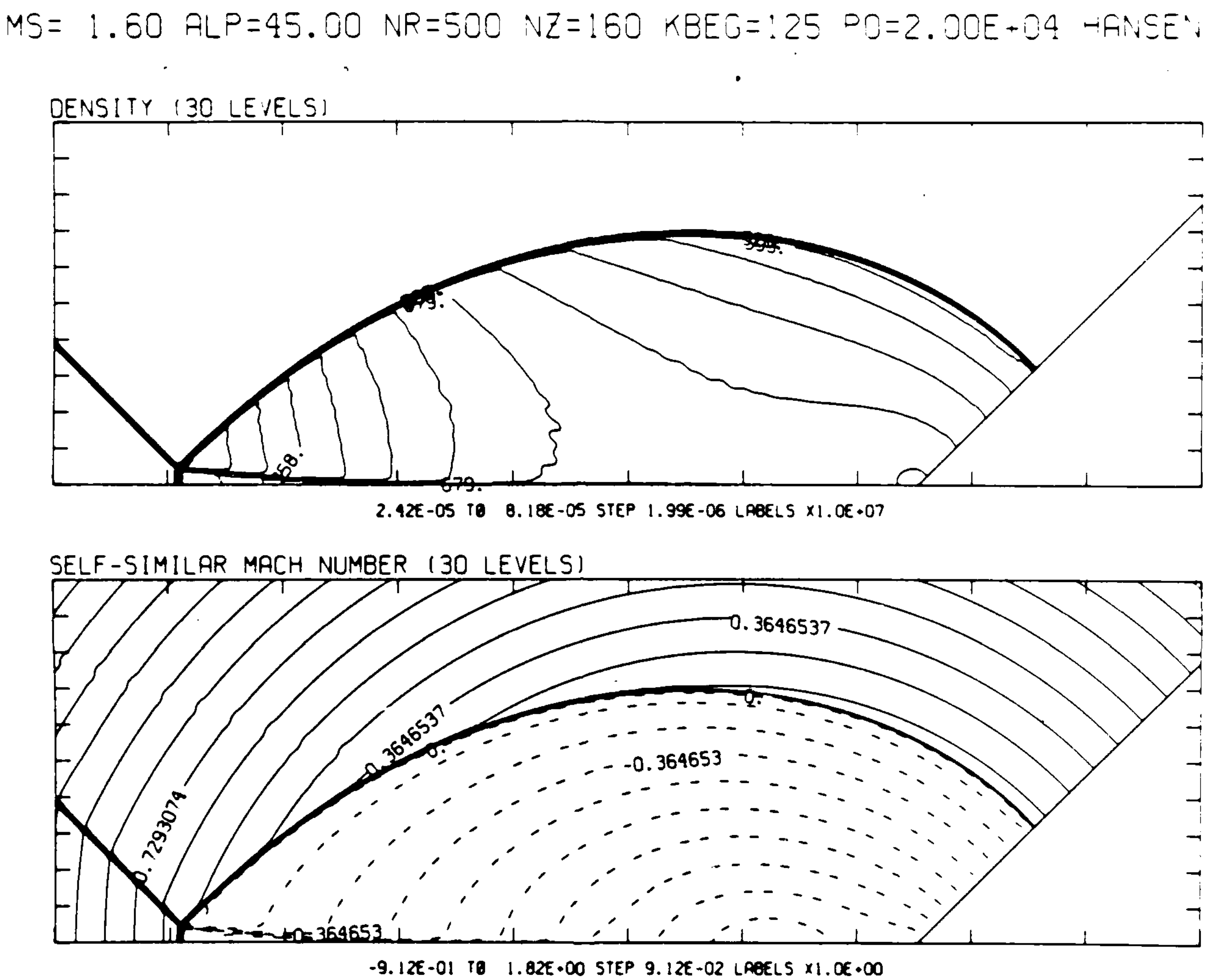

Figure 20.2a. M_S = 1.60, whole-flowfield contour-plots.

Figure 20. Transition set 1, θ_w = 45°, Hansen - continued.

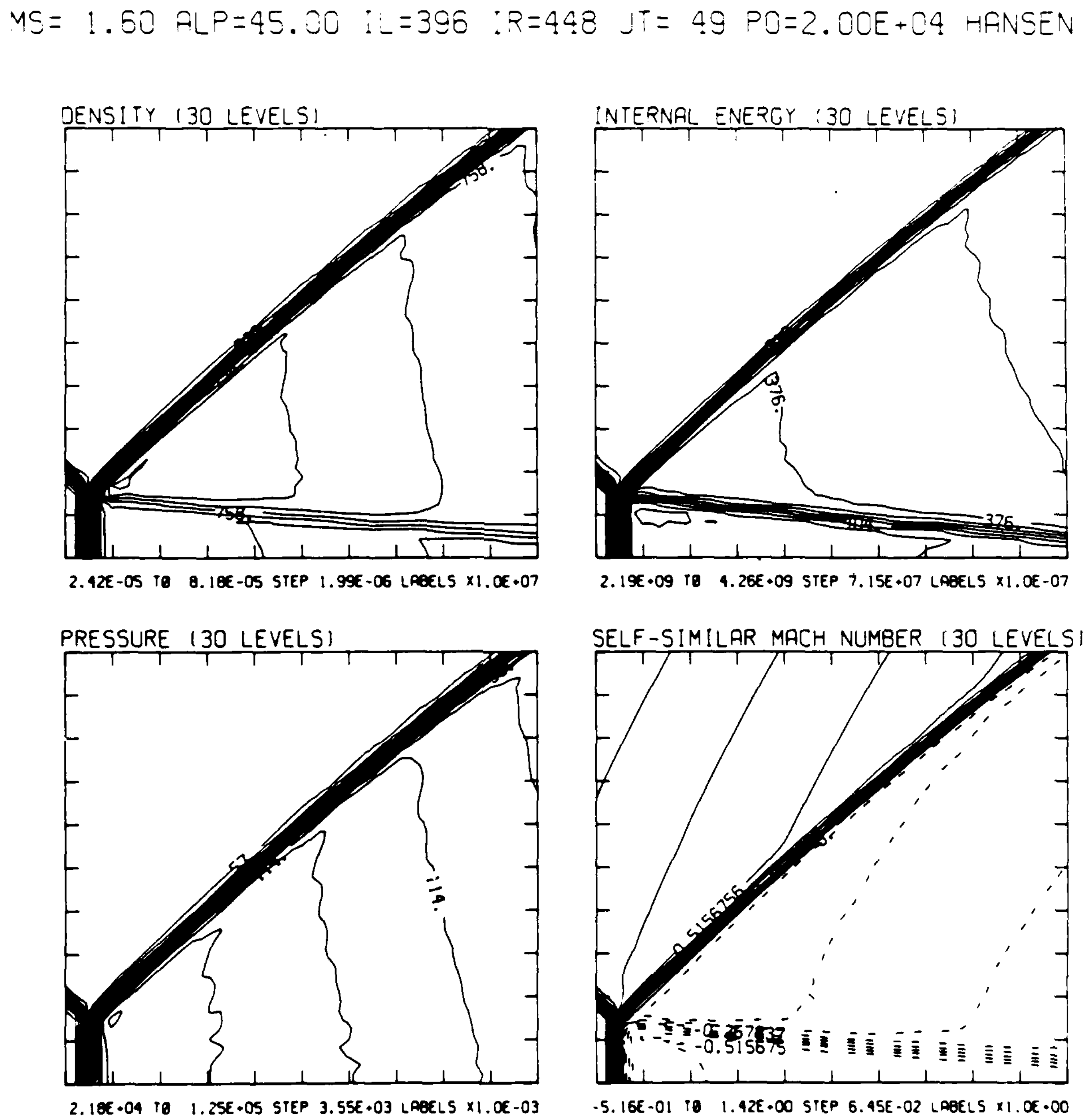

Figure 20.2b. M_s = 1.60, blowup-frame plots.

Figure 20. Transition set 1, θ_w = 45°, Hansen - continued.

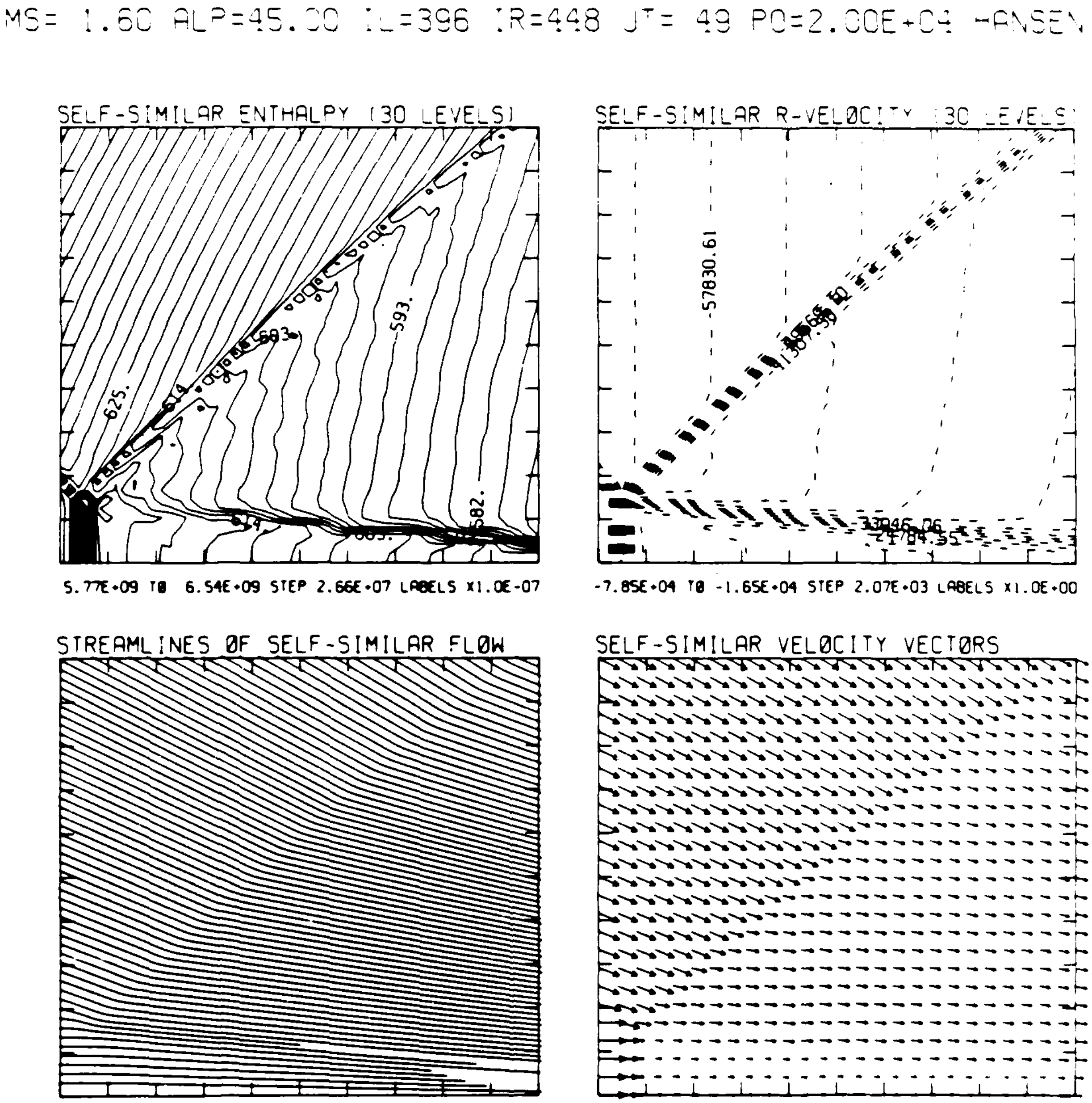

Figure 20.2b. M_s = 1.60, blowup-frame plots - continued.

Figure 20. Transition set 1, θ_w = 45°, Hansen - continued.

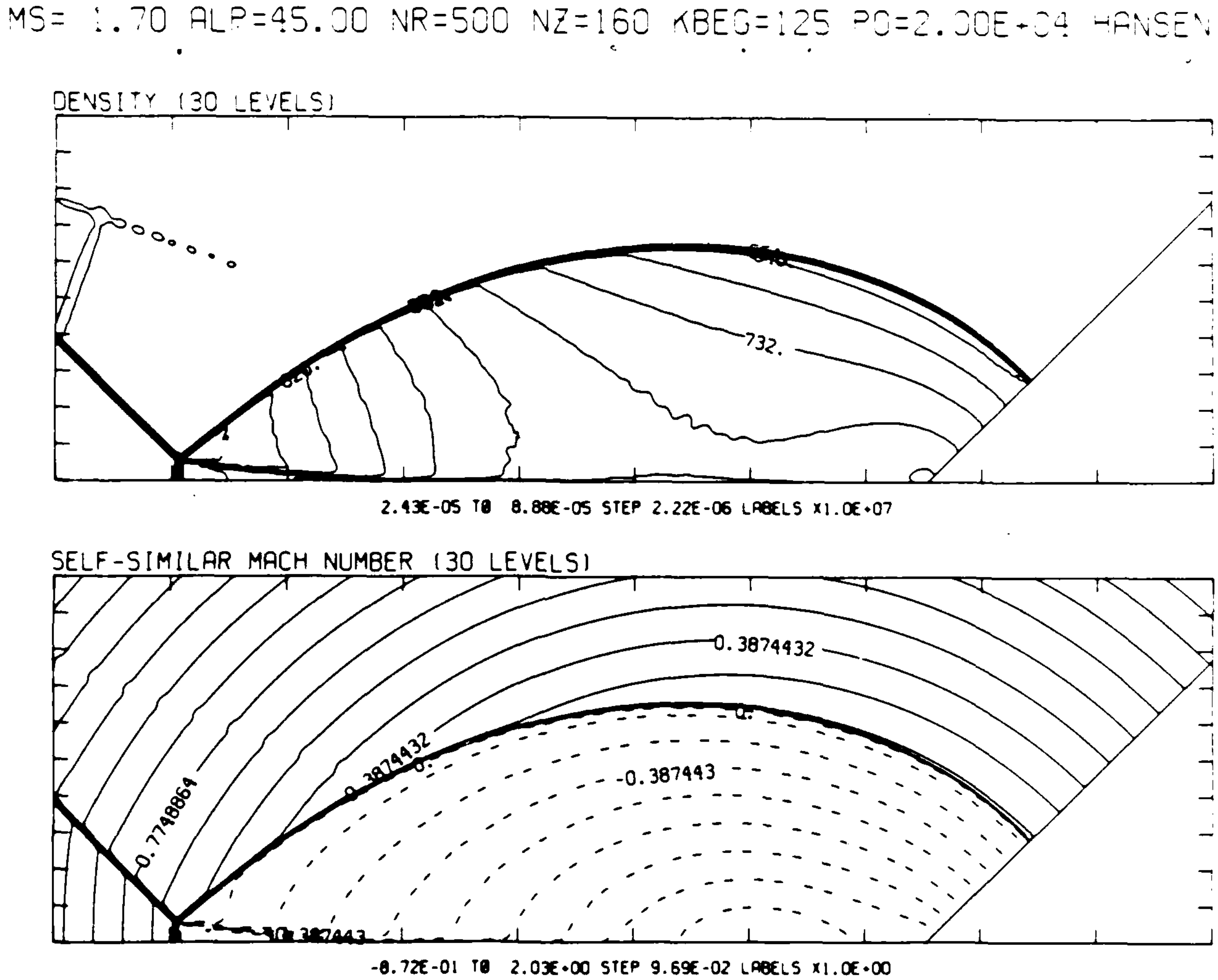

Figure 20.3a. M_S = 1.70, whole-flowfield contour-plots.

Figure 20. Transition set 1, θ_w = 45°, Hansen - continued.

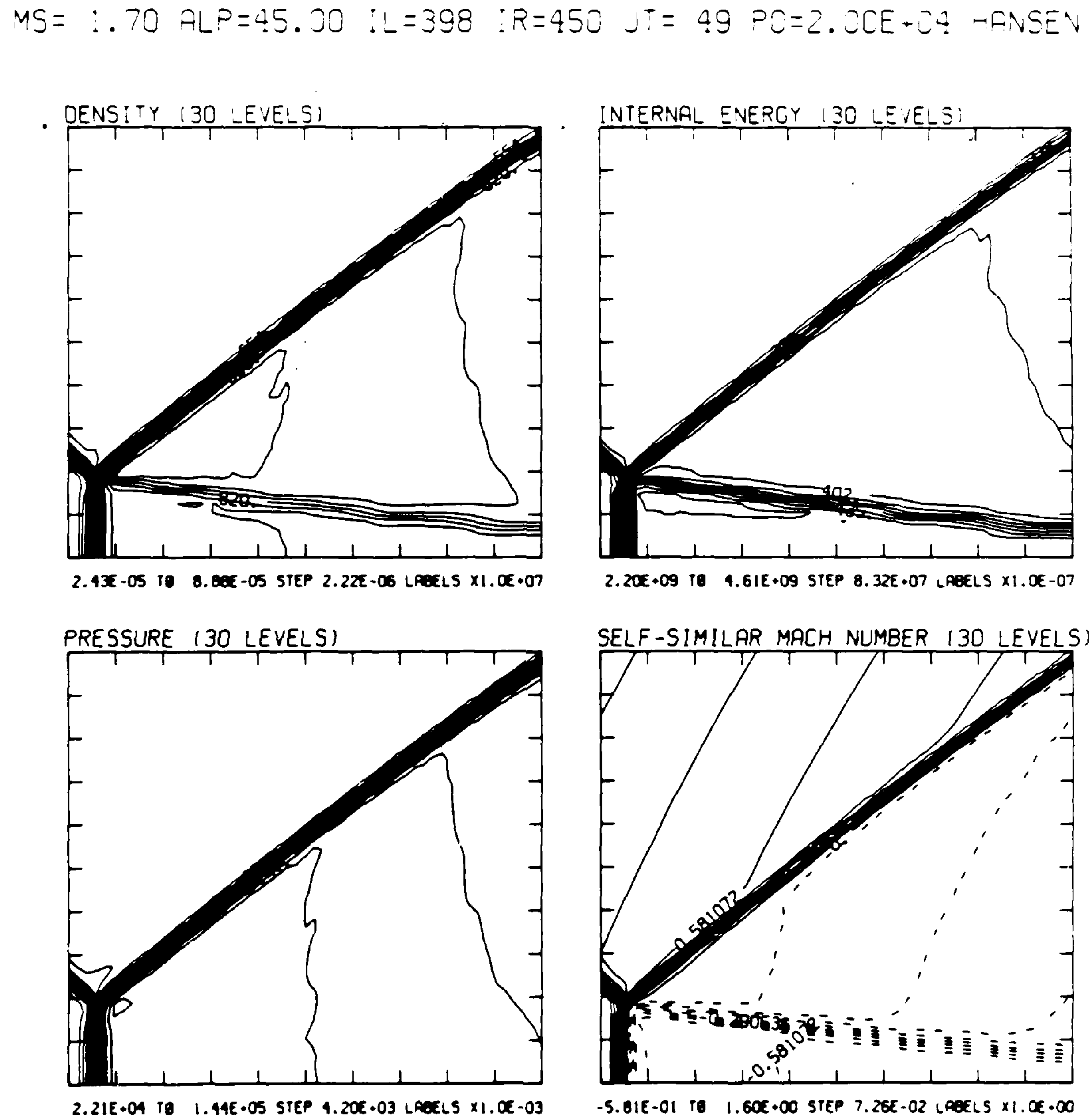

Figure 20.3b. M_s = 1.70, blowup-frame plots.

Figure 20. Transition set 1, θ_w = 45°, Hansen - continued.

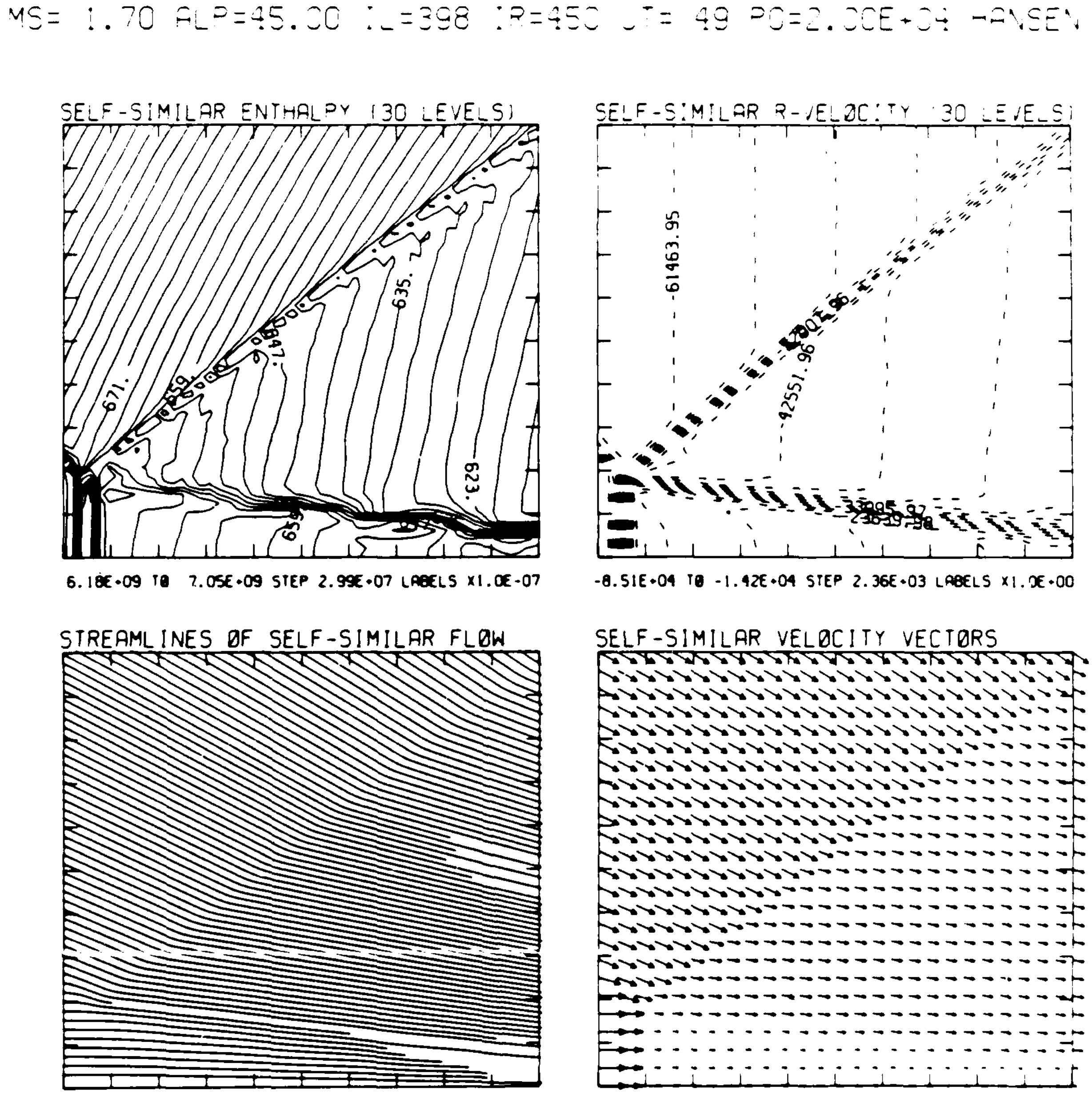

Figure 20.3b. M_s = 1.70, blowup-frame plots - continued.

Figure 20. Transition set 1, θ_w = 45°, Hansen - continued.

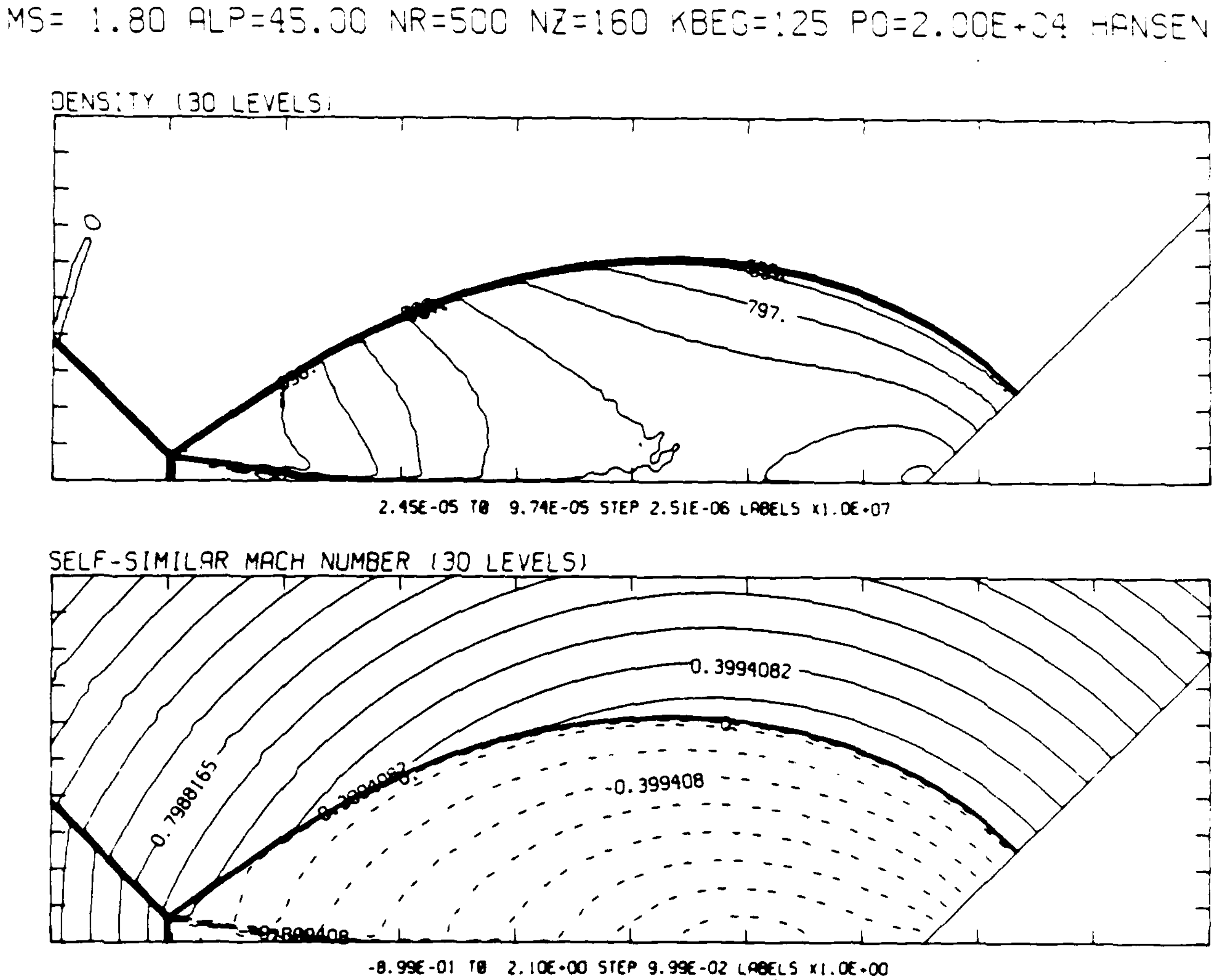

Figure 20.4a. M_S = 1.80, whole-flowfield contour-plots.

Figure 20. Transition set 1, θ_w = 45°, Hansen - continued.

MS= 1.80 ALP=45.00 IL=400 IR=453 JT= 50 PO=2.00E+04 HANSEN

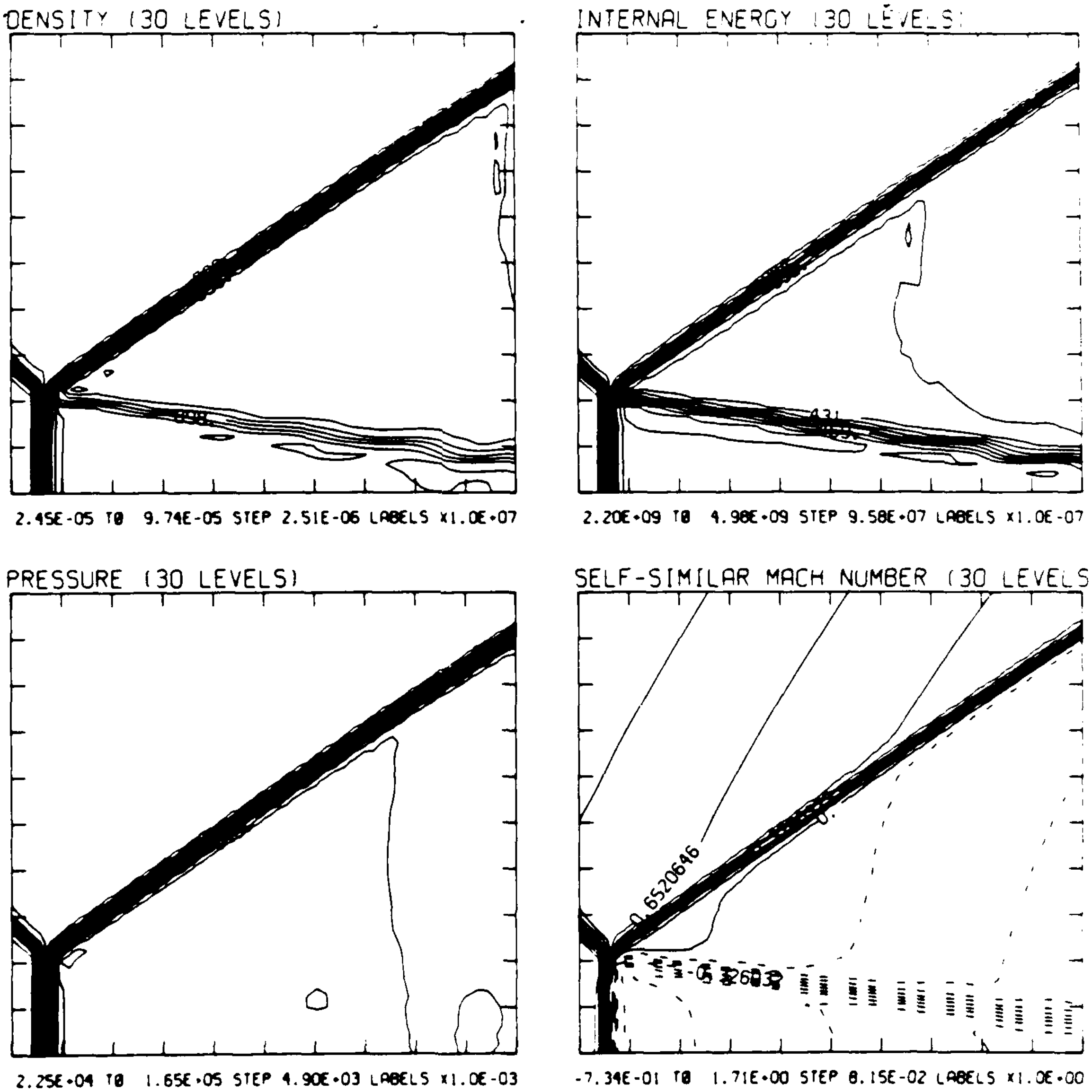

Figure 20.4b. M_s = 1.80, blowup-frame plots.

Figure 20. Transition set 1, θ_w = 45°, Hansen - continued.

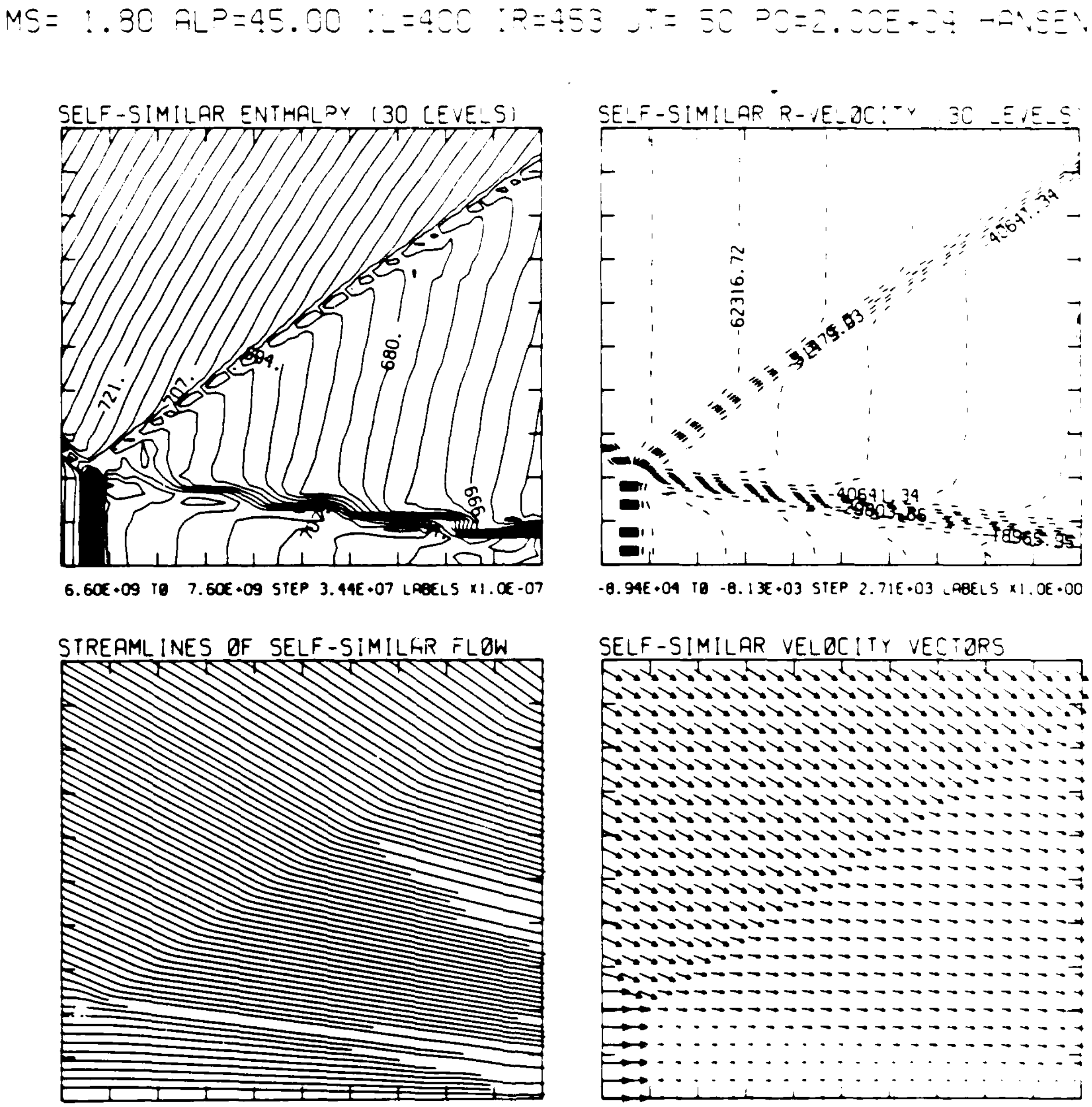

Figure 20.4b. M_s = 1.80, blowup-frame plots - continued.

Figure 20. Transition set 1, θ_w = 45°, Hansen - continued.

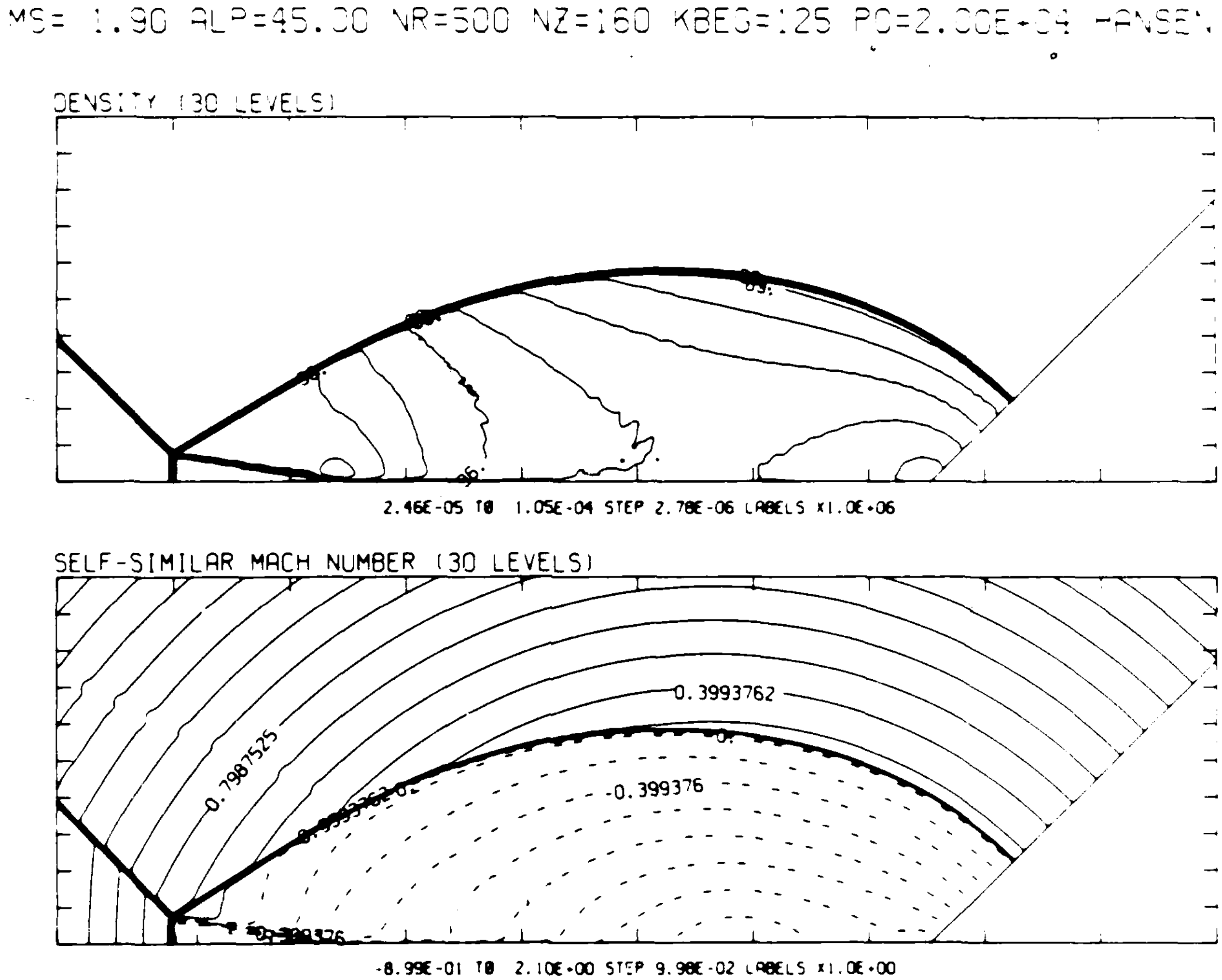

Figure 20.5a. M_s = 1.90, whole-flowfield contour-plots.

Figure 20. Transition set 1, θ_w = 45°, Hansen - continued.

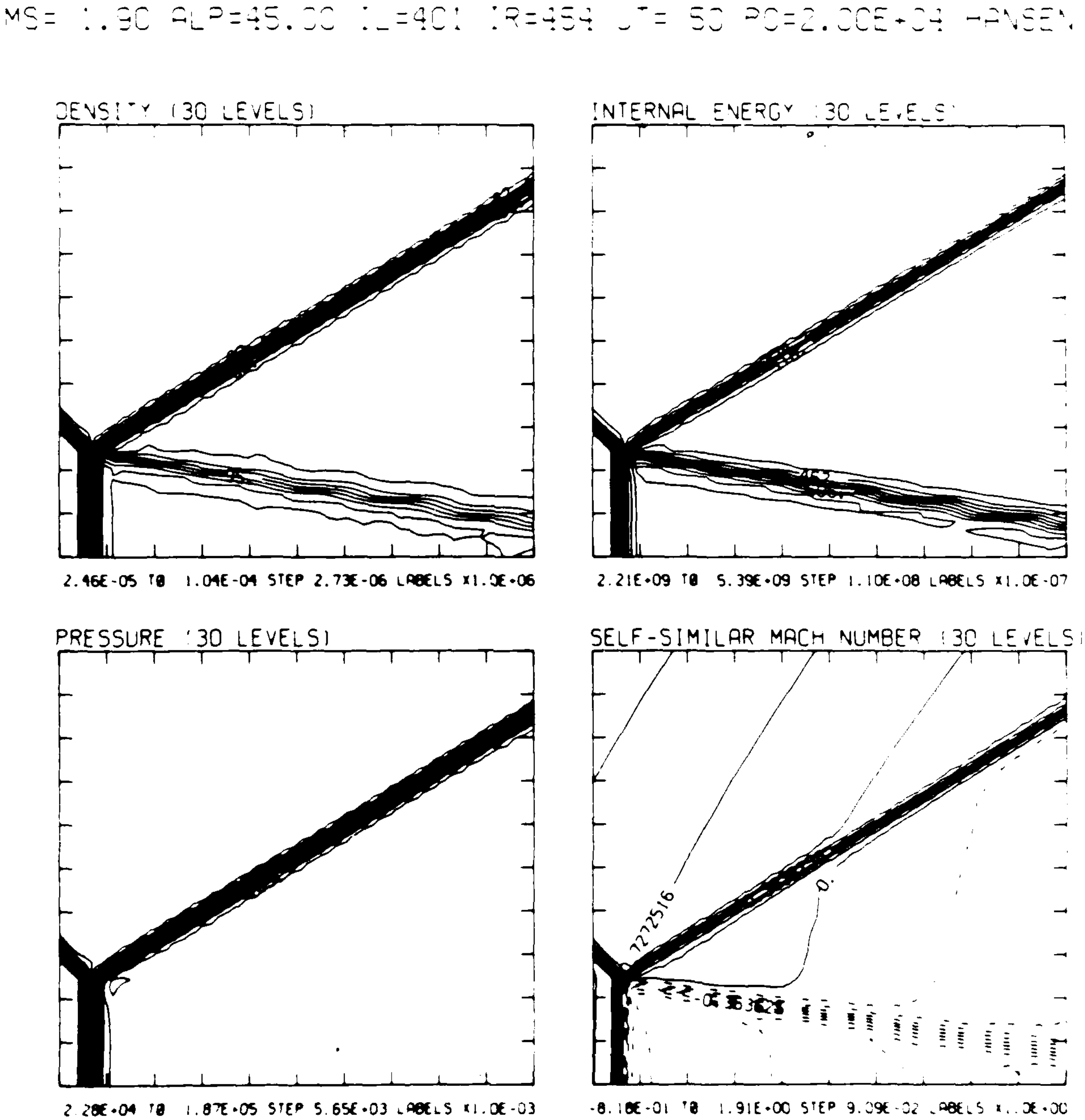

Figure 20.5b. M_s = 1.90, blowup-frame plots.

Figure 20. Transition set 1, θ_w = 45°, Hansen - continued.

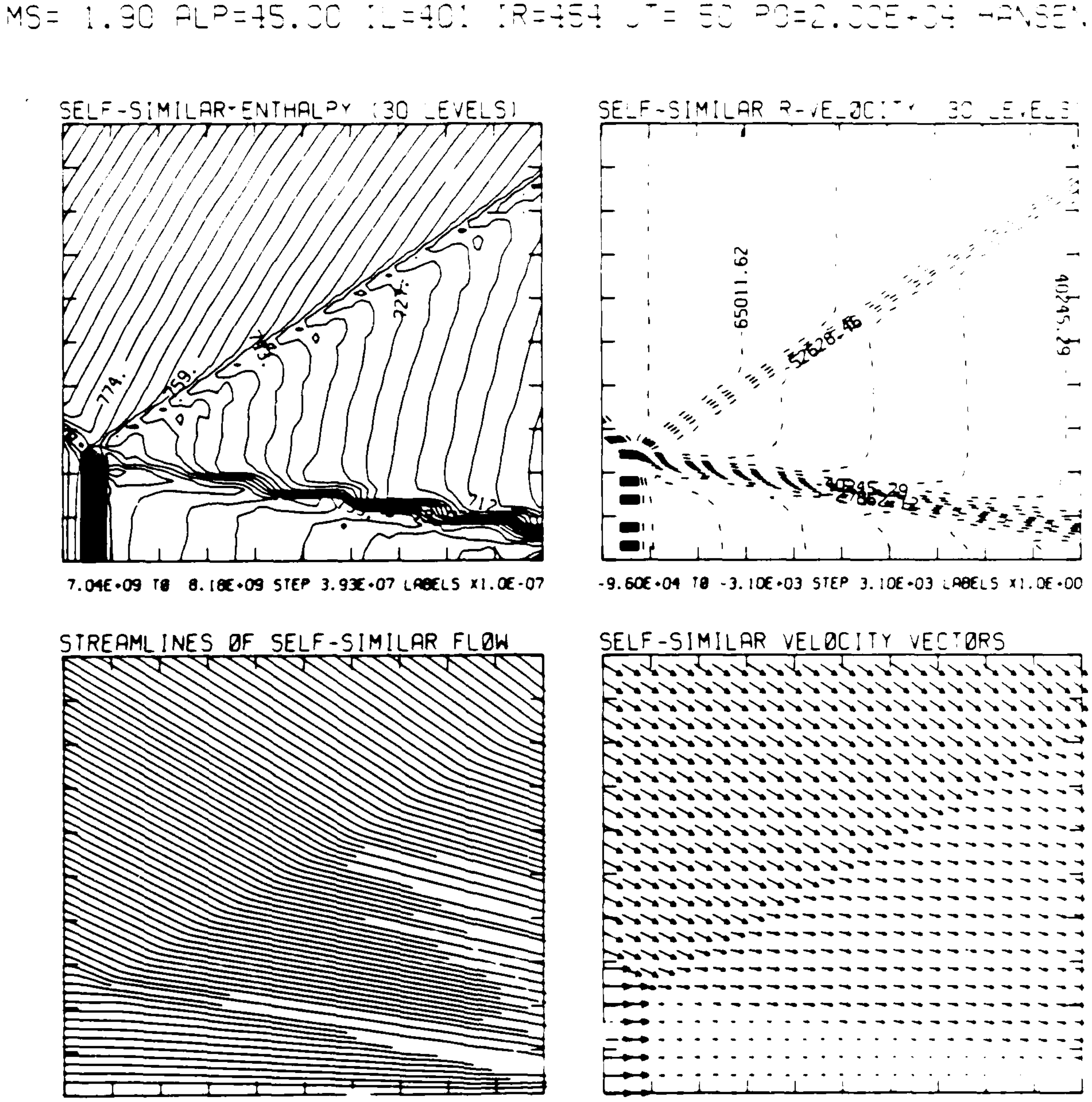

Figure 20.5b. M_s = 1.90, blowup-frame plots - continued.

Figure 20. Transition set 1, θ_w = 45°, Hansen - continued.

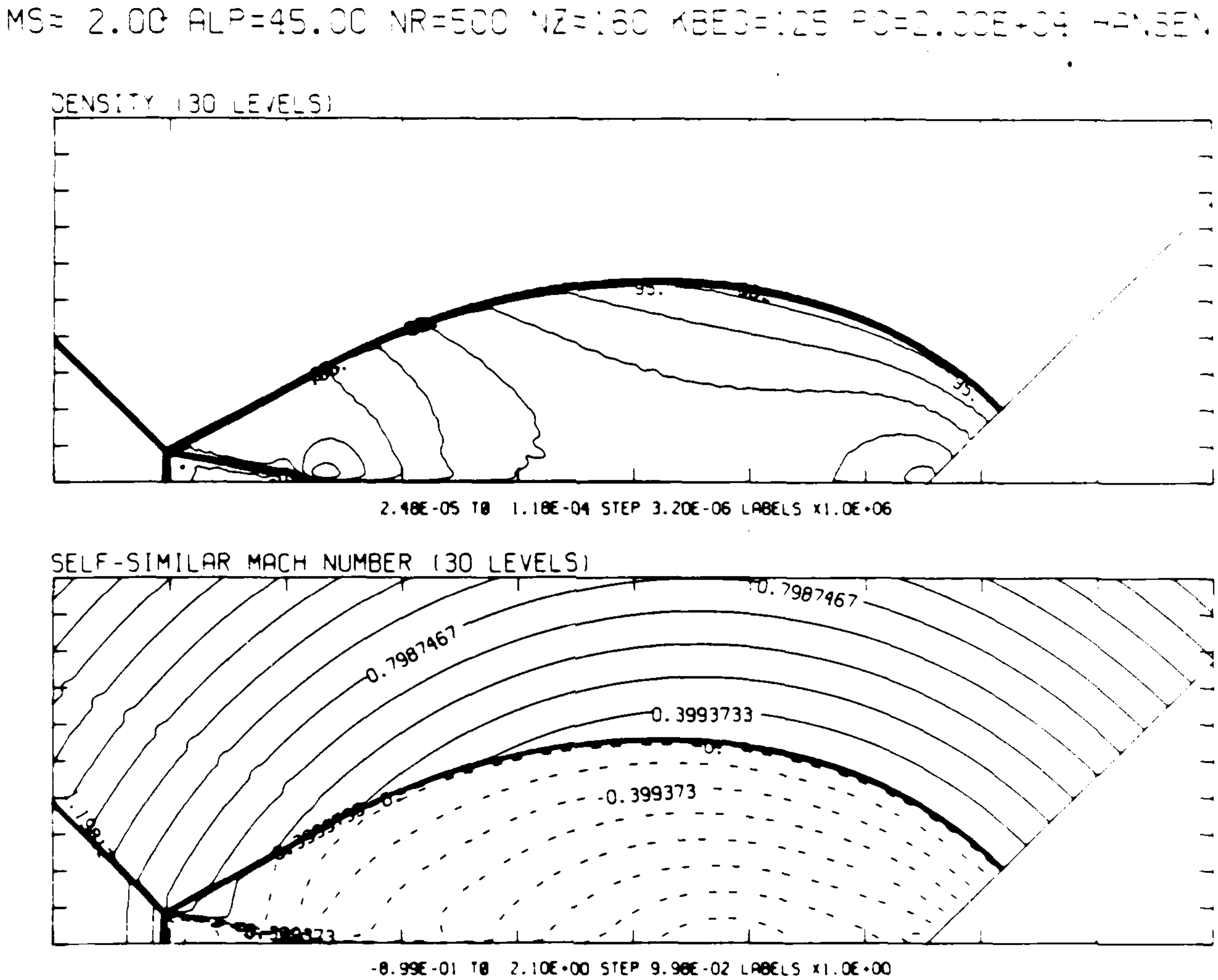

Figure 20.6a. M_s = 2.00, whole-flowfield contour-plots.

Figure 20. Transition set 1, θ_w = 45°, Hansen - continued.

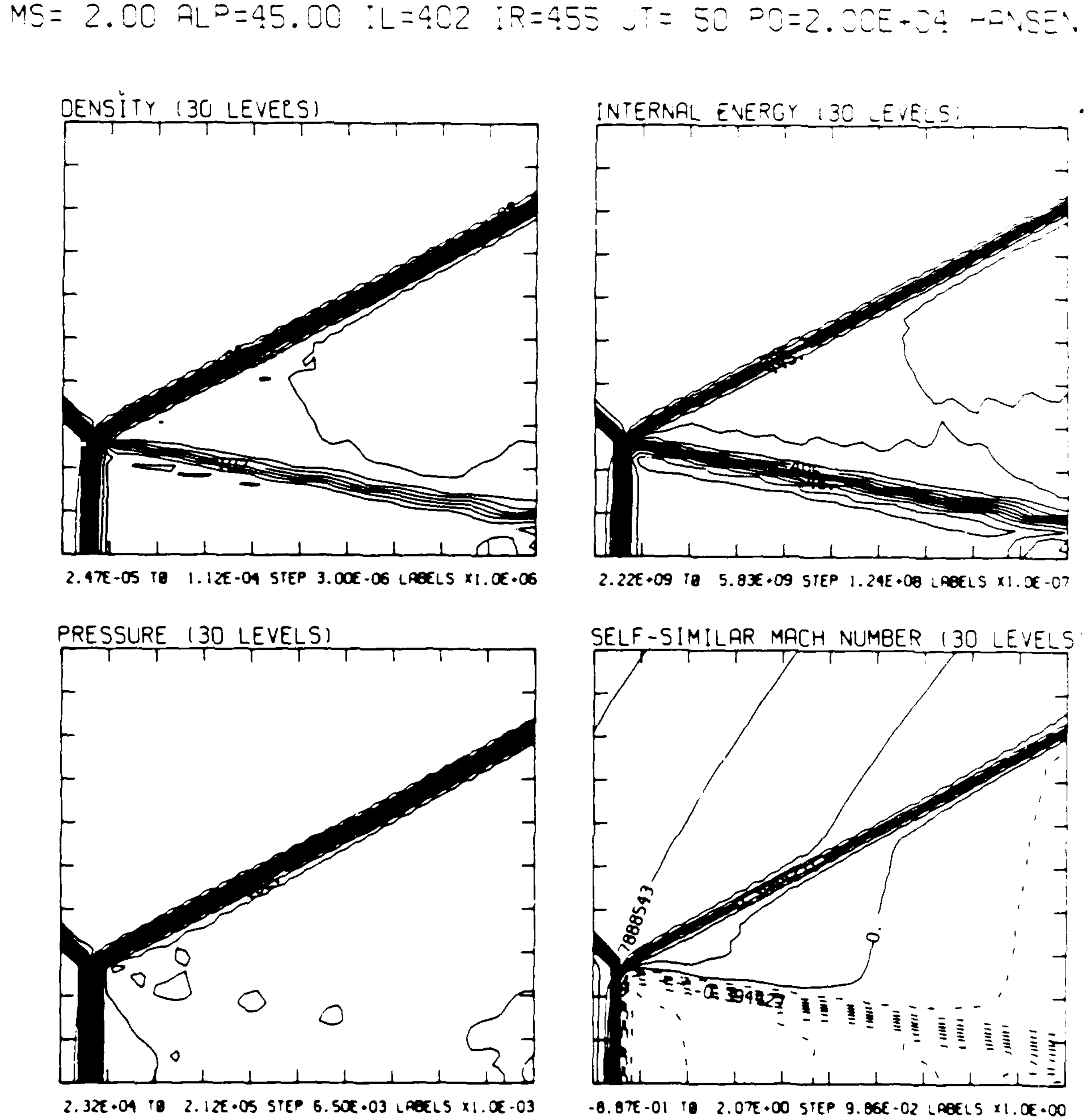

Figure 20.6b. M_s = 2.00, blowup-frame plots.

Figure 20. Transition set 1, θ_w = 45°, Hansen - continued.

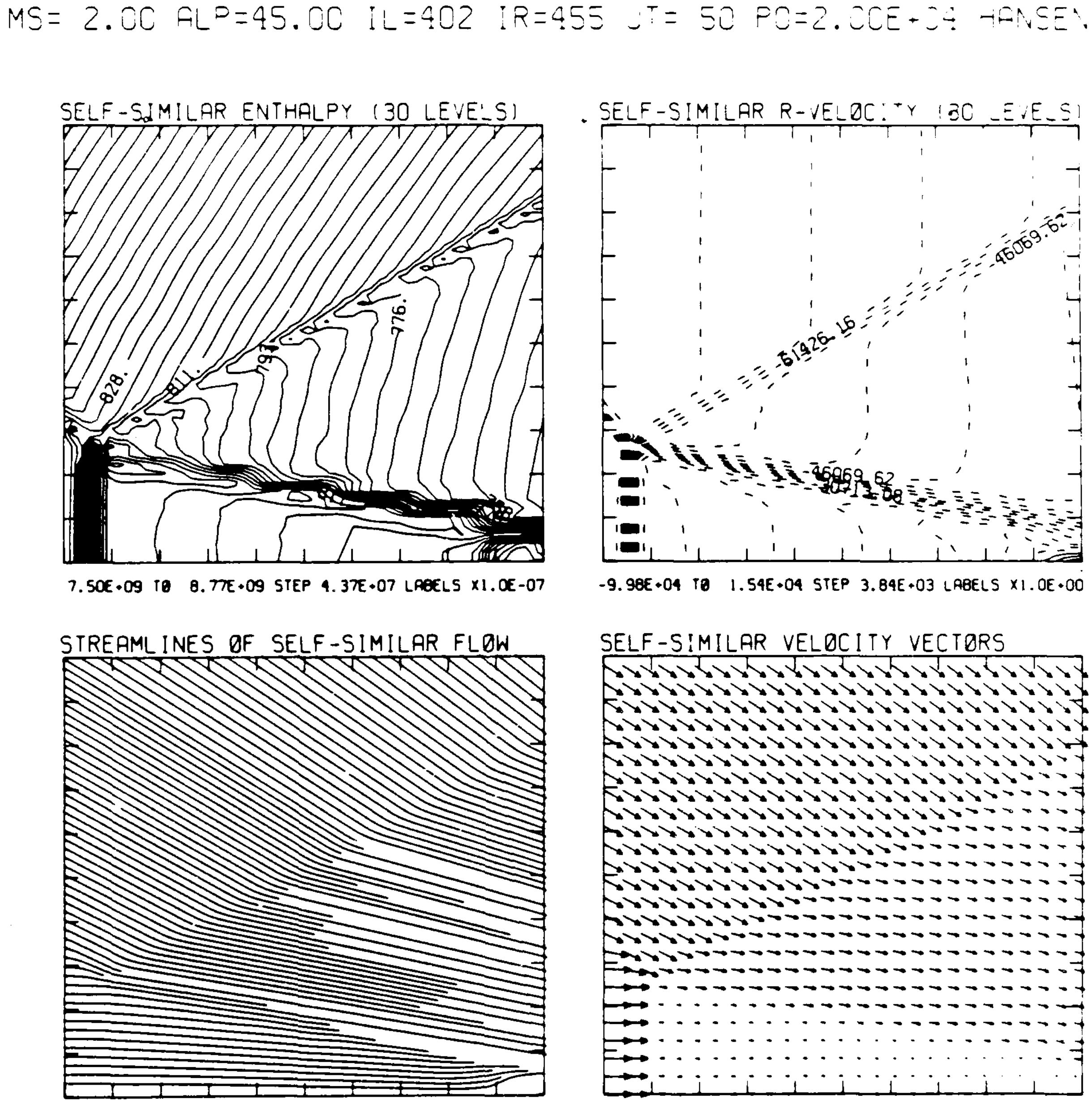

Figure 20.6b. M_S = 2.00, blowup-frame plots - continued.

Figure 20. Transition set 1, θ_w = 45°, Hansen - continued.

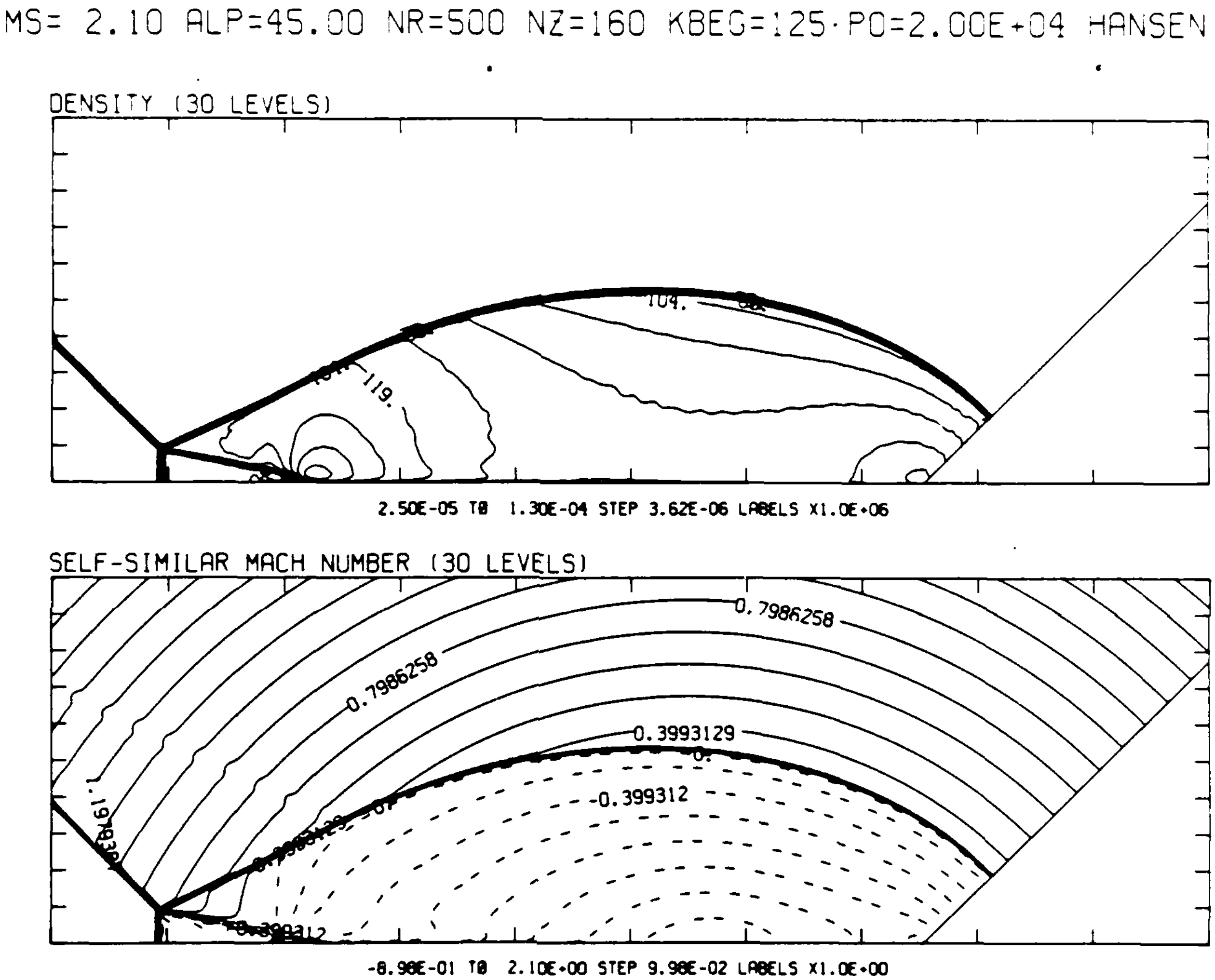

Figure 20.7a. M_s = 2.10, whole-flowfield contour-plots.

Figure 20. Transition set 1, θ_w = 45°, Hansen - continued.

MS= 2.10 ALP=45.00 IL=404 IR=457 JT= 50 PO=2.00E+04 HANSEN

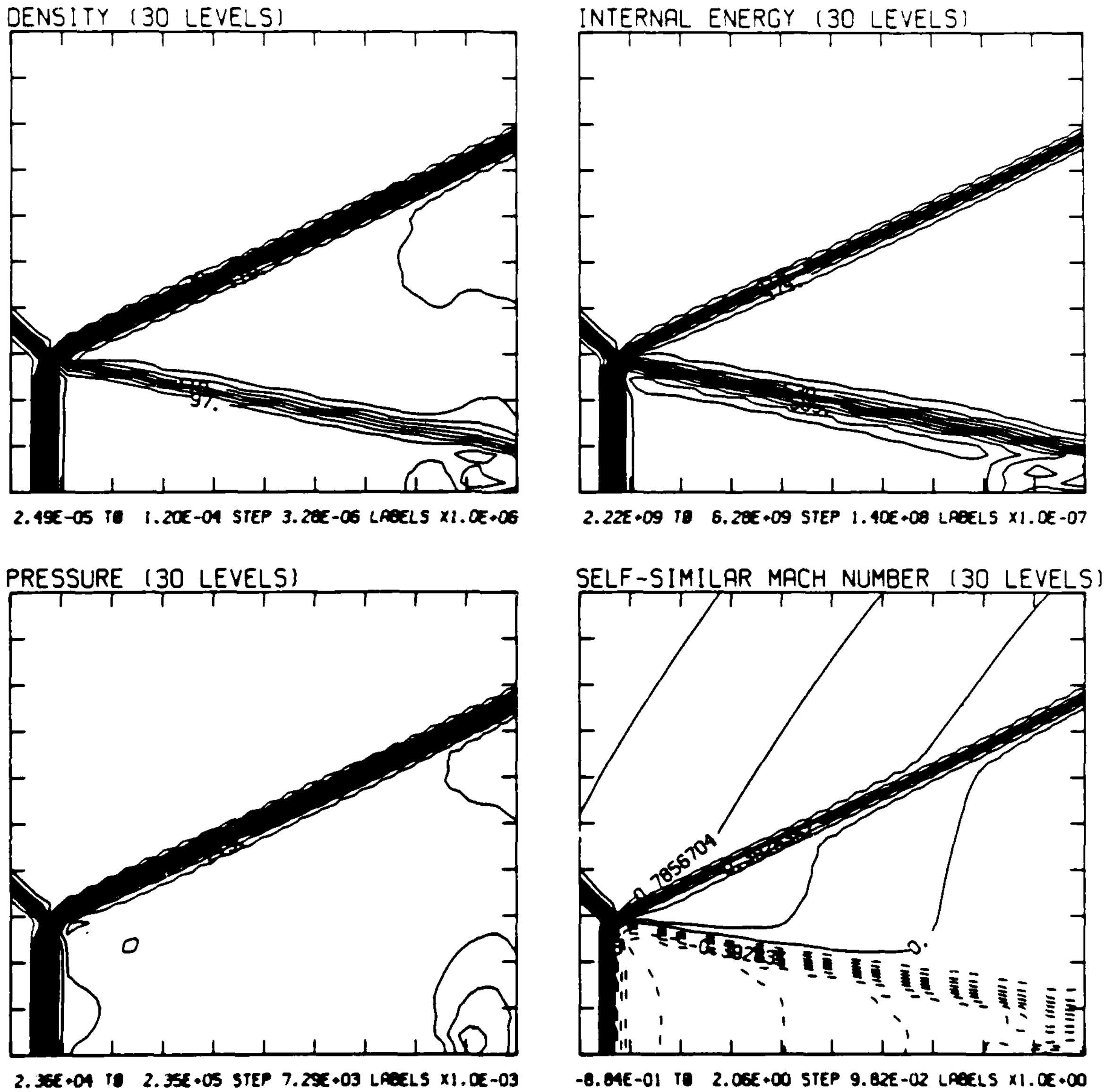

Figure 20.7b. M_s = 2.10, blowup-frame plots.

Figure 20. Transition set 1, θ_w = 45°, Hansen - continued.

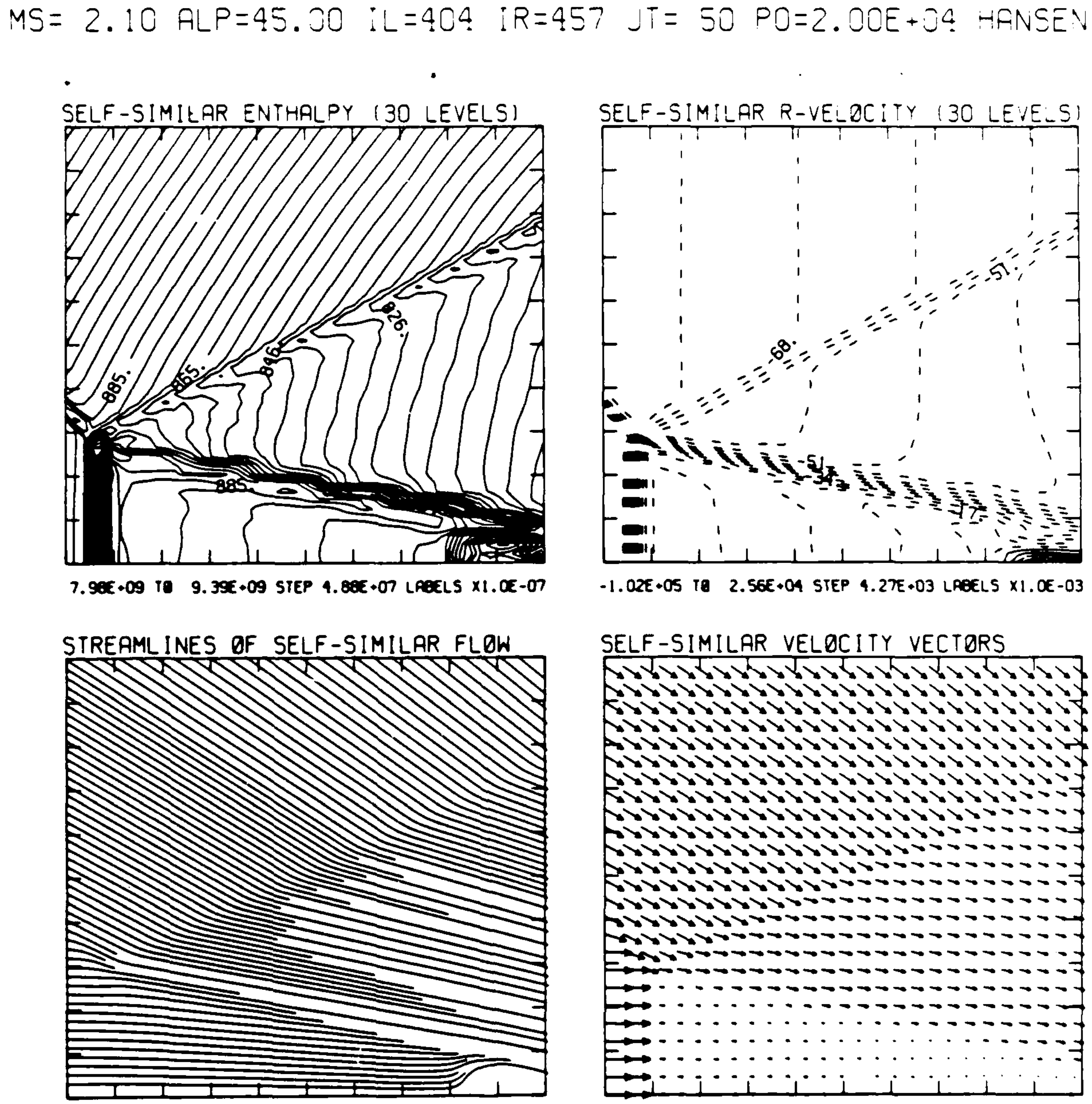

Figure 20.7b. M_s = 2.10, blowup-frame plots - continued.

Figure 20. Transition set 1, θ_w = 45°, Hansen - continued.

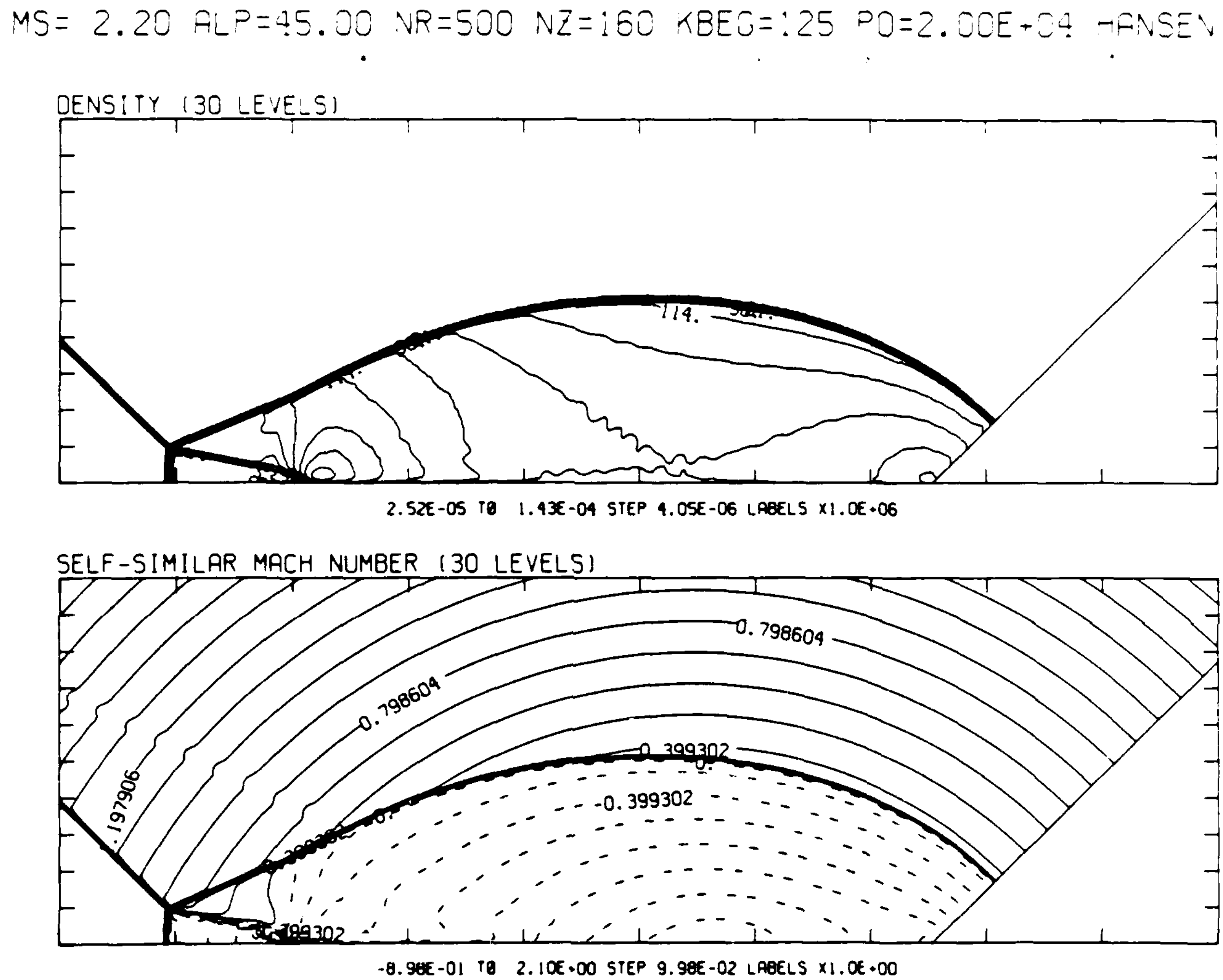

Figure 20.8a. M_s = 2.20, whole-flowfield contour-plots.

Figure 20. Transition set 1, θ_W = 45°, Hansen - continued.

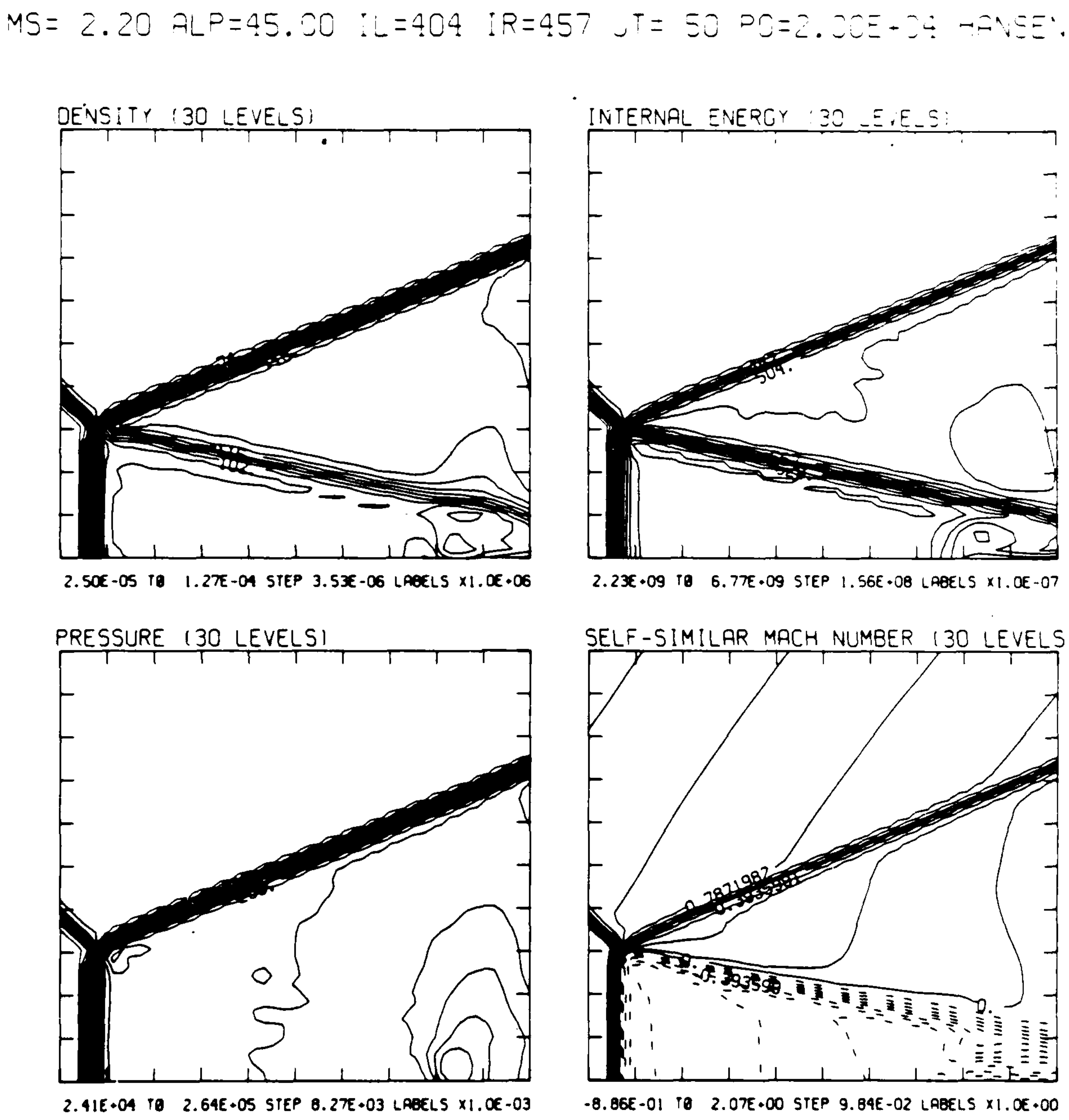

Figure 20.8b. M_s = 2.20, blowup-frame plots.

Figure 20. Transition set 1, θ_w = 45°, Hansen - continued.

MS= 2.20 ALP=45.00 IL=404 IR=457 JT= 50 PO=2.00E+04 HANSEN

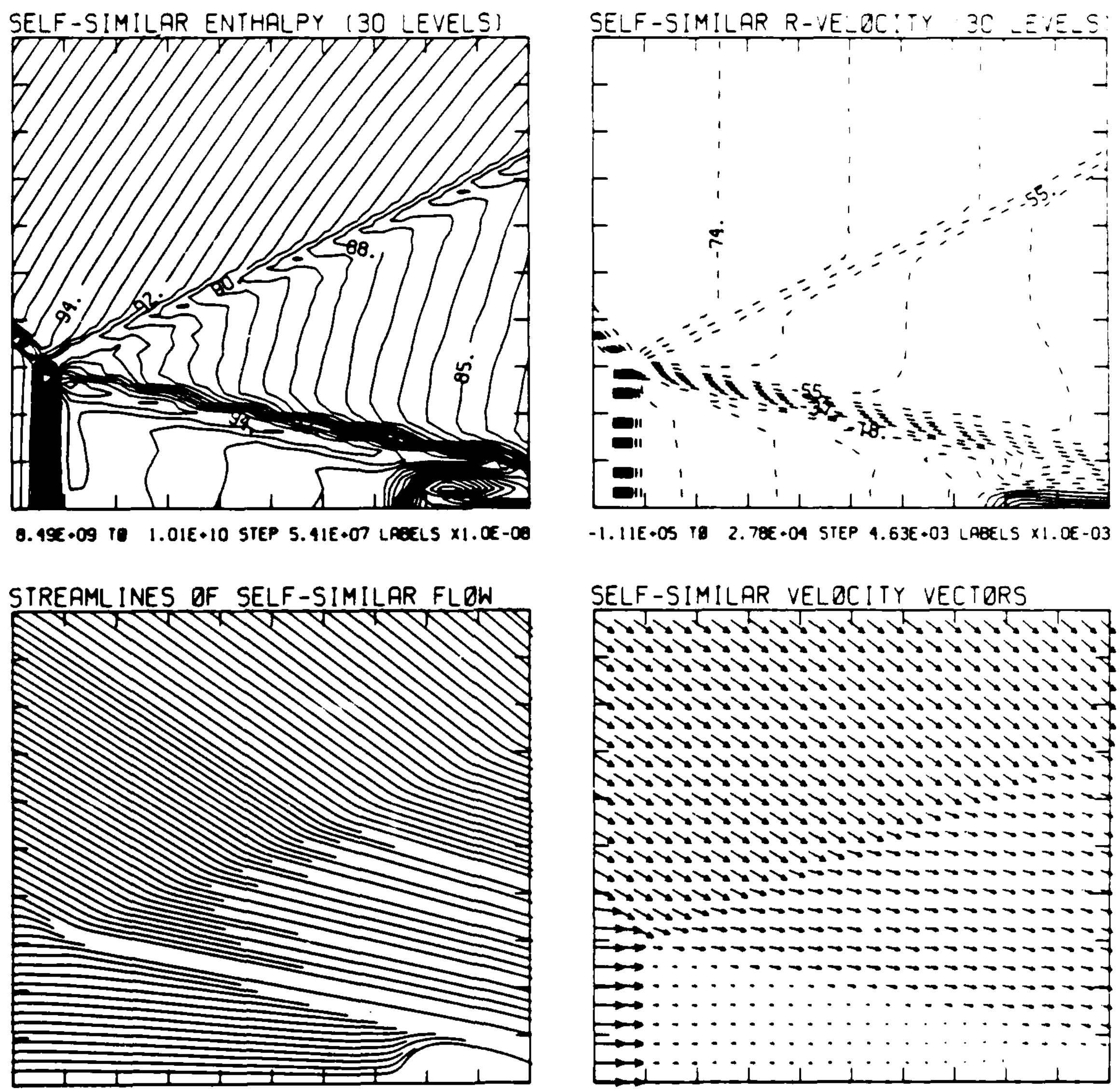

Figure 20.8b. M_S = 2.20, blowup-frame plots - continued.

Figure 20. Transition set 1, θ_W = 45°, Hansen - continued.

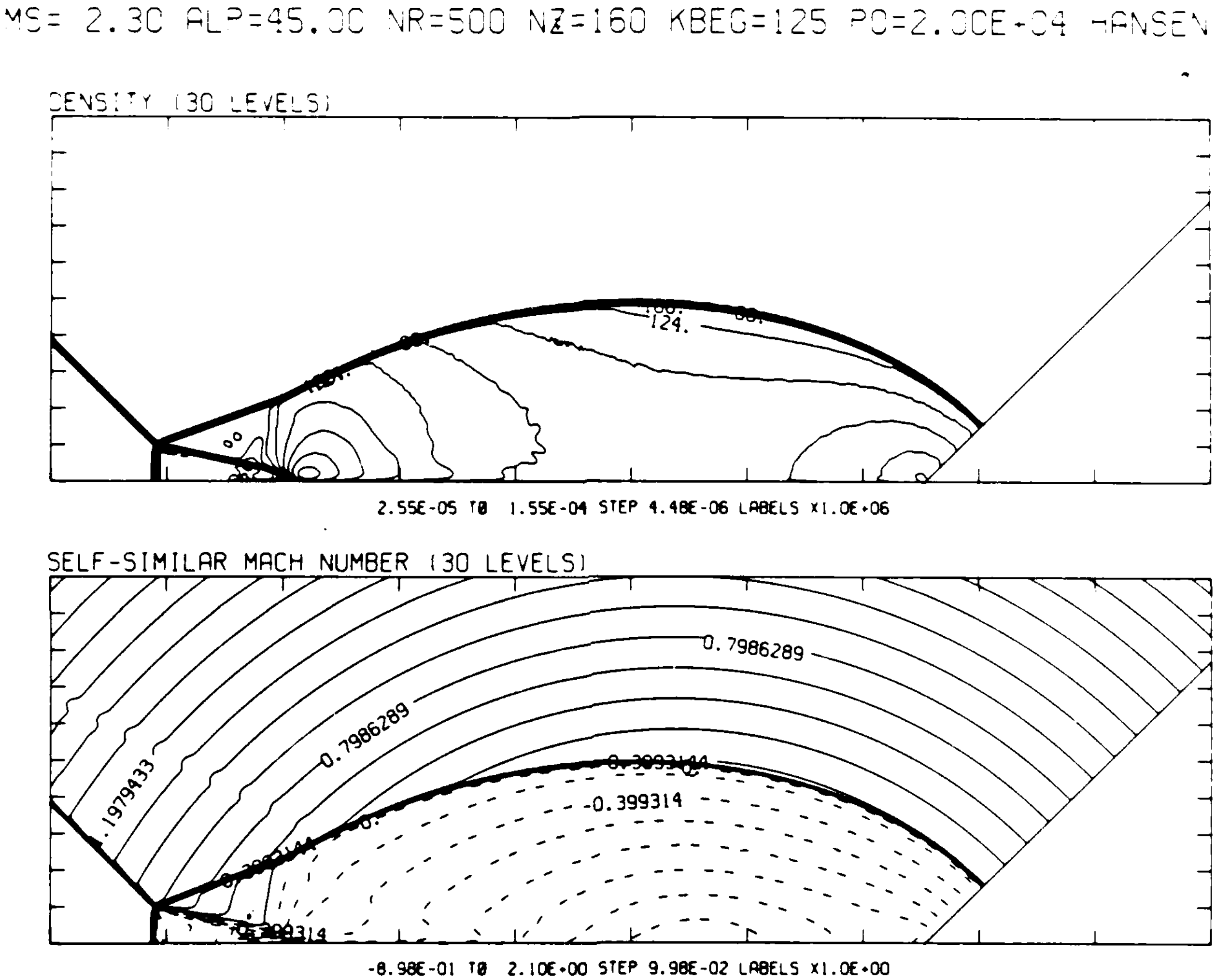

Figure 20.9a. M_s = 2.30, whole-flowfield contour-plots.

Figure 20. Transition set 1, θ_w = 45°, Hansen - continued.

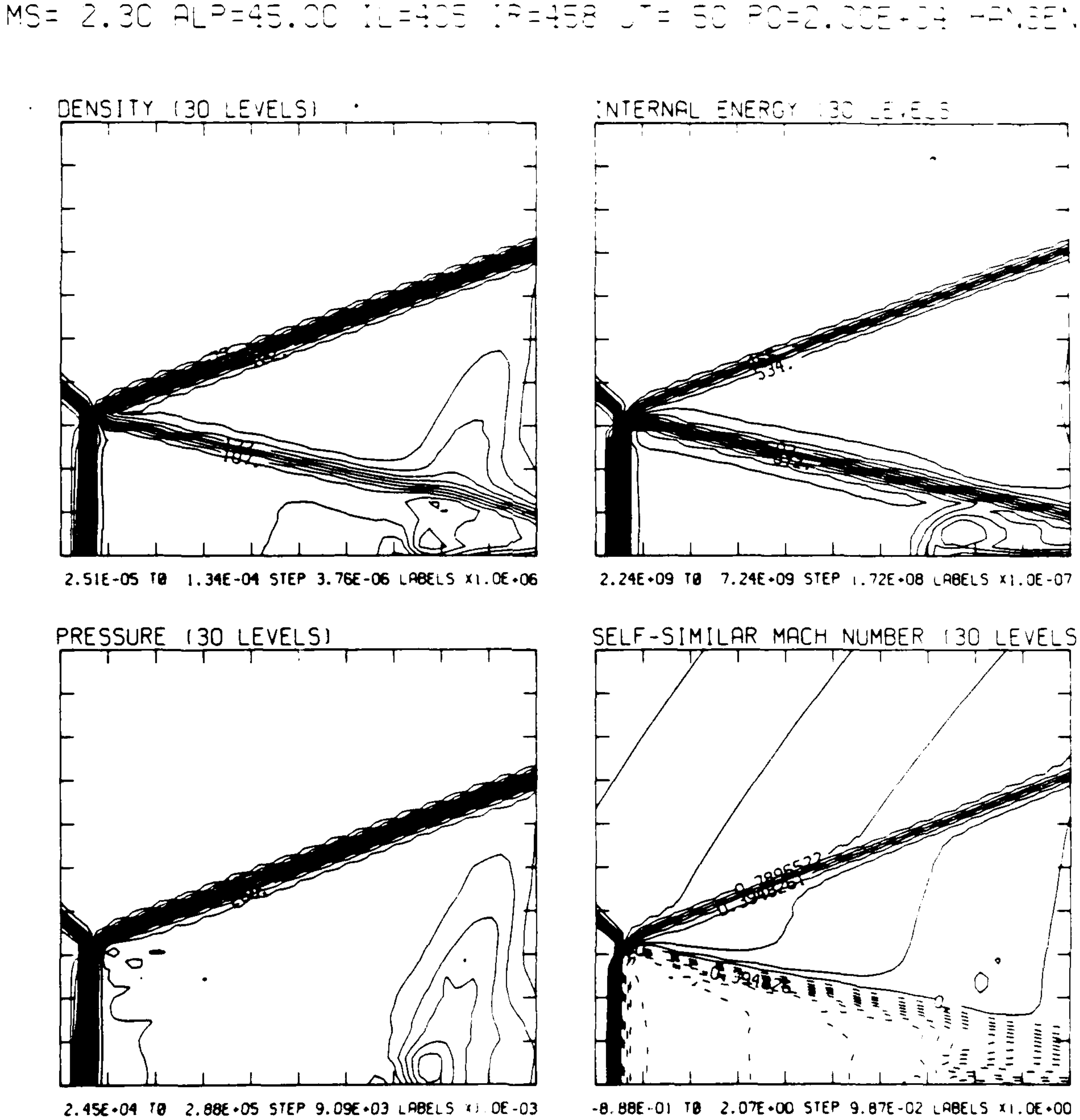

Figure 20.9b. M_s = 2.30, blowup-frame plots.

Figure 20. Transition set 1, θ_w = 45°, Hansen - continued.

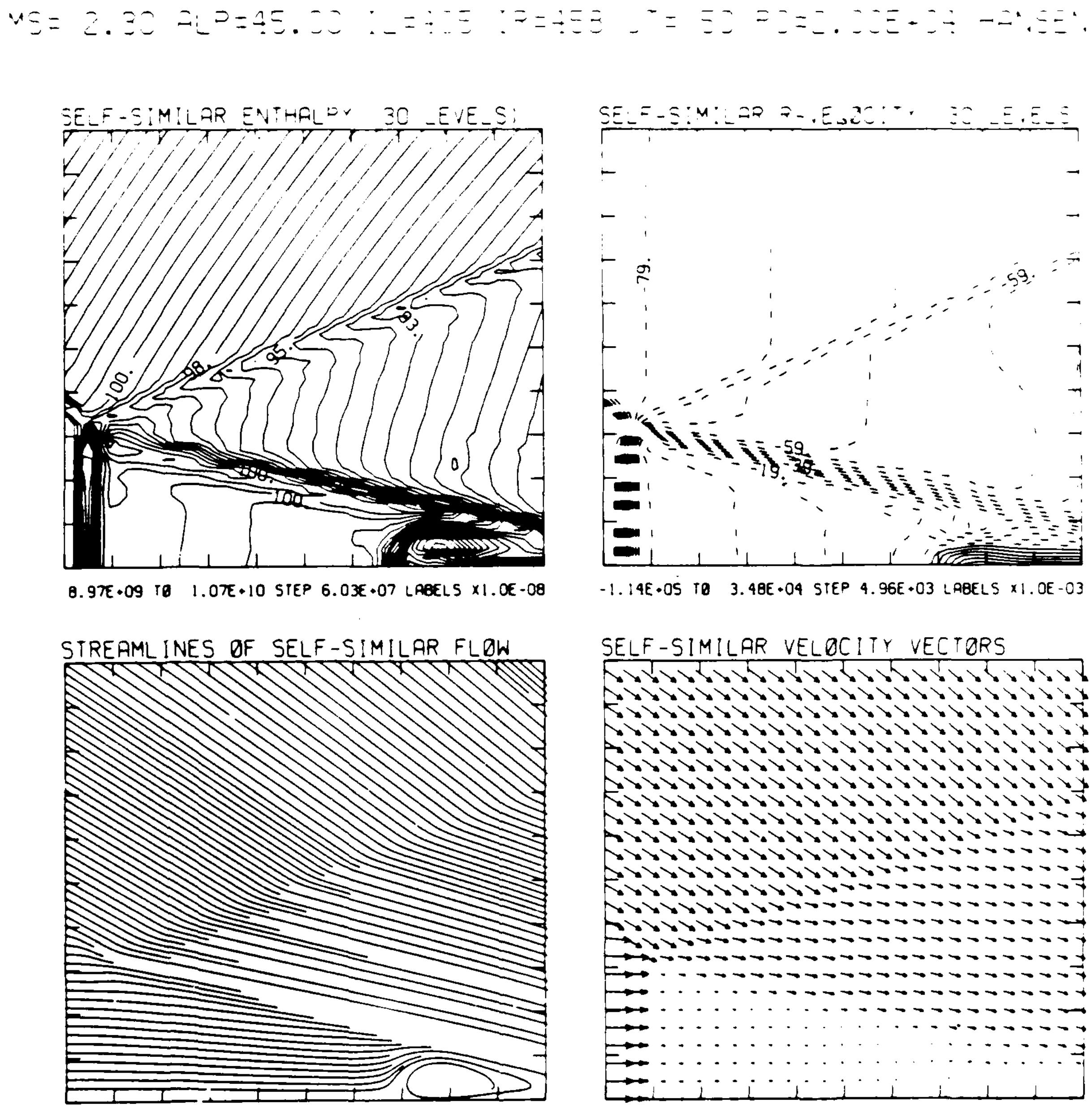

Figure 20.9b. M_s = 2.30, blowup-frame plots - continued.

Figure 20. Transition set 1, θ_w = 45°, Hansen - continued.

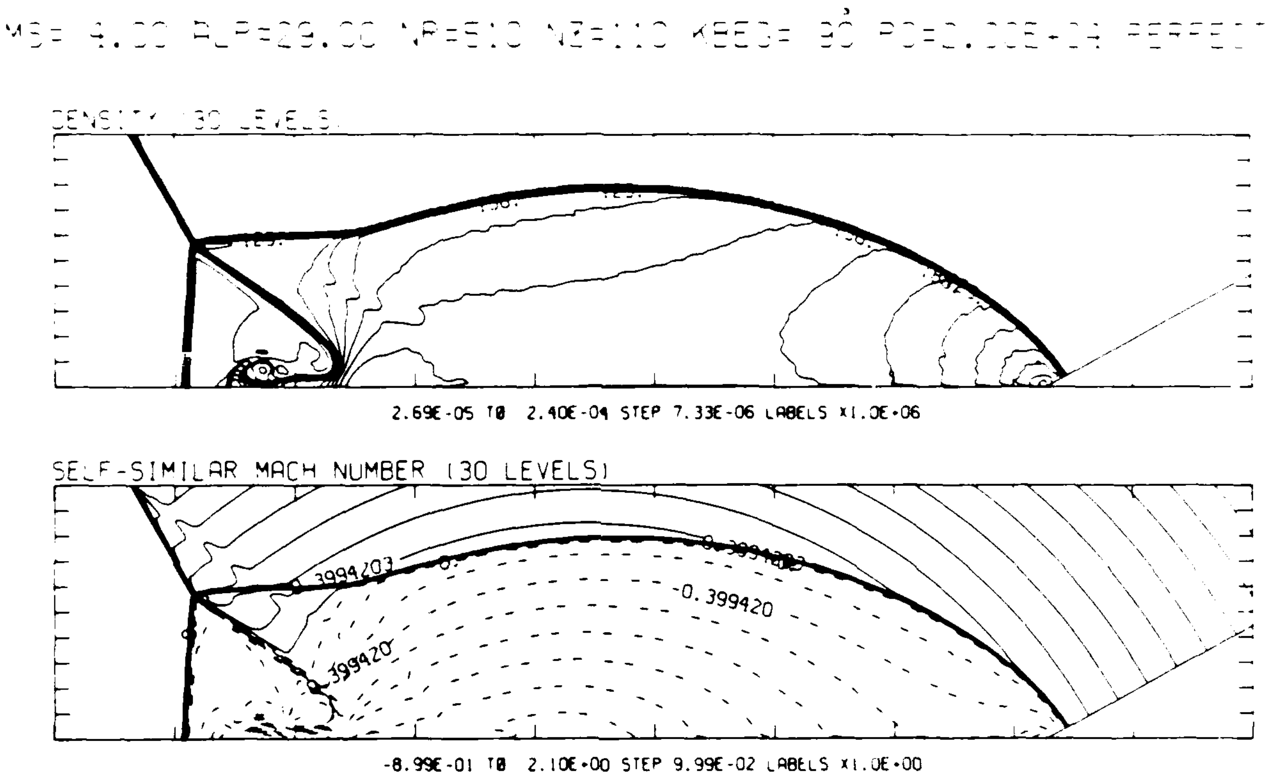

Figure 21.1a. θ_w = 29°, whole-flowfield contour-plots.

Figure 21. Transition set 2, M_s = 4.0, γ = 1.4.

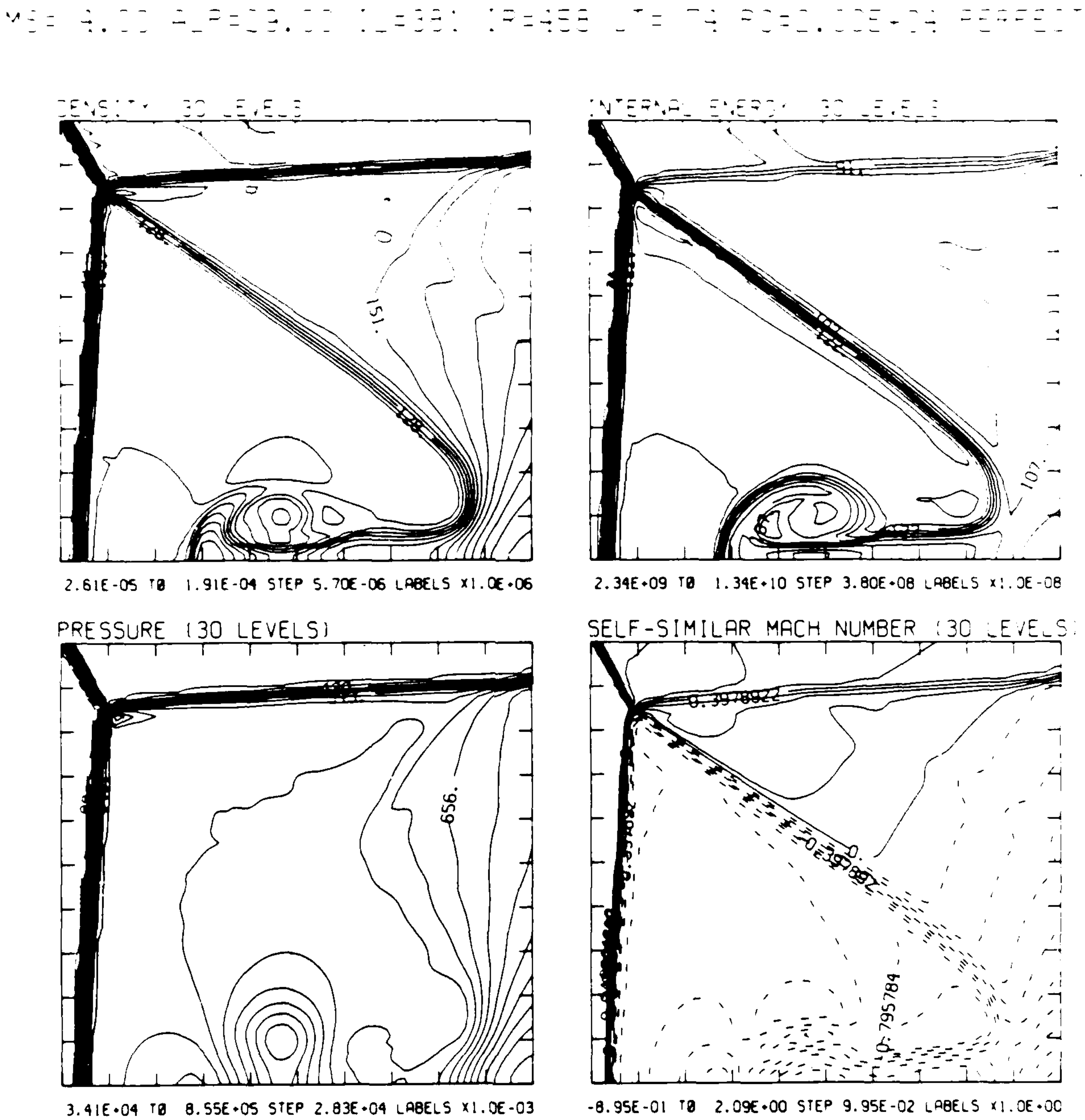

Figure 21.1b. $\theta_w = 29°$, blowup-frame plots.

Figure 21. Transition set 2, $M_s = 4.0$, $\gamma = 1.4$ - continued.

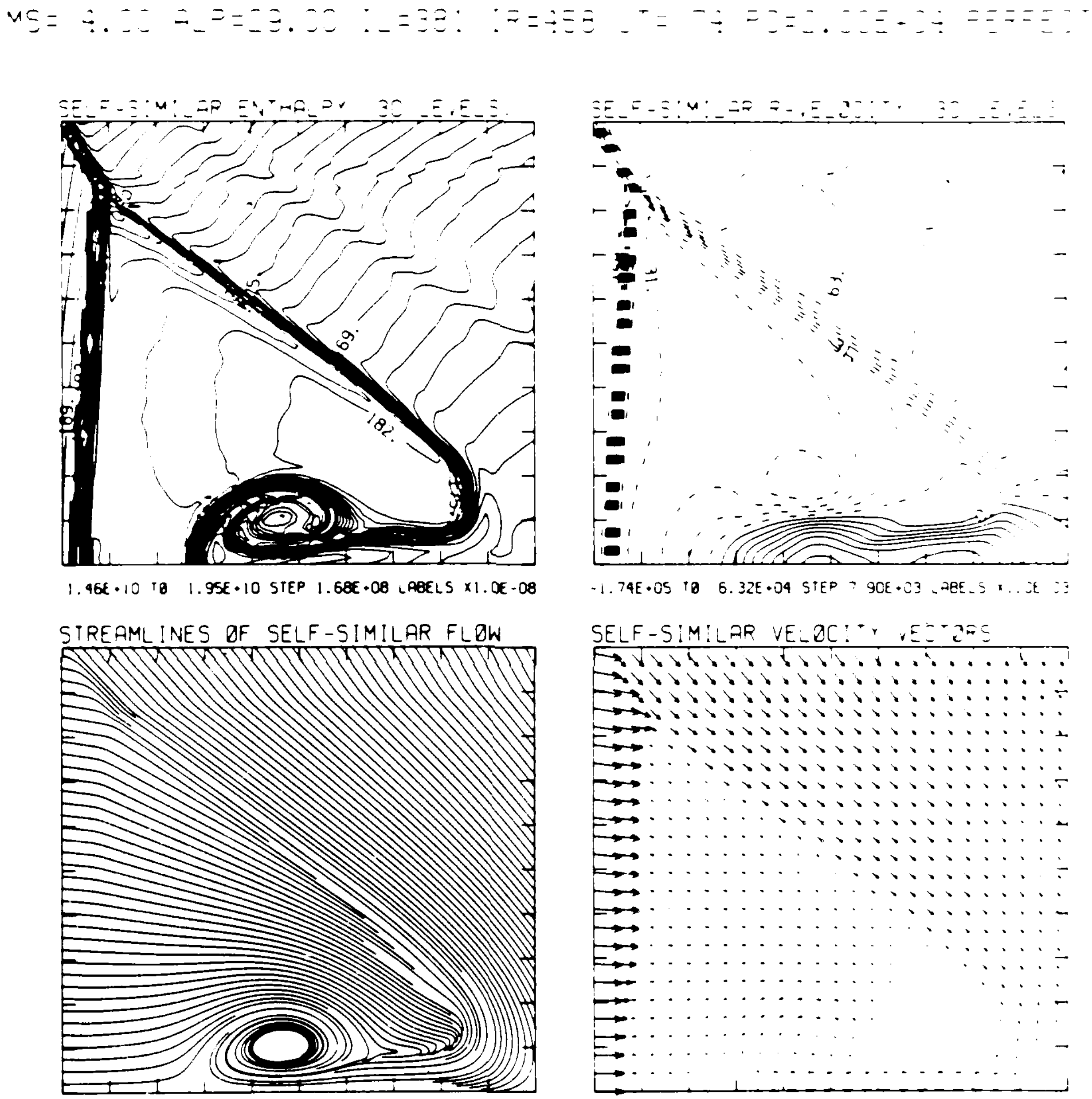

Figure 21.1b. θ_w = 29°, blowup-frame plots - continued.

Figure 21. Transition set 2, M_s = 4.0, γ = 1.4 - continued.

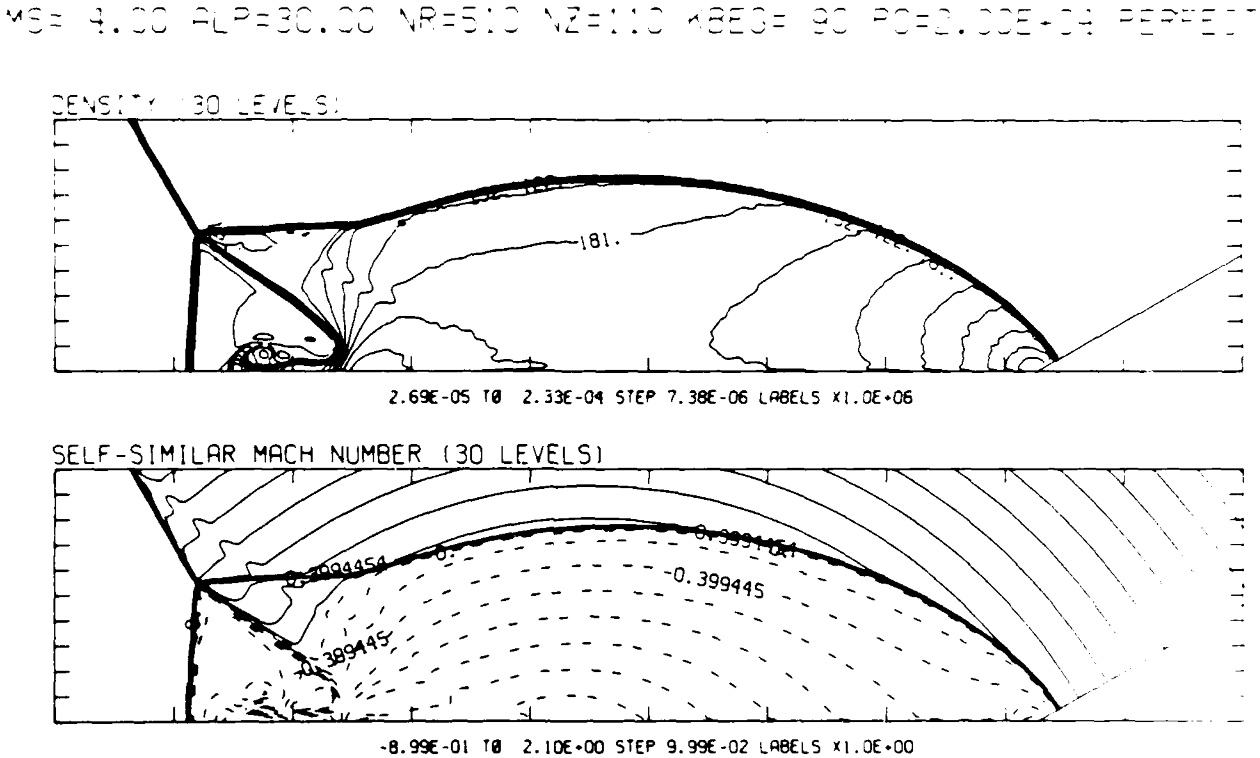

Figure 21.2a. θ_w = 30°, whole-flowfield contour-

Figure 21. Transition set 2, M_s = 4.0,

AD-A186 448 A DETAILED NUMERICAL GRAPHICAL AND EXPERIMENTAL STUDY OF OBLIQUE SHOCK WA (U) TORONTO UNIV DOWNSVIEW (ONTARIO) INST FOR AEROSPACE STUDIES H M GLAZ ET AL 4/5

UNCLASSIFIED 01 AUG 86 UTIAS-285 DNA-TR-86-365 F/G 20/4 NL

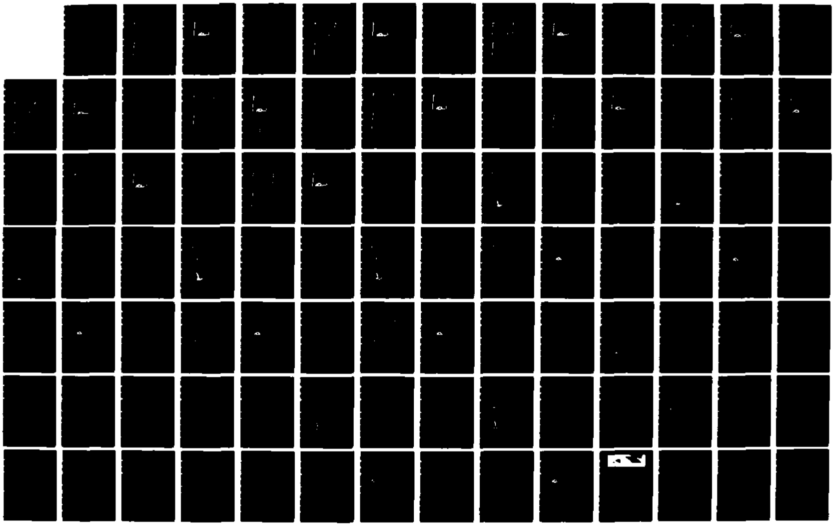

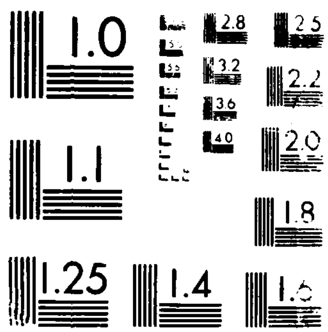
1.0
2.8
2.5
3.2
2.2
3.6
4.0
2.0
1.1
1.8
1.25
1.4

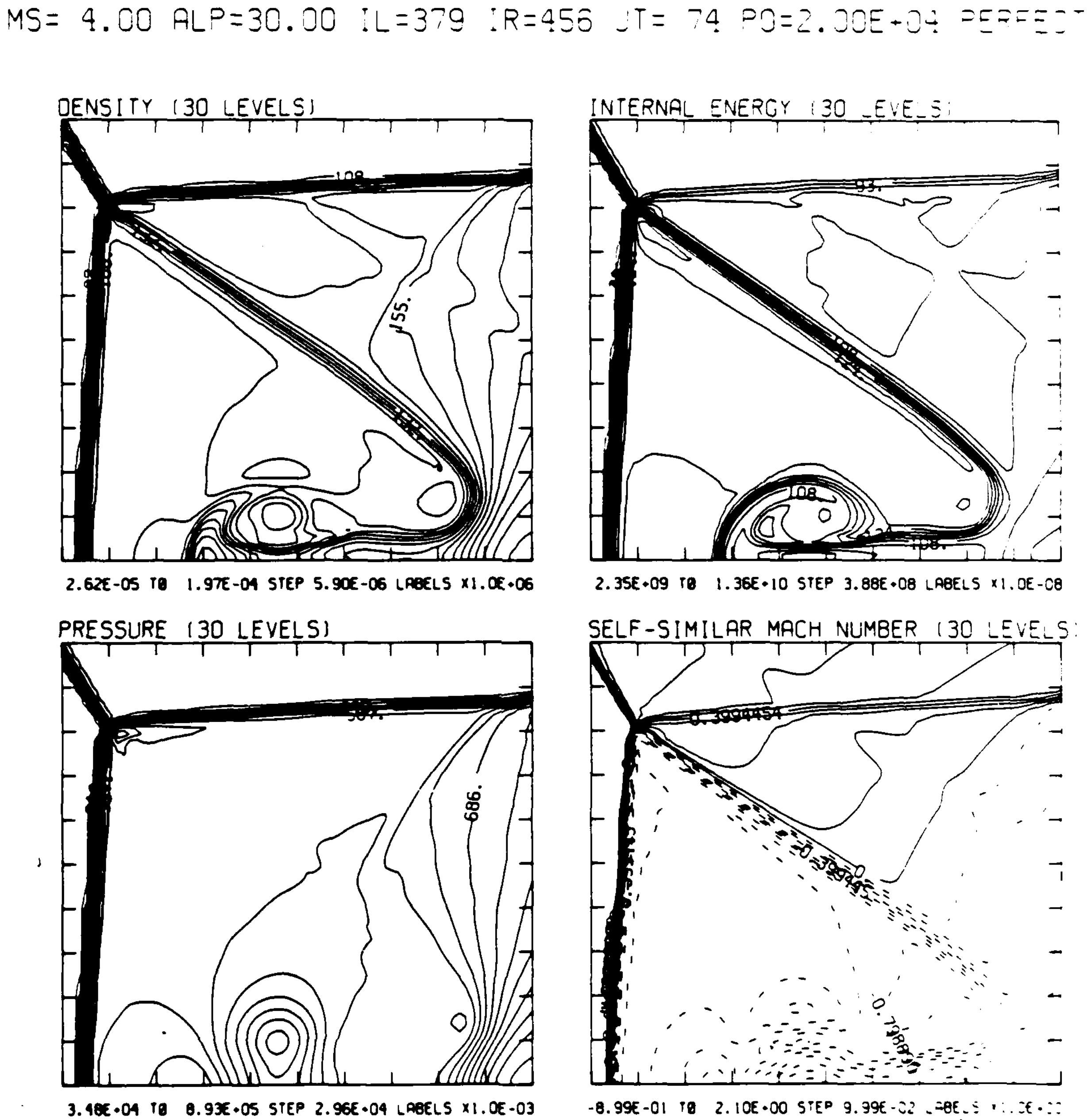

Figure 21.2b. $\theta_w = 30°$, blowup-frame plots.

Figure 21. Transition set 2, $M_s = 4.0$, $\gamma = 1.4$ - continued.

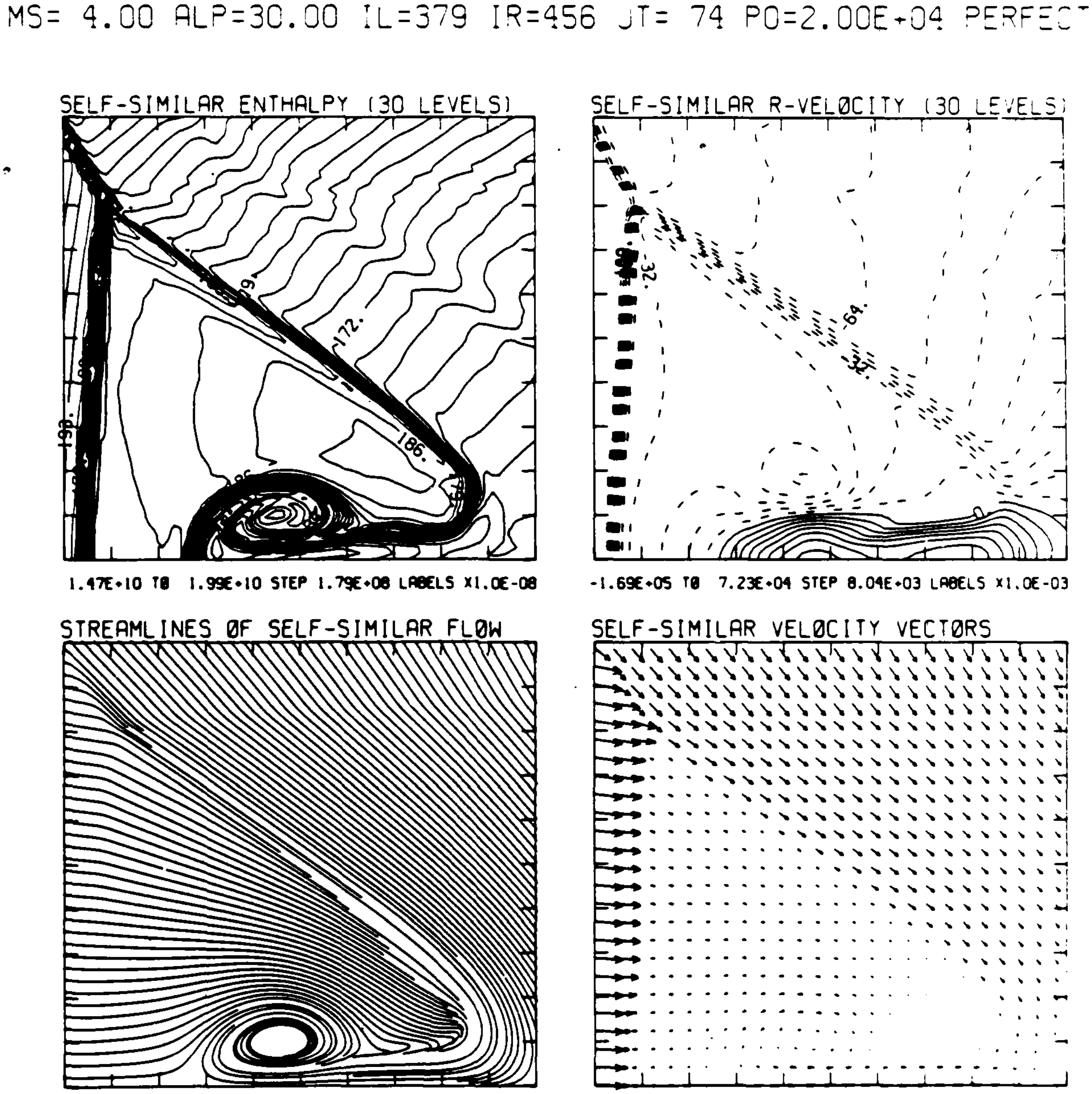

Figure 21.2b. $\theta_w = 30°$, blowup-frame plots - continued.

Figure 21. Transition set 2, $M_s = 4.0$, $\gamma = 1.4$ - continued.

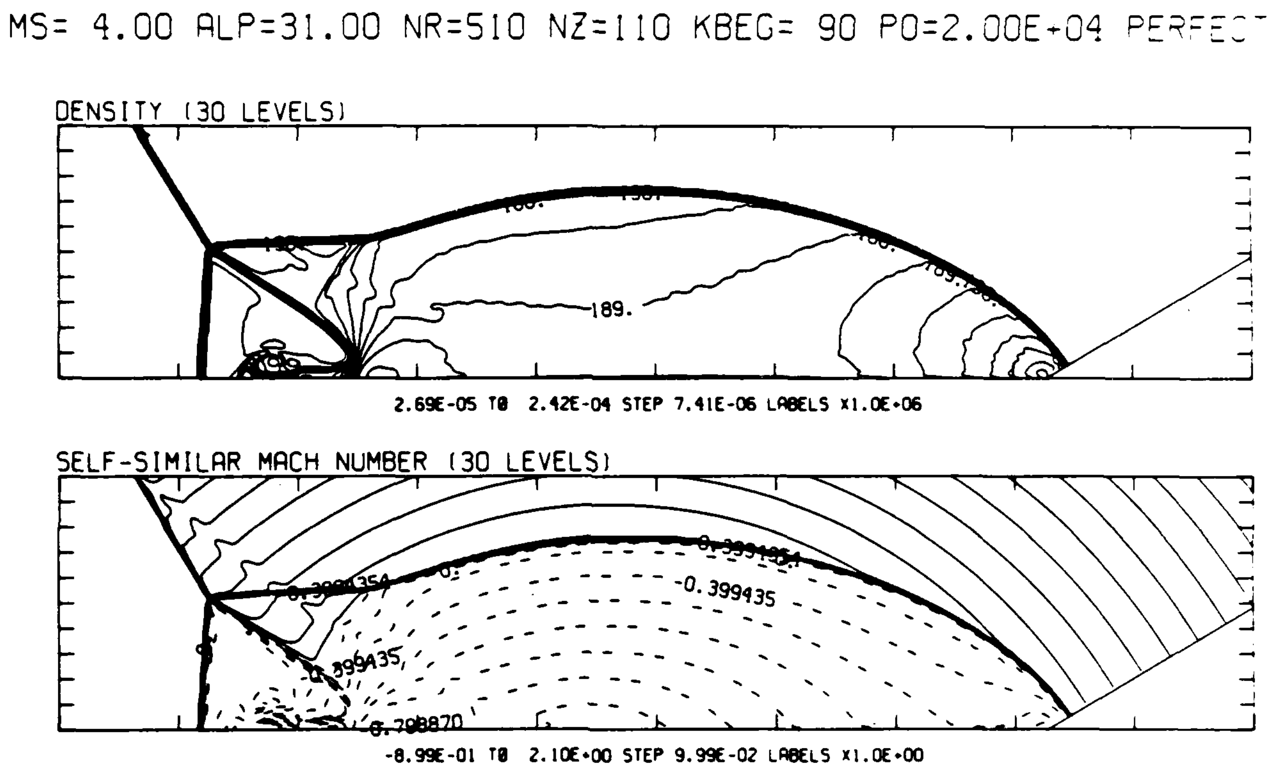

Figure 21.3a. $\theta_w = 31°$, whole-flowfield contour-plots.

Figure 21. Transition set 2, $M_s = 4.0$, $\gamma = 1.4$ - continued.

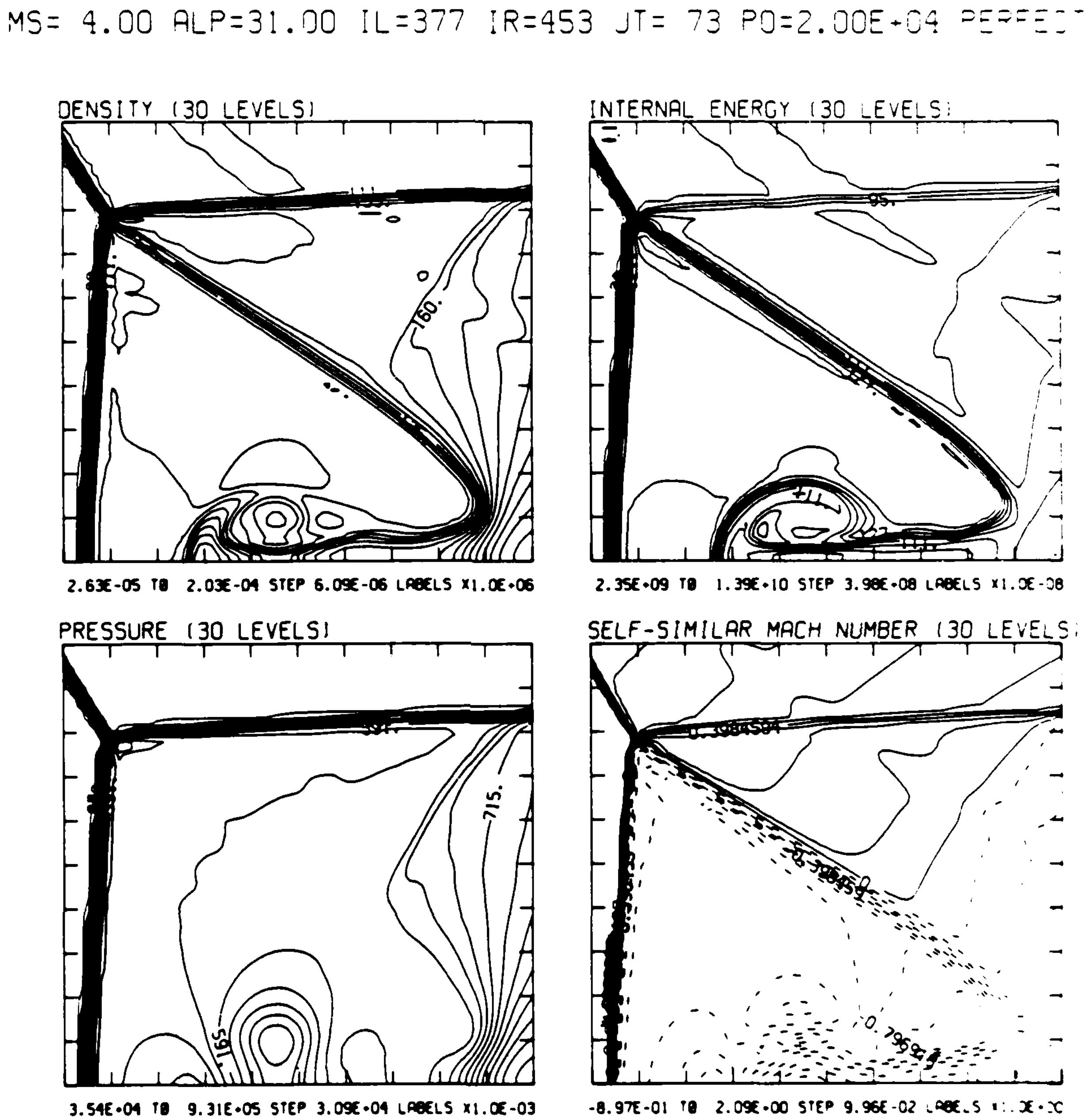

Figure 21.3b. $\theta_w = 31°$, blowup-frame plots.

Figure 21. Transition set 2, $M_s = 4.0$, $\gamma = 1.4$ - continued.

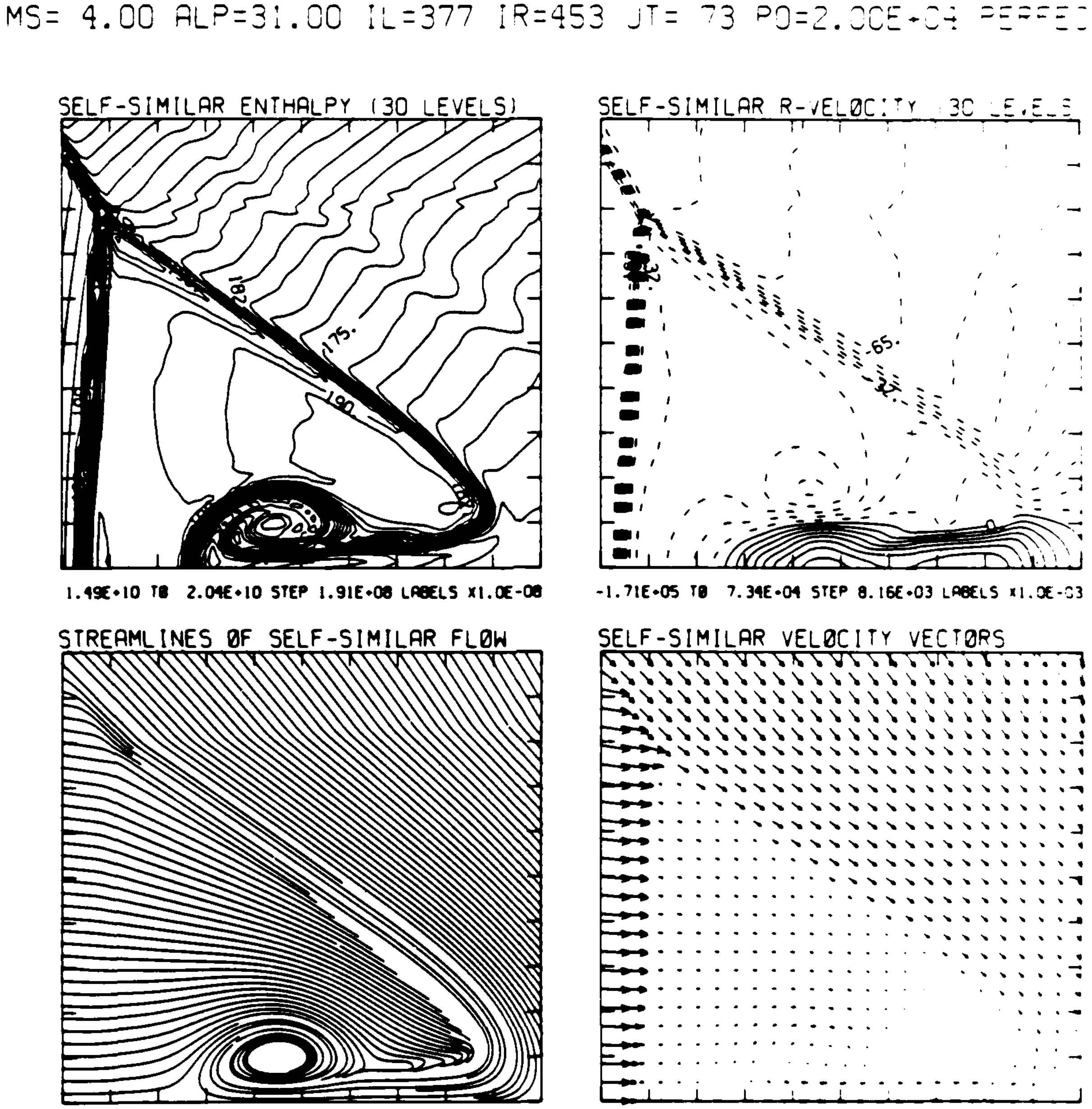

Figure 21.3b. $\theta_w = 31°$, blowup-frame plots - continued.

Figure 21. Transition set 2, $M_s = 4.0$, $\gamma = 1.4$ - continued.

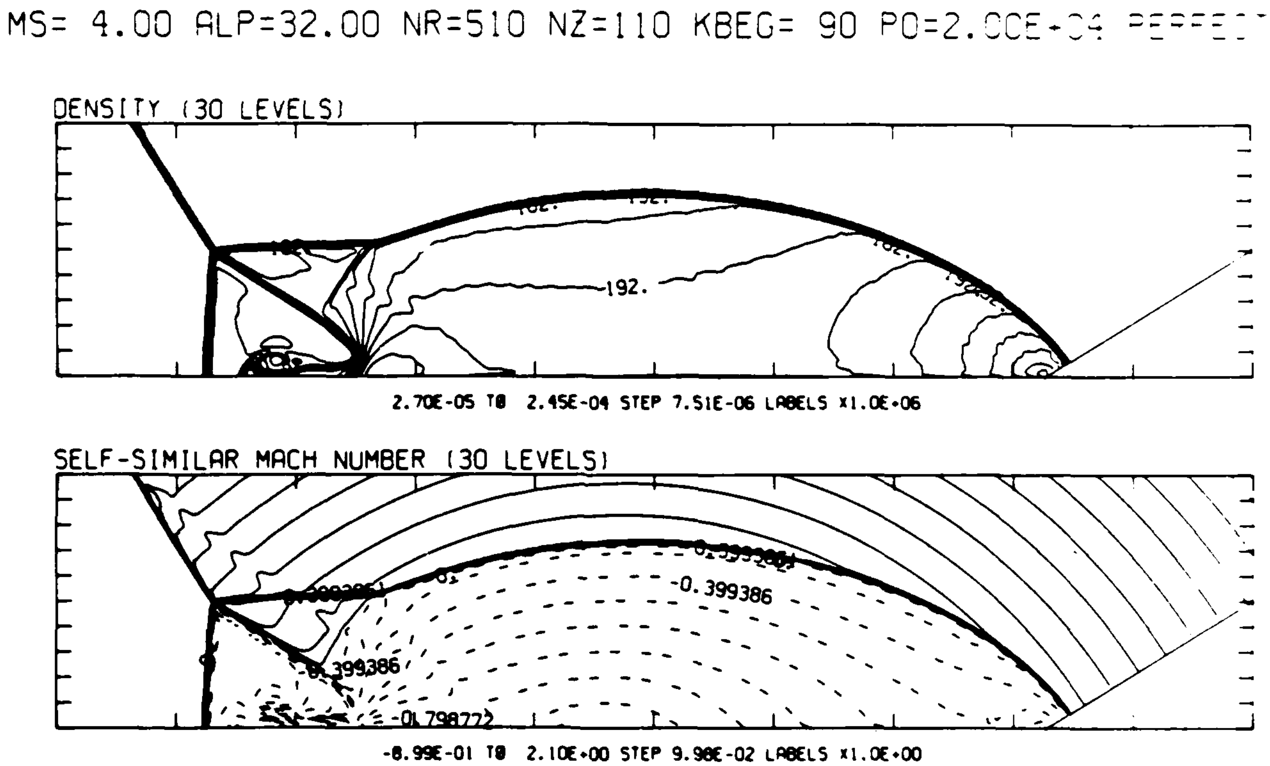

Figure 21.4a. $\theta_w = 32°$, whole-flowfield contour-plots.

Figure 21. Transition set 2, $M_s = 4.0$, $\gamma = 1.4$ - continued.

MS= 4.00 ALP=32.00 IL=375 IR=450 JT= 72 PO=2.00E-04 PERFECT

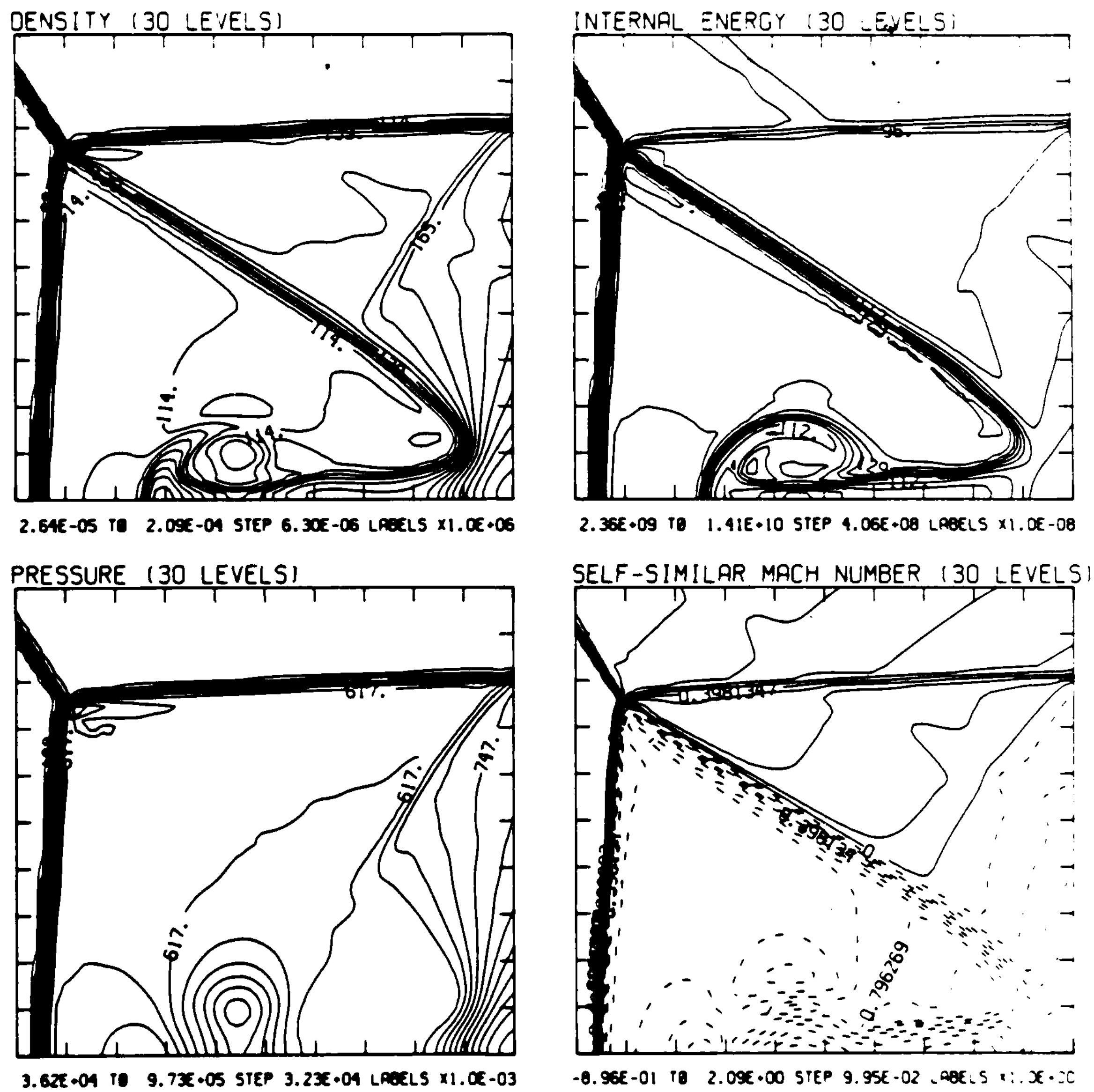

Figure 21.4b. $\theta_w = 32°$, blowup-frame plots.

Figure 21. Transition set 2, $M_s = 4.0$, $\gamma = 1.4$ - continued.

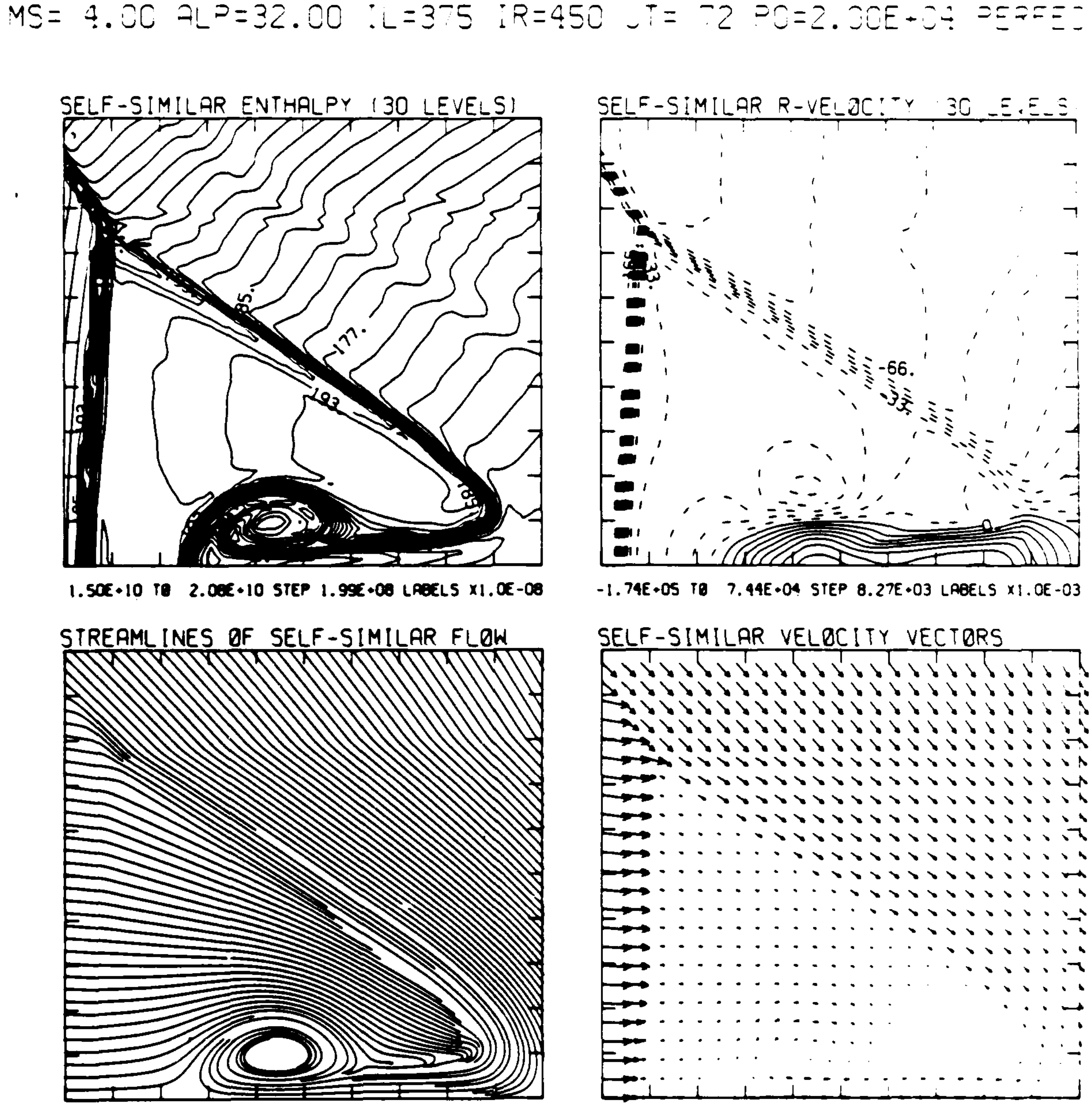

Figure 21.4b. $\theta_w = 32°$, blowup-frame plots - continued.

Figure 21. Transition set 2, $M_s = 4.0$, $\gamma = 1.4$ - continued.

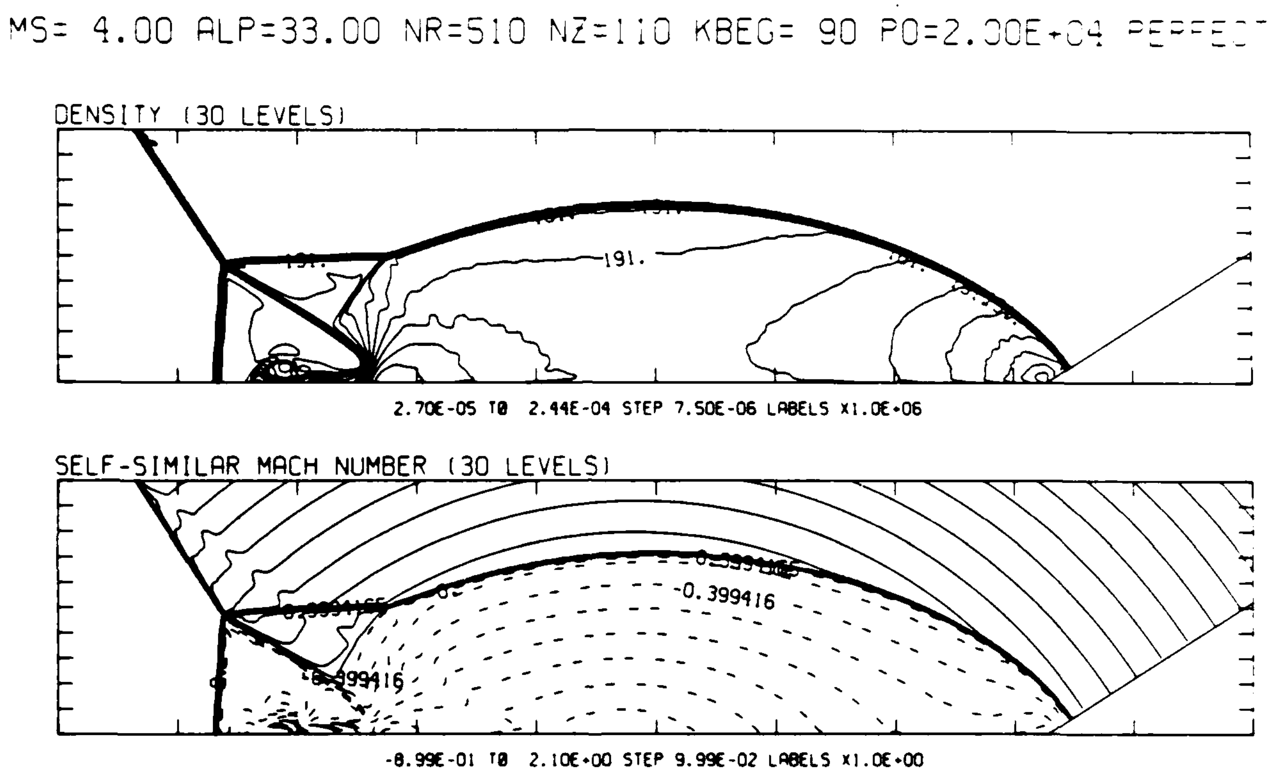

Figure 21.5a. θ_w = 33°, whole-flowfield contour-plots.

Figure 21. Transition set 2, M_s = 4.0, γ = 1.4 - continued.

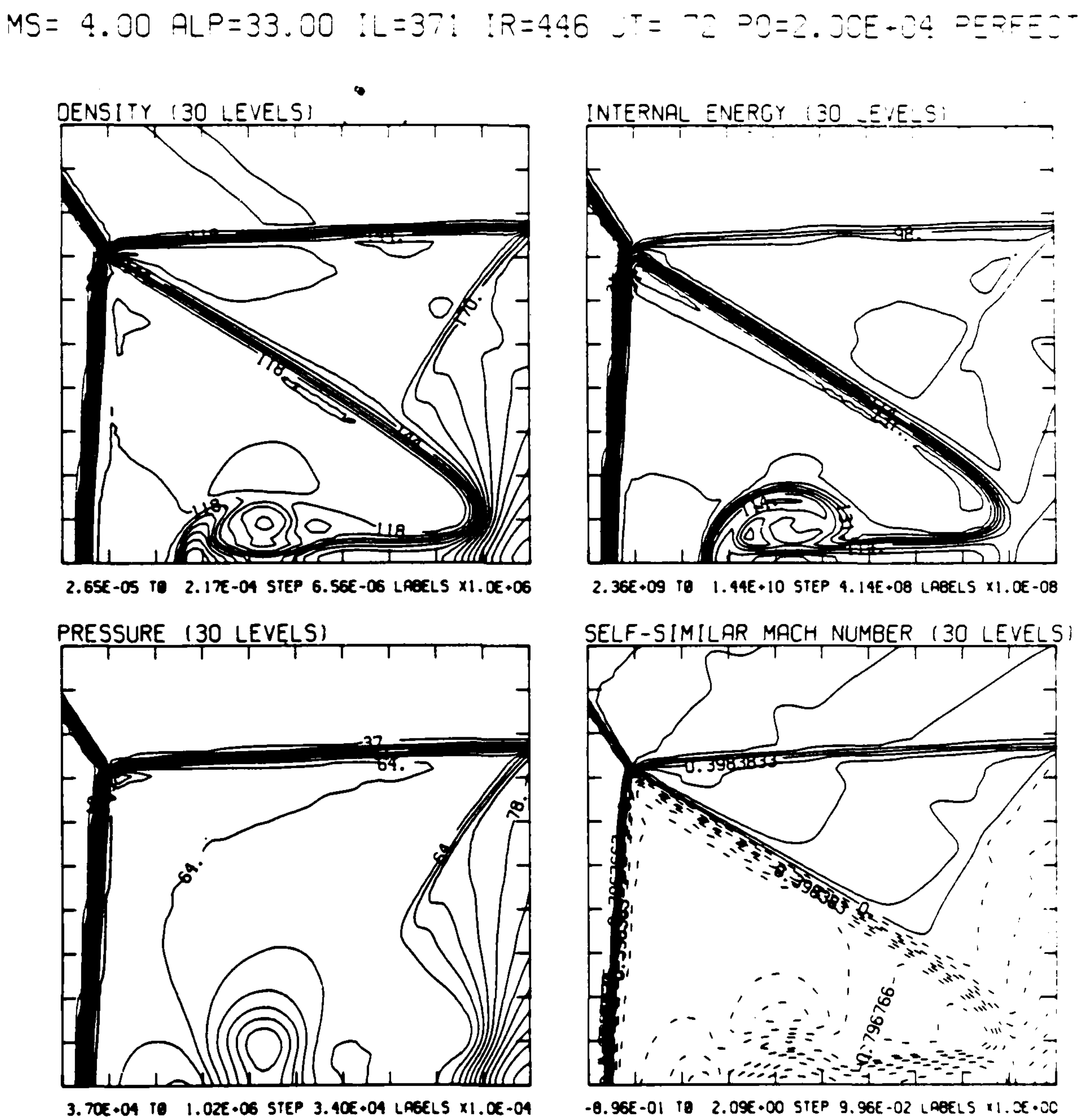

Figure 21.5b. $\theta_w = 33°$, blowup-frame plots.

Figure 21. Transition set 2, $M_s = 4.0$, $\gamma = 1.4$ - continued.

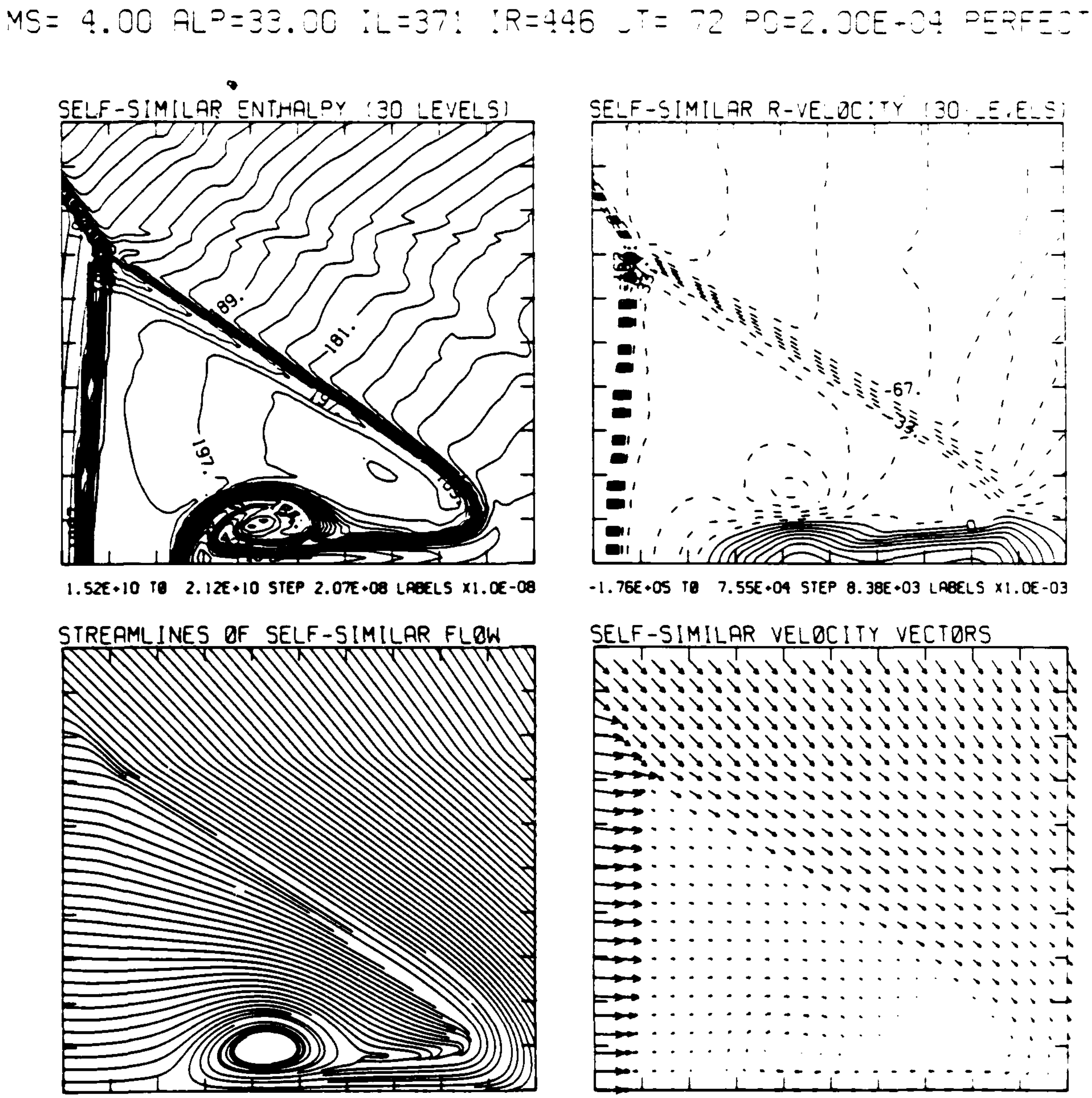

Figure 21.5b. $\theta_w = 33°$, blowup-frame plots - continued.

Figure 21. Transition set 2, $M_s = 4.0$, $\gamma = 1.4$ - continued.

MS= 4.00 ALP=34.00 NR=510 NZ=110 KBEG= 90 PO=2.00E+04 PERFECT

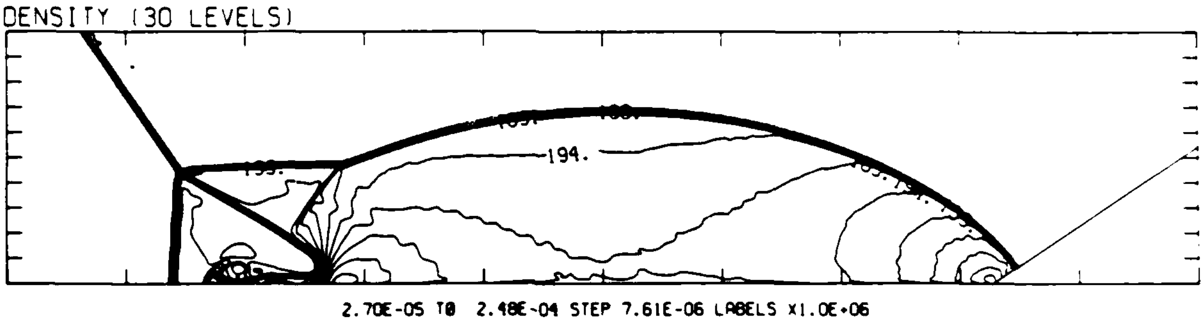

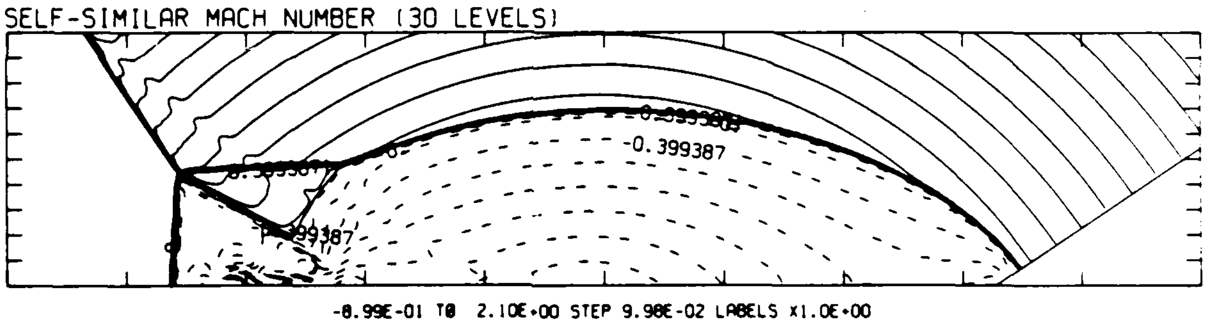

Figure 21.6a. θ_w = 34°, whole-flowfield contour-plots.

Figure 21. Transition set 2, M_s = 4.0, γ = 1.4 - continued.

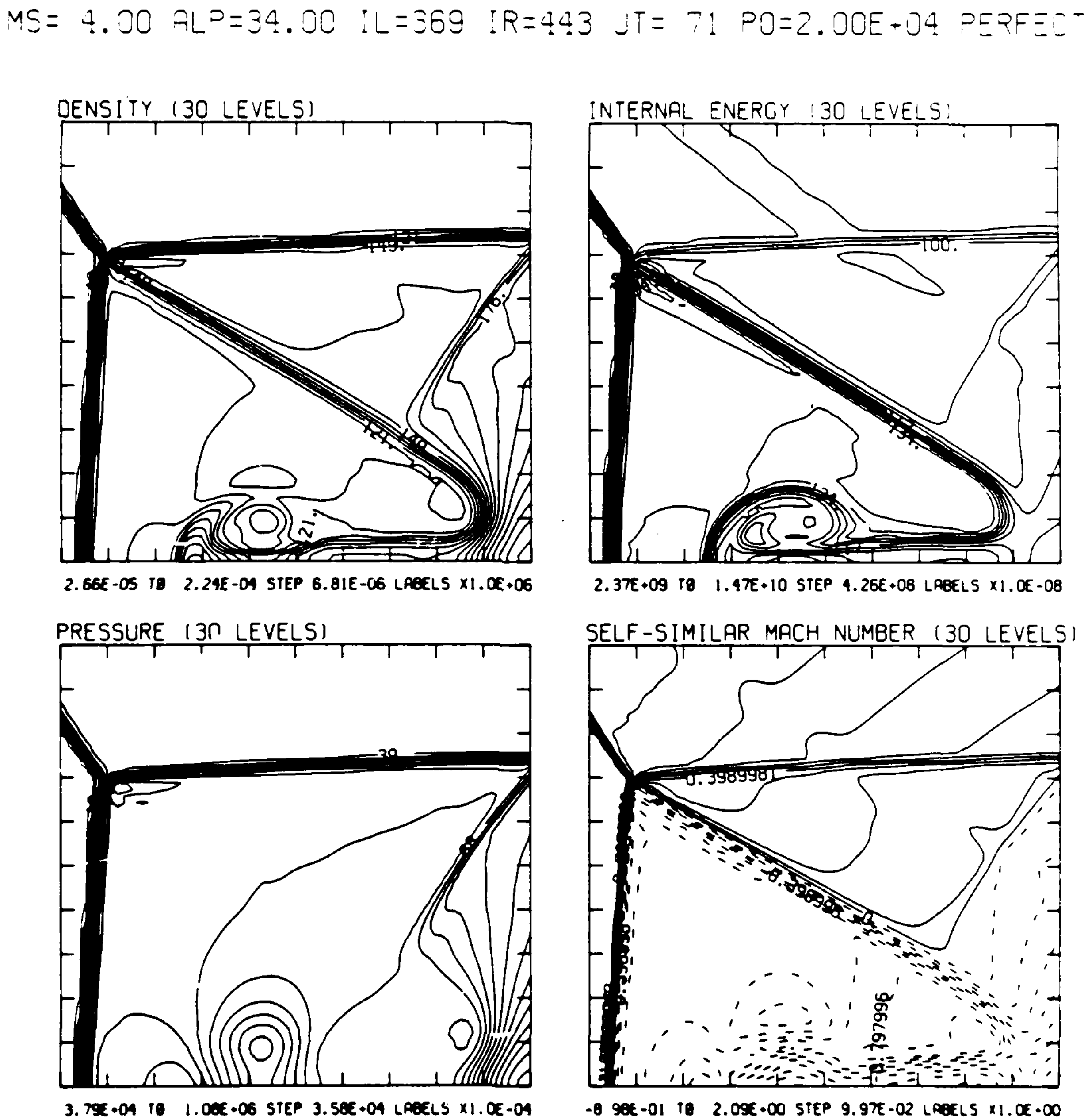

Figure 21.6b. $\theta_w = 34°$, blowup-frame plots.

Figure 21. Transition set 2, $M_s = 4.0$, $\gamma = 1.4$ - continued.

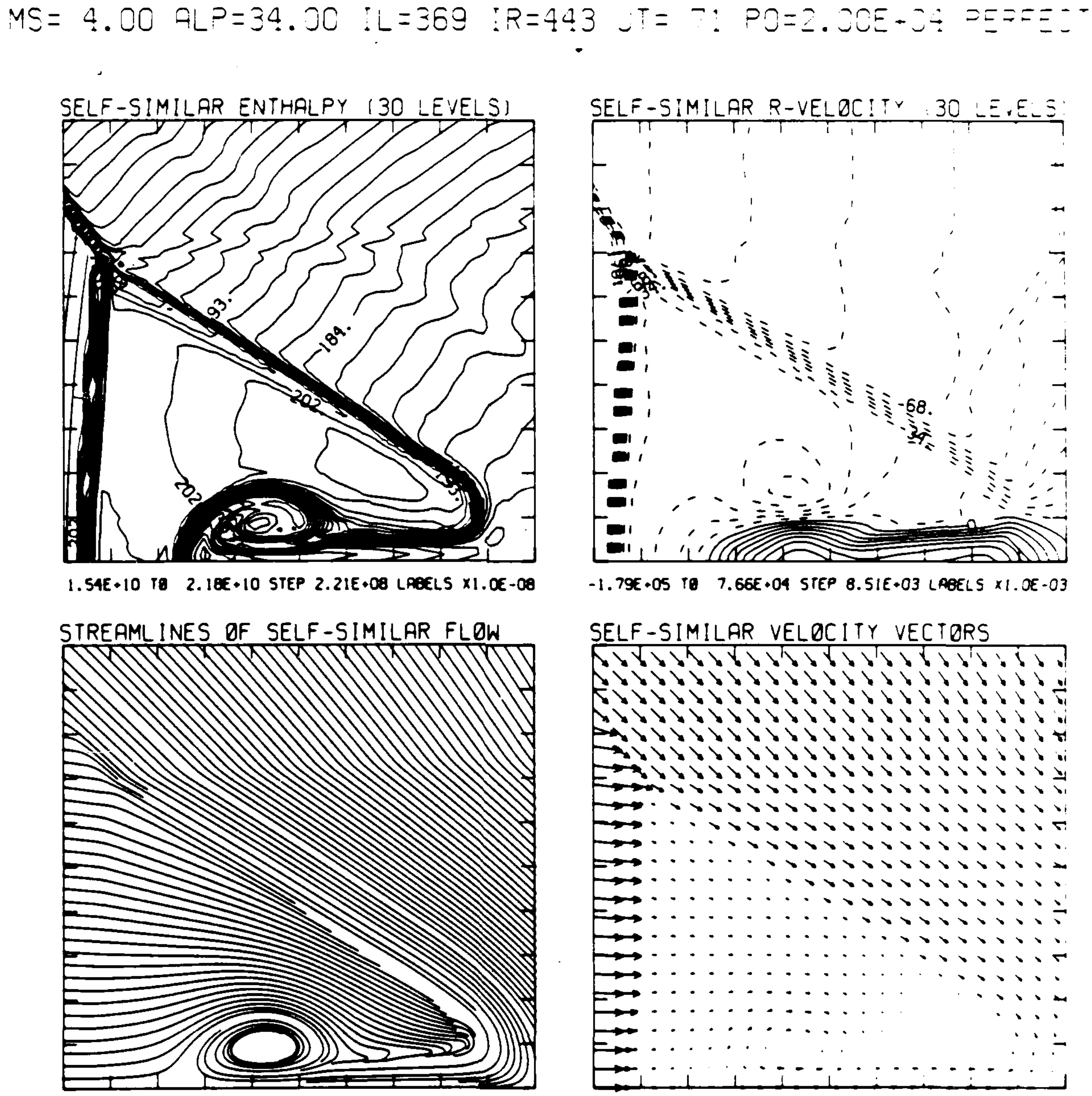

Figure 21.6b. θ_w = 34°, blowup-frame plots - continued.

Figure 21. Transition set 2, M_s = 4.0, γ = 1.4 - continued.

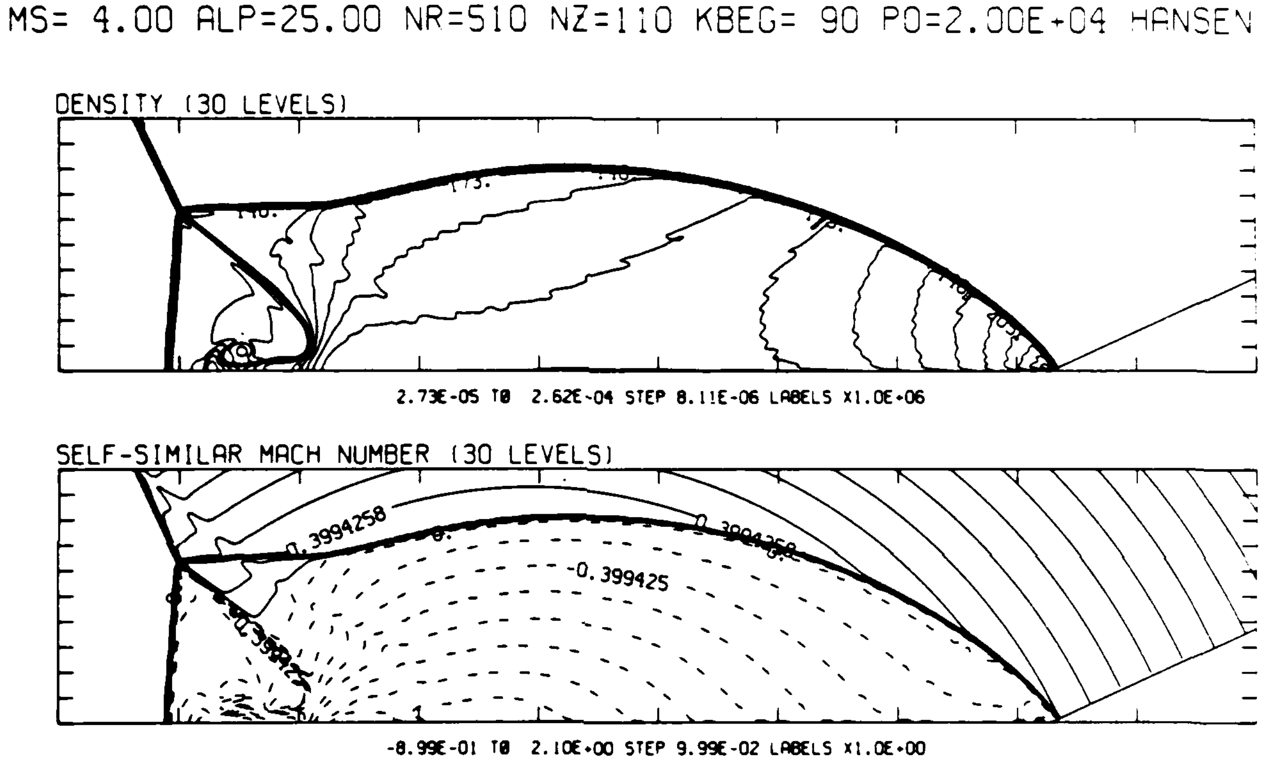

Figure 22.1a. θ_W = 25°, whole-flowfield contour-plots.

Figure 22. Transition set 2, M_S = 4.0, Hansen.

MS= 4.00 ALP=25.00 IL=388 IR=467 JT= 76 PO=2.00E+04 HANSEN

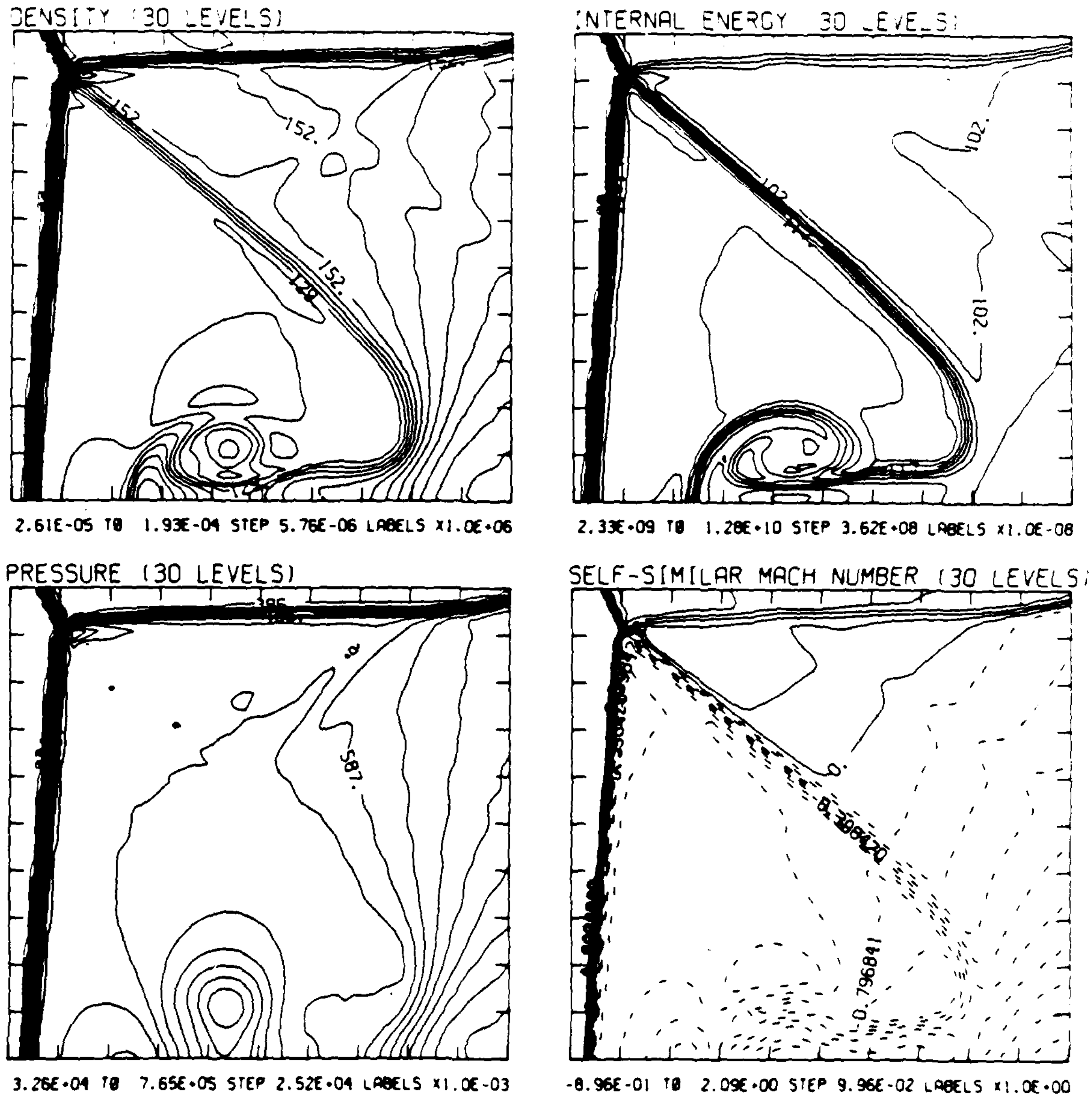

Figure 22.1b. θ_w = 25°, blowup-frame plots.

Figure 22. Transition set 2, M_s = 4.0, Hansen - continued.

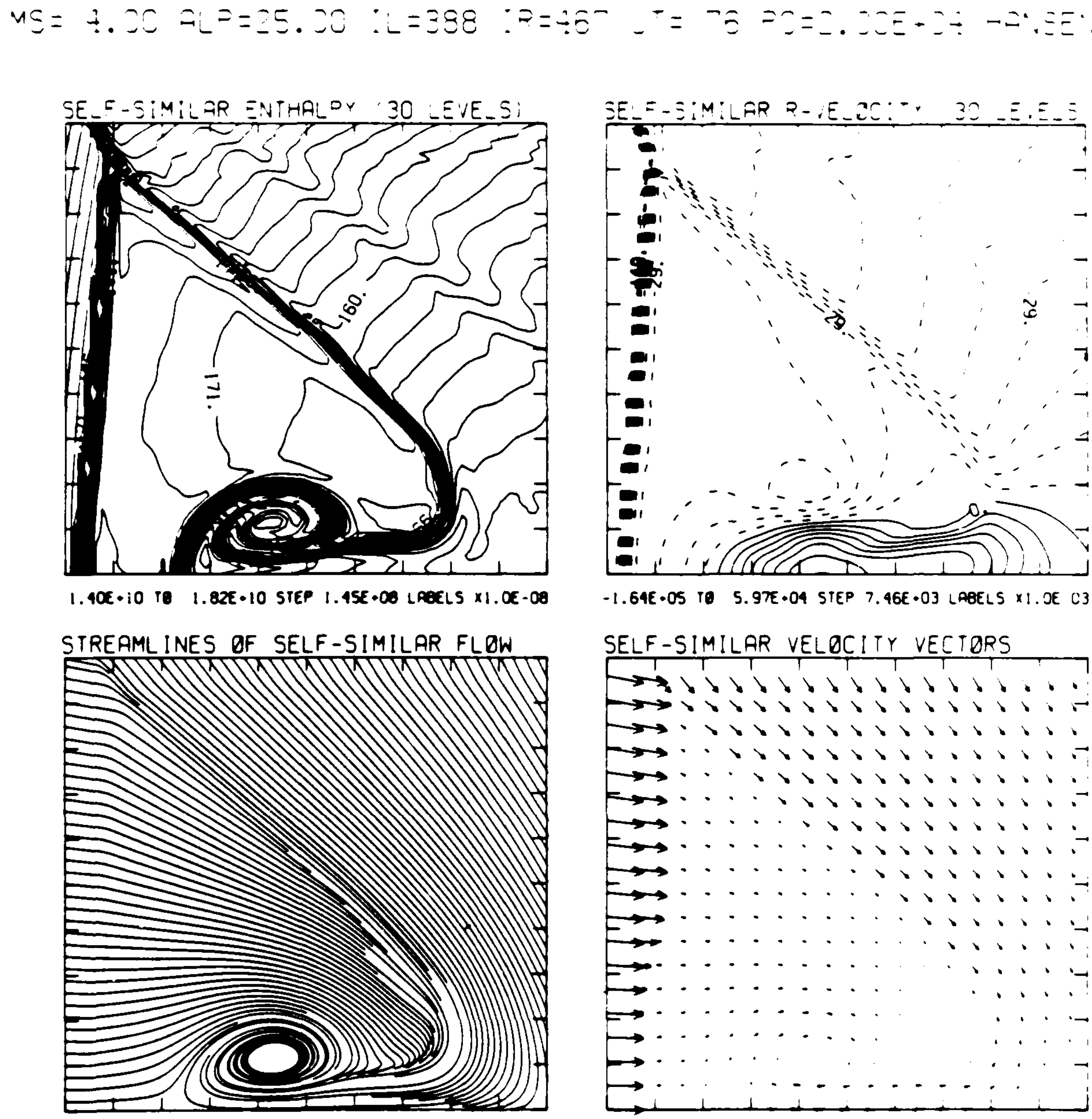

Figure 22.1b. θ_w = 25°, blowup-frame plots - continued.

Figure 22. Transition set 2, M_s = 4.0, Hansen - continued.

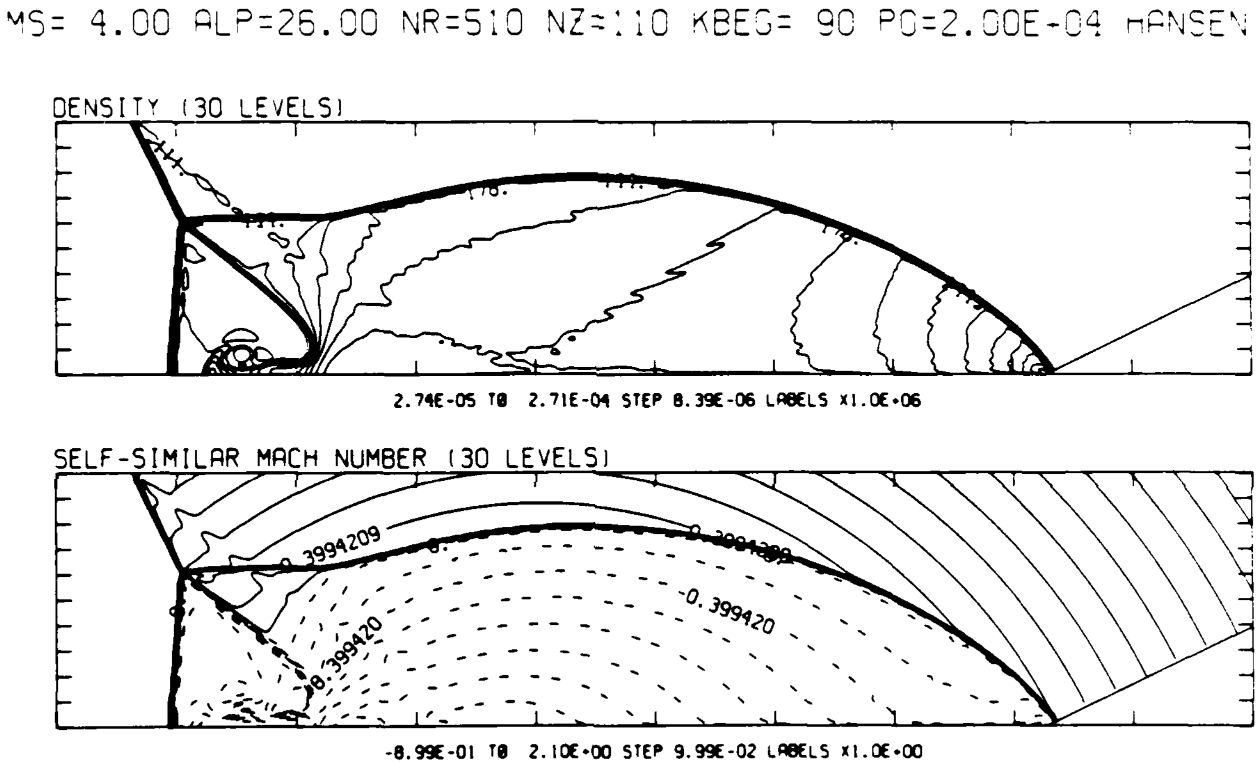

Figure 22.2a. θ_w = 26°, whole-flowfield contour-plots.

Figure 22. Transition set 2, M_s = 4.0, Hansen - continued.

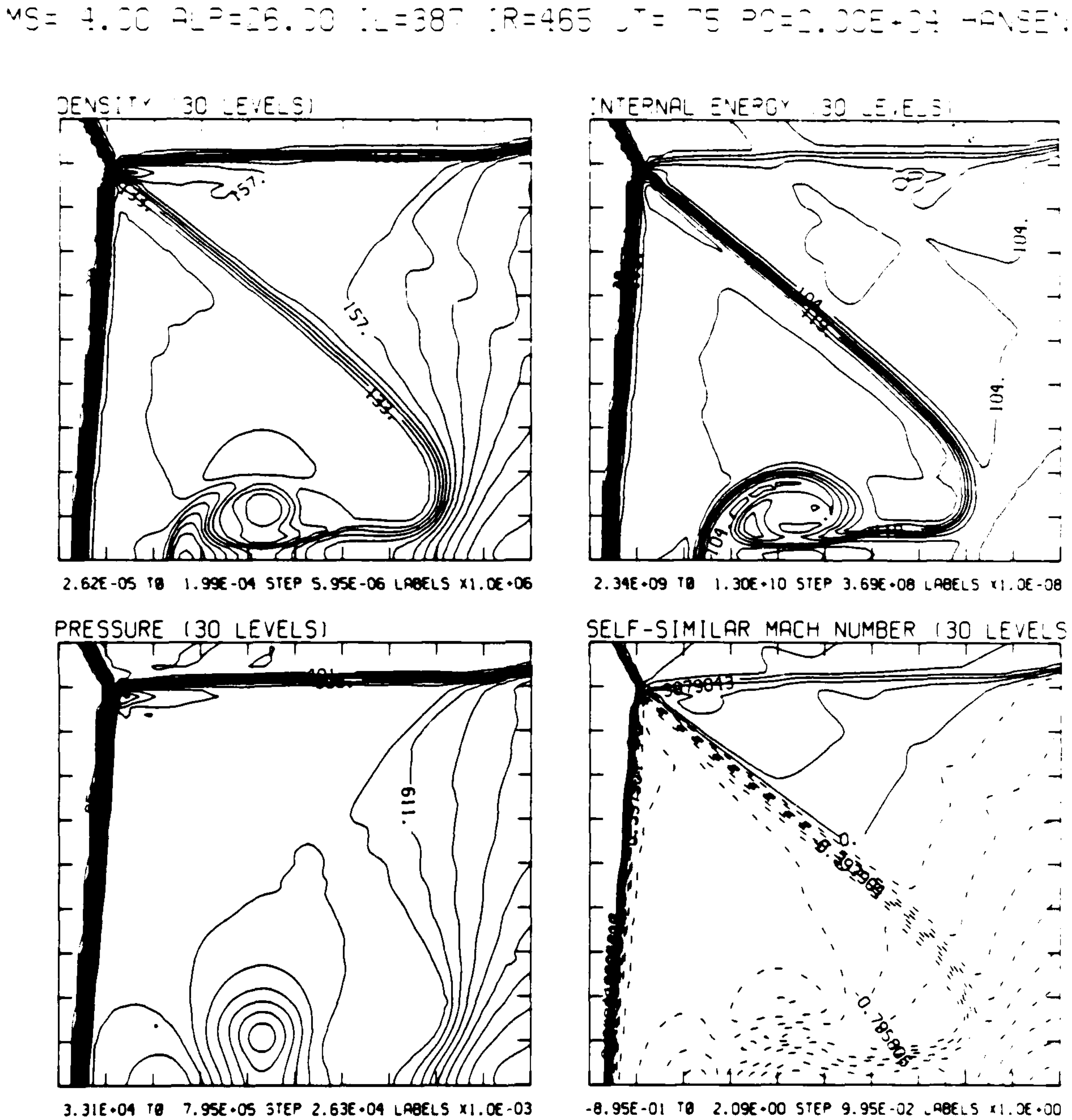

Figure 22.2b. θ_w = 26°, blowup-frame plots.

Figure 22. Transition set 2, M_s = 4.0, Hansen - continued.

MS= 4.00 ALP=26.00 IL=387 IR=465 JT= 75 PC=0.00E+04 HANSEN

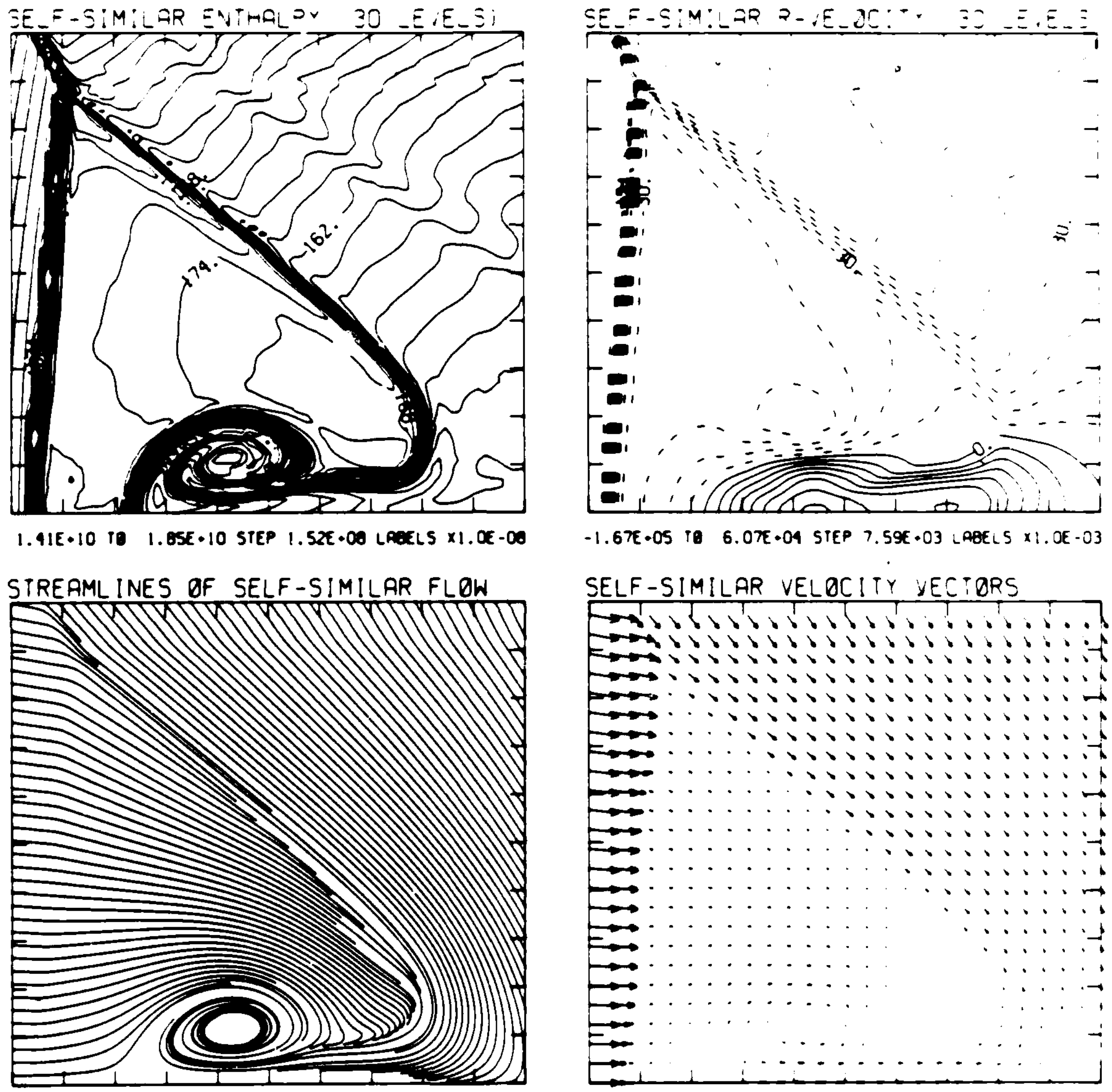

Figure 22.2b. θ_w = 26°, blowup-frame plots - continued.

Figure 22. Transition set 2, M_s = 4.0, Hansen - continued.

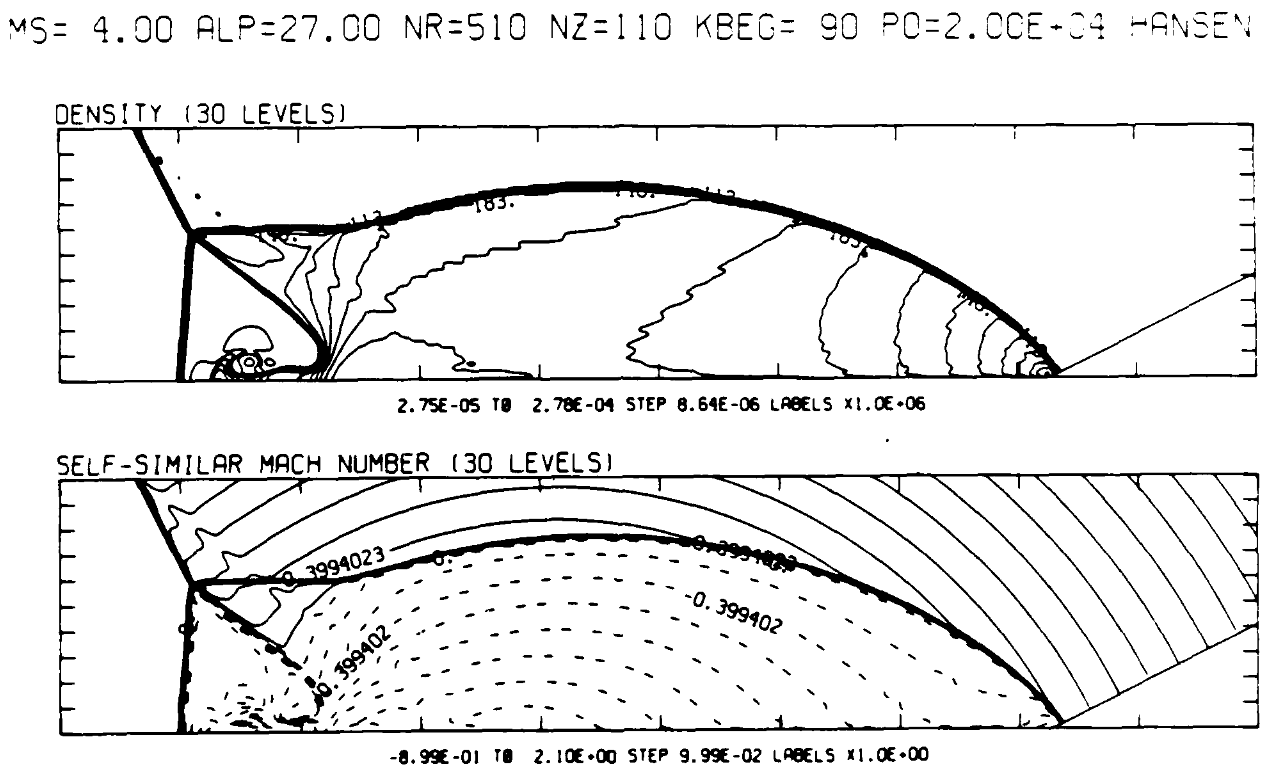

Figure 22.3a. $\theta_w = 27°$, whole-flowfield contour-plots.

Figure 22. Transition set 2, $M_s = 4.0$, Hansen - continued.

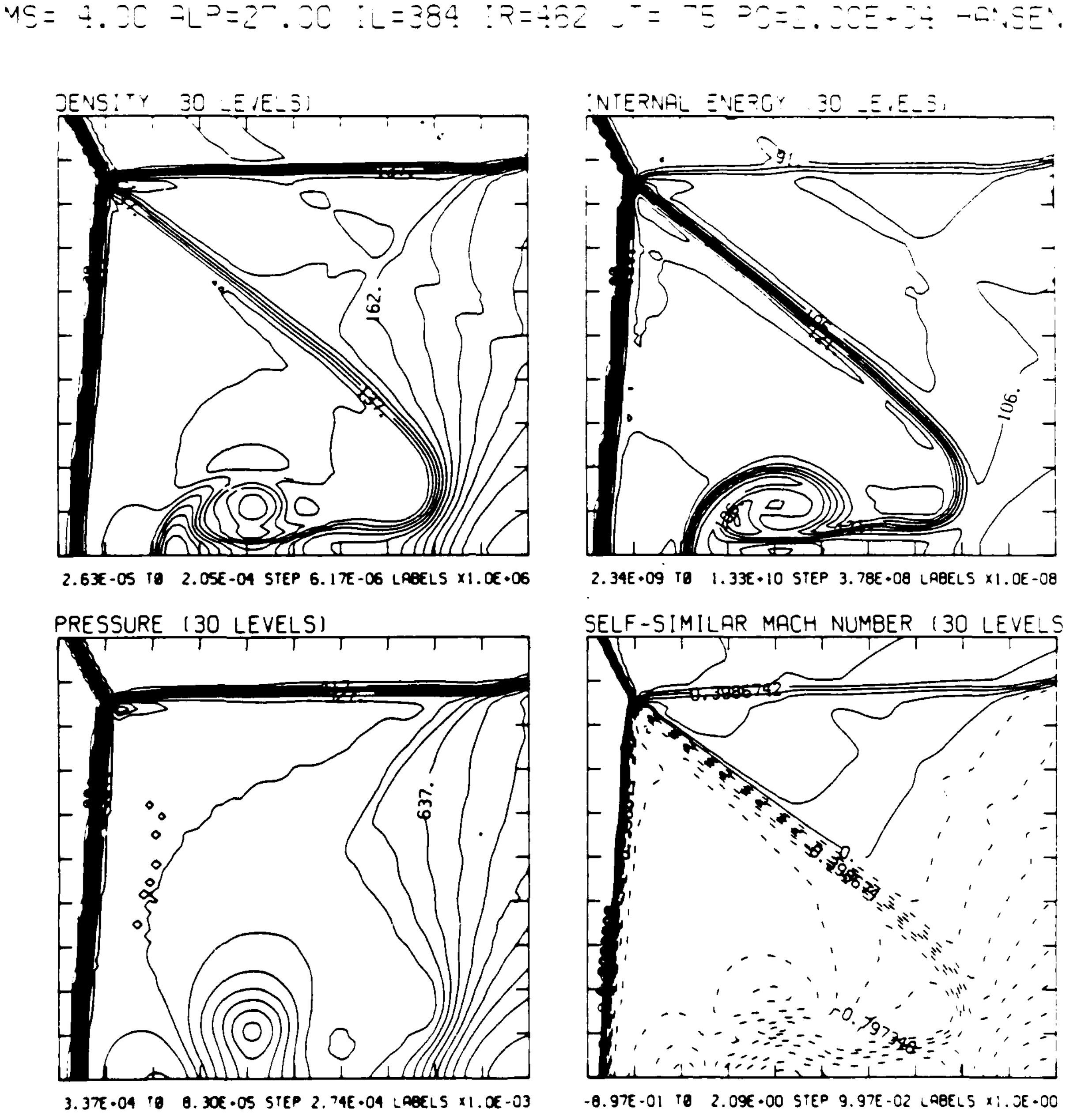

Figure 22.3b. $\theta_w = 27°$, blowup-frame plots.

Figure 22. Transition set 2, $M_s = 4.0$, Hansen - continued.

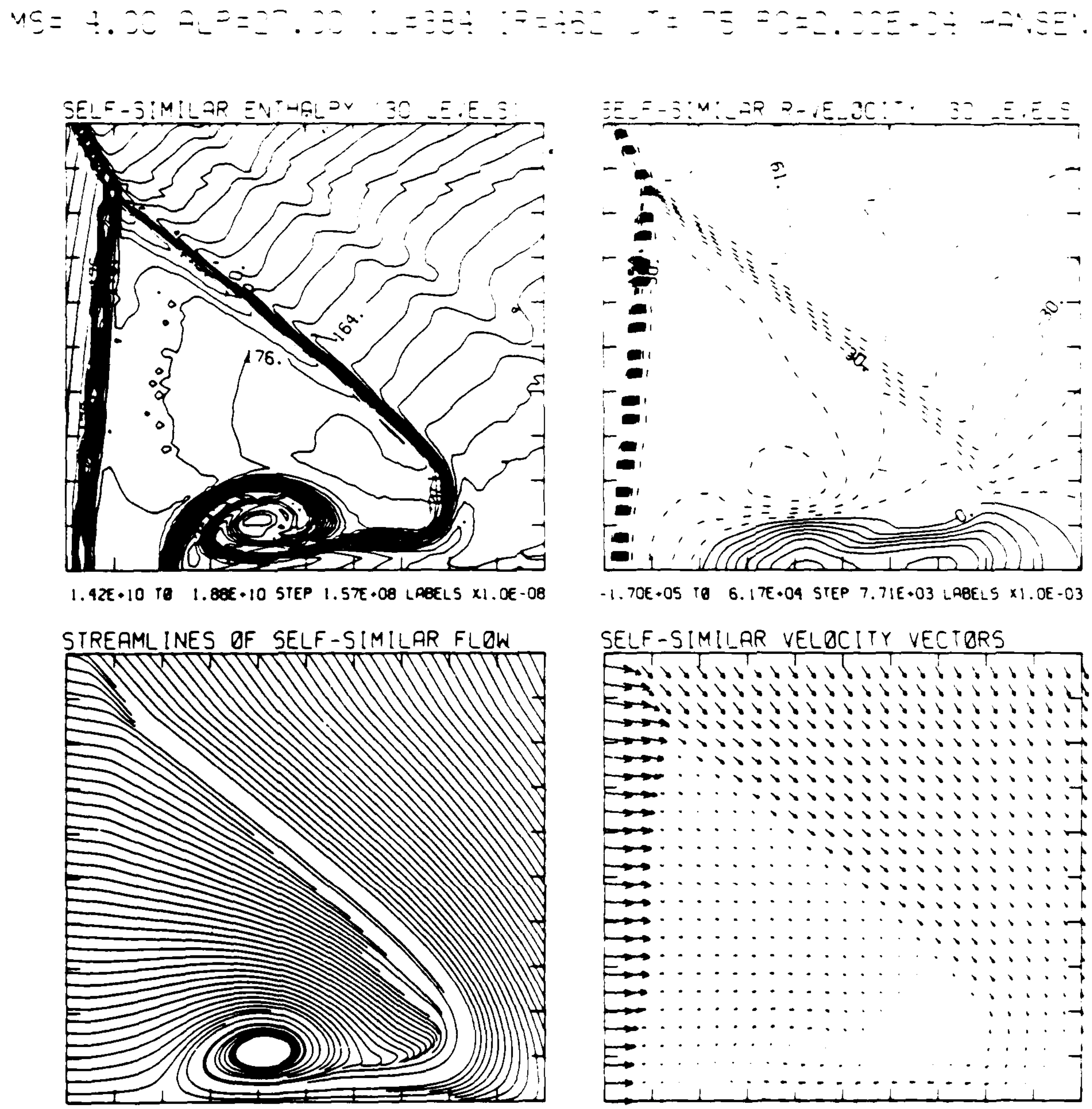

Figure 22.3b. θ_w = 27°, blowup-frame plots - continued.

Figure 22. Transition set 2, M_s = 4.0, Hansen - continued.

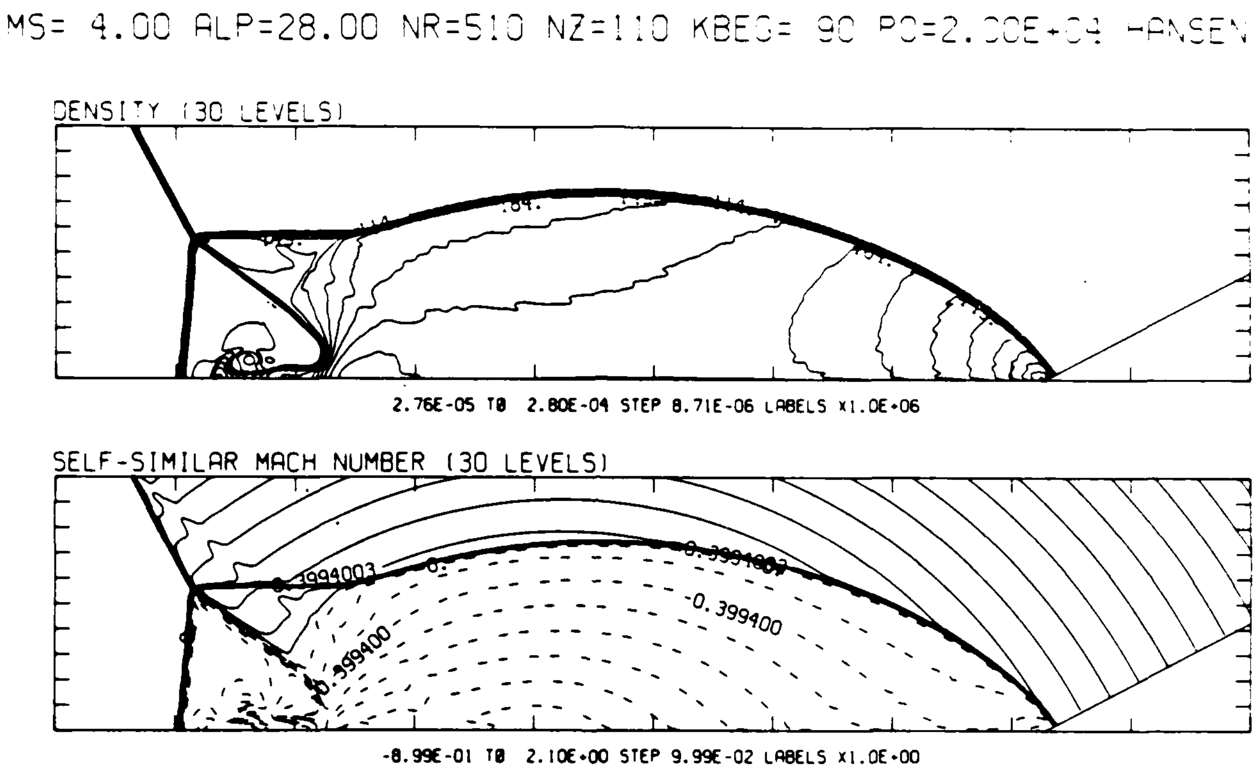

Figure 22.4a. θ_w = 28°, whole-flowfield contour-plots.

Figure 22. Transition set 2, M_s = 4.0, Hansen - continued.

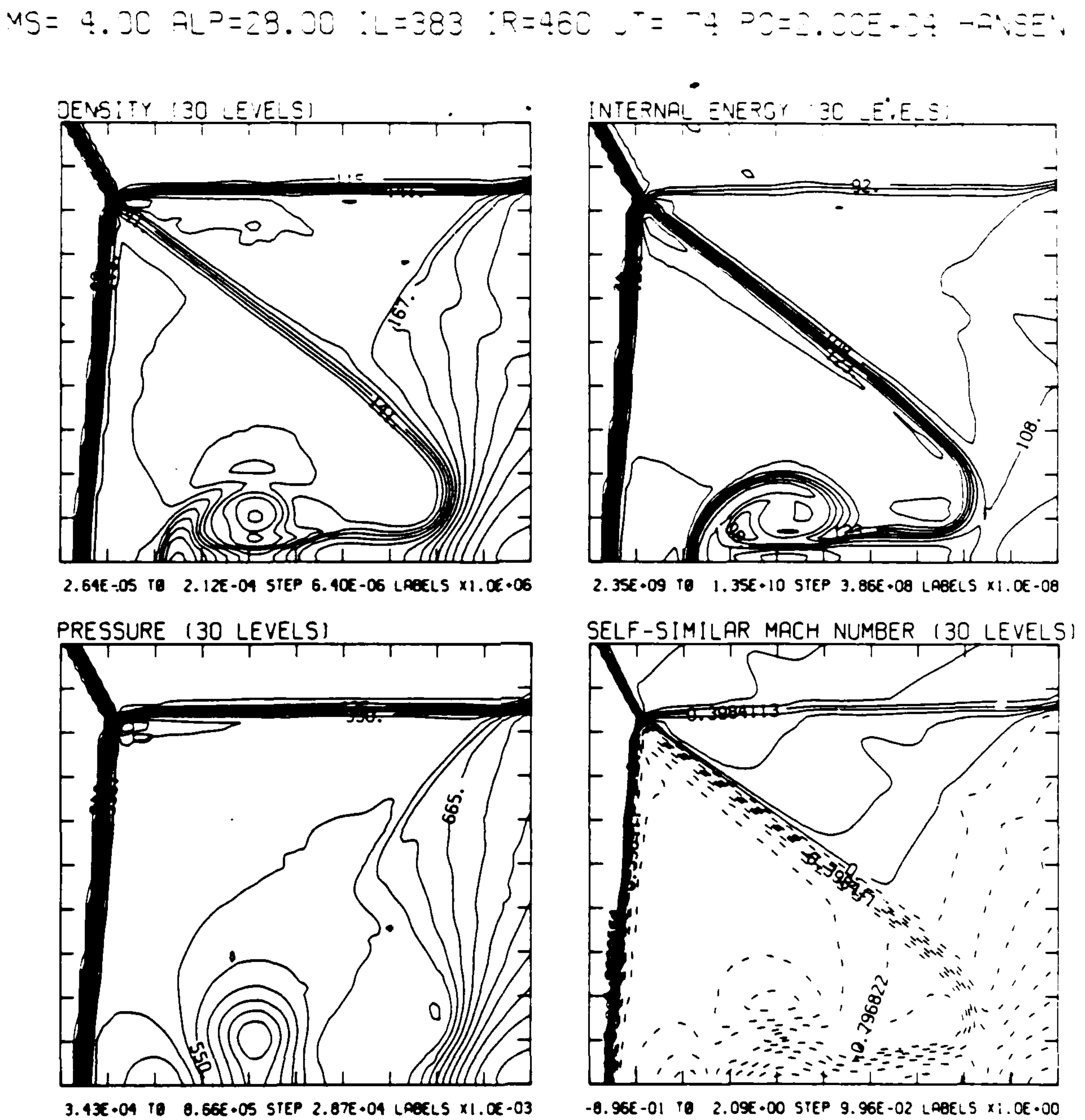

Figure 22.4b. θ_w = 28°, blowup-frame plots.

Figure 22. Transition set 2, M_s = 4.0, Hansen - continued.

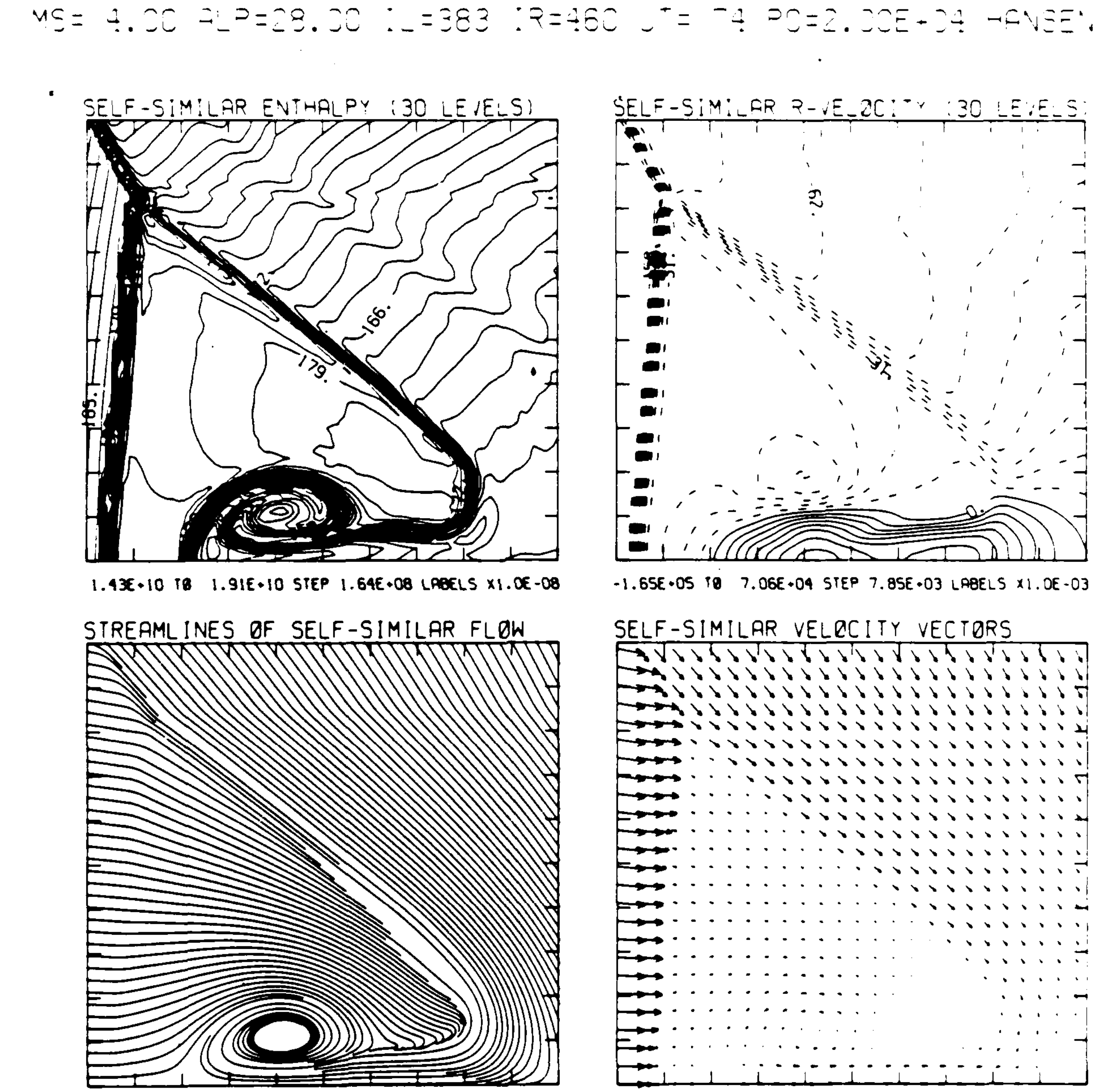

Figure 22.4b. θ_w = 28°, blowup-frame plots - continued.

Figure 22. Transition set 2, M_s = 4.0, Hansen - continued.

MS= 4.00 ALP=29.00 NR=510 NZ=110 KBEG= 90 PO=2.00E+04 HANSEN

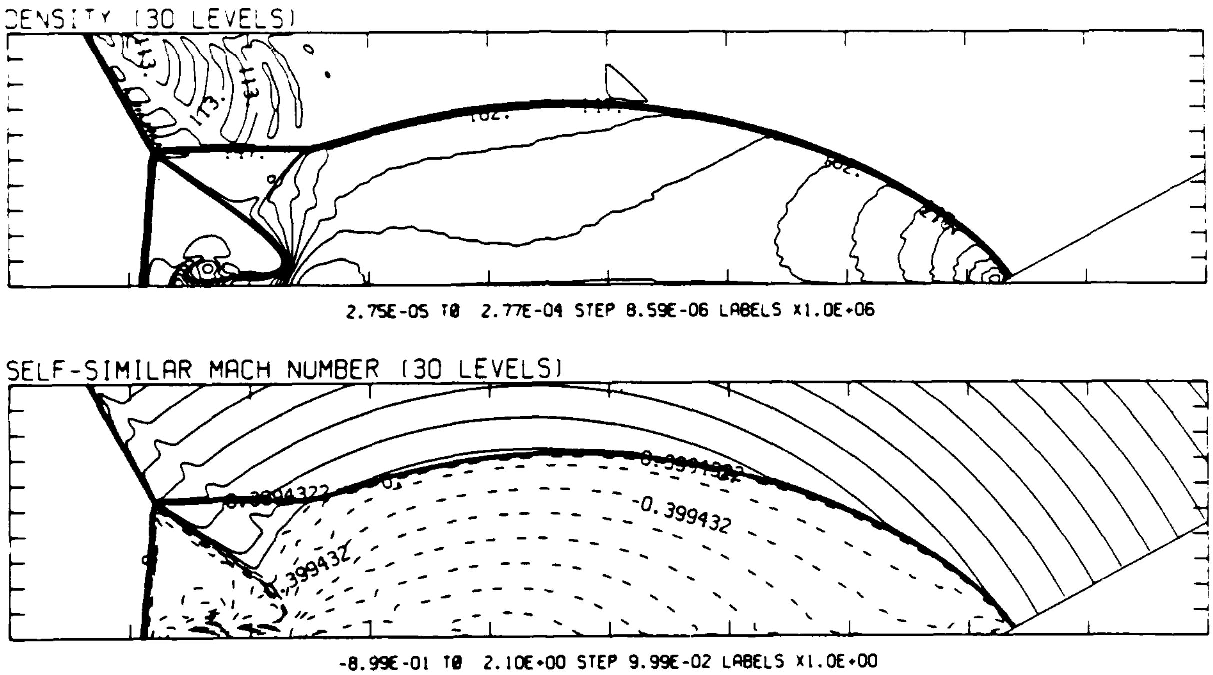

Figure 22.5a. θ_w = 29°, whole-flowfield contour-plots.

Figure 22. Transition set 2, M_s = 4.0, Hansen - continued.

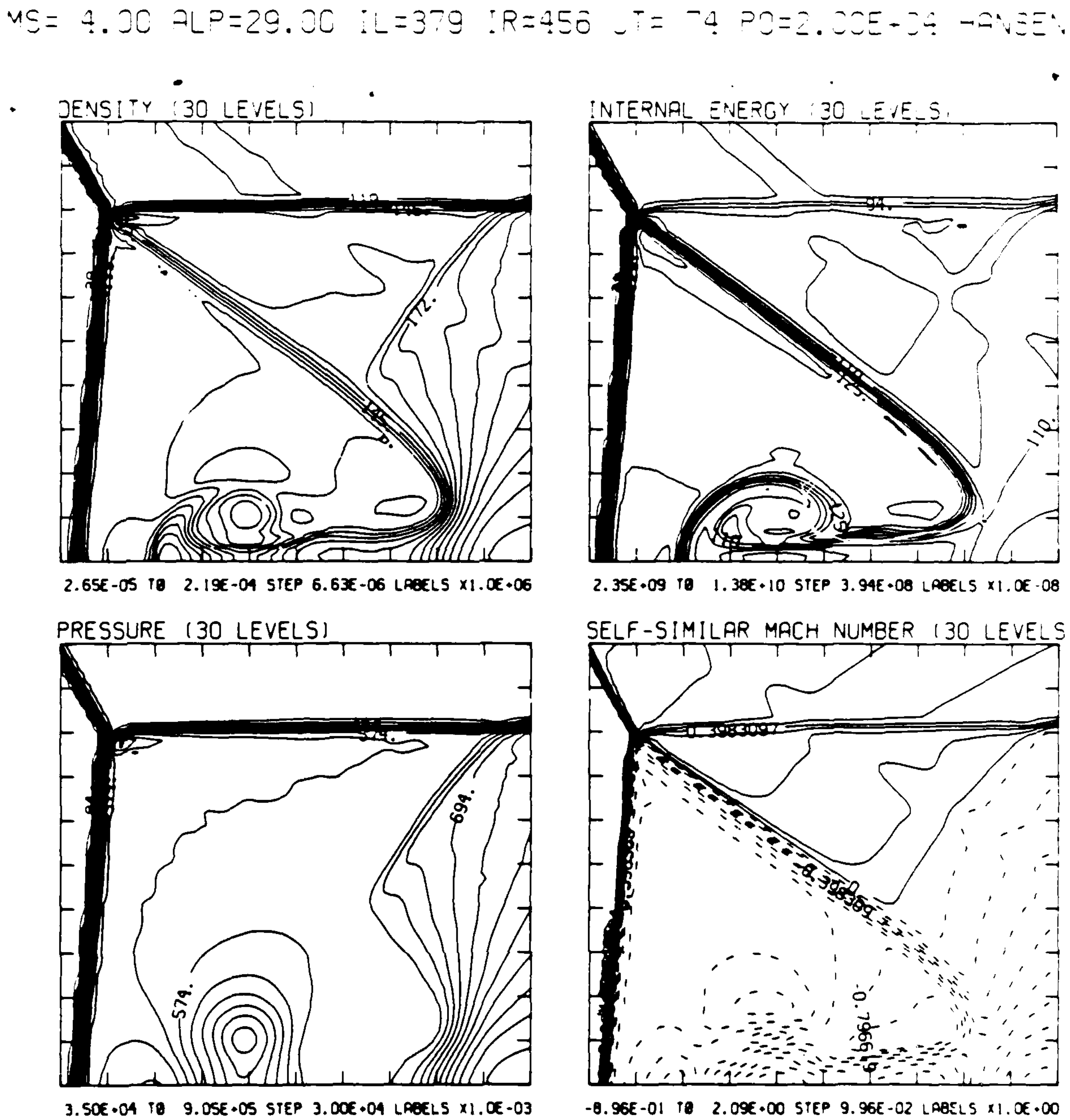

Figure 22.5b. $\theta_W = 29°$, blowup-frame plots.

Figure 22. Transition set 2, $M_S = 4.0$, Hansen - continued.

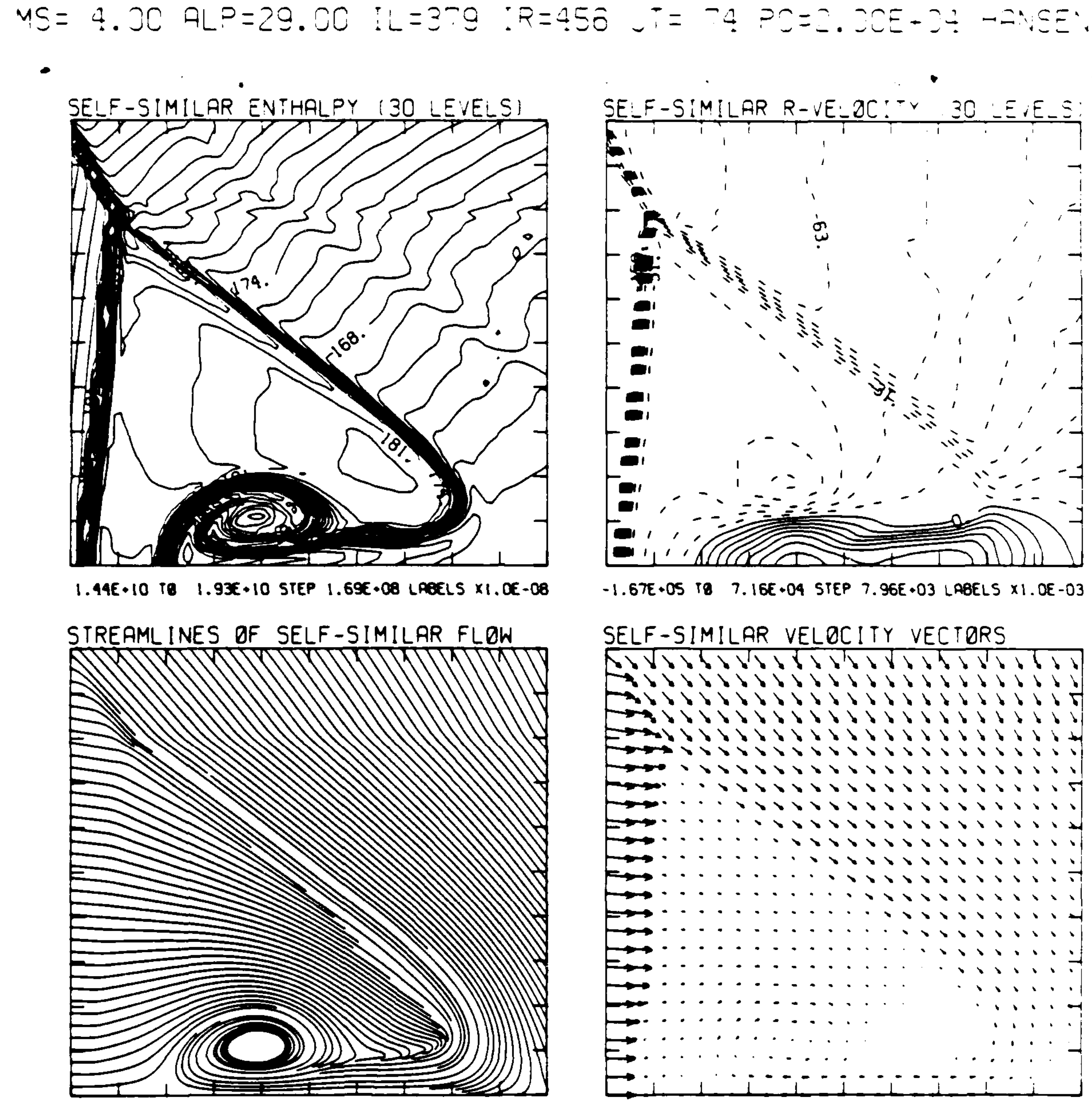

Figure 22.5b. $\theta_W = 29°$, blowup-frame plots - continued.

Figure 22. Transition set 2, $M_S = 4.0$, Hansen - continued.

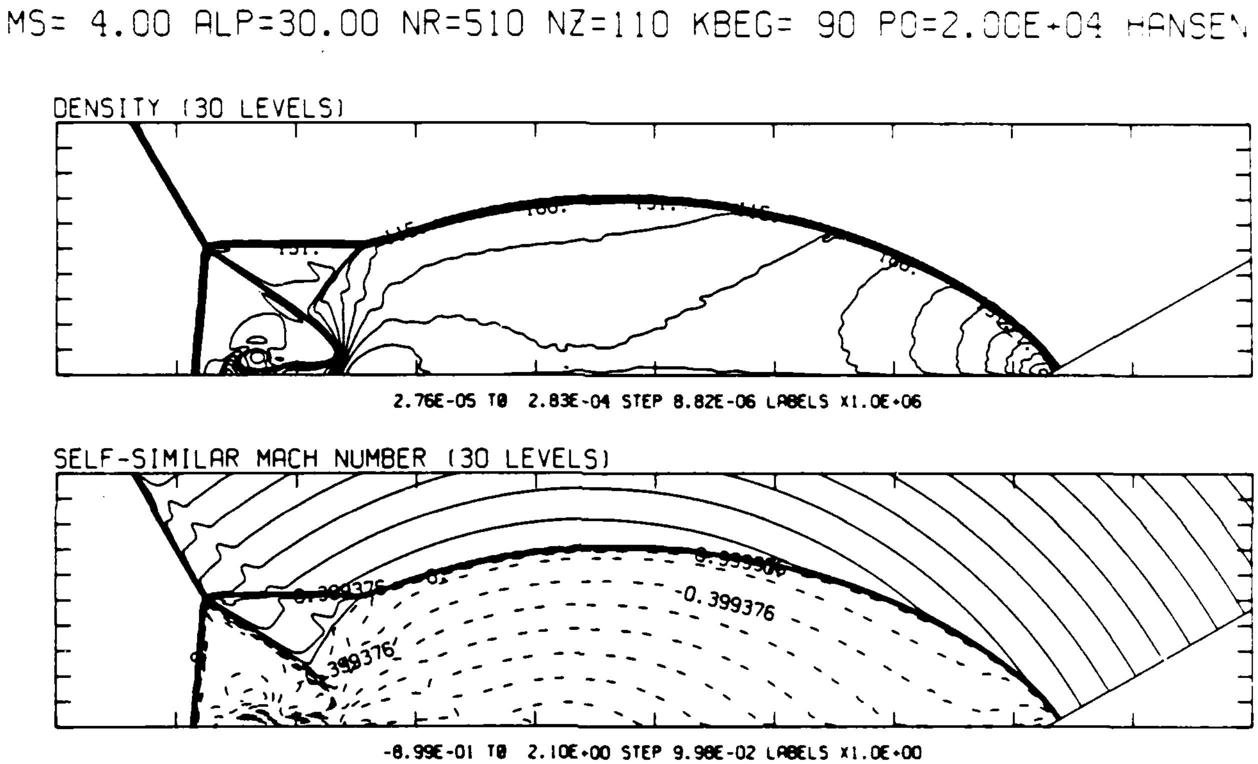

Figure 22.6a. θ_w = 30°, whole-flowfield contour-plots.

Figure 22. Transition set 2, M_s = 4.0, Hansen - continued.

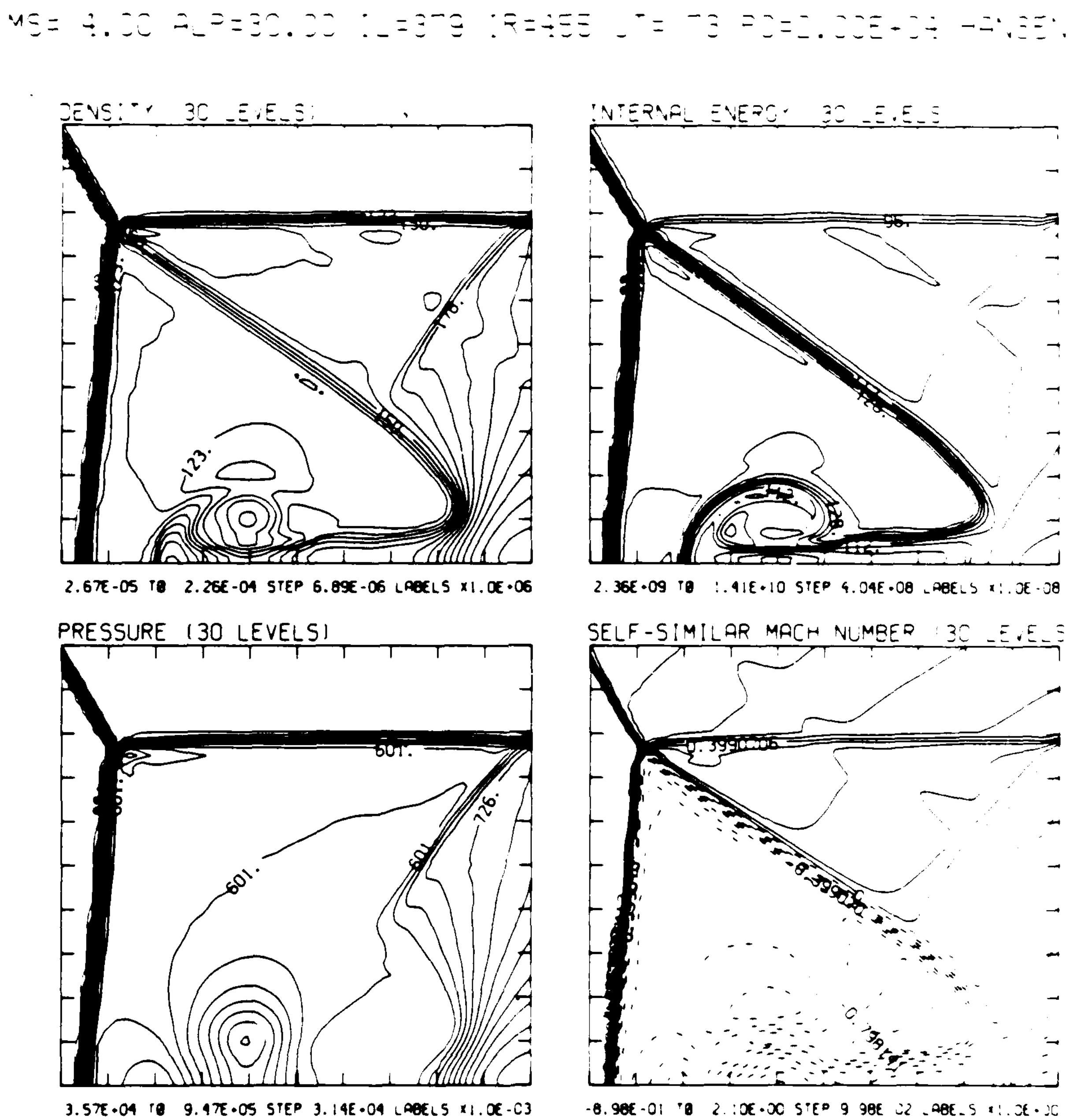

Figure 22.6b. θ_w = 30°, blowup-frame plots.

Figure 22. Transition set 2, M_s = 4.0, Hansen - continued.

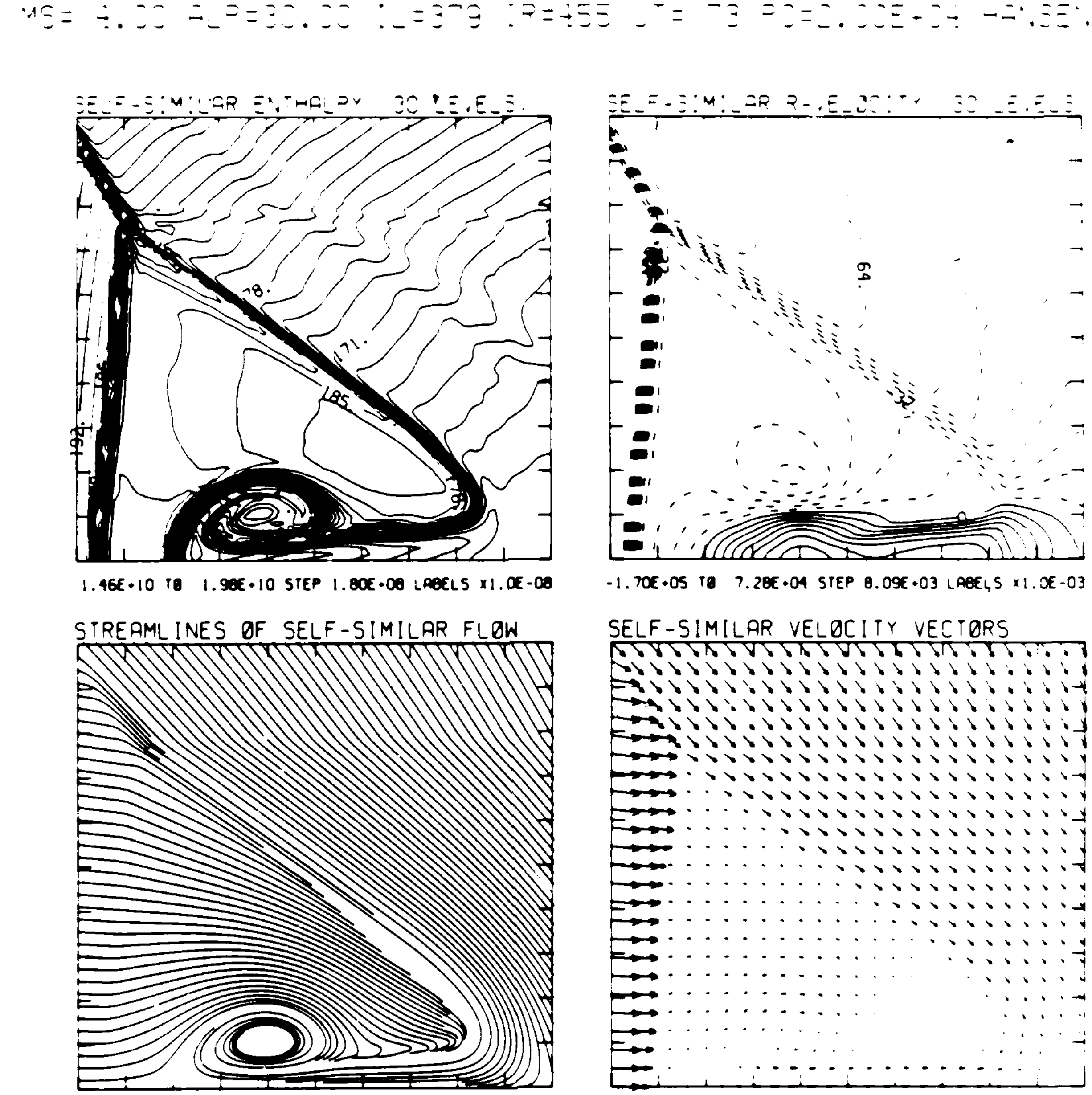

Figure 22.6b. $\theta_w = 30°$, blowup-frame plots - continued.

Figure 22. Transition set 2, $M_s = 4.0$, Hansen - continued.

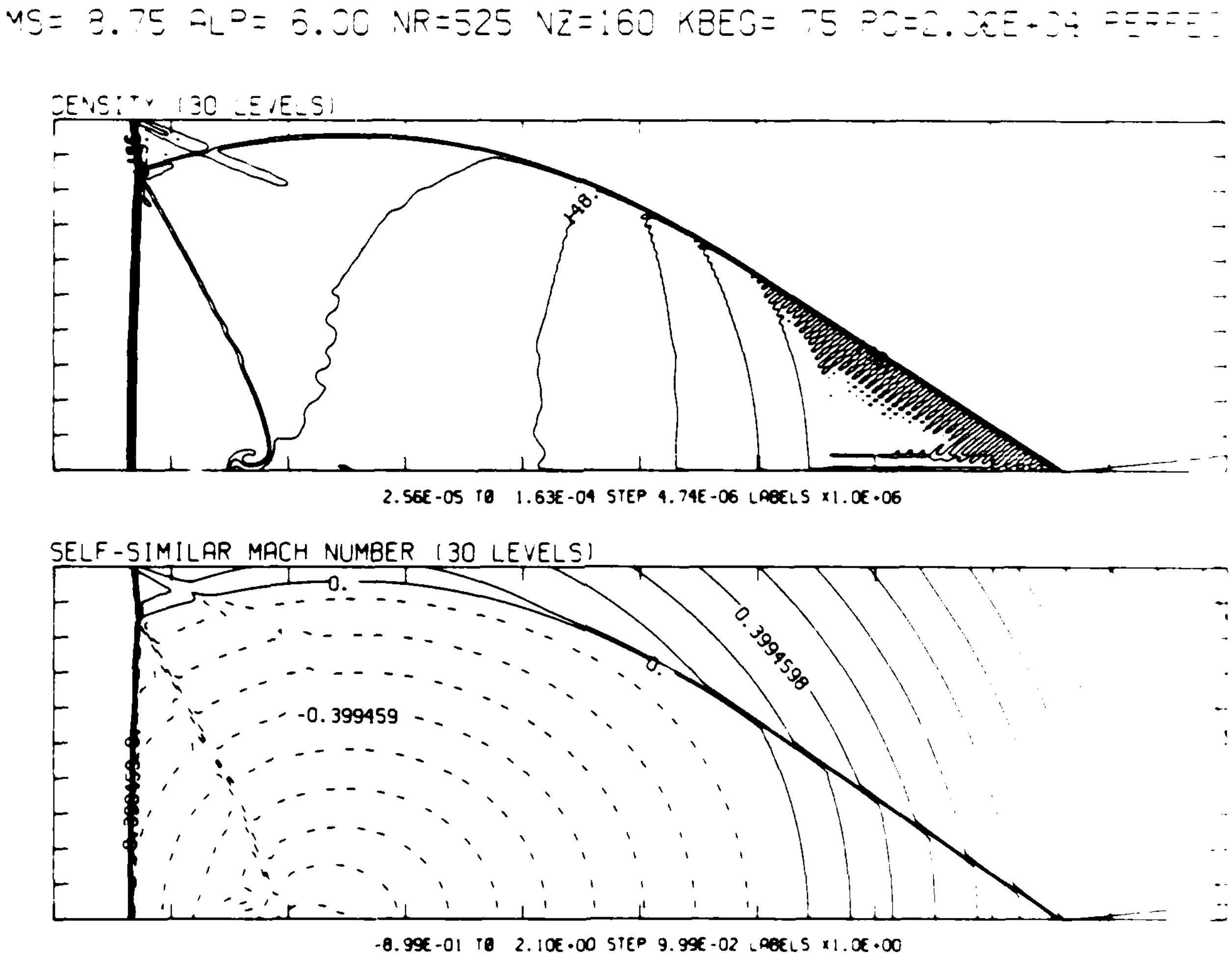

Figure 23.1a. $\theta_w = 6°$, whole-flowfield contour-plots.

Figure 23. Transition set 3, $M_s = 8.75$, $\gamma = 1.4$.

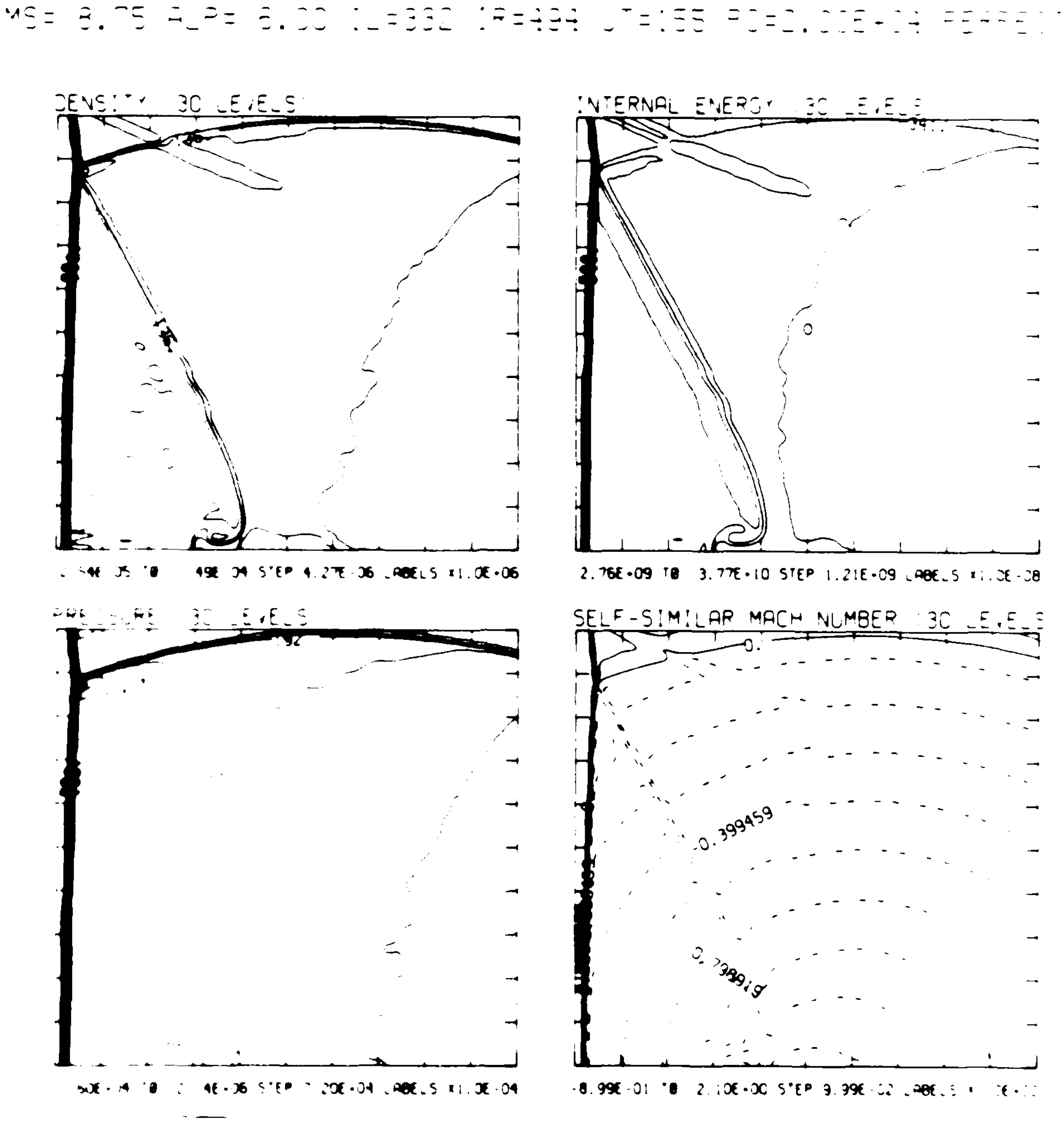

Figure 23.1b. $\theta_w = 6°$, blowup-frame plots.

Figure 23. Transition set 3, $M_s = 8.75$, $\gamma = 1.4$ - continued.

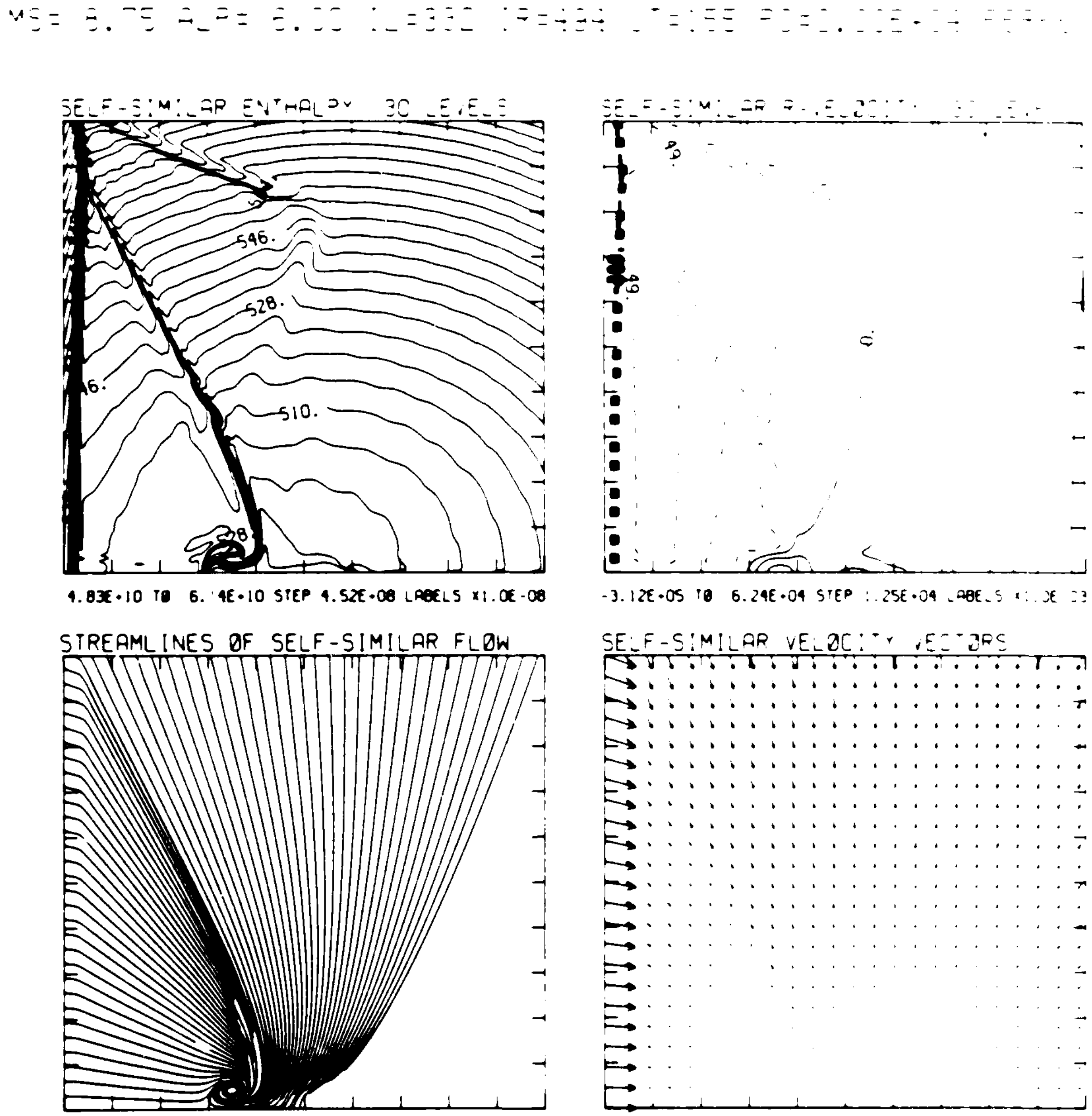

Figure 23.1b. $\theta_w = 6°$, blowup-frame plots - continued.

Figure 23. Transition set 3, $M_s = 8.75$, $\gamma = 1.4$ - continued.

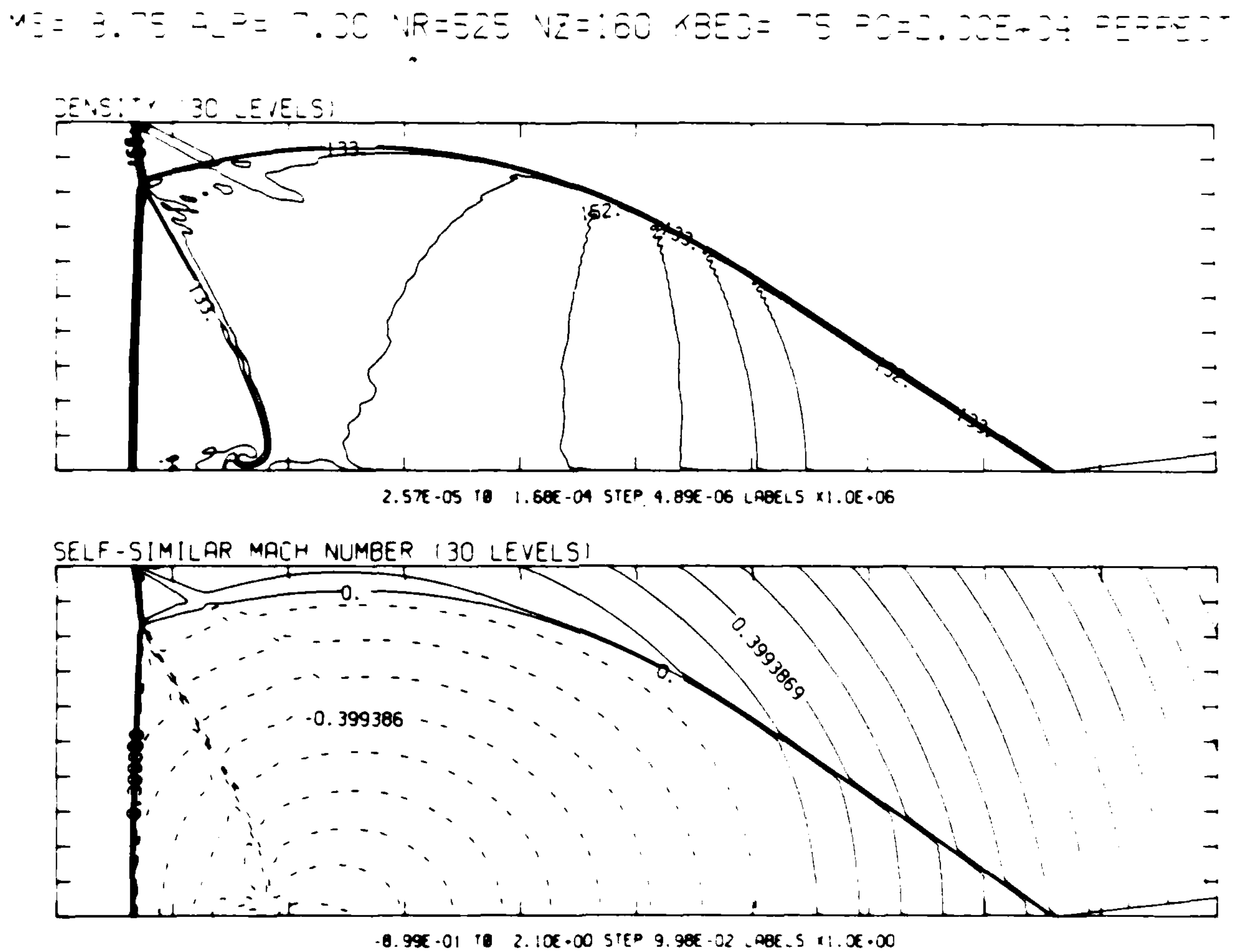

Figure 23.2a. θ_w = 7°, whole-flowfield contour-plots.

Figure 23. Transition set 3, M_s = 8.75, γ = 1.4 - continued.

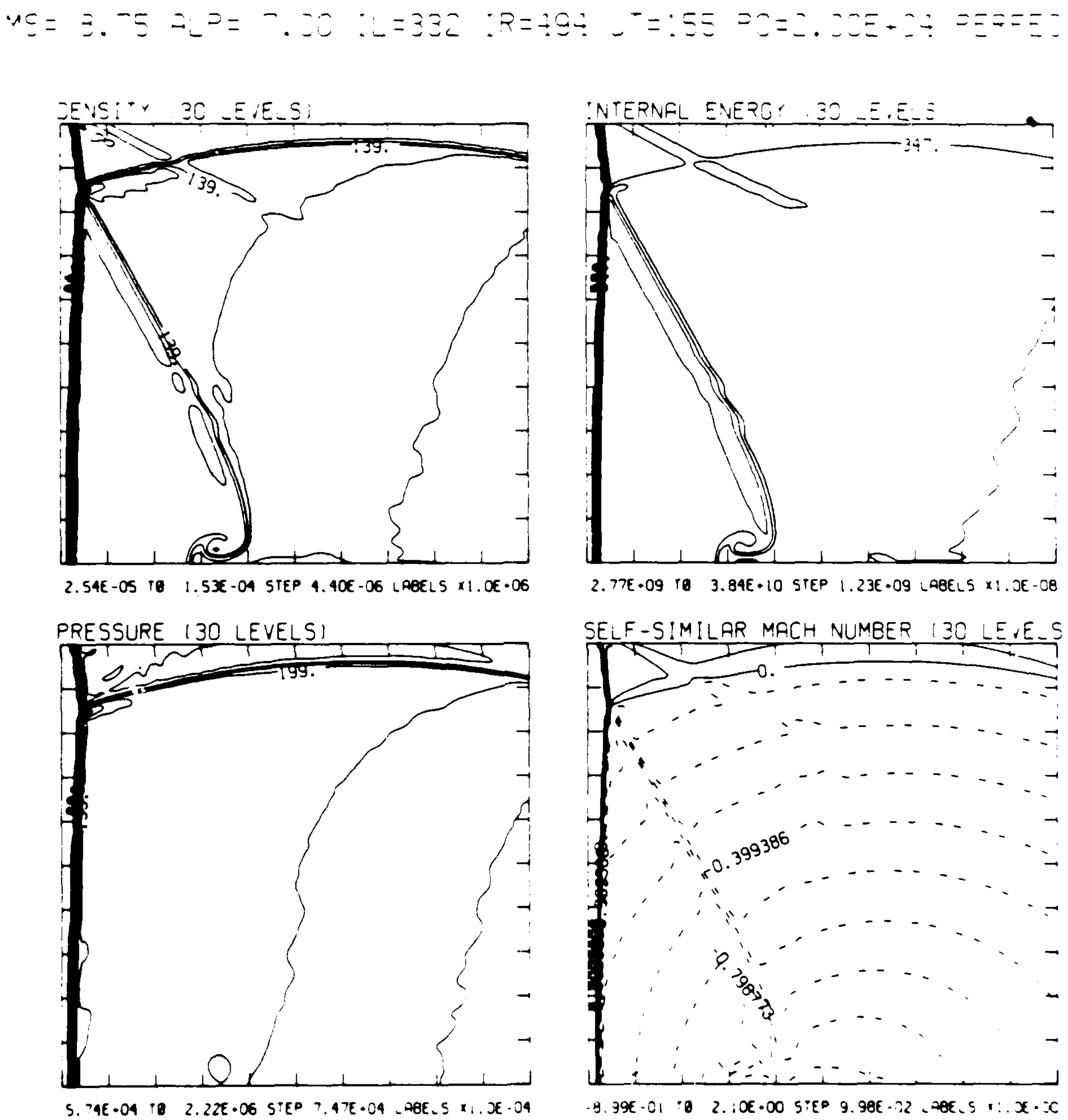

Figure 23.2b. $\theta_w = 7°$, blowup-frame plots.

Figure 23. Transition set 3, $M_s = 8.75$, $\gamma = 1.4$ - continued.

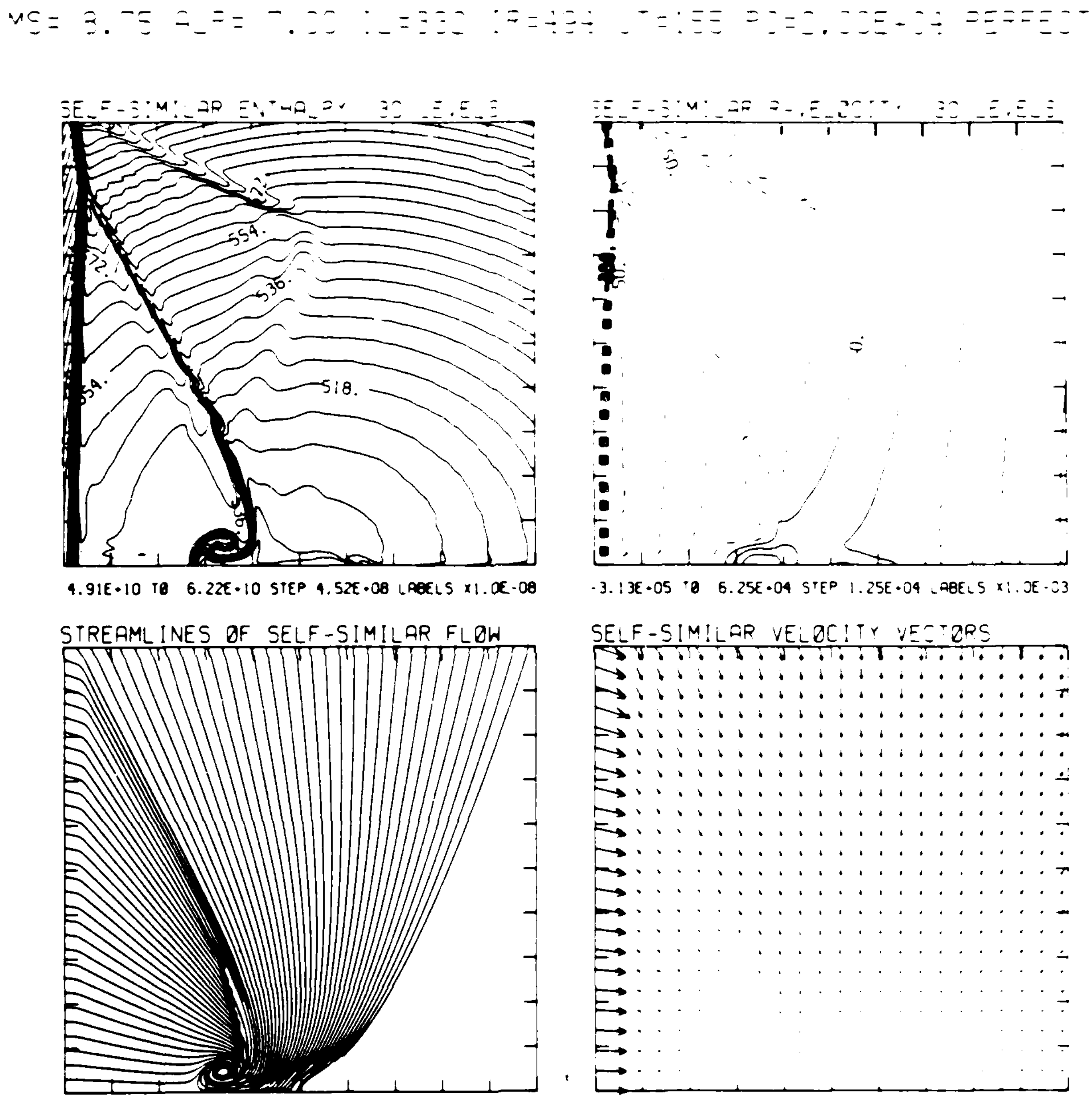

Figure 23.2b. $\theta_w = 7°$, blowup-frame plots - continued.

Figure 23. Transition set 3, $M_s = 8.75$, $\gamma = 1.4$ - continued.

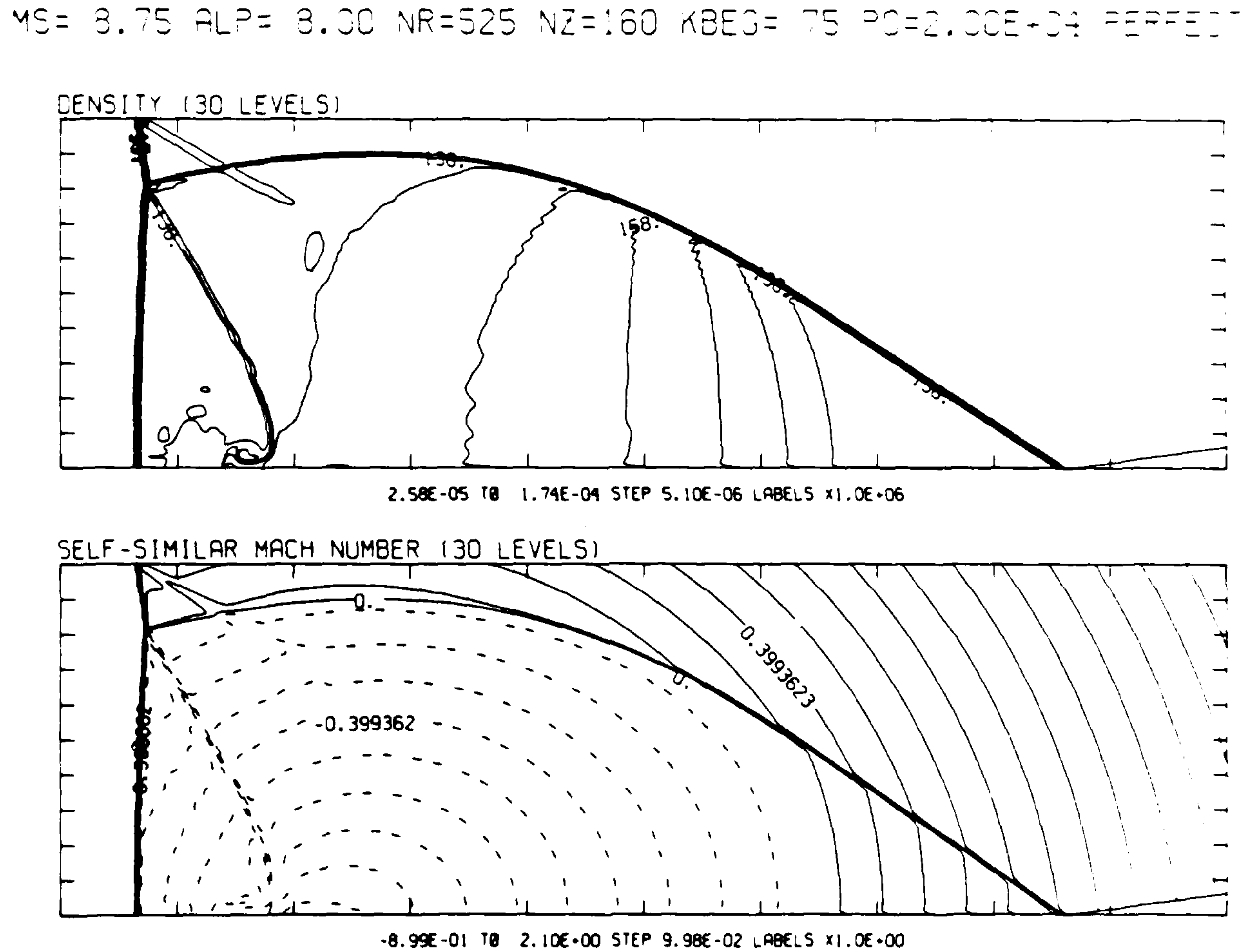

Figure 23.3a. $\theta_w = 8°$, whole-flowfield contour-plots.

Figure 23. Transition set 3, $M_s = 8.75$, $\gamma = 1.4$ - continued.

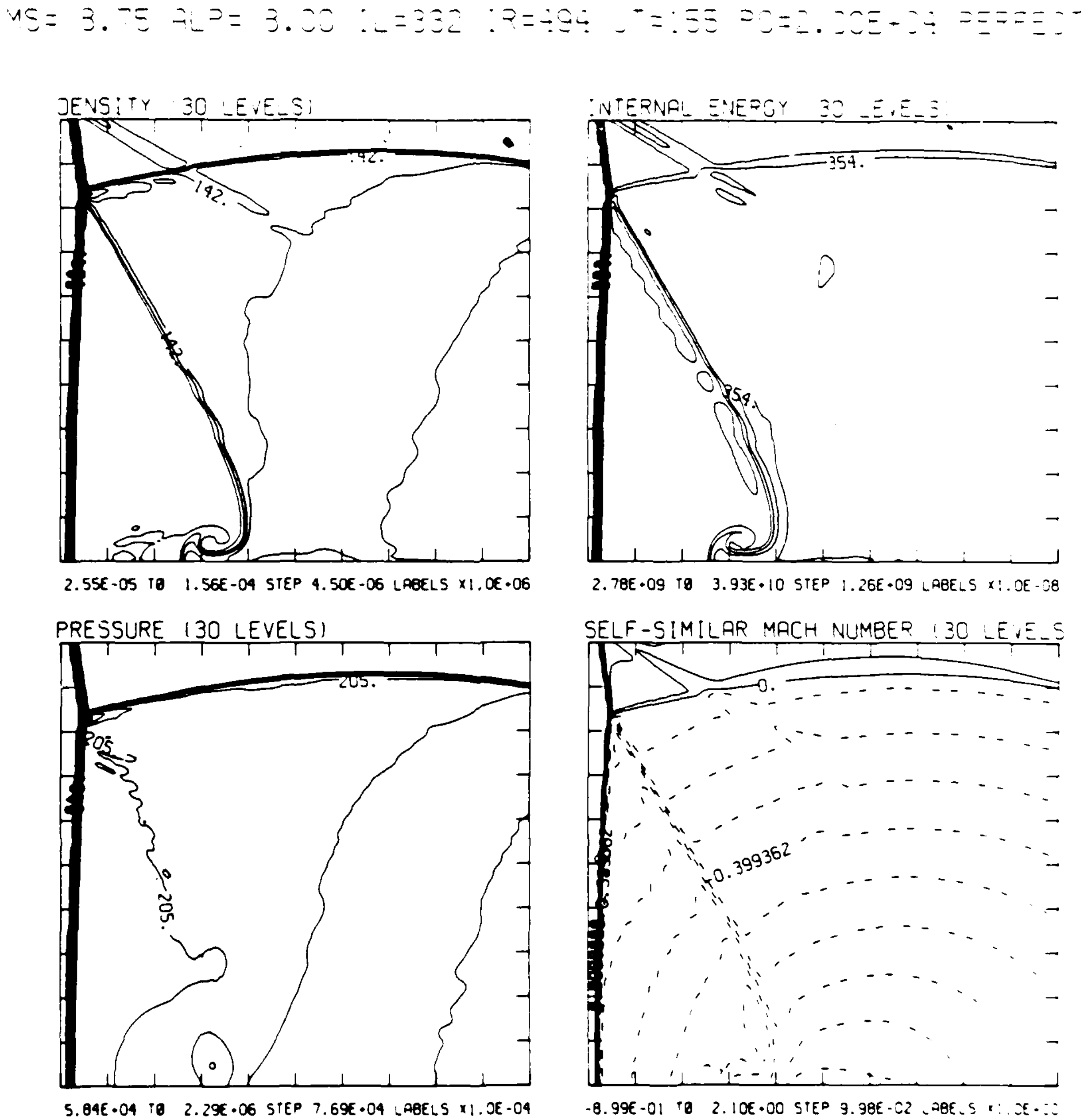

Figure 23.3b. $\theta_w = 8°$, blowup-frame plots.

Figure 23. Transition set 3, $M_s = 8.75$, $\gamma = 1.4$ - continued.

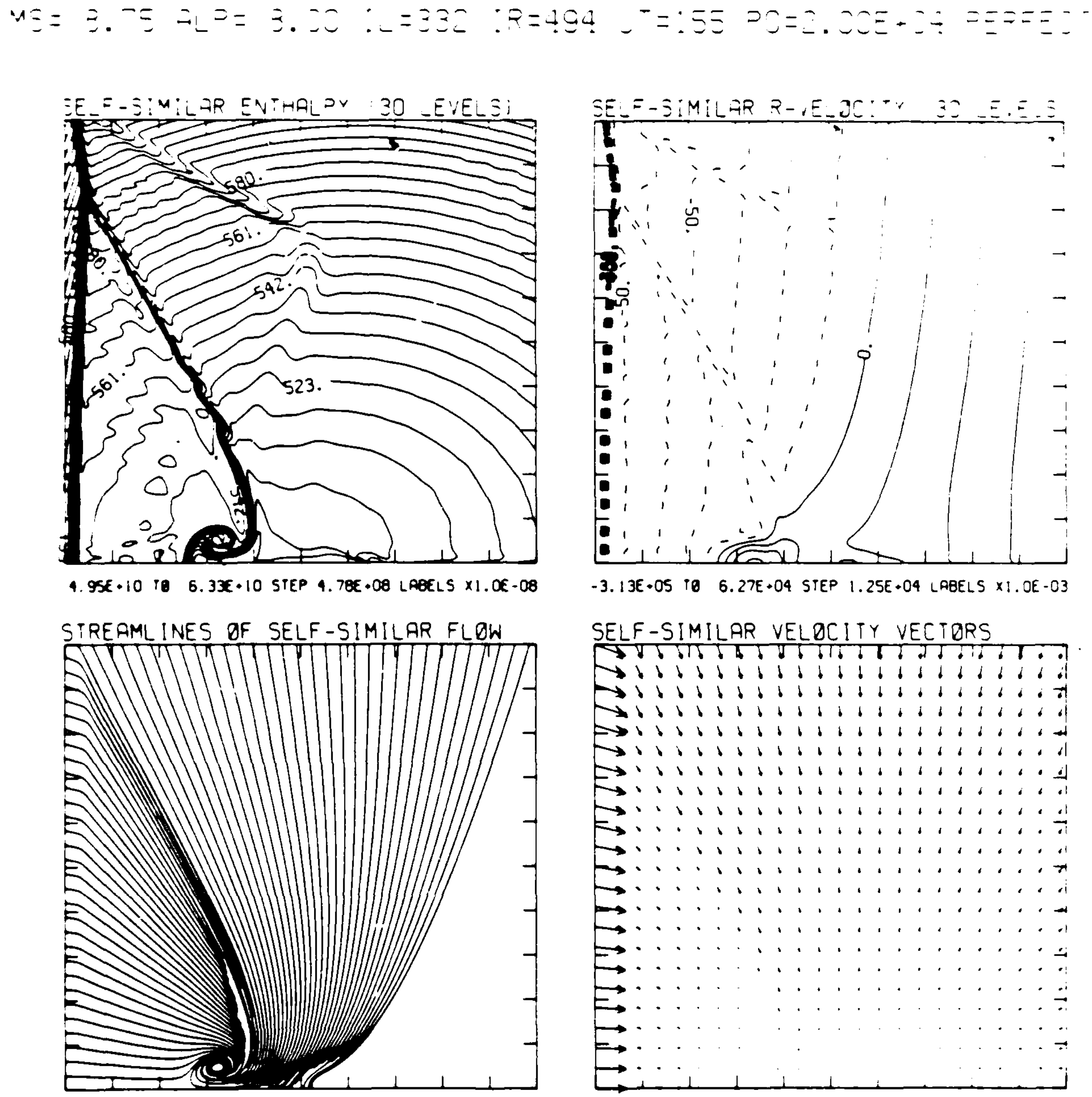

Figure 23.3b. θ_w = 8°, blowup-frame plots - continued.

Figure 23. Transition set 3, M_s = 8.75, γ = 1.4 - continued.

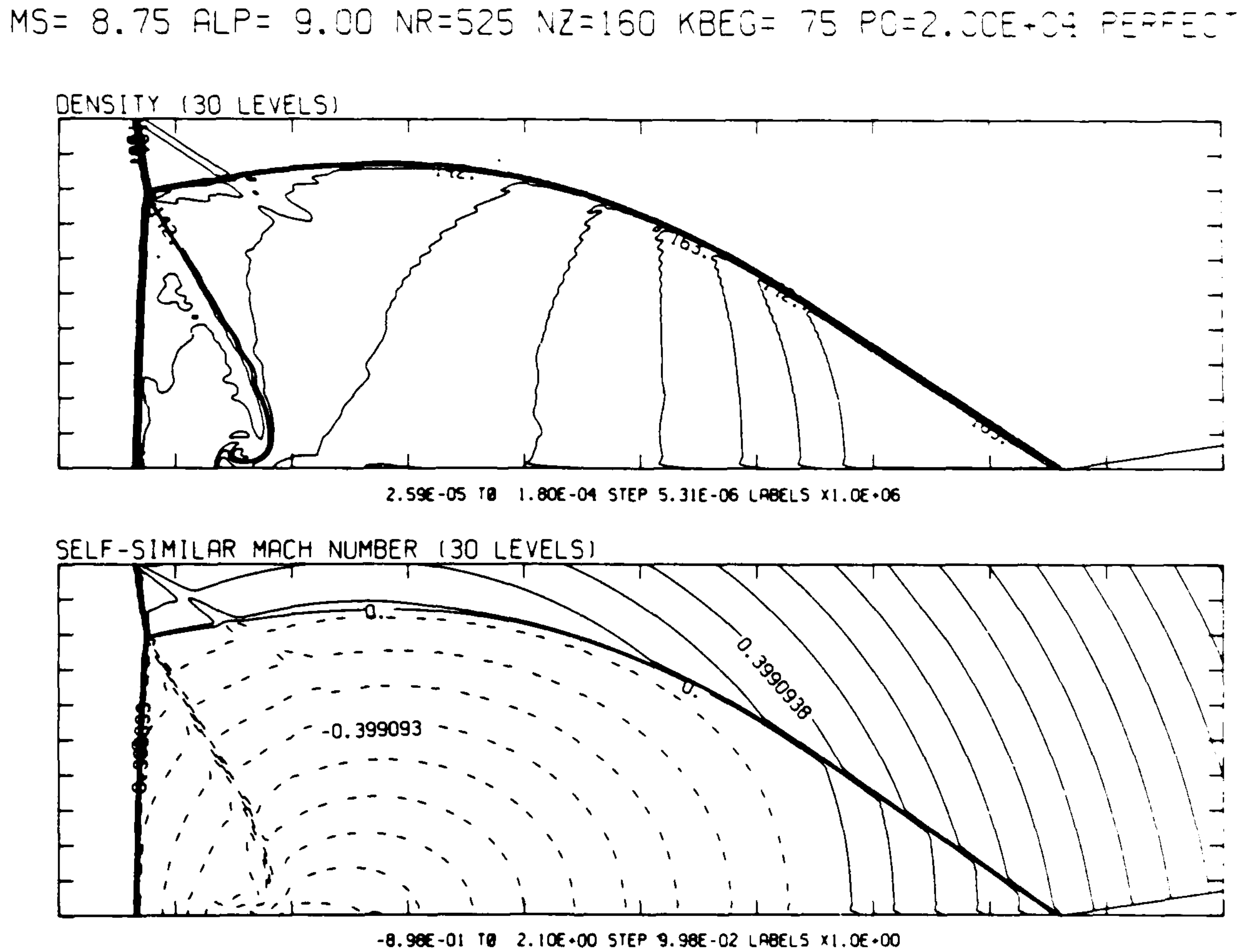

Figure 23.4a. $\theta_w = 9°$, whole-flowfield contour-plots.

Figure 23. Transition set 3, $M_s = 8.75$, $\gamma = 1.4$ - continued.

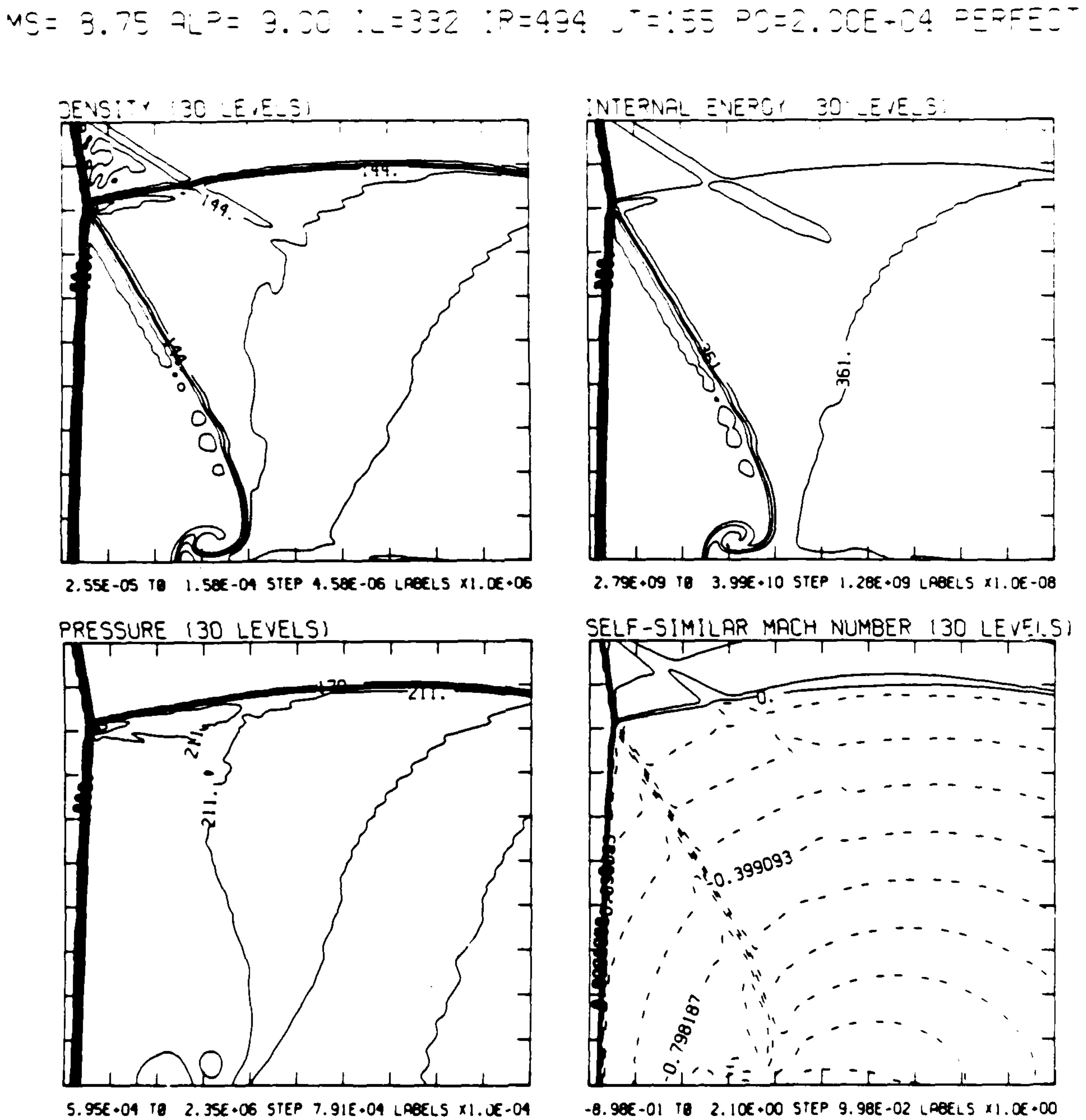

Figure 23.4b. $\theta_w = 9°$, blowup-frame plots.

Figure 23. Transition set 3, $M_s = 8.75$, $\gamma = 1.4$ - continued.

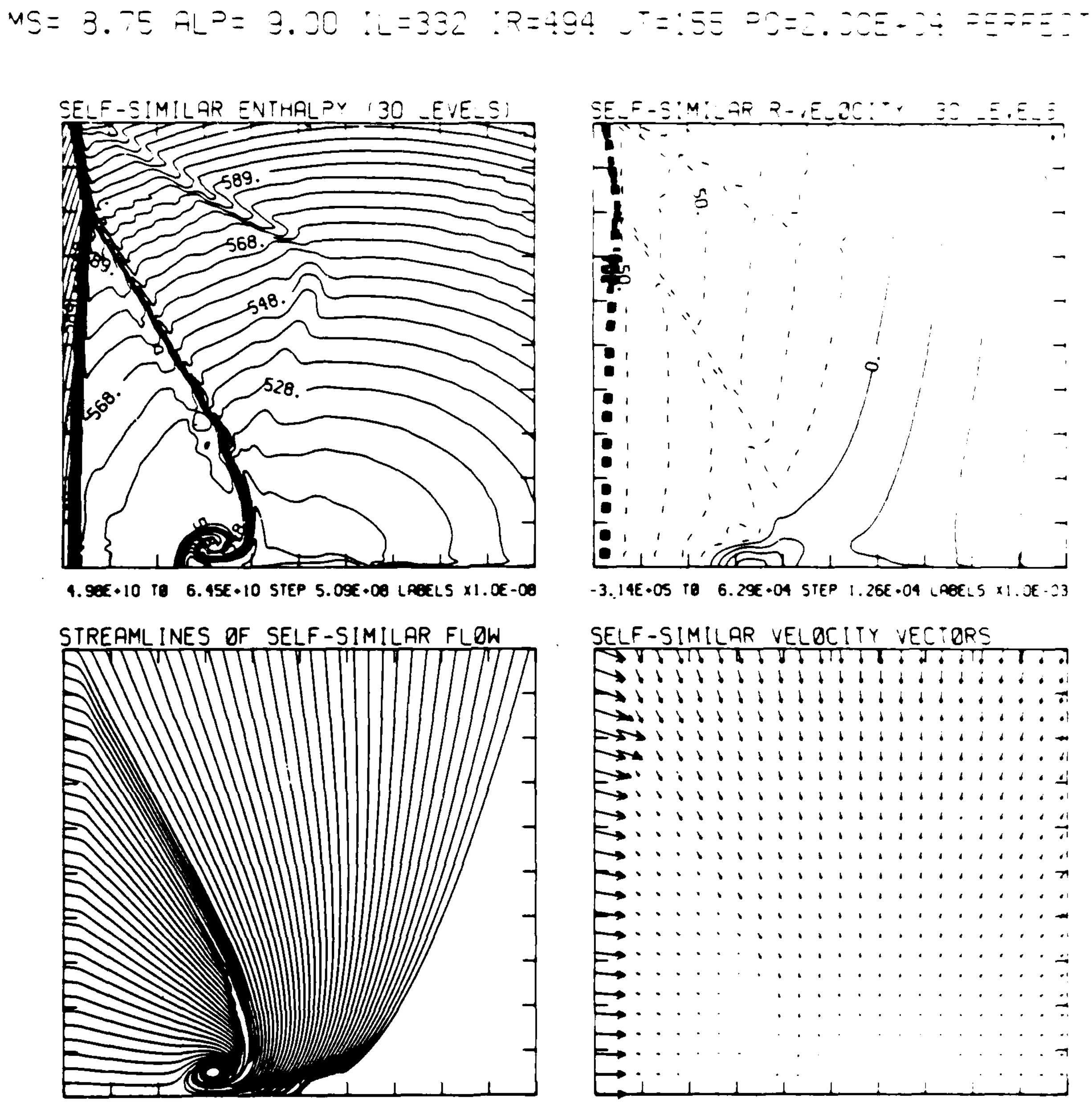

Figure 23.4b. $\theta_w = 9°$, blowup-frame plots - continued.

Figure 23. Transition set 3, $M_s = 8.75$, $\gamma = 1.4$ - continued.

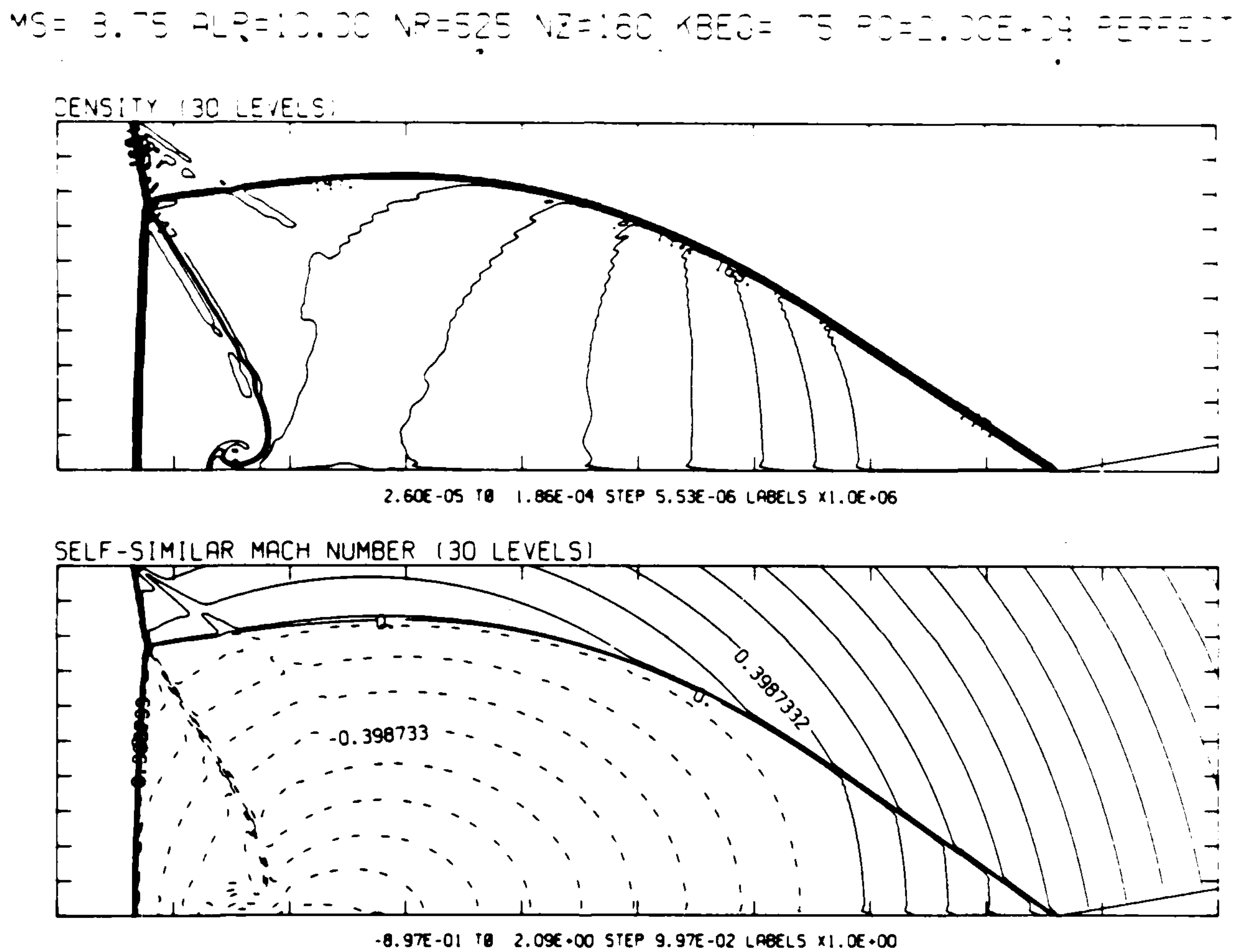

Figure 23.5a. θ_w = 10°, whole-flowfield contour-plots.

Figure 23. Transition set 3, M_s = 8.75, γ = 1.4 - continued.

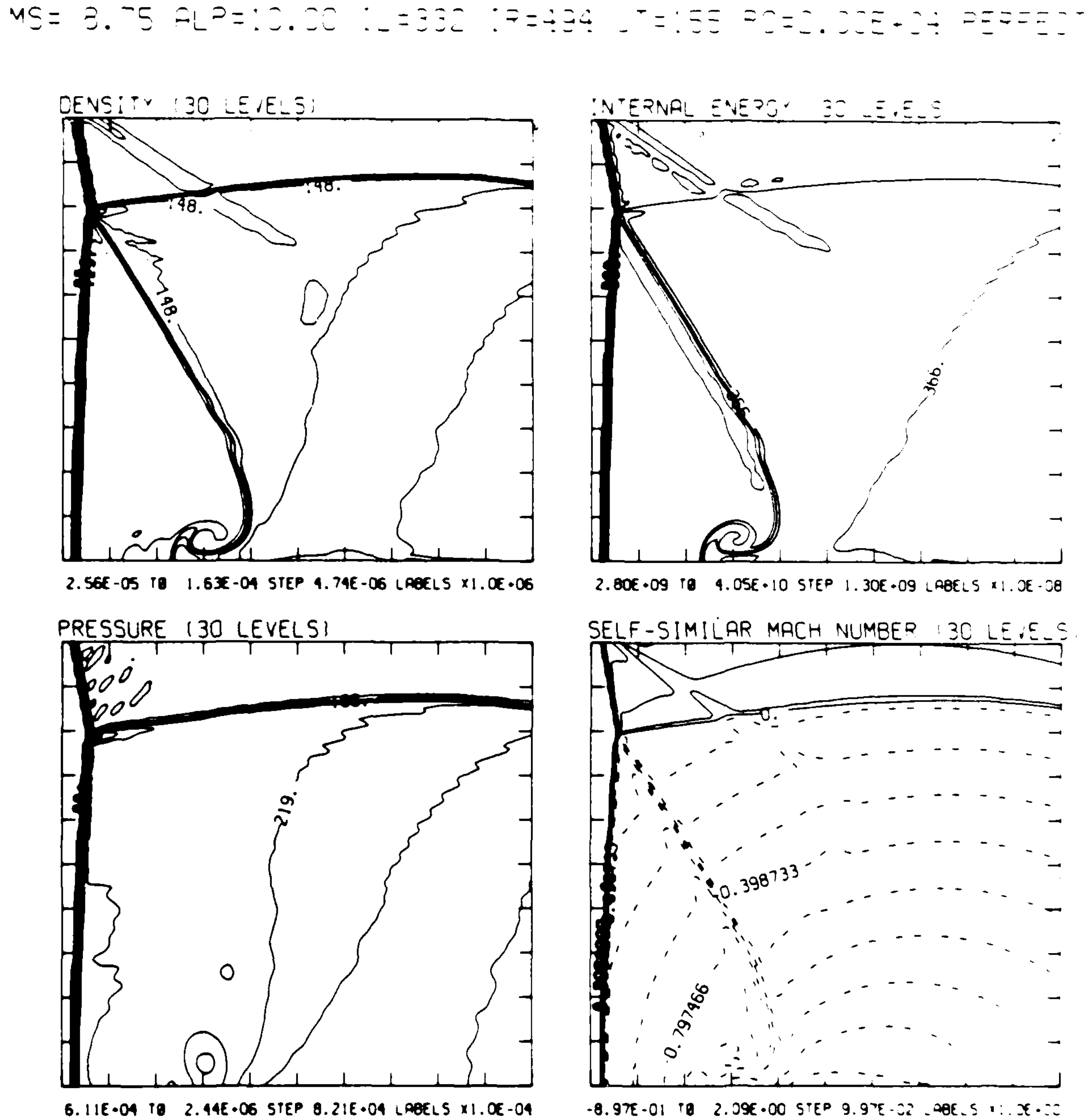

Figure 23.5b. $\theta_w = 10°$, blowup-frame plots.

Figure 23. Transition set 3, $M_s = 8.75$, $\gamma = 1.4$ - continued.

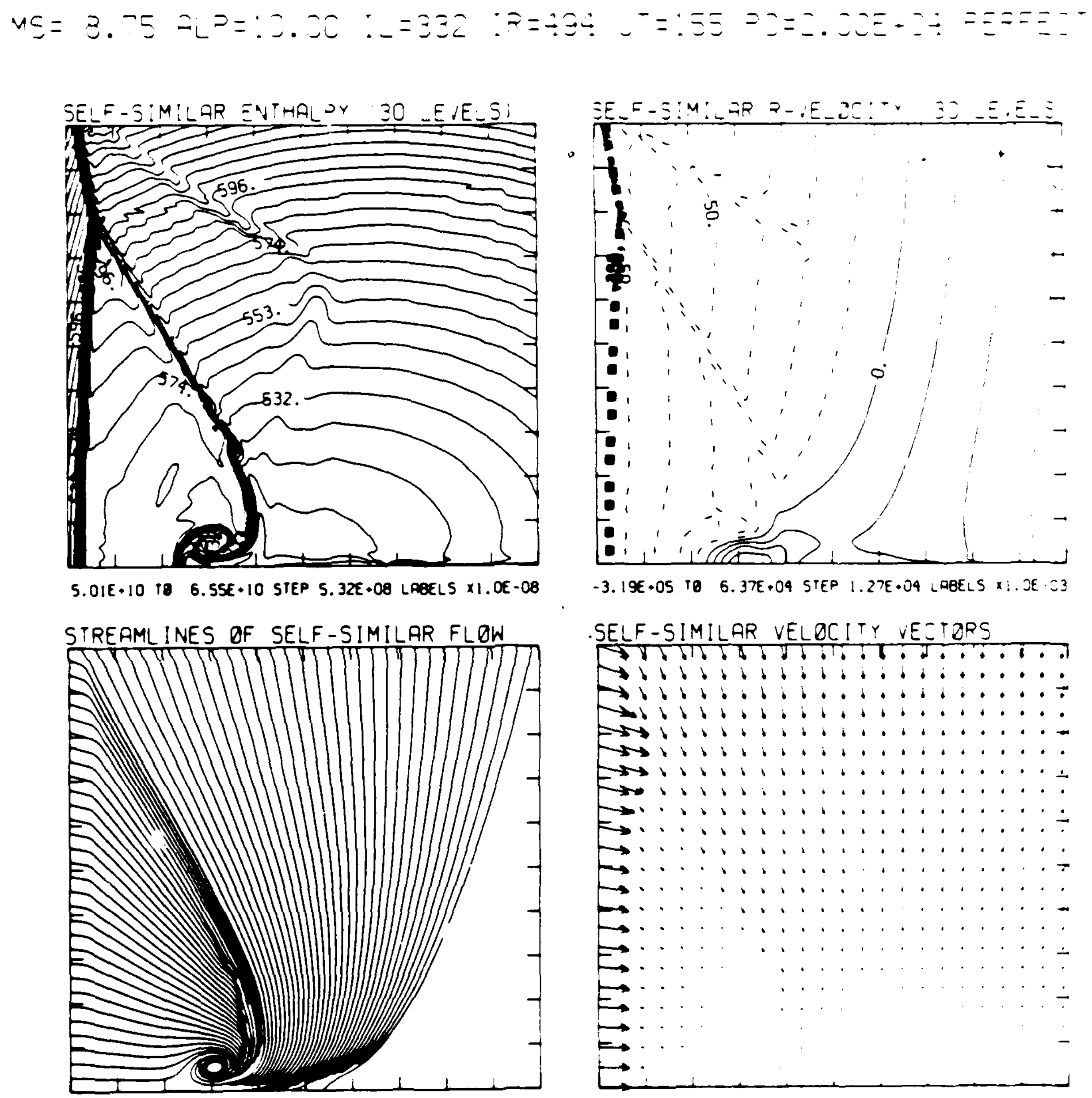

Figure 23.5b. θ_w = 10°, blowup-frame plots - continued.

Figure 23. Transition set 3, M_s = 8.75, γ = 1.4 - continued.

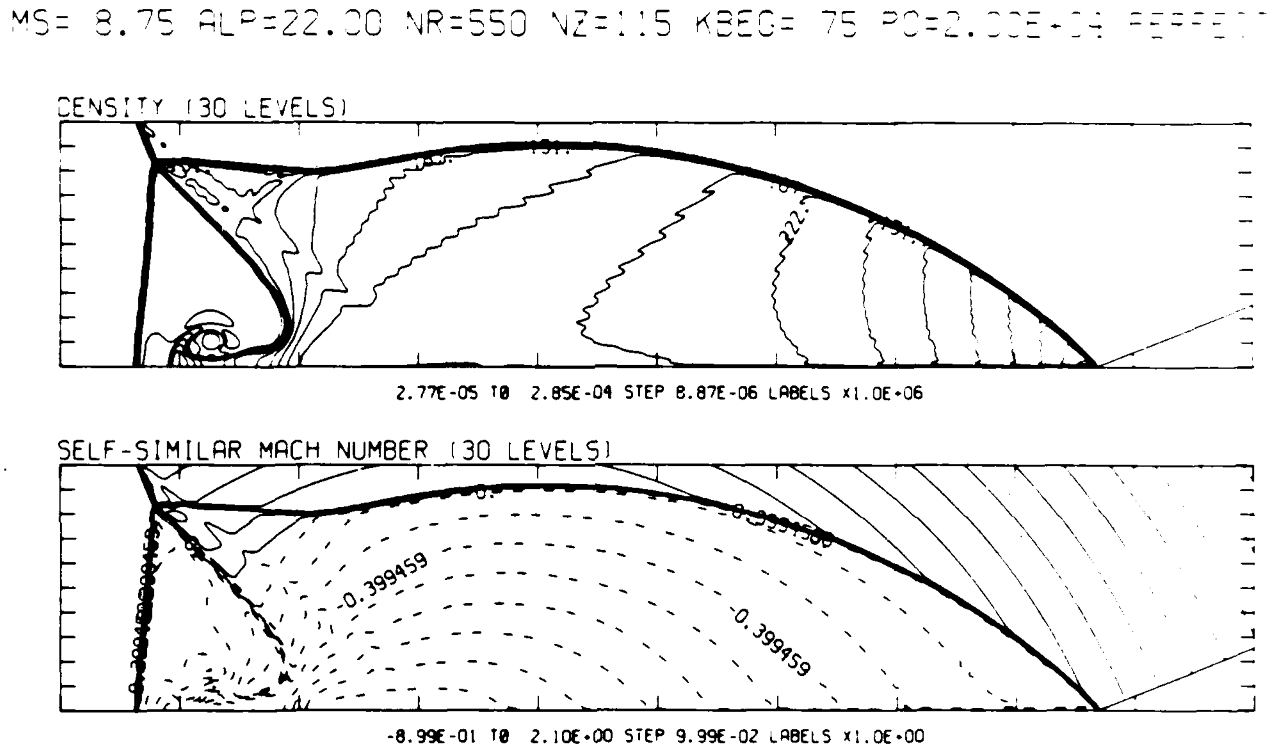

Figure 23.6a. θ_w = 22°, whole-flowfield contour-plots.

Figure 23. Transition set 3, M_s = 8.75, γ = 1.4 - continued.

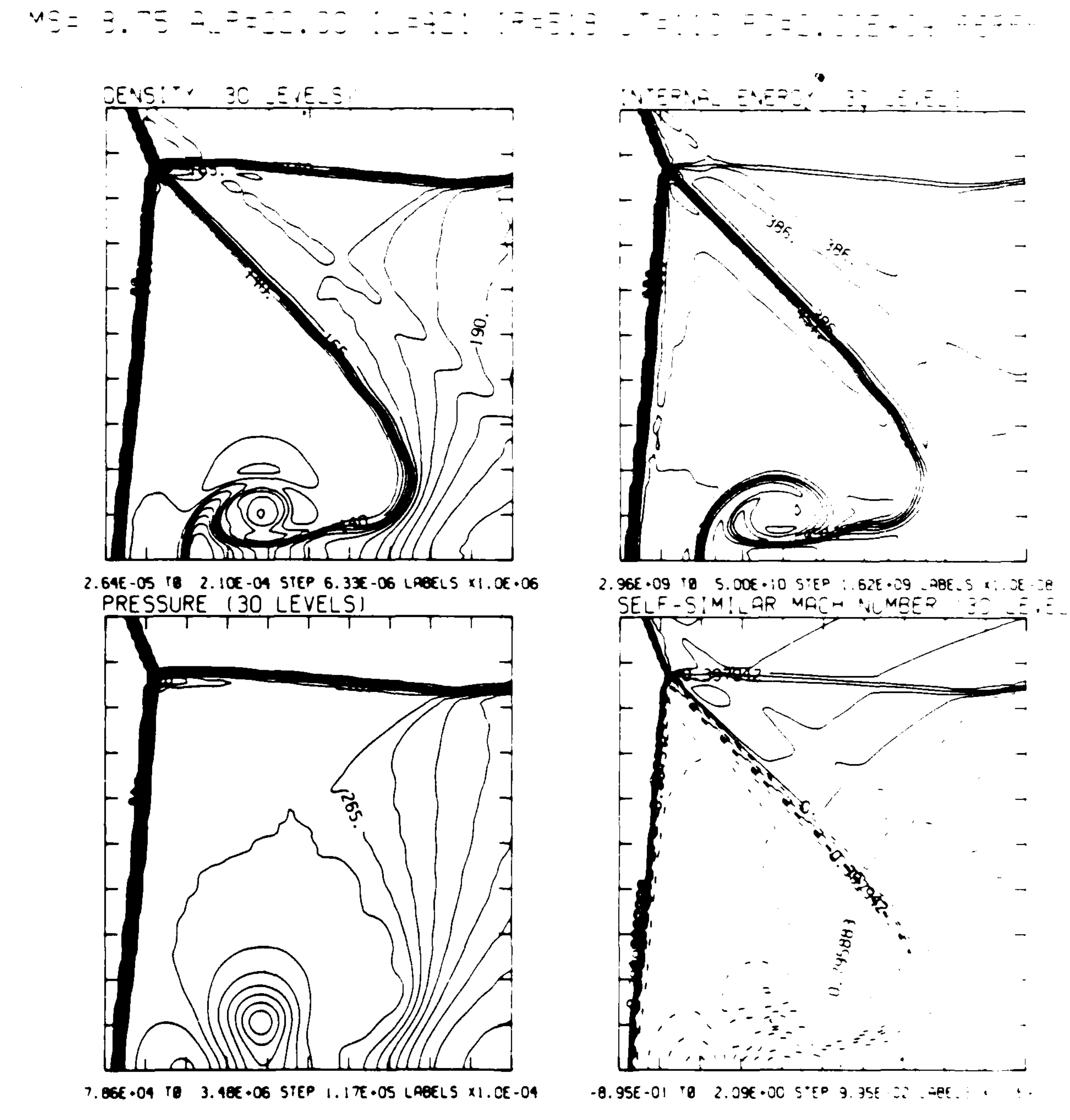

Figure 23.6b. θ_w = 22°, blowup-frame plots.

Figure 23. Transition set 3, M_s = 8.75, γ = 1.4 - continued.

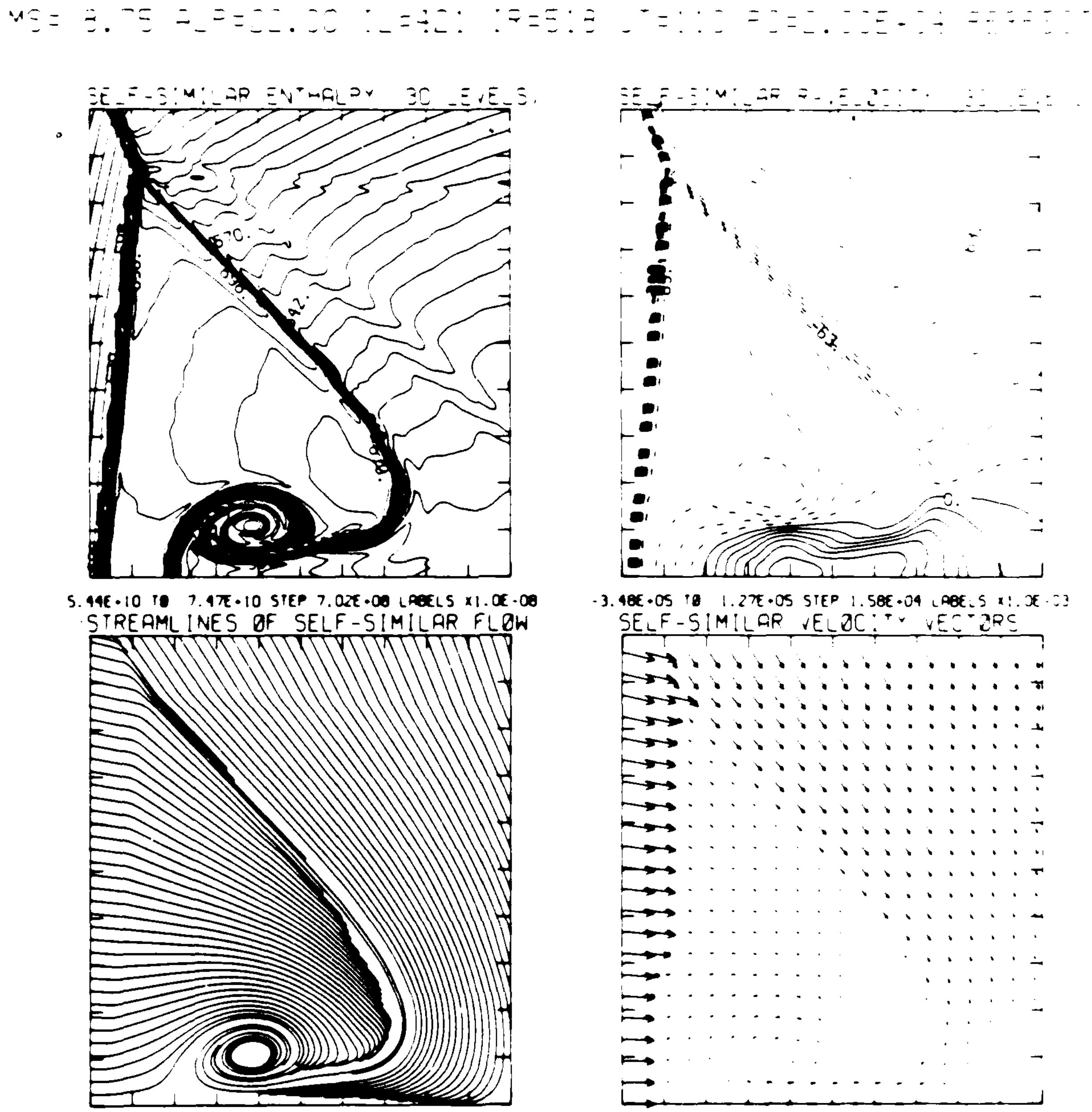

Figure 23.6b. θ_w = 22°, blowup-frame plots - continued.

Figure 23. Transition set 3, M_s = 8.75, γ = 1.4 - continued.

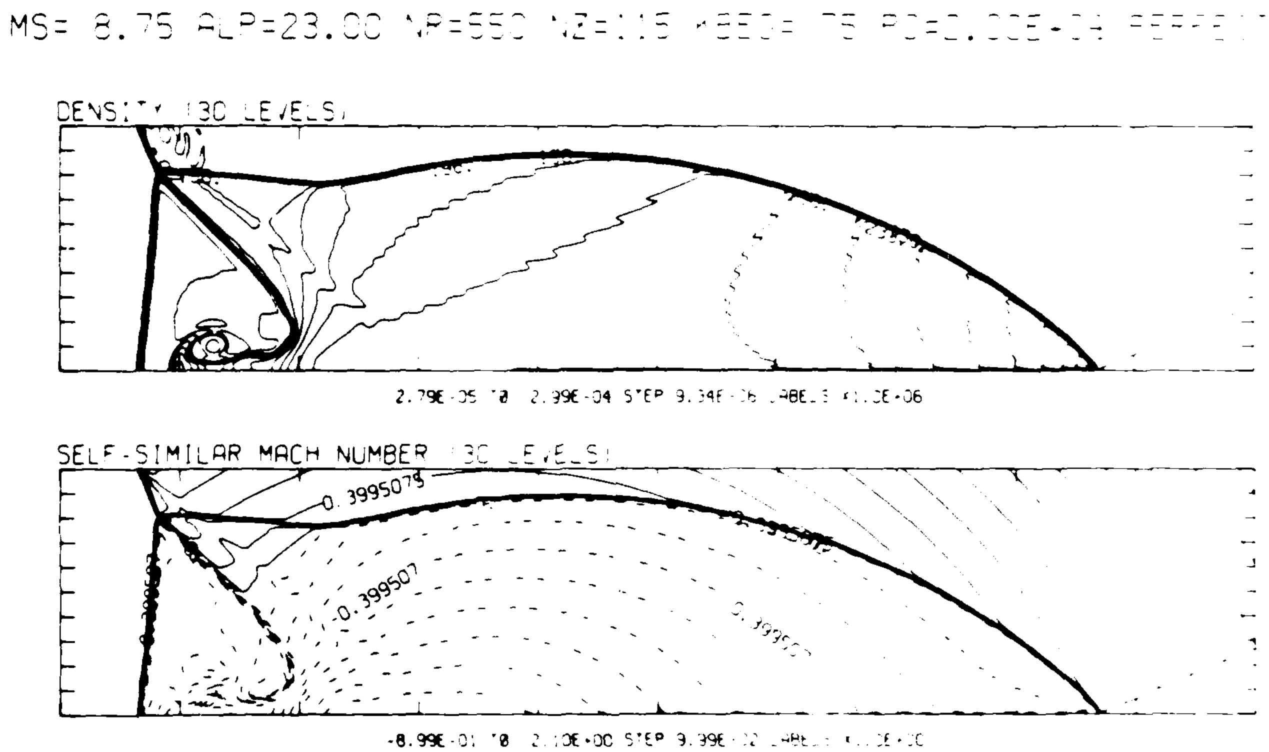

Figure 23.7a. θ_w = 23°, whole-flowfield contour-plots.

Figure 23. Transition set 3, M_s = 8.75, γ = 1.4 - continued.

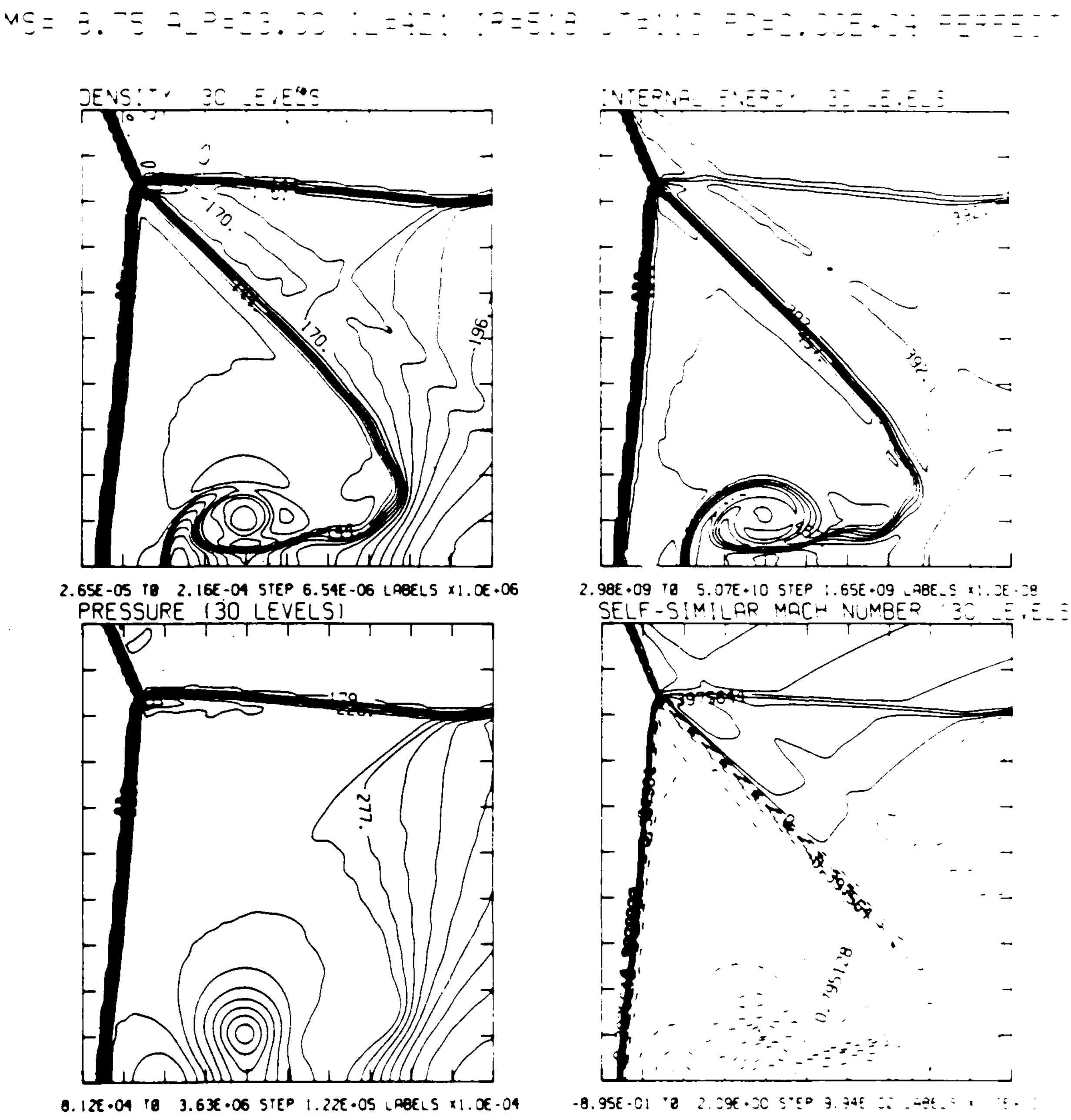

Figure 23.7b. $\theta_w = 23°$, blowup-frame plots.

Figure 23. Transition set 3, $M_s = 8.75$, $\gamma = 1.4$ - continued.

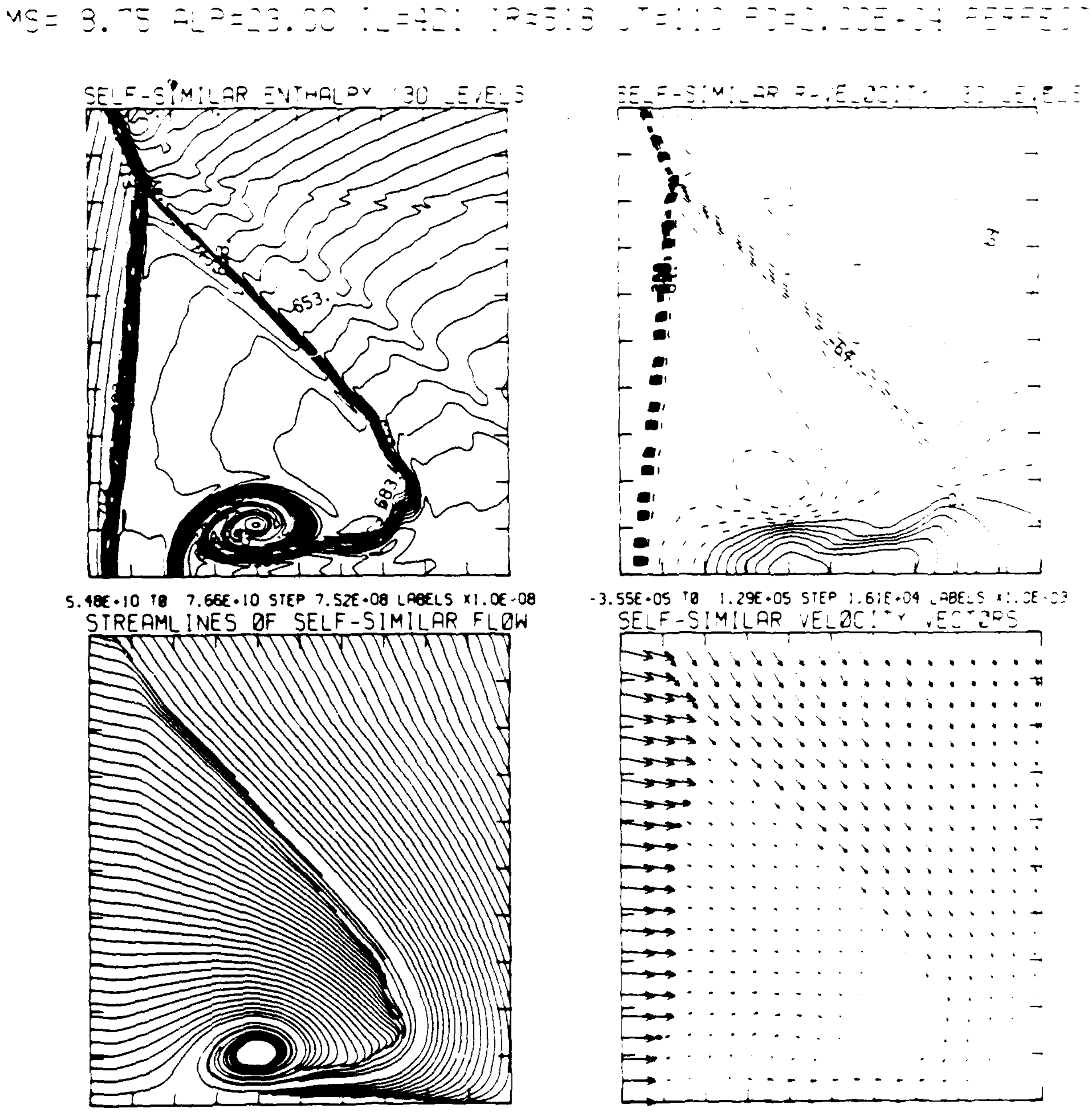

Figure 23.7b. $\theta_w = 23°$, blowup-frame plots - continued.

Figure 23. Transition set 3, $M_s = 8.75$, $\gamma = 1.4$ - continued.

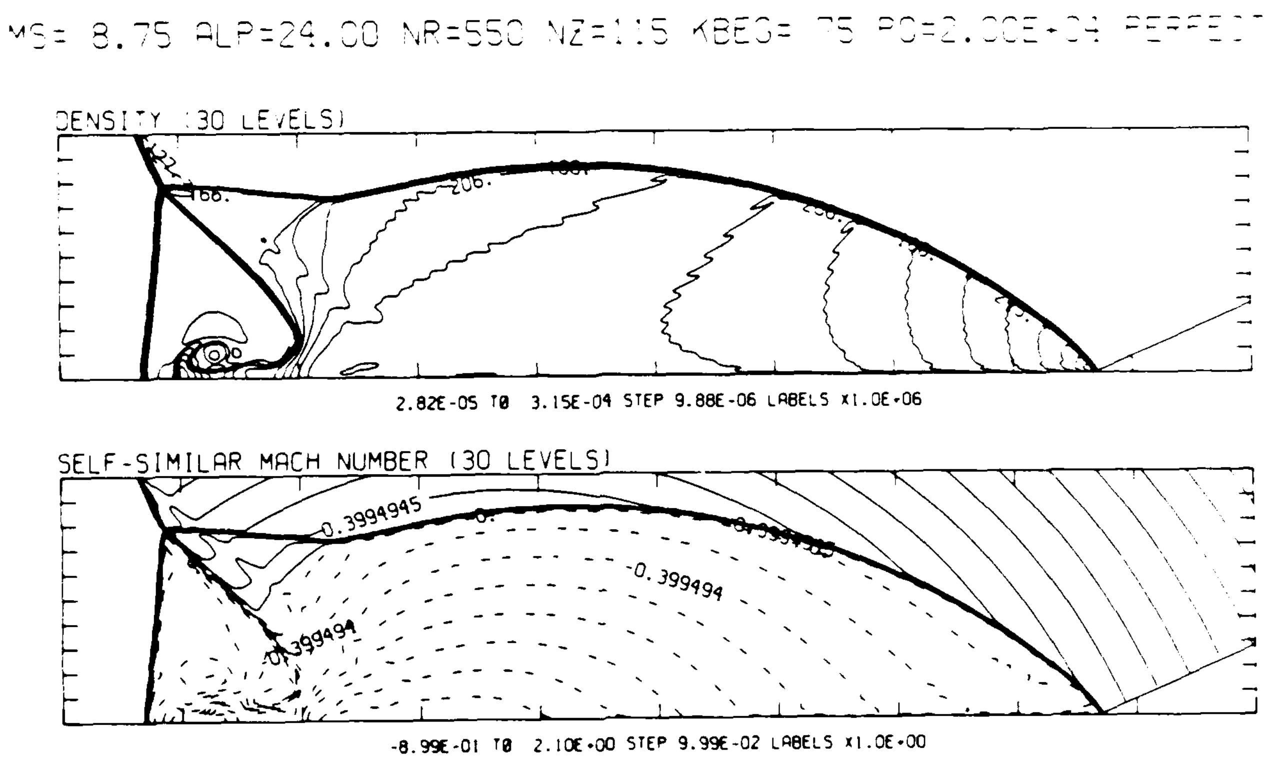

Figure 23.8a. θ_w = 24°, whole-flowfield contour-plots.

Figure 23. Transition set 3, M_s = 8.75, γ = 1.4 - continued.

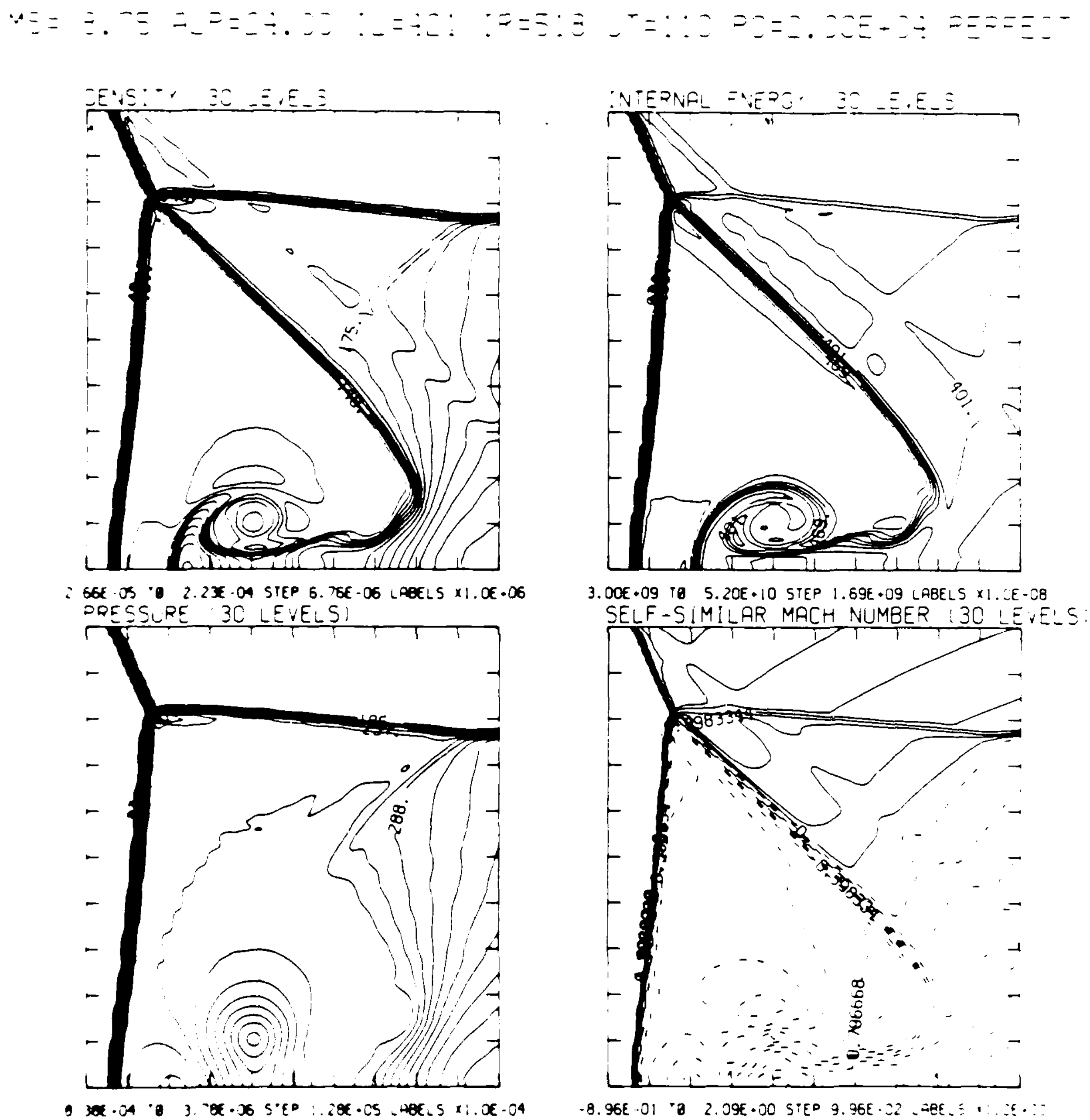

Figure 23.8b. $\theta_w = 24°$, blowup-frame plots.

Figure 23. Transition set 3, $M_s = 8.75$, $\gamma = 1.4$ - continued.

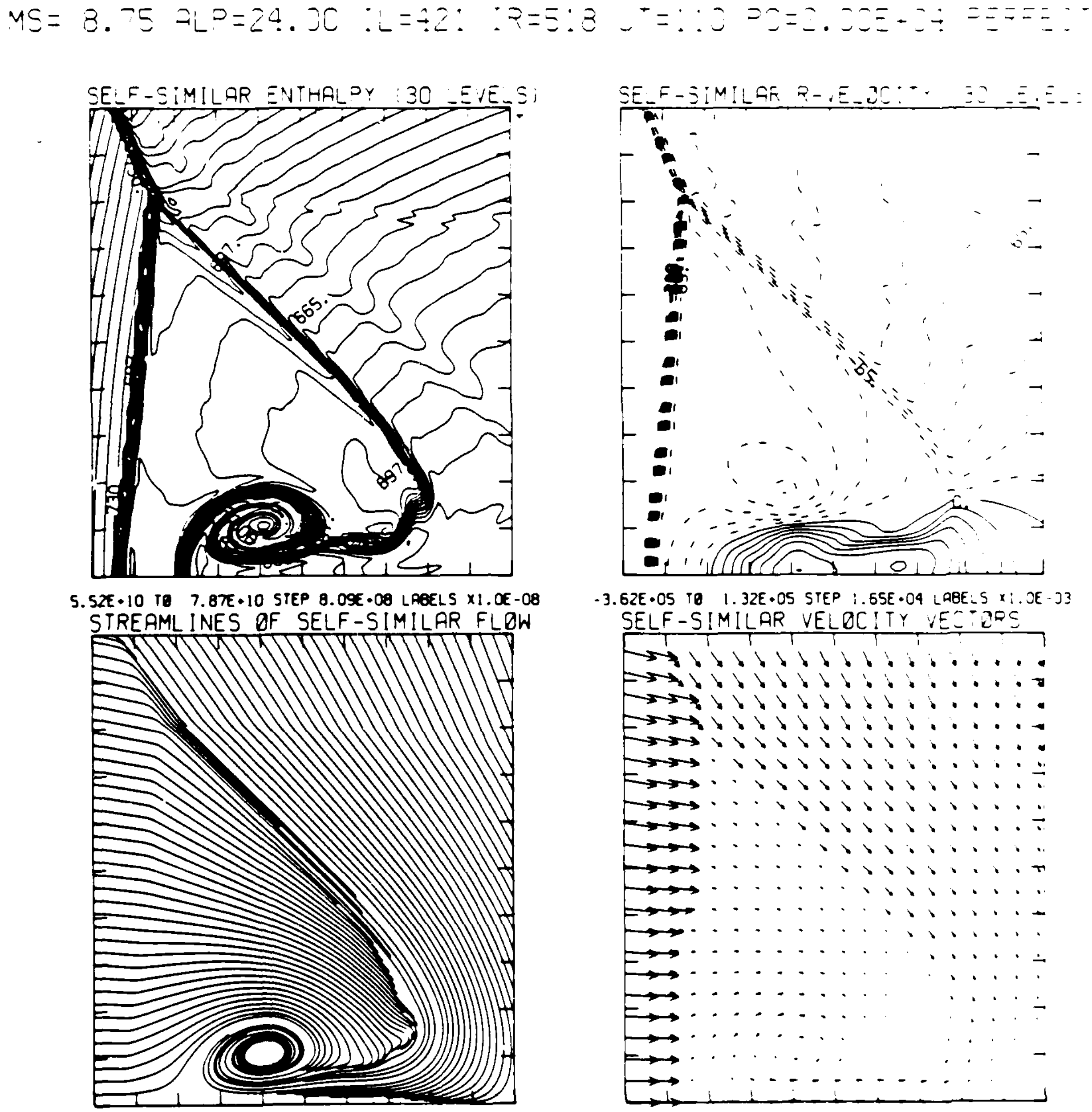

Figure 23.8b. θ_w = 24°, blowup-frame plots - continued.

Figure 23. Transition set 3, M_s = 8.75, γ = 1.4 - continued.

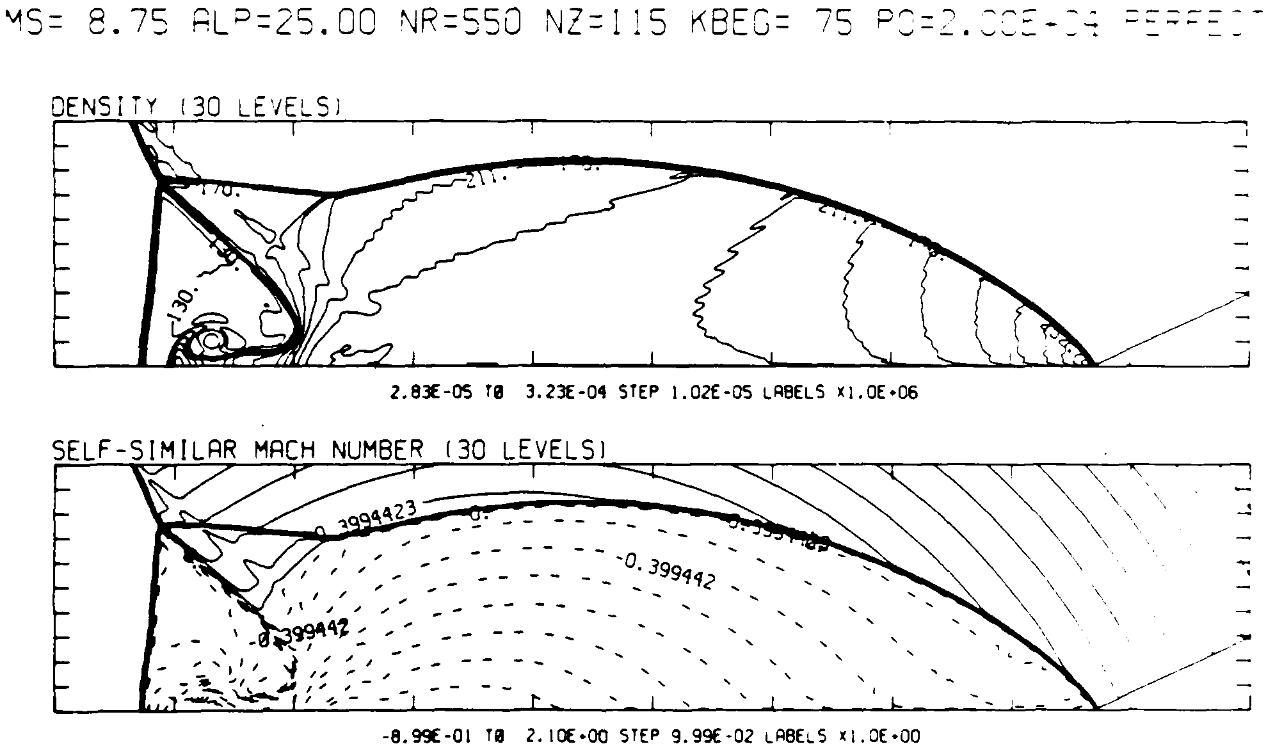

Figure 23.9a. θ_w = 25°, whole-flowfield contour-plots.

Figure 23. Transition set 3, M_s = 8.75, γ = 1.4 - continued.

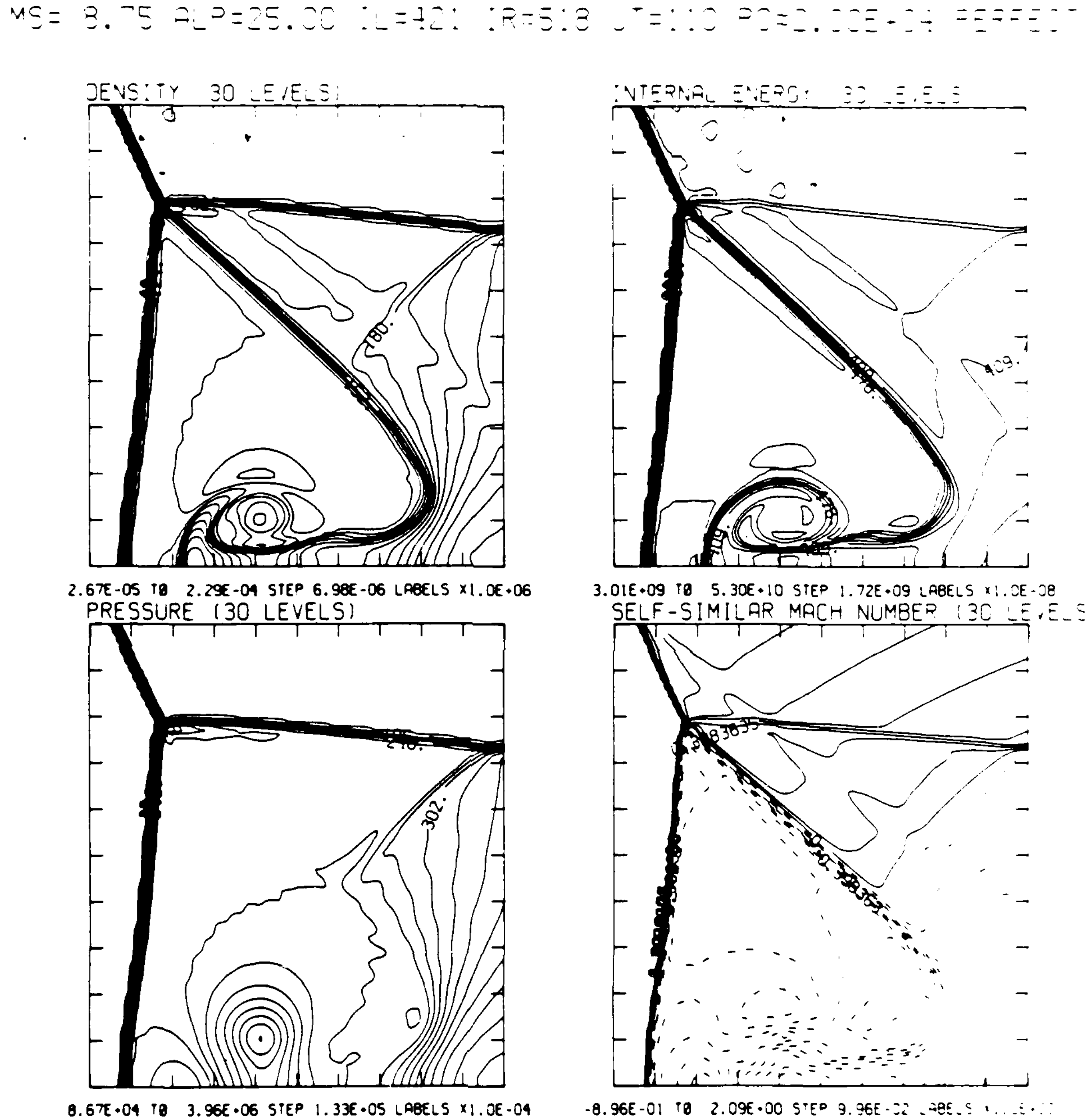

Figure 23.9b. θ_w = 25°, blowup-frame plots.

Figure 23. Transition set 3, M_s = 8.75, γ = 1.4 - continued.

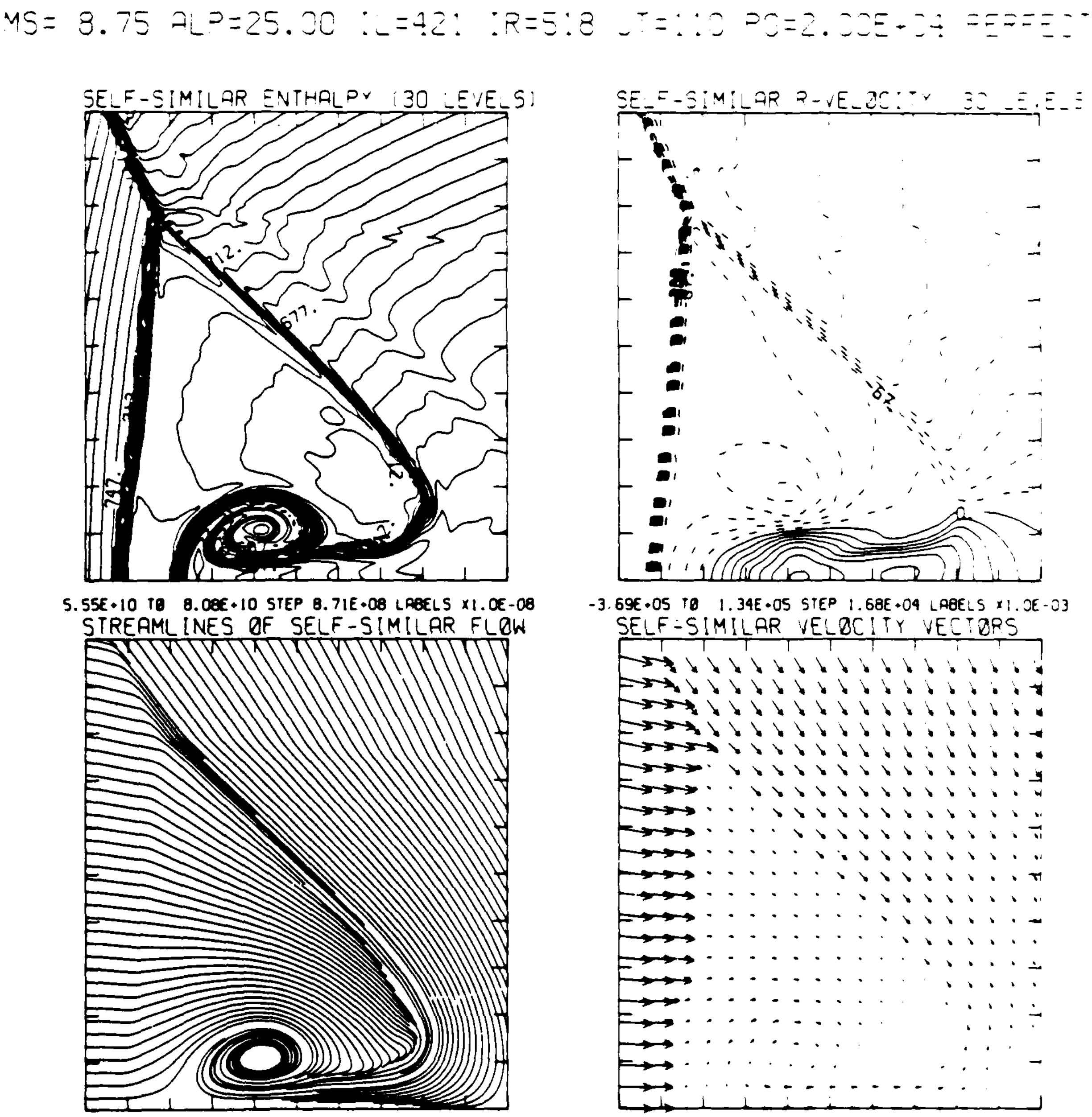

Figure 23.9b. θ_w = 25°, blowup-frame plots - continued.

Figure 23. Transition set 3, M_s = 8.75, γ = 1.4 - continued.

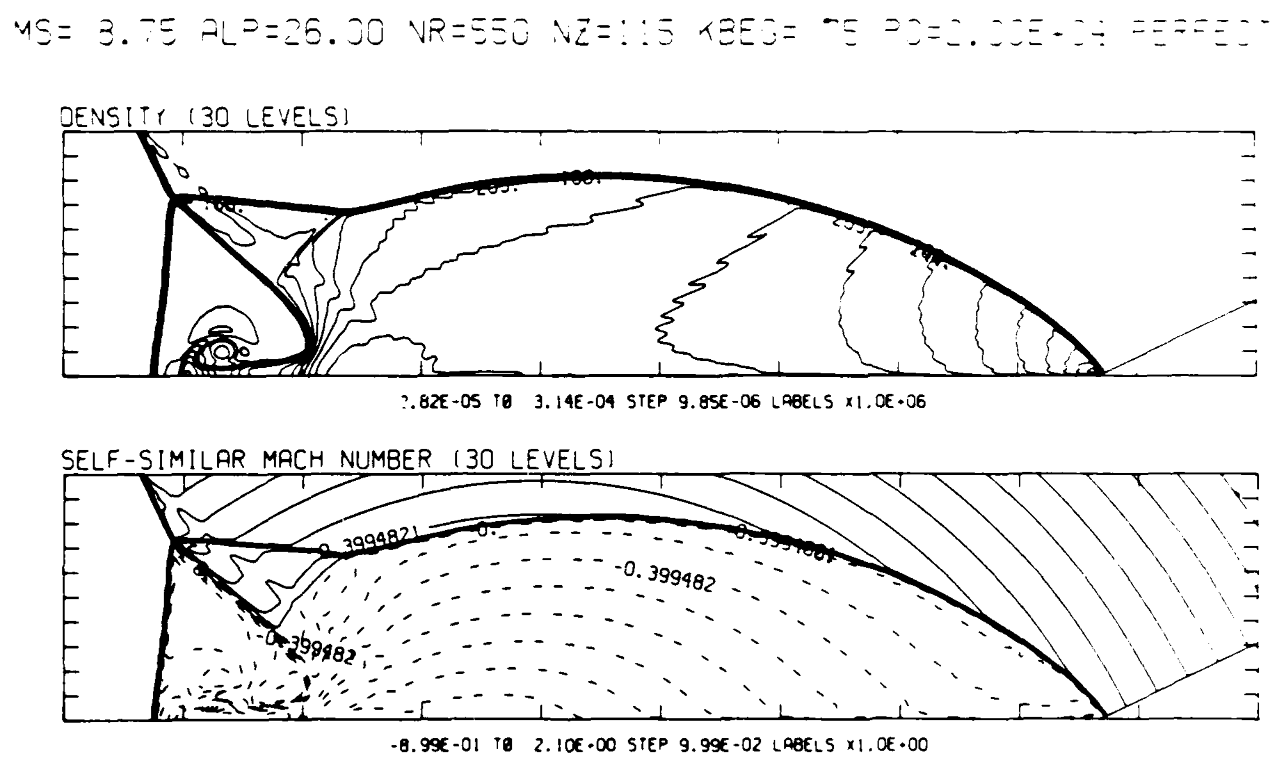

Figure 23.10a. θ_w = 26°, whole-flowfield contour-plots.

Figure 23. Transition set 3, M_s = 8.75, γ = 1.4 - continued.

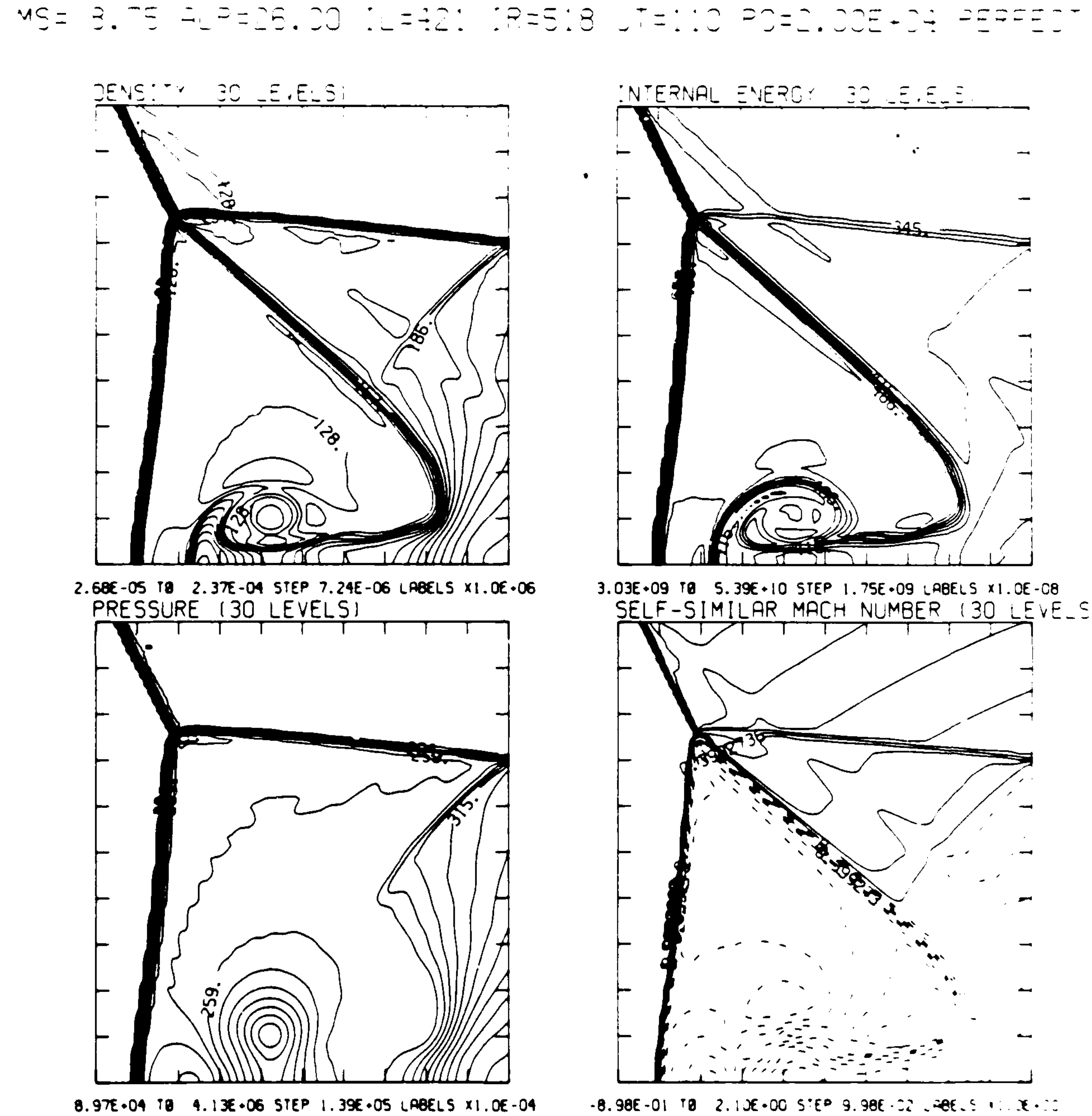

Figure 23.10b. θ_w = 26°, blowup-frame plots.

Figure 23. Transition set 3, M_s = 8.75, γ = 1.4 - continued.

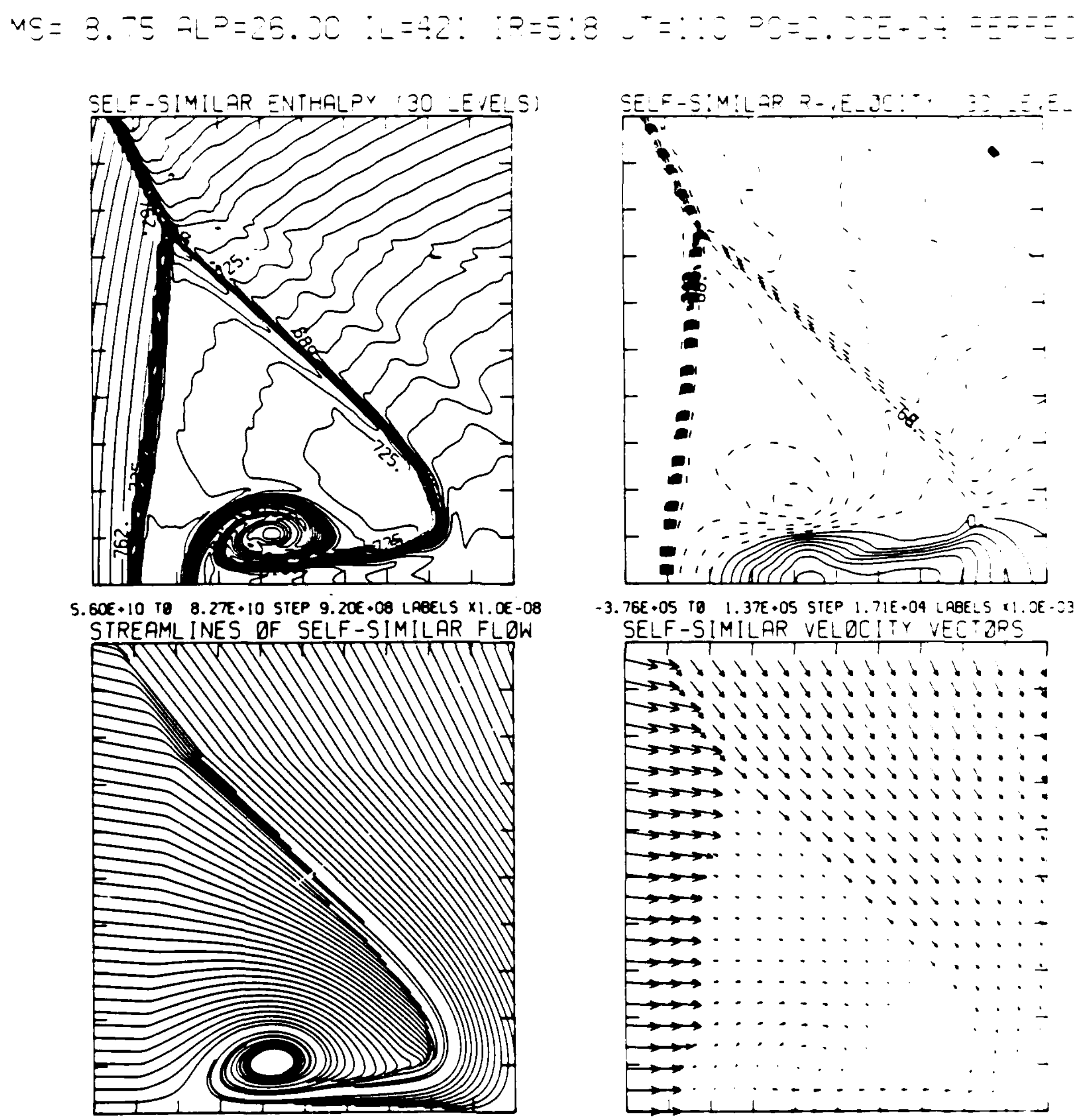

Figure 23.10b. $\theta_w = 26°$, blowup-frame plots - continued.

Figure 23. Transition set 3, $M_s = 8.75$, $\gamma = 1.4$ - continued.

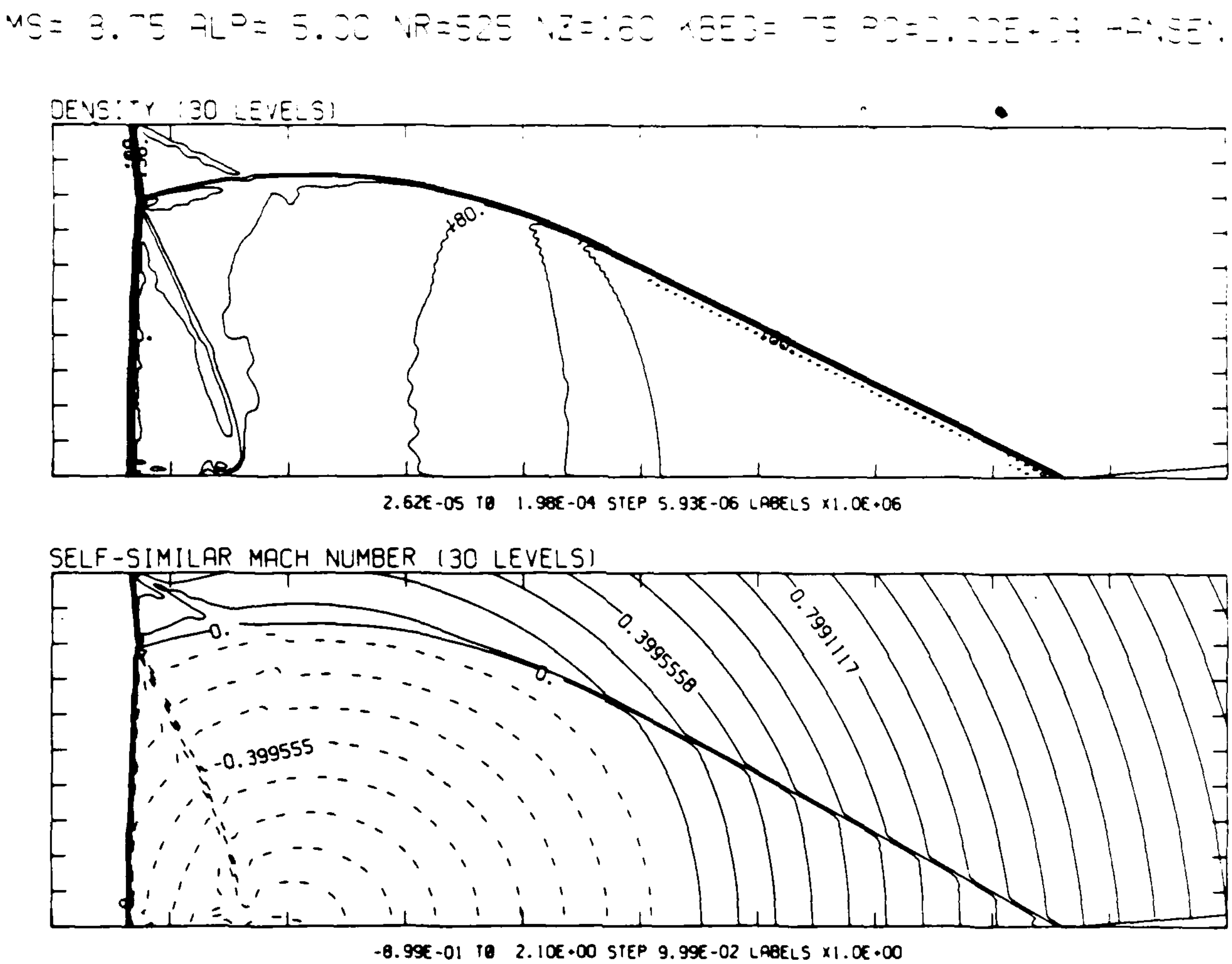

Figure 24.1a. $\theta_w = 5°$, whole-flowfield contour-plots.

Figure 24. Transition set 3, M_s = 8.75, Hansen.

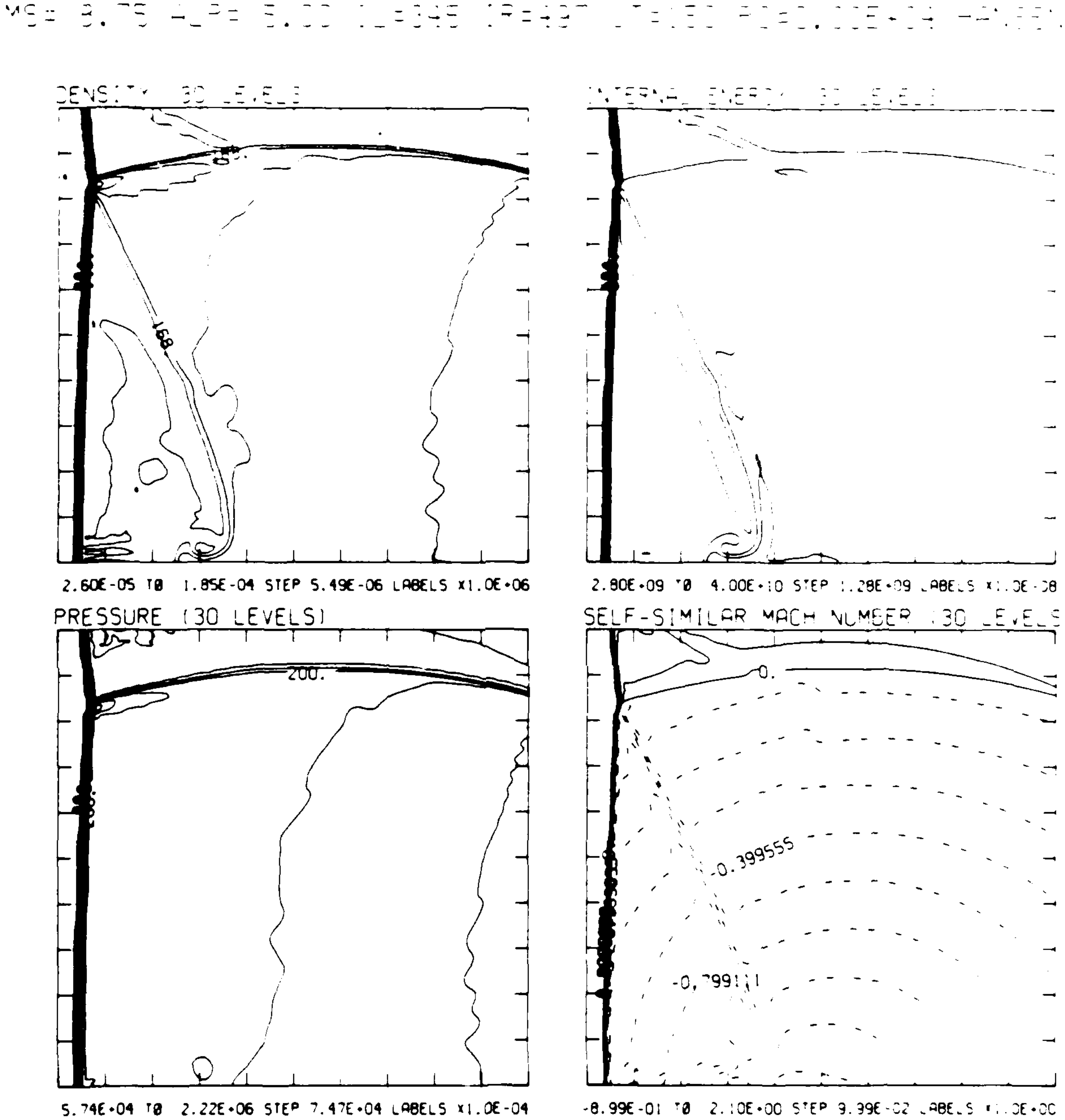

Figure 24.1b. $\theta_w = 5°$, blowup-frame plots.

Figure 24. Transition set 3, $M_s = 8.75$, Hansen - continued.

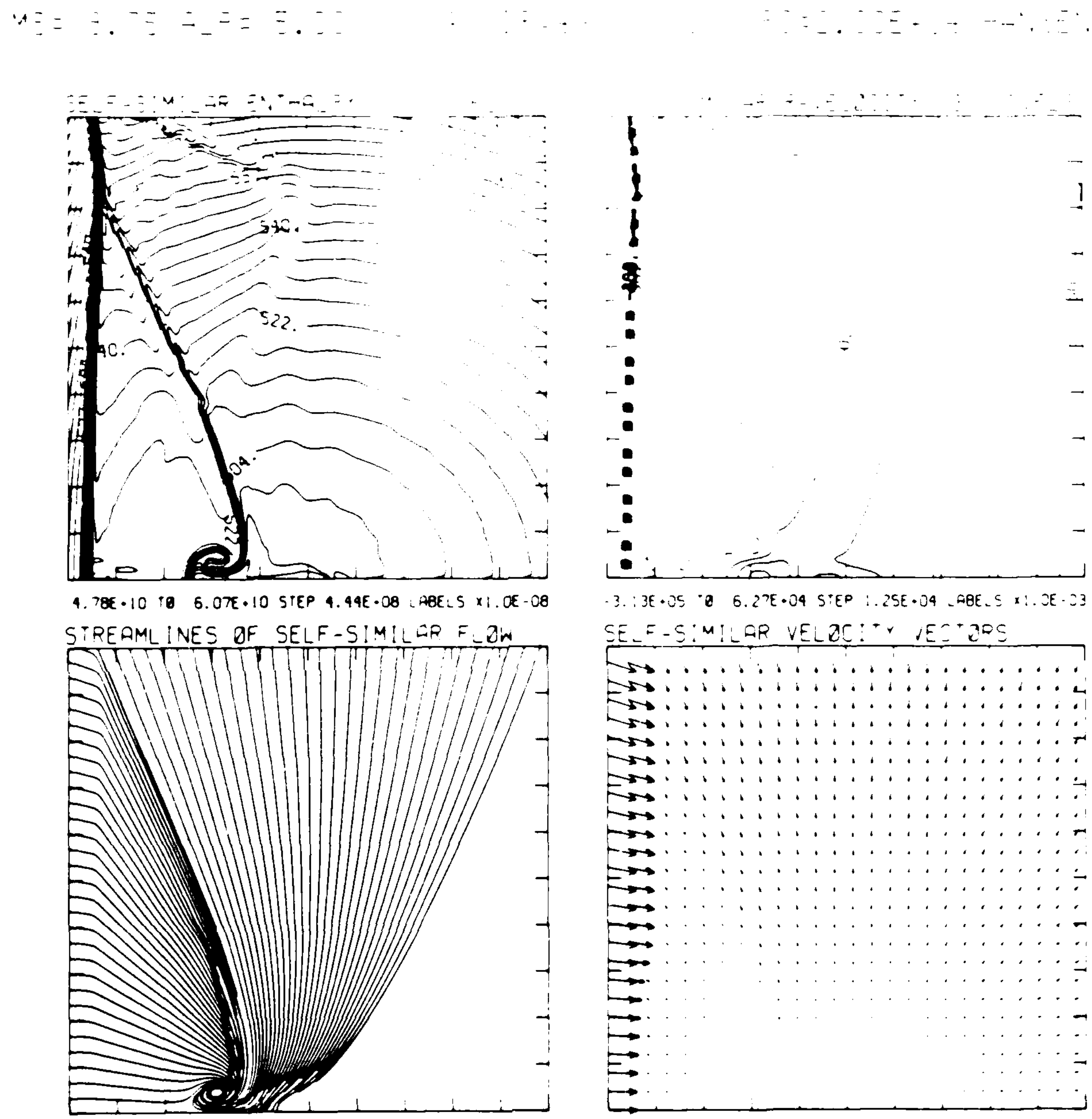

Figure 24.1b. $\theta_w = 5°$, blowup-frame plots - continued.

Figure 24. Transition set 3, M_s = 8.75, Hansen - continued.

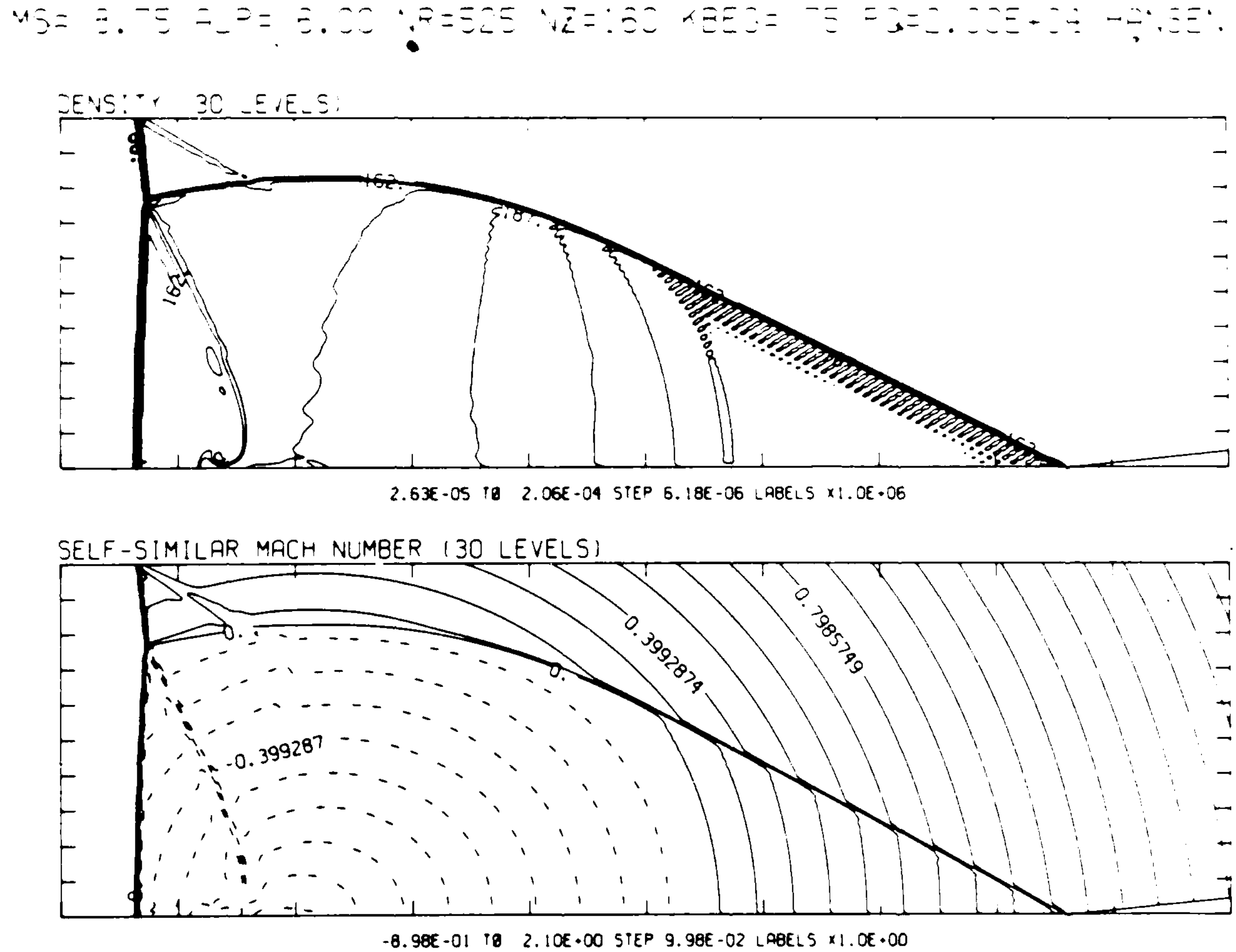

Figure 24.2a. $\theta_w = 6°$, whole-flowfield contour-plots.

Figure 24. Transition set 3, $M_s = 8.75$, Hansen - continued.

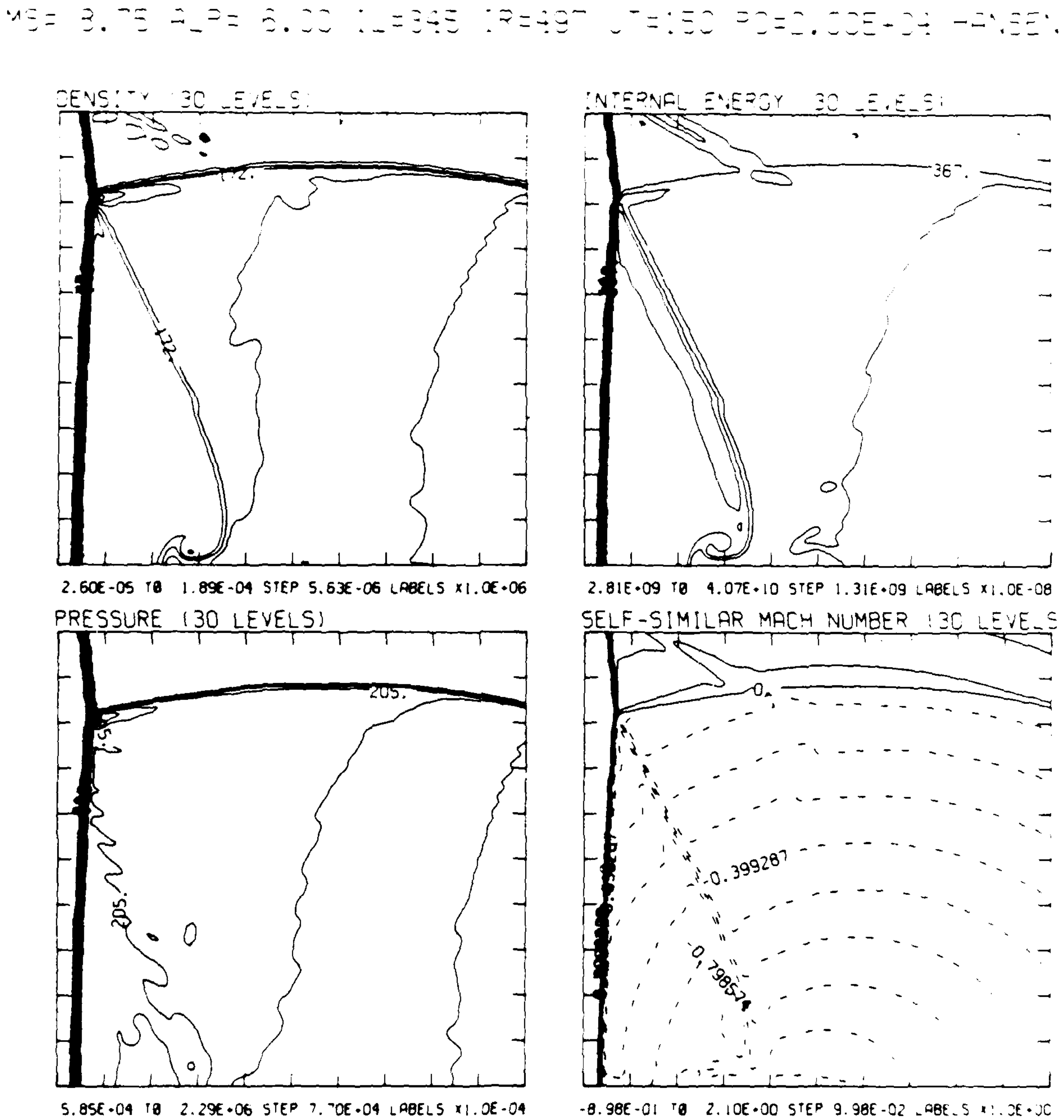

Figure 24.2b. $\theta_w = 6°$, blowup-frame plots.

Figure 24. Transition set 3, $M_s = 8.75$, Hansen - continued.

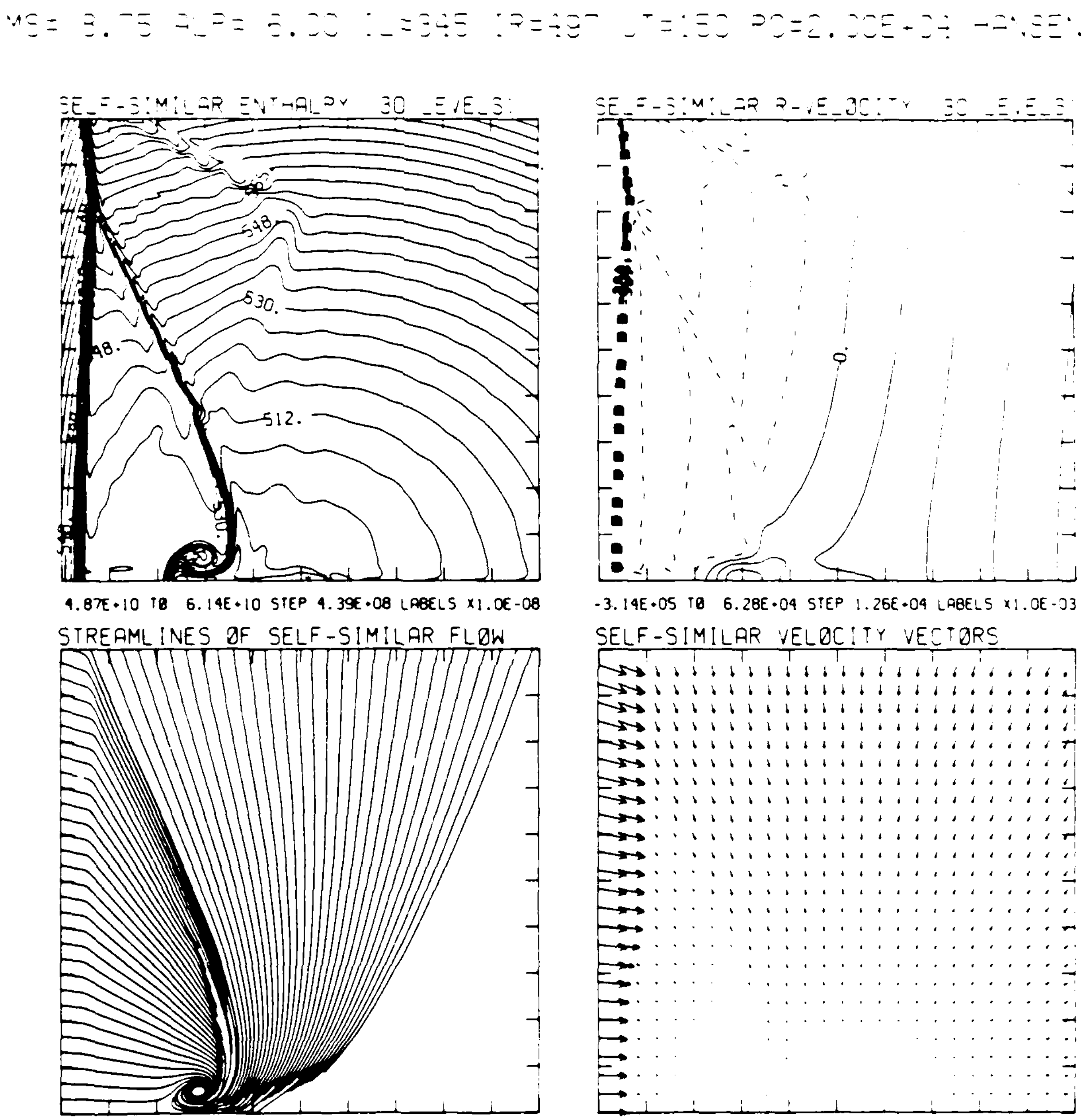

Figure 24.2b. $\theta_w = 6°$, blowup-frame plots - continued.

Figure 24. Transition set 3, $M_s = 8.75$, Hansen - continued.

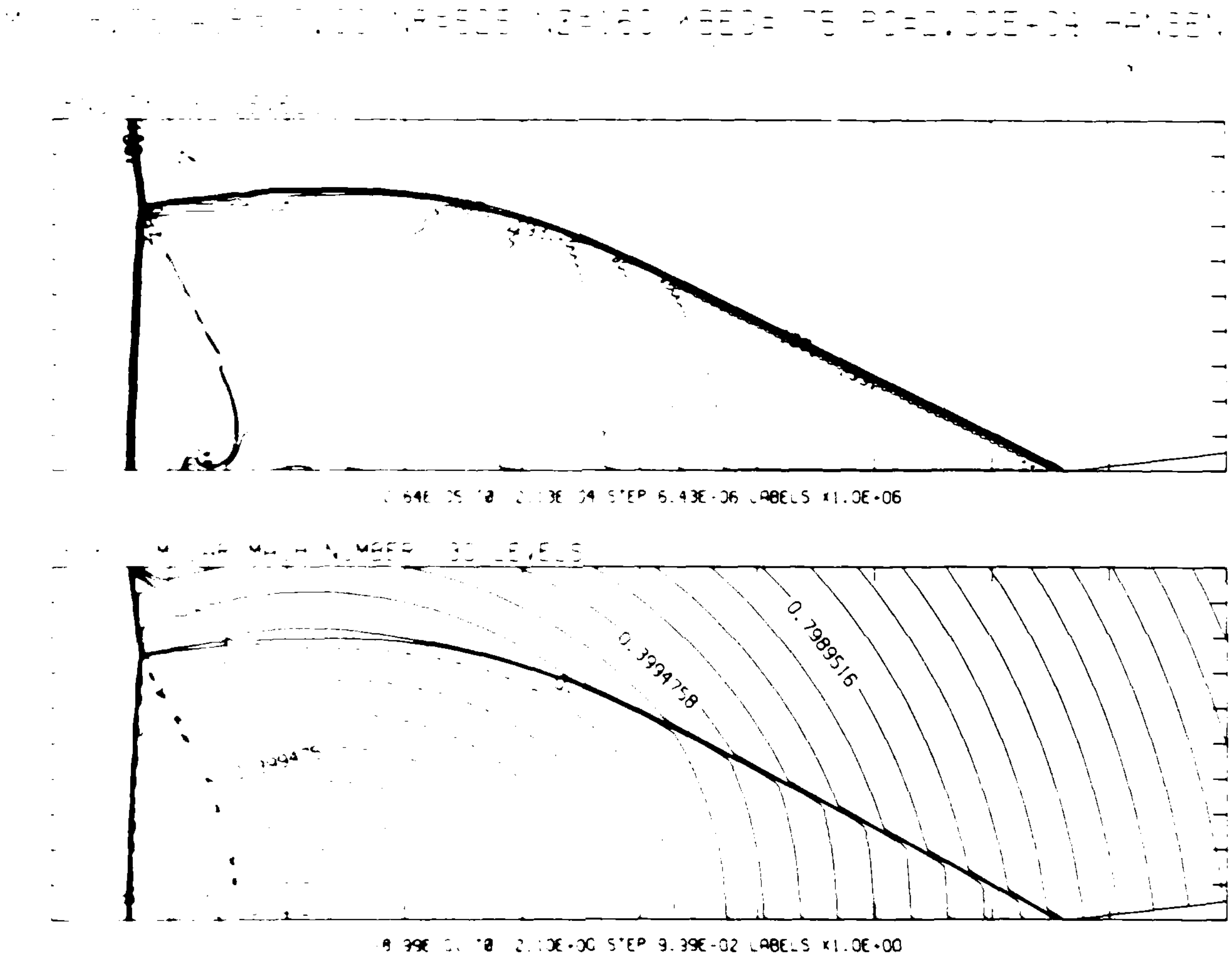

Figure 24.3a. θ_w = 7°, whole-flowfield contour-plots.

Figure 24. Transition set 3, M_s = 8.75, Hansen - continued.

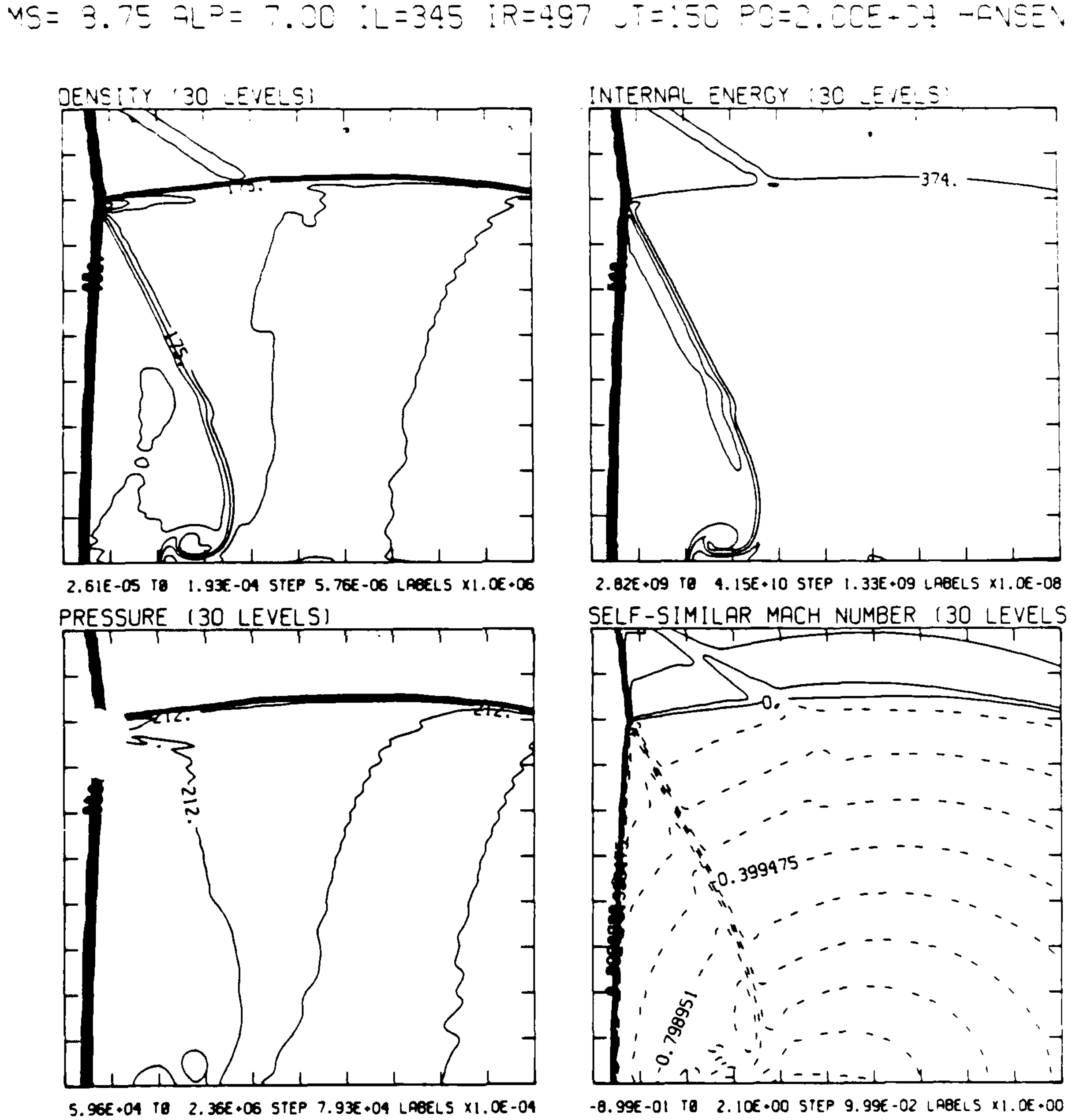

Figure 24.3b. $\theta_w = 7°$, blowup-frame plots.

Figure 24. Transition set 3, $M_s = 8.75$, Hansen - continued.

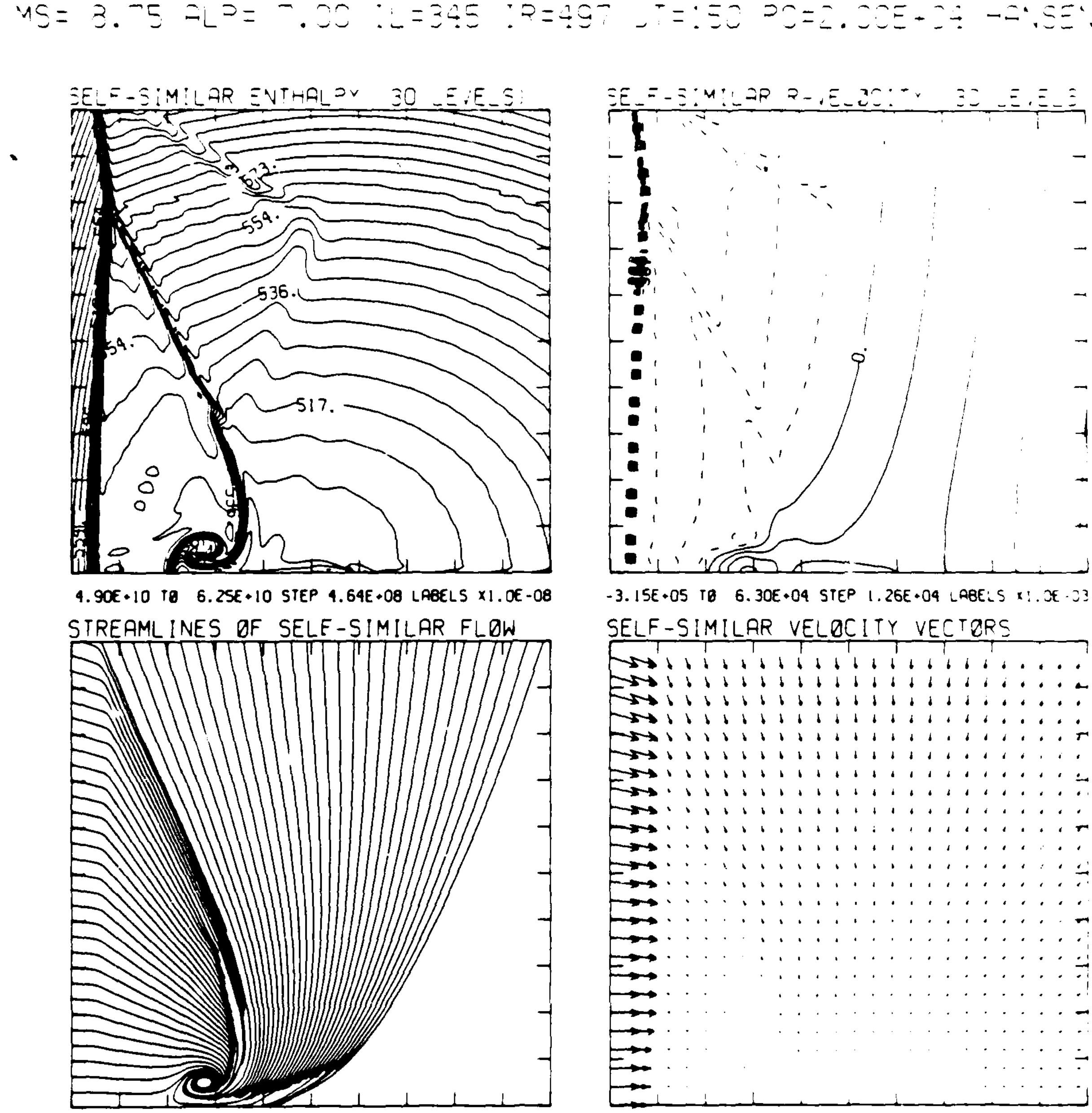

Figure 24.3b. θ_w = 7°, blowup-frame plots - continued.

Figure 24. Transition set 3, M_s = 8.75, Hansen - continued.

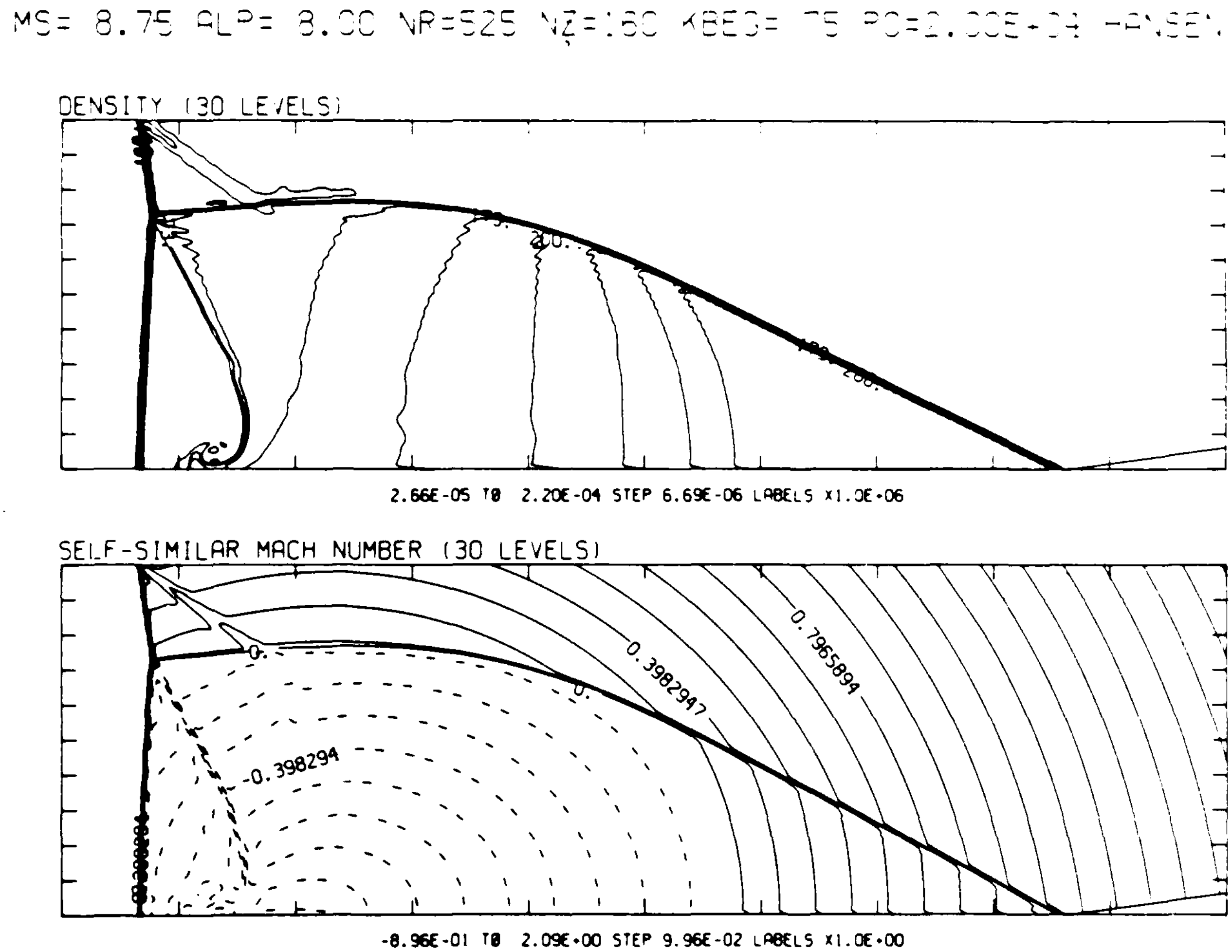

Figure 24.4a. θ_w = 8°, whole-flowfield contour-plots.

Figure 24. Transition set 3, M_s = 8.75, Hansen - continued.

MS= 8.75 ALP= 8.00 IL=345 IR=497 JT=150 PO=1.00E-04 HANSEN

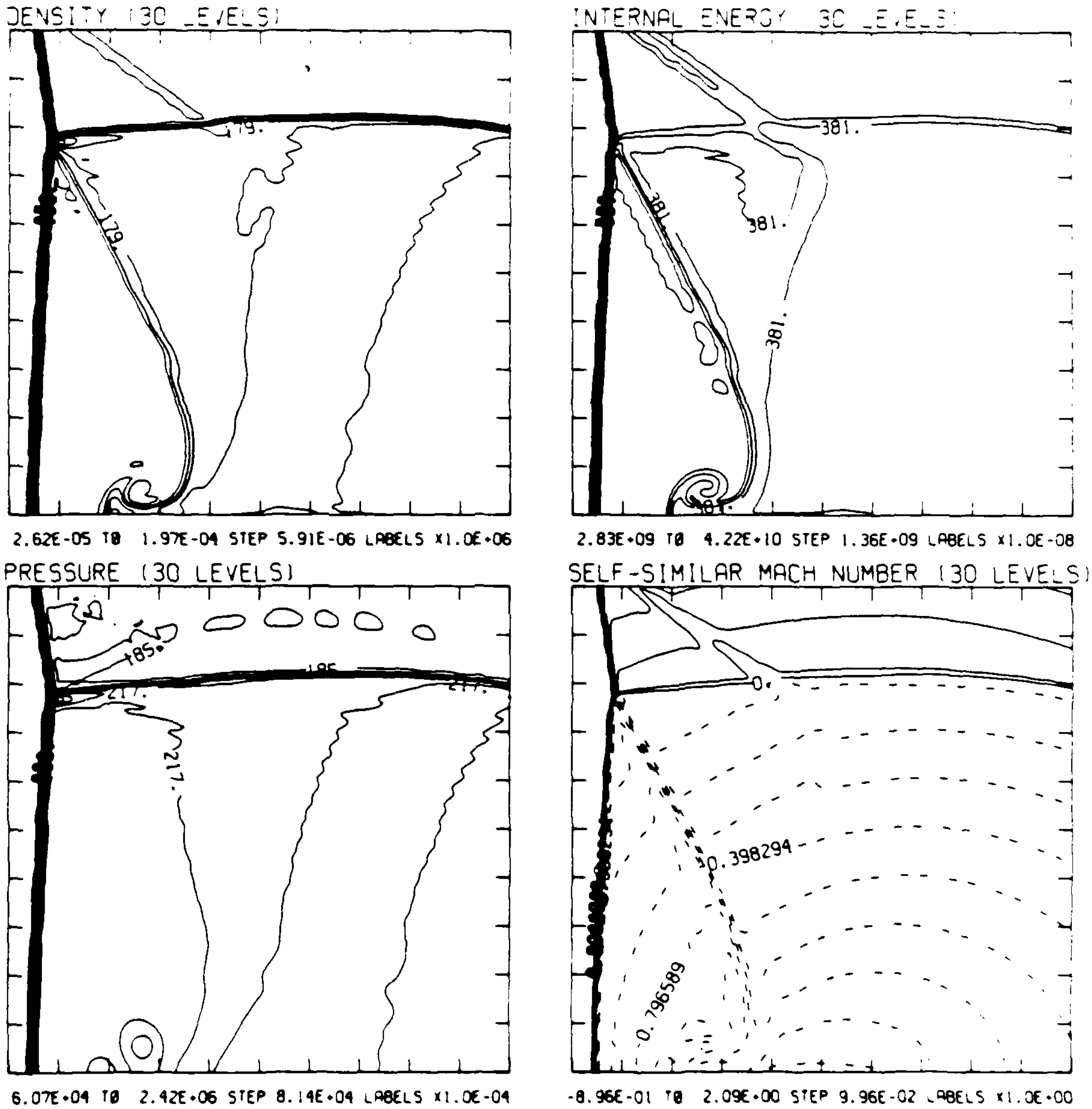

Figure 24.4b. θ_w = 8°, blowup-frame plots.

Figure 24. Transition set 3, M_s = 8.75, Hansen - continued.

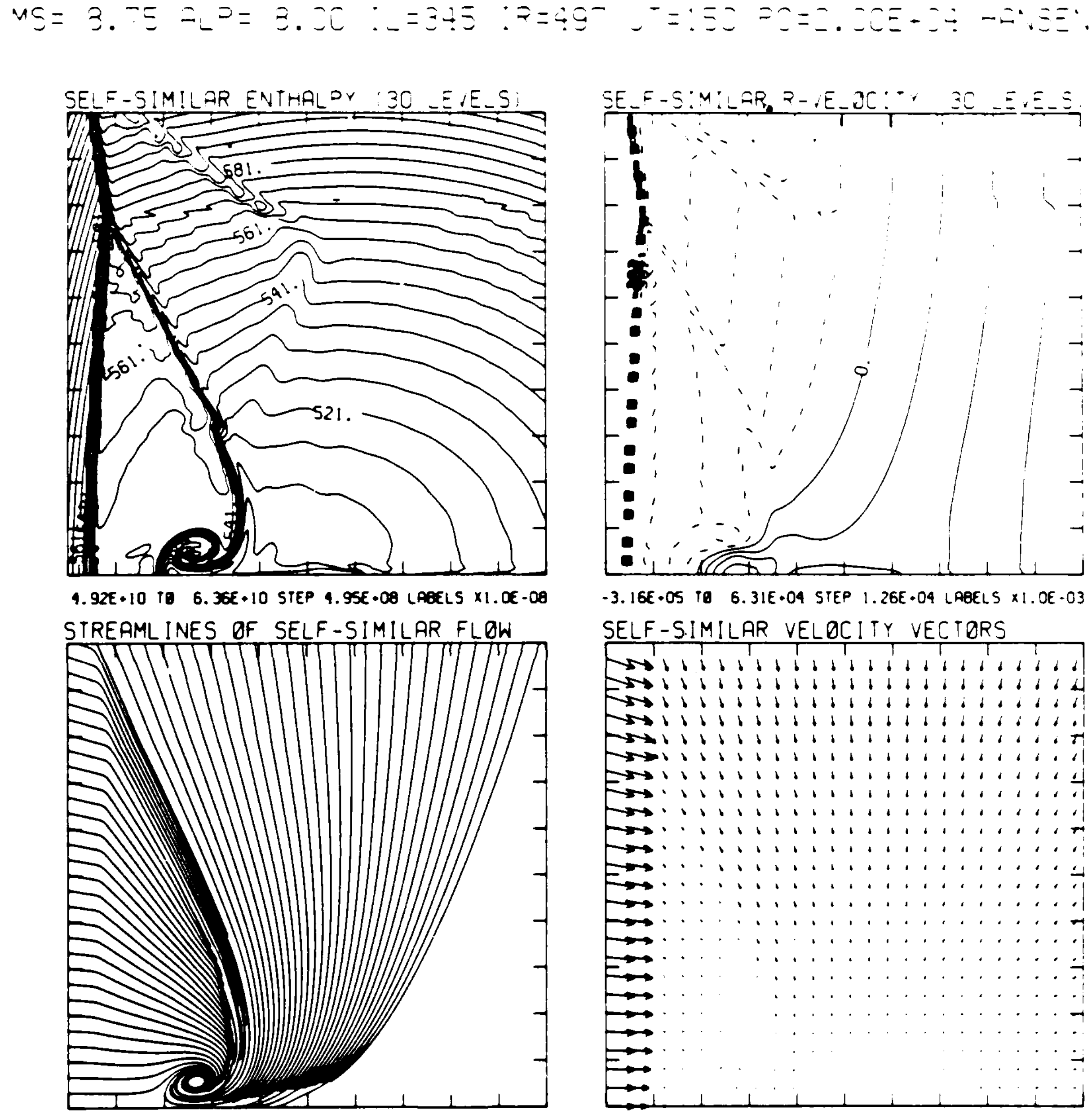

Figure 24.4b. $\theta_w = 8°$, blowup-frame plots - continued.

Figure 24. Transition set 3, $M_s = 8.75$, Hansen - continued.

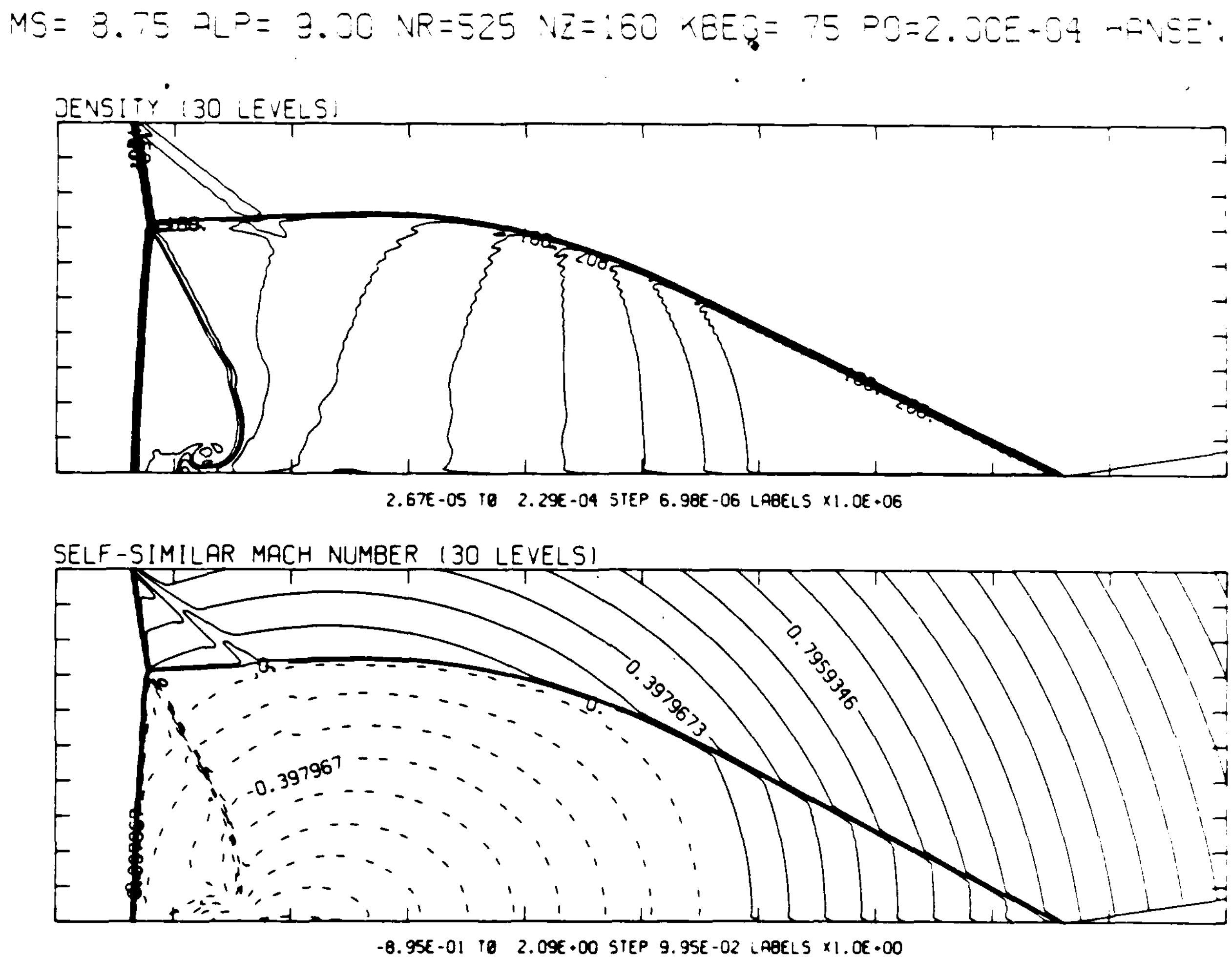

Figure 24.5a. θ_w = 9°, whole-flowfield contour-plots.

Figure 24. Transition set 3, M_s = 8.75, Hansen - continued.

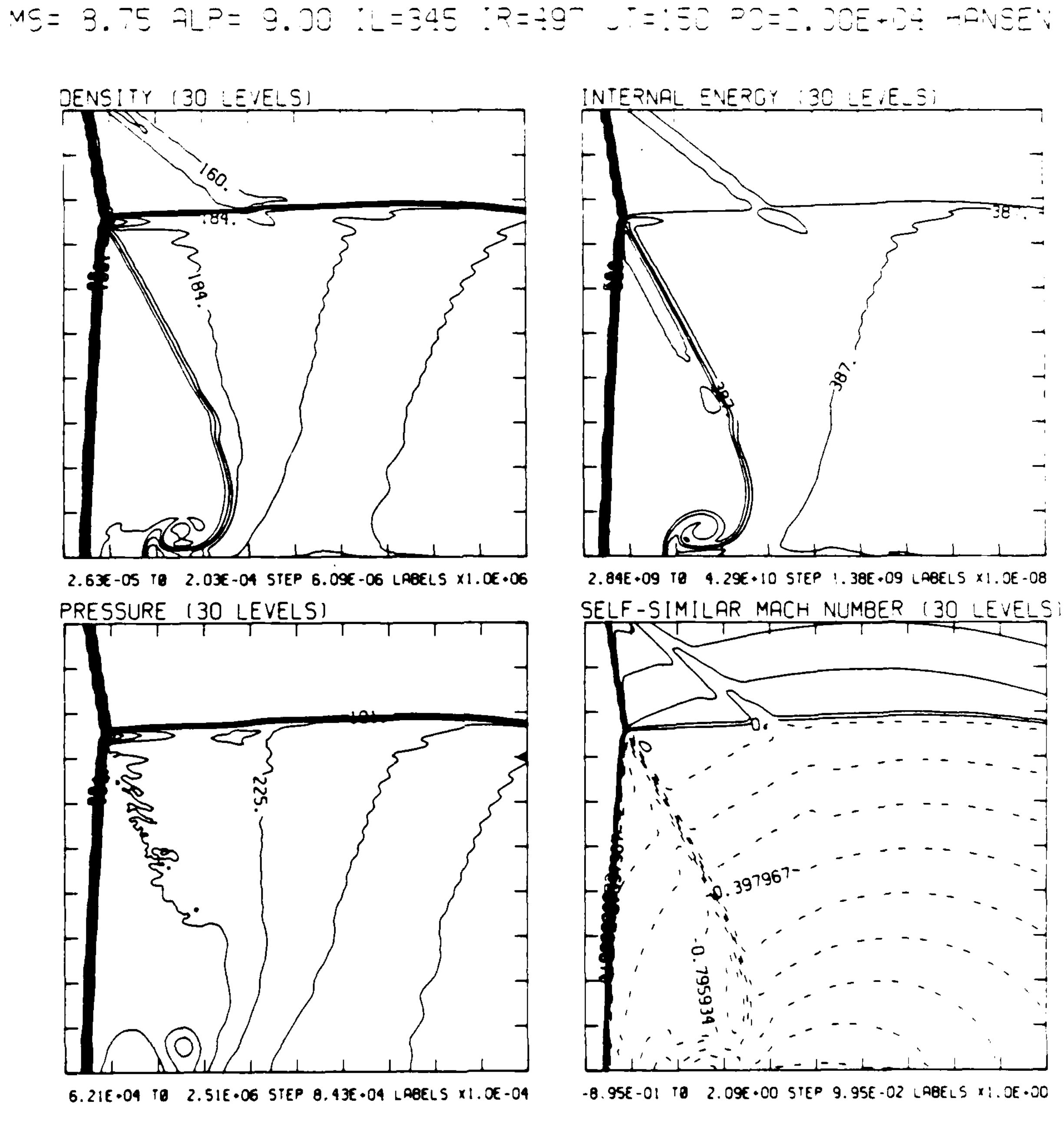

Figure 24.5b. $\theta_w = 9°$, blowup-frame plots.

Figure 24. Transition set 3, $M_s = 8.75$, Hansen - continued.

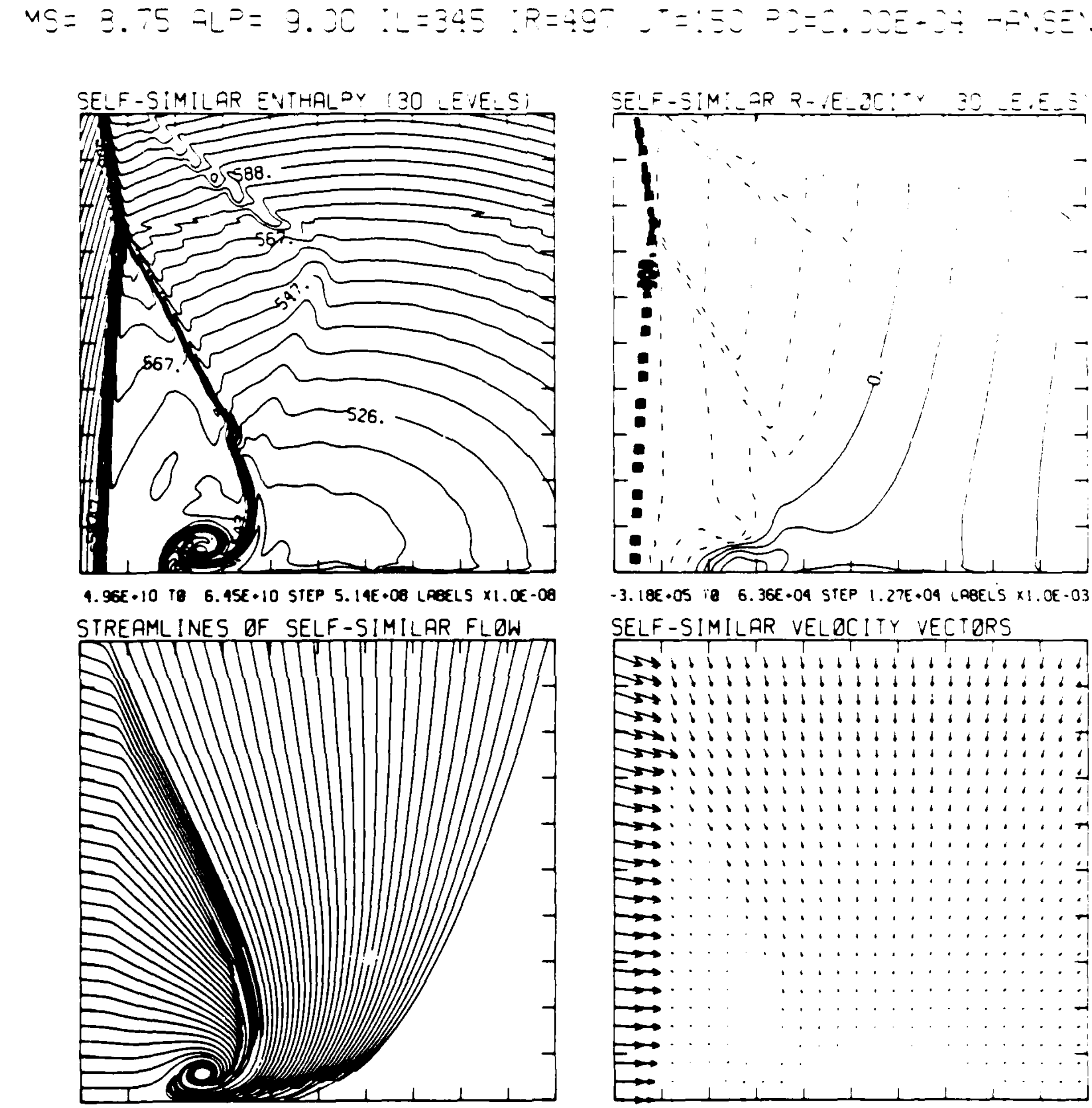

Figure 24.5b. $\theta_w = 9°$, blowup-frame plots - continued.

Figure 24. Transition set 3, $M_s = 8.75$, Hansen - continued.

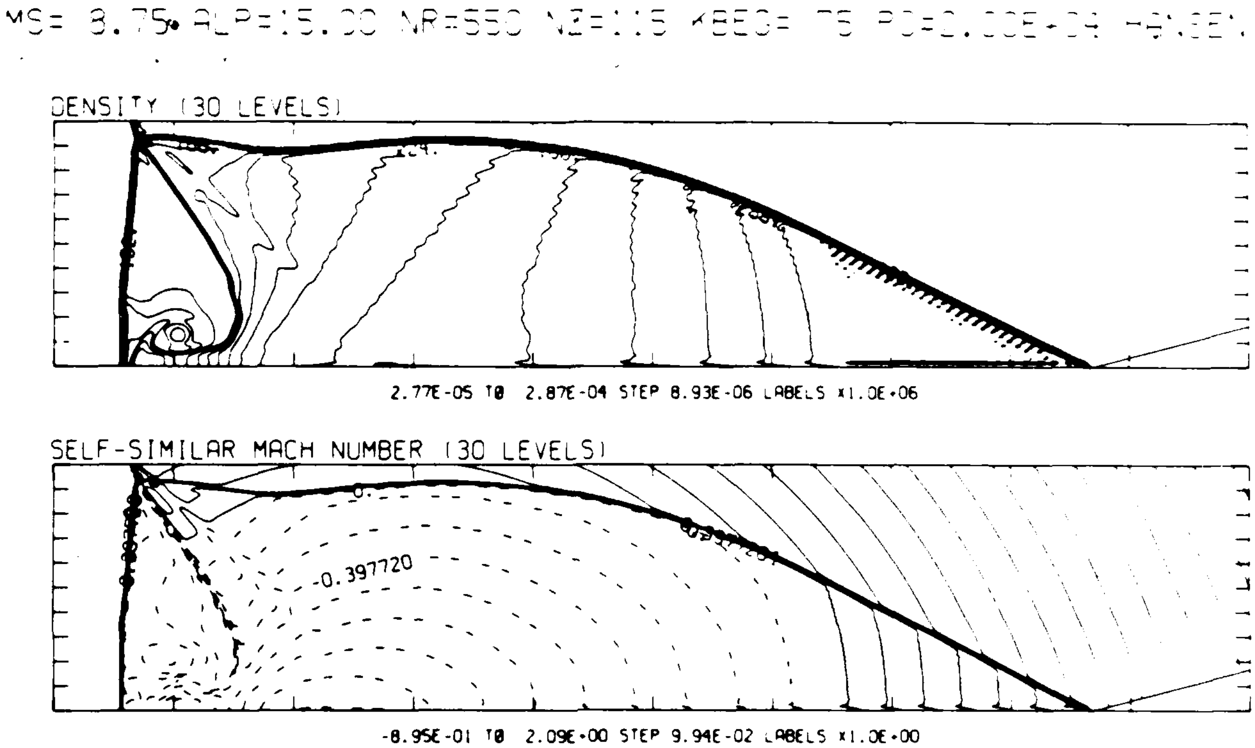

Figure 24.6a. θ_w = 15°, whole-flowfield contour-plots.

Figure 24. Transition set 3, M_s = 8.75, Hansen - continued.

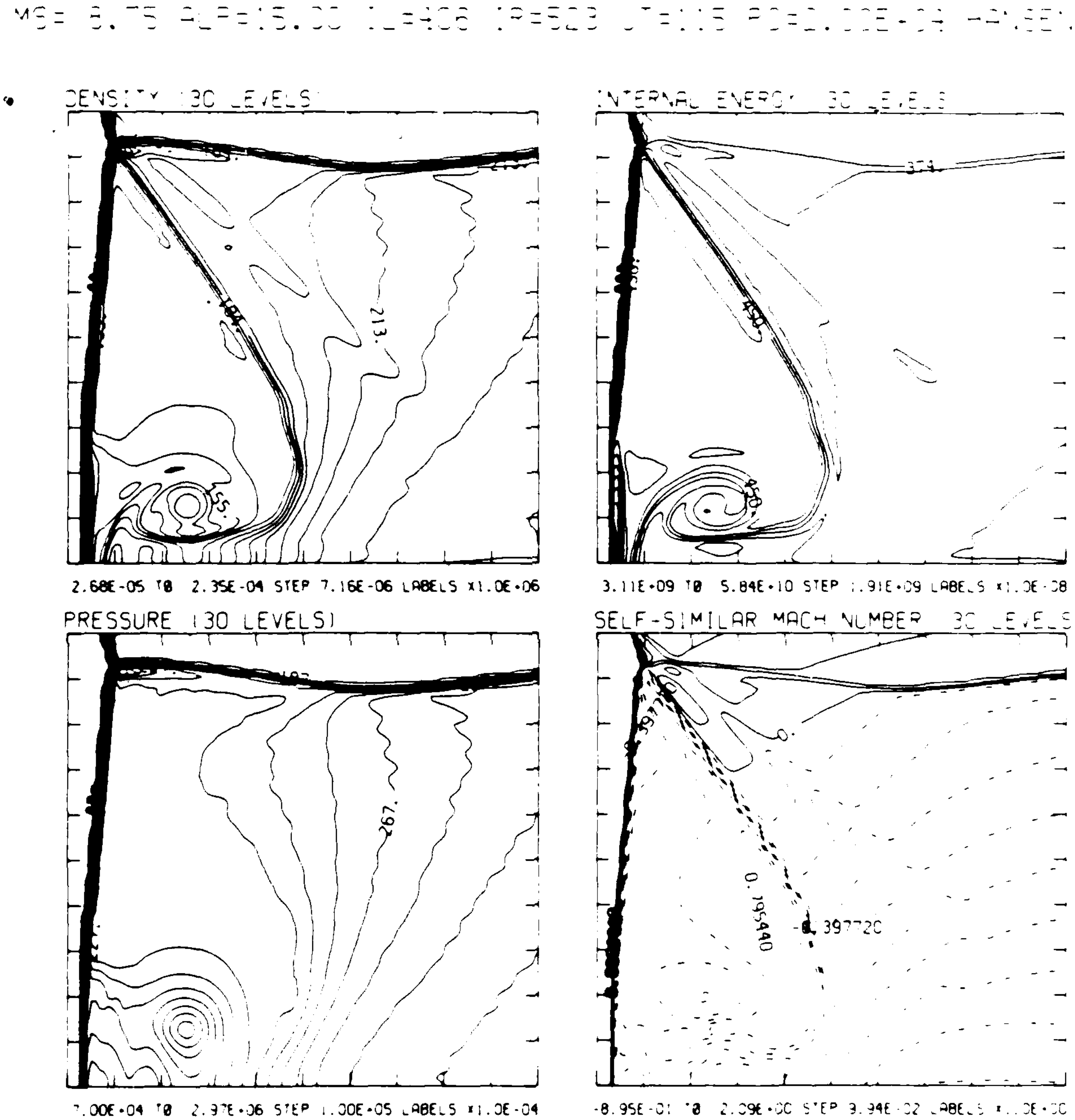

Figure 24.6b. θ_w = 15°, blowup-frame plots.

Figure 24. Transition set 3, M_s = 8.75, Hansen - continued.

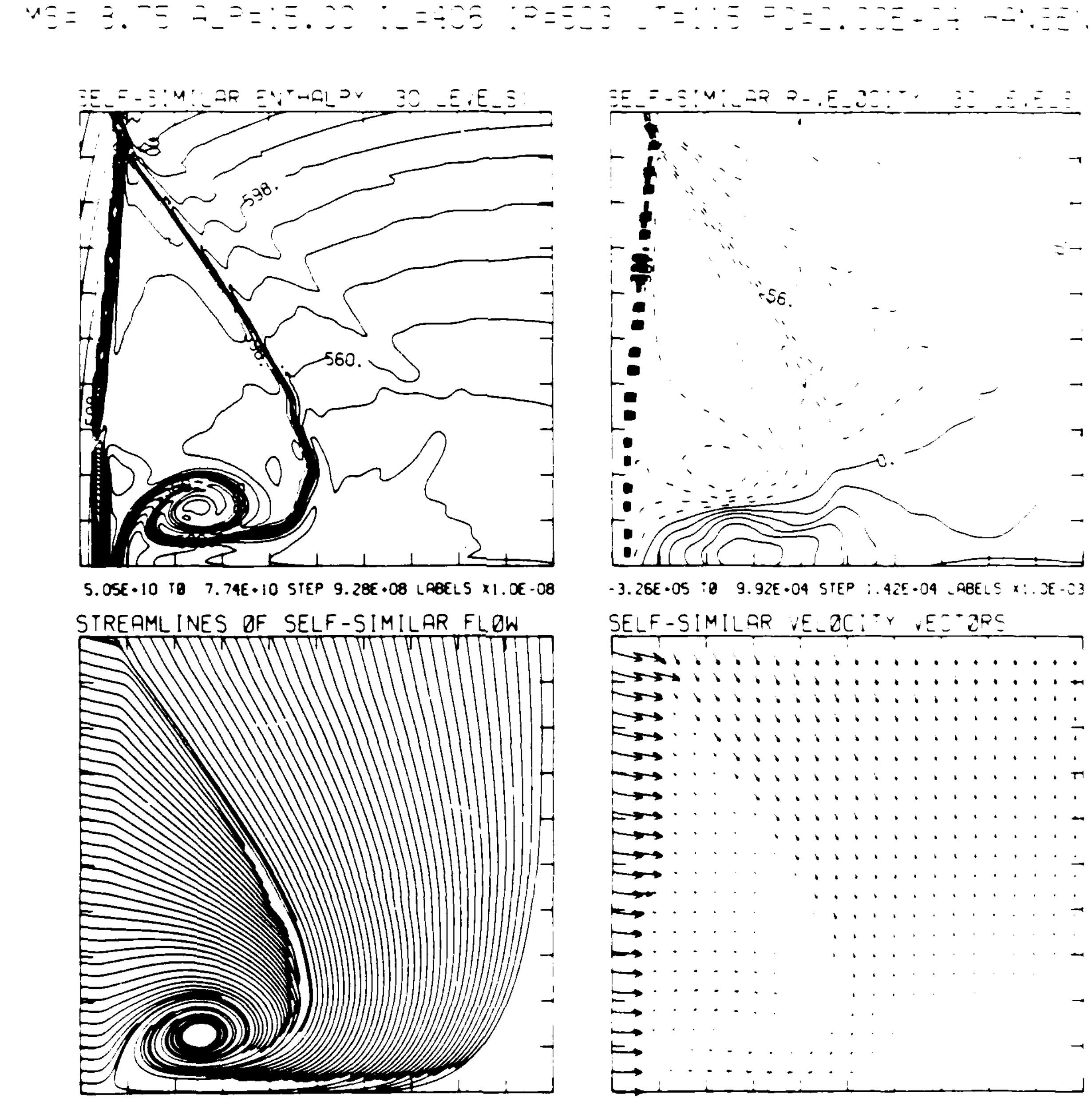

Figure 24.6b. θ_w = 15°, blowup-frame plots - continued.

Figure 24. Transition set 3, M_s = 8.75, Hansen - continued.

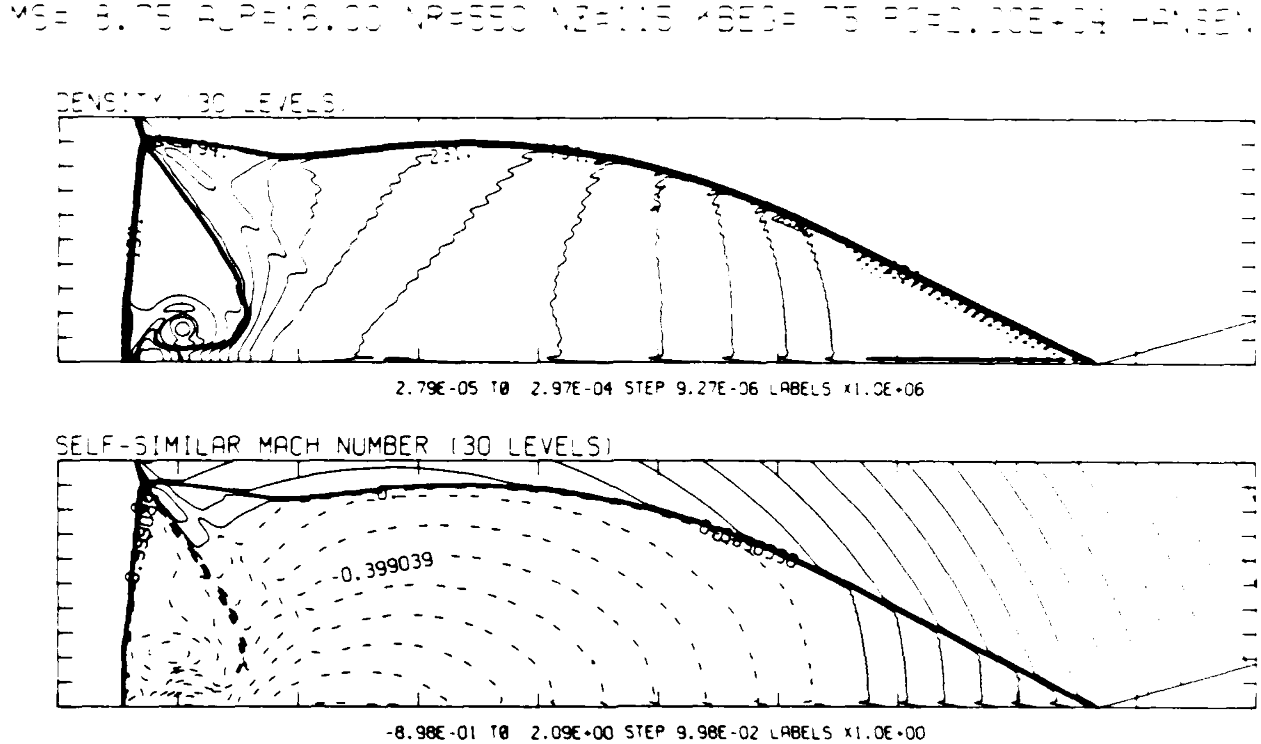

Figure 24.7a. θ_w = 16°, whole-flowfield contour-plots.

Figure 24. Transition set 3, M_s = 8.75, Hansen - continued.

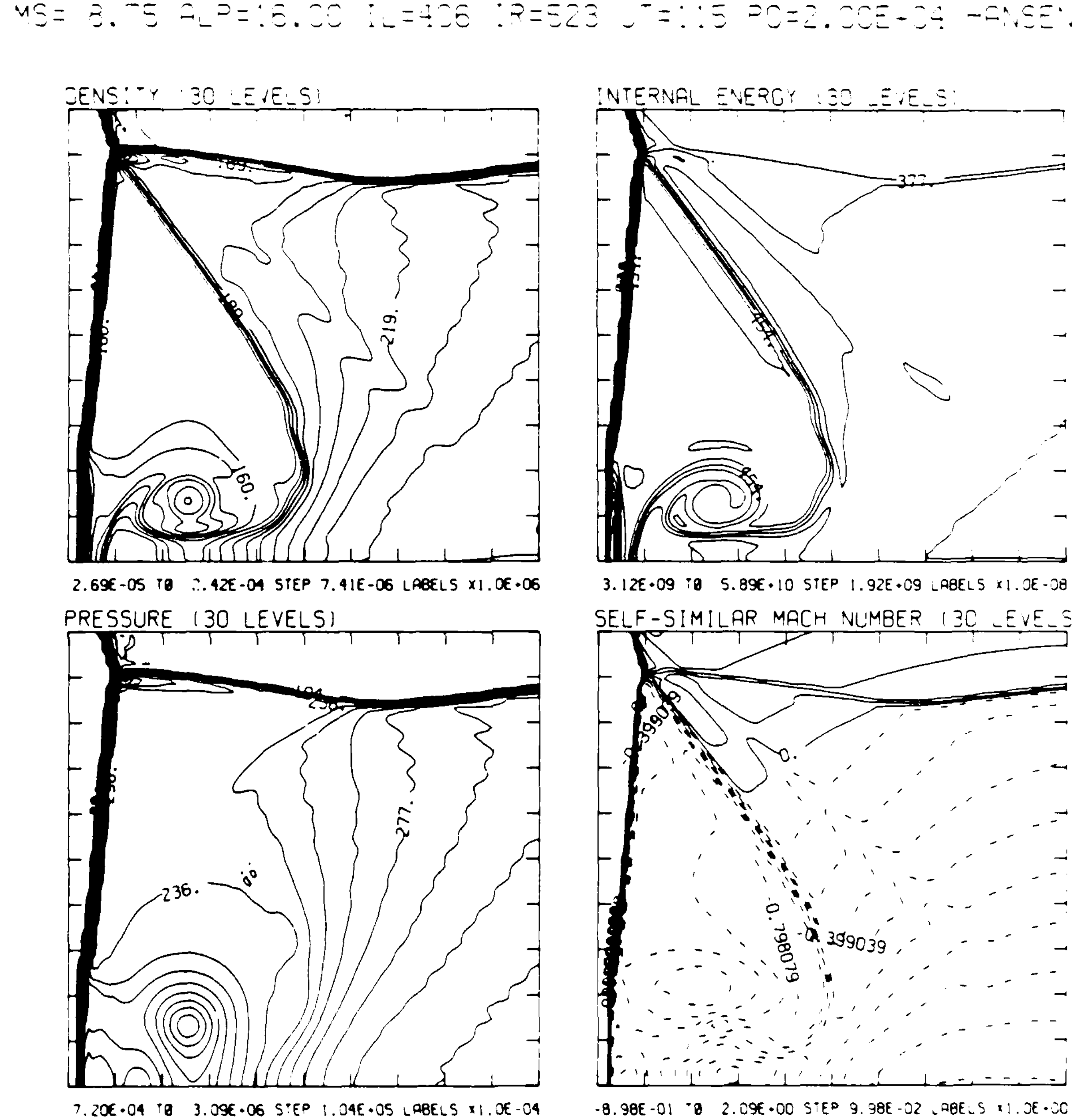

Figure 24.7b. θ_w = 16°, blowup-frame plots.

Figure 24. Transition set 3, M_s = 8.75, Hansen - continued.

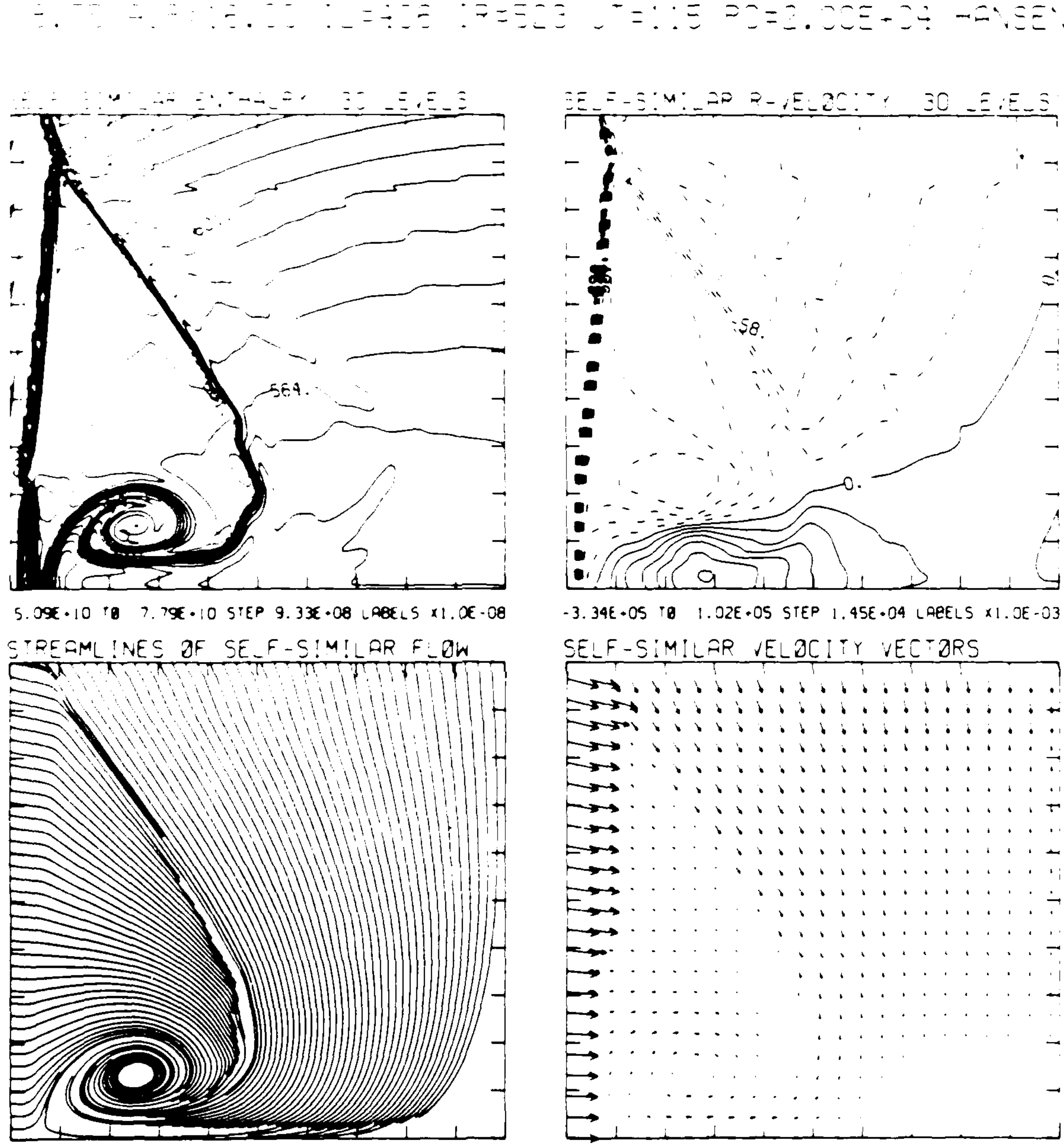

Figure 24.7b. θ_w = 16°, blowup-frame plots - continued.

Figure 24. Transition set 3, M_s = 8.75, Hansen - continued.

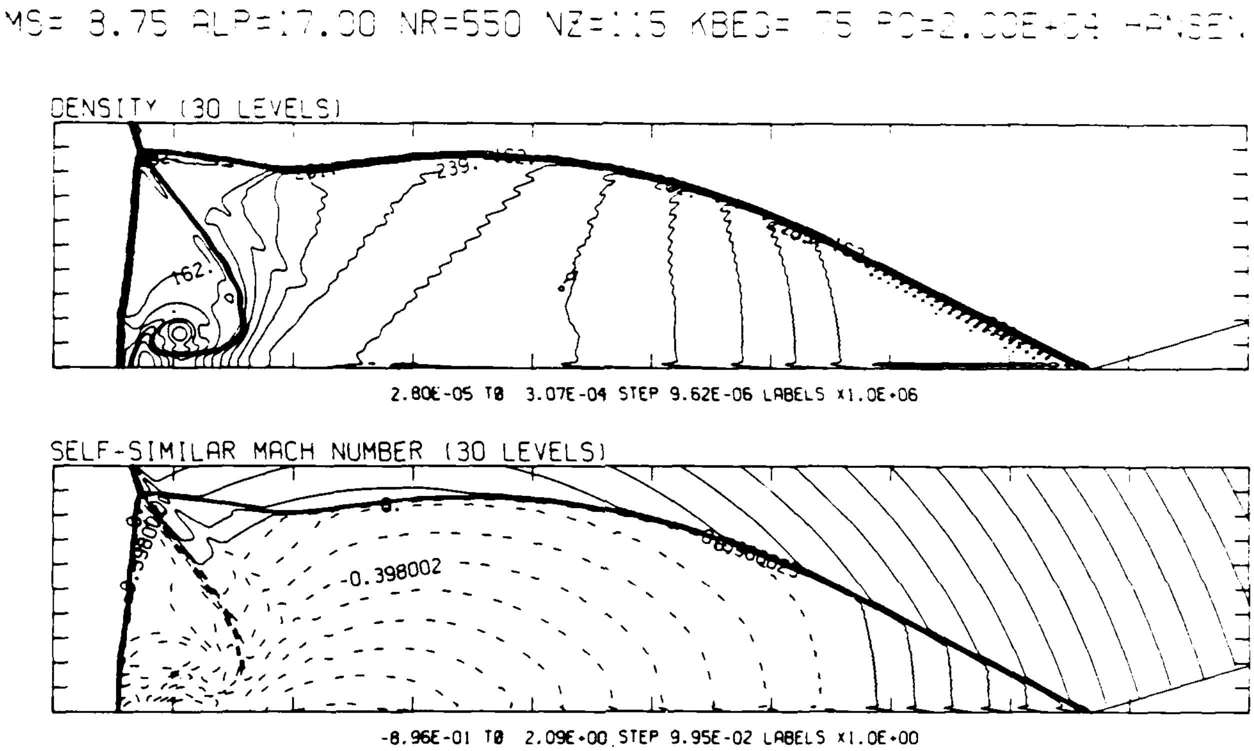

Figure 24.8a. θ_w = 17°, whole-flowfield contour-plots.

Figure 24. Transition set 3, M_s = 8.75, Hansen - continued.

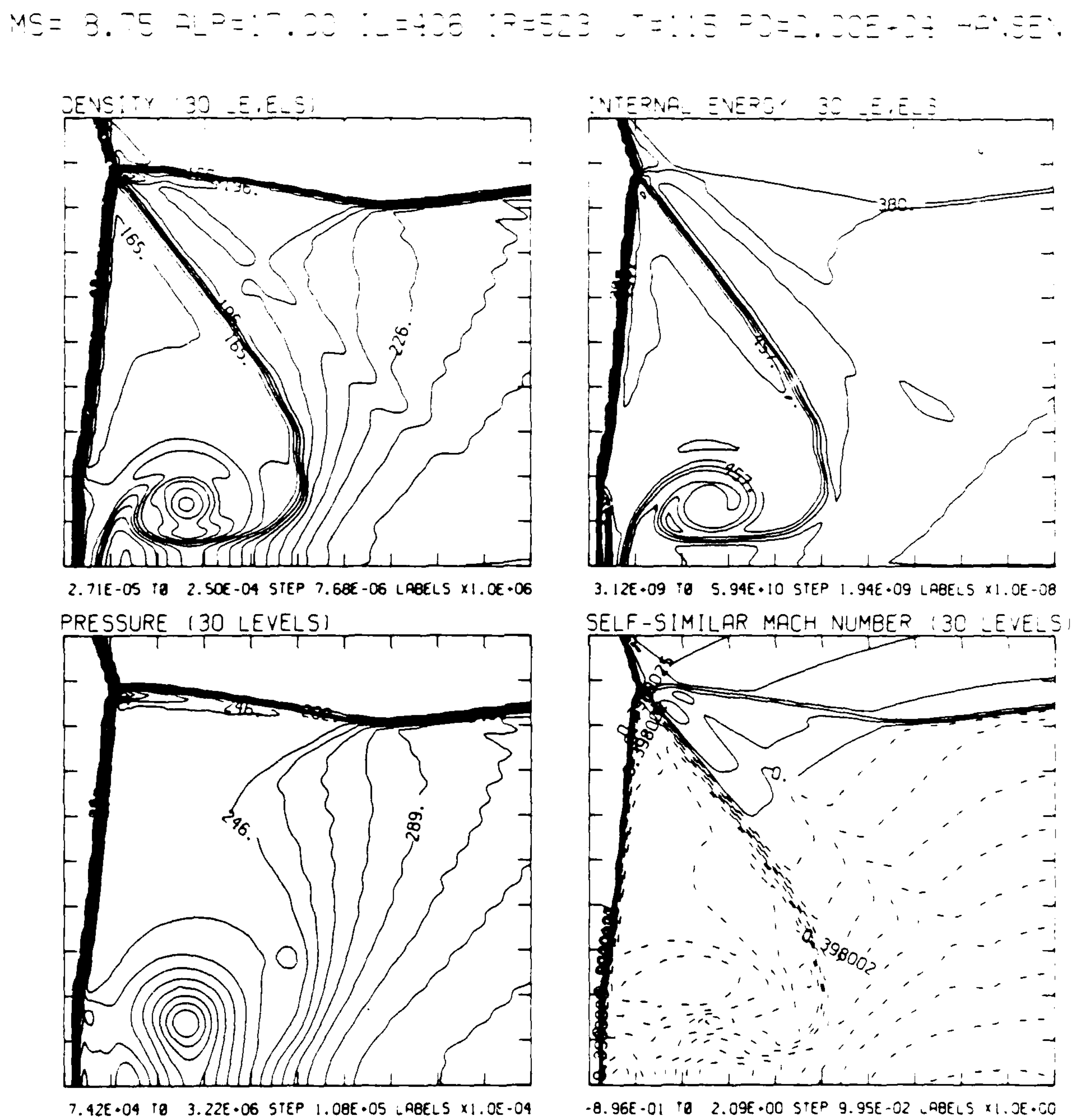

Figure 24.8b. $\theta_w = 17°$, blowup-frame plots.

Figure 24. Transition set 3, $M_s = 8.75$, Hansen - continued.

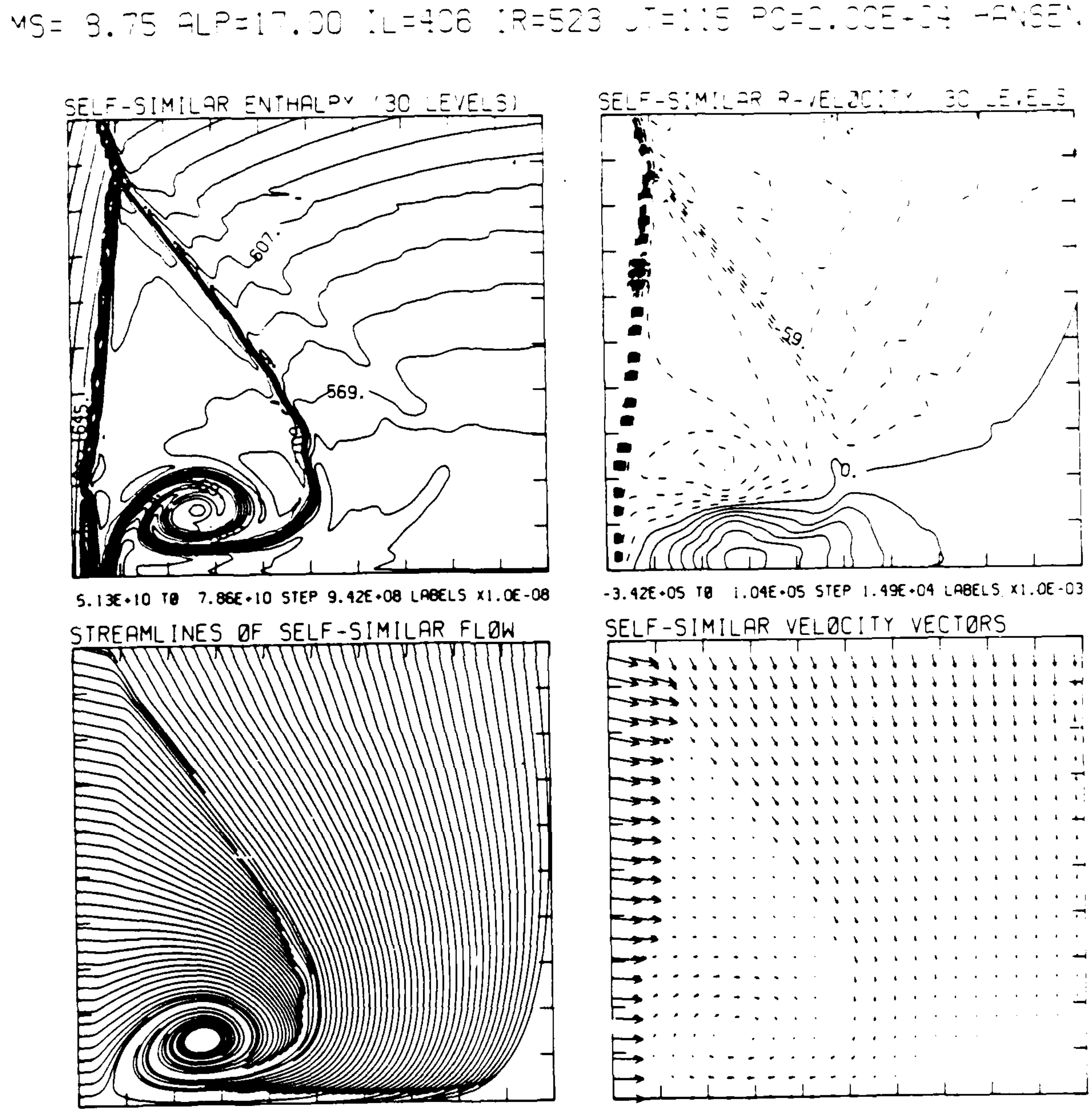

Figure 25.8b. $\theta_W = 17°$, blowup-frame plots - continued.

Figure 24. Transition set 3, $M_S = 8.75$, Hansen - continued.

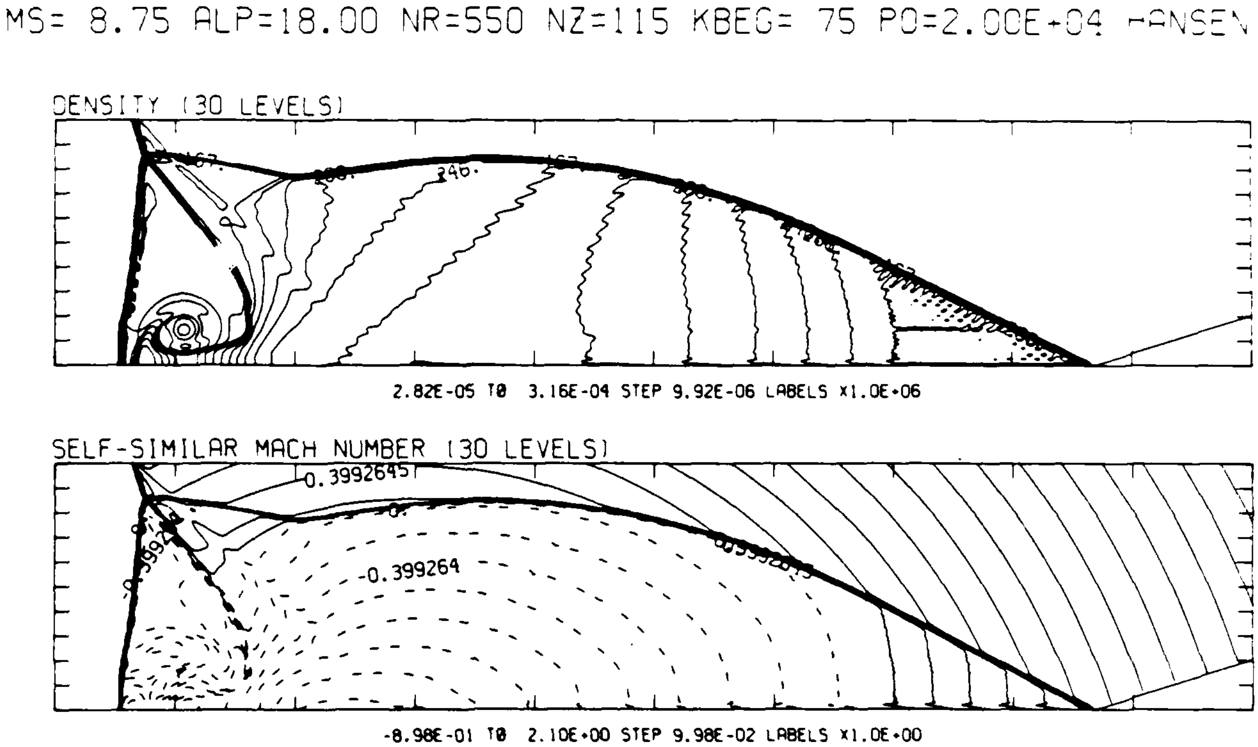

Figure 24.9a. θ_w = 18°, whole-flowfield contour-plots.

Figure 24. Transition set 3, M_s = 8.75, Hansen - continued.

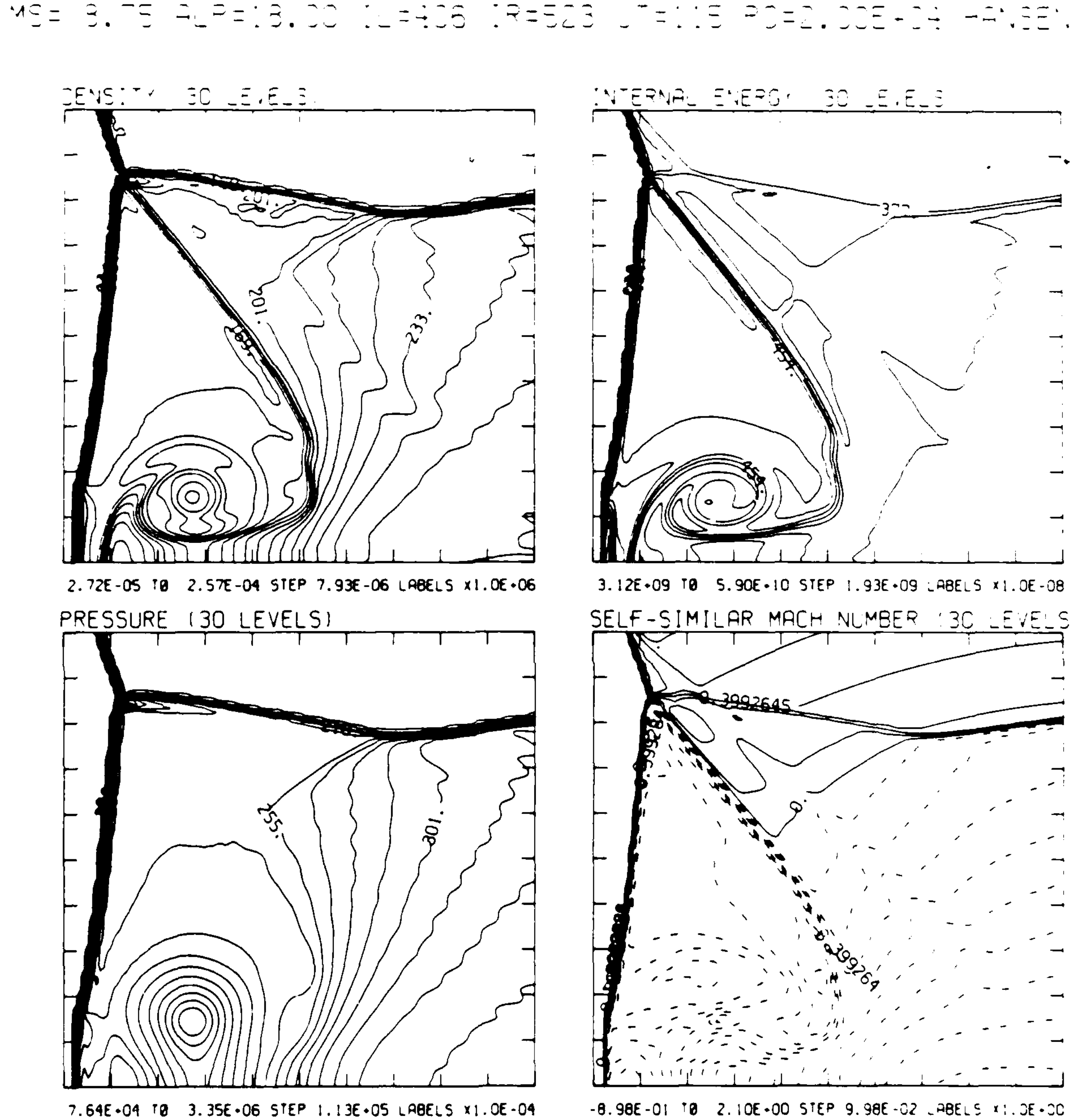

Figure 24.9b. $\theta_w = 18°$, blowup-frame plots.

Figure 24. Transition set 3, M_s = 8.75, Hansen - continued.

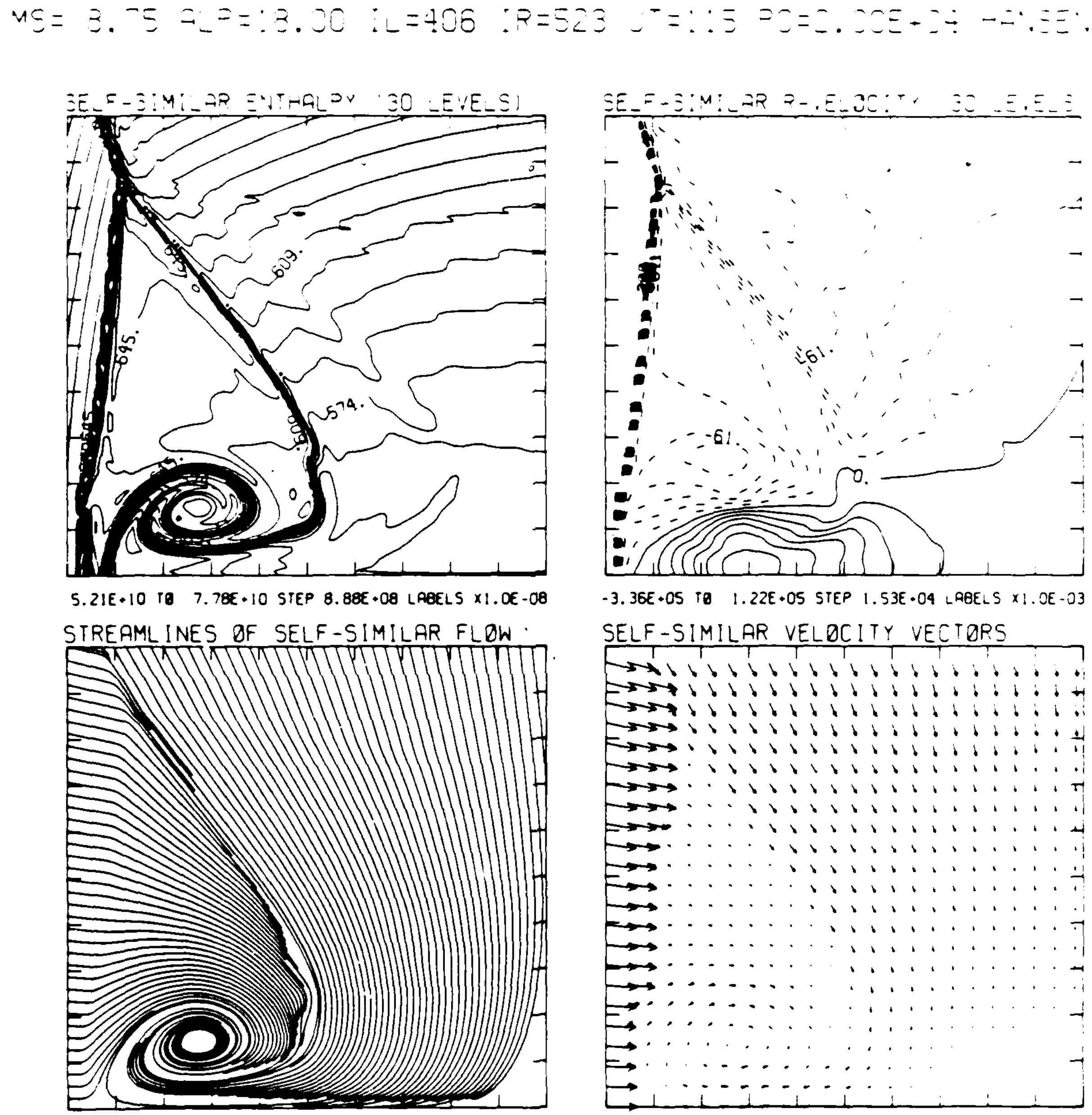

Figure 24.9b. θ_w = 18°, blowup-frame plots - continued.

Figure 24. Transition set 3, M_s = 8.75, Hansen - continued.

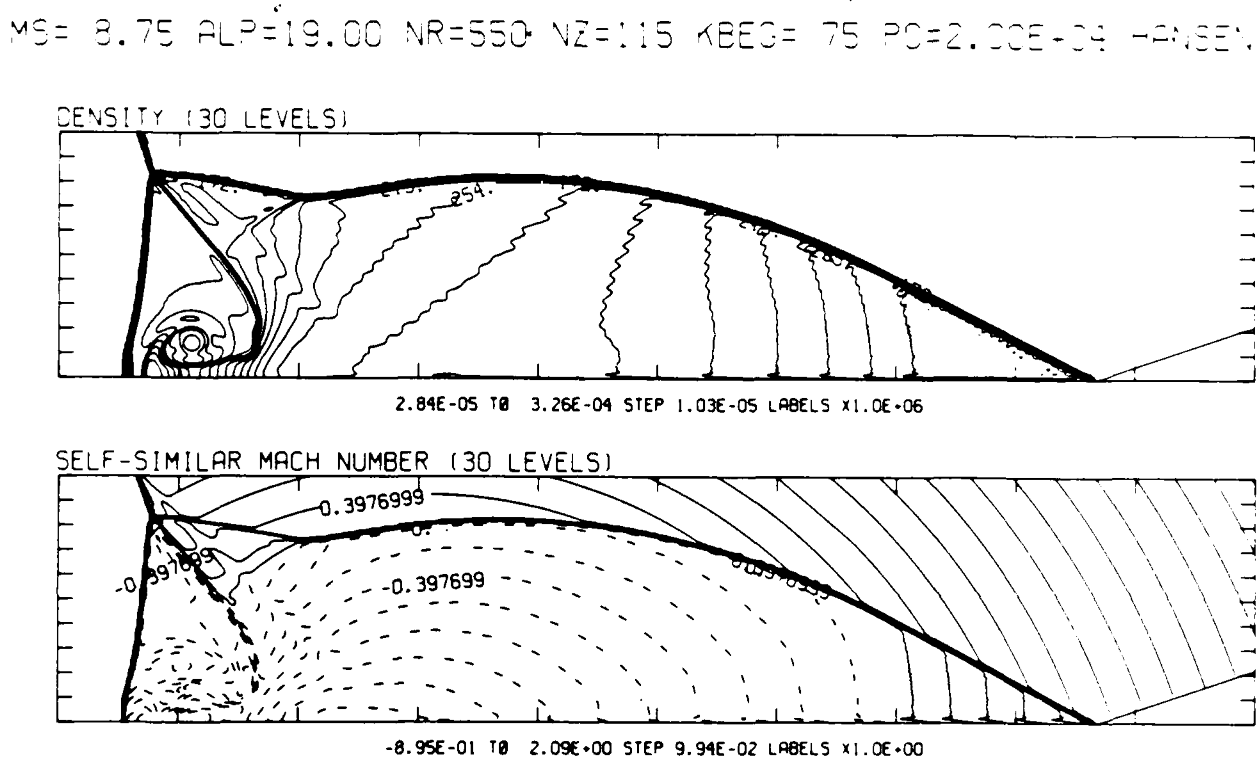

Figure 24.10a. $\theta_w = 19°$, whole-flowfield contour-plots.

Figure 24. Transition set 3, $M_s = 8.75$, Hansen - continued.

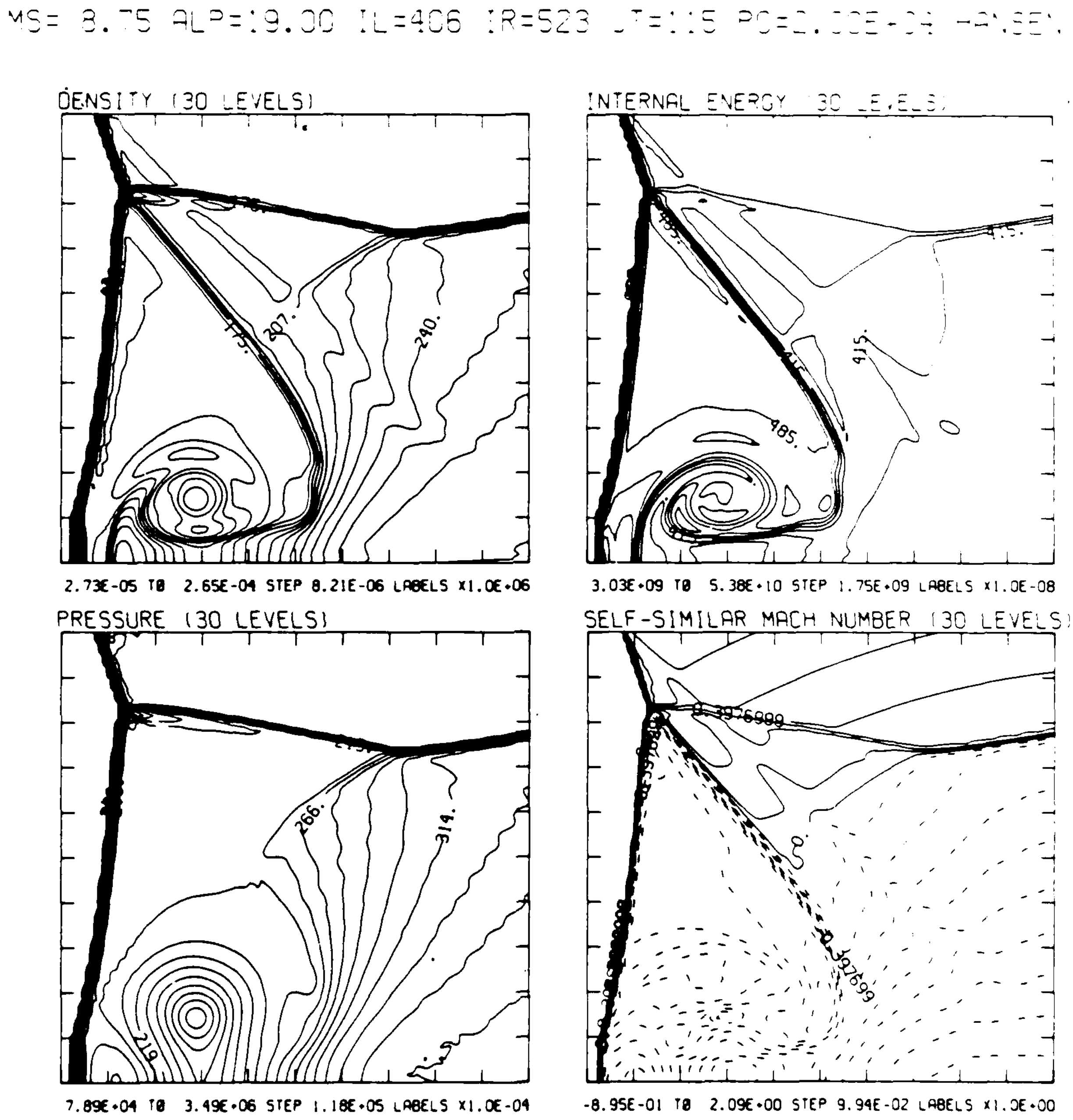

Figure 24.10b. $\theta_w = 19°$, blowup-frame plots.

Figure 24. Transition set 3, $M_s = 8.75$, Hansen - continued.

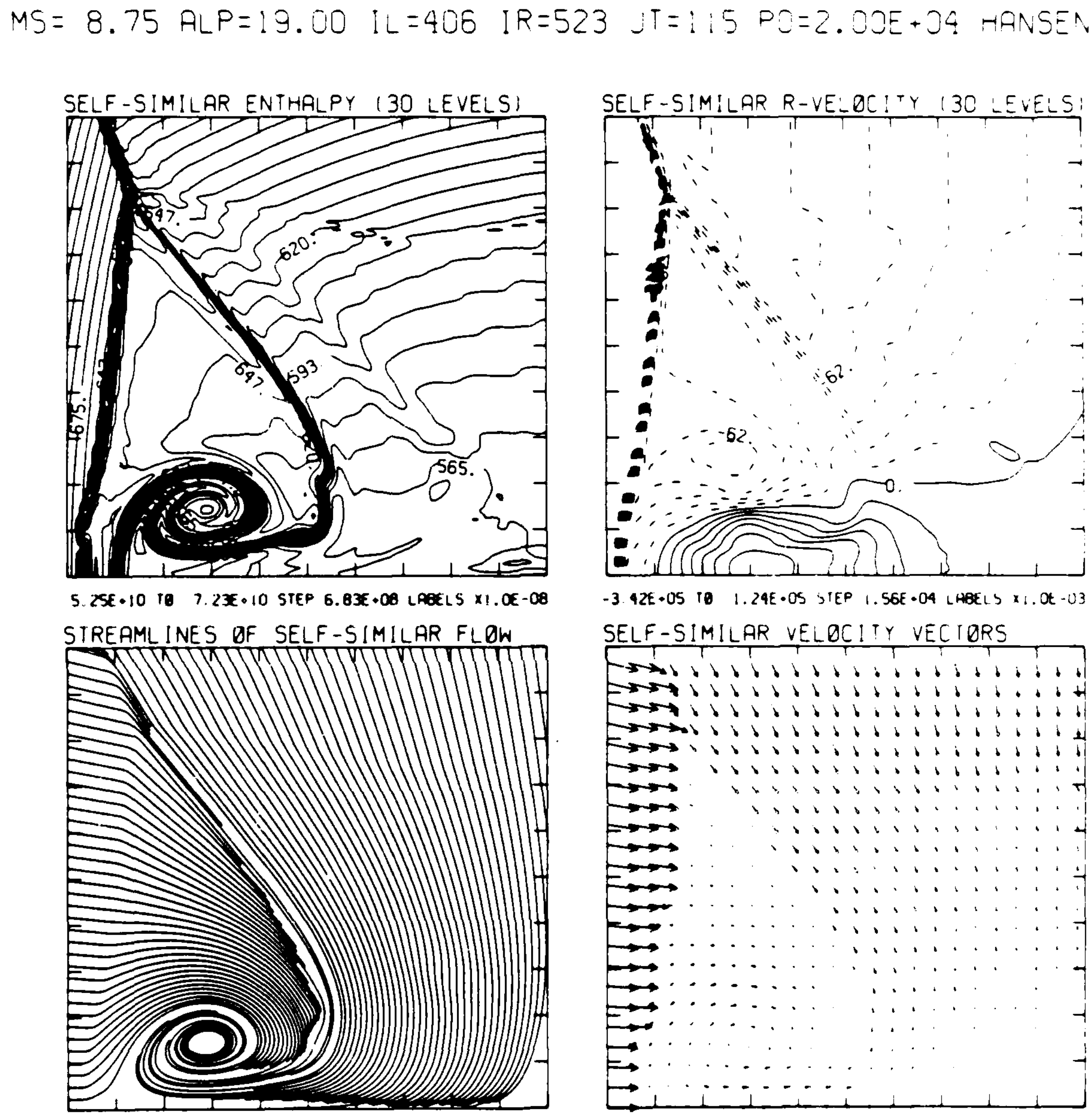

Figure 24.10b. θ_W = 19°, blowup-frame plots - continued.

Figure 24. Transition set 3, M_S = 8.75, Hansen - continued.

Region	ρ/ρ_0
0	1.00
1	3.78
2	6.69
3	3.91
a	7.94
b	9.19
c	6.69
d	5.44

Figure 25a. Interferogram, $\theta_w = 49°$

Figure 25b. $\theta_w = 49°$

XBB 859-7209

Figure 25. Transition set 4, $M_s = 7.10$, $\gamma = 5/3$, density contour-plots

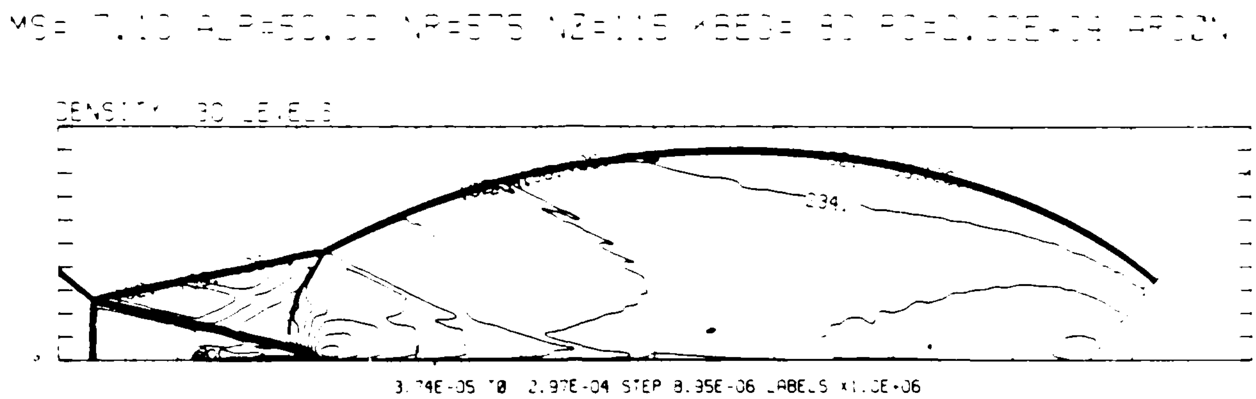

Figure 25c. $\theta_w = 50^0$

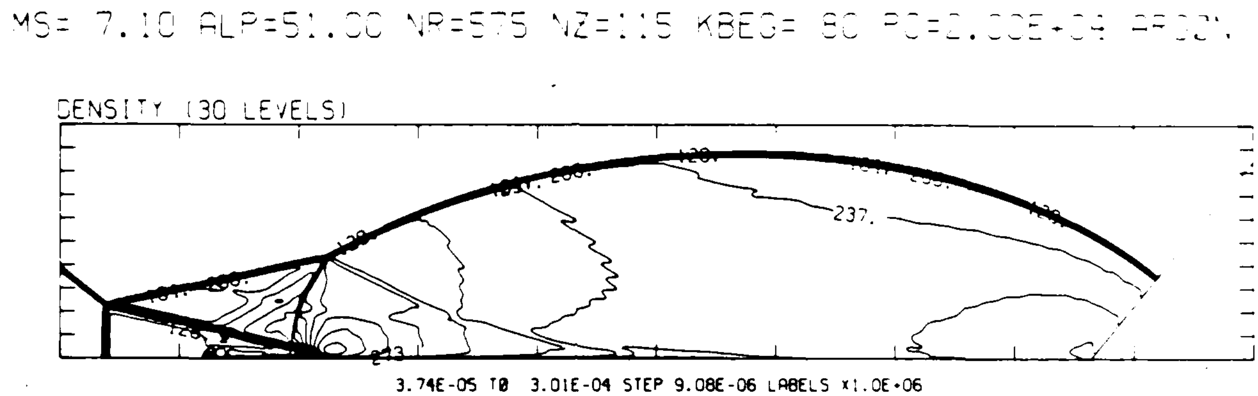

Figure 25d. $\theta_w = 51^0$

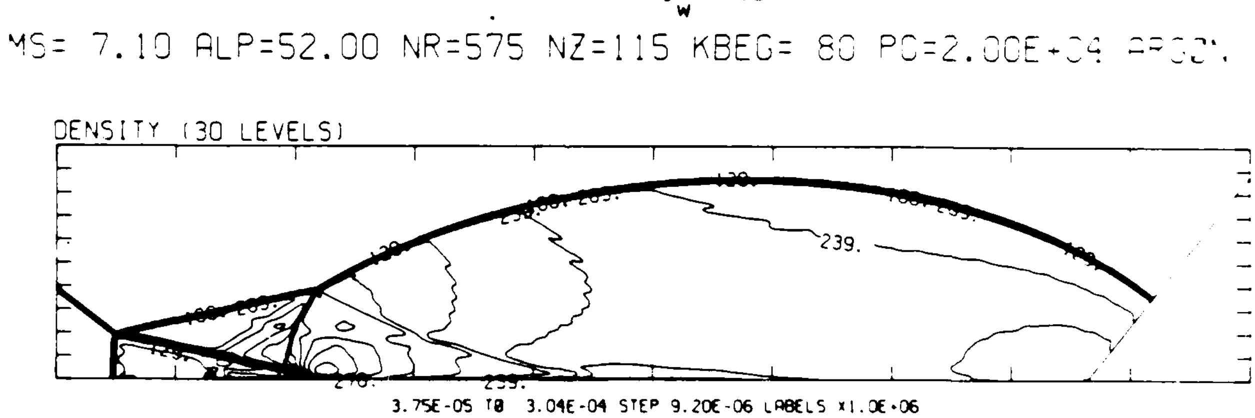

Figure 25e. $\theta_w = 52^0$

Figure 25. Transition set 4, $M_S = 7.10$, $\gamma = 5/3$, density contour plots - continued.

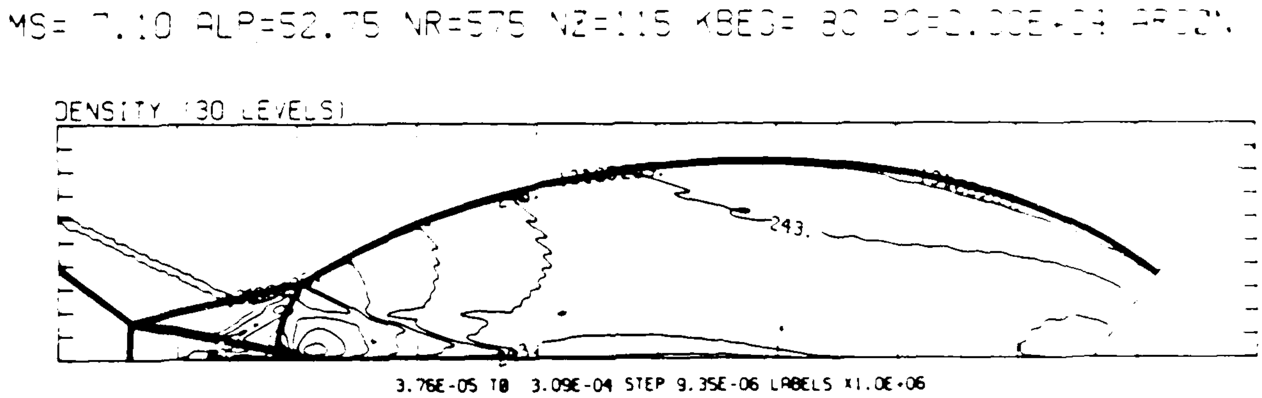

Figure 25f. θ_w = 52.75^0

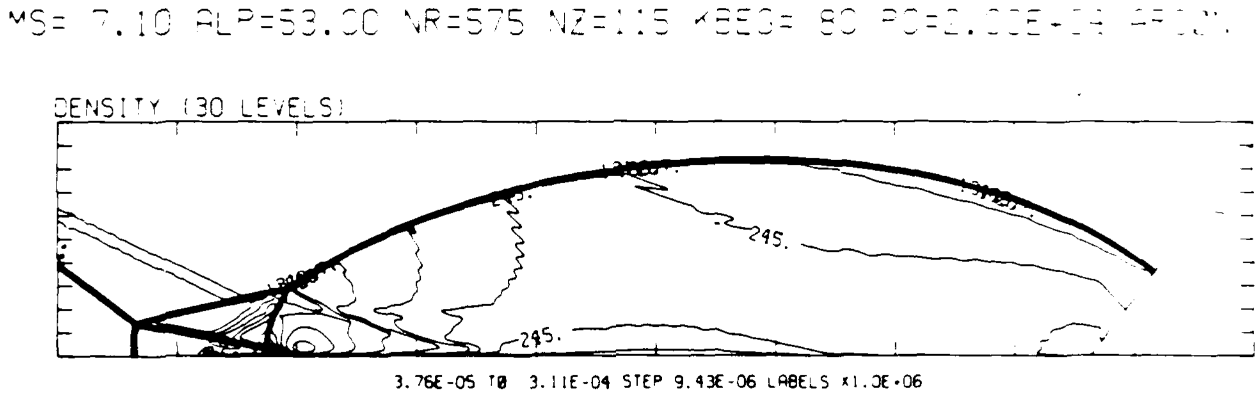

Figure 25g. θ_w = 53.00^0

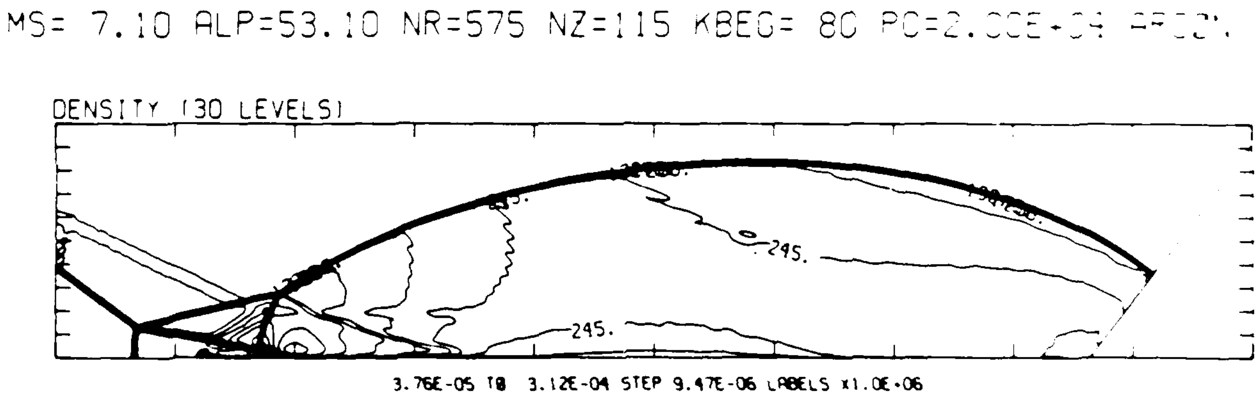

Figure 25h. θ_w = 53.10^0

Figure 25. Transition set 4, M_s = 7.10, γ = 5/3, density contour plots - continued.

MS= 7.10 ALP=53.20 NR=575 NZ=115 KBEG= 80 PO=2.00E-04 ARGON

DENSITY (30 LEVELS)

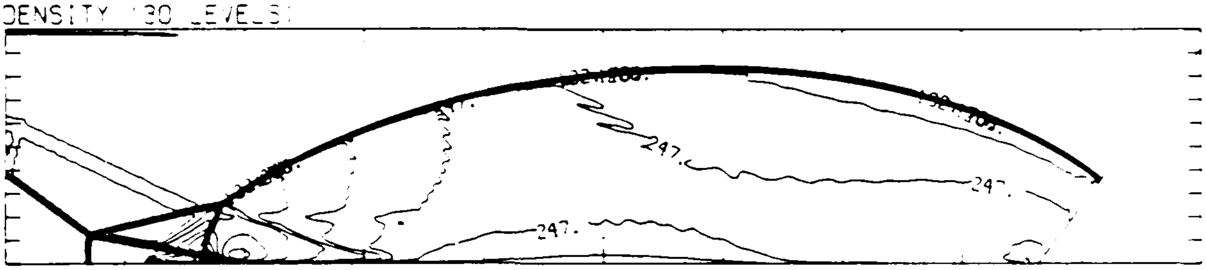

3.77E-05 TO 3.14E-04 STEP 9.52E-06 LABELS X1.0E+06

Figure 25i. $\theta_w = 53.20^0$

MS= 7.10 ALP=53.30 NR=575 NZ=115 KBEG= 80 PO=2.00E-04 ARGON

DENSITY (30 LEVELS)

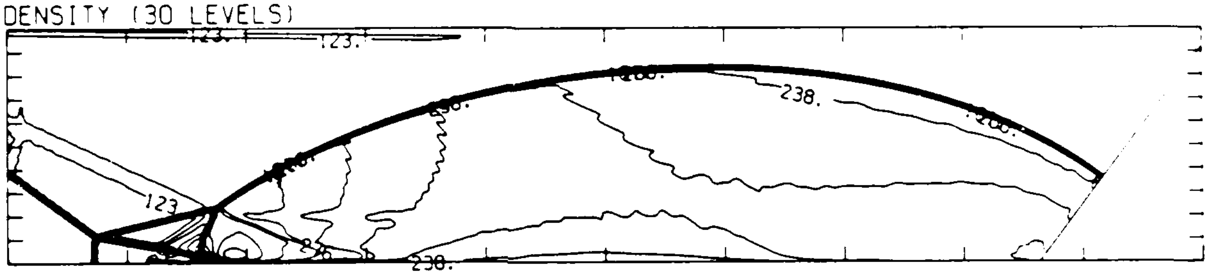

3.77E-05 TO 3.15E-04 STEP 9.55E-06 LABELS X1.0E+06

Figure 25j. $\theta_w = 53.30^0$

MS= 7.10 ALP=53.40 NR=575 NZ=115 KBEG= 80 PO=2.00E-04 ARGON

DENSITY (30 LEVELS)

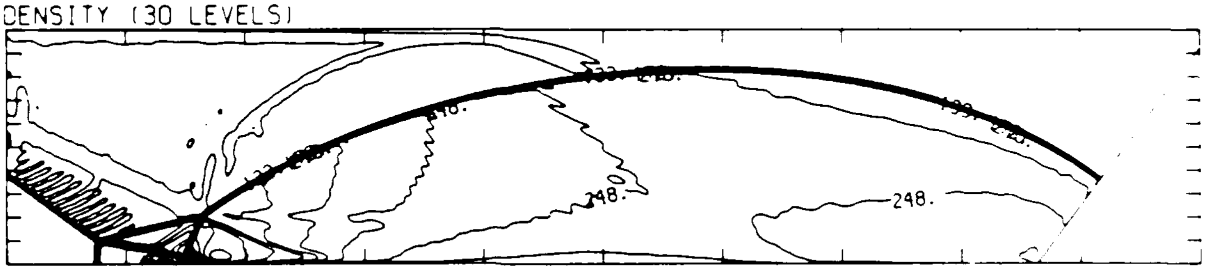

3.77E-05 TO 3.16E-04 STEP 9.60E-06 LABELS X1.0E+06

Figure 25k. $\theta_w = 53.40^0$

Figure 25. Transition set 4, $M_S = 7.10$, $\gamma = 5/3$, density contour plots - continued.

AD-A186 440 A DETAILED NUMERICAL GRAPHICAL AND EXPERIMENTAL STUDY 5/5
OF OBLIQUE SHOCK WA (U) TORONTO UNIV DOWNSVIEW
(ONTARIO) INST FOR AEROSPACE STUDIES H M GLAZ ET AL
UNCLASSIFIED 01 AUG 86 UTIAS-285 DNA-TR-86-365 F/G 20/4 NL

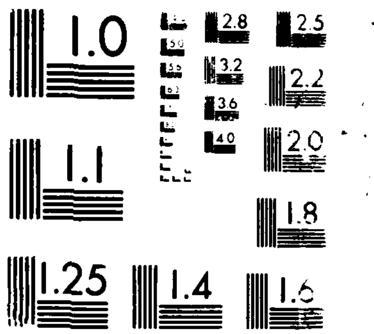

MICROCOPY RESOLUTION TEST CHART
NATIONAL BUREAU OF STANDARDS-1963

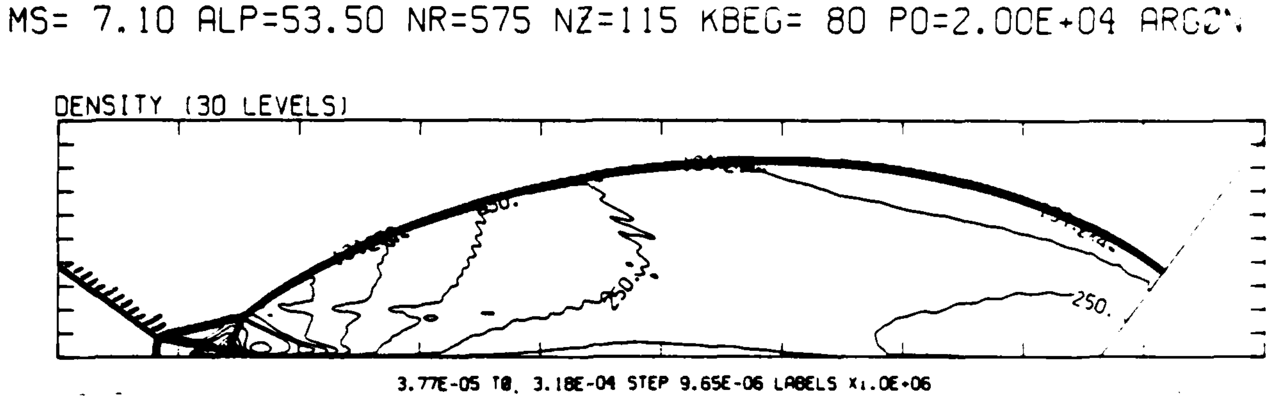

Figure 25l. $\theta_w = 53.50^0$

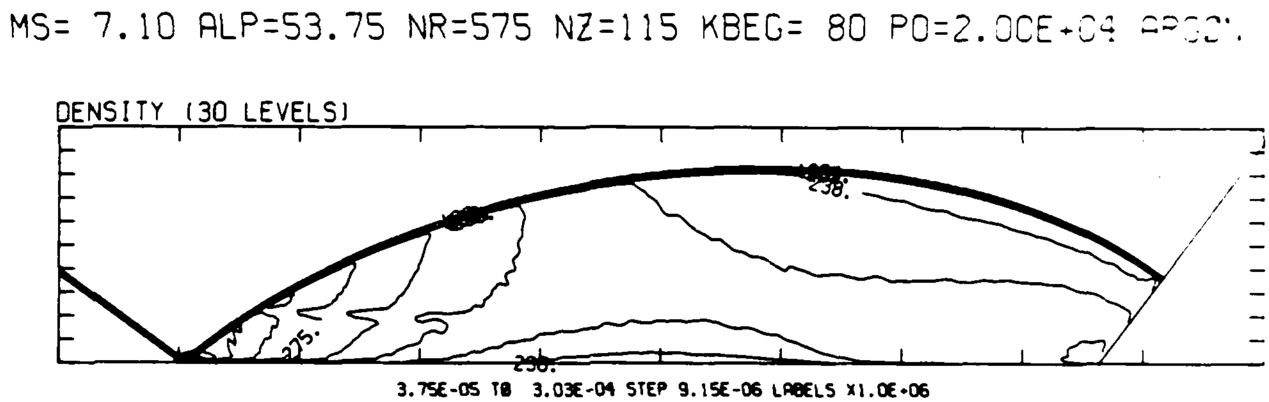

Figure 25m. $\theta_w = 53.75^0$

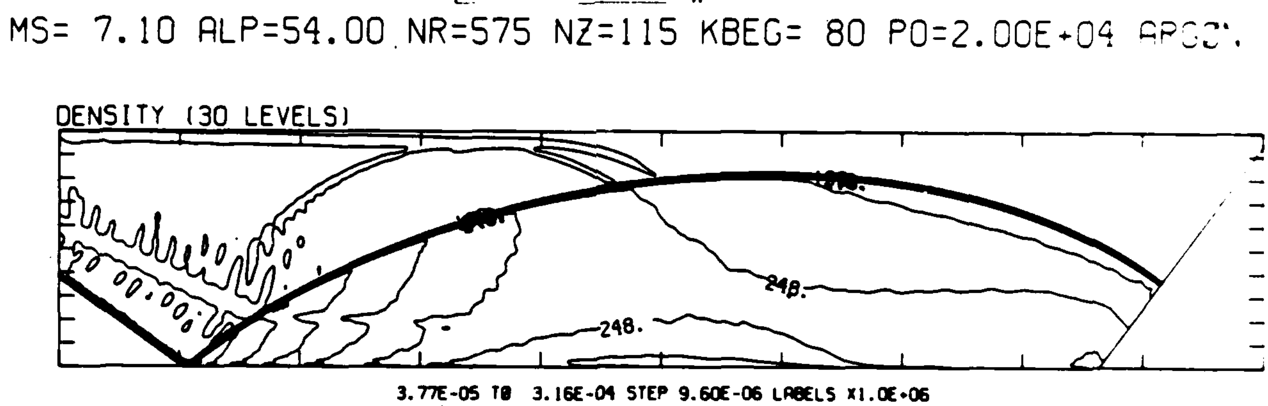

Figure 25n. $\theta_w = 54^0$

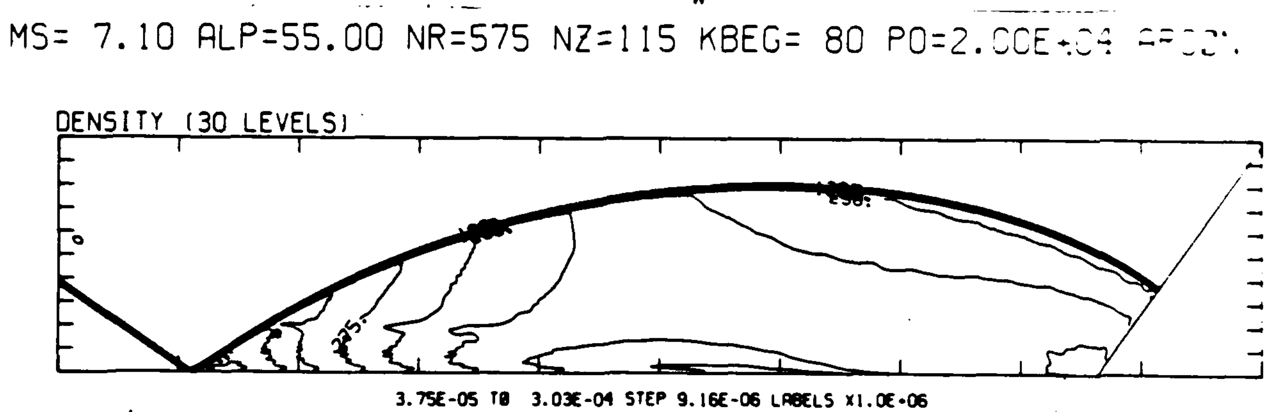

Figure 25o. $\theta_w = 55^0$

Figure 25. Transition set 4, $M_s = 7.10$, $\gamma = 5/3$, density contour plots - continued.

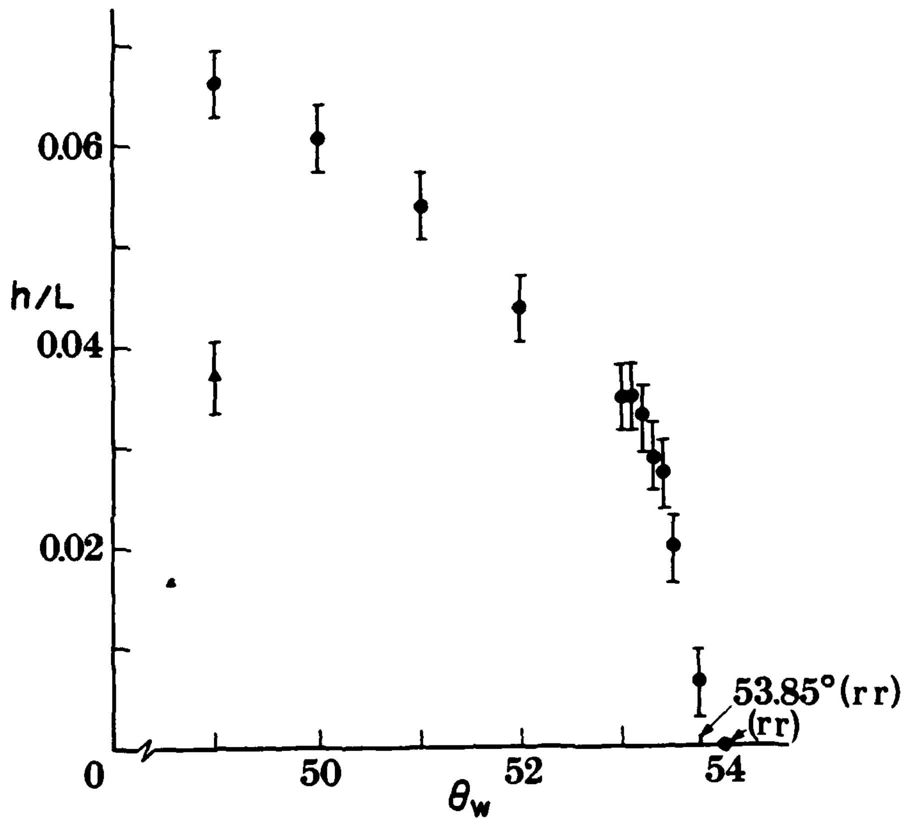

Figure 26. Plot of DMR Mach stem height versus θ_w, extrapolated to zero height for RR($h/L = 0$ for $\theta_w = 53.85^0$), $h/L = 0$ for $\theta_w = 54^0$ is a numerical result

DISTRIBUTION LIST

DEPARTMENT OF DEFENSE

DEF RSCH & ENGRG
ATTN: STRAT & SPACE SYS (OS)
ATTN: STRAT & THTR NUC FOR/F VAJDA

DEFENSE INTELLIGENCE AGENCY
ATTN: RTS-2A (TECH LIB)
ATTN: RTS-2B

DEFENSE NUCLEAR AGENCY
ATTN: DFSP G ULLRICH
ATTN: SPAS C GALLOWAY
ATTN: SPAS D MUNNINGHOFF
ATTN: SPAS R ROHR
4 CYS ATTN: TITL

DEFENSE TECHNICAL INFORMATION CENTER
12 CYS ATTN: DD

FIELD COMMAND DEFENSE NUCLEAR AGENCY
ATTN: FCTXE
ATTN: FTTD
ATTN: FTTD W SUMMA

JOINT STRAT TGT PLANNING STAFF
ATTN: JKCS
ATTN: JPEP
ATTN: JPTM

DEPARTMENT OF THE ARMY

HARRY DIAMOND LABORATORIES
ATTN: SCHLD-NW-P
ATTN: SLCIS-IM-TL (81100) (TECH LIB)

U S ARMY BALLISTIC RESEARCH LAB
ATTN: SLCBR-SS-T (TECH LIB)

U S ARMY CORPS OF ENGINEERS
ATTN: DAEN-ECE-T

U S ARMY ENGINEER CTR & FT BELVOIR
ATTN: TECHNICAL LIBRARY

U S ARMY ENGINEER DIV HUNTSVILLE
ATTN: HNDED-SY

U S ARMY ENGR WATERWAYS EXPER STATION
ATTN: E JACKSON, WESSS-O
ATTN: J JACKSON, WESSD
ATTN: J ZELASKO, WESSD-R

U S ARMY NUCLEAR & CHEMICAL AGENCY
ATTN: LIBRARY
ATTN: MONA-NU MR LONG

U S ARMY STRATEGIC DEFENSE CMD
ATTN: DASD-H-L
ATTN: DASD-H-SAV R K DUDNEY

DEPARTMENT OF THE NAVY

NAVAL RESEARCH LABORATORY
ATTN: CODE 2627 (TECH LIB)
ATTN: CODE 4040 D BOOK
ATTN: CODE 4040 J BORIS

NAVAL SURFACE WEAPONS CENTER
ATTN: CODE R44 H GLAZ
ATTN: CODE X211 (TECH LIB)

NAVAL SURFACE WEAPONS CENTER
ATTN: TECH LIBRARY & INFO SVCS BR

DEPARTMENT OF THE AIR FORCE

AIR FORCE CTR FOR STUDIES & ANALYSIS
ATTN: AFCSA/SAMI (R GRIFFIN)

AIR FORCE INSTITUTE OF TECHNOLOGY/EN
ATTN: LIBRARY/AFIT/LDEE

AIR FORCE WEAPONS LABORATORY, NTAAB
ATTN: NTED-A
ATTN: SUL

BALLISTIC MISSILE OFFICE/DAA
ATTN: ENSN
ATTN: MYEB D GAGE

STRATEGIC AIR COMMAND/NRI-STINFO
ATTN: NRI/STINFO

DEPARTMENT OF ENERGY

LOS ALAMOS NATIONAL LABORATORY
ATTN: C F KELLER
ATTN: M T SANDFORD
ATTN: R WHITAKER

SANDIA NATIONAL LABORATORIES
ATTN: DIV 7111 J W REED
ATTN: J R BANNISTER 7111
ATTN: ORG 7112 A CHABAI

OTHER GOVERNMENT

CENTRAL INTELLIGENCE AGENCY
ATTN: OSWR/NED

DEPARTMENT OF DEFENSE CONTRACTORS

AEROSPACE CORP
ATTN: H MIRELS
ATTN: LIBRARY ACQUISITION

APPLIED RESEARCH ASSOCIATES, INC
ATTN: N HIGGINS

APPLIED RESEARCH ASSOCIATES, INC
ATTN: D PIEPENBURG

BOEING CO
ATTN: G R BURWELL

CALIFORNIA RESEARCH & TECHNOLOGY, INC
ATTN: K KREYENHAGEN
ATTN: LIBRARY

CALIFORNIA RESEARCH & TECHNOLOGY, INC
ATTN: F SAUER

CARPENTER RESEARCH CORP
ATTN: H J CARPENTER

DENVER COLORADO SEMINARY UNIVERSITY OF
ATTN: J WISOTSKI

H & H CONSULTANTS, INC
ATTN: J HALTIWANGER
ATTN: W HALL

H-TECH LABS, INC
ATTN: B HARTENBAUM

KAMAN SCIENCES CORP
ATTN: R RUETENIK

KAMAN TEMPO
ATTN: DASIAC

KAMAN TEMPO
ATTN: DASIAC

MCDONNELL DOUGLAS CORP
ATTN: H HERDMAN
ATTN: R HALPRIN

NEW MEXICO, UNIVERSITY OF
ATTN: J KOVARNA

PACIFIC-SIERRA RESEARCH CORP
ATTN: H BRODE, CHAIRMAN SAGE

PACIFIC-SIERRA RESEARCH CORP
ATTN: D GORMLEY

PACIFICA TECHNOLOGY
ATTN: R ALLEN
ATTN: TECH LIBRARY

PHYSICS INTERNATIONAL CO
ATTN: H W WAMPLER

R & D ASSOCIATES
ATTN: T MAZZOLA
ATTN: TECHNICAL INFO CENTER

R & D ASSOCIATES
ATTN: A POLK
ATTN: B WEBSTER

R & D ASSOCIATES
ATTN: G GANONG

RAND CORP
ATTN: B BENNETT

S-CUBED
ATTN: B PYATT
ATTN: C DISMUKES
ATTN: J BARTHEL
ATTN: LIBRARY

S-CUBED
ATTN: C NEEDHAM

SCIENCE APPLICATIONS INTL CORP
ATTN: H WILSON
ATTN: R SCHLAUG
ATTN: TECHNICAL LIBRARY

SCIENCE APPLICATIONS INTL CORP
ATTN: J COCKAYNE
ATTN: W LAYSON

SCIENCE APPLICATIONS INTL CORP
ATTN: G BINNINGER

SRI INTERNATIONAL
ATTN: J COLTON

TELEDYNE BROWN ENGINEERING
ATTN: D ORMOND
ATTN: F LEOPARD

TRW ELECTRONICS & DEFENSE SECTOR
ATTN: A ZIMMERMAN
ATTN: M SEIZEW
ATTN: TECH INFO CTR, DOC ACQ

TRW ELECTRONICS & DEFENSE SECTOR
ATTN: N GUILES
ATTN: N LIPNER

UNIVERSITY OF TORONTO
2 CYS ATTN: H GLAZ
2 CYS ATTN: I GLASS
2 CYS ATTN: R DESCHAMBAULT
2 CYS ATTN: T COLELLA

WEIDLINGER ASSOC. CONSULTING ENGRG
ATTN: I SANDLER

END
DATE
FILMED
JAN
1988